Tesi di Dottorato di MATTEO PELUCCHI
Matricola 812527

POLITECNICO
MILANO 1863

DIPARTIMENTO DI CHIMICA, MATERIALI E INGEGNERIA CHIMICA "Giulio Natta"

Development of kinetic mechanisms for the combustion of renewable fuels.

Dottorato di Ricerca in Chimica Industriale e Ingegneria Chimica (CII)

PhD in Industrial Chemistry and Chemical Engineering

XXIX ciclo
2013 - 2016

Relatore: Prof. Tiziano Faravelli

Coordinatore: Prof. Alessio Frassoldati

To my family

Publications

- E. Ranzi; A. Frassoldati; A. Stagni; **M. Pelucchi**; A. Cuoci; T. Faravelli, *Reduced Kinetic Schemes of Complex Reaction Systems: Fossil and Biomass-Derived Transportation Fuels*, International Journal of Chemical Kinetics 46 (9) (2014) 512-542

- **M. Pelucchi**; M. Bissoli; C. Cavallotti; A. Cuoci; T. Faravelli; A. Frassoldati; E. Ranzi; A. Stagni, *Improved kinetic model of the low-temperature oxidation of n-heptane*, Energy & Fuels 28 (11) (2014) 7178-7193

- **M. Pelucchi**; A. Frassoldati; T. Faravelli; B. Ruscic; P. Glarborg, *High-temperature chemistry of HCl and Cl_2*, Combustion and Flame 162 (6) (2015) 2693-2704

- **M. Pelucchi**; E. Ranzi; A. Frassoldati; T. Faravelli, *Alkyl radicals rule the low temperature oxidation of long chain aldehydes*, Proceedings of the Combustion Institute (2016)

- **M. Pelucchi**; K. P. Somers; K. Yasunaga; U. Burke; A. Frassoldati; E. Ranzi; H. J. Curran; T. Faravelli, *An experimental and kinetic modeling study of the pyrolysis and oxidation of n-C_3– C_5 aldehydes in shock tubes*, Combustion and Flame 162 (2) (2015) 265-286

- E. Ranzi; C. Cavallotti; A. Cuoci; A. Frassoldati; **M. Pelucchi**; T. Faravelli, *New reaction classes in the kinetic modeling of low temperature oxidation of n-alkanes*, Combustion and flame 162 (5) (2015) 1679-1691

- D. Nativel; **M. Pelucchi**; A. Frassoldati; A. Comandini; A. Cuoci; E. Ranzi; N. Chaumeix; T. Faravelli, *Laminar flame speeds of pentanol isomers: An experimental and modeling study*, Combustion and Flame 166 (2016) 1-18

- P. E. A. Debiagi; G. Gentile; **M. Pelucchi**; A. Frassoldati; A. Cuoci; T. Faravelli; E. Ranzi, *Detailed kinetic mechanism of gas-phase reactions of volatiles released from biomass pyrolysis*, Biomass and Bioenergy 93 (2016) 60-71

- M. Bernardi; **M. Pelucchi**; A. Stagni; L. Sangalli; A. Cuoci; A. Frassoldati; P. Secchi; T. Faravelli, *Curve matching, a generalized framework for models/experiments comparison: An application to n-heptane combustion kinetic mechanisms*, Combustion and Flame 168 (2016) 186-203

- **M. Pelucchi**, C. Cavallotti, E. Ranzi, A. Frassoldati, T. Faravelli *Relative reactivity of oxygenated fuels: alcohols, aldehydes, ketones and methyl esters.* Energy & Fuels 30 (2016) 8665-8679.

- **M. Pelucchi**, K.P. Somers, U. Burke, C. Saggese, A. Frassoldati, E. Ranzi, H.J. Curran, T. Faravelli, *Kinetic modelling of Biofuels: Pyrolysis and Auto-Ignition of Aldehydes*, Chemical Engineering Transactions, (2014), 37, 871–876.

Contributions to Meetings and Symposia

- **6th European Combustion Meeting**, Lund, Sweden, 25th -28th June 2013. **Poster:** "Experimental and kinetic modeling study of n-butanal auto-ignition in shock tube"

- **4th COST Annual Meeting**, CM0901 Detailed Chemical Models For Cleaner Combustion. Università di Perugia, Italy. **Oral presentation**: "Experimental and kinetic modeling study of $C_3–C_5$ n-aldehydes auto-ignition and pyrolysis in shock tubes"

- **French-Italian Joint Combustion Meeting**, Hotel San Ranieri, Pisa, Italy, 22nd-24th April 2014. **Poster**: "Kinetic modeling of $C_1–C_5$ aldehydes in shock tubes"

- **1st International Conference on Biomass**. Firenze, Italy, 3rd-7th May 2014. **Oral Presentation**: "Kinetic modeling of biofuels: pyrolysis of aldehydes"

- **7th European Combustion Meeting,** Budapest, Hungary, 30th March – 2nd April 2015. **Oral Presentation** at the 3rd Topical Workshop on Taming Uncertainty In Combustion Chemistry: experiments and models: "Curve matching: a generalized framework for combustion model validation"

- **CleanAir Conference 2015**, Instituto Tecnico Superior, Lisbon, Portugal. 5th -9th July 2015. **Oral Presentation**, invited speaker for young researchers colloquium: "Detailed kinetic mechanisms for practical applications: new reaction classes and model reduction"

- **28th Meeting of the Italian Section of the Combustion Institute**. Università di Lecce, Lecce, Italy. 21st-23rd September 2015. **Poster[1]**: "Kinetic modeling of the low temperature cool flames of acetaldehyde in a well stirred reactor", **Poster[2]**: "Oxidation of C_3 and n-C_4 aldehydes at low temperatures"

- **36th International Symposium on Combustion**, Seoul, South Korea, 1st-5th August 2016. **Oral Presentation**: "Alkyl Radicals Rule the Low Temperature Oxidation of long chain aldehydes"

- **Convegno Nazionale GRICU**, Anacapri, Napoli, Italy. 12th-14th September 2016. **Poster**: "Theoretical and master equation study of the potential energy surface of benzyl + O_2".

- **2nd General Meeting and Workshop on Smart Energy Carriers in Industry**, COST Action 1404. Instituto Tecnico Superior, Lisbon, Portugal. 14th-16th November 2016. **Oral presentation**: "Toward a fully automated system to develop, validate and evaluate combustion kinetic mechanisms". **Poster**: "Extension of the ReSpecTh database for application in a fully automated system for the development and validation of kinetic mechanisms"

- **The 10th International Conference on Chemical Kinetics,** Chicago, USA, 21st-25th May 2017 **Oral presentation**: "Ab Initio and Kinetic Modelling Study of Toluene Oxidation" and co-author in "From electronic structure calculations to temperature and pressure dependent rate constants: a new computational environment"

- **13th International Conference on Engines & Vehicles**, Capri, Napoli, Italy 10th-14th September 2017. **Oral presentation**: "A kinetic modelling study of alcohols operating regimes in a HCCI engine"

Table of Contents

List of Figures

List of Tables

Abstract

Pursuing a sustainable energy scenario for transportation requires the blending of fuels from renewable sources (alcohols, methylesters etc.) into hydrocarbon fuels from fossil sources (gasoline, diesels, jet fuels etc.). In fact, while effective alternatives to combustion exist for electricity production (nuclear, hydroelectricity, solar, wind etc.), the high energy density required for road, sea and air transport endorses biofuels as the only viable and realistic option. Moreover, from an environmental perspective, undeniable and dramatic climate change phenomena imply the need for long term sustainable solutions for reducing greenhouse gases, NO_x and soot emissions. If on one side the production of biofuels from biomasses satisfies the requirement of a net *zero-CO_2* balance, new fuels and new engine technologies have been investigated to improve fuel economy and reduce pollutant emissions. The correct characterization of a fuel or fuel mixture reactivity and the evaluation of its compatibility with existing engine infrastructure in terms of pollution and efficiency is, for a major part, a chemical kinetics problem.

Combustion kinetic modelling, which is the topic of *this thesis*, has been driving fuel and engine developments for the last ~25 years. While most of the focus in the first decade has been devoted to the understanding of alkane chemistry, the need for better representing commercial fuels by means of surrogate mixtures extended the interest to aromatics and finally to oxygenated fuels from renewable sources. The aim of *this thesis* is to extend the knowledge of the chemistry involved in alkanes (e.g. n-heptane), aromatics (e.g. toluene) and oxygenated (e.g. alcohols, aldehydes, ketones etc.) fuels combustion, by means of an effective coupling of theory and experiments, within the POLIMI (Politecnico di Milano) approach to combustion kinetics developed in the last 30 years of research activity in the CRECK group. The model obtained by coupling the different revised portions, accurately reproduces recent experimental measurements of surrogate mixtures representative of real fuels. Suggestions for future refinement of the presented models have been provided throughout the discussion, highlighting for example the need of a hierarchical revision starting from the core C_0–C_4 portion of the POLIMI mechanism or a better assessment of other key channels, whose parameters still carry high degrees of uncertainty.

Beside the definition of key model parameters and standard kinetic mechanisms validation procedures, other important challenges of modern kinetic modelling have been a topic of research. The necessity of automatically assessing the validity of increasingly complex kinetic mechanisms has been tackled, providing an innovative and effective method, of application also to mechanism reduction and optimization, and to experimental design.

Abstract

Perspectives concerning the possibility and potentials of effectively and extensively exploiting theoretical kinetics, and the necessity of fully automated procedures of kinetic mechanism development are also discussed, providing directions for future research efforts.

Chapter 1 – Introduction

1.1 The Global Energy and Environmental Scenario

Humanity is nowadays facing multifaceted and complex energy-related challenges. As summarized in Figure 1, the income growth driving population growth (+30% between 2010 and 2040 [1]), led to an unprecedented expansion of the middle class which, as a consequence of increasing living standards, generates higher and more diverse demands for energy and goods (food, education, health assistance etc.). The thrust for this phenomena arises mainly from developing countries such as China, India, Vietnam, Philippines and Nigeria in which some 3 billion people are expected to access the middle class by 2040 [1].
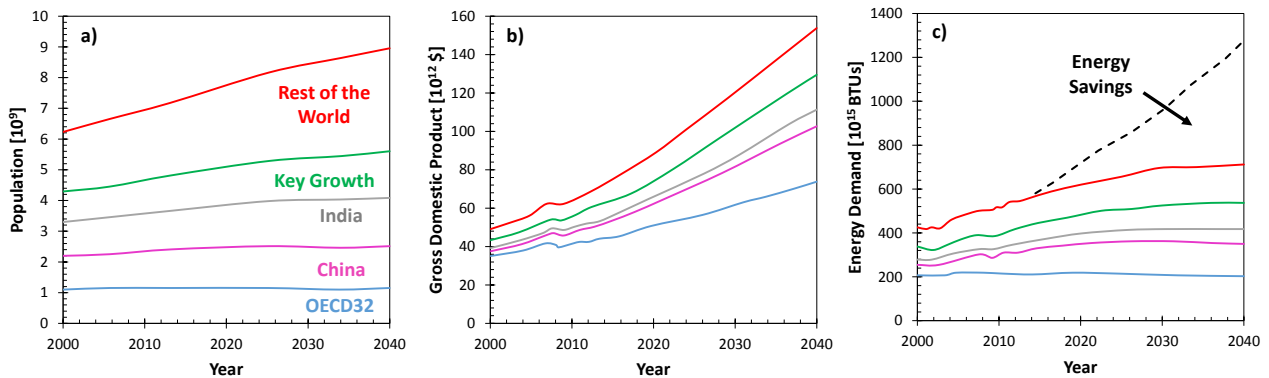
Figure 1: Projections of population growth (a), GDP (b) and energy demand (c) [1].

While the second half of the previous century was characterized by the bilateral interaction between developed and emerging economies, seeking for perspectives of improved global welfare, nowadays both the old and the new players are putting efforts in exploiting the benefits of modern technologies and diverse energy sources in more efficient ways, while protecting the environment. In other words while the estimated Gross Domestic Product (GDP) is expected to increase by ~140% by 2040, improved energy efficiency will allow the rise in energy demand to be limited to ~35% [1].

It is unavoidable that a sustainable energy scenario relies also on smart practical choices at different levels: governments, individuals and industries. A simple example can be observed in metropolitan areas where the continuous expansion and implementations of public transport networks, together with car and bike sharing programs, allow more efficient, cleaner and sometimes cheaper ways to travel or simply to commute to work.

However, projections for the next 20-30 years foresee the use of fossil sources (natural gas, petroleum and coal) to keep driving energy production, mainly through combustion. In fact, while reliable alternatives exist for power generation (hydroelectricity, wind, solar, wave or nuclear energy), road, air and sea transportation

requires high-density energy sources which are, and will be, primarily provided by petroleum-derived liquid fuels (gasoline, diesel, kerosene and naphta).

Nonetheless, due to associated greenhouse gas emissions, combustion of fossil-fuels has been identified as the main reason for deterioration of air quality and, ultimately, for climate change. After the activation of the Kyoto Protocol in 2005 [2], another milestone was recently settled in Paris [3] where 150 state presidents and prime ministers, together with a large number of other non-state players reached a key agreement providing new directions to tackle environmental issues and climate change.

Beyond environmental aspects, other factors such as unstable petroleum prices, the intrinsic finite nature of fossil resource and the dependence on politically unstable regions for imports, are the major motivations for pursuing biofuels. Particularly, considering forms of transportation for which electrical propulsion is not suitable due to low energy density and storage limitations (long distance trucking, shipping and aviation), it is clear that biofuels represent the most likely near term alternative to fossil fuels.

The coupling of increased energy demand with environmental and geo-political issues, makes the optimization of combustion systems mandatory, at both fuels and engines levels.

Bioethanol, mainly produced in USA and Brazil from fermentation of corn or sugar cane, is the most widely used biofuel today. The European Union ranks third in terms of bioethanol production, while leading the production of biodiesels (fatty acid methyl esters from esterification of vegetal and animal fats). Most of the bioethanol is blended with gasoline for use in passenger vehicles. Gasoline with up to 10% ethanol (E10) can be used in most vehicles without further modification, while only flexible fuel vehicles can use a gasoline-ethanol blend with up to 85% ethanol (E85). According to the Environmental Protection Agency (EPA), most of the vehicles manufactured after 2001 can run with up to 15% ethanol (E15) without modifications.

Beside ethanol, longer chain alcohols (C_3–C_6) are foreseen as possible alternatives, in particular for spark ignition engines (SI). From a chemical perspective, the influence of the hydroxyl moiety in terms of lower heating values (LHV) fades when increasing the chain length, making the energy density of longer alcohols more similar to that of gasoline and diesels (30-35 MJ/L). Therefore fuels such as butanol and pentanol isomers (LHV: 26.9-28.5 MJ/L) [4] are considered interesting for improved fuel economy. As reported in Table 1, other physical-chemical properties such as boiling point, octane rating and octane sensitivity (Section 1.2) endorse these compounds as reliable alternatives to fossil fuels.

Fuel	Air/Fuel ratio	LHV (MJ/L)	B.P. (°C)	RON	MON

Gasoline	~14.5	30-33	27-225	88-98	80-88
Diesel	~15.0	~35	125-400	<0	<0
n-propanol	10.3	24.7	97	104	89
n-butanol	11.2	26.9	118	98	85
n-pentanol	11.7	28.5	138	80	74
n-hexanol	12.2	29.3	157	56	46

Table 1: Properties of alcohols, gasolines and diesel fuels. Adapted from [4].

Biobutanol is of particular interest for a number of different reasons. Firstly, it can be used in pure form, or blended with gasoline in any concentration, without requiring modification to commercial engines. Biobutanol allows direct blending at the refinery, differently from ethanol which is blended with gasoline shortly before being distributed. Furthermore, its lower corrosive nature allows distribution in current infrastructures (tanks, pipelines, pumps, filling stations, etc.). In the United States the Octamix waiver [5] already allows 12.5-16% biobutanol blends with gasolines as an equivalent to E10 gasolines. Potentials of higher molecular weight alcohols/gasoline blends have been highlighted in engine experiments since the early 2000 [6]. Despite some technical issues mostly related to corrosion, the "Alternative Fuels and Biofuels for Aircraft Development program" [7] highlighted the high thermal stability and soot reduction potential of a 20% n-hexanol / 80% Gas-to-Liquid Jet fuel.

Biodiesel is primarily produced from soybean oil in the United States and from rapeseed oil in Europe. The most common blend is 20% biodiesel/80% petroleum diesel (B20), as higher percentages might require system modifications.

As recently reviewed by Sadeghinezhad et al. [8], despite the fact that the use of biofuels generally reduces particulate matter (PM), carbon monoxide (CO), unburned hydrocarbons (HC) and aromatic compounds emissions, carbonyl compounds (aldehydes and ketones) emissions increase. Some controversial findings are reported in the literature with respect to NOx emissions.

As the use of raw materials such as sugar and vegetable oils to produce "first generation biofuels" has raised ethical concerns about driving food prices higher, the use of lignocellulosic biomass is considered a better route for the production of renewable "second-generation" biofuels, through thermochemical or biochemical processes. The most promising route is the conversion of biomass to syngas, further transformed into liquid fuels through the Fischer-Tropsch process [9], in the so-called biomass to liquid (BTL) route. Another option is the conversion of the biomass to a bio-oil through pyrolysis. The product is then further

processed to give a various range of hydrocarbons. The more recent "third generation biofuels" derive from algae, and, to some extent, from recycling CO_2 to feed algae.

Differently from ethanol and fatty acid methyl esters, biomass derived fuels are a mixture of different component like petroleum fuels.

The main concern with any new fuel being investigated is whether or not it could be directly and efficiently used in current engines or distribution infrastructures, without requiring major and often inconvenient adjustments. To meet this necessity a modern research approach is the development of "drop-in" biofuels, which, by definition are "liquid bio-hydrocarbons that are functionally equivalent to petroleum fuels and are fully compatible with existing petroleum infrastructure" [10]. The main aim of this approach is to tackle limitations of first and second generation biofuels in terms of blending issues (i.e. ethanol and biodiesel cannot be used in neat form in engines but only within specific blending ratios), energy security (production volume to decrease energy dependence from petroleum) and infrastructure incompatibility (e.g. ethanol and biodiesels have to be delivered through different tanks and pipelines than those in use for regular fuels), making them directly usable in engines.

The approach required for the identification of "drop-in" biofuels is multidisciplinary. It involves the implementation of a sustainable production process and the evaluation of many different physical-chemical properties (LHV, viscosity, stability, acidity, boiling point, heat of evaporation, solubility in water etc.) to ensure complete compatibility. Finally, the assessment of its reactivity at engine relevant conditions plays the major role in determining if the product would ever be able to access the market.

Despite promising long-term solutions such as the "drop-in" biofuels, the short and mid-term transport scenario will see increasing amounts of biofuels blended with regular gasoline and diesel fuels.

Overall, the coupling of quite stable reserve-to-production ratio limiting fossil fuels prices, criticism in biofuels production processes, demanding technology modification required for use of neat biofuels, with additional stringent goals to limit climate change and the rather unstable political situation of key areas (e.g. Middle East), encourages the academic and the industrial communities to focus research efforts on the combustion of new gasoline and diesel fuel formulations, obtained from blending bio and fossil fuels.

Beside the need for further exploring features of oxygenated biofuels such as alcohols, ketones and methyl esters, a deeper and more accurate assessment of hydrocarbon fuels (n- and iso-alkanes, aromatics) combustion properties is driven by increased experimental, theoretical and modeling capabilities.

1.2 Combustion Chemistry and Fuels for Internal Combustion Engines

Correctly assessing the reactivity of a given fuel or fuel mixture such as a new formulation of gasoline, is a chemical kinetics problem. A better understanding of specific chemical compounds effects on combustion performances and emissions potential of a fuel, allows the tailoring of a fuel or a fuel blend for an existing technology or, conversely, the tuning of an engine for a given fuel. Researchers and industries are currently pursuing the first solution, and most likely will continue to do so in the near future [11]. The capability of a fuel to access the market is defined based on standards, measured according to a specific test procedure. These specifications guarantee that, for example, the engine will start easily in cold weather, provide good fuel economy or produce low emissions.

The main properties are autoignition quality measures such as Research Octane Number (RON) and Motor Octane Number (MON) for gasoline spark ignited (SI) engines, or the Cetane Number (CN) for diesel compression ignition (CI) engines. The RON test is performed in a single-cylinder cooperative fuels research engine (CFR) running at 600 rpm, with an intake temperature of 52°C. The MON test is performed at 900 rpm and 149°C intake temperature. The true antiknock quality of a gasoline is better defined by the Octane Index (OI = RON − KS) [12, 13] where K is an empirical parameter depending on the temperature and pressure traces and S is the Octane Sensitivity (S = MON − RON), which measures the differences in the autoignition propensity of a given fuel compared to the Primary Reference Fuels (PRFs). Indeed, RON and MON are defined by referring to the main components of gasoline surrogates: n-heptane (RON=MON=0) and iso-octane (RON=MON=100). As is clear from the definition, binary mixture of PRFs are not able to replicate autoignition properties of commercial octane sensitive (S>0) gasolines, therefore toluene (RON=120, MON=109, S=11) has been recently included in gasoline surrogates formulation [14]. These indicators serve the goal of characterizing the knocking propensity of a fuel: the lower the knocking propensity, the higher the pressure the engine can be run at and thus the higher the efficiency.

In SI engines, fuel and air are premixed before entering the cylinder and their pressure and temperature increase along the engine cycle. Due to temperature inhomogeneity, autoignition can start at some "hot spots" where a flame kernel propagates ahead of the piston head. This causes a sharp rise in the heat release rate, which translates into pressure waves propagation producing a characteristic metallic sound. The engine is "knocking" once the threshold value of ~20 kPa noise in pressure is reached. Another common parameter is the knock-limited spark advance (KLSA), which represents the advance in the spark timing that induces the phenomena and defines the "knock limit" of a given fuel. The larger the KLSA, the more a fuel resists knocking at a given condition. When engine knock is detected in modern cars, the control system acts to retard the spark timing (i.e. moving it towards or beyond the top-dead-center), reducing the power release and therefore the overall efficiency.

Current trends to improve engine efficiency by increasing compression ratios (i.e. downsizing with consequent increase in pressure) and implement turbocharging [13] make knocking, or "*superknocking*", more likely to occur and the accurate assessment of fuel ignition propensity mandatory for advances in the transport sector.

Engine knock mostly depends on chemical kinetics phenomena such as cool flames and autoignition at low temperatures (~500–1000 K), and their competition with flame fronts propagating from higher temperatures "hot spots". Progress in combustion kinetics historically guided engine design to improve engine efficiency by means of a thorough understanding of these autoignition phenomena [14-18].

As recently summarized by Kalghatgi [13] three reasons can lead to "*superknock*":

1) Formation of a "hot spot" that satisfies the ignition criterion (autoignition);
2) Development of an expanding flame front with high enough laminar flame speed to propagate (preignition). This will increase the temperature of the end gas possibly causing autoignition and extremely heavy knock;
3) Increasing knock intensity for increasing knock temperature and pressure (developing detonation).

Figure 2 shows a plot of the crank angle degree at which ignition occurs using a RON pressure time history for a series of PRFs mixtures (from n-heptane to iso-octane), linear alkanes, alkyl benzenes, olefins and alcohols. These results were recently reported by Westbrook et al. [19].
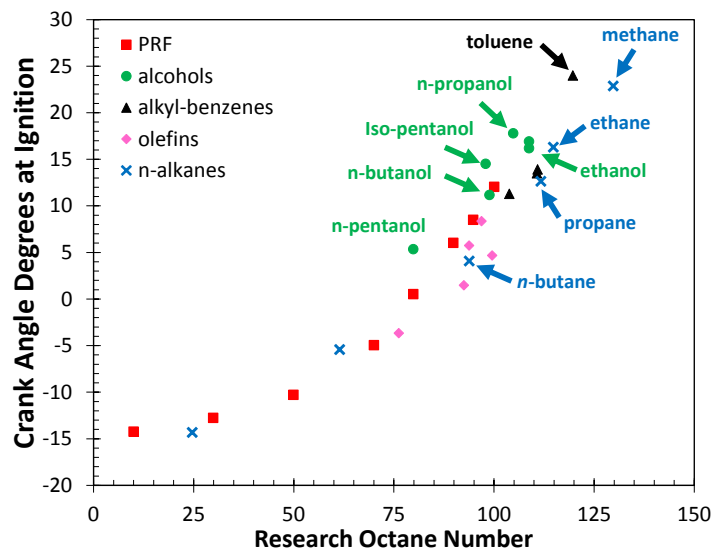
Figure 2: Autoignition crank angle degree for selected fuel classes using a RON-like pressure history. Adapted from Westbrook et al. [19].

The fundamental combustion properties (autoignition, laminar flame speed, NO_x and soot formation etc.) of advanced biofuels and their blends with petroleum based fuels influence engine performance and emissions.

While at high temperatures oxygenated and synthetic-hydrocarbon biofuels (BTL) behave similarly to conventional hydrocarbon fuels, the low-temperature chemistry, important for determining the octane rating, differ significantly due to the different reactivity of the portions of the molecules neighboring the functional group. The main goal of kinetic modelling of combustion is to characterize and quantify the impact of these different molecular features.

Along with short term perspectives of developing new fuels to be used in existing engines, new engine technologies are also being investigated.

Despite some critical aspects in terms of maximum load achievable and phasing control, Homogeneous Charge Compression Ignition (HCCI) engines allow for a reduction in NOx and soot formation while delivering high efficiency. As in SI engines, the charge of fuel and air is premixed and ignited by compression, as in CI engines.

Premixed Compression Ignition (PCI) or Gasoline Compression Ignition (GCI) requires an earlier injection of fuel compared to diesel engines to allow for proper mixing. The lack of perfect mixing ensures that the ignition occurs somewhere, in contrast with HCCI where the perfectly mixed charge might not be at ignition conditions and not ignite at all. The optimum RON for such technology appears to be between 70 and 85, which is much lower than market gasolines and comparable with longer alcohols (n-pentanol, n-hexanol) ignition propensity. Due to the higher combustion stability, GCI engines appear to be a promising alternative to CI engines [13].

Reactivity Controlled Compression Ignition (RCCI) [20] uses high octane commercial gasolines, or gasolines/ethanol mixtures, triggering the ignition through the injection of a more reactive diesel fuel (dual-fuel). Despite the higher costs associated with the dual-fuel injection system, RCCI ensure very promising NOx and soot levels and high efficiency.

1.3 Kinetic Modelling of Combustion

Figure 3 shows the typical flow chart of the research approach guiding the implementation of a new fuel or fuel mixture into existing infrastructures.

As partly discussed in Section 1.1, the identification of a new fuel or fuel mixture candidate, is mostly based on the sustainability of its production process, on a few physico-chemical properties ensuring its compatibility with existing infrastructure and efficient blending with hydrocarbon fuels, or driven by new international regulations forcing increasing biofuel content into gasoline or diesel fuels.

The second step requires the development and validation of reliable kinetic mechanisms describing the oxidation of their components as neat fuels (alcohols, methyl esters, n- and iso-alkanes, cycloalkanes, aromatics etc.), to correctly describe the chemistry involved in low and high temperature autoignition phenomena and to correctly predict pollutants formation.
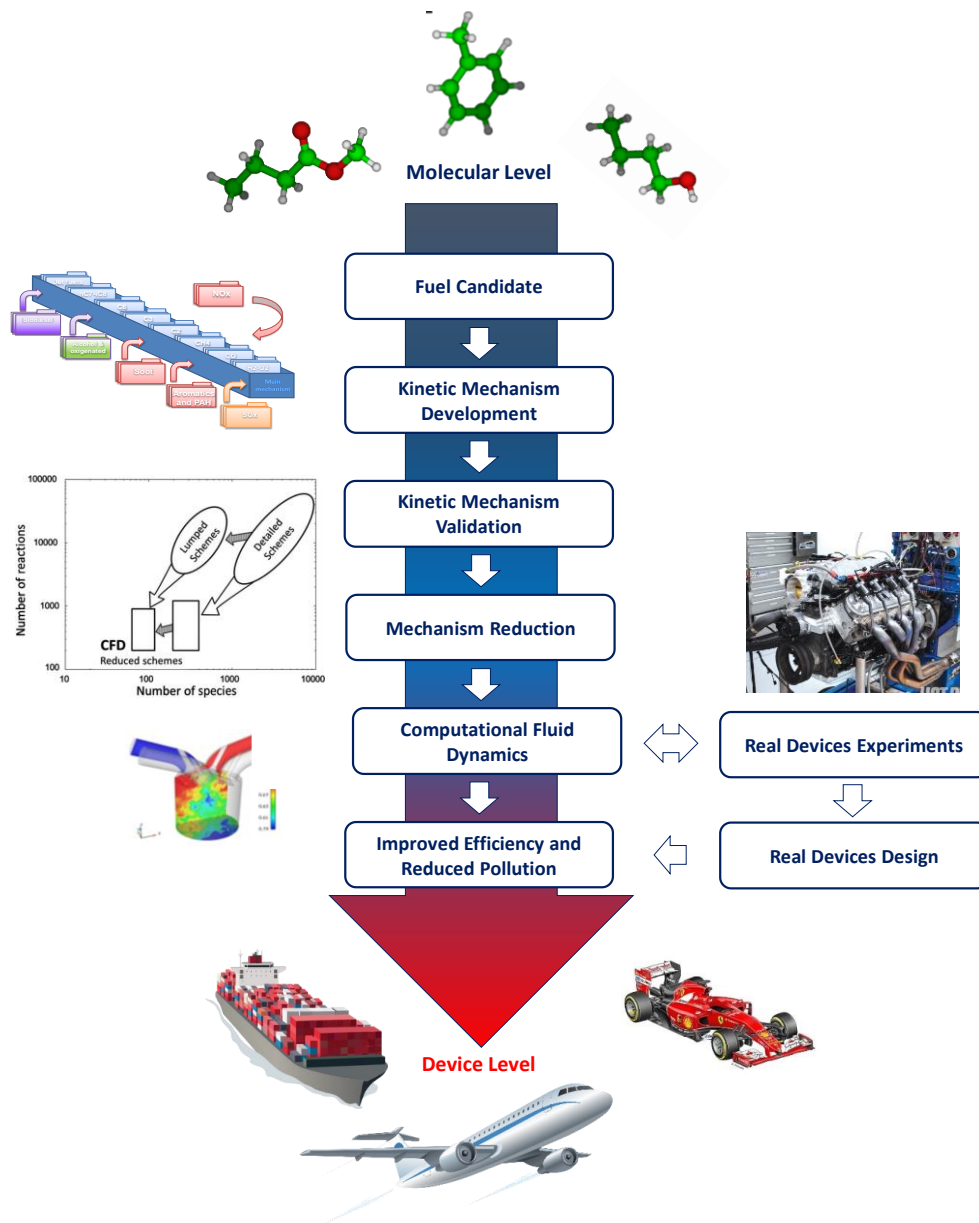
Figure 3: Flow chart of the engineering process for the development or improvement of novel practical fuels and/or combustion devices.

Practical fuels are too complex for really detailed and comprehensive chemical kinetic schemes to be developed for them. While the biofuel portion might be a pure compound (ethanol, butanol etc.) the fossil portion is usually a mixture of 100s–1000s of different components [21]. This issue is tackled by defining surrogate mixtures of a limited number of reference components (e.g. n-heptane, iso-octane, toluene, n-butanol etc.), usefully applied to mimic the behavior of real fuels with respect to specific validation targets

(viscosity, ignitability, boiling point etc.) [22-25]. Table 2 reports the components of gasoline surrogates investigated in the literature. Beside primary reference fuels, toluene reference fuels are commonly considered together with the addition of olefins, cycloalkanes and oxygenated species such as alcohols to represent biogasolines.

Reference	Components
Gauthier et al. [26]	*iso*-octane, *n*-heptane, toluene
Naik et al. [27]	*iso*-octane, *n*-heptane, toluene, methylcyclohexane, 1-pentene
Vanhove et al. [28]	*iso*-octane, *n*-heptane, toluene, 1-hexene
Haas et al. [29]	*iso*-octane, *n*-heptane, ethanol
Lenhert et al. [30]	*iso*-octane, *n*-heptane, toluene, 1-pentene
Mehl et al. [14]	*iso*-octane, *n*-heptane, toluene, 1-hexene
Sileghem et al. [31]	*iso*-octane, *n*-heptane, methanol, ethanol
Fikri et al. [32]	*iso*-octane, *n*-heptane, ethanol
Saisirirat et al. [33]	*n*-heptane, *n*-butanol, ethanol
Kumar et al. [34]	*iso*-octane, *n*-heptane, butanol
Agbro et al. [35]	*iso*-octane, *n*-heptane, toluene, butanol

Table 2: Components of gasoline surrogates from the literature.

Another task in combustion kinetics relates to the complexity of detailed mechanisms. This complexity increases even more when mixtures of different components are considered. Even for pure components, a large number of species ($\sim 10^2$–10^3) and reactions ($\sim 10^3$–10^4) need to be included for an accurate description of the variables of interest for real applications (ignition delay times, laminar flame speed, heat release rate, intermediates, products and pollutants formation). A classical representation of the size of different kinetic mechanisms from the literature is reported in Figure 4. Considering for example the LLNL (Lawrence Livermore National Laboratory, USA) biodiesel mechanism [36], it involves about 4800 species. This fact on one hand supports the necessity of automatically generated kinetic schemes, and on the other hand shows that the number of intermediate species increases exponentially for increasing molecular weight of the fuel.

For a completely balanced and physically significant model, the decomposition and oxidation pathways of such intermediates must be included.

Postponing the discussion concerning the obvious challenges related to the inclusion of every elementary step, or the critical management in light of updates and parameter modification (see Chapter 7), it is clear that models of such complexity are computationally hardly manageable even in 1D laminar flame simulations due to the large number of species. Simplification techniques aimed at reducing the number of species are therefore mandatory when such detailed mechanism need to be successfully used in large scale computations, where the computational costs scale by the second/third power of the number of species.
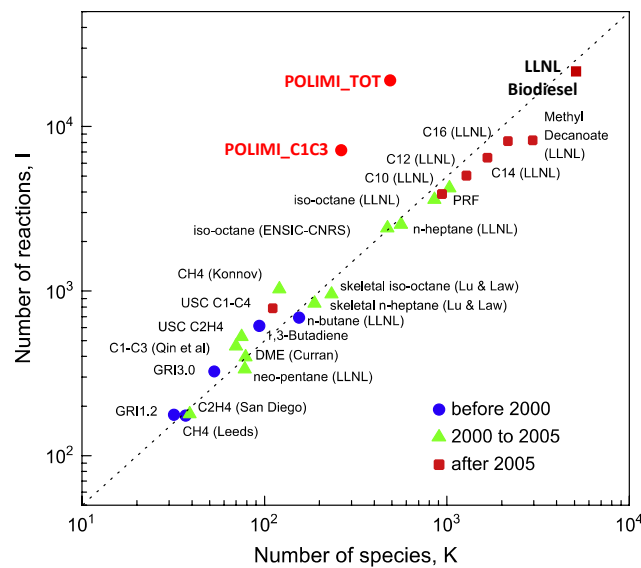
Figure 4: Number of reactions and species of detailed and lumped mechanisms for hydrocarbon and oxygenated fuels from the literature, adapted from [37].

Beside the chemical lumping procedure adopted in the Chemical Reaction Engineering and Chemical Kinetics (CRECK) group at Politecnico di Milano (POLIMI) since Ranzi et al. [17, 38] and better discussed in Section 3.3, skeletal reduction approaches are used to detect and eliminate species and reactions which are of negligible importance in the operating conditions (temperature, pressure and equivalence ratio) of interest [39]. Figure 5 shows possible strategies for the reduction of detailed kinetic mechanisms as recently discussed in Ranzi et al. [40].
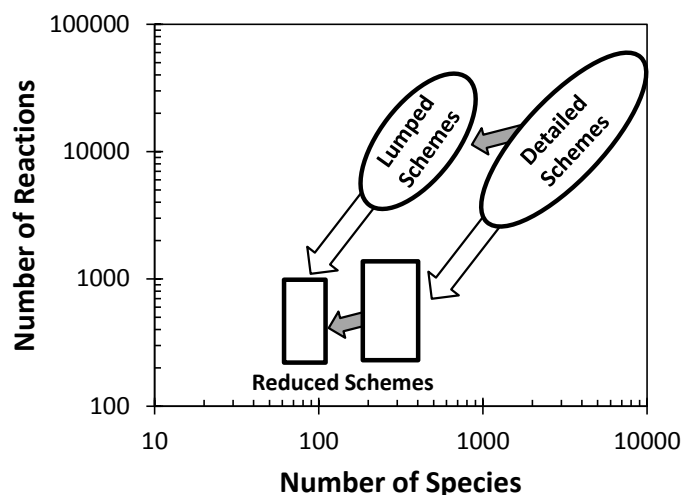
Figure 5: Strategies for the reduction of lumped and detailed kinetic schemes. Grey arrows represent the lumping phases, white arrows represent skeletal reduction phases. Adapted from [40].

Despite the qualitative purpose of such representation, recent experiences proved that skeletal mechanisms obtained from a lumped mechanism, required a lower number of species for a desired accuracy [41]. Therefore, the application of skeletal reduction to a detailed mechanism would require a successive lumping to obtain a comparable number of species and to be of even more effective use in Computational Fluid Dynamics simulations (CFD).

The inclusion of complex fuel chemistry and its interaction with turbulence in CFD simulations allows for a realistic description of a large variety of combustion regimes that are typical of real systems, where autoignition and flame propagation occur in wide range of temperatures, pressure and stoichiometry. Finally, the coupling of CFD results with experimental measurements from real devices guides fues and engine optimization for improved efficiency and reduced pollution [42].

The procedure behind the development, update, extension and the validation of the POLIMI chemical kinetic mechanism, which constitutes the core of *this thesis*, is discussed in the following and represented in Figure 6.
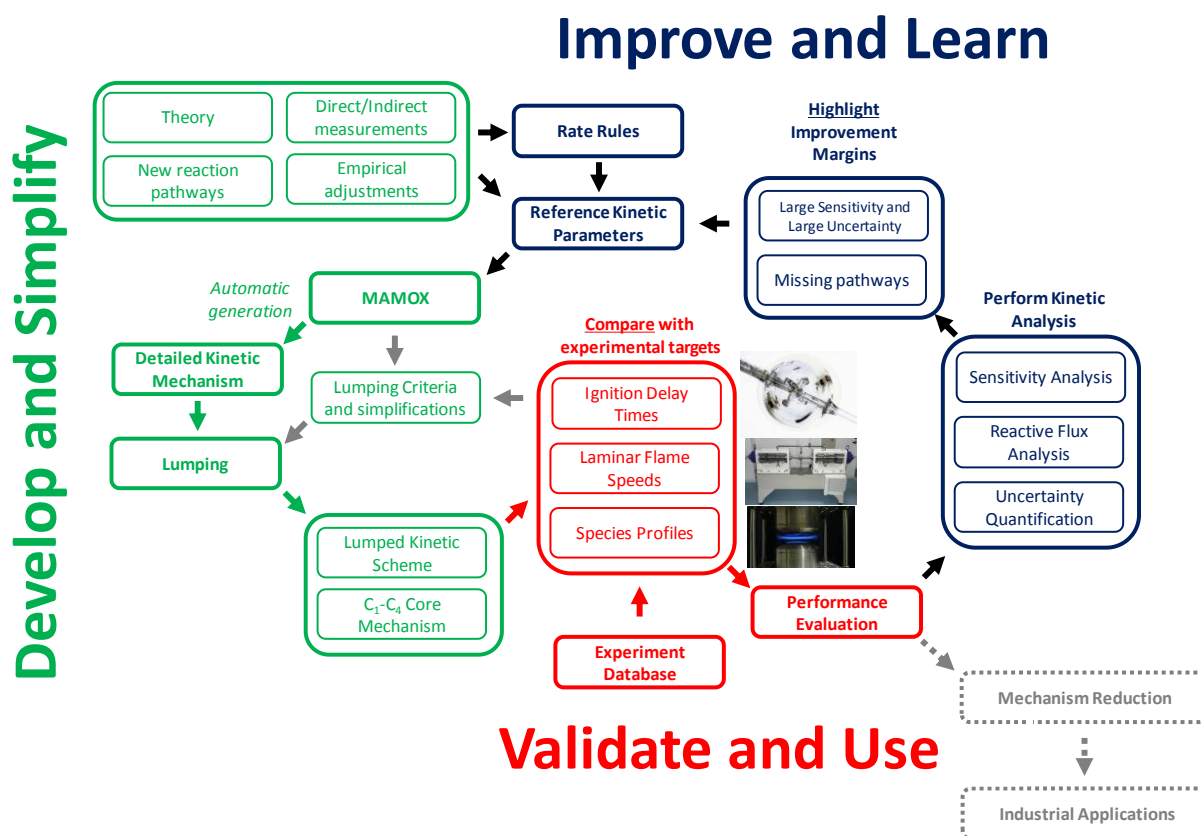
Figure 6: Development and validation procedure of the chemical kinetic mechanisms for pyrolysis and combustion of hydrocarbon fuels.

Different phases of this procedure have been the subject of *this work* and will be discussed in detail in specific Sections. It is important to underline that, beside some features such as lumping or the automatic generation of the mechanism, which are specific to the approach in use in the CRECK group, the procedure discussed below is completely general and applies to any kinetic model being developed, not only within the combustion community.

The POLIMI mechanism has been conceived and developed in a hierarchical, modular and general way in the last ~35 years [40, 43, 44] in the CRECK group (http://creckmodeling.chem.polimi.it). It is able to describe the oxidation and pyrolysis of any fuel from hydrogen and syngas to heavy biodiesels, including oxygenated species such as alcohols, aldehydes and ethers. A schematic representation of the hierarchical modularity of the POLIMI mechanism is provided in Figure 7.
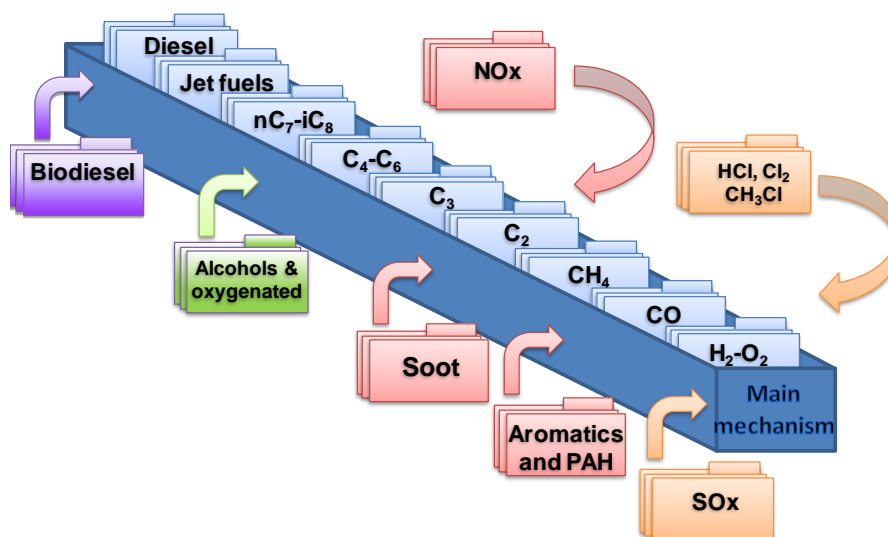
Figure 7: Schematic representation of the hierarchical modularity of the POLIMI kinetic mechanism.

The hierarchical structure reflects the intrinsic nature of combustion. Any detailed kinetic mechanism is in fact developed on top of a core mechanism. Starting from the simplest H_2/O_2 sub-system whose radical species ($\dot{H}$, $\dot{O}H$, $H\dot{O}_2$, $\ddot{O}$) dominate the reactivity of any fuel, the C_1 portion (CH_4, $\dot{C}H_3$, CH_2O, CO and CO_2) is implemented together with C_2 species (C_2H_6, C_2H_4, C_2H_2) as ethane can be formed from the recombination of two methyl radicals in methane oxidation and pyrolysis ($\dot{C}H_3+\dot{C}H_3+M=C_2H_6+M$). In a similar fashion C_3 hydrocarbons are introduced (C_3H_8, C_3H_6 etc.). All the successive modules to describe the pyrolysis and oxidation of higher molecular weight hydrocarbons, include the same elementary reaction steps already contained in the underlying systems. Whenever a new module is implemented only the primary reactions have to be defined, as the intermediate or product species would be already accounted for in the lower level framework [38]. Such primary reactions are introduced according to reaction classes that will be better discussed in Section 3.1.

Another feature of the modularity refers to pollutants chemistry (NOx, SOx, PAH and soot formation). For example, it is possible to exclude such modules if the interest is limited to the time scale of fuel reactivity (ignition delay times, laminar flame speed, speciation in isothermal reactors). Finally, the lumping approach (Section 3.3) limiting the size of the mechanism in terms of species allows for the efficient use of a single general mechanism for any molecular weight fuel. Overall, the POLIMI mechanism contains ~500 species and ~19000 reactions.

The first step in the development of a kinetic mechanism requires the definition of the primary reaction pathways involving the fuel (reaction classes) and the assignment of appropriate reference kinetic parameters and thermodynamic properties.

Historically, kinetic mechanism development has strongly relied on direct experimental measurements for the assignment of kinetic rate constants and thermochemistry parameters. Clearly, beside an unavoidable intrinsic uncertainty, the experimental data represents the ideal source for such parameters. However it is equally clear that, considering the number of parameters needed in a typical kinetic model (~10^4 reactions), relying totally on direct experimental measurements is impossible. Additionally, inevitable limitations in the experimental facilities used for such measurements do not allow a complete coverage of the conditions of temperature (~500–2500K) and pressure (~1–100 atm) of interest in combustion.

Despite the fact that "*the underlying physical laws necessary for the mathematical theory…of physics and the whole of chemistry*" have been *"…completely known*" [45] since the beginning of the 1900's, computational limitations did not allow for direct application of theoretical chemistry in chemical kinetic modelling of such complex reactive systems. The breakthrough happened in the last 20-30 years, with the advent of high-end computing facilities and the implementation of commercial quantum chemistry software packages [46, 47] allowing for the computation of fundamental data for complex species. Further advancements in algorithms and in computational capabilities keep driving improvements in the accuracy of a priori theoretical methods to levels which are now comparable to those of experiments [48]. These progresses transformed theoretical chemical kinetics from an empirical science mostly used to extrapolate measurements to conditions of interest to combustion, to a fully predictive science bridging between fundamental molecular properties and laboratory scale experiments. For such reasons, theoretical chemistry is nowadays a necessary and a powerful tool for advances in kinetic modelling and therefore in combustion science and engineering.

Since the formalization of the bond increment theory of Benson and Buss [49] it has been possible to classify the elementary reactions composing a mechanistic kinetic model into classes, and determine kinetic parameters for reactions belonging to the same class according to analogy rules. The analogy rules relied partially on thermokinetic theory by assuming that transition states, molecules and radicals in an elementary reaction obey additivity rules of bond properties, and largely on macroscopic experimental data (i.e. intermediates and products yields), the only solid basis for assigning rate parameters for most of the 20th century. Considering the obvious limitations in collecting data for every parameter needed for kinetic modelling purposes, the work of Benson [50] provided the theoretical basis for an intensive use of analogy rules. The core concept behind the use of analogy rules is that only a small portion of the molecule influences rate parameters, as the dominant forces between atoms are short range. For example, in an addition reaction the rate constant mainly depends on the atoms and groups in α and β to the double bond.

The first field of application of such approach can be summarized in the groundbreaking activity performed at Politecnico di Milano by Dente, Ranzi and coworkers [43, 44] in modeling steam cracking processes. The same approach initially used for the kinetic modeling of pyrolysis processes [51, 52], was gradually and

naturally extended to the combustion of hydrocarbons [53, 54] where the primary reactions are defined according to classes and rate rules. As reported in Figure 6, the different sources of kinetic parameters previously discussed (theoretical chemistry, direct measurements, macroscopic data) constitutes the basis for the definition of such rate rules. The recent work of Bugler et al. [55], revisited the thermochemistry and the kinetics of alkane oxidation at low temperatures in light of recent theoretically derived rate coefficients, providing updates to the rate rules of Curran et al. [54]. This praiseworthy effort clearly shows the potentialities of an effective coupling of theoretical chemistry and kinetic modelling, obtained by checking and eventually updating those rate rules whose definition has been, is and will be the key for the systematic development of kinetic mechanisms for combustion applications.

Given the complexity of reaction mechanisms involving $\sim 10^2$-10^3 species and $\sim 10^3$-10^4 reactions, their manual construction is very time consuming and highly prone to error. Over the last 20 years, the use of computer-based expert systems provided a very efficient alternative for automatic generation of kinetic mechanisms. From the experience gained in the manual development, the definition of rate rules can be converted into algorithms [56]. As reviewed by Ranzi et al. [17] these algorithms for the implementation of kinetic generators can be divided into two categories [57]. The first are able to generate a whole set of possible reactions, while the second, having recognized the compounds as belonging to a certain class, only generate reactions known to be characteristic of that class. Many examples of such algorithms exist in the literature [43, 57-62]. In particular since the work of Dente, Ranzi and coworkers [38, 43] the MAMOX code [63] is used to generate all those primary reaction steps needed whenever a new fuel module is implemented in the main mechanism of Figure 7.

Summarizing, the classification of the primary reaction classes and the definition of their specific rate rules yield a limited number of reference kinetic parameters needed for the automatic generation of the detailed kinetic mechanism. A clear example can be found in *this thesis,* where the systematic analysis of series of compounds belonging to the same class (aldehydes, alcohols, n-alkanes etc.) resulted in the definition of rate rules.

The final simplified mechanism is then obtained through the lumping approach discussed in Section 3.3 and coupled with the detailed core mechanism covering the C_0–C_4 species. Similarly to the definition of rate rules used for the detailed mechanism, once the lumped rate constants are obtained for a specific compound it is convenient to extend such rate constants to heavier molecular weight species belonging to the same class (n-alkanes, iso-alkanes, aromatics etc.) without generating a detailed mechanism upstream. Ranzi et al. [64] discussed the successful extension of the lumped kinetic mechanism for *n*-pentane and *n*-heptane to heavier *n*-alkanes (*n*-decane, *n*-dodecane and *n*-hexadecane). The marginal variations in product selectivities allow for the description of low temperature oxidation of longer alkanes with the same lumped kinetic parameters

used for *n*-heptane, limiting the differences to some reaction step typical of the high temperature oxidation (unimolecular initiation reactions) and directly related to the different size of the molecules (i.e. larger number of H-atom for H-abstractions, size of the ring intermediate for internal H-abstractions).

Once the kinetic mechanism is fully implemented, together with thermodynamic and transport properties for every species, they can be handled by CHEMKIN or similar commercial packages [65] or by open source solvers such as OpenSMOKE++ [66]. Results from kinetic simulations thus obtained are compared with experimental measurements in ideal reactors to check for consistency between model and experiments. This part of the procedure is commonly called "*validation*".

Ignition delay time measurements in rapid compression machines or shock tubes, laminar flame speed measurements and speciation in different types of burners (premixed, counterflow etc.), species measurements in ideal reactors such as jet stirred reactors (JSR) and flow reactors (PFR), are the most common experimental targets used to validate the mechanism. Clearly the wider is the range of temperature, pressure and stoichiometry conditions covered experimentally and used for the validation, the higher is the confidence in the accuracy and reliability of a kinetic mechanism.

While it is clear that the kinetic model should be designed to perform well under a wide range of conditions, it is useful to also distinguish at least two different objectives concerning the validation targets of the kinetic model. From one side, it is possible to have a greater interest and attention to combustion properties, such as ignition delay times and laminar flame speeds of fuel/air mixtures. These quantities directly impact the design of real devices as discussed in Section 1.2. Speciation measurements on the other hand allow extremely detailed insights into the evolution of the reactive system, particularly for the characterization of pollutant formation in combustion processes. A common example refers to speciation measurements in low pressure flames (~0.04 atm), useful to explore in detail the evolution of the chemistry within a flame, but far from the operating conditions of real applications.

An effective example also refers to the modularity features previously discussed. The chemistry behind NOx and soot formation involves longer time scales (10^{-2}-10^{0} s), often not interacting with the ignition chemistry (10^{-4}-10^{-1} s). For these reasons, it is possible to exclude such modules, strongly simplifying the mechanism and the model. Exceptions are the interactions between NOx in exhaust-gas-recirculation (EGR) with the ignition chemistry, or the radiative effect of soot in industrial furnaces.

As recently discussed by Wang and Sheen [67], model validation is a "poorly posed" problem. In fact, both model and experimental uncertainties would need to be precisely quantified to overcome usual "agree–disagree" statements, mostly based on subjective assumptions. The rigorous quantification of the uncertainty in complex kinetic mechanisms has been widely reported in the literature and constitutes one of

nowadays most challenging topics in combustion [68]. To some extent, the increase in the number of kinetic mechanisms available for a given fuel already maps the underlying uncertainty of kinetic parameters [67].

Anyway, the primary goal of chemical kinetic modeling remains the *making of predictions.* Therefore the performance evaluation phase through model/experiment comparison plays the critical role of determining the need for further iterations along the "*predict-measure-learn* loop" [69] schematically reported in Figure 6. All these comparisons are usually performed using plots in which the experimental data and the calculated curves are plotted together. Very often though, this qualitative and rather subjective evaluation is not efficient, particularly when a very large number of comparisons have to be performed. Agreement assessment methods are emerging in the literature [70], but they still carry some limitations which have been tackled in *this work* as discussed in Chapter 7. Moreover, the aforementioned quantitative evaluation becomes strictly necessary when aiming at an automatic and iterative validation procedure, which, in turn is the main meaning of the representation of Figure 6 and the ambitious goal of kinetic modelling of the 21st century.

As mentioned above other critical challenges lie in the "*performance evaluation*" phase. With regards to the uncertainty quantification (UQ) of the experiments, it is clear that the sources of error are various and sometimes difficult to quantify (i.e. mass and heat transfer in different parts of the facility, irregularity of temperature or flow profiles, poor mixing and heterogeneous interactions with reactors walls). Some of these issues have been solved through gradual and continuous improvements to the experimental facilities in the attempt to approach the "ideal" behavior, to focus the measurements exclusively on kinetic phenomena. Other non-ideal effects, like those in shock tubes and rapid compression machines, can be correctly accounted for in standard kinetic simulations. Experimentalist have been focusing more and more on providing valuable error quantification, which is vital for kinetic modelers regularly involved in balancing model accuracy, simplification and computational efforts.

The management of this large amount of experimental information is already complex itself. How should experimental data be stored to be promptly and effectively available for kinetic modeling purposes? The formatting issue was firstly tackled with the PrIMe project (http://www.primekinetics.org) of Frenklach and coworkers [71]. Other databases such as the CloudFlame (https://cloudflame.kaust.edu.sa/) at King Abdullah University of Science and Technology (Saudi Arabia), or the ReSpecTh database (http://respecth.hu) of the Chemical Kinetics Laboratory at Eötvös Loránd University (Budapest, Hungary) have been developed afterward, but the establishment of a common formatting still has not been completely achieved. Similar standardization problems apply to species nomenclature. For fuels and parent species larger than C_2, in fact, names differ between mechanisms (or experimental datasets) coming from different research groups, making the automation of pre or post-processing steps more complicated than expected.

The correct and exhaustive evaluation of uncertainties in model parameters (kinetic rate constants, thermochemistry and transport properties) is still one of the most challenging topics in combustion science, particularly if "*we are looking for models which not only describe accurately broad sets of existing experimental data, but which are also predictive in the sense that they can be applied in situations where experiments are expensive or difficult to perform*" [68]. Often the operating conditions accessible experimentally do not entirely reflect those typical of real systems (e.g. ~100 atm pressure for diesel engines) due to issues of a different nature, making the kinetic mechanisms not necessarily reliable beyond those validation targets in which they are iteratively implemented.

As previously discussed and summarized in Figure 6, whenever the model is evaluated to be accurate enough, a successive skeletal reduction phase makes it suitable for large scale computation. Conversely, if the model poorly predicts the experimental targets under some specific regimes of temperature, pressure or dilution, standard kinetic analysis tools allow for a clear highlighting of its deficiencies and improvement margins. Sensitivity analysis identifies those parameters with the biggest influence on predictions. Specifically, in kinetic modelling of complex reaction systems sensitivity analysis highlights which rate constants most strongly affect a key model output (flame speed, ignition delay time, formation of a particular species). A rigorous use of this information would require a proper weighing of the sensitivity coefficients obtained from such an analysis over the relative uncertainty of those parameters. Indeed, it would be fundamentally erroneous and worthless to take action through empirical adjustment, theory or new measurements on those parameters which are well known or, in other words, for which different studies from the literature already induced a natural uncertainty bounds minimization according to the obvious inverse proportionality linking knowledge and uncertainty. Better estimates are instead needed for those parameters with lower sensitivity coefficients and larger uncertainty. Rate-of-production analysis (ROPA) is another useful tool to determine the contribution of each reaction to the net production or destruction rates of a species. Another source of improved predictive capabilities for kinetic models comes from the identification of missing reaction pathways. These new pathways might come from theoretical studies highlighting channels not observable experimentally, or from detailed experimental measurements interpreted with chemical intuition and further confirmed by theory as in the new reaction classes in n-alkane low temperature oxidation recently proposed by Ranzi et al. [72, 73] and discussed in Section 5.1.

Concluding, pursuing the idea of a fully predictive model is the goal of the modern approach to kinetic modelling. This ambitious goal needs the full and, more importantly, wise implementation of the powerful tool of theoretical chemistry. Being aware of the strong sensitivity of such complex systems to modifications of core parts, even if extremely accurate, is in fact as important and forces a cautious blending. Moreover,

the synthesis of the large amount of outputs coming from theoretical chemistry into validated simplification methods (rate rules, lumping etc.) is needed.

This full coupling is however at hand, but first requires the solution of other critical problems. The management of big data in terms of formatting and storage of a large amount of experimental data used for kinetic mechanisms validation plays a key role in the full automation of the flow chart summarized in Figure 6. Again, the definition of quantitative and robust methods to evaluate model performances is strictly necessary to control systems tending to exponentially increase in size for the reasons discussed throughout this Section.

1.4 Goals and Overview of This Thesis

The goals of *this study* were to develop, revise and update the kinetic mechanism of key components or intermediates of new gasolines surrogates derived from blending biofuels with fossil fuels. Beside the more fundamental kinetic modelling activity, some other key parts of the procedure in Figure 6 have been investigated and will be discussed.

Chapter 1 provided a brief overview on the global energy scenario and discussed perspectives and challenges in today's kinetic modelling approach, focusing on key aspects that will often be recalled in the following Sections. *Chapter 2* provides an overview of concepts central to the construction of kinetic mechanisms. *Chapter 3* provides insight to the specific approach to kinetic modelling conceived and developed at POLIMI. Theoretical methods used to derive kinetic parameters via computational chemistry for some parts of the activity are described in *Chapter 4*. *Chapter 5* discusses the kinetic mechanisms for the hydrocarbon components of gasoline surrogates: n-alkanes and toluene. The biofuel and key intermediates portion (alcohols and aldehydes) is reported in *Chapter 6* together with an investigation of the relative reactivity of different oxygenated components of relevance as biofuels (ketones and methyl esters). The POLIMI kinetic mechanism thus obtained is compared with recent biogasoline surrogate experimental data from the literature. The curve matching approach to comparing model and experiments is described in *Chapter 7*. Finally, *Chapter 8* draws conclusions, providing directions for further investigations and future perspectives of kinetic modelling.

It has to be noted that a large part of *Chapter 5* (*n*-alkanes) and the whole of *Chapter 6* and *Chapter 7* are based on peer-reviewed publications authored and coauthored during the PhD program in Industrial Chemistry and Chemical Engineering [40, 72-78]. Additional publications produced within the research activity are reported in the *Appendix*.

Chapter 2 – Fundamentals of Chemical Kinetic Modelling

This chapter is meant to provide an overview of some fundamental concepts underlying chemical kinetic modelling. Relevant theoretical principles are briefly discussed, possibly allowing a more detailed reading of the upcoming sections.

2.1 Radical-chain Reactions

The overall and apparent combustion of any fuel can be written as

$$C_xH_yO_z + \left(x + \frac{y}{4} - \frac{z}{2}\right)O_2 = xCO_2 + \frac{y}{2}H_2O + Energy$$
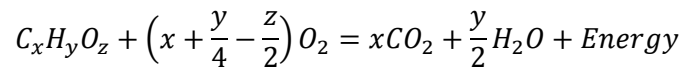
Such simplistic representation does not describe the true nature of the combustion process, involving the progression of many intermediate species over different time scales. About 30 years ago, simplified single or double step kinetic mechanisms provided the first insights into macroscopic phenomena such as flame propagation at a very limited computational cost [79]. However, nowadays the rapid increase in computational capabilities allows for a detailed treatment of combustion chemistry as a complicated network of elementary reaction steps.

The conversion of fuel and oxidizer into CO_2, H_2O and energy is a complex radical-chain reaction and the detailed understanding of the mechanism underlying the overall process is the first step in the development of a kinetic model.

If we consider the simplest system involving the combustion of molecular hydrogen (H_2) the global reaction would be written as

$$H_2 + 0.5\, O_2 = H_2O$$
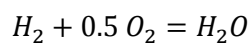
At a fundamental level, the process is initiated by *chain initiation reactions* converting stable species into radicals. In particular, three initiation reactions can activate hydrogen combustion:

$$H_2 = \dot{H} + \dot{H}$$

$$O_2 = \ddot{O} + \ddot{O}$$

$$H_2 + O_2 = H\dot{O}_2 + \dot{H}$$
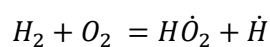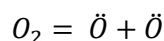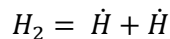
As free radicals are by definition species containing at least one unpaired electron in their valence electron shell, they will naturally tend to a more stable configuration satisfying the octet rule. For this reason these

very reactive, or short-lived, intermediates will propagate the chain reaction further and allow the full conversion of fuel and oxidizer into products. *Chain propagation reactions* convert one radical species into another radical species. This step can occur via a unimolecular process

$$H\dot{O}_2 = O_2 + \dot{H}$$
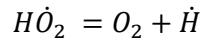
or through a bimolecular process, where a radical and a stable species are converted into another radical and another stable species.

$$H_2 + H\dot{O}_2 = \dot{H} + H_2O_2$$
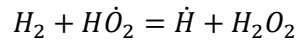
These *chain propagation* channels define the high pressure limit (second limit) of the H_2/O_2 explosion diagram reported in Figure 8. The net result of this reaction network is

$$H_2 + O_2 = H_2O_2$$
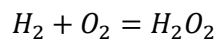
Further decomposing, at higher temperature, *via*

$$H_2O_2 = 2\dot{O}H$$
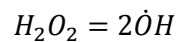
If the chain propagation process results in an increased number of radicals, the reaction is termed *chain branching*:

$$\dot{H} + O_2 = \ddot{O} + \dot{O}H$$

$$H_2 + \ddot{O} = \dot{O}H + \dot{H}$$
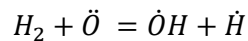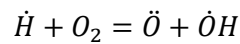
The *chain branching* channels define the low pressure limit (*first limit* in Figure 8) whose net result is

$$H_2 + O_2 = 2\dot{O}H$$
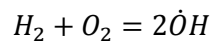
While chain propagation and chain branching reactions are responsible for promoting reactivity, chain termination reactions inhibit the overall process by converting radicals into stable species.

$$H\dot{O}_2 + H\dot{O}_2 = O_2 + H_2O_2$$

$$H\dot{O}_2, \dot{H}, \ddot{O} \rightarrow Wall$$
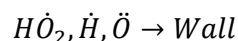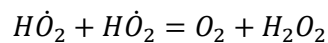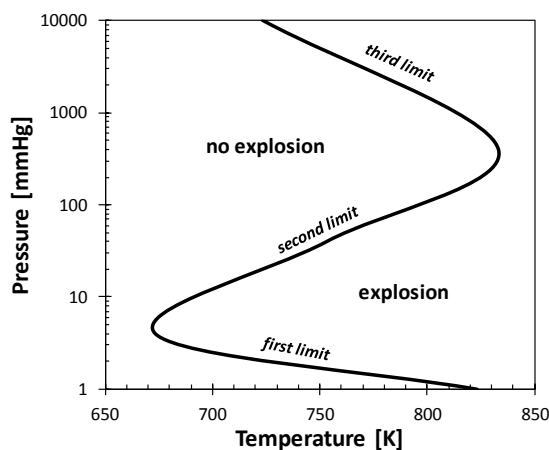
Figure 8: Explosion limits of the H₂/O₂ system.

The identification of initiation, propagation, branching and termination reactions is the first step in the development of a kinetic model. Quantitative predictions require the understanding of the rate at which such reactions occur and the amount of energy consumed (endothermic reaction) or released (exothermic reaction).

2.2 Chemical Kinetics Principles

2.2.1 Rate Laws and Rate Constants

Chemical kinetics is the branch of chemistry dealing with the rate at which chemical reaction occur. Applications of chemical kinetics range from organic synthesis to nuclear, biological, atmospheric and combustion chemistry. Chemical reaction engineering considers reactor design for industrial applications through optimization of reaction kinetics and its interactions with flow phenomena, mass and heat transfer. The following discussion on rate laws and rate constants is mostly based on standard physical chemistry, kinetics and combustion monographs [50, 80-83].

Considering the simplest irreversible reaction $aA \rightarrow bB$ where A is an arbitrary reactant and B a product, the rate of consumption of A, $-d[A]/dt$ is proportional to its concentration $[A]$ raised to the power of its stoichiometric coefficient, a.

$$-\frac{d[A]}{dt} \propto [A]^a$$

$[A]$ is given by the number of moles of A (N_A) over the volume V. Similarly, the rate of formation of B can be written as

$$\frac{d[B]}{dt} \propto [A]^a$$

With a proportionality constant k the equality can be written as

$$-\frac{d[A]}{dt} = \frac{d[B]}{dt} = k[A]^a$$

The determination of the complex dependence of such proportionality constant k on temperature (T) and pressure (p) is the main object of chemical kinetic modelling and therefore central to *this thesis*.

The above equations highlight that the rate of a chemical reaction depends on both the rate constant and the concentration of reactants. Different types of reaction exist. Considering once again the generic reaction $aA \rightarrow bB$ where $a = b = 1$, the rate law can be written as

$$-\frac{d[A]}{dt} = k[A]^1$$

The reaction is *first order* where the *th* order is the *th* power to which the concentration of species is raised in the rate law.

Considering the reaction $aA + bB \rightarrow products$ the rate law becomes

$$-\frac{d[A]}{dt} = -\frac{d[B]}{dt} = k[A]^a[B]^b$$

If $a = b = 1$ the reaction is bimolecular and specifically of the first order in A and B and of the *second order* overall. Other reactions with *molecularity* larger than 2 can exist as $2A + B \rightarrow products$ but the probability of the three partners to efficiently collide is so low that no *third order* reaction can be found in typical combustion kinetic models ideally involving only elementary steps.

As the rate law is always expressed in mol cm^{-3} s^{-1} the units of rate constants are s^{-1} and cm^3 mol^{-1} s^{-1} for unimolecular and bimolecular reactions respectively.

Before proceeding to describe the T and p dependence of k, it is important to note that the expression of the rate law for a global reaction step must be determined experimentally. For example the rate law for the gas phase reaction $H_2 + Br_2 = 2HBr$ can be expressed as

$$\frac{d[HBr]}{dt} = \frac{k[H_2][Br_2]^{1.5}}{[Br_2] + k'[HBr]}$$

meaning that the reaction is first order in H_2 but has no defined order in Br_2 or HBr. Clearly this is an example of a non-elementary reaction, whose elementary steps have been deeply discussed in the literature [84].

The integration of the rate law of a first order reaction

$$-\frac{d[A]}{dt} = k[A]$$

$$\int_{[A]_0}^{[A]} \frac{d[A]}{[A]} = -k \int_0^t dt$$

$$\ln([A]/[A]_0) = -kt$$

leads to an expression for the concentration of A at a given time expressed as

$$[A] = [A]_0 \exp(-kt)$$

Integrating the rate laws of second order reactions such as $2A \rightarrow products$ and $A + B \rightarrow products$ leads to the following expressions for determining $A(t)$ and $B(t)$

$$[A]_t = \frac{[A]_0}{1 + kt[A]_0}$$

$$\frac{1}{[B]_0 - [A]_0} \ln \frac{[B]_t[A]_0}{[A]_t[B]_0} = kt$$

While this section highlighted the dependence of rate laws on the concentrations of reactants and on the rate constant, the next section will discuss the temperature dependence of k.

2.2.2 Temperature Dependence of the Rate Constant

The relationship between the reaction rate constant k and temperature was experimentally investigated by Van't Hoff [85] and Arrhenius [86] late in the 19th century. Arrhenius deduced that a plot of $\ln(k)$ versus $1/T$ showed a linear dependence as reported in the linearized Arrhenius equation

$$\ln(k) = \ln(A) - E_A/RT$$

where R is the ideal gas constant (1.987 $cal\ mol^{-1}K^{-1}$) and T is the temperature. The parameters A and E_A were found to be constant for a given chemical reaction. The former is the frequency factor and has the same unit as the rate constant k. The latter was termed the activation energy of the reaction with units of molar energy ($cal\ mol^{-1}$). The Arrhenius expression is usually given in its exponential form as

$$k = A \exp(-E_A/RT)$$

The exponential factor $\exp(-E_A/RT)$ is also known as the Boltzmann factor, a distribution function describing the fractional population of reactive species with sufficient energy to overcome the reaction barrier at a given temperature. This factor ranges between 0 and 1, moving from infinitely low to infinitely high temperature.

Over temperature ranges wider than 100 K, the majority of chemical reactions show non-linearity. The so-called modified Arrhenius expression adds a curvature term to the non-modified expression given above

$$k = A\,T^n \exp(-E_A/RT)$$

The Arrhenius parameters A, n, E_A beside representing a rate constant over a wide temperature range are the key inputs of kinetic models. The Arrhenius expression is often referred to as an empirical correlation, where A, n, E_A are determined from fitting.

2.2.3 Pressure-Dependent Reactions and Fall-off

In the early part of the 20th century it was shown that in order for a unimolecular reaction $A \rightarrow products$ to proceed, the molecule A must undergo a non-reactive collision with another molecule to gain the necessary energy to form products. The inconsistency implicit in the need for a bimolecular collision process for a unimolecular reaction to proceed was solved by Lindemann [87] proposing the following mechanism. A molecule A undergoes collision with another molecule M (bath gas) forming an energized molecule A^*through the *thermal activation* process:

$$A + M \overset{k_1}{\rightarrow} A^* + M$$
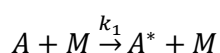
k_1 is the rate constant for the collisional activation in the form

$$k_1 = Z_{AM}\exp(-E_0/kT)$$

where Z_{AM} is the rate of collision of A with M and the Boltzmann factor defines the likelihood that the collision supplied sufficient energy to overcome the barrier E_0.

The fate of the molecule A^* is then twofold, it can be deactivated with another *third body* collision

$$A^* + M \overset{k_{-1}}{\rightarrow} A + M$$
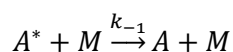
or it can react to form products:

$$A^* \overset{k_2}{\rightarrow} Products$$

The theory was proved to be wrong when the model was compared with experiments. Reasons behind the failure were mostly related to the simplistic assumption of the single step activation/deactivation process. However the idea of Lindemann provided the basis for further developments such as the Rice-Ramsperger-Kassel (RRK), Quantum-Rice-Ramsperger-Kassel (QRRK) and ultimately Rice-Ramsperger-Kassel-Marcus

(RRKM) theories, which are nowadays the standards in modeling pressure-dependent single channel reactions. A more detailed description of QRRK and RRKM will be given in Section 4.3.

To determine the rate of formation of products one should know $[A^*]$

$$\frac{d[P]}{dt} = k_2[A^*]$$

which is formed by the activation process and consumed partly by the deactivation and partly by the reaction to products

$$\frac{d[A^*]}{dt} = k_1[A][M] - (k_{-1}[A^*][M] + k_2[A^*])$$

The concentration of the third body $[M]$ is that of the bath gas in the system and from the ideal gas equation $[M] = n/V = p/RT$.

Assuming that A^* has a short lifetime compared to A, the steady state approximation allows one to write

$$\frac{d[A^*]}{dt} = k_1[A][M] - (k_{-1}[A^*][M] + k_2[A^*]) = 0$$

therefore

$$k_1[A][M] = k_{-1}[A^*][M] + k_2[A^*]$$

$$[A^*] = \frac{k_1[A][M]}{k_{-1}[M] + k_2}$$

Further simplification can be obtained by considering two limiting cases: infinitely high pressure and infinitely low pressure. In the first case $[M]$ is high, therefore $k_{-1}[M] \gg k_2$ as collisional deactivation becomes much faster than chemical reaction. $d[P]/dt$ can be written as:

$$\frac{d[P]}{dt} \approx \frac{k_1 k_2 [A][M]}{k_{-1}[M]} = \frac{k_1 k_2 [A]}{k_{-1}}$$

meaning that the rate constant is no longer dependent on the bath gas concentration, and the reaction becomes independent of pressure as it is in its *high pressure limit*. In other words activation and deactivation reach an equilibrium where a steady state population of A^* is achieved and the unimolecular reaction of A^* is the rate limiting step. The rate constant for the formation of products is therefore

$$k_\infty = \frac{k_1 k_2}{k_{-1}}$$

with units of inverse time, thus the reaction is first order in $[A]$. The Lindemann mechanism rationalizes the perplexity of a bimolecular process obeying first order kinetics.

At infinitely low pressures $k_2 \gg k_{-1}[M]$ leading to

$$\frac{d[P]}{dt} \approx \frac{k_1 k_2 [A][M]}{k_2} = k_1 [A][M]$$

The formation of products is now limited by the rate of activation of A and the reaction becomes second order overall and reaches its *low pressure limit*. In other words, at infinitely low pressures the rate of consumption of A^* through chemical reaction is much faster than deactivation. Technically every molecule of A^* that is formed will react to form products with the rate limiting step being the formation of A^*.

In between the two limiting cases, the rate of formation cannot be described by either equation: the reaction is in the *fall-off* regime. *Figure 9* shows the pressure dependent behavior of unimolecular reactions. The example is that of the unimolecular initiation reaction of propionaldehyde (propanal) $C_2H_5CHO=C_2H_5+HCO$ as calculated by Pelucchi et al. [72] at T=1600 K. At 10 atm for example the fall-off effect results in a unimolecular rate constant which is ~18% lower than the high pressure limit. At 2000 K and 10 atm pressure this effect increases to ~45 %. For pressure below 1 atm, of limited interest for combustion applications, the omission of a proper fall-off treatment could result in ~1-3 orders of magnitude overestimation of the rate constant. The reason behind a more pronounced effect at higher temperatures and lower pressures is that at high temperatures the rate of chemical reaction is extremely fast due to high thermal energy. Therefore, the population of A^* depletes quickly, but, due to low pressure, the collisional activation of A to A^* is not fast enough to re-populate those molecules with high enough energy to react.
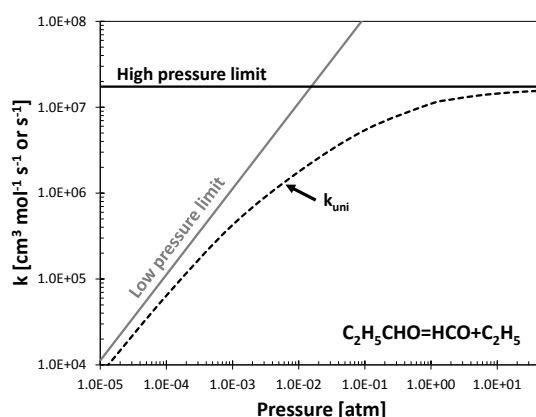
Figure 9: Unimolecular rate constant for the reaction $C_2H_5CHO=C_2H_5+HCO$ [72] as a function of pressure at 1600 K.

At lower temperatures, reactions exhibit less fall-off firstly because the population of A^* above the energy threshold is quite small due to the low temperature. Moreover, this small population is restored quickly by

collisional activation. In other words, in the high pressure limit the average energy of dissociating molecules is proportional to T. At lower temperatures the average energy is lower and therefore the dissociation is lower, allowing the maintainance of the thermal population through the collisional activation process. *Figure 10* shows the temperature dependence of the rate constants for the reaction in Figure 9 at different pressures.
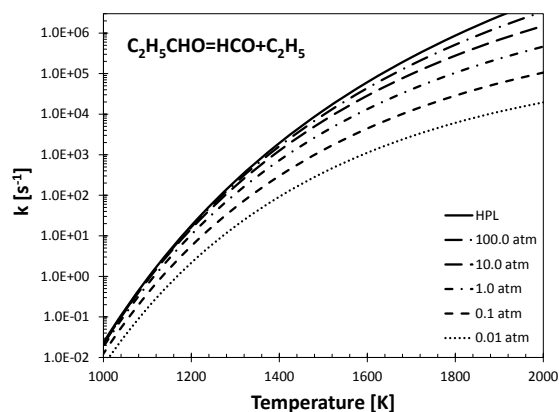
Figure 10: Unimolecular rate constant for the reaction C₂H₅CHO=C₂H₅+HCO [72] as a function of temperature.

The competition between collisional and chemical processes discussed above is not limited to unimolecular reactions, but is of concern also for many bimolecular reactions such as radical-radical recombination or radical-molecule interactions (e.g. addition reactions). In such cases, the formation of a new chemical bond releases potential energy which must be conserved within the system. The chemical activation involves the formation of a ro-vibrationally excited molecule as

$$A + B \xrightarrow{k_1} AB^*$$

$$AB^* \xrightarrow{k_{-1}} A + B$$
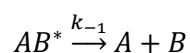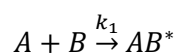
The excited molecule can undergo unimolecular reaction via k_{-1} or isomerize or dissociate to other products

$$AB^* \xrightarrow{k_2} Products$$
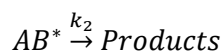
Thermalization, i.e. the collision with a third body removing excess energy from the adduct, is also possible

$$AB^* + M \xrightarrow{k_3} AB + M$$
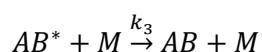
The mechanism is similar to the unimolecular process described above, resulting in another class of pressure dependent reactions.

Accounting for pressure dependent reactions is important in chemical kinetic modelling as virtually all the reactions display this behavior. Methods to determine $k(T,p)$ will be discussed in Section 4.3.

2.2.4 Thermodynamics and Chemical Equilibria

Thermodynamics is the study of energy transformation, heat and work. Kinetics and thermodynamics are unavoidably linked and our ability to build a predictive kinetic model of combustion is as much dependent on the latter as on the former. The second law of thermodynamics states that every closed, isolated system will approach an "equilibrium" state in which its properties are independent of time [50]. The fundamental thermodynamic properties of interest are the enthalpy (H), entropy (S) and heat capacity $(C_p$ or $C_v)$ that need to be determined for any species involved in the kinetic mechanism. Knowing these properties effectively characterizes the equilibrium state. Thermodynamics cannot tell anything about the time required to reach the equilibrium state, or about the evolution of the system. These problems in fact are a matter of chemical kinetics describing properties as a function of time.

The enthalpy of a system is obtained as

$$H = U + pV$$

which for ideal gases can also be written as

$$H = U + nRT$$

where U is the internal energy, p the pressure of the system and V the volume. The internal energy is a measure of the kinetic and potential energy stored in all the components (atoms and molecules) of the system. The second term stands for the energy to be supplied to bring n moles of gas of volume V, pressure p and temperature T to its present state from the reference state. Therefore the standard enthalpy of formation ΔH_f of any chemical species is the energy required to form one mole of that species from the elements in their reference state. ΔH_f is also used to compute the enthalpy of the reaction j as:

$$\Delta H_{r,j} = \sum_{i=1}^{N} \nu_{i,j} \, \Delta H_{f,i}$$

where N is the number of species (products and reactants) involved in the reaction, according to a certain stoichiometry represented by the coefficient ν. The heat of reaction is the difference between the enthalpy of the products and that of reactants. If a reaction forms products that are enthalpically more stable than reactants $(\Delta H_{r,j} < 0)$ the reaction is termed exothermic, otherwise $(\Delta H_{r,j} > 0)$ it is endothermic and energy must be supplied for the reaction to happen. As in *Figure 11* most chemical reactions proceed through a reaction barrier, which, to a large extent, relates to the activation energy E_a qualitatively introduced in

Section 2.2.2. This barrier lies enthalpically above both reactants and products, therefore $\Delta H_{r,j}$ already provides an estimate of the minimum barrier of the reaction. Exothermic reactions (reactant to product in *Figure 11*) will proceed through smaller barriers compared to the reverse reaction going from products to reactants.
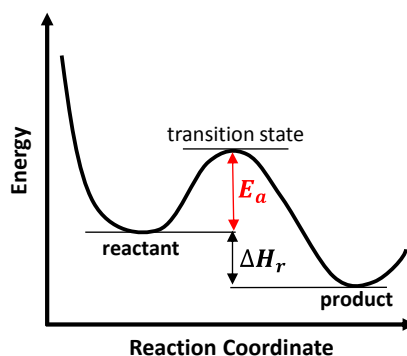
Figure 11: Energy-reaction coordinate diagram for an exothermic unimolecular reaction.

Considering barrierless reactions of relevance in combustion systems like radical-radical recombination reactions ($A + B \rightarrow AB$) the enthalpy is clearly the barrier associated with the corresponding reverse unimolecular dissociation step ($AB \rightarrow A + B$). The energy diagram for a typical barrierless recombination reaction is reported in Figure 12.

Another typical example of the relevance of reaction enthalpy refers to the bond dissociation energy (BDE), a standard measure of the strength of a chemical bond. Its determination is of key importance to understanding which reaction sites would be more likely to undergo unimolecular cleavage or free radical attack. It is defined as the molar enthalpy required to homolytically break a bond. For the reaction reported in Figure 12 the BDE coincides with the energy change required for the reaction $AB \rightarrow A + B$ to proceed.
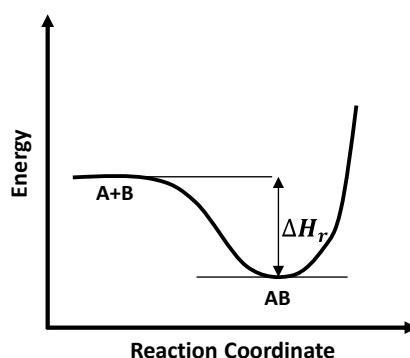
Figure 12: Energy-reaction coordinate diagram for a radical-radical recombination reaction.

This feature is frequently exploited by kinetic modelers in relationships such as Evans-Polanyi [88] that are useful for rate rule extrapolations [89].

Beside the kinetic importance of the reaction enthalpy other important parameters in combustion modelling are directly related to this thermodynamic property. The heat of combustion of a fuel-oxidizer mixture or the adiabatic flame temperature are the primary examples.

Another essential thermodynamic property is the entropy, S which is the measure of the disorder of a system. The physical meaning of entropy mostly relates to the concept of a *spontaneous change*, which is a process occurring without any work being done. In any spontaneous process the system will naturally tend to be more disordered, or chaotic. The entropy change, ΔS, reflects this spontaneous evolution. Similarly to the enthalpy change, the entropy change is defined as

$$\Delta S_{r,j} = \sum_{i=1}^{N} \nu_{i,j} \, \Delta S_{f,i}$$

At fixed energy, a spontaneous process requires $\Delta S_{r,j} > 0$, therefore reactions proceeding with a net increase in entropy will tend to be favored over others.

Enthalpy and entropy can be combined to obtain another key property, the Gibbs Free Energy, G. By definition the Gibbs Free Energy change is

$$\Delta G_f = \Delta H_f - T\Delta S_f$$

It measures the energy available in the system to do work (ΔH_f) less the quantity of energy stored in random motion of the molecules ($T\Delta S_f$). Once again the Gibbs Free Energy change in a reaction can be defined as

$$\Delta G_{r,j} = \sum_{i=1}^{N} \nu_{i,j} \, \Delta G_{f,i}$$

Consider now a simple reversible reaction j where k_f and k_r are the forward and backward rate constants, respectively

$$aA + bB \rightleftharpoons qQ + rR$$
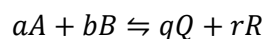
Assuming this reaction happens in a closed system, it will reach an equilibrium state where the concentrations of reactants and products do not vary with time:

$$-\frac{1}{a}\frac{d[A]}{dt} = -\frac{1}{b}\frac{d[B]}{dt} = \frac{1}{q}\frac{d[Q]}{dt} = \frac{1}{r}\frac{d[R]}{dt} = 0$$

As previously discussed, kinetics tell us the time required for this equilibration to occur, but the final concentrations are determined by the equilibrium constant, K_p

$$K_p = \prod_{i=1}^{N} \left(a_i(T, p, p_r, x)^{\nu_i} \right)$$

where a_i is the *activity*, i.e. the ratio between a species *fugacity* in the specific condition of T, p and composition x of the system and an arbitrary reference state at the same temperature and at a reference pressure p_r. Considering a perfect gas in an ideal mixture the fugacity is its partial pressure $p_i = px_i$, and therefore in the specific reaction j

$$K_p = \prod_{i=1}^{N} px_i^{\nu_i} = p^{\Delta n} \frac{x_Q{}^q \, x_R{}^r}{x_A{}^a \, x_B{}^b}$$

where $\Delta n = q + r - a - b$ is the change of mole in the reaction.

In turn the equilibrium constant for the reaction is related to the Gibbs Energy change of the reaction

$$K_p = \exp\left(\frac{-\Delta G_R(T)}{RT} \right)$$

At any given temperature, knowing the enthalpy and entropy change, it is possible to determine the equilibrium constant and therefore the final composition.

Moreover, knowing the rate constant for either the forward or reverse direction, from the thermodynamic properties it is possible to compute the rate constant for the opposite process, according to the principle of *microscopic reversibility*

$$K_p = \frac{k_f}{k_r}$$

Figure 13 shows the forward and reverse rate constants of the reaction $CO+OH=CO_2+H$. As suggested by the expression for $\Delta G_r(T)$, when $\Delta G_r = 0$, $K_p = 1$ and $k_f = k_r$.
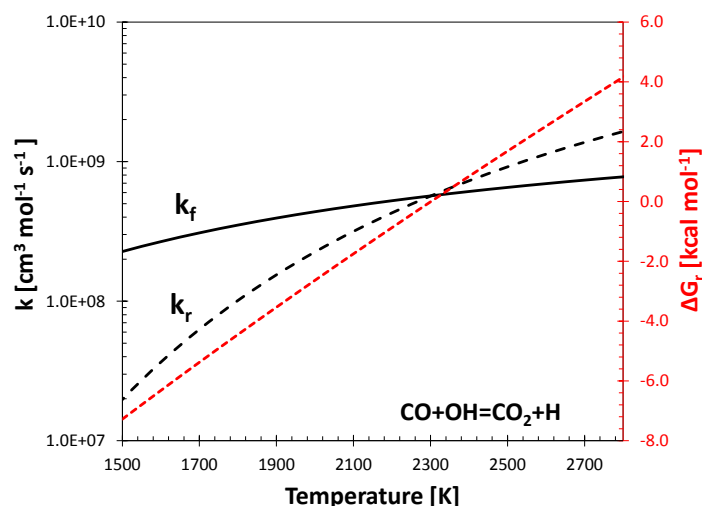
Figure 13: Black lines are forward (solid) and reverse (dashed) rate constant for CO+OH=CO₂+H as in POLIMI mechanism [40], red line is $\Delta G_R(T)$.

Sometimes analogy rules make extensive use of the microscopic reversibility principle. For instance the decomposition of radicals through β-scission reaction, corresponds to the reverse elementary step of radical addition to a double bond. Once the high pressure limit rate constant is systematically defined for different systems involving radical addition to olefins (e.g. $CH_3+C_3H_6 \rightarrow n$-$C_4H_9$) [90] it is possible to obtain the decomposition rate constant of a similar system (e.g. n-$C_5H_{11} \rightarrow CH_3+1$-$C_4H_8$) by assigning the rate parameters in the addition direction (i.e. CH_3+1-$C_4H_8 \rightarrow n$-C_5H_{11}).

The heat capacity, C, is the remaining thermodynamic property needed for the development of a kinetic mechanism. C measures the responsiveness of a system to the supply of heat in terms of temperature variation. In particular, it tells us the heat energy required to change the temperature of one mole of a substance by one degree. Two analogous definition are commonly used, because *heat*, in contrast with enthalpy, entropy and Gibbs free energy, is not a *state function,* and thus depends on the type of transformation. The first definition is the constant pressure heat capacity defined as

$$C_p = \left(\frac{\partial H}{\partial T}\right)_p$$

and the second is the constant volume heat capacity

$$C_v = \left(\frac{\partial U}{\partial T}\right)_v$$

The relation between the two definitions is that

$$C_p - C_v = R$$

The heat capacity is also used to extrapolate enthalpy and entropies to conditions different from the reference state through the following relations

$$\Delta H_f(T) = \Delta H_{f,0}(T_0) + \int_{T_0}^{T} C_p(T)dT$$

$$\Delta S(T) = \Delta S_0(T_0) + \int_{T_0}^{T} \frac{C_p(T)}{T}dT$$

The thermodynamic properties for every species included in the kinetic mechanism are traditionally estimated through group additivity methods [49, 50] implemented in software such as THERM [91] or THERGAS [92]. This programs can generate thermochemistry of radicals and stable molecules in NASA format, providing $C_p(T)$, $\Delta H_f(298\ K)$ and $\Delta S_f(298\ K)$ as inputs.

Theoretical chemistry provides high accuracy predictions of thermodynamic properties[93-95]. The powerful coupling of theory and experimental data is expressed in what nowadays constitutes the reference for thermochemical data: the Active Thermochemical Tables (ATcT) [95-99]. The state-of-the-art theoretical data and all the available experimental measurements constitutes the underlying Thermochemical Network (TN) to determine enthalpies of formation, Gibbs energies of formation, bond dissociation energies, reaction enthalpies, etc. for stable, reactive, and transient chemical species.

From the point of view of a systematic and hierarchical approach to the kinetic modelling of combustion processes, the *ATcT/databases* guided update of group properties for use in THERM and similar software seems to be a great value practice. An interesting example is the work of Burke et al. showing the promising perspectives of such an approach in generating quite accurate estimates of the properties of higher molecular weight species. The optimization of group properties based on experimental and theoretical data for C_1–C_2 species provided good estimates when extended to C_4 species [100].

2.2.5 Transport Properties

Shock-tube, perfectly-stirred, plug-flow and batch reactors are commonly used for kinetic mechanism validation as design and construction features ensure kinetically controlled regimes. However other phenomena that might occur in reacting flows such as diffusion, convection and conduction can have similar timescales to the kinetic phenomena. When such phenomena are accounted for in the mass, energy and momentum equations some other properties such as diffusion coefficients, viscosities, thermal conductivities and thermal diffusion need to be estimated for any species in the mechanism. The common example for kinetic modelers is the study of laminar flames, to determine the laminar flame speed or

reproduce speciation measurements. Pursuing the goal of comprehensive kinetic mechanisms requires the correct assessment of flame chemistry as a key target, despite the predominance of the core C_0-C_3 chemistry for laminar flame propagation has been largely discussed in the literature [101]. The reader is referred to standard literature monographs [102, 103] for further details.

	Index	ε/k_B (K)	σ (Å)	μ (D)	α (Å³)	Z_{rot}
H	0	145.000	2.050	0.000	0.000	0.000
H_2	1	38.000	2.920	0.000	0.790	280.000
H_2O	2	572.400	2.605	1.844	0.000	4.000

Table 3: Example of transport coefficient data to be included for kinetic simulations.

Table 3 shows an example of transport data input file. The first term represents the name of the species, the second column contains an index which is 0 for atomic species, 1 for a linear molecule and 2 for a non-linear molecule. The second term ε/k_B is the Lennard-Jones well-depth and σ is the hard-sphere collision diameter. These parameters are used to calculated the Lennard-Jones potential [104] which describes the forces acting between two molecules. Longest range interactions are accounted for with the addition of a third term together with a third parameter: the dipole moment μ. The Stockmayer potential [105] thus obtained reduces to the Lennard-Jones potential if, in a binary mixture, one or both the dipole moments are zero. α is the polarizability and the final term is the temperature-dependent rotational relaxation collision number at 298 K.

As recently reported by Brown and coworkers [106] the combustion community has invested much more in improving chemical mechanisms through more and more accurate assessment of rate parameters and thermodynamic properties, but has not focused with the same intensity on the treatment of molecular transport. However, as already discussed in the literature [101, 107] fuel/air flame propagation is very sensitive to N_2 properties, and mostly to O_2-N_2 binary diffusion coefficient. A significant role is also played by H_2-N_2 binary coefficients, mostly due to the relevant backward diffusion of H radical towards the unburned gas mixture, but no sensitivity is found to the fuel properties.

2.3 Kinetic Modeling Software: OpenSMOKE++

The kinetic simulations presented in *this thesis* where performed with the OpenSMOKE++ code of Cuoci et al. [66]. The main features of relevance for the following discussion are briefly summarized in this Section.

OpenSMOKE++ is an open-source framework conceived to perform numerical simulations of combustion processes involving large size detailed kinetic mechanism. It is written in C++ according to the Object-

Oriented Programming. The modular approach based on classes representing the components of a simulation (gas mixture, reactors, kinetic models, ordinary differential equations integrators etc.) allows extensions and modifications to meet the needs of the users.

Figure 14 shows a schematic diagram of the different portions of the OpenSMOKE++ Suite. The main components of the kinetic models discussed in the previous Section 2.2 are: the kinetic mechanism including every reaction with its kinetic parameters (A, n, E_a) in the modified Arrhenius form, the thermodynamic data in the NASA polynomial format [108] and the transport properties for every species computed according to the standard kinetic theory [102]. The kinetic pre-processor reads, checks and analyzes kinetic mechanisms in the standard CHEMKIN® format [65].The mechanism is written in a XML format and is ready to be used by the other solvers. The collection of solvers to simulate chemical reactors includes: batch, perfectly stirred, plug-flow reactors and shock-tubes. They all need the same pre-processed kinetic mechanism together with an input file specifying the operating conditions (gas mixture composition and conditions, reactor conditions and parameters, ODE parameters, output options etc.). The simulation results are saved both in XML and in ASCII format. The XML file can be then used in the graphical post-processor to directly plot profiles, or read kinetic analyses results.
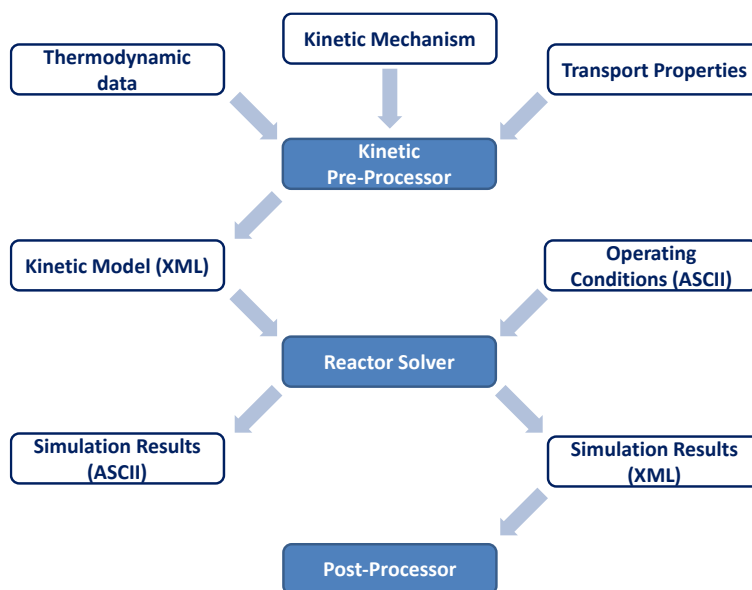
Figure 14: Structure of the OpenSMOKE++ Suite, adapted from [66].

Some useful features of the Kinetic Pre-Processor include a consistency check on the thermodynamic properties, the reaction stoichiometry and for the existence of duplicate reactions.

As mentioned above, the thermodynamic properties described in Section 2.2.4 are written in the thermodynamic data file according to the NASA format which consists of two sets of 7 coefficients. The molar specific thermodynamic properties for a species i as functions of temperature are expressed as:

$$\frac{\tilde{C}_{p,i}}{R} = a_{i,1} + a_{i,2}T + a_{i,3}T^2 + a_{i,4}T^3 + a_{i,5}T^4$$

$$\frac{\tilde{H}_i}{RT} = a_{i,1} + \frac{a_{i,2}}{2}T + \frac{a_{i,3}}{3}T^2 + \frac{a_{i,4}}{4}T^3 + \frac{a_{i,5}}{5}T^4 + \frac{a_{i,6}}{T}$$

$$\frac{\tilde{S}_i}{R} = a_{i,1}\ln T + a_{i,2}T + \frac{a_{i,3}}{2}T^2 + \frac{a_{i,4}}{3}T^3 + \frac{a_{i,5}}{4}T^4 + a_{i,7}$$

The two sets of coefficients are used to determine the properties in two adjacent temperature intervals. Obviously the continuity over the two intervals must be guaranteed, and if the relative error exceeds 0.1% the user is asked to modify the parameters. Such modifications might also positively affect the integration of the ODE system as discussed in Cuoci et al. [66].

Table 4 lists the coefficients of the NASA polynomials used to calculate the thermodynamic properties of molecular hydrogen as function of temperature.

H_2		T_{min}=300 K	T_{max}=4000 K	T_{med}=1000 K
2.991422E+00	7.000644E-04	-5.633828E-08	-9.231578E-12	1.582752E-15
-8.350335E+02	-1.355106E+00	3.298124E+00	8.249441E-04	-8.143015E-07
-9.475434E-11	4.134872E-13	-1.012521E+03	-3.294094E+00	

Table 4: NASA coefficients for the thermodynamic properties of H₂ as in the POLIMI mechanism.

Other features include the computation of the kinetic parameters for the reverse rate constants together with explicit ΔG_r, ΔH_r, ΔS_r and the equilibrium constant for every reversible reaction in the mechanism.

A CHEMKIN® [65] format mechanism contains a list of elements

```
ELEMENTS
C
H
CL
O
N
AR
HE
END
```

a list of species

```
SPECIES
HE        AR        N2        O2        H2
H2O       H2O2      CO        CO2       CH2O
```

```
CH4      CH3OH    CH3OOH   C2H2     CH2CO
...
END
```

and the list of chemical reactions with the respective kinetic parameters A, n and E_a with cm³, calories and mole based units

```
REACTIONS
H+O2=OH+O              .9600E+15    -.200   16625.0
O+H2=OH+H              .4330E+14     .000   10000.0
OH+HO2=H2O+O2          .5000E+14     .000    1000.0
...
END
```

Several options can be adopted to define a chemical reaction. For instance reversible reactions are written as

```
A+B=C              A          n          E_a
```

while for irreversible the syntax is

```
A+B=>C             A          n          E_a
```

The most common options to write pressure-dependent rate constants are the Troe formalism and the logarithmic interpolation (PLOG).

The effective rate constant of a pressure-dependent reaction derives from the combination of the high ($k_{\infty,j}^f$) and the low pressure limit ($k_{0,j}^f$) rate constants discussed in Section 2.2.3:

$$k_j^f = k_{\infty,j}^f \frac{P_r^j}{1 + P_r^j} F_j^{PD}$$

where F_j^{PD} is a blending function and P_r^j is the reduced pressure:

$$P_r^j = \frac{k_{0,j}^f [M_{eff}]}{k_{\infty,j}^f}$$

Three formalism for estimating F_j^{PD} are allowed in OpenSMOKE++. In the most common Troe approach

$$\log F_j^{PD} = \left[1 + \left(\frac{\log P_r^j + c_j}{n_j - d_j(\log P_r^j + c_j)} \right)^2 \right]^{-1} \log F_j^{cent}$$

where

$$c_j = -0.4 - 0.67 \log F_j^{cent}$$

$$n_j = 0.75 - 1.27 \log F_j^{cent}$$

$$d_j = 0.14$$

$$F_j^{cent} = (1 - \alpha_j)e^{-\frac{T}{T_j^{***}}} + \alpha_j e^{-\frac{T}{T_j^*}} + \alpha_j e^{-\frac{T_j^{**}}{T}}$$

Despite the lengthy expressions, α_j, T_j^*, T_j^{**}, T_j^{***} are the specific parameters of each pressure dependent reaction. An example is reported below: in the first line the chemical equation for the third body reaction is given together with the parameters for $k_{\infty,j}^f$, the second line reports the low pressure limit $k_{0,j}^f$ and the third line contains the four coefficients to determine F_j^{PD}. The third body efficiencies for different bath gases are reported in the last line.

```
OH+OH(+M)=H2O2(+M)          .7400E+14   -.370          .0
LOW/   .1300E+19    -.900   -1700.0/
TROE/   .7346 94.00 1756. 5182./
H2/2.0/ H2O/6.0/ CH4/2.0/ CO/1.5/ CO2/2.0/ C2H6/3.0/ AR/.7/ N2/.9/
```

These collisional efficiencies represent the enhancing effect due to the presence of species other than those directly participating in the reaction. This effect is obtained according to an "effective concentration" through which it is possible to compute M_{eff} as

$$M_{eff} = \sum_{i=1}^{N_{species}} \alpha_{i,j} \, C_i$$

As reviewed recently by Klippenstein [48] relevant progresses in theoretical predictions bring to light some limitations in current modeling software. Many of these shortcomings are related to a correct and *a priori* determination of collisional efficiency. Recent studies highlighted in fact how reference mechanisms from the literature, failed in predicting oxidation data in highly diluted, MILD combustion conditions [109]. Moreover, the Troe parametrization has fitting accuracy (~50-90 % for widely studied reactions such as $\dot{H}+O_2+M=H\dot{O}_2+M$ [110]) which is often lower than that of theoretical predictions, making highly accurate estimations of rate constant worthless.

Other formalism for expressing F_j^{PD} include the SRI and the Lindemann approaches, not further discussed herein.

The PLOG formulation describes the pressure dependence of a rate constant as an interpolation of reaction rates specified at individual pressures. For a given reaction the usual Arrhenius parameters are estimated for a set of P_k pressures. This is the typical output obtained from some Master Equation codes, as discussed in Section 4.3.4. For a pressure between P and P_k the rate constant can be obtained as:

$$\ln k_j^f = \ln k_{j,k}^f + (\ln k_{j,k+1}^f - \ln k_j^f)\frac{\ln P - \ln P_k}{\ln P_{k+1} - \ln P_k}$$

An example of such expression is reported below:

```
C7H7+O2=C7H7O2   5.589E+07     1.250    -1376.06
PLOG / 0.1       8.603E+33    -7.457     4997.99/
PLOG / 1.0       4.203E+23    -3.967     2719.75/
PLOG / 10.0      1.621E+17    -1.817     1234.19/
PLOG / 100.0     7.636E+13    -0.703      472.42/
PLOG / 1000.0    8.879E+10     0.251     -317.65/
```

The first line reports the high pressure limit rate constant from which the different rate constants at different pressure are derived. Despite being reported this is never used in kinetic simulations. If the pressure being simulated is below the range of pressures defined, the lowest pressure rate constant will be used and *vice versa* for the highest pressure.

Despite a better accuracy compared to the Troe formalism, the PLOG formulation in present kinetic solvers do not allow to provide any information on different colliders and their mixtures. The modular structure of OpenSMOKE++ already allowed the implementation of more accurate expressions, which will be included in an upcoming release.

As reported in Figure 14, once the kinetic mechanism is interpreted, the XML file can be used in any OpenSMOKE++ solver. Such solvers are independent programs that, in addition to the kinetic model, need the specification of operating conditions (temperature, pressure, mixture composition, geometry, residence time etc.) listed in an input ASCII file. Some of the solvers available in the current version of OpenSMOKE++ and typically used for kinetic mechanism validations are reported in Table 5 together with different specific features available. Other more recent solvers include microgravity droplet and laminar flamelets simulations.

Reactor type	Mode
Batch Reactor	Isothermal, Non-Isothermal/Adiabatic, Constant Volume, Constant Pressure
Perfectly Stirred Reactor	Isothermal, Non-Isothermal, Constant Pressure, Heat Exchange

Plug Flow Reactor	Isothermal, Non-Isothermal, Temperature Profile, Heat Exchange, Constant Pressure, Pressure Drop
Shock Tube Reactor	Before and After Incident Shock, After Reflected Shock
Premixed Laminar Flame 1D	Flame Speed, Burner Stabilized

Table 5: List of ideal reactors solvers available in the current version of OpenSMOKE++ and reactor modes typically used in kinetic mechanisms validation.

The mathematical details of the different models are not discussed herein and can be found in Cuoci et al. [66].

The OpenSMOKE++ framework also provides several useful tools for the kinetic analysis, which, as discussed in Section 1.3, is a key part of the iterative process of development and validation of a kinetic mechanism. The typical examples are the sensitivity analysis (SA) and the rate of production analysis (ROP).

The sensitivity analysis qualitatively and quantitatively highlights how the solution of the governing equations is influenced by the model parameters, i.e. the kinetic rate constants. The numerical method used to calculate the sensitivity coefficients was already discussed [66] and will be briefly reiterated here.

The numerical method exploits the linearity of the differential equations governing the evolution of such coefficients, regardless of any non-linearities in the problem itself.

Defining y as the N unknowns and N_P parameters α (the kinetic parameters), the system under investigation is generally defined by the following system of ordinary differential equations (ODE):

$$\frac{d\boldsymbol{y}}{d\xi} = \boldsymbol{f}(\boldsymbol{y}, \xi; \boldsymbol{\alpha})$$

The first-order sensitivity coefficients is defined as

$$s_{i,j} = \frac{\partial y_i}{\partial \alpha_j}$$

where j refers to the variable and i to the parameter. For large kinetic mechanisms ($N = 1000$ species and $N_P = 10000$) the number of coefficients can be equal to 10^8. Therefore including the vector $\boldsymbol{s_j} = \left[\frac{\partial y_1}{\partial \alpha_j}, \frac{\partial y_2}{\partial \alpha_j} \dots \frac{\partial y_N}{\partial \alpha_j}\right]$ and differentiating the previous ODE with respect to the parameters we obtain N_P additional terms in the ODE system.

$$\begin{cases} \dfrac{d\boldsymbol{s}_j}{d\xi} = \boldsymbol{J}\boldsymbol{s}_j + \dfrac{\partial \boldsymbol{f}}{\partial \alpha_j} \\ \boldsymbol{s}_j(\xi_0) = \boldsymbol{0} \end{cases}$$

where $\boldsymbol{J}$ is the Jacobian matrix of the ODE system, i.e. $J_{ij} = \dfrac{\partial f_i}{\partial y_j}$. Overall it is possible to solve N_P independent systems instead of the whole ODE system. Of course the computational cost of this would be prohibitive for large detailed mechanisms. A further simplification involves the solution of the sensitivity equations separately but sequentially with the model equations. Defining the step of integration $\Delta \xi = \xi_{n+1} - \xi_n$ for the model equations, the sensitivity equations are solved over the same step adopting the backward Euler method obtaining N_P independent linear systems where the unknowns are $\boldsymbol{s}_j^{n+1}$ as

$$(\boldsymbol{I} - \Delta\xi \boldsymbol{J}^{n+1})\boldsymbol{s}_j^{n+1} = \boldsymbol{s}_j^{n+1} + \Delta\xi \left.\frac{\partial \boldsymbol{f}}{\partial \alpha_j}\right|^{n+1} \quad j = 1, \dots, N_P$$

where $\boldsymbol{I}$ is the identity matrix. Since the sensitivity equations and the model equations are decoupled it is possible and often convenient to solve them in parallel or on distributed or shared memory.

Finally, the raw sensitivity coefficients are normalized in the form of logarithmic derivatives for direct use in analyses and comparisons:

$$\tilde{s}_{ij} = \frac{\partial \ln y_i}{\partial \ln \alpha_j} = \frac{\alpha_j}{y_i} s_{ij}$$

In some cases the sensitivity coefficients are more useful if normalized over the maximum value of each independent variable

$$\hat{s}_{ij} = \frac{\alpha_j}{\max y_i} s_{ij}$$

this avoids unreasonably high sensitivity coefficients due to numerical errors.

The rate of production analysis provides insights in reacting flow by determining the contribution of each reaction to the production and destruction rates of a species. As in [65] for each species i and reaction j it is possible to define a normalized production term C_{ij}^p and a normalized destruction term C_{ij}^d:

$$C_{ij}^p = \frac{\max\left(v_{ij}^f - v_{ij}^b, 0\right) r_j}{\sum_{k=1}^{N_R} \max\left(v_{ij}^f - v_{ij}^b, 0\right) r_k}$$

$$C_{ij}^d = \frac{\min\left(v_{ij}^f - v_{ij}^b, 0\right) r_j}{\sum_{k=1}^{N_R} \min\left(v_{ij}^f - v_{ij}^b, 0\right) r_k}$$

where v_{ij}^f is the stoichiometric coefficient of the reactant species in the forward direction and v_{ij}^b is that in the reverse direction. r stands for the reaction rate. It is always verified that $\sum_{j=1}^{N_R} C_{ij}^p = 1$ and $\sum_{j=1}^{N_R} C_{ij}^d = 1$

The results from the numerical simulations are available both in ASCII and XML format. The XML file can be used in the graphical post-processor to plot typical (x, y) profiles and kinetic analysis results.

2.4 Summary

This Chapter reviewed some theoretical and fundamental principles of chemical kinetics and thermodynamics, the core of any chemical kinetic models.

Summarizing, when developing a kinetic model it is necessary to:

1. Identify and define the reaction network responsible for the conversion of fuel and oxygen to products. While this step might be accomplished by an automatic mechanism generator, chemical intuition, experience and analogy serve as the basis for a complete characterization and also for a thorough understanding of the reacting flow.
2. Determine the thermodynamic functions for any species involved in the kinetic mechanism and fit them into NASA format polynomials.
3. Determine the transport properties for every species in the mechanism.
4. Estimate rate constants parameters for each reaction in the most accurate way. Theory, experimental measurements and analogy can guide the formulation of rules as discussed in different parts of *this thesis*.
5. Preserve at any cost the internal consistency reflecting the hierarchical and systematic nature of combustion. Particularly, when dealing with the modeling of large kinetic schemes for the simulation of complex reacting systems, it is important to accurately assess the relative importance of the different reaction channels characterizing a fuel's reactivity.

Unavoidably, this standard procedure has to be contextualized in the engineering approach to pyrolysis and combustion kinetics conceived and developed over the years at POLIMI [17, 43, 44, 101, 111]. The systematic, hierarchical and *application-oriented* nature behind the definition of reference kinetic parameters, the automatic generation and the simplification through lumping, makes the POLIMI kinetics framework more applicable to complex systems [112-116], without losing the kinetic detail essential to the understanding of combustion processes in real devices. The description of these features is the main topic of the next Chapter.

Chapter 3 – Kinetic Modelling of Hydrocarbon Pyrolysis and Oxidation and Lumping Technique

This Chapter discusses the general approach to the development of the POLIMI kinetic mechanism. Starting from the definition of reaction classes needed to describe the pyrolysis and oxidation of hydrocarbon fuels, their reference kinetic parameters (rate rules) are provided and discussed. The lumping technique used to tackle the size related issues of complex combustion kinetic mechanisms previously highlighted is also described.

3.1 Reaction Classes of Primary Propagation Reactions

The kinetic modelling of hydrocarbon pyrolysis has been a powerful tool for reactors and process design since the second half of the previous century [43, 117]. Since then, the correct prediction of product yields and performances achieved through a systematic characterization of the chemical kinetics phenomena allows optimal design and flexibility in systems whose complexity mainly derives from the variability in feedstocks and other operational criteria [43]. Although advances in computational, theoretical and experimental capabilities experienced over the years guided improvements and extensions, the systematicity of pyrolysis kinetics was already quite well understood.

Figure 15 shows the primary reactions of *n*-heptane (n-C_7H_{16}) pyrolysis. Clearly, beside possible extensions to fuel specific reaction classes, the same fundamental reaction network applies for any fuel.
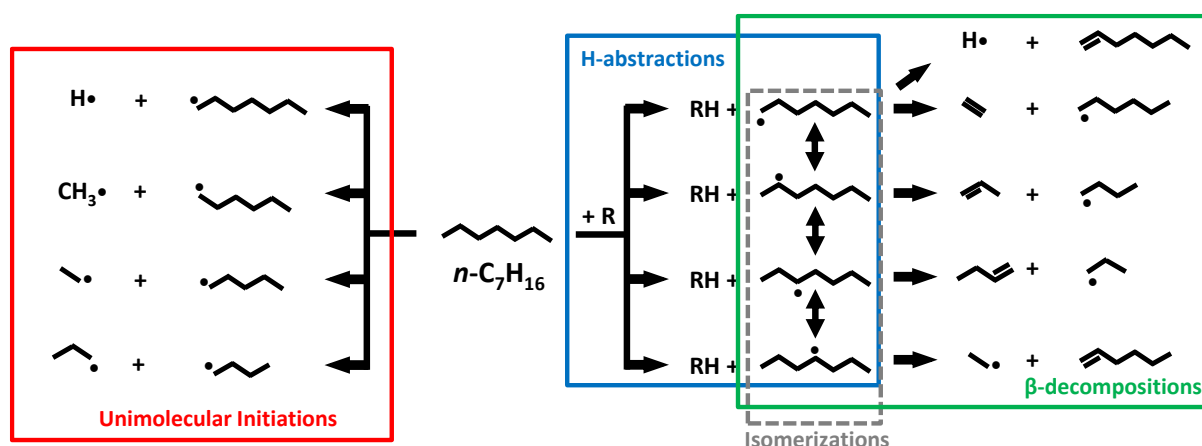
Figure 15: Primary pyrolysis reaction classes for n-heptane pyrolysis.

1. Unimolecular Initiation reactions: the fuel molecule undergoes C–C or C–H bond fission.

$$Fuel \rightarrow R \cdot + R' \cdot$$

$$Fuel \rightarrow R \cdot + H \cdot$$
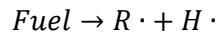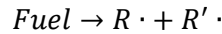
The net result is the formation of two radical species giving rise to the formation of the radical pool. This extremely endothermic process (i.e. on the order of ~80-90 kcal/mol) requires very high temperatures (T>~1200 K) to sensibly contribute to the fuel consumption. However, it is sufficient to form a limited amount of radicals to activate the chain degeneracy at any temperature.

The relevance of the reverse barrierless radical-radical recombination is limited to resonance-stabilized radicals (e.g. allyl, benzyl, …) whose stability allows relatively higher concentrations.

2. <u>H-abstraction reactions</u> are chain propagation reactions forming alkyl radicals. A radical can abstract a H-atom from a stable molecule forming another stable molecule and another radical, thus propagating the reactivity.

$$R \cdot + R'H \rightarrow RH + R' \cdot$$
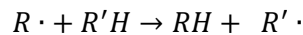
In principle any alkyl radical in the system can abstract. In the case of saturated fuel molecules this possibility is governed by the competition between the bimolecular H-abstractions and the subsequent unimolecular fate (isomerizations, β-decomposition). Once again the H-abstraction becomes more likely when resonance-stabilized radicals are involved, although termination steps are also more favored.

In pyrolytic systems the main abstracting radicals are H and methyl ($\dot{C}H_3$). Figure 16 shows a comparison of literature rate constants for such reactions [14, 54, 73, 118-120].
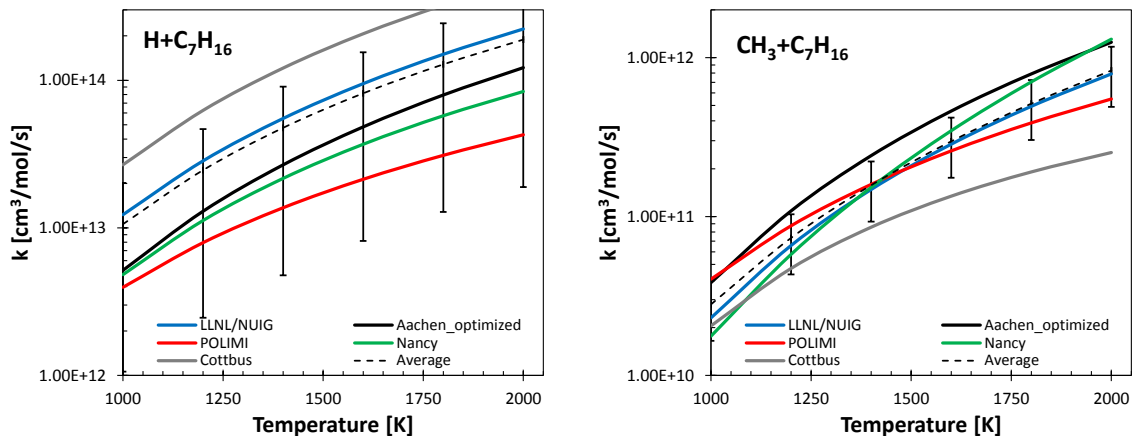
Figure 16: Total H-abstraction reaction rate constant by H and $\dot{C}H_3$ according to different kinetic mechanisms from the literature [14, 54, 73, 118-120]. Dashed lines are the average values $\overline{x}$ and error bars are derived from standard deviation σ as $\sigma/\overline{x}$.

The deviations observed are not surprising as every mechanism is developed on top of different C_0–C_1 sub-mechanisms. This causes the concentrations of $\dot{H}$ or $\dot{C}H_3$ in the system to be very different from mechanism to mechanism. A more significant comparison is obtained when calculating an apparent rate constant as $k_{app} = k\,[R \cdot]$. As discussed in Section 6.2.1, this is due to the fact that in

different kinetic frameworks, the abstracting radicals are managed by different C_0–C_4 subsets. Therefore, they might show different concentrations histories, to some extent counterbalanced by different rate constants of propagation reactions.

3. <u>β-decomposition reactions:</u> involve the cleavage of the bond sited in β to the radical position. The resulting products are a smaller radical and an unsaturated molecule.

$$R \cdot \rightarrow \ R' \cdot \ + (R - C = R)$$
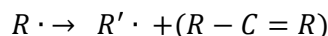
These propagation reactions are endothermic of about 30 kcal/mol, therefore requiring relatively high temperature to become of relevance (T>~850 K). The reverse exothermic alkyl radical addition to a double bond is also accounted for by introducing reversible β-scission reactions.

4. <u>Isomerization reactions</u> involve a H-atom transfer from one site to the radical site *via* internal H-abstraction reactions, involving the formation of a ring transition state (Figure 17). The competition between entropic and energetic factors, determines the rate constants for this reaction class as discussed in Section 3.2.4 and their competition with β-scission reactions.
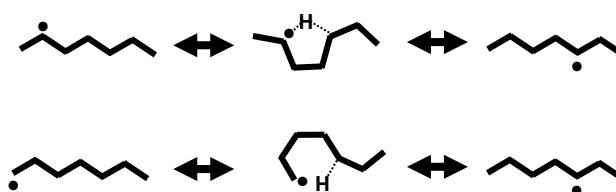
Figure 17: 5- and 6- membered transition states in H-transfer reactions of alkyl radicals (Isomerizations).

The competition of these reactions with decomposition reactions of alkyl radicals has a strong impact on product yields.

It is worth mentioning that 4- or 6-membered concerted reaction pathways can play a significant role too. Typical activation energies for such processes are in the order of ~70-80 kcal/mol. In particular they include: dehydrogenation of a saturated molecule to form an alkene, further dehydrogenation reaction of alkenes to form dienes or the decomposition through *ene-mechanism* [17] to form two alkenes, the Diels-Alder reactions between a diene and an alkene to form cyclohexene species and olefin isomerizations via four center reactions.
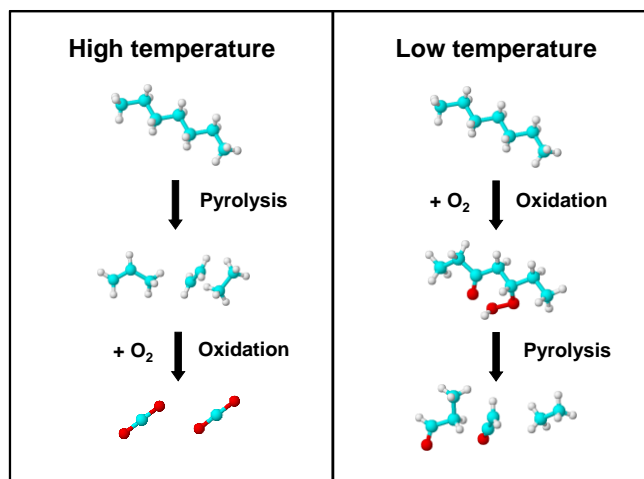
Figure 18: Simplified interpretation of high and low temperature combustion of n-heptane.

The overall exothermic combustion process proceeds through the coexistence of pyrolytic and oxidative steps. As summarized in Figure 18, at high temperatures (T>~1000 K), the energy of the system is high enough to allow for endothermic pyrolytic steps breaking the bonds in the fuel radicals derived through H-abstractions or, at very high temperatures (T>~1800 K), directly in the fuel molecules. Only then the fragments are oxidized, releasing energy. Conversely, at low temperatures (T<~1000 K), the fuel radicals derived through lower barrier H-abstractions interact with oxygen before bond breakings take place. The complexity of combustion is somehow related to the competition between these two macroscopic phenomena.

For high temperature combustion the same pyrolysis reactions apply, with the difference mostly lying in the presence of highly reactive oxygenated radicals such as $\dot{O}H$, $H\dot{O}_2$ and $\ddot{O}$. Also molecular oxygen (O₂) in some cases contributes to fuel consumption through H-atom abstraction. These reactions are, in turn, bimolecular initiation reactions as they convert two stable molecules into radicals. As discussed in Section 5.2.1 a relevant contribution of these H-abstractions is highlighted when unsaturated species such as olefins and aromatics are involved due to the formation of resonance stabilized radicals. As previously discussed, due to microscopic reversibility, addition of O and OH to double bonds are accounted for in the alkyl radical decomposition reactions.

Figure 19 shows a simplified reaction scheme for n-heptane oxidation at low temperatures, highlighting characteristic reaction classes.
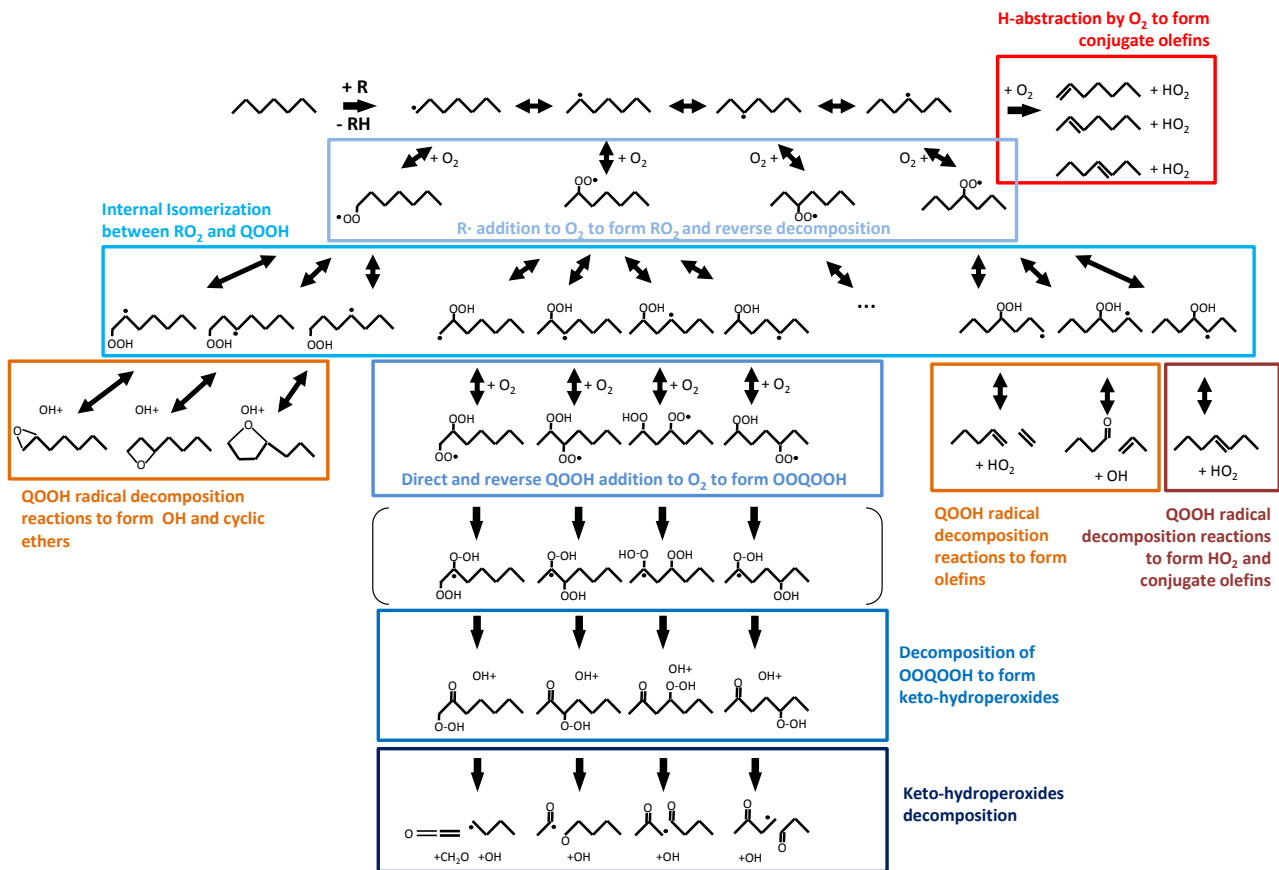
Figure 19: Simplified reaction scheme and reaction classes in n-heptane low temperature oxidation.

5. <u>H-abstraction by O$_2$ to form conjugate olefins from alkyl radicals</u>: in a particular regime of transition between high and low temperature combustion O$_2$ can interact with alkyl radicals by abstracting an H atom to form $H\dot{O}_2$ and the conjugate olefin.

6. <u>Alkyl radical addition to O$_2$ to form peroxyl radicals (RO$_2$)</u> characterizes the transition to low temperature combustion. The equilibrium of $\dot{R} + O_2 \leftrightarrow R\dot{O}_2$ defines the ceiling temperature ($T_{ceiling}$) as the temperature where the two radicals have the same concentration ($[R\dot{O}_2]/[\dot{R}] = 1$). For $T > T_{ceiling}$ the equilibrium is shifted toward the alkyl radical, which might undergo decomposition according to the reaction class (3). If $T < T_{ceiling}$ the peroxyl radical lives long enough to allow for isomerization steps (7). While the addition reaction is barrierless, the activation energy for the decomposition reaction is on the order of ~28-30 kcal/mol, therefore there is a strong temperature dependence to the equilibrium rate constant. From its definition

$$\frac{[\dot{R}]}{[R\dot{O}_2]} = \frac{k_{RO_2 \rightarrow R+O_2}}{k_{R+O_2 \rightarrow RO_2}[O_2]} = \frac{k_{RO_2 \rightarrow R+O_2}}{k_{R+O_2 \rightarrow RO_2}\left(\dfrac{P}{RT_{ceiling}}\right)x_{O_2}} = 1$$

the pressure dependence of $T_{ceiling}$ emerges clearly. For increasing pressure the bimolecular channel is favored over the unimolecular decomposition. In other words the low temperature regime survives longer for increasing pressures.

7. <u>Internal isomerization between RO₂ and QOOH</u>: peroxyl radicals (RO₂) isomerize via 5-, 6- or 7-membered ring transition states to form alkyl hydroperoxyl radicals (QOOH) (*Figure 20*).
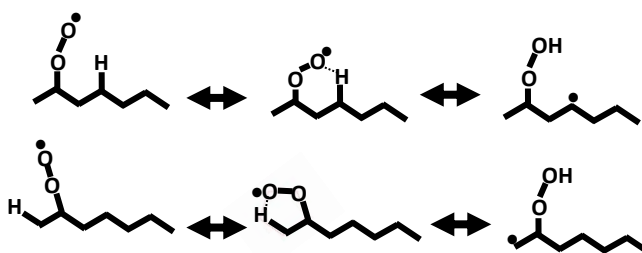
Figure 20: 5- and 6- membered transition states in H-transfer reactions of peroxyl radicals.

This step is responsible for the exponential increase in the number of species in low temperature kinetic mechanisms. For example, while the RO₂ radicals are only four in the case of heptane, there are 15 possible QOOH isomers produced by internal H-abstraction by RO₂ radicals. The same approach as in reaction class (4) is used to estimate the rate constants, whose parameters strongly depend on the competition between energetic and entropic factors.

8. <u>Decomposition of QOOH to form OH and cyclic ethers</u> involves the breaking of a O-O bond coupled with the formation of a cyclic ether. Similarly to other reactions involving the formation of a ring, the activation energy depends on its size.

9. <u>Decomposition of QOOH to form olefins</u>: QOOH species produced through a six-membered ring structure can undergo β-scission. The possible products are usually chosen based on the weakest C–C bond in the molecule, which is usually α to the O-OH substitution due to the higher electronegativity of oxygen. One olefin is formed together with an OH radical and the carbonyl compound (R-(C=O)H) derived from the O-O broken bond. This reaction is not elementary as it involves two successive β-scissions and three products, therefore the rate of the reverse termolecular reaction is assumed to be negligible.

10. <u>Decomposition of QOOH to form $H\dot{O}_2$ and conjugate olefins</u>: a QOOH species produced through a five-membered cyclic transition state can decompose, yielding $H\dot{O}_2$ and the conjugate olefin. This channel is the main source of olefins at low temperatures. In contrast with the previous QOOH decomposition channels (9 and 10), which are chain propagating steps producing one radical starting from one radical consumed in the H-abstraction from the fuel, this last channel propagates the chain through formation of a less reactive radical ($H\dot{O}_2$). For this reason, this reaction class is responsible

for a large part of the negative temperature coefficient behavior (NTC), which is a reduction in reactivity for increasing temperature.

11. <u>Hydroperoxyl-alkyl radical (QOOH) addition to O_2</u>: similarly to reaction class (7), hydroperoxyl-alkyl radicals can also add to oxygen to form hydroperoxyalkyl peroxy radicals OOQOOH. The reverse decomposition reaction is accounted for as in alkyl radicals addition to O_2.

12. <u>Decomposition of OOQOOH to form ketohydroperoxide and OH</u>: this reaction class includes an isomerization reaction similar to $R\dot{O}_2 \leftrightarrow \dot{Q}OOH$ followed by a unimolecular decomposition to form a ketohydroperoxide and OH. The internal H-abstraction involves the weakly bound H-atom at the O-OH substituted carbon site and the further β-decomposition breaking the O-O bond yielding a carbonyl functionality (R-(C=O)-R).

13. <u>Ketohydroperoxide decomposition:</u> the unimolecular decomposition of ketohydroperoxide produces another hydroxyl radical together with another radical species, giving chain branching. The activation energy for the O-OH bond cleavage is on the order of ~42-45 kcal/mol, ensuring an induction time in which ketohydroperoxide concentration builds up, strongly enhancing fuel consumption once the decomposition occurs. Overall, the formation and the decomposition of a ketohydroperoxide produce two hydroxyl radicals. This chain branching phenomena constitutes the core of low temperature reactivity.

Curran et al. [54] identified 25 reaction classes for the description of high and low temperature combustion regimes, while the formulation of Ranzi et al. [17, 38], as reported in this study, only includes 13. The difference lies in the fact that, for example, Curran et al. explicitly include addition reactions, which for the *microscopic reversibility* principle are already included in the β-decomposition reactions according to Ranzi and coworkers. Other classes introduced by Curran et al. deal with successive reactions of intermediates such as cyclic ethers and olefins. Even though the reactivity of alkenes and ethers is very different from that of n-alkanes due to a different molecular structure and to different bond strengths, the primary reactions to be included in a detailed approach are similar to those described above. Finally seven further classes refer to recombination reactions of peroxyl radicals, of relevance only at very low temperature as discussed in Ranzi et al. [64] and in Section 5.1.

The complexity of kinetic mechanisms for combustion is further highlighted in *Table 6* and Table 7. The former reports the total number of reactions in the oxidation mechanisms of *n*-alkanes, following the fate of alkyl radicals from the isomerization step (reaction class 4) throughout the low temperature branching pathway. The latter reports the number of primary propagating radicals and primary products to account for.

Reaction Class	Generic Form	n-C$_7$H$_{16}$	n-C$_{10}$H$_{22}$	n-C$_{12}$H$_{26}$	n-C$_{14}$H$_{30}$	n-C$_{16}$H$_{34}$
R3	$R \cdot \leftrightarrow R' \cdot + alkene$	6	8	10	12	14
R4	$R \cdot \leftrightarrow R' \cdot$	10	18	24	30	36
R6	$R \cdot + O_2 \leftrightarrow C_nH_{2n} + HO_2$	7	9	11	13	15
R7	$\dot{R} + O_2 \leftrightarrow R\dot{O}_2$	8	10	12	14	16
R8	$R\dot{O}_2 \leftrightarrow \dot{Q}OOH$	33	48	60	72	84
R9	$\dot{Q}OOH \leftrightarrow cyclic\ ether + \dot{O}H$	15	24	30	36	42
R10	$\dot{Q}OOH \leftrightarrow C_nH_{2n} + R(C=O)H + \dot{O}H$	5	8	10	12	14
R11	$\dot{Q}OOH \leftrightarrow H\dot{O}_2 + C_nH_{2n}$	6	9	11	13	15
R12	$\dot{Q}OOH + O_2 \leftrightarrow \dot{O}OQOOH$	30	48	60	72	84
R13	$\dot{O}OQOOH \leftrightarrow OQOOH + \dot{O}H$	15	24	30	36	42
R14	$OQOOH \leftrightarrow R'' + \dot{O}H$	15	24	30	36	42
total		150	230	288	346	404

Table 6: Detailed mechanism of n-alkane oxidation: number of primary propagation reactions.

Considering n-heptane, i.e. the smallest fuel used in surrogate formulations to replicate the properties of commercial fuels, there are 38 primary radicals and 26 primary products, excluding hydroperoxides (ROOH) further discussed in Section 3.2.13. The total number of reactions, excluding unimolecular initiations and H-abstraction reactions, is ~150, increasing to ~400 for n-C$_{16}$H$_{34}$. Clearly, the detailed description of successive reactions of all these new intermediate species makes detailed mechanisms hardly manageable. Moreover, the n-alkane example is even more favorable due to molecular symmetry greatly reducing the number of species and reactions needed to describe their oxidation. Typically branched alkanes and oxygenated molecules lack such symmetry, therefore, for a given carbon number, the number of species greatly increases.

	Primary propagating radicals				Primary products				
Fuel	R·	ROO·	·QOOH	·OOQOOH	Alkene	Cyclic ethers	ROOH	OQOOH	Total
n-C$_7$H$_{16}$	4	4	15	15	3	8	4	15	68

$n\text{-}C_{10}H_{22}$	5	5	24	24	5	13	5	24	105
$n\text{-}C_{12}H_{26}$	6	6	30	30	6	16	6	30	130
$n\text{-}C_{14}H_{30}$	7	7	36	36	7	19	7	36	155
$n\text{-}C_{16}H_{34}$	8	8	42	42	8	22	8	42	180

Table 7: Detailed mechanism of n-alkane oxidation: number of primary propagating radicals and products.

3.2 Reference Kinetic Parameters

The previous discussion of Chapter 1 already highlighted how the complexity of low- and high-temperature mechanisms of pyrolysis and oxidation of hydrocarbon fuels encouraged the development of expert systems for the automatic generation of kinetic mechanisms. The possibility of always applying the same general rules to the reaction classes described in Section 3.1 effectively served this goal since the dawn of the detailed modeling of hydrocarbon combustion kinetics. Aim of this Section is to summarize the approach in use at POLIMI in terms of the definition of a few reference kinetic parameters, of easy extension to similar classes of compounds through analogy and similarity rules.

3.2.1 Unimolecular Initiation Reactions

Before discussing the propagation reactions the first reactions to be included in the mechanism are the unimolecular initiation reactions. The reference rate parameter for the simple fission of a C–C bond between secondary C atoms is

$$k_{ref} = 5 \cdot 10^{16} \exp(-81.5/RT)$$

An extra 2 kcal/mol are required to break a terminal methyl group. Taking into account the fuel symmetry the initiation for *n*-heptane previously reported in Figure 15 can be expressed as

$$n\text{-}C_7H_{16} = CH_3 + p\text{-}C_6H_{13} \quad k = 10^{17} \exp(-83.5/RT)$$

$$n\text{-}C_7H_{16} = C_2H_5 + p\text{-}C_5H_{11} \quad k = 10^{17} \exp(-81.5/RT)$$

$$n\text{-}C_7H_{16} = p\text{-}C_3H_7 + p\text{-}C_4H_9 \quad k = 10^{17} \exp(-81.5/RT)$$
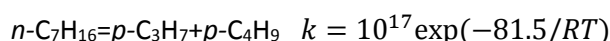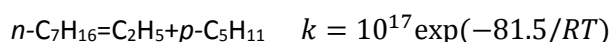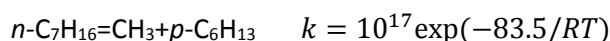
The proposed values are thermodynamically consistent with a recombination reaction rate constant on the order of 10^{12}-10^{13} cm^3/mol/s [64]. For the higher barrier reactions leading to alkyl radical and H-atoms a recombination rate constant of 10^{14} cm^3/mol/s is assumed. The higher activation energy of these pathways

(~10 kcal/mol higher than C–C fissions) makes them less likely to occur as initiation step, but in some instances such as flames they serve as sinks of H-atoms, globally reducing reactivity [101].

The reference kinetic parameters for propagation steps in pyrolysis processes are reported in Table 8 [17] and will be discussed in the following Sections.

H-abstraction reactions

	Primary H-atom	Secondary H-atom	Tertiary H-atom
Primary radical	10^{11} exp(-13.5/RT)	10^{11} exp(-11.2/RT)	10^{11} exp(-9/RT)
Secondary radical	10^{11} exp(-14.5/RT)	10^{11} exp(-12.2/RT)	10^{11} exp(-10/RT)
Tertiary radical	10^{11} exp(-15/RT)	10^{11} exp(-12.7/RT)	10^{11} exp(-10.5/RT)

Isomerization reactions (transfer of a primary H-atom[a])

	1-4 H-transfer	1-5 H-transfer	1-6 H-transfer
Primary radical[b]	10^{11} exp(-20.6/RT)	$10^{10.2}$ exp(-14.5/RT)	$10^{9.7}$ exp(-14.5/RT)

Alkyl radical decomposition reactions to form primary radicals

Primary radical	Secondary radical	Tertiary radical
$3 \cdot 10^{13}$ exp(-30/RT)	$3 \cdot 10^{13}$ exp(-31/RT)	$3 \cdot 10^{13}$ exp(-31.5/RT)

Corrections in activation energy (kcal/mol) to form		
Methyl radical	Secondary radical	Tertiary radical
+2	-2	-3

[a] Corrections for secondary and tertiary H-atoms are the same as for H-abstractions

[b] Rate values for secondary and tertiary radicals are obtained by adding 1 and 1.5 kcal/mol to the activation energy

Table 8: Reference kinetic parameters for pyrolysis processes [17].

3.2.2 H-abstraction Reactions

The rate coefficients for the generic H-abstraction reactions

$$R \cdot + R'H \rightarrow RH + \ R' \cdot$$
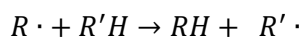
are determined according to the approach proposed by Ranzi et al. [52], based on the group contribution method of Benson et al. [50]. The rate constant for the forward reaction k_f is only a function of the abstracting radical $R\cdot$ and of the type of hydrogen in the molecule $R'H$. It is possible to write the rate constant as

$$k_f = k_{ref,R}^0 C_{R'H}$$

where $k_{ref,R}^0$ is the reference rate parameter representing the reactivity of $R\cdot$, and $C_{R'H}$ represents the reactivity of the removed H-atom. Both terms can be expressed in the Arrhenius form

$$k_f = A_{ref,R}^0 \exp\left(E_{ref,R}^0/RT\right) AC_{R'H} \exp(EC_{R'H}/RT) = A_{ref,R}^0 AC_{R'H} \exp\left(\left(E_{ref,R}^0 + EC_{R'H}\right)/RT\right)$$

explicitly expressing the correction to the frequency factor and to the activation energy directly depending on the H-atom being abstracted.

Based on this formulation the values given in Table 8 for H-abstraction reactions provide guidance to the determination of the rate values. Considering for example a primary radical (e.g. C_2H_5) removing a primary H-atom according to the reaction $C_2H_5+n\text{-}C_4H_{10}=C_2H_6+p\text{-}C_4H_9$ the reference rate constant, on a per H-atom basis, is $10^{11} \, exp(-13.5/RT)$. Figure 21 summarizes the bond dissociation energies for n- and iso-butane, highlighting the different bond strengths of primary, secondary and tertiary C–H bonds. The unimolecular cleavage of a primary C–H bond costs about 99.7 kcal/mol. The secondary and tertiary C–H bonds are respectively ~2.5 and ~4.3 kcal/mol weaker. As in Table 8, these differences are coherently reflected in the reference values for a secondary and tertiary H-atom abstraction, whose rate constants are $10^{11} \, exp(-11.2/RT)$ and $10^{11} \, exp(-9.0/RT)$ respectively. The same activation energy correction for the type of H-atom is applied for any abstracting radical.
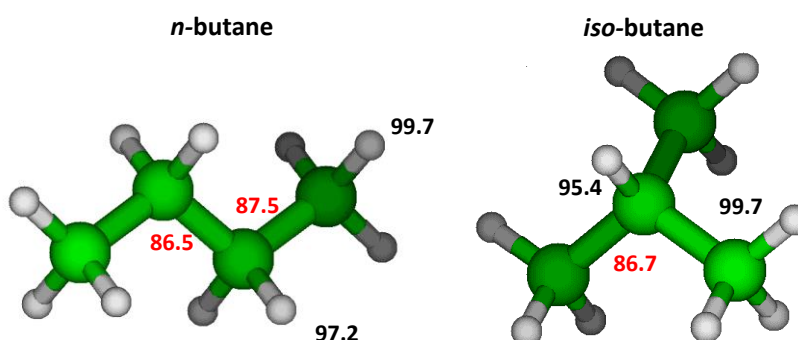
Figure 21: Bond dissociation energies (BDE) calculated at G4 level (298 K) of n- and iso-butane. C–H (black) and C–C (red).

Consider for example the H-abstractions by OH from *n*-butane to form a primary (*p*-C$_4$H$_9$) and secondary (*s*-C$_4$H$_9$) radical

$$OH + n\text{-}C_4H_{10} = H_2O + p\text{-}C_4H_9 \qquad (1)$$

$$OH + n\text{-}C_4H_{10} = H_2O + s\text{-}C_4H_9 \qquad (2)$$
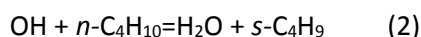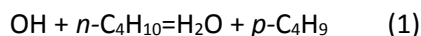
and *iso*-butane to form a primary and a tertiary radical (*t*-C$_4$H$_9$)

$$OH + iso\text{-}C_4H_{10} = H_2O + p\text{-}C_4H_9 \qquad (3)$$

$$OH + iso\text{-}C_4H_{10} = H_2O + t\text{-}C_4H_9 \qquad (4)$$
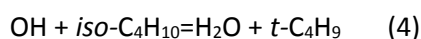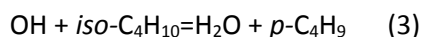
The reference rate constant for a primary H-atom is $3 \cdot 10^{12} \exp(-3.7/RT)$. Referring to *n*-butane a correction to the frequency factor ($AC_{R'H} = 6$) has to be applied to account for the 6 H-atoms available on the terminal methyl groups. In a similar way, the 9 primary H-atoms available in iso-butane have to be accounted for, therefore $AC_{R'H} = 9$. Overall, the rate constants for reactions (1) and (3) are $k_1 = 1.8 \cdot 10^{13} \exp(-3.7/RT)$ and $k_4 = 2.7 \cdot 10^{13} \exp(-3.7/RT)$ respectively. Applying $EC_{R'H} = -2.3$ kcal/mol and $AC_{R'H} = 4$ yields to obtain the rate constant for (2) as $k_2 = 1.2 \cdot 10^{13} \exp(-1.4/RT)$. With regards to the only tertiary H-atom in *iso*-butane the rate constant becomes $k_4 = 3 \cdot 10^{12} \exp(0.8/RT)$. Figure 22 shows such rate values on a per H-atom basis. A similar approach is used to estimate and automatically generate rate constants for ~40 different abstracting radicals on different abstraction sites (allyl, vinyl etc.).
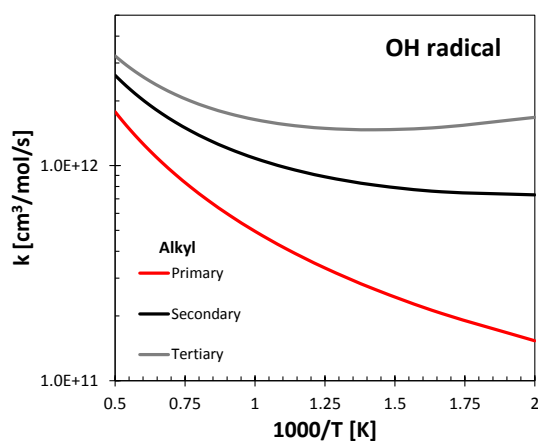
Figure 22: H-abstraction reactions. Calculated rate constants (per H-atom) for simple primary, secondary, tertiary H-atoms.

*Figure **23*** compares the total rate constants of H-abstraction by OH obtained according to the rate rules above with available experimental data for C$_5$-C$_7$ linear alkanes. The agreement is within a factor of 1.4 to 1.7.
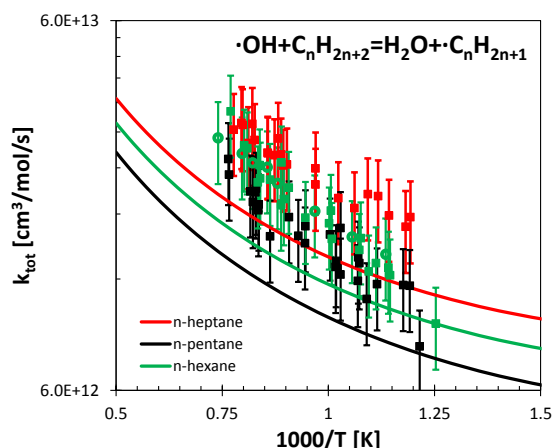
Figure 23: Arrhenius plot of the total OH+alkane rate constants. Experimental data from Sivaramakrishnan and Michael [121] (squares) and from Badra et al. [122] (circles).

The rate of bimolecular reactions such as H-abstractions depends linearly on the concentration of the abstracting radicals as for example $r_{abs} = k_{abs}[\dot{R}][R'H]$ (mol/cm^3/s). Due to the hierarchical modularity according to which kinetic mechanisms are developed, the reactivity, through the concentration of small radicals $[\dot{R}]$, is extremely dependent on the C$_0$-C$_2$ subset. Moving beyond the simple rate constant and its physical meaning (energy barrier, frequency of collisions etc.), many insights can be obtained by looking at the apparent unimolecular rate constant obtained as $k_{abs}[\dot{R}]$ (s^{-1}). *Figure 24* shows these apparent rate constants as a function of time for the oxidation of a stoichiometric n-heptane/air mixture in an isothermal plug flow reactor at *p*=10 atm. The four most reactive radicals commonly found in pyrolysis and oxidation processes are considered: $\dot{H}, \dot{C}H_3, \dot{O}H, H\dot{O}_2$ at three different temperatures *T*=700, 1000 and 1300 K.
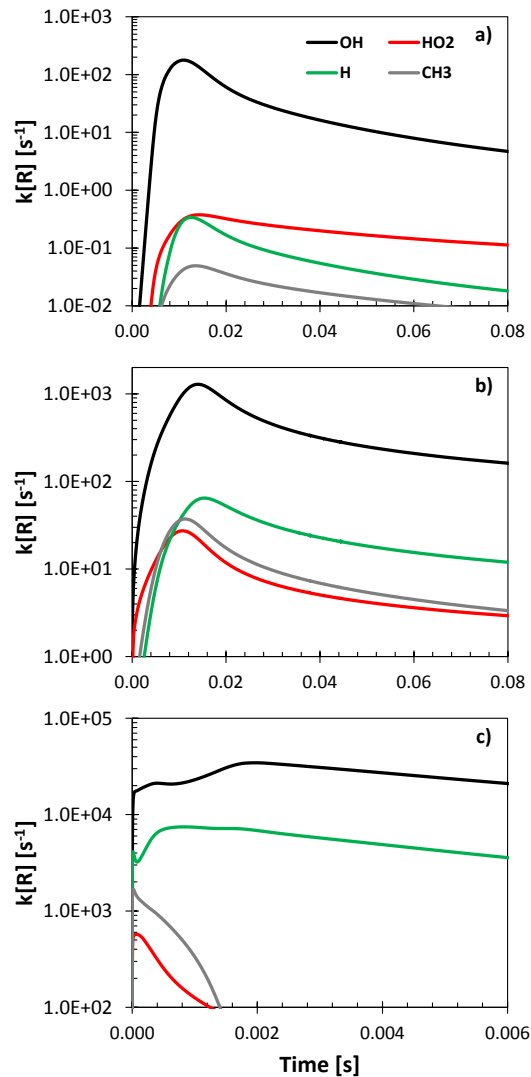
Figure 24: $k_{abs}[\dot{R}]$ as a function of time in the oxidation of a stoichiometric n-heptane/air mixture in an isothermal plug flow reactor at p=10 atm. a) T=700 K, b) T=1000 K and c) T=1300 K.

At every temperature condition, the abstraction by OH dominates over the other channels. At low temperatures, for every OH molecule consumed via H-abstraction two are promptly produced by the low temperature branching. H radical is globally consumed by the reaction $\dot{H}+O_2+M=H\dot{O}_2+M$ producing $H\dot{O}_2$. The termination reaction $H\dot{O}_2+H\dot{O}_2+M$ produces hydrogen peroxide (H$_2$O$_2$) which undergoes H-abstraction restoring $H\dot{O}_2$. Additional amounts of $H\dot{O}_2$ come from the interactions between $\dot{C}H_3$ and O$_2$, and the successive fate of CH$_3$O$_2$ and CH$_3$O. For increasing temperature, the relevance of H radicals increases. This is due to the increasing importance of radical decomposition pathways forming alkyl radicals such as C$_3$H$_7$, C$_2$H$_5$ and $\dot{C}H_3$. Subsequent decompositions (C$_2$H$_5$+M=H+C$_2$H$_4$+M, C$_3$H$_7$=C$_2$H$_4$+CH$_3$) and recombination reactions (CH$_3$+CH$_3$+M=C$_2$H$_5$+H) justify the higher concentration of H and to some extent the higher apparent rate. At intermediate temperatures (panel b, T=1000 K) H$_2$O$_2$ is rapidly consumed via the third body reaction

producing two OH ($H_2O_2+M=2OH+M$). At higher temperatures $H\dot{O}_2$ and $\dot{C}H_3$ rapidly react producing CH_4 and O2, or CH_3O and OH. Clearly this branching strongly influences the reactivity counterposing a termination and a branching step. $\dot{C}H_3$ is produced by $CH_3+CH_3+M=C_2H_5+H$ and rapidly consumed to form ethane from which C_2H_5 is reobtained through H-abstraction. H and OH levels are controlled by the branching reaction $H+O_2+M=OH+O+M$, additional amounts of OH are produced via the propagation reaction $H+HO_2+M=2OH+M$. In light of this picture the deviations of Figure 16 appear to be less dramatic: the correct prediction of a fuel chemistry strongly depends on smaller species, particularly at high temperatures. Deviations between rate constants adopted in different mechanisms not only originates from different approaches and rate rules, but also from differences in the C_0-C_2 subset governing radical species concentrations. A rigorous approach would require first a revision of core subsets for which theoretical chemistry constitutes a reliable, efficient and relatively fast source of parameters.

3.2.3 β-Decomposition Reactions

Alkyl radical β-decomposition is an endothermic process, often studied in the reverse exothermic direction of a radical addition to an olefin. A wide investigation of such reactions involving C_1-C_4 alkyl and alkoxy radicals was presented by Curran [90]. Based on literature experimental data, recommended rate values for different addition reactions were provided in the form of rate rules.

Considering the simple β-decomposition of the primary butyl radical p-$C_4H_9=C_2H_4+C_2H_5$ and of the secondary butyl radical s-$C_4H_9=C_3H_6+CH_3$, rate rules from Table 8 would recommend $k_p = 3\ 10^{13} \exp(-30/RT)$ and $k_s = 3\ 10^{13} \exp(-33/RT)$, accounting in the latter for the correction due to the formation of methyl radical. Microscopic reversibility allows for the computation of the reverse additions, resulting in $k_{-p} = 8.95\ 10^3\ T^{2.355} \exp(-5.77/RT)$ and $k_{-s} = 1.70\ 10^6\ T^{1.767} \exp(-6.33/RT)$. These values and those proposed by Curran [90] are compared in *Figure 25*, showing a factor of ~2-3 deviation.

Similarly Figure 26 shows the same kind of comparison for H-atom addition to propylene to form a primary or a secondary propyl radical (*iso*-C_3H_7). The addition can occur at the internal carbon atom producing n-C_3H_7 or at the terminal carbon atom, yielding iso-C_3H_7. Assuming reference rate constants for the β-scission reaction of $k_{nC3H7} = 5\ 10^{13} \exp(-41/RT)$ and $k_{iC3H7} = 2\ 10^{13} \exp(-39/RT)$ it is possible to obtain the rates of addition from microscopic reversibility. In this case the agreement between the rate rules and the values from Curran [90] is within a factor of ~0.7–1.3.
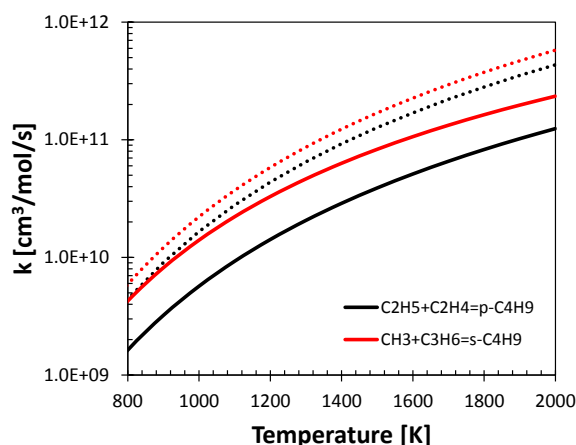
Figure 25: Rate constants for $C_2H_5+C_2H_4=p$-C_4H_9 (black lines) and $C_3H_6+CH_3=s$-C_4H_9 (red lines). Dashed lines are the values proposed by Curran [90], solid lines are those derived from rate rules through microscopic reversibility.
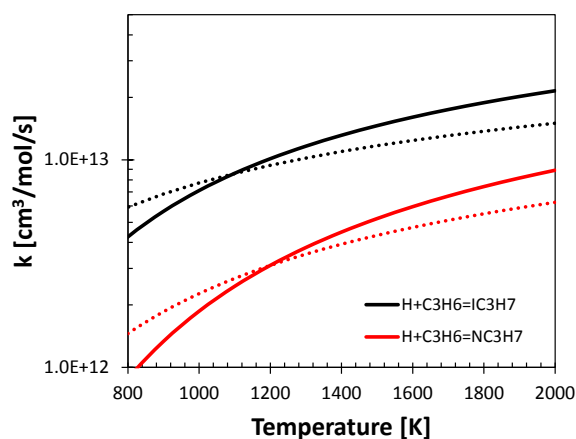
Figure 26: Rate constants for $H+C_3H_6=iso$-C_3H_7 (black lines) and $H+C_3H_6=n$-C_3H_7 (red lines). Dashed lines are the values proposed by Curran [90], solid lines are those derived from rate rules through microscopic reversibility.

3.2.4 Isomerization Reactions

Alkyl radicals can also isomerize through 5-, 6- or 7- membered cyclic transition states as discussed previously. Based on the work of Benson [50], the rate constants for isomerization reactions are described in terms of the number of atoms in the transition state structure and the type of H-atom to be abstracted. The activation energy of the process can be expressed as

$$E_a = E_{rs} + E_{abs}$$

where E_{rs} is the additional barrier due to ring strain and E_{abs} is the activation energy for the equivalent H-abstraction reaction. The frequency factor A of the rate constant should decrease for increasing ring size, as the number of hindered rotations tied up in the transition state increases. Referring to Table 8 consider the following 1-5 H-transfer
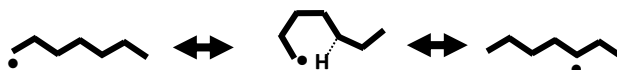
where a primary radical abstracts from a secondary site through a 6-membered ring transition state. The formation of a 6-membered ring has only 1 kcal/mol of ring strain, therefore the activation energy of such a process would be equal to that of an H-abstraction of a secondary H-atom by a primary radical, i.e. 11.2 kcal/mol, plus the ring strain. The resulting activation energy is $E_a = 12.2$ kcal/mol as reported in Table 8. For every rotor tied-up a decrease of $10^{0.8}$ in the frequency factor is considered, starting from the collisional limit of ~$10^{13.5}$ (A=3E+13) for the unimolecular β-decomposition. The 1-5 H-transfer involving four hindered rotations thus has a frequency factor $A = 10^{10.2}$ s^{-1}. When considering a 1-4 H-transfer, via a 5-membered ring transition state and three hindered rotors
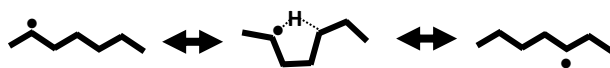
the activation energy is computed as $E_a = 12.2 + 7.1 = 19.3$ kcal/mol. The formation of a 5-membered ring involves in fact a 7.1 kcal/mol ring strain [50]. From an entropic point of view this reaction is more favored than the previous 1-5 H-transfer and requires a frequency factor $A = 10^{11}$ s^{-1}. 4-membered rings have strain energies of ~27.0 kcal/mol. Thus their contribution are negligible as are those from smaller cyclic transition states.

Figure 27 compares the rate constants of the isomerization reactions described above and the alkyl radical decomposition discussed in Section 3.2.3, highlighting the strong competition between the channels over the temperature range 800-1200 K.
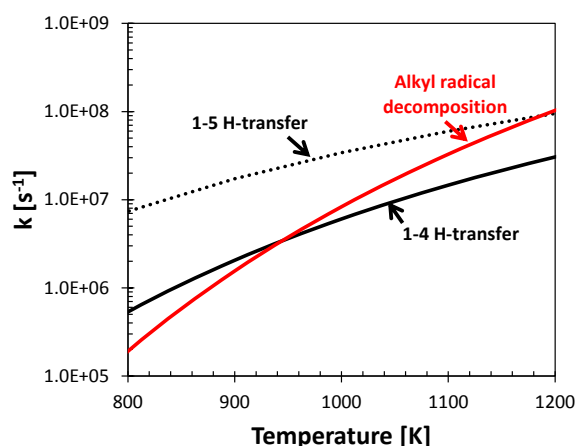
Figure 27: Comparison of isomerization and decomposition reactions of primary alkyl radicals according to rate rules.

Matheu and coworkers [123] also proposed rate rules for this reaction class. Energy barriers were determined for a set of possible H-transfer reactions and an Evans-Polanyi correlation allowed for an extension of the rule to other systems without performing any additional calculation. The activation energy is expressed as

$$E_a = E_{rs} + a + b\Delta H_r^{298}$$

where a and b were derived from fitting. Depending on the size of the ring the frequency factors were also determined by taking into account hindered rotations. *Figure 28* compares the rate constants for a 1-4 H-transfer reaction as obtained from the rate rules of Table 8
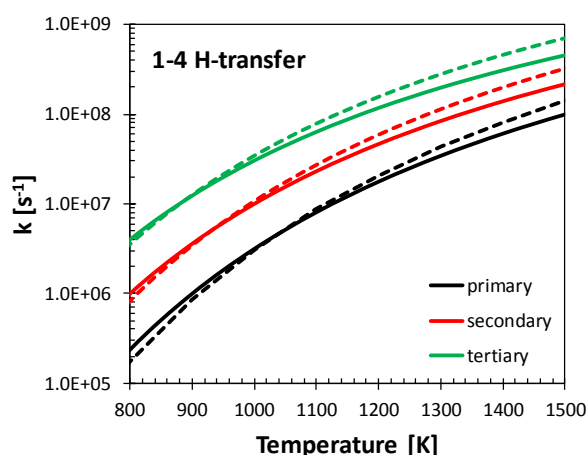
Figure 28: Comparison of 5-member isomerizations of a primary radical to form a primary (black), secondary (red) or tertiary (green) radical. Dashed lines (Matheu et al. [123]), solid lines (POLIMI).

3.2.5 H-abstraction by O₂ to form Conjugate Olefins

In the region of transition between high and low temperature oxidation (~800–1100 K), the interactions of alkyl radicals with O₂ and their competition with decomposition reactions govern the reactivity. As will be more and more clear to the reader, the production of $H\dot{O}_2$ rather than OH through the low temperature branching pathway, or vice versa, is what determines the ignitability of a fuel over the conditions of interest in real systems. In particular, while R+O₂ can give rise to the low temperature branching pathway if RO₂ is stabilized (see Section 3.2.6, reaction class 6 and followings), at higher temperatures, it might decompose to $H\dot{O}_2$ and conjugate olefin according to the following steps

$$R + O_2 \leftrightarrow RO_2 \rightarrow HO_2 + olefin$$
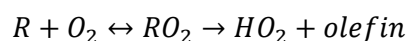
A correct analysis of the chemically activated channel would suggest the introduction of both the direct bimolecular reaction

$$R + O_2 \rightarrow HO_2 + olefin$$

and the unimolecular RO_2 decomposition

$$RO_2 \rightarrow HO_2 + olefin$$
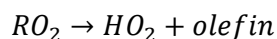
However, as reported in Ranzi et al. [17], the contribution of such channel is limited under conditions of interest (~5-10%, 800–1100 K, 10 atm), allowing the introduction of a single global step without dramatically affecting the overall reactivity. *Figure 29* illustrates a comparison between the rate constant for the reaction of 1-pentyl radical with O_2 directly forming 1-pentene and $H\dot{O}_2$ according to the POLIMI mechanism and the global step obtained from the *n*-pentane mechanism of Bugler et al. [55].
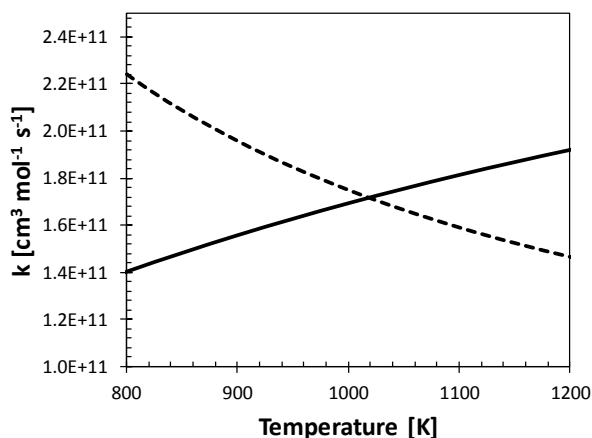
Figure 29: Comparison between the single step rate constant from rate rules in POLIMI mechanism (solid line) and that obtained from Bugler et al. [55] (dashed line).

The apparent rate constant k_{app} was obtained by assuming the steady state for RO_2. Overall the production of $H\dot{O}_2$ (and the conjugate olefin) from these channels can be expressed as

$$R_{HO_2} = \left(\frac{k_{RO_2=HO_2+olefin} \cdot k_{R+O_2=RO_2}}{k_{RO_2=R+O_2} + k_{RO_2=HO_2+olefin}} + k_{R+O_2=HO_2+olefin} \right) [O_2][R] = k_{app}[O_2][R]$$

Figure 30 compares the rate constants for $RO_2 \rightarrow HO_2 + olefin$ with its alternative isomerization or backward decomposition channels as in the mechanism of Bugler et al. [55]. Such visualization highlights the limited contribution of these reaction class, further supporting the single step formalism. Many theoretical studies have been devoted to a complete assessment of RO_2 reactivity. Starting from the work of Miller et al. [124], De Sain [125] and Goldsmith and coworkers [126] characterized the reactivity of ethyl and propyl radicals at low temperatures. As illustrated in Figure 30, at low temperatures RO_2 stabilizes and mostly isomerizes to QOOH. As the temperature increases the pathway to $H\dot{O}_2$ and alkene becomes dominant as the equilibrium for $RO_2=R+O_2$ shifts backward. RO_2 concentration is controlled by this equilibrium and by the competition with the rate of β-scission as discussed in the following Section 3.2.6.
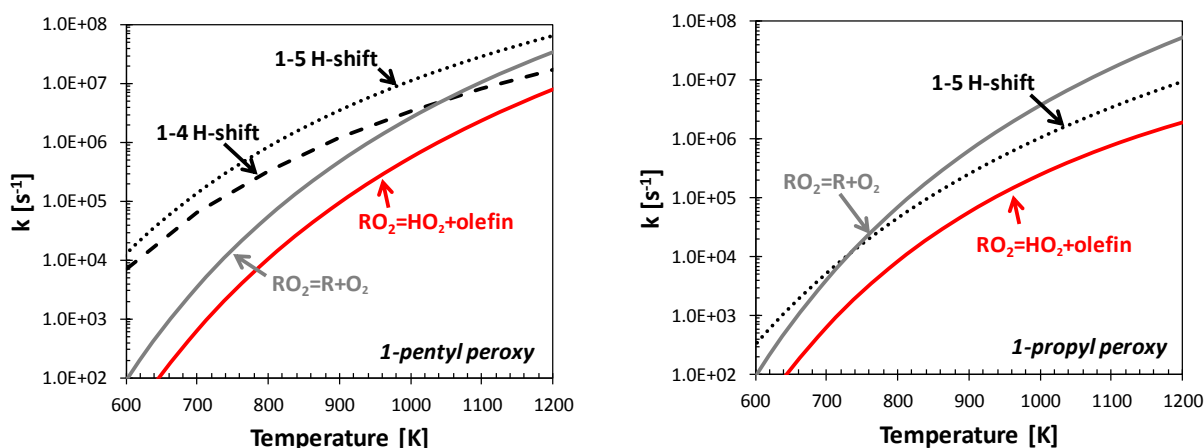
Figure 30: Comparison between RO$_2$=QOOH channels (black lines), $R\dot{O}_2$= $H\dot{O}_2$+olefin (red line) and RO$_2$=O$_2$+R (grey line) for 1-pentyl peroxyl radical as in Bugler et al. [55] and for 1-propyl peroxyl radical as in DeSain et al. [125].

3.2.6 Alkyl Radical Addition to O$_2$ to form Peroxyl Radicals (RO$_2$) and Reverse Decomposition Reactions

The transition between high and low temperature regimes depends on the competition between alkyl radical β-scission and on their addition to O$_2$. Although this step does not determine the rate of chain branching, the correct description of the relative concentrations of alkyl and peroxyl radicals is a necessary condition to fully characterize low temperature ignition phenomena.

$$R + O_2 \leftrightarrow RO_2$$
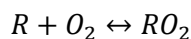
Peroxyl radicals decrease in stability as the temperature increases, moving the equilibrium backwards and giving rise to pathways alternative to the low temperature branching. The first row of *Figure 31* compares the rate rules of Bugler et al. [55, 127, 128] with those in use at POLIMI, reported in *Table 9*. The rate rules of Bugler have been obtained from a number of theoretical studies available in the literature [124-126, 129-135], allowing the definition of uncertainty bounds, also reported in *Figure 31*.

More than the forward or the reverse reaction rate constants, the key aspect is the correct definition of the equilibrium constant. The second row of *Figure 31* shows the equilibrium constants from the *n*-pentane mechanism of Bugler et al. [55], theoretical calculations for n- and iso-propyl radicals of Goldsmith et al. [126] and the rate rules adopted in POLIMI mechanism. It is important to mention that such a comparison is generically valid within the POLIMI kinetics framework as both the direct and inverse rate constants of any reversible low temperature reaction discussed in this and in the following Sections, are explicitly assigned. The reverse decomposition rate constants reflect the stability of alkyl-peroxy radicals as

tertiary>secondary>primary (-36.7, -35.2, -33.2 kcal/mol [126, 135]). The activation energy is assumed to be 30 kcal/mol and the frequency factor A varies between $1 - 3 \ 10^{13} \ s^{-1}$.

Alkyl radical addition to O₂		
Primary radical	*Secondary radical*	*Tertiary radical*
$1 \ 10^{12}$	$2 \ 10^{12}$	$3 \ 10^{12}$

H-abstraction reactions			
	Primary H-atom	*Secondary H-atom*	*Tertiary H-atom*
Peroxyl radical	$10^{11.7} \exp(-21.5/RT)$	$10^{11.7} \exp(-18.8/RT)$	$10^{11.7} \exp(-16.5/RT)$

Isomerization reactions (transfer of a primary H-atom[a])			
	1-4 H-transfer	*1-5 H-transfer*	*1-6 H-transfer*
Peroxyl radical [b]	$10^{11.8} \exp(-28.5/RT)$	$10^{11.0} \exp(-22.5/RT)$	$10^{10.6} \exp(-22.5/RT)$

Hydroperoxy-alkyl radical (QOOH) decomposition reactions to form		
$H\dot{O}_2$ *and conjugate olefins*		*Smaller olefins*
$10^{14} \exp(-23.0/RT)$		$10^{13.2} \exp(-22.5/RT)$
	Cyclic ethers	
Oxiranes	*Oxetanes*	*Furans*
$10^{12} \exp(-18.0/RT)$	$10^{11.2} \exp(-17.0/RT)$	$10^{10.4} \exp(-8.5/RT)$

Table 9: Reference kinetic parameters for low temperature processes [17]. [a]Corrections for secondary and tertiary H-atoms are the same as for H-abstractions. Units are kcal, cm³, mol, s.
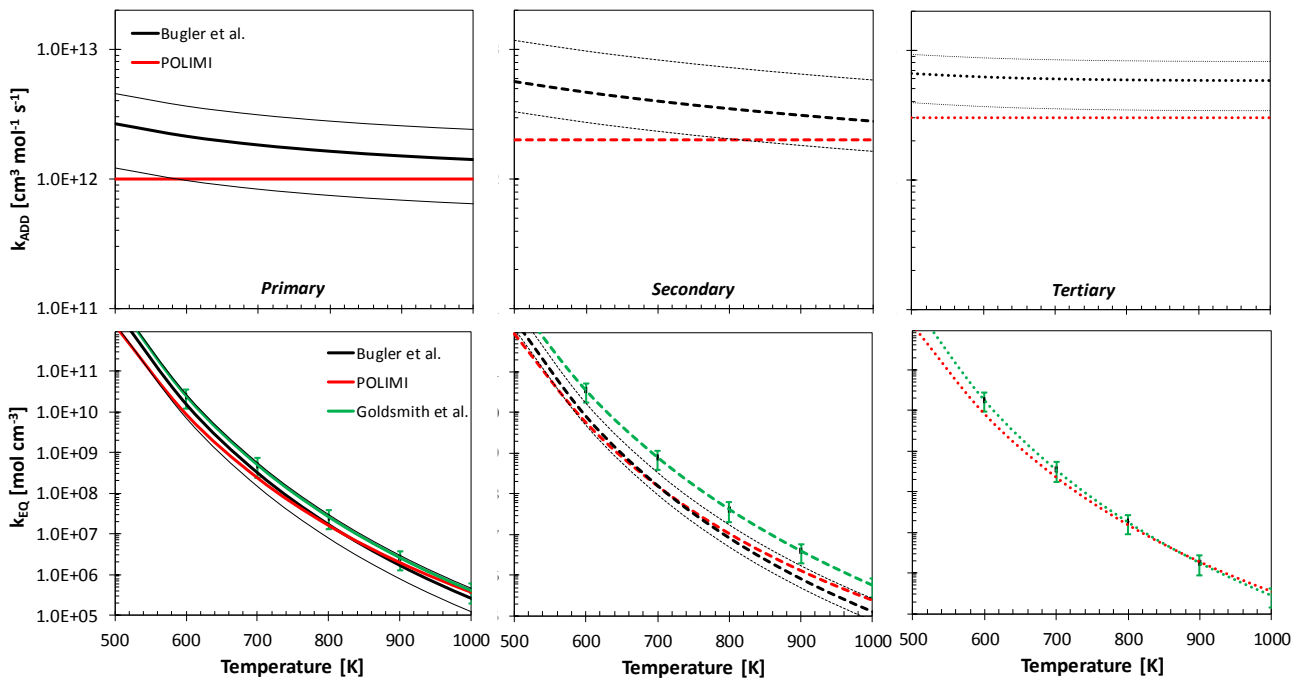
Figure 31: First row: rate constant for primary, secondary and tertiary alkyl radical addition to O_2 according to Bugler et al. [56] (black lines) and POLIMI mechanism (red lines). Thin black lines are uncertainty bounds [56]. Second row: comparison of equilibrium constant for $R+O_2=RO_2$ reactions as in the pentane mechanism of Bugler et al. [56] from calculation of Goldsmith et al. for propyl radicals [126] and in POLIMI mechanism..

The *ceiling temperature* is defined as the temperature where the concentration of alkyl radicals equals that of peroxyl radicals as

$$\frac{[R]}{[RO_2]} = \frac{k_{DEC}}{k_{ADD}[O_2]} = 1$$

Figure 32 shows concentration profiles of pentyl and pentyl-peroxyl radicals of a stoichiometric n-pentane/air mixture in an adiabatic constant volume batch reactor, at initial temperature of 850 K and initial pressures of 1, 10 and 100 atm. It is possible to locate the ceiling temperature in correspondence of $[R] = [RO_2]$. As expected, the ceiling temperature increases for increasing pressure, meaning that peroxyl radicals stabilize more at higher pressures, building up in concentration and *feeding* the low temperature branching pathway, resulting in enhanced overall reactivity. Evidence of this is the clear first stage ignition (i.e. low temperature ignition, cool flame) associated to the peak of peroxyl radicals concentration in the case at 100 atm.
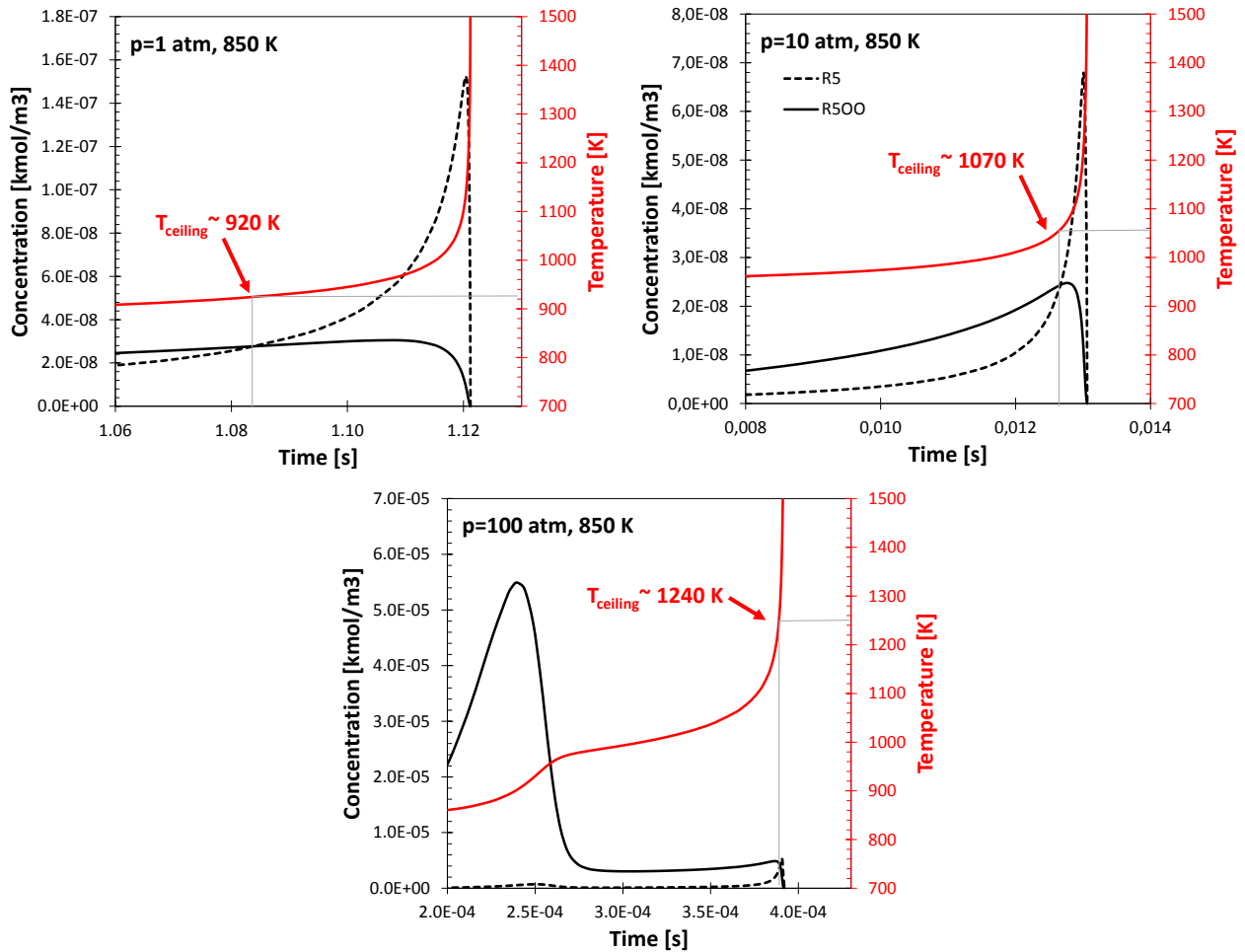
Figure 32: Concentration (black) and temperature (red) versus time profile of stoichiometric n-pentane/air mixtures. Dashed lines: pentyl radical, solid lines: pentyl peroxyl radical. Adiabatic constant volume batch reactor, T_0=850 K and p_0=1–100 atm.

Qualitatively it is also possible to visualize the *ceiling temperature* by computing the apparent unimolecular rate of addition (s^{-1}) as the product of the rate of addition (cm3 mol^{-1} s^{-1}) and the oxygen concentration (mol cm^{-3}) and comparing it with the RO_2 decomposition rate constant. Figure 33 shows the qualitative agreement with Figure 32 obtained assuming oxygen concentrations equal to that where the condition $[R] = [RO_2]$ is satisfied.
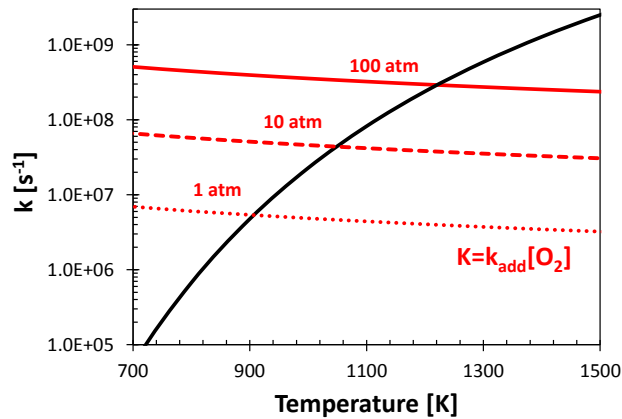
Figure 33: Rate constants plot of alkyl peroxyl radical decomposition versus apparent rate of addition to O_2 (K = k_{add} [O_2]).

Figure 34 shows a schematic representation of the reaction pathways of n-heptane, and in general n-alkane oxidation. Once the branching between peroxyl radical addition and decomposition is accurately established, the low temperature oxidation mostly requires a correct definition of selectivity to products. The formation of two OH and another radical starting from one single fuel radical enhances reactivity (low temperature branching) Alternatively, the side decomposition channels produce either one $\dot{O}H$ or one less reactive $H\dot{O}_2$ radical and other products (propagation). The competition of these alternative channels produces the negative temperature coefficient (NTC) behavior, where for increasing temperature the overall reactivity decreases.
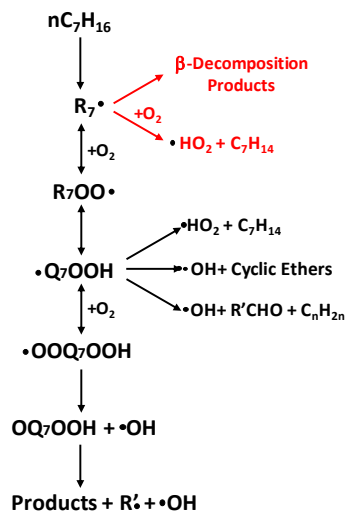
Figure 34: Reaction path diagram of n-heptane oxidation. Black: low temperature, red: high temperature.

The competition between low, intermediate and high temperature channels gives rise to a variety of behaviors such as oscillatory cool flames or single and multi-stage ignitions, whose correct prediction directly impacts fuel efficiency in real systems [136, 137]. From a modelling perspective, an accurate description of

the selectivity (i.e. relative rates) to the different alternative pathways is often more important than absolute rate values.

An example supporting such a statement is given in the following. Pelucchi et al. [73] at POLIMI and Zhang et al. [138] at National University of Ireland, recently updated their respective *n*-heptane mechanisms in light of new reaction classes and updated rate rules. As reported in the study of Zhang, despite different rate rules in use in the different frameworks, the predicted ignition delay times agree well within experimental uncertainty (~15-20%).

Figure 35 reports molar selectivity plots of $\dot{O}H$ and $H\dot{O}_2$ for a stoichiometric n-heptane/air mixture at 13.5 bar and 750 K obtained with the two mechanisms. The definition of selectivity in this case is based on n-heptane conversion as function of time. In other words, it tells how much of the converted n-heptane forms OH or $H\dot{O}_2$ as a function of time. As discussed above, such profiles can be directly related to the relative importance of the low temperature branching, producing $\dot{O}H$, and of the alternative intermediate channels, producing $H\dot{O}_2$. At lower temperatures the $\dot{O}H$ concentration builds up slightly and is consumed via H-abstraction from the fuel, exponentially enhancing $\dot{O}H$ production resulting in the second stage ignition. The selectivity to $H\dot{O}_2$ is instead controlled by the rate of production from side pathways producing olefins and by the termination rate of $HO_2+HO_2=O_2+H_2O_2$.
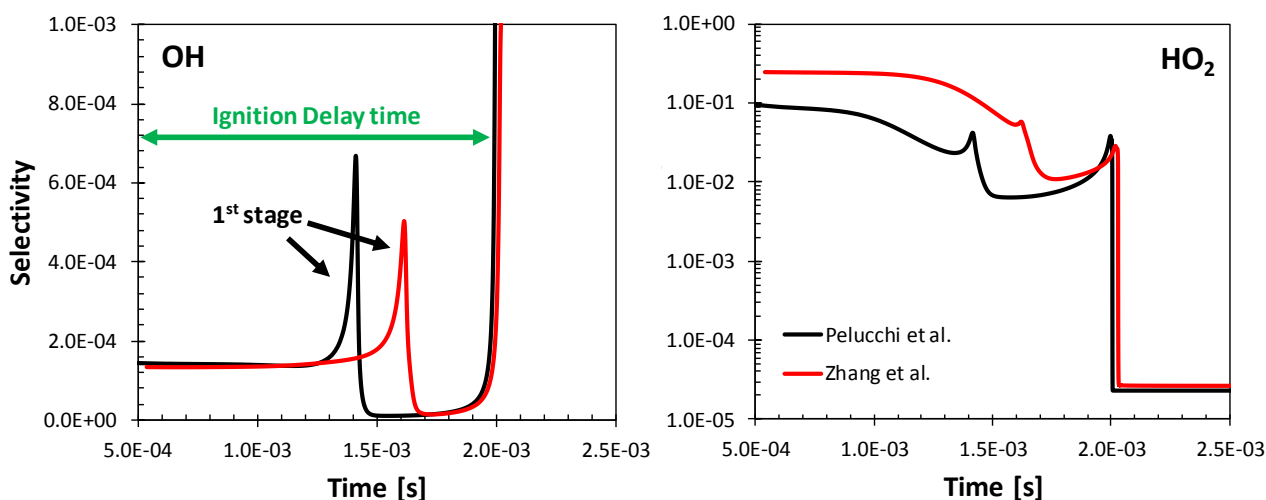
Figure 35: Selectivity to $\dot{O}H$ and $H\dot{O}_2$ according to POLIMI mechanism (black) and Zhang et al. (red) for a stoichiometric n-heptane/air mixture. Adiabatic constant volume batch reactor, T_0=750 K and p_0=13.5 bar.

Despite similar ignition delay times, timing and selectivity to OH at the first stage ignition differ quite significantly. The mechanism of Zhang predicts a longer induction time for the first stage ignition. The similar amount of peroxy heptyl radicals (*Figure 36*) provides a very similar radical pool to the low temperature branching channels. Differences in the first stage ignition derive from the factor of 2 difference in selectivity to $H\dot{O}_2$, associated with higher alkenes yields, resulting in a delayed fuel consumption.
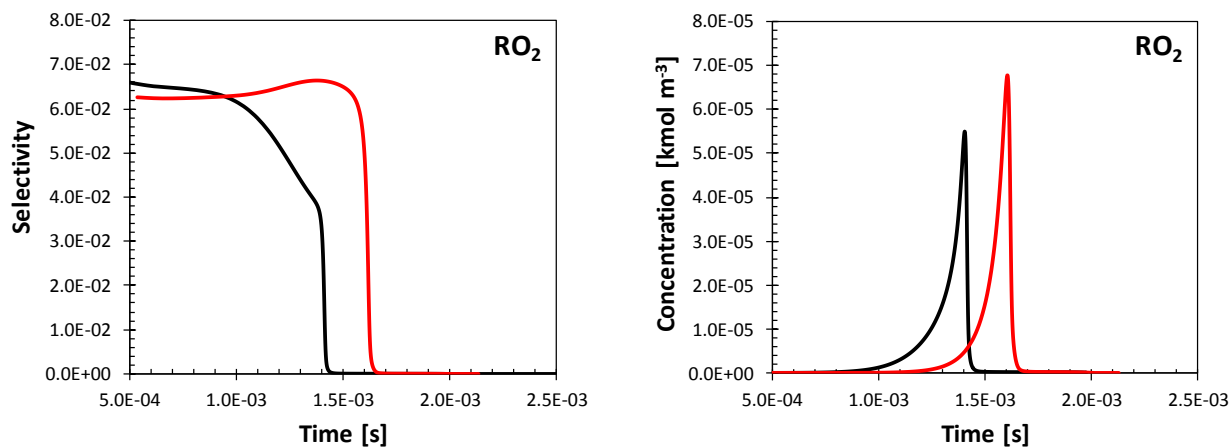
Figure 36: Selectivity and concentration of RO$_2$ according to POLIMI mechanism (black) and Zhang et al. (red) for a stoichiometric n-pentane/air mixtures. Adiabatic constant volume batch reactor, T$_0$=750 K and p$_0$=10 atm.

Despite the clear importance of the relative relevance of the competing channels, the capability to accurately evaluate absolute rate values nowadays by means of an effective coupling of theory and experimental data plays a major role in making kinetic models increasingly more predictive and less empirical. In particular, many unknown pathways at low temperatures have been recently proposed [72, 139-141] pursuing such an approach. Their correct implementation in existing mechanism requires a better characterization of competing channels, at a consistent level of accuracy.

The rate rules in use at POLIMI refer to the high pressure limit rate constants. A non-negligible effect of fall-off generally emerges at high temperatures (T>1200 K) and its inclusion for unimolecular initiation and β-scissions is necessary to correctly model speciation, flame speeds, high temperature ignition delay times. The simplifications from using only the high pressure limit for low temperature reactions do not dramatically impact model results at the conditions of interest in real systems. Similar conclusions were reported by Miyoshi [130] for the reaction class discussed in this Section. Bugler et al. [55] also confirmed through the evidence from the literature [129, 142] that the use of high-pressure limit rate coefficients for the important low-temperature reaction classes of alkanes is adequate under practical combustion operating conditions. An additional example is reported in the following *Figure 37*. Ignition delay times of stoichiometric propane/air mixtures at 750 K have been simulated at 1, 10 and 100 bar. Firstly, only the high pressure limit rate coefficients for O$_2$+n-C$_3$H$_7$ and O$_2$+iso-C$_3$H$_7$ from Goldsmith [126] (black lines in *Figure 37*) have been included. The same simulations have then been performed including the proper pressure dependent kinetics (red lines) from the same study. The two results show very limited deviations (~5%) further supporting the above assumption. This is due to the fact that the addition and the reverse decomposition reactions have the same pressure fall-off, and their inclusion does not affect the relative amount of peroxyl radicals formed or decomposed backwards.
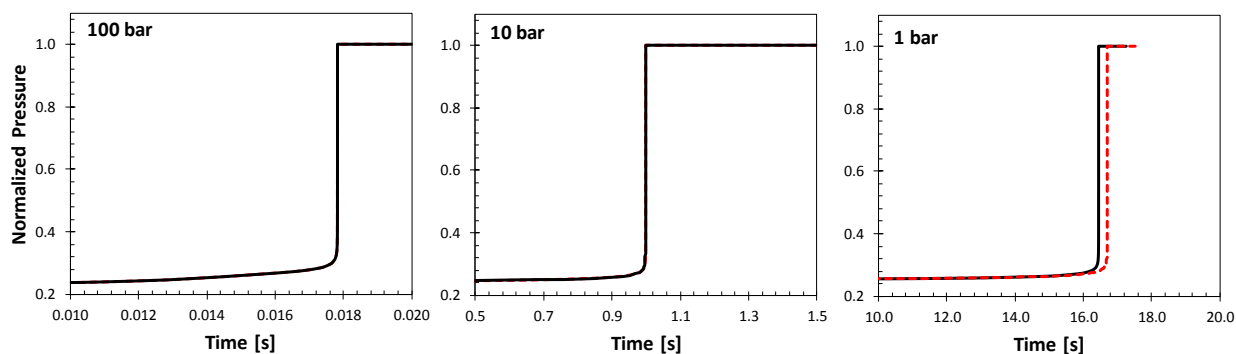
Figure 37: Pressure profiles of ignition delay time simulations for propane/air mixtures at T_0=750 K, P_0=100, 10 and 1 bar. Black lines: only high pressure limit rate constants [126] for R+O_2=RO_2, red lines: pressure dependent rate coefficients [126].

3.2.7 Internal Isomerization between RO$_2$ and QOOH

Peroxyl radicals can isomerize through internal H-abstraction forming hydroperoxy-alkyl radicals (QOOH). This step is treated similarly to alkyl radical isomerization reactions (Section 3.2.4), taking into account the differences in the rate of H-abstractions by a peroxyl radical ($H\dot{O}_2$, $CH_3\dot{O}_2$ etc.) as discussed in Section 3.2.5. *Figure 38* shows examples of internal isomerization of peroxyl radicals. The first reaction involves a 5-membered ring transition state, with the tie-up of 3 internal rotors. The activation energy is computed as

$$E_a = E_{ref,R}^0 + EC_{R'H} + E_{rs}$$

Where $E_{ref,R}^0$ is the reference activation energy for a peroxyl radical abstracting a primary H-atom (21.5 kcal/mol), $EC_{R'H}$ is the correction to account for the type of H-atom abstracted (0 kcal/mol, primary H-atom) and E_{rs} is the ring strain (~7 kcal/mol). Overall, the activation energy is ~28.5 kcal/mol. The reference frequency factor is $10^{11.8}$ s^{-1}. This value decreases by multiples of $10^{0.8}$ for increasing ring size, and has to be multiplied by the number of H-atoms. Taking these considerations into account, the overall rate constant for the 1-4 H shift in *Figure 38* is $k_{1-4,p} = 3 \; 10^{11.8} \exp(-28.5/RT)$ s^{-1}. A rate constant of $k_{1-5,p} = 3 \; 10^{11} \exp(-22.5/RT)$ s^{-1} is obtained for the second reaction of *Figure 38*. Only reactions involving 5-, 6- and 7-membered ring structures are considered. The same approach is used to estimate the rate constants of the reverse QOOH→RO$_2$ reactions.

1-4 H-transfer, 5-membered ring
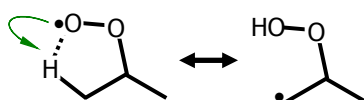
1-5 H-transfer, 6-membered ring
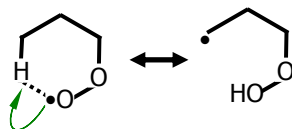
Figure 38: Peroxyl radical isomerization to form hydroperoxy-alkyl radicals. 1-4 H-transfer of a primary H-atom through 5-membered ring (top) and 1-5 H-transfer through 6-membered ring (bottom).

The first backward reaction requires an activation energy of ~18 kcal mol^{-1}, resulting from the reference 13.5 kcal mol^{-1} of H-abstraction of a primary H-atom (Table 8) corrected by -2.6 kcal mol^{-1} to account for the weakly bound H-atom at the hydroxyl moiety [52] and incremented by ~7 kcal mol^{-1} for the ring strain. The frequency factor is that of a 5-membered alkyl radical isomerization ($A = 10^{11}$ s^{-1}). In a similar way it is possible to obtain the reverse rate constant for the second reaction as $k_{1-5,rev} = 1.5 \cdot 10^{11} \exp(-12/RT)\ s^{-1}$.
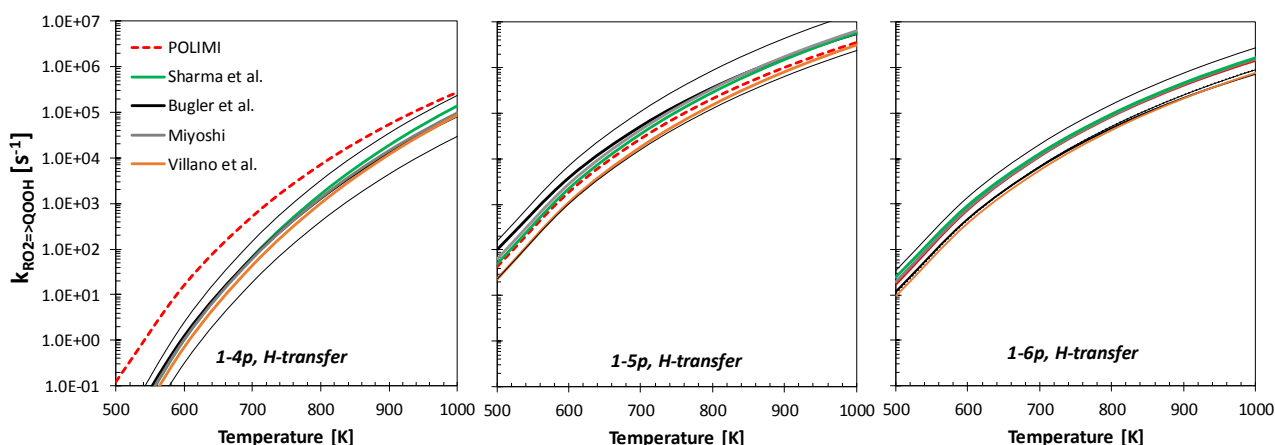
Figure 39: Rate constants for RO$_2$=QOOH H-transfer reactions of a primary H-atom through a 5-, 6- or 7- membered ring. Red lines: POLIMI, black lines: rate rules from Bugler et al. [55] (thinner lines:uncertainty bounds), green lines: calculations by Sharma et al. [143], grey lines: calculation from Miyoshi [144], orange lines: calculations from Villano et al. [129].

Figure 39 compares the rate constants from the rate rules reported in Table 9 and rate rules or calculations from the literature [55, 129, 143, 144]. The rate rules adopted in the POLIMI mechanism agree within a factor of ~2 of the other cases, while deviations on the order of a factor of ~3-5 are observed for the 1-4 H-transfer. These deviations are most probably related to activation energies that are ~2-3 kcal mol^{-1} lower than those reported in the literature (~32 kcal mol^{-1}).

An instructive example of the application of RO₂=QOOH rate coefficient estimation refers to iso-octane and n-heptane, which are primary reference fuels commonly used to simulate ignition propensity and other combustion characteristics of commercial gasolines. At 800 K ~25% of *iso*-octane undergoes H-abstraction at the tertiary site. The most probable isomerization channel of the tertiary RO₂ radical derived from addition to O₂ is the one involving a 5-membered ring and one of the two central secondary H-atoms (top of *Figure 40*). Considering *n*-heptane, ~20% percent of the H-abstraction occurs at the central secondary carbon site. The RO₂ radical obtained via H-addition preferentially undergoes internal isomerization through a 6-membered ring, abstracting one of the four secondary H-atoms available.
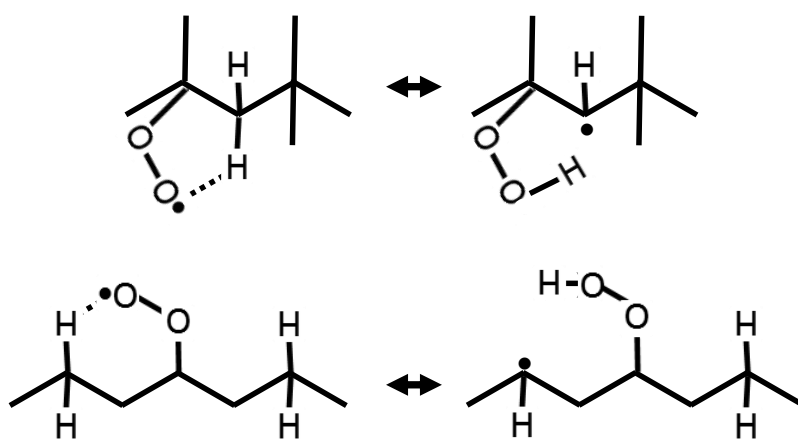
Figure 40: RO2=QOOH isomerization channels in iso-octane (top) and n-heptane (bottom).

According to the rate rules, the reference kinetic parameters for the reaction involving *iso*-octane are $k_{ref,1-4,p} = 10^{11.8} \exp(-28.5/RT)\, s^{-1}$, accounting for the two secondary H-atoms available, both the frequency factor (2x) and the activation energy (-2.3 kcal mol⁻¹) have to be corrected. The rate constant thus obtained is $k_{i-c8} = 2\,10^{11.8} \exp(-26.2/RT)\, s^{-1}$. In a similar way it is possible to estimate the isomerization rate constant for *n*-heptane starting from the reference 1-5 H-shift $k_{ref,1-5,p} = 10^{11} \exp(-22.5/RT)\, s^{-1}$, and correcting the activation energy (-2.3 kcal mol⁻¹) and the frequency factor (4x), thus obtaining $k_{n-c7} = 4\,10^{11} \exp(-20.2/RT)\, s^{-1}$. Overall the isomerization rate of iso-octane isomerization turns out to be ~15 times slower than that of n-heptane at 800 K, as illustrated in *Figure 41*.
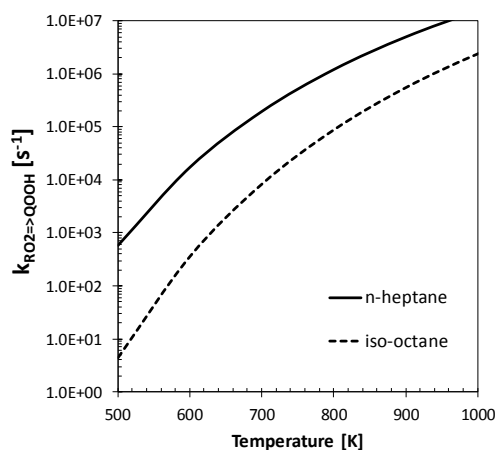
Figure 41: Rate constants of n-heptane and iso-octane isomerizations reported in Figure 40.

This feature directly impacts the anti-knocking propensity of these primary fuels, whose systematic definition is a key feature in correctly assessing real fuels properties. A comparison of ignition delay times of the two fuels is reported in *Figure 42*. At temperatures lower than 900 K, n-heptane is ~10-20 times faster to ignite under the investigated conditions.
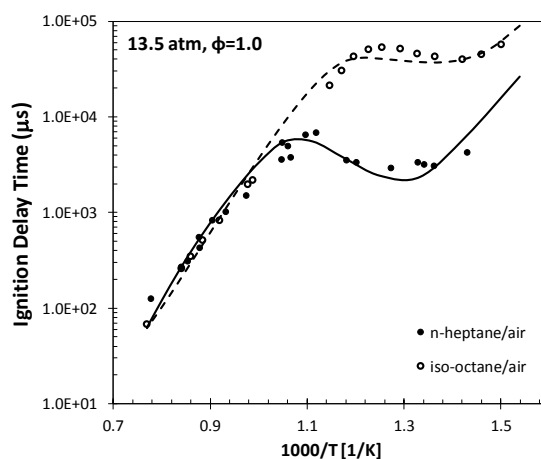
Figure 42: Ignition delay times of stoichiometric mixtures of n-heptane and iso-octane/air. Symbols: experimental data [145, 146], lines: POLIMI mechanism.

3.2.8 Decomposition of QOOH to form OH and Cyclic Ethers

These propagation reactions involve the breaking of an O-O bond and the formation of cyclic species together with a hydroxyl radical. Once again the energy barrier and the frequency factor depend on the size of the cyclic species formed. Specifically, an activation energy of 18 kcal mol^{-1} is assumed for the formation of oxiranes (3-membered cyclic ethers), this decreases to 17 kcal mol^{-1} for oxetanes (4-membered cyclic ethers) and to 8.5 kcal mol^{-1} for furans (5-membered cyclic ethers). The frequency factor ranges from 10^{12} s^{-1} to 10$^{10.4}$ s^{-1} decreasing of 10$^{0.8}$ s^{-1} for any rotor tie-up. The three examples are reported in Figure 43 for the case of n-heptane hydroperoxy-alkyl radicals.
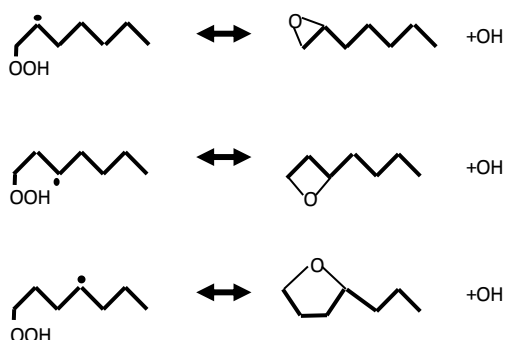
Figure 43: Examples of QOOH=OH + cyclic ether reactions for n-heptane.

The recent study of Bugler et al. [55] highlighted some major discrepancies between literature values, reflected in quite large uncertainty bounds for the proposed rate rules. These uncertainties are reported in *Figure 44* together with other rate values from the literature [55, 144, 147] and the rate constant adopted in the POLIMI mechanism, confirming such large discrepancies. The activation energy adopted in the rate rules of POLIMI exceeds by ~7-8 kcal mol^{-1} that obtained from theoretical calculations in the case of oxiranes formation. Although the revision of such parameters was not within the goals of this thesis, improvements in the rate rules are recommended. More recently Bugler and coworkers reported some systematic theoretical calculation for C_3, C_4 and C_5 hydroperoxy-alkyl radical species aiming at reducing existing uncertainties [148].
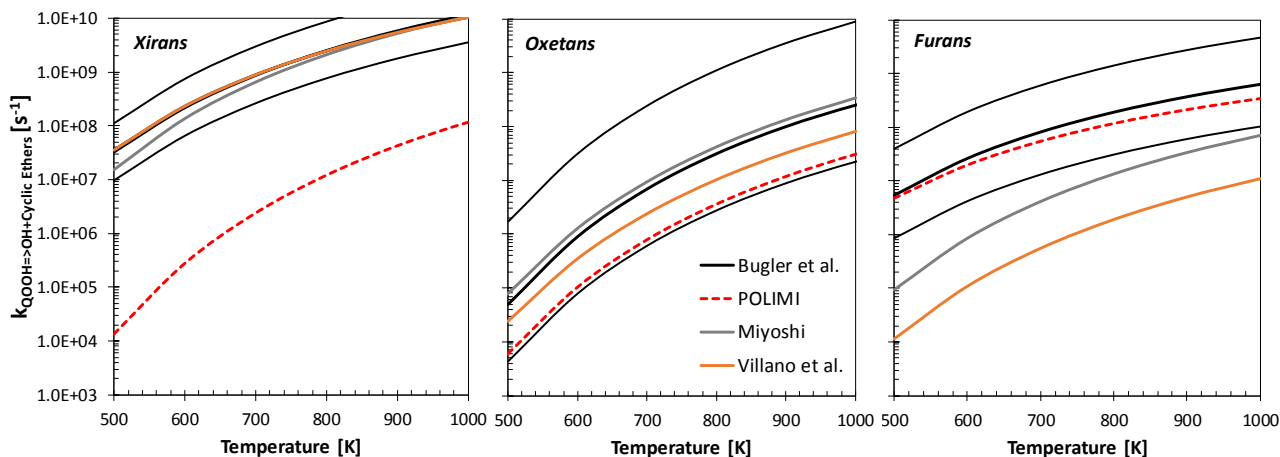
Figure 44: Rate constants for QOOH=OH + cyclic ethers. Red lines: POLIMI, black lines: rate rules from Bugler et al. [55] with uncertainty bounds, orange lines: rate rules from Villano et al.[147], grey lines: calculations from Miyoshi [144].

However it is worth noting that, recent detailed speciation measurements from Herbinet et al. [149] would suggest a large predominance of furanic species, accounting for ~80% of the total amount of cyclic ethers between 600 and 700 K, in agreement with the rate rules adopted in the POLIMI mechanism.

3.2.9 Decomposition of QOOH to form Olefins

QOOH radicals produced by a 6- or 7-membered ring intermediate (γ- or δ-QOOH) can decompose via β-scission to form smaller olefins, carbonyl compounds and OH or smaller olefins and smaller β-QOOH respectively. Examples from n-heptane oxidation are reported in Figure 45.
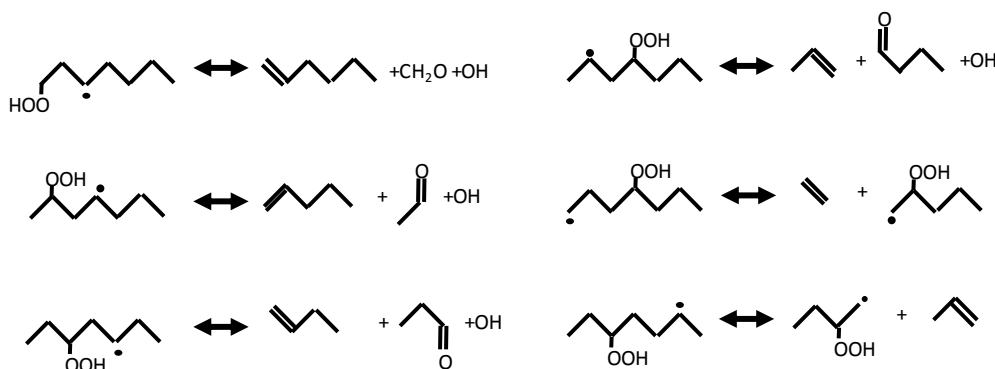
Figure 45: Examples of γ- and δ-QOOH decomposition reactions to form olefins and other products.

Rate constants for a few reactions belonging to this class were calculated by Villano and coworkers [143]. The activation energy of the rate rules obtained was expressed according to an Evans-Polanyi correlation [88], as a function of the reaction enthalpy. γ-QOOH radical decomposition to an olefin, a carbonyl compound and OH is exothermic by ~10-17 kcal mol^{-1}, and according to Villano $E_a = 0.53\,\Delta H_{r,298} + 32.4$ kcal mol^{-1}. Overall it is possible to obtain an average E_a of ~25 kcal mol^{-1}, with a frequency factor of ~3.08E+13 s^{-1}. In a similar way they proposed $E_a = 0.93\,\Delta H_{r,298} + 7.2$ kcal mol^{-1} for δ-QOOH radicals endothermic decompositions. The average reaction enthalpy is ~24 kcal mol^{-1}, therefore the activation energy is ~29 kcal mol^{-1}. For this second case the frequency factor is ~1.4E+14 s^{-1}. A single reference rate constant is assumed in the POLIMI mechanism, $k_{ref} = 10^{13.2}\exp(-22.5/RT)$. *Figure 46* compares rate rules from Villano et al. [147] and Bugler et al. [55] with the reference rate constant of POLIMI, which are seen to agree within the uncertainty limit reported by Bugler.
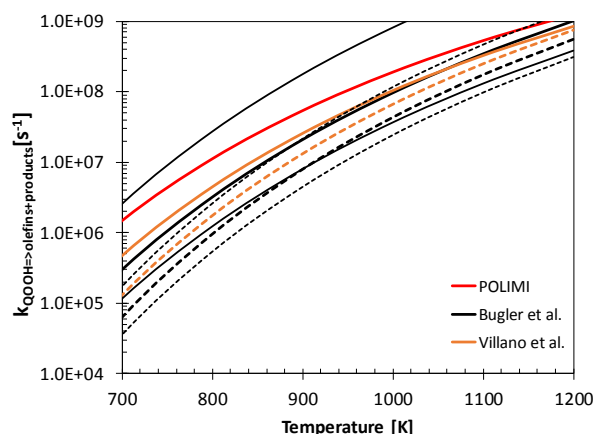
Figure 46: Rate constants for γ-QOOH (solid lines) δ-QOOH (dashed lines) decomposition reactions. Red lines: POLIMI, black lines: rate rules from Bugler et al. [55] with uncertainty bounds (thin lines), orange lines: rate rule from Villano et al. [147].

3.2.10 Decomposition of QOOH to form $H\dot{O}_2$ and Conjugate Olefins

QOOH radicals carrying a radical site in β (i.e. formed through a 5-membered ring intermediate) can decompose to form $H\dot{O}_2$ and a conjugate olefin. Examples from the n-heptane oxidation kinetic scheme are reported in Figure 47.
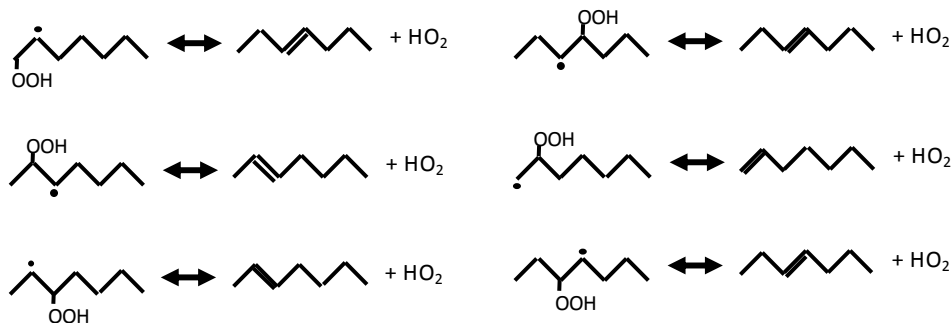
Figure 47: Examples of QOOH= $H\dot{O}_2$ + conjugate olefin reactions for n-heptane.

According to the rate rules reported in Table 9 the reference rate constant is $k_{ref} = 10^{14} \exp(-23.0/RT)$. Recent calculations [144, 147] suggest activation energies on the order of ~15-17 kcal mol^{-1} and frequency factors ~5-7 times lower than those assumed here. However, the overestimation of both the activation energy and of the frequency factor balance out in the temperature range where these reactions are relevant as highlighted in Figure 48.
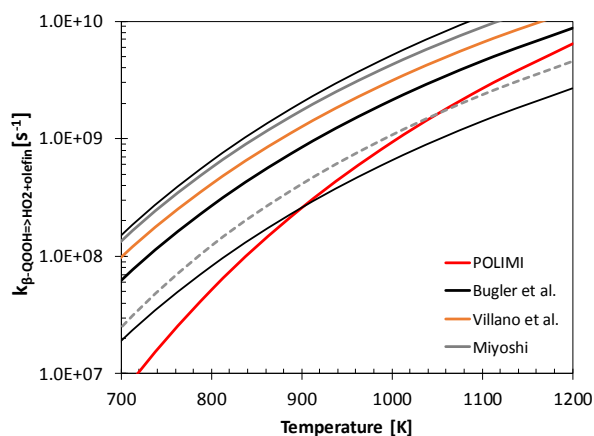
Figure 48: Rate constants for QOOH= $H\dot{O}_2$+ alkene. Red lines: POLIMI, black lines: rate rules from Bugler et al. [55] with uncertainty bounds (thin lines), orange lines: rate rule from Villano et al.[147], grey lines: highest (solid) and lowest (dashed) rate from calculations by Miyoshi [144].

3.2.11 Hydroperoxyalkyl Radicals (QOOH) Addition to O₂

The fourth major reaction channel involving QOOH radicals is the addition to molecular oxygen to form hydroperoxy-alkylperoxy radicals (OOQOOH). The same rate constants adopted for R+O₂ and discussed in Section 3.2.6 are assumed, both in the forward and backward direction.

3.2.12 Decomposition of OOQOOH to form Ketohydroperoxide and OH

This channel in the traditional approach is a "lumped" isomerization/decomposition step. The isomerization of hydroperoxy-alkylperoxy radicals involves the H-atom at the carbon site bound to the hydroperoxy group. Some examples from n-heptane oxidation are given in *Figure 49*.
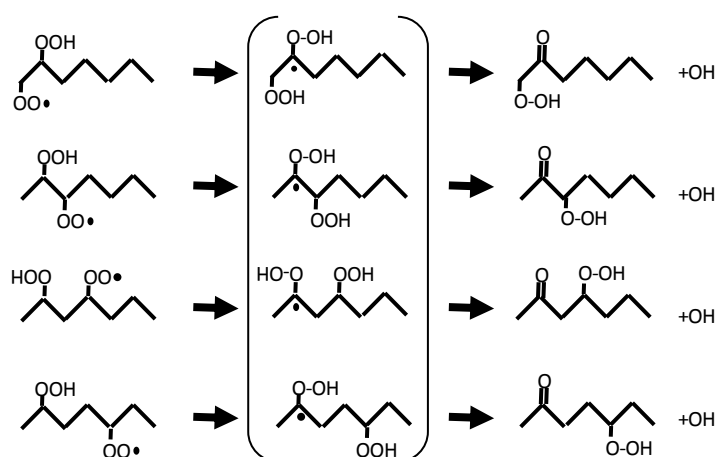
Figure 49: Isomerization/decomposition of hydroperoxy-alkylperoxy radicals to form ketohydroperoxides.

Rate constants are estimated according to the rate rules discussed in Section 3.2.7, lowering the activation energies by 2.5 kcal mol^{-1} to account for the weaker C–H bond.

The recent study of Bugler et al. [55] reexamined the findings of Silke et al. [150] regarding which alternative pathways to the traditional "lumped" isomerization/decomposition to ketohydroperoxides and OH exist for OOQOOH radicals. Such pathways are analogous to those involving RO$_2$ radicals: an isomerization step leads to the formation of dihydroperoxyalkyl radicals (P(OOH)$_2$ [55]), which can decompose in a similar way to that described in Sections 3.2.8, 3.2.9 and 3.2.10, or lead to chain branching by producing carbonyl-hydroperoxides and OH. Figure 50, adapted from Bugler et al. [55], summarizes this possibility.
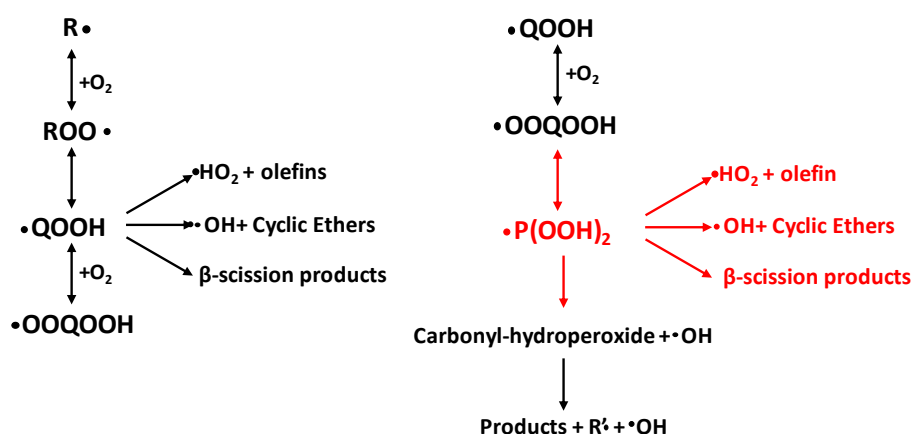
Figure 50: Simplified kinetic scheme of the primary oxidation reactions of alkanes, including possible alternative pathways (red). Adapted from [55].

In contrast with Silke, Bugler et al. did not find much influence of such alternative pathways on alkane reactivity, although a rigorous approach to combustion chemistry would strongly suggest their inclusion. The reason for this disagreement "*is likely a result of the use of more accurate thermochemistry values and rate coefficients to those used previously*" [55]. The updated thermochemistry led in fact to a shift of R+O$_2$⟷RO$_2$ and of RO$_2$⟷QOOH toward the reactants, resulting in a large decrease in reactivity that justified the revision of the rate rules previously adopted [54] in light of more accurate information available in the literature. An example of the impact of the updated thermochemistry is displayed in Figure 51, adapted from Bugler et al. [55].
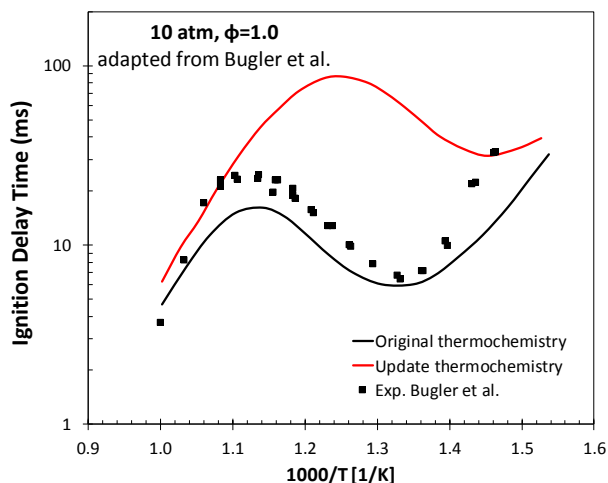
Figure 51: Effect of updated thermochemistry on the n-pentane starting mechanism of Bugler et al. [55].

It is worth mentioning that such alternative pathways might be of relevance for branched alkanes (e.g. iso-octane), whose tertiary alkyl radical addition to O_2 would degenerate in a "*dead-end*" [55] after the formation of a OOQOOH radical, as these radicals cannot produce carbonyl-hydroperoxides. As is clear from Figure 52 the H-atom involved in the traditional isomerization channel is not available for the case of iso-octane.
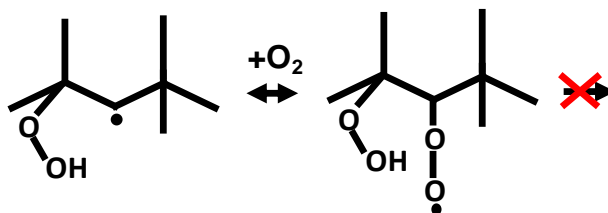
Figure 52: "Dead-end" channel in the oxidation of iso-octane.

3.2.13 Ketohydroperoxide Decomposition

The typical low temperature branching is given from the formation and the decomposition of ketohydroperoxides (or carbonyl hydroperoxides when the carbonyl group (R-C=O) is terminal). The decomposition of these species occurs via the cleavage of the O-OH bond, producing another OH radical, carbonyl species (mostly aldehydes) and another radical as reported in *Figure 53*. The OH radicals formed from this and from the previous step lead to chain branching.
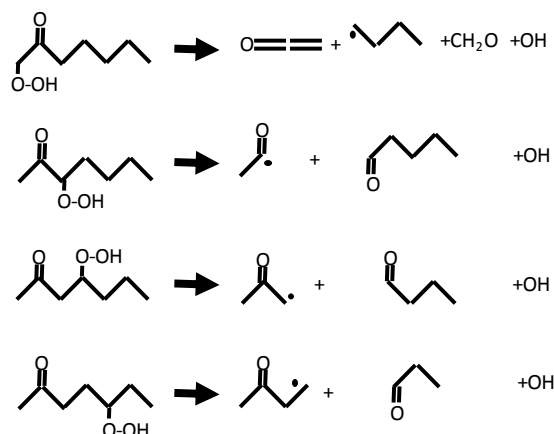
Figure 53: Examples of ketohydroperoxide decomposition reactions from n-heptane oxidation.

New reaction classes introduced in alkane oxidation [72, 73] and discussed in *this thesis* (Section 5.1) compete with these branching steps, reducing the overall reactivity.

The reference rate constant for this reaction class is $k_{ref} = 10^{16}\exp(-43000/RT)$ s^{-1}, in agreement with that proposed by Bugler et al. [55].

3.3 Lumping of Detailed Kinetic Mechanisms

Simplification techniques aiming at reducing the number of species are necessary when detailed mechanisms have to be used in large scale computations, where the computational costs scale by the second/third power of the number of species. As summarized by Huang et al. [151], lumping of species is a well-established technique in model reduction. The pioneeristic work of Dente, Ranzi and coworkers [17, 38, 43, 44, 152] applied simplification and lumping techniques to the kinetic modelling of combustion and pyrolysis processes. The main issues to be tackled when applying lumping techniques are: 1) define which species have to be lumped, 2) determine how the lumped species contribute to the lumped one and 3) estimate lumped kinetic parameters.

The approach of Ranzi et al. [17] aims at reducing the number of species involved in pyrolysis and oxidation schemes without losing predictive capability. In this way the detailed model can be extended to heavier compounds according to a hierarchical approach, with a "linear" increase of the number of species [64].

Table 6 and Table 7 in Section 3.1 already showed the number of species and reactions to be included in detailed mechanisms of n-alkane oxidation, from n-heptane to n-hexadecane. Table 6 highlighted the need of ~68 and ~180 species to describe the oxidation of the two fuels respectively, lumping techniques allow for a treatment of the same system with only 9 species (including the fuel). Table 7 showed the number of reactions, ranging between ~150 and ~404.

Following the observations above, the lumping can be performed at three different levels: 1) lumping of reactions, 2) lumping of species (horizontal lumping) and 3) vertical lumping.

3.3.1 Lumping of Reactions and of Alkyl Radicals

At high temperatures (T > 1000 K) the interactions between alkyl radials heavier than C_4 and the reacting mixtures are very weak, as the lifetime of such radicals is on the order of a tenth of a microsecond (10^{-7} s) as derived from the reference rate constant for β-scission reactions as discussed in Section 3.2.3 ($k_{ref,p} = 3 \: 10^{13} \exp(-30/RT)$). By assuming a steady state for intermediate radicals, the product distributions (i.e. selectivities) can be calculated by solving the following linear system of N equations for N alkyl radicals

$$r_j(0) + \sum_{i \neq j} k_{ij} R_i - \left(\sum_{i \neq j} k_{ji} + k_{dj} \right) R_j = 0 \qquad j = 1 \dots N$$

where $r_j(0)$ is the direct formation rate of the alkyl radical R_j, k_{dj} is the total rate constant for the decomposition reaction of R_j, k_{ji} is the rate constant of the isomerization reaction $R_j \leftrightarrow R_i$ and k_{ij} the rate constant for $R_j \leftrightarrow R_i$. Once the values of R_j are evaluated, a single lumped reaction can be written for the decomposition of the lumped alkyl radical. This reaction, already accounting for the isomerization contributions at the evaluation temperature (T=1000 K) is written in the general form as

$$R_{lumped} \rightarrow \sum_{j=1}^{N} \nu_j P_j$$

where ν_j are stoichiometric coefficient representing the distribution of products P_j specific of the j alkyl radical isomers. An example for the lumped heptyl radical is reported below, Figure 54 shows the radical position of the four heptyl radicals of n-heptane whose decomposition products have already been reported in Figure 15.
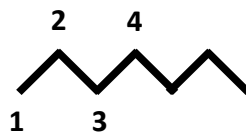
Figure 54: n-heptane alkyl radicals position.

$$r_1(0) + k_{21}R_2 + k_{31}R_3 + k_{41}R_4 - (k_{12} + k_{13} + k_{14} + k_{d1})R_1 = 0$$

$$r_2(0) + k_{12}R_1 + k_{32}R_3 + k_{42}R_4 - (k_{21} + k_{23} + k_{24} + k_{d2})R_2 = 0$$

$$r_3(0) + k_{13}R_1 + k_{23}R_2 + k_{43}R_4 - (k_{31} + k_{32} + k_{34} + k_{d3})R_3 = 0$$

$$r_4(0) + k_{14}R_1 + k_{24}R_2 + k_{34}R_3 - (k_{41} + k_{42} + k_{44} + k_{d4})R_4 = 0$$

At 1000 K the internal distribution (%) of radicals is 17:43:24:16 ($R_1:R_2:R_3:R_4$) therefore the lumped decomposition reaction can be written as:

$$C_7H_{15} \rightarrow 0.17C_2H_4 + 0.17C_5H_{11} + 0.43C_4H_9 + 0.43C_3H_6 + 0.20C_4H_8 + 0.20C_3H_7 + 0.16C_5H_{10}$$
$$+ 0.16C_2H_5 + 0.04C_6H_{12} + 0.04CH_3$$
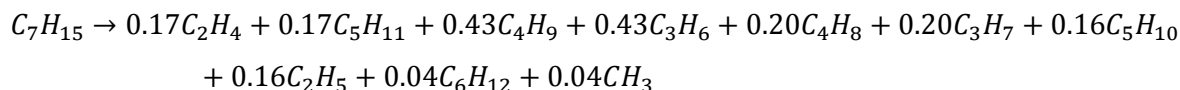
The dependence of this lumped stoichiometry on temperature is weak and mostly related to the different temperature dependence of the rate of H-abstraction reactions leading to the four different radicals. Accounting for the activation energy correction previously discussed for secondary H-atoms (Section 3.2.2) it is possible to obtain the selectivities to the four abstraction sites. Figure 55 shows the dependence of such selectivities on temperature, showing limited variations for the secondary sites (~2-3%) and variation on the order of ~10 % for the higher activation energy primary site over a quite broad range of temperature (1000–1800 K). The differences between the stoichiometric coefficients of the lumped reaction above and the selectivity values of Figure 55 are due to contributions from isomerization reactions.
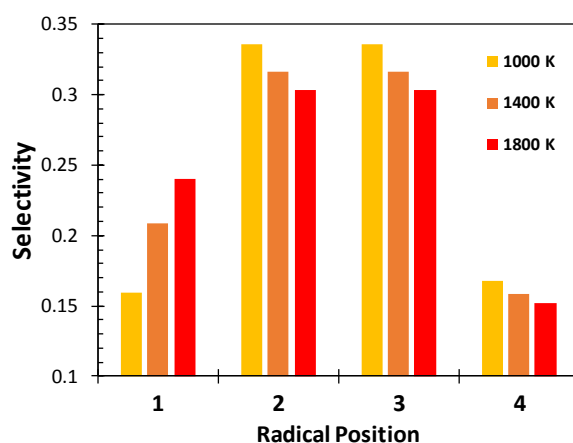
Figure 55: Selectivity of H-abstractions as function of temperature for n-heptane.

Figure 56 justifies the assumption according to which alkyl radicals larger than C4 do not interact significantly with the remaining mixture. The decomposition of a primary alkyl radical according to the reference kinetic parameters is compared with the apparent unimolecular rate constant obtained as the product of the bimolecular rate constant of H-abstraction by a primary alkyl radical, and the concentration of the fuel at 20% of its conversion. The rate of abstraction is at least 3 orders of magnitude lower than the β-decomposition, supporting the assumption.
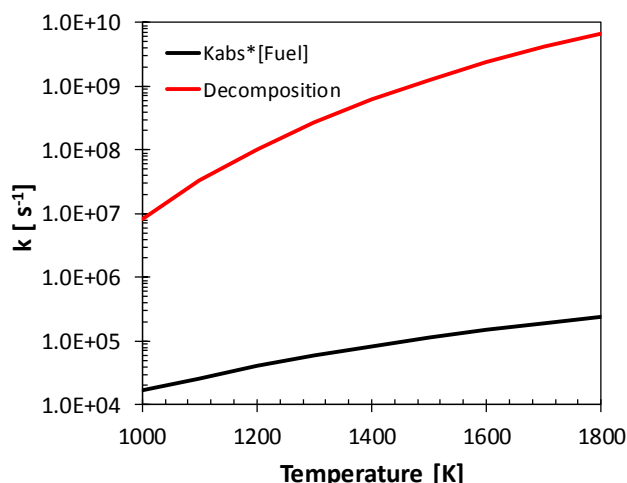
Figure 56: Heptyl radical decomposition rate constant (red lines) versus apparent unimolecular rate of H-abstraction of a primary heptyl radical from the fuel (black lines). Concentration of the fuel at 20% of its consumption are obtained from a constant volume batch simulation at T=1000–1800 K and p=13.5 bar for a stoichiometric mixture of n-heptane and air.

Accepting this assumption, at high temperatures, where the alkyl radicals do not interact with oxygen forming peroxy radicals and pursuing the low temperature pathway, the generic H-abstraction reaction can be written as

$$R + Fuel \rightarrow RH + \sum_{j=1}^{N} \nu_j P_j$$
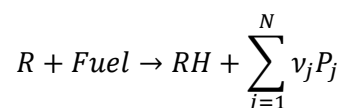
largely simplifying the kinetic mechanisms. As reported by Ranzi et al. [17] the generic H-abstraction on iso-octane written as

$$R + iC_8H_{18} \rightarrow RH + Products$$
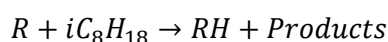
is equivalent to ~300 elementary steps. Clearly, the lumping procedure prevents the possibility of analyzing the decomposition of a pure compound which has been lumped, without a precedent process of "*delumping*".

3.3.2 Lumping of Species: Horizontal Lumping

The kinetic scheme can be greatly simplified by introducing *pseudospecies* representative of the 8 classes of primary intermediates (radical and stable species) reported in Table 7. A schematic representation of this approach is reported in Figure 57. Beside the computational advantage of this important reduction in the number of species, the introduction of one single lumped components for any intermediate radicals and compounds makes the comprehensive description of their successive reactions easier to manage and also to understand and interpret. Detailed kinetic mechanisms available in the literature in fact tend to treat the kinetic mechanism of large hydrocarbons in a very detailed fashion, up until where the explosion of the

number of species (e.g. in ketohydroperoxides) forces the treatment of every isomer with the same kinetic rate constant. This coexistence of the aim for a high level of detail and difficulties in managing the complexity of combustion kinetic mechanisms further supports the suitability and efficiency of the approach used in the CRECK modeling group for the last 30 years.
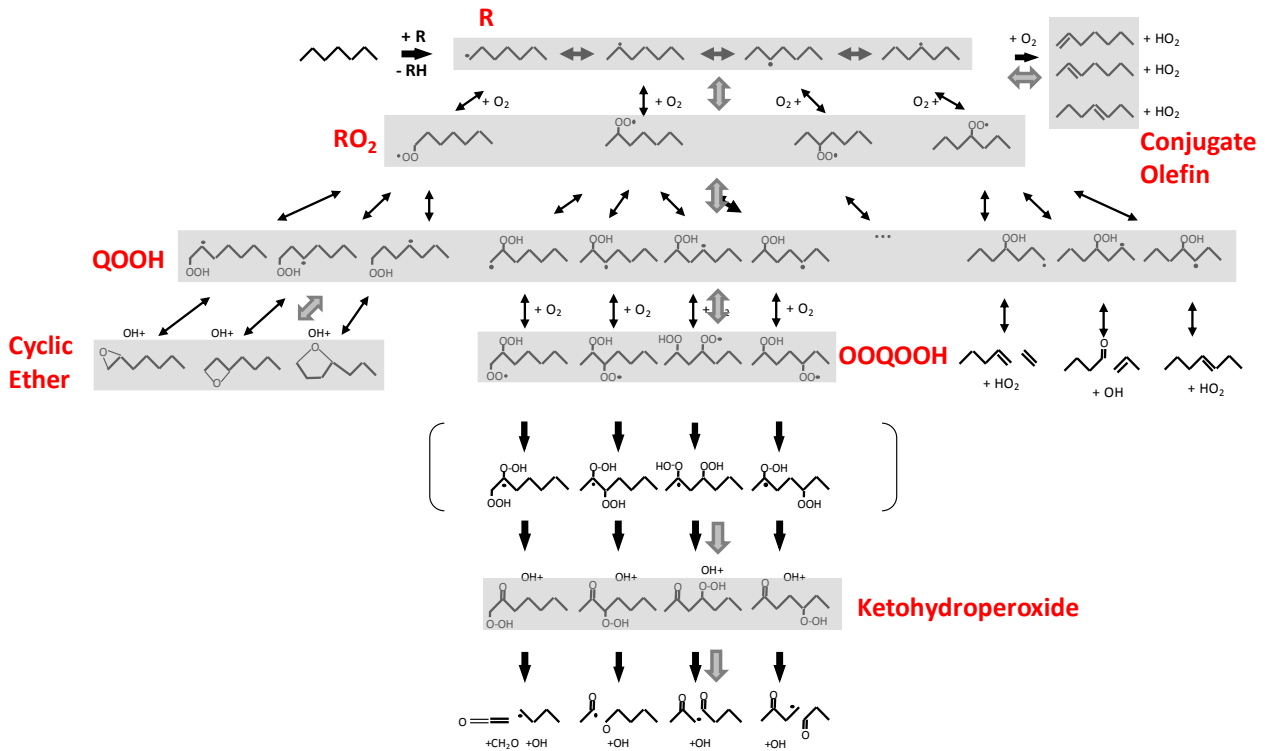
Figure 57: Species lumping (horizontal lumping) in the oxidation of n-heptane.

As summarized from the grey arrows in Figure 57 the detailed kinetic rate constants describing the successive reactions of the single species are replaced by a limited number of lumped rate constants. The 10 primary propagation reactions described in previous Sections (3.2.4 to 3.2.13) and listed in Table 1 allow a direct evaluation of the distribution of the primary products from fuel pyrolysis and oxidation. The lumped kinetics are then derived through an optimization process aimed at minimizing the deviation in the selectivities to final products between the original detailed mechanism and the lumped one. The objective function involved in such a process is

$$\min_{\boldsymbol{k}} \varepsilon = \min_{\boldsymbol{k}} \int_{P_0}^{P} \int_{T_0}^{T} \sum_{j=1}^{N} \left[\sigma_{detailed,j} - \sigma_{lumped,j}(\boldsymbol{k}) \right]^2 dT \, dP$$

where n is the number of products, $\boldsymbol{k}$ is the vector of lumped kinetic constants and σ_j the product selectivities. The range of temperature and pressure are the conditions at which the starting detailed kinetic

mechanism was validated. The MAMOX++© code is used to perform such minimization, with the details of the code discussed in previous studies [64, 152].

The discussion in Section 3.2 already pointed out the fact that the correct description of the low temperature phenomena (cool flames, ignition, negative temperature coefficient region) strongly depends on the correct assessment of the relative role of chain branching and chain propagating channels, or, in other words, on the correct evaluation of product distributions. Figure 58 compares selectivities from the n-heptane detailed mechanism and the lumped version as included in the POLIMI mechanism. Starting from low temperatures characterized by high yields of branching agents (ketohydroperoxides formation), the transition to higher temperatures leads to an increase in selectivity to propagation channels typical of the NTC region, until the alkyl radical decomposition products highlight the increasing importance of high temperature reactions. As expected the selectivity to branching channels shows a wider temperature window for increasing pressure, due to stabilization of peroxy radicals. The simplified mechanism (dashed lines) coherently reproduces the product distribution obtained with the detailed mechanism.
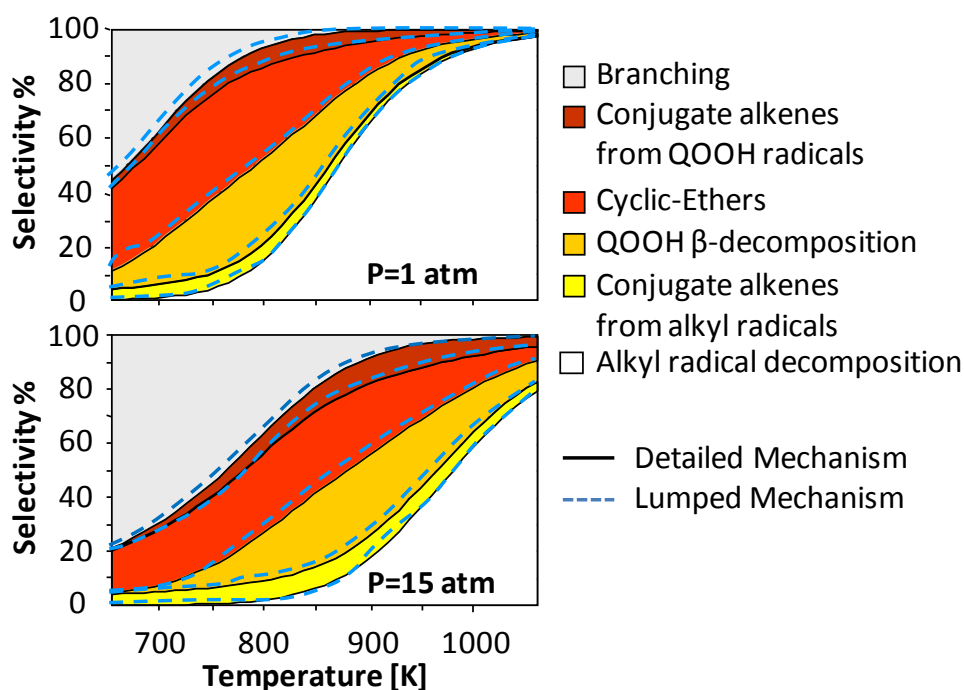
Figure 58: Selectivities to products in the oxidation of n-heptane in air at 1 and 15 atm. Comparisons between the predictions of the detailed (solid line) and the lumped (dashed lines) kinetic mechanisms.

Ranzi et al. [64] observed very marginal variations to these selectivities when considering n-hexadecane (n-$C_{16}H_{34}$) oxidation. For this reason, the primary lumped reactions always appear with very similar, often identical, kinetic parameters for compounds belonging to the same class.

In this regard, *Table 10* compares the lumped kinetic parameters for n-heptane (C_7), n-decane (C_{10}) and n-hexadecane (C_{16}) adopted in the POLIMI mechanism. A thorough validation of these real fuels surrogate components was recently reported [40]. The differences between the fuels are evident for initiation reactions and H-abstraction reactions where the rate constants increase for increasing chain length. Similarly, the isomerization steps reflect the increasing availability of 5- 6- and 7-membered intermediates in longer alkanes, resulting in a more pronounced low temperature reactivity. This is also reflected in the different decomposition rates of ketohydroperoxides. Some minor differences (within a factor of ~3) are observed in β-QOOH → $H\dot{O}_2$ + olefin reactions, due to a recent revision of the lumped kinetic parameters of *n*-heptane where new reaction classes were introduced based on new experimental evidence and theoretical calculations [72, 73] (Section 5.1).

Overall, *Table 10* highlights another advantage of this simplified approach which is the possibility of easily extending the mechanism to larger fuels belonging to the same class of compounds, by simply adopting the same lumped kinetics. The obtained kinetic scheme, which might need revisions and refinements depending on the availability of more accurate parameters from the literature (e.g. revision of rate rules, introduction of new reaction classes), only causes a limited increase in the global mechanism size, allowing good predictive capability.

Lumped reactions	n-C_7H_{16}			n-$C_{10}H_{22}$			n-$C_{16}H_{34}$		
	A	*n*	*Ea*	*A*	*n*	*Ea*	*A*	*n*	*Ea*
Initiation (total)	**2.00E+17**	**0**	**82000**	**3.00E+17**	**0**	**81500**	**7.00E+17**	**0**	**81500**
H-abstractions by OH (total)	**4.79E+06**	**2**	**-2260**	**6.80E+06**	**2**	**-2260**	**1.20E+07**	**2**	**-2260**
Abstraction sites	$10H_s$	$6H_p$		$16H_s$	$6H_p$		$28H_s$	$6H_p$	
R → β-decomposition	3.00E+13	0	30000	3.00E+13	0	30000	3.00E+13	0	30000
O_2+R = $H\dot{O}_2$+ conjugate olefin	5.00E+11	0	3500	5.00E+11	0	3500	5.00E+11	0	3500
$R+O_2$ → RO_2	2.00E+12	0	0	2.00E+12	0	0	2.00E+12	0	0
RO_2 → R + O_2	5.00E+13	0	31000	5.00E+13	0	31000	5.00E+13	0	31000
RO_2 → QOOH	**3.00E+12**	**0**	**25100**	**3.00E+12**	**0**	**24800**	**3.00E+12**	**0**	**24000**
QOOH → RO_2	2.00E+10	0	16100	2.00E+10	0	16100	2.00E+10	0	16100
QOOH → Cyclic Ether + OH	1.00E+10	0	14100	1.50E+10	0	14100	1.50E+10	0	14100

β-QOOH $\rightarrow$ $H\dot{O}_2$ + Olefin	**2.00E+12**	**0**	**24000**	**3.00E+11**	**0**	**19000**	**3.00E+11**	**0**	**19000**
γ/δ-QOOH $\rightarrow$ OH + Olefins	2.00E+12	0	22500	2.00E+12	0	22500	2.00E+12	0	22500
QOOH + O_2 $\rightarrow$ OOQOOH	2.00E+12	0	0	2.00E+12	0	0	2.00E+12	0	0
OOQOOH $\rightarrow$ QOOH + O_2	2.00E+14	0	29000	2.00E+14	0	29000	2.00E+14	0	29000
OOQOOH $\rightarrow$ OQOOH + OH	**1.00E+12**	**0**	**24500**	**1.50E+12**	**0**	**24500**	**2.60E+12**	**0**	**24500**
OQOOH $\rightarrow$ OH + Products	7.00E+15	0	42000	8.00E+15	0	42000	1.50E+16	0	42000

Table 10: Kinetic parameters of the lumped oxidation reactions of n-alkanes (units are mol, cm, s, cal). Values in bold are those differing from one fuel to another. Updated from Ranzi et al. [65].

The hierarchical approach, reflecting the intrinsic nature of combustion kinetics, is even more evident from *Figure 59* where the bar diagrams show the rate constants at varying temperatures for those reactions specifically characterizing each fuel: initiation, H-abstractions and isomerization reactions. Rate constants for initiation, H-abstraction and isomerization reactions coherently increase moving to large fuels. These features result in the reactivity trend reported in the bottom-right panel of *Figure 59*, showing a comparison of the ignition delay times of stoichiometric fuel/air mixtures at *p*=10 bar.
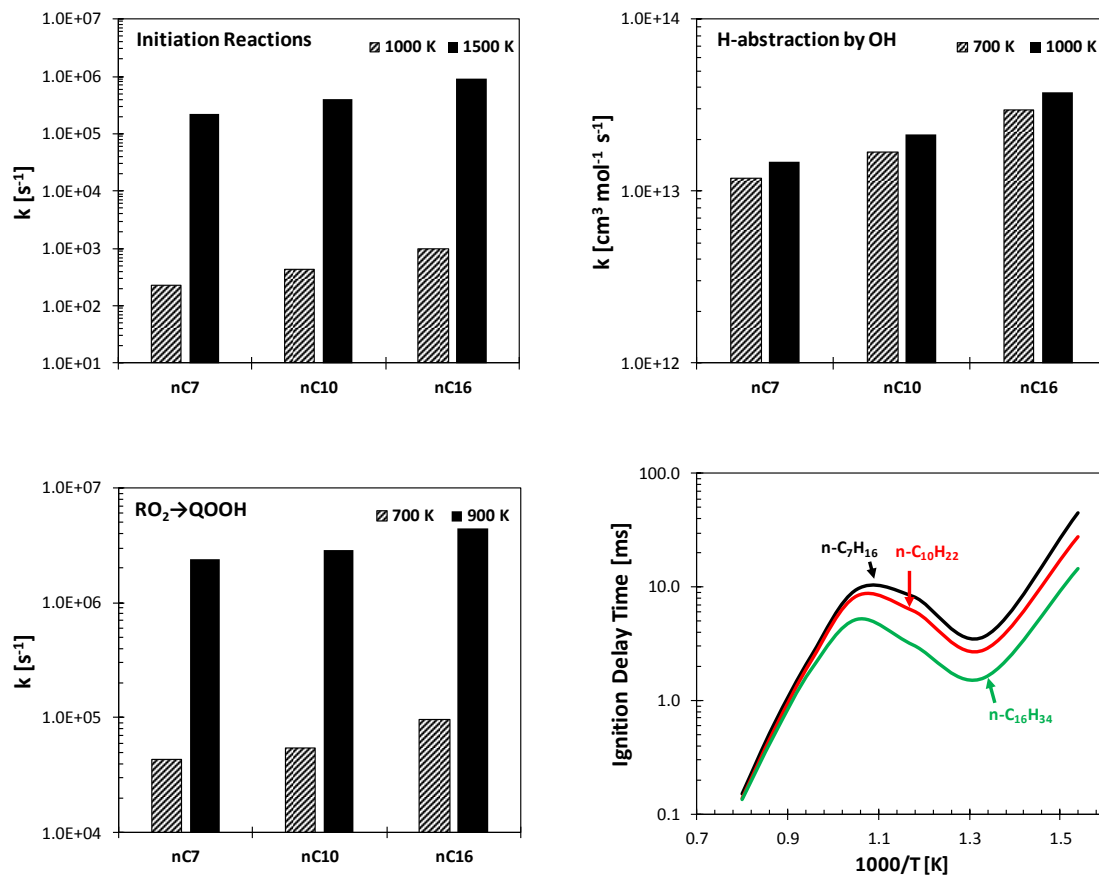
Figure 59: Comparison between rate constants of n-C_7, C_{10} and C_{16} alkanes at different temperatures. Ignition delay time comparison for stoichiometric fuel/air mixtures at p=10 bar. Adiabatic constant volume batch reactor simulations.

3.3.3 Vertical Lumping

The similar reactivity and product yields from the pyrolysis and combustion of homologous species allows a further simplification of the overall kinetic scheme. Instead of including all the n-alkanes from *n*-pentane up to *n*-hexadecane (12 species), it is possible to consider only some reference species C_5, C_7, C_{10}, C_{12} and C_{16}, with a reduction of more than 50% for the final scheme.

Following the previous discussion, is not surprising that further reduction of the number of species belonging to the kinetic mechanism can be achieved by only considering some reference species (n-butane, n-heptane, n-decane etc.) for a given family (n-alkanes). The species which are not included in the mechanism are represented by splitting them between the closest species through the lever rule. For example, n-hexane oxidation can be investigated by considering a mixture of 50% n-pentane and 50% n-heptane, as summarized in Figure 60 together with other examples.
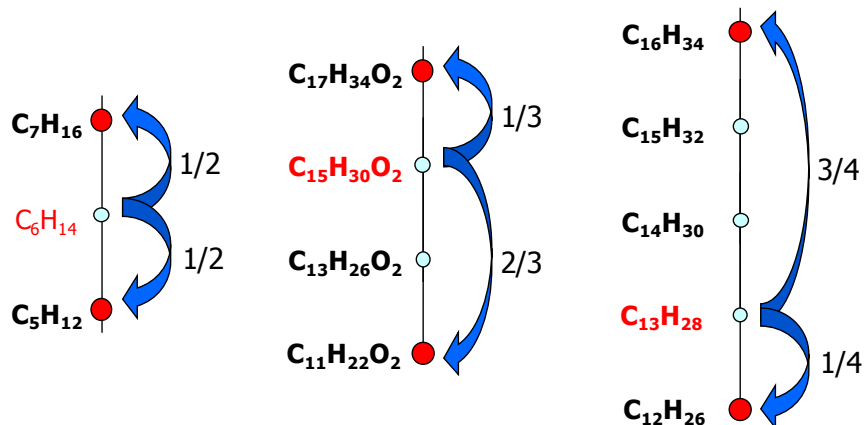
Figure 60: Approach to intermediate fuel analysis through vertical lumping. From left to right: n-hexane, methyl-myristate, and tridecane.

A recent study of Zhang et al. [153] presented a new kinetic model for n-hexane oxidation, together with some detailed ignition delay time measurement in shock tubes and rapid compression machines. The POLIMI kinetic mechanism was used to simulate these data, by considering a stoichiometric in air mixture of 50% n-heptane and 50% n-pentane to represent n-hexane. Satisfactory agreement supporting the reliability of the vertical lumping is reported in *Figure 61*.
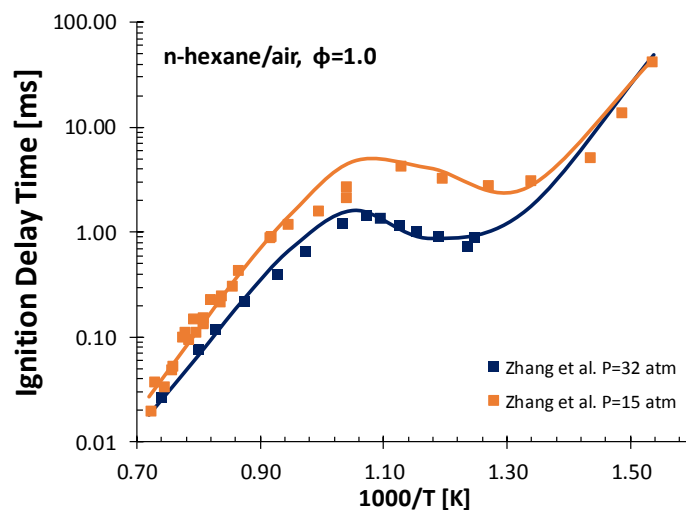
Figure 61: Ignition delay times of stoichiometric n-hexane/air mixtures at p=15 and 32 atm. Symbols: experimental data of Zhang et al. [153], lines: POLIMI mechanism (n-hexane=50% n-pentane, 50% n-heptane).

3.4 Summary

This Section described the reaction classes and the reference kinetic parameters used to model pyrolysis and combustion of alkanes [17].

The revision of these rate rules was not the goal of this study, therefore the discussion is limited to a comparison of the kinetic parameters in use at POLIMI with more recent theoretical calculations systematically summarized by Bugler et al. [55]. In most of the cases the agreement was found to be within the existing uncertainty. Other classes need better refinement either because a systematic evaluation aimed at reducing the uncertainty is missing from the literature or because the adopted parameters greatly deviates from more accurate values. This necessity constitutes one of the outcome of this work and motivates the discussion carried out in this chapter. However it has to be stressed that the revision must be systematic, starting from the inclusion of more accurate thermodynamic data [97, 100] and from a comprehensive update of the C_0-C_4 submechanism. The key features of pyrolysis, high and low temperature oxidation kinetics have been discussed pointing out how the relative importance of reaction channels is often more important than extremely accurate absolute values. However, the availability of theoretical knowledge and computational capabilities makes the thorough and hierarchical revision of rate parameters necessary for enhanced predictive capabilities, in particular at those conditions of interest for real systems where experimental measurements are hardly available [48, 68]. Moreover, as it should be in the nature of scientists and engineers, the thrust to dig deeper in the understanding and representation of reality with improved models should always be within the main goals of our scientific research. In combustion kinetics, this opportunity is nowadays at hand and should be exploited.

Simplification techniques such as lumping aimed at reducing the complexity of combustion kinetic mechanisms have been also discussed in this Section, highlighting pros and cons involved in such approaches.

The next Chapter focuses on the theoretical estimation of gas phase reaction rate constants, discussing available methods used to estimate rate constants for some of the systems investigated in *this thesis*.

Chapter 4 – Theoretical Gas Phase Kinetics

Historically the development of kinetic mechanisms has been based on direct experimental measurements of elementary reaction steps and thermodynamic properties. The impossibility of measuring every reaction rate constant involved in the kinetic model has driven the extensive use of analogy rules, whose coupling with thermochemical kinetics [50], chemical intuition and empirical adjustment allowed the development of mechanisms of increasing complexity. In this scenario, as already discussed in Section 1.3, the limitations to the direct application of theoretical chemistry to kinetic modelling have to be referred to limited computational capabilities, overcome in the last three decades with the advent of high-end computing hardware. This Chapter provides an overview of current methods used for the theoretical estimation of gas phase rate constants, with direct reference to those methods adopted in different parts of *this study*. As the detailed explanation of the underlying theory is outside the scope of this study, the reader is referred to standard monographs on computational chemistry [81, 82, 154] and to the specific scientific literature.

4.1 Electronic Structure Methods

The power of applied computational chemistry lies in the ability to support and rationalize experimental findings, allowing the estimation of model parameters starting from molecular level information. The quality of such approaches may vary depending on the computational feasibility of the problem, which is determined by: 1) the level of accuracy required, 2) the size of the system (i.e. the number of heavy atoms in the molecules). The accuracy (and the computational cost) increases as one moves from molecular mechanics, to semi-empirical quantum mechanics, to density functional theory (DFT) and *ab initio* methods.

Large molecular systems (e.g. proteins, 10^5 atoms) are investigated through molecular mechanics while semi-empirical quantum mechanics, based on approximate solutions of the Schröedinger equation, is used for systems where DFT or *ab initio* methods are computationally impractical. These latter are typically employed for the investigation of gas-phase combustion reactions whose characterization requires firstly the knowledge of the potential energy surface (PES) on which the reaction takes place. This involves the knowledge of 1) the molecular geometry, 2) the vibrational frequencies and 3) the electronic energies of the reactants, the transition state and the products involved in the reactions. Theoretical chemistry allows to calculate these properties *ab initio,* through the direct solution of the time-independent Schröedinger equation [155]

$$(T_e + H_{e-e} + H_{n-e})\Psi_e = E_e\Psi_e$$

obtaining a *single point energy*, which is the electronic energy of the molecule for a particular configuration of the nuclei. The remaining properties are evaluated based on the knowledge of energy gradients and of the

hessian matrix. The energy gradients (first derivative) characterize the effect of electronic energy on the nuclei. At the equilibrium geometry, the forces acting on a nucleus must vanish (first derivative equals zero). The vibrational analysis requires the knowledge of the hessian which is the second derivative matrix of the electronic energy.

In the Schröedinger equation reported above E_e is the electron energy, T_e is the electron kinetic energy, H_{n-e} is the nuclei-electron interaction potential, H_{e-e} is the electron-electron interaction potential and Ψ_e is the electron wave function. Most of the complexity of this equation lies in the electron-electron interaction. The dynamics of a many-electron systems is very complex, and consequently requires elaborate computational methods. The introduction of independent-particle models, where the motion of one electron is considered to be independent of the dynamics of all other electrons allows for significant simplification of the problem. An independent-particle model requires the approximation of the interactions between particles considering only the most important one, or by taking all interactions into account in an average fashion.

The Hartree-Fock (HF) method [156-158] is the basic method to approach the solution of the Schröedinger equation. In this case the H_{e-e} term is replaced by an average interaction covering up to 99% of the total energy for large basis sets. The remaining 1% is however very significant and the difference between the HF solution and that explicitly considering H_{e-e} is defined as the electronic correlation energy (EC).

Since the implementation of the Hartree-Fock, other methods have been developed to calculate the electronic correlation energy. *Post-Hartree-Fock* approaches include single-reference and multi-reference methods.

Within the first class the coupled-cluster singles and doubles with triples excitations (CCSDT [159]) with subsequent extrapolation of the energies to the basis-set limit is the desirable standard. As this is hardly achievable, more common methods include the CCSD(T) methods, with perturbative inclusion of triples [160]. The application of such methods to systems with up to ~10 "heavy" or "non-hydrogen" atoms requires the adoption of a computationally suitable basis set. The subsequent extrapolation allows the refinement of the computed energies.

Multi-reference methods come from the necessity to overcome issues coming from "spin contamination" effects as thoroughly described in chapter 4 of the book "Introduction to Computational Chemistry" of Jensen [154]. Neglecting such effects leads to undesirable inaccuracy in single point energies, and therefore in kinetic rate constants. Methods such as CASPT2 [161-164] with adequate basis sets provide accurate treatments of such systems. Both single and multi-reference methods are efficiently implemented in commercial software such as Gaussian [46] and Molpro [47], with the only difference that CASPT2 requires the knowledge of the

orbitals showing spin contamination and involved in the reaction, making these methods less straightforward.

In terms of accuracy the methods briefly introduced above have proven to be accurate within ~1 kcal/mol for large enough basis sets, when compared with well-known experimental information.

As already pointed out the major problem of *Post-Hartree-Fock* methods is the high computational effort required for systems with more than 10 heavy atoms. Such cases are more efficiently investigated with density functional theory (DFT) methods.

According to the Hohenberg and Kohn theorem [165] the electronic energy is completely determined by the electron density. This assumption simplifies the treatment of the so called *many-body problem* according to which the exact solution of the Schröedinger equation only exists for 1-electron systems, reducing the number of degrees of freedom from 3N (N is the number of electrons) to 3. Therefore, even if a wave function complexity increases with the number of electrons, the electron density is only a scalar function of space coordinates, therefore is independent on the system size. The only challenge is to define a functional creating this one-to-one connection between electron density and electron energy. Among these methods the most common is the B3LYP functional [166, 167], commonly adopted for the calculation of frequencies and geometries. The main limitation of DFT methods lies in neglecting dispersion interaction that might be relevant for large systems. This normally leads to accuracies within ~5 kcal/mol. New DFT functionals have been recently proposed to overcome this problem: for example the M05- and M06-2X of Zhao and Truhlar [168] and the B2PLYP-D3 of Grimme and coworkers [169, 170].

Overall, if on one hand DFT methods provide lower accuracy at lower computational costs, *Post-Hartree-Fock* high level methods provide highly accurate energies at a significant computational cost. This scenario drove the implementation of approximate procedures commonly known as compound methods. These methods consist of a pre-defined routine of cost-effective calculations intended to achieve high-accuracy (~1-2 kcal/mol).

The CBS-QB3 method [171] consists of the following sequence:

    1. B3LYP/CBSB7 geometry optimization and vibrational frequencies calculation

    2. CCSD(T)/6-31+G(d') single point energy

    3. MP4(SDQ)/CBSB4 single point energy

    4. UMP2/CBSB3 single point energy with complete basis-set extrapolation

The G4 [172] method uses the following calculations:

1. B3LYP/6-31G(2df,p) geometry optimization and vibrational frequencies calculation

2. HF/limit single point energy

3. MP4/6-31G(d) single point energy

4. MP4/6-31+G(d) single point energy

5. MP4/6-31G(2df,p) single point energy

6. CCSD(T)/6-31G(d) single point energy

7. MP2(full)/G3LargeXP

In the latter G4 methods the computed energies are combined as reported in the paper of Curtiss et al. [172]. Other procedures such as those proposed by Martin [173, 174] and coworkers and by Stanton and coworkers [95, 175, 176], aim at even higher accuracy (~0.1-0.2 kcal/mol), but can only be extensively applied to rather small molecules.

Figure 62 summarizes standard methods and basis sets used in electronic structure calculations. Accuracy and computational costs increase moving from left to right in terms of methods and from bottom to top in terms of basis set.
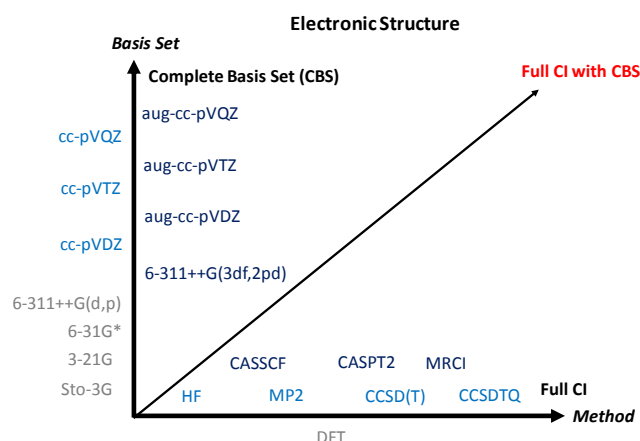
Figure 62: Basis set and methods commonly used in electronic structure calculations. Adapted from Klippenstein [177].

4.2 Statistical Thermodynamics

Before introducing the kinetic theories commonly used to calculate rate constants for combustion kinetic mechanisms it is necessary to briefly discuss some statistical thermodynamics concepts central to the derivation of thermodynamic and kinetic parameters from atomic and molecular properties (vibrational

frequencies, rotational constants etc.) obtained from quantum chemical calculations. The connection between the two parts is through the definition of the *partition function Q*. For a system of N molecules the number of molecules N_i in a given state of the system with energy e_i, is given by the Boltzmann distribution as

$$N_i = \frac{N \, exp(-e_i/k_BT)}{Q}$$

Where k_B is the Boltzmann constant (~1.381 × 10^{-23} m² kg s^{-2} K^{-1}).

Q is defined as

$$Q = \sum_i g_i \, exp(-e_i/k_BT)$$

and g_i is the degeneracy of the ith level. In other words the partition function Q is the total number of states accessible to a molecule at a given temperature T. Assuming separable degrees of freedom where the energy can be stored, it can be derived that Q is the product of individual partition functions representative of these degrees of freedom. In the phase space (x, y, z) each non-linear molecule with N atoms has $3N$ degrees of freedom. Three are related to translational motion, three are external rotations of the molecules center of mass with respect to the axes, and the remaining $(3N - 6)$ are vibrational modes. For linear molecules only two distinguishable external rotations are possible, therefore the vibrational frequencies are $(3N - 5)$. Translational motion Q_T considers a molecule of mass m moving in a volume V at temperature T

$$Q_T = \frac{(2\pi m k_B T)^{\frac{3}{2}}V}{h^3}$$

Where h is the Planck constant (~6.626 × 10^{-34} m² kg s^{-1}).

The partition function Q_R represents the external rotational motion, which for a non-linear molecule is expressed as a function of the three rotational constants A, B, C

$$Q_R = \left(\frac{k_B T}{h}\right)^{\frac{3}{2}} (ABC)^{-\frac{1}{2}}\pi^{\frac{1}{2}}\sigma^{-1}$$

While for a linear molecule it is

$$Q_R = \left(\frac{k_B T}{h\sigma B}\right)$$

These two expressions derive from the approximate solution of the Schrödinger equation through the rigid-rotor assumption. This means that the rotational constants are assumed to be unperturbed by the rotations or the vibrations of the molecule, and the influence of centrifugal forces is assumed to be negligible.

The partition function for vibrational motion is directly calculated from the frequencies ν_i as

$$Q_V = \prod_i [1 - \exp(-h\,\nu_i / k_B T)]^{-1}$$

The harmonic oscillator assumption is assumed to derive the above expression. In many cases a more accurate treatment of Q_V is necessary as some of the $(3N - 6)$ vibrational modes may correspond to tortional motion over a dihedral angle and not to a proper vibration. A simple example is provided in *Figure 63* for acetic acid. The rotation of the methyl group ($-CH_3$) corresponding to the dihedral angle 4-1-2-3, has a barrier of ~0.47 kcal/mol at the M06-2x/6-311+g(d,p) level.
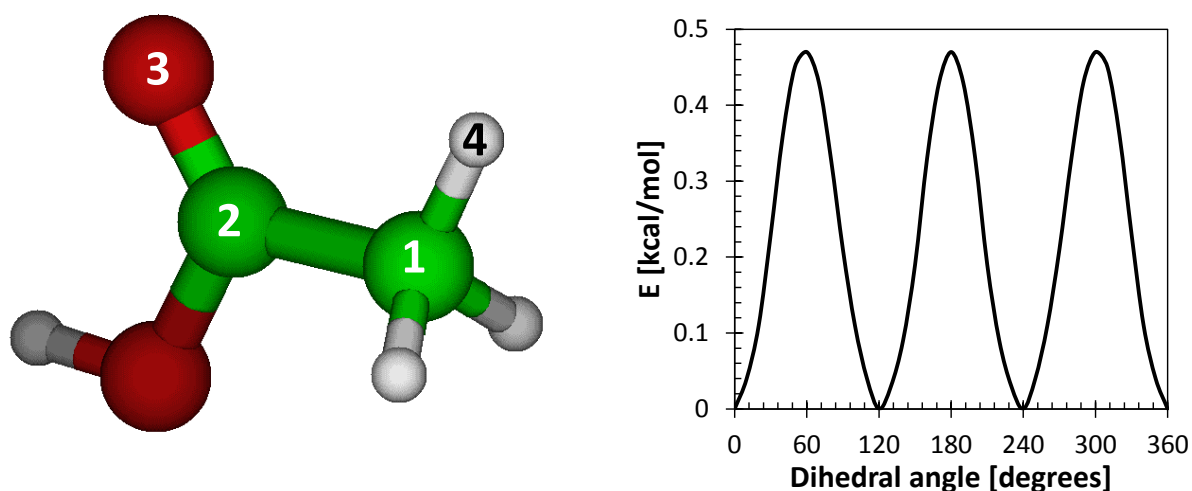
Figure 63: Potential energy as a function of the dihedral angle 4-1-2-3 of acetic acid calculated at M06-2x/6-311+g(d,p) level.

Depending on the thermal energy of the system, RT, this barrier is more or less likely to be overcome. At room temperature (298 K) the thermal energy is ~0.59 (207 cm^{-1}) kcal/mol, therefore a consistent portion of the population of molecules would have energy in excess of the rotational barrier. Even more for increasing temperatures, where for example at 1000 K the thermal energy is ~1.987 kcal/mol (695 cm^{-1}). For this reason, this mode should be rigorously treated with a tortional partition function (Q_{IR}), incorporating the transition of the hindered rotation to a free rotation, which in this case is very likely at temperatures of interest for combustion. Incorporating a fitting of this potential energy in the Schröedinger equation allows us to determine Q_{IR} for the hindered rotor case, while for free rotors the partition function can be expressed as

$$Q_{IR,free} = (\sigma_v h)^{-1} (8\pi^3 I_{int} k_B T)^{\frac{1}{2}}$$

Where σ_v is the symmetry number for the internal rotation and I_{int} is the reduced moment of inertia. In the case of a free rotor, both the treatments would produce the same result. A brief overview of the different approaches from the literature [178-181] is reported in a recent work of Klippenstein et al. [182] highlighting the importance of rigorous treatments of free rotors mainly for oxygenated molecules, where hydrogen bonding effects can be relevant.

The last partition function of interest is the electronic partition function Q_E computed as

$$Q_E = \sum_i g_i \exp(-\varepsilon_i/k_B T)$$

Where g_i is the degeneracy of the ith electronic state of energy ε_i. For closed shell molecules, only the ground state ($\varepsilon_i = 0$) is normally considered, therefore $Q_E = g_E$, i.e. the number of unpaired electrons in the molecular orbitals plus 1. Defining a net electron spin $S = n/2$, with n the number of unpaired electrons and expressing $g_i = 2S + 1$ it derives that $g_E = 2$ for radicals and 3 for molecules that are triplets in their fundamental state (e.g. O_2).

The total partition function Q introduced at the beginning of this section can be computed as

$$Q = Q_T Q_R Q_V Q_{IR} Q_E$$

Its application to the calculation of kinetic rate constants will be discussed in the next Section 4.3.

4.3 Kinetic Theories

Figure 64 shows an example potential energy surface with three stationary points: two minima and one transition state. The minima can be global or local and they are located in a potential well. The transition state lies at the maximum (saddle-point) between the two minima, although it is itself a minimum in all other coordinates.
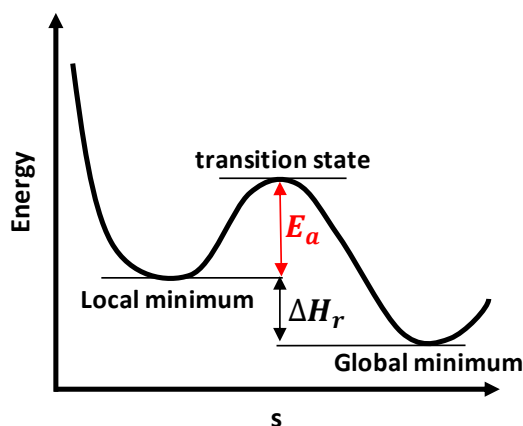
Figure 64: Potential energy surface for a generic unimolecular reaction.

The plot of Figure 64 is obtained from the qualitative plot of Figure 65, sliced over the *s* reaction coordinate, a curvilinear path connecting reactant and products following the minimum energy path (MEP).
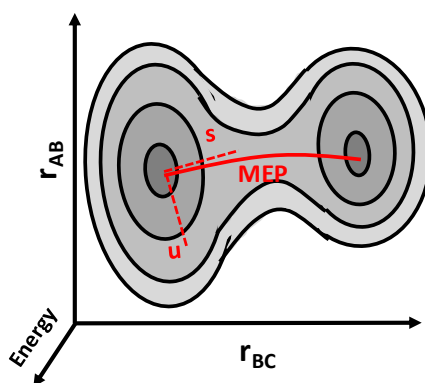
Figure 65: Representation in the (rAB, rBC) plane of the triatomic system of the new set of reaction coordinates (s,u).

Reactions can be classified based on the shape of their PES. The clear maximum of Figure 64 is defined as a "simple barrier reaction" proceeding through a "tight" transition state. "Barrierless" reactions like radical-radical recombination reactions typically show a "loose" transition state as the PES smoothly changes from reactant to products, without a clear saddle-point.

4.3.1 Transition State Theory

Transition state theory (TST) was developed in the 1930s by Eyring [183], and Evans and Polanyi [184]. Transition state theory is based on two fundamental hypotheses and on three restrictive hypotheses that limit its field of applicability. The two fundamental hypotheses are:

1) The Born-Oppenheimer approximation states that it is possible to treat the motion of electrons and of nuclei independently: during the translation of nuclei, electrons are always in the equilibrium position, in the lowest quantum state.

   a. Like in classical mechanics, the nuclei move according to the potential generated by the electronic energy of the reacting molecule. This leaves out quantum effects such as quantum tunneling, that might be relevant for accurate calculation of rate constants.

   b. The *adiabatic assumption* concerning the lowest quantum state excludes the treatment of spin forbidden reactions, involving an intersystem crossing (e.g. jump from a singlet to a triplet potential energy surface as in singlet-to-triplet reactions).

2) The velocity distribution of molecules is defined by the Maxwell-Boltzmann distribution function.

The three restrictive hypotheses are:

1) The *non-recrossing* approximation states that reactant molecules that have overcome the transition state, proceed until the formation of the products, without possibility of return to the reactant conformation. As this is not always verified, the transition state theory only provides an upper bound of the "true" rate coefficients. This is the most limiting hypothesis on which TST is based.

2) At the transition state the motion along the reaction coordinate can be separated by the other internal motions and can be treated as a translation. It is possible in fact to define an interval of arbitrary length δ along the reaction coordinate where the potential is constant.

3) The reactant lies in a quasi-equilibrium with the transition state (TS, $\neq$), which is located at the maximum potential energy between reactants and products.

Considering the reaction

$$A \leftrightarrow A^{\neq} \rightarrow P$$
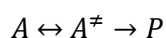
The equilibrium constant is defined as

$$K^{\neq} = [A]^{\neq} \Big/ [A]$$

And the rate of formation of P is therefore given by the first order law as discussed in Section 2.2.1

$$\frac{dP}{dt} = k^{\neq}[A]^{\neq} = k^{\neq}K^{\neq}[A]$$

It is possible to derive [80] that $k^{\neq} = \lambda k_B T / h$ where λ is a transmission coefficient, k_B is the Boltzmann constant, T is the temperature and h the Planck constant. The equilibrium constant $K^{\neq}$ can be expressed in terms of Gibbs free energy as $K^{\neq} = \exp(-\Delta G^{\neq}/RT)$ where $\Delta G^{\neq}$ is the Gibbs free energy of activation ($\Delta G^{A\neq} - \Delta G^{A}$). Therefore, if we take the transmission coefficient to be unity, we obtain

$$k_{TST} = \left(\frac{k_B T}{h}\right) \exp\left(\frac{\Delta S^{\neq}}{R}\right) \exp\left(-\frac{\Delta H^{\neq}}{RT}\right)$$

Comparing the last equation with the Arrhenius equation

$$k = A \exp\left(-\frac{E_a}{RT}\right)$$

suggests that A corresponds to $(k_B T/h) \exp(\Delta S^{\neq}/R)$, and is proportional to the entropy of activation, while the activation energy E_a closely corresponds to the enthalpy of activation of the reaction $\Delta H^{\neq}$.

TST can be formulated also in terms of partition functions Q as

$$k_{TST} = \left(\frac{k_B T}{h}\right)\left(\frac{Q^{\neq}}{Q^{A}}\right) \exp\left(-\frac{E_a}{RT}\right)$$

Canonical Transition State Theory (CTST) assumes that energy levels are thermally occupied and the partition functions represent a canonical ensemble of reactants and transition state. For this reason the theory is applicable for the computation of the high pressure limiting rate constant where the Boltzmann energy distribution can be safely assumed for reactants.

As introduced in Section 4.2 within the TST approach molecular rotations and vibrations are generally treated according to the rigid-rotor harmonic-oscillator (RRHO) model. The treatment of centrifugal corrections for molecular rotations and corrections for anharmonicity is not a common practice for large molecules, but recent studies quantitatively highlighted the impact of a rigorous treatment of torsional anharmonicity [185].

Also quantum tunneling has a non-negligible impact on rate estimation. While in classical mechanics a particle can overcome a barrier only if the sum of its kinetic and potential energy is higher than that of the barrier, according to quantum mechanics the same particle is able to overcome the barrier even if its energy is lower. This phenomenon is known as tunneling. The most common approaches from the literature are the Eckart model [186] introducing a functional form to approximate the shape of the potential energy surface. This formulation led to a relatively simple expression of the transmission coefficient λ. More recently, starting from the work of Marcus and Coltrin [187], the following studies of Miller et al. [188] and of Truhlar et al. [189] led to the implementation of the Small Curvature Tunneling theory, currently among the most effective approaches for the accurate calculation of quantum tunneling.

Recently the effects of intersystem crossing (ISC) in systems of interest for combustion are also being largely investigated. For example $\ddot{O}$ atom addition to unsaturated hydrocarbons, has been studied by Cavallotti, Casavecchia and coworkers [190] and by Li et al. [191].

4.3.2 Variational Transition State Theory

CTST can be applied also to reactions characterized by a "loose" transition state. The lack of a saddle-point prevents the identification of a molecular configuration for the transition state, but the application of the variational principle still allows for the computation of the rate coefficient. In terms of the reactive flux, the transition state is located where the flux of molecule going from reactant to product configuration is minimum, as summarized in Figure 66. From a practical point of view the calculation of $k(T)$ requires the consideration of multiple transition state configurations along the reaction coordinate as the minimum moves depending on temperature.
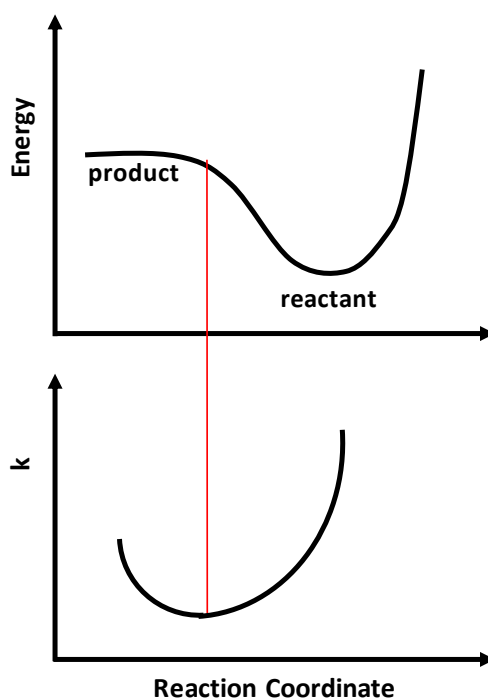
Figure 66: Identification of the transition state through the variational approach.

As reported in *Figure 67* for the recombination of $\dot{C}H_3$ and $\dot{C}l$ to form chloromethane (CH₃Cl) in fact the minimum moves toward shorter distances for increasing temperature. Calculations were performed as part of *this thesis* at the CASPT2/cc-pVDZ level, with an active space of 6 electrons in 4 orbitals (6e4o). Further details of the calculations, final results and the kinetic mechanism describing pyrolysis and oxidation of chloromethane are reported in Appendix A3 as in Pelucchi et al. [192].
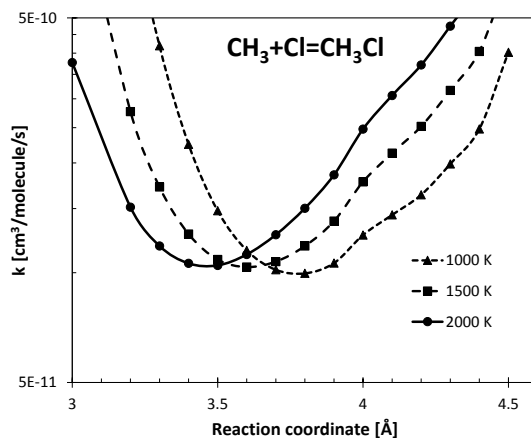
Figure 67: Reactive flux as a function of the reaction coordinate at T=1000, 1500 and 2000 K for the recombination reaction $\dot{C}H_3+\dot{C}l=CH_3Cl$. Calculations performed at the CASPT2/cc-pVDZ, with a 6e4o active space.

4.3.3 The RRKM Theory

Conventional TST does not take into account any pressure dependence of rate coefficients. The realization of the strong pressure dependence of small molecules kinetics led to the development of the RRKM Theory.

Starting from Rice and Ramsperger [193, 194], and Kassel [195] in the late 1920s, Marcus implemented RRK theory into TST [196, 197]. The concept central to pressure dependent kinetics is that molecules in the gas-phase can increase their internal energy through excitation induced by a collision with other molecules in the bath gas. Revisiting the previous discussion of Section 2.2.3, the Lindemann mechanism involves activation, deactivation and a chemical reaction steps, with the overall unimolecular reaction depending on k_1, k_{-1} and k_2

$$A + M \overset{k_1}{\Leftrightarrow} A^{\neq} + M$$

$$A^{\neq} \overset{k_2}{\Rightarrow} P$$
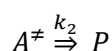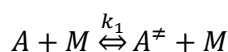
The inability of Lindemann theory to describe the pressure dependence of unimolecular reactions is due to the hypothesis that the activated state can be described by only one molecular conformation. Actually, the identity of the activated state is a function of the vibrational energy level reached for the translational vibrational energy transfer due to the intermolecular collisions. In such perspective, a reactant molecule A does not exist just in its fundamental vibrational energy state (i.e. the one defined by the zero point energy ZPE), but in N energy states, where N varies from 1 to ∞ and describes systems with increasing energy, whose existence is possible for the capability of a vibration to store energy in quanta $h\nu$ and whose population is defined by the dynamics of intermolecular collision and tends, at high pressure, to an equilibrium value. Figure 68 shows a simplified representation of collision and reaction events involving levels of the generic reactant A with energy E.
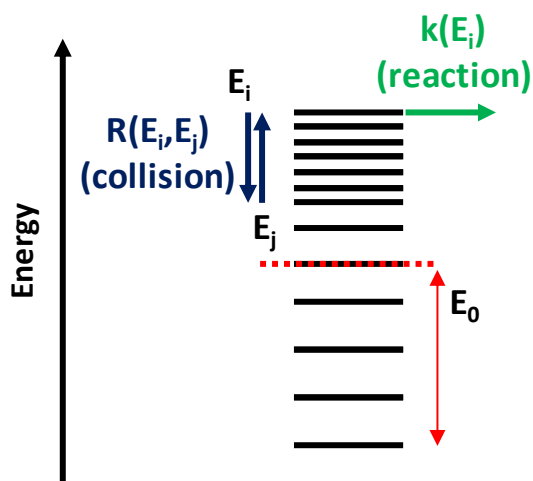
Figure 68: Energy levels involved in the collision and reaction events of the reactant A.

The three steps involved in the umimolecular process are specific functions of the ro-vibrational energy, E, and the reaction mechanism of the RRKM theory can also be written as

$$A + M \underset{}{\overset{k_1(E)}{\Longleftrightarrow}} A^{\neq} + M$$

$$A^{\neq} \overset{k_2(E)}{\Longrightarrow} P$$
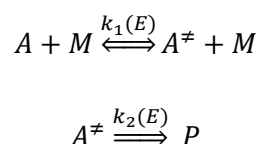
The rate of formation of P can be expressed as

$$\frac{dP}{dt} = \frac{k_1(E)k_2(E)[A][M]}{k_{-1}(E)[M] + k_2(E)}$$

The approximate derivation of the RRKM rate constant assumes that all active degrees of freedom exchange energy randomly, on time-scales much shorter than that of chemical reaction, therefore the energy is statistically distributed amongst all of them.

The microscopic (microcanonical) unimolecular rate constant $k_2(E)$ is given by

$$k_2(E) = L^{\neq} \frac{g_e^{\neq} G^{\neq}(E - E_0)}{g_e \, h \, \rho(E)}$$

Where g_e is the electronic state degeneracy of the reactants or the transition state ($\neq$), $G^{\neq}(E - E_0)$ is the sum of states of the transition state, $\rho(E)$ is the density of states of the reactants and h is Planck's constant. $L^{\neq}$, referred to as the reaction path degeneracy, accounts for statistically equivalent reaction paths and is expressed as

$$L^{\neq} = \left(\frac{m^{\neq}}{m}\right)\left(\frac{\sigma}{\sigma^{\neq}}\right)$$

Where $m^{\neq}$ and m are the number of optical isomers, and $\sigma^{\neq}$ and σ are the external symmetry numbers.

Clearly the evaluation of $k_2(E)$ critically depends on the ability of evaluating the sums and densities of states for each reaction. The unsuitability of a manual counting led to the development of algorithmic approaches to evaluate $G^{\neq}(E - E_0)$ and $\rho(E)$ [198-201] since the second half of the previous century. It is worthwhile mentioning that the Boltzmann averaged microcanonical rate coefficient $k_2(E)$ corresponds to the canonical $k_{TST}(T)$, which is of relevance to the high pressure limit.

In order for energy to be transferred between reactant molecules and the bath gas molecule M a collision must occur. The frequency ω of this event is given by

$$\omega = k_c[M]$$

Where k_c is the bimolecular rate constant for inelastic collisions and is derived according to standard gas kinetic theory as reported in Gilbert and Smith [82]. Once the frequency ω is assessed, one must consider how much energy is transferred per collision. The most widely used model is the exponential-down [202] model for collisional energy transfer. The model assumes that for a molecule in the energy range E' to $E' + dE'$ the probability $P(E, E')$ of a deactivating collision decreasing the energy to the range E to $E + dE$ is given by

$$P(E, E') = \frac{1}{N(E')} \exp\left(-\frac{E' - E}{\alpha}\right) \, for \, E' > E$$

The term $1/N(E')$ ensures that the probability of a molecule transitioning from its current state to another state in the range $0 \rightarrow \infty$ closes to unity. In other words

$$\int_0^\infty P(E, E') \, dE = 1$$

α represents the average energy transferred in a deactivating collision, commonly referred to as $< \Delta E_d >$ (delta-E-down). The average energy transferred for an activating collision is linked to that for a deactivating via detailed balance (microscopic reversibility) through the density of states at energy E and the Boltzmann constant k_B

$$\frac{P(E, E')}{P(E', E)} = \frac{\rho(E)}{\rho(E')} \exp\left(-\frac{E - E'}{k_B T}\right)$$

The actual rate of an energy transition can be deduced as

$$R(E, E') = \omega \, P(E, E')$$

Considering the case of infinitely high pressure

$$\frac{dP}{dt} = \frac{k_1(E)}{k_{-1}(E)} L^{\neq} \frac{g_e^{\neq} G^{\neq}(E - E_0)}{g_e \, h \, \rho(E)}$$

The term $k_1(E)/k_{-1}(E)$ is the equilibrium constant between A and A^* and can be written in terms of partition functions as

$$\frac{k_1(E)}{k_{-1}(E)} = \frac{Q_{A*}}{Q_A}$$

Q_{A*} is the partition function of the molecules with energy in the range E^* and $E^* + dE^*$ and Q_A is the partition function of the reactant molecule. Assuming small dE^*, Q_{A*} resolves to

$$Q_{A*} = \rho(E) \exp(-E/k_B T) dE$$

And the production of P becomes

$$\frac{dP}{dt} = \frac{\rho(E) \exp\left(-\dfrac{E}{k_B T}\right)}{Q_A} L^{\neq} \frac{g_e^{\neq} G^{\neq}(E - E_0)}{g_e \, h \, \rho(E)} dE$$

$$= \frac{\exp\left(-\dfrac{E}{k_B T}\right)}{Q_A} L^{\neq} \frac{g_e^{\neq} G^{\neq}(E - E_0)}{g_e \, h} dE$$

The latter expression has to be integrated over all energies E. $G^{\neq}(E - E_0)$ is the sum of states of the transition state, determined by integration and summation of densities of states of the activated complex from $E = 0$ to $(E - E_0)$, i.e.

$$G^{\neq}(E - E_0) = \int_0^{\infty} \rho^{\neq}(E_+) dE_+$$

The exponential term $\exp(-E/k_B T)$ has also to be integrated over all relevant energies giving the following equation

$$\frac{dP}{dt} = \frac{L^{\neq}}{Q_A h} \int_0^{\infty} \rho^{\neq}(E_+) dE_+ \left[\int_{E_+ + E_0}^{\infty} \exp\left(-\frac{E}{k_B T}\right) dE \right] = \frac{L^{\neq} k_B T}{Q_A h} \exp(-E_0/k_B T) \int_0^{\infty} \rho^{\neq}(E_+)(-E_+/k_B T) dE_+$$

When integrated over all energy levels the term within the integral is the partition function of the transition state, therefore

$$\frac{dP}{dt} = \frac{L^{\neq} k_B T}{h} \frac{Q_{\neq}}{Q_A} \exp(-E_0/k_B T)$$

Which is totally consistent with the transition state theory formulation.

It has to be noted that in the high-pressure limiting unimolecular rate constant the 2-dimensional external rotation (J-rotor) is adiabatic, and therefore it is not included in the calculation of the sums and densities of states. The RRKM result must be therefore corrected by the ratio of the partition functions for the 2-D external rotation in reactants and activated complex

$$\frac{dP}{dt} = \frac{L^{\neq} k_B T}{h} \frac{Q_{2D,\neq} Q_{\neq}}{Q_{2D,A} Q_A} \exp(-E_0/k_B T)$$

For infinitely low pressures

$$\frac{dP}{dt} = k_1(E)[A][M]$$

Or, as the rate of energization and of de-energization are assumed to be equivalent

$$\frac{dP}{dt} = k_{-1}(E)[A][M] \frac{Q_{A*}}{Q_A}$$

As clear from the above expression, no knowledge of the ro-vibrational states of the transition state is needed at the low pressure limit. Although the deactivation rate constant $k_{-1}(E)$ is expressed as a function of E, the strong collision model used in the original formulation of RRKM assumed this step as energy independent. Available programs for RRKM simulations [178, 203] consider this term as energy dependent.

When the system is in between the limiting cases of the HPL and LPL, the solution of the Master Equation (ME) provides the phenomenological rate coefficients. Before the description of the multiple-well time-dependent ME in the next Section some limitations of the RRKM theory have to be mentioned. In fact, being based on the transition state approximation it suffers from similar limitations as in the TST such as the impossibility of treating spin-forbidden reactions or to account for quantum effects such as tunneling. Moreover, it requires the existence of a saddle point, and barrierless reactions have to be treated according to a variational implementation of the theory. However, due to the failures of the microcanonical implementation of the RRHO based versions of VTST to reproduce experimental data, in the last 25 year Klippenstein and co-workers formulated and developed the Variable Reaction Coordinate TST (VRC-TST) [204-207].

4.3.4 Solution of the Master Equation

The general ME for a single-well unimolecular process incorporates three terms: 1) the rate of collisional energy transfer (CET) into energy states in the range $E \rightarrow E + dE$, 2) the rate of CET out of the energy states

in the range $E \rightarrow E + dE$ and 3) the rate of unimolecular chemical reaction at energy E consuming the reactant

$$\frac{dn(E,t)}{dt} = \int_0^\infty R(E,E')\, n(E',t)dE - \int_0^\infty R(E',E)\, n(E,t)dE - \sum_i^{channels} k_i(E)n(E,t)$$

Where the left term is the rate of decrease in concentration of a molecule n with energy E.

Both the first and the second term on the right side depend on ω (collision frequency) and the energy transferred in a deactivating collision α. ω is derived from gas kinetic theory and therefore needs the specification of Lennard-Jones hard sphere collision diameter and well depth. Empirical methods are available for the estimation of such parameters [208]. The average energy transferred α is one of nowadays topic of debate. Simple power law expressions

$$\alpha = \alpha_{300} \left(\frac{T}{300} \right)^\beta$$

allow for reproduction of experimental data over a wide range of temperature and pressure with reasonable accuracy. However α is typically used as a semi-empirical fitting parameter where in the absence of fundamental kinetic data, analogy with similar chemical systems is widely pursued. The research activity of Jasper and co-workers is strongly focused on the calculation of such parameters from a fundamental level by using direct molecular dynamics (classical trajectories) [209, 210]. The relevance of such activity extend well beyond fundamental kinetic studies, and will hopefully allow the proper exploration of MILD combustion or EGR (exhaust-gas-recirculation) systems in the near future.

The third term is derived from quantum chemical calculations already discussed in the previous Sections.

Figure 69 shows a generic multiple-well reactive system for which it is possible to formulate the master equation [211] for a generic isomer m as:

$$\frac{dp_m(E)}{dt} = \omega \int_{E_{0m}}^\infty P(E,E')\, p_m(E')dE' - \omega p_m(E) + \sum_{n \neq m}^M k_{m \rightarrow n}(E)p_n(E) - \sum_{n \neq m}^M k_{n \rightarrow m}(E)p_m(E)$$

$$- k_{Pm}(E)p_m(E) + K_{Rm}^{eq} k_{Rm}(E) \frac{\rho_m(E)e^{-\frac{E}{k_B T}}}{Q_m(T)} n_A p_B - k_{Rm}(E)p_m(E)$$
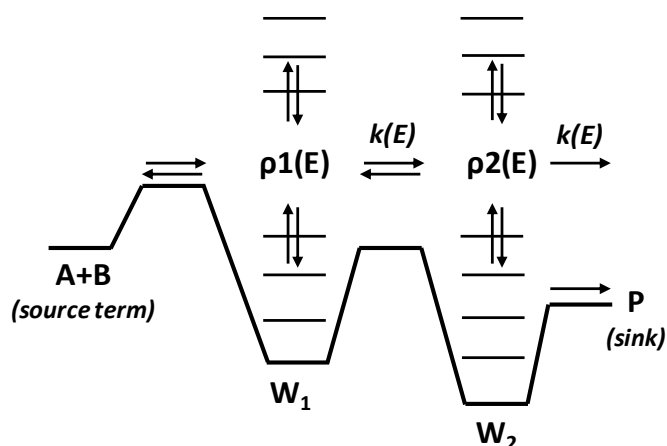
Figure 69: Generic multiple-well PES. Adapted from [211].

p_m is the ro-vibrational population density within an energy grain E. The positive terms correspond to population flux into the state (m, E), the negative terms are flux out of (m, E). The first term is a population gain of the isomer m at energy E due to collisional energy transfer, the second term is a population loss. The third and the fourth term describe population gain or loss through reactions transferring population for the isomer 1 to the isomer 2 and vice versa. $k_{n \to m}(E)$ and $k_{m \to n}(E)$ are microcanonical rate coefficients for the population transfer. The fifth term is an irreversible population loss due to reaction of isomer m to products P. The last two terms represent the bimolecular association source term and apply only to those isomers that are populated through a bimolecular association reaction, in which it is assumed that reactant A is in significant excess compared to reactant B.

If a bimolecular step is involved it is necessary to define also p_B, adding a differential equation

$$\frac{dp_B}{dt} = \sum_{m=1}^{M} \int_{E_{0i}}^{\infty} k_{Rm} \, p_m(E) dE - n_A p_B \sum_{m=1}^{M} K_{Rm}^{eq} \int_{E_{0i}}^{\infty} k_{Rm}(E) \frac{\rho_m(E) e^{-\frac{E}{k_B T}}}{Q_m(T)} dE$$

Different approaches exist to solve the coupled system of ordinary differential equation thus obtained. Stochastic approaches include the Multiwell Program Suite of Barker and coworkers [178] and that of Barbato et al. [212]. Within those using matrix diagonalization techniques are the MESMER program of Glowacki et al. [211], VariFlex of Klippenstein et al. [213] and the more recent MESS from Georgievskii, Klippenstein et al. [203]. In the development of *this thesis* the code of Barbato et al. [212] and MESS [203] have been used at different instances.

4.3.5   The QRRK Theory

Another derivation of classical RRK theory is the quantum Rice-Ramsperger-Kassel (QRRK) theory. The RRK approach assumes that the rate constant for the unimolecular reaction step in the usual Lindemann mechanism is proportional to the probability that a molecule containing s oscillators ($3N - 6$ or $3N - 5$ for

non-linear or linear molecules, respectively) with a total energy E will have energy higher than the reaction barrier E_0 localized in one of these oscillators. This probability is statistically derived by

$$\frac{\rho(E - E_0)}{\rho(E)}$$

With the energy dependent chemical step given by

$$k(E) = \frac{A\,\rho(E - E_0)}{\rho(E)}\ s^{-1}$$

Typically A and E_0 were derived from experiment and assumed to correspond to the parameters of the Arrhenius expression of the rate constant. RRK theory therefore assumes that the energy dependent rate constant is proportional only to the number of vibrational degrees of freedom in the molecule, s. No transition state information is required because the different contributions of the s oscillators to the active energy E are not distinguished.

The approach of QRRK is very similar to that of the classical RRK. It assumes again that there are s oscillators in the system, but each is assigned the same vibrational frequency, v. The barrier to reaction, E_0, is an integer function of these quantized vibrational energies where $E_0 = mhv$ and m is therefore the critical number of quanta required for the vibrational energy to be in excess of E_0, $m = E_0/hv$. If s oscillators contain n quanta of energy, such that the total energy is given by $E = nhv$ the probability that one of the s oscillators contains the minima quanta of energy for reaction, m, is statistically given by

$$P_{E \geq E_0} = \frac{n!\,(n - m + s - 1)}{(n - m)!\,(n + s - 1)!}$$

In turn the energy dependent rate constant is given by $k(E) = AP_{E \geq E_0}$ where A and E_0 are again assumed as those in the Arrhenius equation. Details on QRRK theory can be found elsewhere [214-216] and the following discussion will further highlight the reasons behind the gradual drop out observed in the use of QRRK theory.

1. Sums and densities of states for reactants and transition states in RRKM/ME are computed by direct count methods based on ro-vibrational properties from quantum chemical calculations. An approximate state counting is instead applied in QRRK/MSC approaches, without knowledge of transition state properties.

2. RRKM/ME uses a master equation to describe activating and deactivating steps. Differently from the MSC where every collision activates or deactivates a molecule depending on whether the molecule is above or below the threshold, the method used by RRKM/ME is called weak collision approach: many collisions are needed to activate or deactivate an excited ground state molecule

3. QRRK does not distinguish between the contributions of the different degrees of freedom

It is worth mentioning that the use in *this thesis* of the QRRK theory in its Modified Strong Collision approximation as implemented in the CHEMDIS program of Bozzelli and coworkers [214], although limited (Section 6.2), was accompanied by a comparison with RRKM/ME results. This comparison was thoroughly extended in the Ph.D. Thesis of Kieran P. Somers at National University of Ireland [217]. The main conclusion of such comparison was that the main advantage of QRRK/MSC is to provide a coarse and computationally effective sense of the extent of pressure dependence in unimolecular reactions, before undertaking more accurate but at the same time more complex and computationally expensive RRKM/ME calculation. The average deviations between QRRK/MSC and RRKM/ME were found to be within a factor of ~2-4.

4.4 Summary

Modern theoretical chemistry has reached a level of accuracy and computational cost effectiveness that its use is becoming standard practice in the development of combustion kinetic mechanisms. This Chapter provided a brief overview of methods and theories adopted at different instances during the development of *this thesis*. In many parts, the reader is referred to the available scientific literature and to standard books on the topic for a deeper understanding of the concepts here discussed.

The potential of applied theoretical chemistry will be shown in some of the next chapters and the challenge for future developments of the POLIMI mechanism would be to effectively integrate such methods in the systematic, modular and hierarchical approach developed in the last 30-40 years of research activity in thermal processes kinetics described in the previous Chapter 3.

Chapter 5 – Kinetic Modeling of Hydrocarbon Fuels: n-alkanes and toluene

This Chapter reports results from the research activity carried out on hydrocarbon fuels pyrolysis and oxidation. Fuel and engine design largely relies on the definition of surrogate mixtures consisting of representative components of families of species commonly found in commercial fuels components. Historically, mixtures of primary reference fuels such as n-heptane and iso-octane were considered (PRFs). The need for reproducing the Octane Sensitivity of real fuels discussed in Section 1.2, led to the introduction of toluene as the third component in the so-called toluene reference fuels mixture (TRFs). The activity reported in this Chapter aimed at refining n-alkane chemistry at low temperatures, and to advance the knowledge of toluene pyrolysis and oxidation chemistry. Recent research efforts in fact highlighted on one side a lack of knowledge in alkane combustion chemistry [149] brought to light from advances in experimental techniques, and on the other side a whole controversial and inconsistent literature on toluene oxidation [218, 219].

Section 5.1 introduces new reaction classes in the kinetic modelling of n-alkane oxidation at low temperature. Starting from propane and n-butane, the new reaction classes have been implemented also into the n-heptane mechanism. The updated mechanism has been validated both for standard targets such as flames, species profiles and ignition delay times and in more complex applications such as droplet microgravity conditions and HCCI engines. This Section is mostly based on peer-reviewed publications authored and coauthored during the PhD program in Industrial Chemistry and Chemical Engineering. For the mentioned Supporting Information the reader is referred to the web version of the papers.

Section 5.2 reports results from theoretical calculation of toluene oxidation reactions. The activity features the investigation of relevant reaction channels and was performed under the co-supervision of Dr. Stephen Klippenstein and Prof. Carlo Cavallotti at Argonne National Laboratory, IL, USA. Results from this Section are in preparation for submission to peer-reviewed journals for publication.

5.1 New Reaction Classes in the Kinetic Modeling of Low Temperature Oxidation of Alkanes [72]

5.1.1 Propane and n-butane

1. **Introduction**

The understanding of the elementary reactions that govern the chemistry of low-temperature combustion and autoignition in internal combustion engines is in continuous progress, mainly due to the rapid advances both in theoretical kinetics and in experimental methods [220]. After several comprehensive reviews [16, 18, 221-223], the more recent work of Zádor et al. [220] highlighted the fundamental role of key elementary reactions involved in the low-temperature oxidation and ignition chemistry, where reactions of peroxy and hydroperoxy radical species are important [126]. In particular, they emphasized the ways in which computational chemistry and improved experimental capabilities enable a more detailed characterization of complex oxidation reactions. They also concluded that while the reactions of alkyl radicals with O_2 are better clarified, the mechanism of the second oxygen addition and related chemistry is nowadays an important unanswered question for ignition chemistry research [126]. Moreover, new experimental data of low-temperature oxidation of propane, n-butane and n-heptane in a jet stirred reactor (JSR) were recently presented and discussed [224-230]. The joint research efforts of Nancy and Hefei produced very detailed experimental measurements of reaction products of stoichiometric mixtures at low temperatures and atmospheric pressure in a JSR. The reaction products were analyzed using gas chromatography analysis and mass spectrometry. The mass spectrometer was combined with tunable synchrotron vacuum ultraviolet photoionization and coupled with a JSR via a molecular-beam sampling system. In this way, a large detail of reaction products of propane and n-butane oxidation have been quantified, including hydrogen peroxide and several oxygenated organic compounds, such as ketones, cyclic ethers, alcohols, acetic acid, alkyl- and carbonyl-hydroperoxides [225]. Similar attention was also paid to the formation of reaction products involved in the low-temperature oxidation of n-heptane highlighting that diones and di-oxygenated products other than carbonyl-hydroperoxides (CHP) or keto-hydroperoxides are important intermediates in the low-temperature oxidation of n-alkanes, but their formation was usually not accounted for in the detailed or lumped kinetic models of hydrocarbon fuel combustion [15, 64, 231-236].

The aim of this paper is to critically revise the low temperature oxidation mechanism, taking advantage of this new comprehensive and detailed information. Moving from the systematic deviations between model predictions and experimental measurements, Section 2 discusses the new reaction classes added to the low temperature oxidation mechanism of hydrocarbon fuels. Particularly, H-abstraction reactions on hydroperoxides and carbonyl-hydroperoxides are firstly analyzed. Then, successive molecular reactions of carbonyl-hydroperoxides, as well as recombination/disproportionation reactions of peroxy radicals are also discussed. Section 3 presents some theoretical calculations to determine preliminary rate constants for relevant reactions used in this work. Section 4 finally presents complete comparisons between model predictions and experimental data of the low temperature oxidation of propane and n-butane.

2. Low temperature oxidation mechanism and new reaction classes

Since the pioneering work of Westbrook et al. [237], who proposed the first detailed low- and high-temperature oxidation mechanism of n-heptane, the chain radical oxidation mechanism of n-alkanes, with the formation of extremely reactive hydroperoxide species, was identified and commonly accepted [38, 233, 238]. *Figure 70* schematically shows the oxidation mechanism of propane [239]. The two addition reactions of molecular oxygen to alkyl radicals (R• and •QOOH), together with the successive isomerization reactions of peroxy radicals (ROO• and •OOQOOH), and the formation of hydroperoxide and carbonyl-hydroperoxide species are critical to the low temperature oxidation chemistry of hydrocarbon fuels [126].

As clearly discussed by Battin-Leclerc [18], the formation of peroxides is extremely important, because they include an O-OH bond, which can easily be broken and lead to the formation of two radicals, which can in turn react with fuel molecules to give alkyl radicals. These degenerate branching steps involve an increase of the number of radicals, which induces an exponential acceleration of reaction rates leading in some conditions to spontaneous autoignition. The works of Curran et al. [54, 240] defined the oxidation mechanisms for primary reference fuels in terms of 25 specific reaction classes and exploited a modular form for the construction of kinetic schemes that is largely accepted and employed. Due to the low dissociation energy of the O-OH bond and the high reactivity of hydroperoxide species, only the class of unimolecular decomposition reactions was considered for these species. This oxidation mechanism was extensively applied to different linear and branched alkanes, up to normal hexadecane [63, 241, 242], as well as heavy branched alkanes [236, 243].
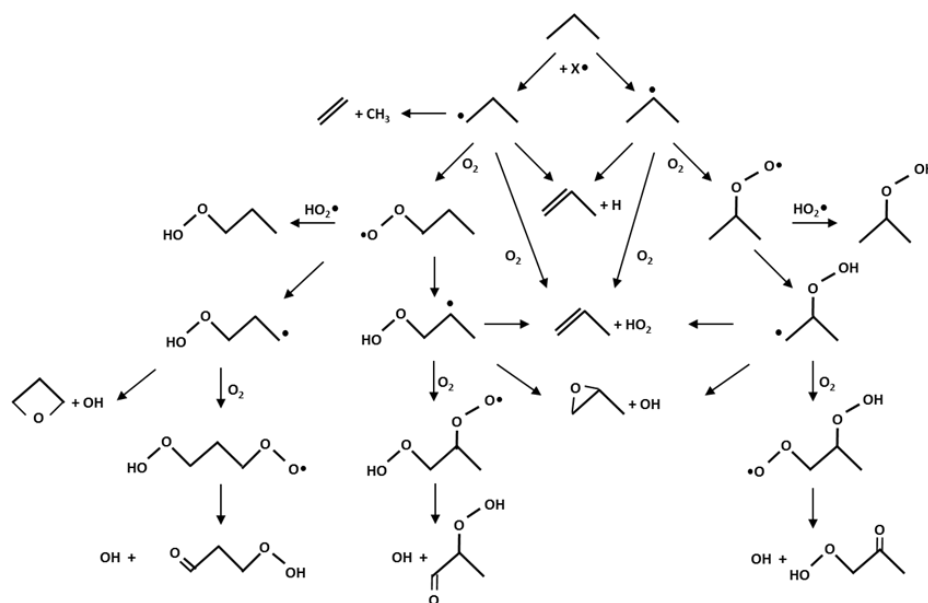
Figure 70: Chain radical mechanism of propane oxidation.

The recent data obtained by Nancy and Hefei research teams [224-230] allow to critically revise and highlight the limits of the existing low temperature mechanisms in the proper prediction of oxygenated species. As

already observed by Herbinet et al. [225, 226] in n-butane and n-heptane oxidation, while detailed kinetic models [224] satisfactorily reproduce the global reactivity and the usual oxidation products, their predictions partially deteriorate in the case of the formation of organic acids and species with two carbonyl groups. To account for these discrepancies, Battin-Leclerc et al. [224, 244] and Herbinet et al. [226] already analyzed possible pathways for the formation of acids and molecules including two carbonyl groups, or molecules with one carbonyl and one alcohol. Despite the addition of these new reaction pathways, the formation of carboxylic acids and compounds with two carbonyl groups was not completely explained, and they observed the need of an increased accuracy of the kinetic models [245].

The presence of very sharp peaks of some oxygenated species at low temperatures [226] can be well explained on the basis of successive reactions of carbonyl-hydroperoxides involving activation energies lower than those typical of the unimolecular decomposition reactions, i.e. the O-OH bond dissociation energy (40-45 kcal/mol). Indeed, the formation of molecules including two carbonyl groups can be easily explained on the basis of H-abstraction reactions on the site of the hydroperoxyl substitution and the subsequent decomposition of the O–OH bond, as shown in Figure 71. Thus, 3-oxobutanal can be obtained from H-abstraction on 2-acetyl-ethyl hydroperoxide:
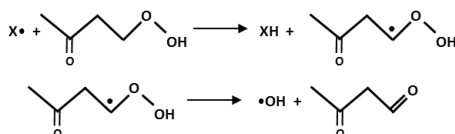
Figure 71: H-abstraction from 2-acetyl-ethyl hydroperoxide and radical decomposition to form 3-oxobutanal.

As will be better shown in Section 3, the intermediate C_4 radical is instantaneously decomposed to form OH radical and the corresponding 3-oxobutanal. At temperatures lower than 600 K and the oxidation conditions here analyzed, OH radicals largely dominate the H-abstraction reactions and this radical reaction to form C_4-molecules including two carbonyl groups can also prevail over the previously proposed reaction channels [224, 226, 244]. At these low temperatures, the H-abstraction reactions on carbonyl-hydroperoxides can play a significant role, thus decreasing the chain branching effect of the competing initiation reactions. The net consequence is a reduction of the overall conversion, at temperatures lower than 550-600 K, while only at higher temperatures the unimolecular decomposition of CHP remains the dominant reaction path. Referring to the low temperature oxidation of n-butane [228], *Figure 72* shows the clear reduction of reactivity and the better agreement with the experiments mainly at 550-600 K. Moreover, the sharp peak at the very low temperatures (~600K) in the production of C_4-molecules including two carbonyl groups, previously completely disregarded, is reasonably reproduced.

Similar considerations of the importance of the H-abstraction reactions need to be extended also to all the hydroperoxides. Thus, butanal and methyl-ethyl-ketone (MEK) are the expected products of H-abstractions on C_4-hydroperoxides.
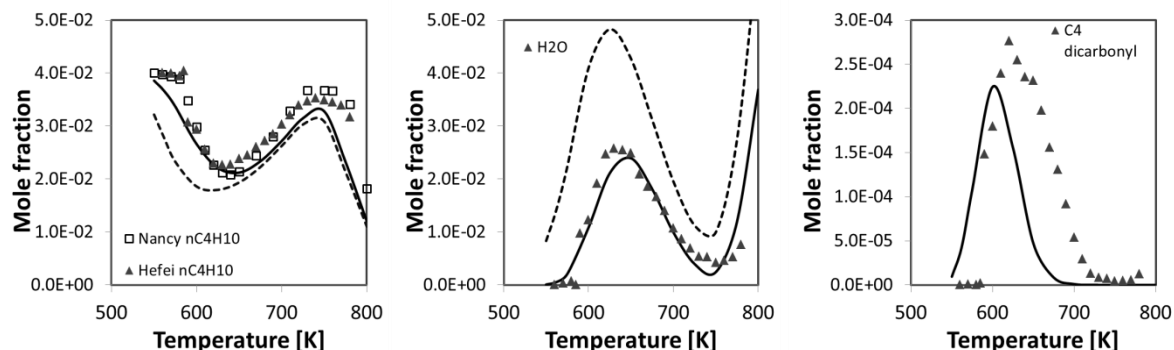
Figure 72: Oxidation of n-butane in jet stirred reactor (n-butane/O_2/Ar = 4/26/70 mol%; 1.04 atm; residence time 6 s) [225, 228]. Comparison of experimental mole fractions of n-butane, water, and C_4-molecules including two carbonyl groups measured at Nancy [squares] and Hefei [triangles] with model predictions with [solid lines] and without the new reactions [dashed lines].

All these considerations clearly confirm the importance of successive reactions of hydroperoxide species. With reference to the low temperature oxidation mechanism of propane, Figure 73 and Figure 74 show the H-abstraction reactions on C_3-hydroperoxides and the most favored C_3-carbonyl-hydroperoxides, respectively.

Figure 73: H-abstraction reactions on propyl-hydroperoxides to form propanal and acetone.

In their general form, the following classes of H-abstraction reactions are likely to be included in the low temperature oxidation mechanism of hydrocarbon fuels:

a) H-abstractions on alkyl-hydroperoxides:

$$X\bullet + C_nH_{2n+1}OOH \rightarrow XH + \bullet C_nH_{2n}OOH \rightarrow XH + C_nH_{2n}O + \bullet OH$$
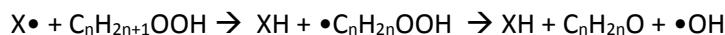
b) H-abstractions on carbonyl-hydroperoxides:

$$X\bullet + OC_nH_{2n-1}OOH \rightarrow XH + OC_nH_{2n-2}O + \bullet OH$$

$$X\bullet + OC_nH_{2n-1}OOH \rightarrow XH + C_mH_{2m-2}O + C_kH_{2k}O + \bullet OH \quad (m+k=n)$$

$$X\bullet + OC_nH_{2n-1}OOH \rightarrow XH + C_nH_{2n-2}O + \bullet HO_2$$
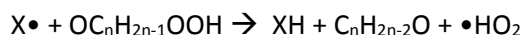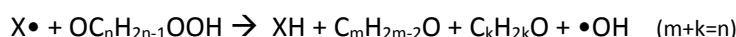
These H-abstraction reactions on hydroperoxides and carbonyl-hydroperoxides, whose kinetic parameters are reasonably estimated on the basis of analogy and similarity rules [52], have already been applied to atmospheric chemistry studies [246-248]. For the first time, they are included in the kinetic model of hydrocarbon fuel combustion, to justify the formation of some oxygenated species. The role of these H-abstraction reactions, as well as the importance of molecular reactions involving carbonyl-hydroperoxides is better highlighted through the systematic comparisons between model predictions and experimental data reported in Section 4.
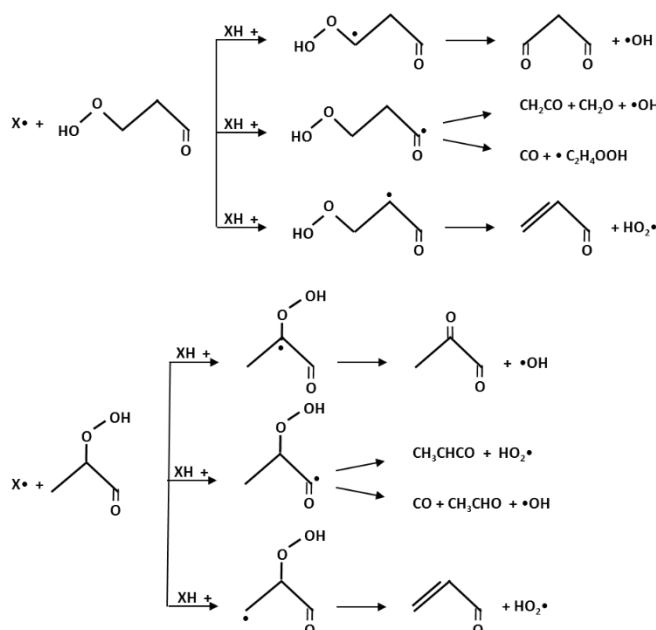
Figure 74: H-abstraction reactions on the most favored C3-carbonyl-hydroperoxides.

As far as the formation of organic acids is concerned, recently Jalan et al. [249] presented new reaction pathways of ketohydroperoxides relevant to low-temperature gas phase oxidation of propane. Ab initio calculations identified new exothermic reactions forming a cyclic peroxide isomer, which decomposes via concerted reactions into carbonyl and carboxylic acid products (Korcek Mechanism). This reaction is very useful to explain the formation of formic and acetic acids, mainly at low temperatures and in liquid phase. The same reaction path also explains the formation of propanoic acid from CHPs of C_4 and heavier species.

Moreover, an important source of acetic acid is the recombination/disproportionation reaction of peracetyl ($CH_3COOO\bullet$) and methyl-peroxy radicals ($CH_3O_2\bullet$):

$$CH_3COOO\bullet + CH_3O_2\bullet \rightarrow CH_3COOH + CH_2O + O_2$$
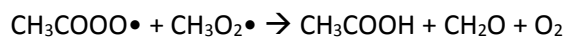
This reaction was already considered in a previous paper on methane oxidation, where the acetaldehyde low temperature reactions were also discussed [250]. Similarly, the recombination/disproportionation of alkyl-peroxy radicals forms O_2 and a di-alkyl-peroxide, which rapidly forms an alcohol and a carbonyl component. Thus, propyl peroxide radicals can form propanol and propanal:

$C_3H_7OO\bullet + C_3H_7OO\bullet \rightarrow O_2 + C_3H_7OOC_3H_7$

$C_3H_7OOC_3H_7 \rightarrow C_3H_7OH + C_2H_5CHO$
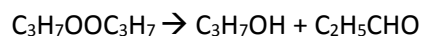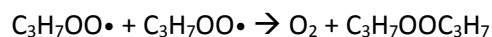
Kinetic parameters for this reaction class are similar to those for the recombination reactions (Class 15 and 16), as suggested by Curran et al. [233, 240].

Thus, in addition to the 25 reaction classes usually considered in the low and high temperature oxidation schemes of alkanes [233, 240], the following new reaction classes are here included:

1- H-abstraction reactions on alkyl and carbonyl-hydroperoxides.

2- Molecular reactions of carbonyl-hydroperoxides to form organic acids (Korcek mechanism).

3- Recombination/disproportionation reactions of peroxy radicals.

The approach used to validate the capability of the proposed reaction mechanism is based on the comparison with experimental measurements for propane and n-butane and on the use of theoretical calculations to determine preliminary rate constants for reaction channels for which no estimate based on analogy rules is possible. This was useful both to check the predictive capability of the similarity and analogy rules for some key reactions, as well as to provide preliminary estimates of rate constants of molecular processes that can be hardly determined through analogy. The purpose of these calculations, and more generally of the present work, is not to provide the most accurate estimate of the rate constant for the investigated reactions, but rather to identify a set of reactions that have the potential to contribute significantly to the low temperature reactivity of the investigated systems. For this purpose the theoretical rate constant estimate was performed at a level that allowed to evaluate rate parameters with an uncertainty factor of about three, which, combined with the satisfactory comparisons with experimental data, is useful to determine whether a reaction channel has the potential to have a significant impact on the system reactivity or not. All the rate constants here determined were evaluated using conventional transition state theory calculating the necessary parameters either using the CBS-QB3 method or at the CCSD(T) level with extension to the complete basis set (CBS) using geometries and vibrational frequencies calculated at the M062X/6-311+G(d,p) level. The rate constant was corrected for tunneling using the Eckart model. The CBS extrapolation was performed through a scheme developed by Martin [251] using single point energies computed with the aug-cc-pVDZ and aug-cc-pVTZ basis sets [252]. One reaction that has multireference character was investigated

through CASPT2 calculations. All calculations were performed using the G09 suite of programs [253], except for the CCSD(T) and CASPT2 calculations, which were performed using Molpro 2008.1 [254].

3. Theoretical rate constant calculations and estimation

The theoretical analysis was focused on three different sets of reactions:

3.1- H-abstractions from the hydroperoxyl substitution site.

3.2- Carbonyl-hydroperoxide decomposition through the Korcek mechanism.

3.3- Molecular decomposition of acetyl-methyl-hydroperoxide.

The calculated unimolecular rate constants are high-pressure values, though at atmospheric pressure and between 500 and 700 K, where these reactions are most likely to play a significant role, the pressure dependence is expected to be small.

3.1 H-abstractions from the hydroperoxyl substitution site

The reactions of H-abstraction from carbonyl-hydroperoxides play an important role, as they are the main source of dicarbonyl compounds, as shown in Figure 71. It was thus decided to determine the rate constant for one of these reaction channels, namely H-abstraction of the hydrogen atoms from a primary carbon atom functionalized with the hydroperoxyl group, as this is the one for which analogy rules are least established. The molecular model used in the simulations was 2-acetyl-ethyl-hydroperoxide ($CH_3COCH_2CH_2OOH$), whose reactivity is expected to be the same as that of 2-formyl-ethyl-hydroperoxide (C_3CHP). The considered extracting agent is the OH radical, as it is the most effective radical in the conditions considered in the present study. Simulations were performed for the two minimum energy conformers of $CH_3COCH_2CH_2OOH$. Abstraction is possible from two $\dot{H}$ atoms, which are differentiated by the relative orientation of the OH group of the OOH moiety. Two distinct rate constants were thus computed for each conformer, which were distinguished as cis or trans depending on the proximity to the OOH group. The rate constants were then summed up after performing a Boltzmann weight of the relative population of the two conformers and a global rate constant was determined. Further computational details are reported in the Supplemental Material.

The rate constants of the four reactions calculated using CBS-QB3 energy barriers, the global rate constant and the rate constant determined using analogy rules are reported in Figure 75, while the cis and trans transition state structures for the minimum energy conformer are reported in Figure S1 in the Supplemental Material. On the whole, given the approximations discussed above, we expect that the uncertainty factor for the rate constant calculated theoretically is within a factor of about 2-3. The ratio between the rate constant calculated using analogy rules and the one calculated theoretically using CBS-QB3 energy barriers is a factor of 1.3 in the 400 − 700 K temperature range (that is when the low temperature reactivity of CHPs is relevant)

and grows to 2.0 using CCSD(T)/cc-pVTZ energy barriers corrected for basis set size effects with MP2/aug-cc-pVTZ energies. It can thus be concluded that the analogy rules allow calculating rate constants for H-abstraction reactions whose uncertainty is within the level that was considered reasonable to identify a major reaction channel in the present study.
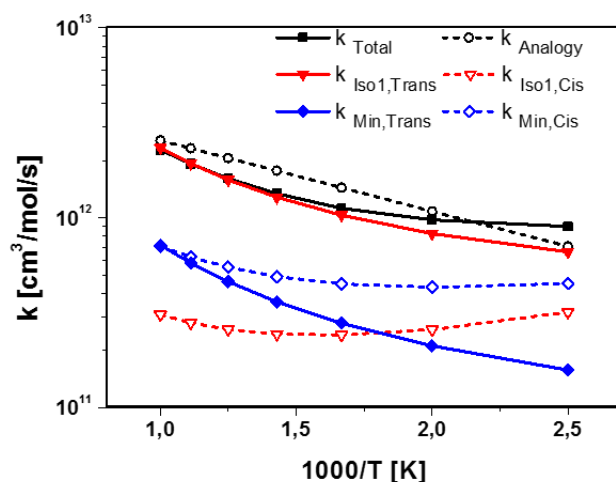
Figure 75: Comparison between the rate constant calculated using analogy rules (k analogy) and the one determined theoretically (k total) summing up the rate constants of cis and trans addition to the minimum energy conformer of CH₃COCH₂CH₂OOH (k minimum cis and k minimum trans) and those of the conformer that is closest in energy (k Iso1 cis and k Iso1 trans), weighted over the Boltzmann population of the conformers.

An analysis of the expected products of the H-abstraction reaction was performed using an Intrinsic Reaction Coordinate (IRC) scan from the cis transition state of the minimum energy conformer. Simulations were performed starting from the transition state structure using a step of 0.1 Bohr updating the Hessian every 5 steps. It was found that following H-abstraction, an intermediate structure stabilized by the formation of an H bond with the $\ddot{O}$ atom of the carbonyl group is formed, which successively loses the OH group and forms the molecule including two carbonyl groups, which was thus considered as the reaction product. Similarly, for the other H-abstraction reactions considered in this work, it was assumed that H-abstractions from carbonyl-hydroperoxides are followed by the fast decomposition of the radical product, as assumed in Figure 71.

3.2. Carbonyl-hydroperoxide decomposition through the Korcek mechanism

The second set of reactions here investigated is the decomposition of CHPs through the Korcek mechanism. The mechanism of this reaction for 2-formyl-ethyl-hydroperoxide (C₃CHP) has been recently studied by Jalan et al. [249]. The reaction is started by a cyclization reaction to form a cyclic peroxide, which can subsequently decompose either to acetic acid and formaldehyde or to acetaldehyde and formic acid. The latter reaction channel is the fastest, while the rate determining step is the cyclization reaction. Beside H-abstraction

reactions, cyclization is in competition with C_3CHP decomposition to OH radical, formaldehyde, and vinoxy radical. The rate constants of the cyclization reaction of C_3CHP and its analogous C_4CHP (2-acetyl-ethyl-hydroperoxide: $CH_3COCH_2CH_2OOH$ and 2-formyl-isopropyl-hydroperoxide: $CHOCH_2CHOOHCH_3$) were here computed using conventional transition state theory, correcting the rate constants for tunneling using the asymmetric Eckart model [186, 255]. Channel specific rate constants for cyclic peroxide decomposition were computed using the rate parameters calculated by Jalan et al. [249] for the decomposition of the species formed by C_3CHP cyclization. The rate parameters calculated for the cyclization of C_3CHP and C_4CHP are reported in Table 11, while further details of the calculations are reported as Supplemental Material.

Temperature (K)	$k_c(s^{-1})$		
	C_3CHP	$CHOCH_2CHOOHCH_3$	$CH_3COCH_2CH_2OOH$
400 K [a]	4.2E-7	1.9E-6	1.9E-7
500 K [a]	3.6E-4	1.5E-3	1.8E-4
600 K [a]	3.6E-2	1.6E-1	2.1E-2
600 K [b]	1.5E-2	-	-
600 K [c]	1.3E-2	-	-

a) Rate constants computed using CCSD(T)/CBS energy barriers; b) Rate constant calculated using the energy barrier computed at the CCSD(T)/cc-pVTZ level; c) Rate constant computed by Jalan et al. [249];

Table 11: *Rate parameters for the reaction of cyclization of C_3CHP and C_4CHP to the cyclic peroxide intermediate whose decomposition represent an important pathway for the formation of acids and aldehydes.*

As it can be observed, the reaction of cyclization of $CHOCH_2CHOOHCH_3$ is about a factor of 5 faster than that calculated for C_3CHP, while the cyclization reaction of $CH_3COCH_2CH_2OOH$ is slightly slower. This is due to the different contribution of the additional methyl group for the two isomers, which hinders the rotational motion for $CHOCH_2CHOOHCH_3$ and favors that of $CH_3COCH_2CH_2OOH$, thus leading to a decrease of the density of states for $CHOCH_2CHOOHCH_3$ and to a slight increase for $CH_3COCH_2CH_2OOH$ with respect to C_3CHP. Channel specific rate constants were determined for the decomposition of the cyclic peroxide formed by $CHOCH_2CHOOHCH_3$ using the same branching ratios used for C_3CHP. In the case of $CH_3COCH_2CH_2OOH$, the absence of the tertiary hydrogen in the cyclic peroxide intermediate implies that the only possible reaction channel is decomposition to acetic acid and acetaldehyde. The rate constants calculated for the fragmentation of C_3CHP and C_4CHP to the possible products and used in the simulations are summarized, with a schematic of the Korcek mechanism in Figure 76 (see also Table S1 of the Supplemental Material).
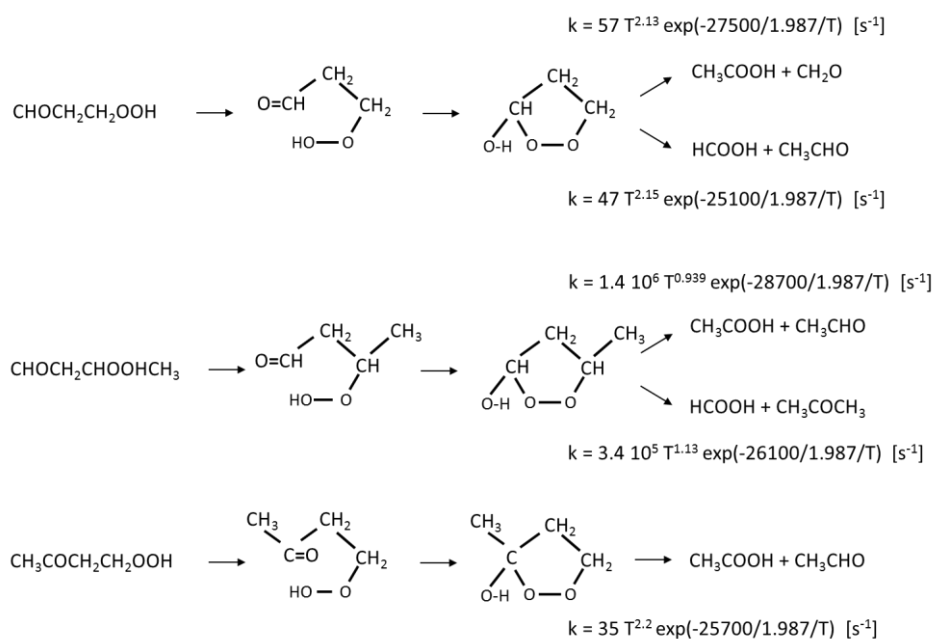
Figure 76: Schematic of Korcek mechanism and rate constants for the decomposition of C_3CHP and C_4CHPs interpolated between 400 and 1000 K in the modified Arrhenius form.

3.3 Molecular decomposition of acetyl-methyl-hydroperoxide.

The last reaction that was studied is the concerted one step molecular decomposition of acetyl-methyl-hydroperoxide (CH_3COCH_2OOH). The reason for this study is that, while H-abstraction reactions on CHP and the Korcek decomposition of CHP have the potential to explain the formation of several oxygenated species from propane and butane oxidation, the kinetic simulations reported in Figure 80 clearly show that the predicted formation of acetic acid underestimates the experimental data. There is thus potential for the existence of alternative reaction routes. Here it is explored the molecular decomposition of acetyl-methyl-hydroperoxide, one of the simplest CHP species. Since this reaction has multireference character, as found by calculating the T1 diagnostic of the CBS-QB3 transition state for decomposition to acetic acid, calculations were performed at the CASPT2 level. Computational details are reported as Supplemental Material. Though no transition state that directly connects the reactant to acetic acid could be found, two distinct three body transition states leading to decomposition into OH radical, formaldehyde, and the acetyl radical were found. A further transition state leading to the formation of a peroxide cyclic species similar to that of the Korcek mechanism was also found. An internal reaction coordinate investigation of the two three body decomposition reactions showed that the product of both reactions are the acetyl radical and a complex formed by formaldehyde and the OH radical, stabilized by the formation of a hydrogen bond between the two. Barrier heights for the three reaction channels were determined from the geometries optimized using the minimal active space and the cc-pVDZ basis set by increasing the basis set to the aug-cc-pVTZ level and the size of the active space. The calculated barrier heights are reported in Table 12.

	Energy Barrier (kcal/mol)			ZPE correction
Reaction	(4e,4o)	(6e,6o)	(8e,8o)	(4e,4o)/(6e6o)
$CH_3COCH_2OOH \rightarrow CH_3CO + OH + H_2CO$ (cis)	44.6	45.7	44.7	-4.4
$CH_3COCH_2OOH \rightarrow CH_3CO + OH + H_2CO$ (trans)	44.8	46.6	45.7	-5.1
$CH_3COCH_2OOH \rightarrow C_4$ cyclization	-	46.2	45.8	-2.8

Table 12: *Barrier heights (kcal/mol) for the unimolecular decomposition of acetyl-methyl-hydroperoxide and for peroxy cyclization. Barrier heights are not corrected for Zero Point Energies, which were calculated from unscaled frequencies determined at the CASPT2/cc-pVDZ level using the minimal active space here considered and are reported separately in the last column. All calculations performed at the CASPT2/aug-cc-pVTZ level using different active spaces.*

The most interesting aspect of this system is that the final decomposition products of the reactive flux passing from the cis transition state may actually differ from the acetyl radical, $\dot{O}H$, and formaldehyde. An energy minimization performed starting from the final step of the IRC scan of the cis transition state in fact converged to acetic acid and formaldehyde. An analysis of the intermediate geometries visited during the energy minimization protocol showed that following dissociation from the hydroperoxy group the hydroxyl radical remains in proximity of the acetyl radical center, so that after the CH_3CO–CH_2OOH bond distance increases to about 3 Å it becomes possible for the hydroxyl group to react with CH_3CO and form acetic acid. This reaction path will most probably be in competition with the three body decomposition path, which will be progressively favored with increasing temperature, due to the higher density of states of its transition state, as is the case for roaming reactions. However, it is possible that at low temperatures, such as those considered in the present work, a non-negligible contribution to the formation of minor reaction products may come from this pathway. Further studies are needed to determine whether this reaction mechanism may be competitive with the other low temperature reaction classes proposed in this work.

4. Comparisons with experimental measurements

All simulations required for the comparisons with the experimental measurements of the low temperature oxidation of propane and n-butane in JSR [224-230, 245] were performed with OpenSMOKE++ code [66], by using the kinetic scheme POLIMI attached as Supplemental Material (in Chemkin format with thermo and transport properties), and also available in the CreckModeling web site (http://creckmodeling.chem.polimi.it).

4.1 Oxidation of propane [227]

Cord et al. [227] investigated the low-temperature oxidation of propane using a jet-stirred reactor. Mole fractions of reactants and reaction products were measured as a function of the reactor temperature (550-730 K), with a particular attention to intermediate reaction products. As already mentioned, to widen the range of analyzed species, they used two different analytical methods: online gas chromatography (GC) in

Nancy and synchrotron vacuum ultraviolet photoionization mass spectrometry (SVUV-PIMS) in Hefei. Experiments were performed under stoichiometric conditions with a large mole fraction of propane (0.12), at atmospheric pressure, residence time of 6 s, and the mixture was diluted in an inert gas (helium in Nancy and argon in Hefei). As shown in *Figure 70*, 1- and 2-propyl radical additions on oxygen compete with their high temperature β-decomposition reactions to form ethylene and propene. Thus at low temperatures, two successive O_2 addition and isomerization reactions (occurring via intramolecular H-abstractions through cyclic transition states) form peroxy and propyl-hydroperoxy radicals up to the formation of three different carbonyl-hydroperoxides. Peroxy radicals can also form propyl hydroperoxides, mainly via recombination/disproportionation reactions with $H\dot{O}_2$ radicals:

$C_3H_7OO\bullet + HO_2\bullet \rightarrow C_3H_7OOH + O_2$
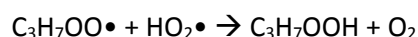
All these hydroperoxides are the main source of the chain branching occurring at low temperatures. Detailed comparisons between experimental data and model predictions for propane, oxygen, and several intermediates are reported in Figure **77**. Simulations show that the system reactivity is not affected by the two different inert gases. This is firstly due to the very similar collisional efficiency of Ar and He adopted in the POLIMI kinetic scheme. Moreover, it was also verified that the system sensitivity to collisional efficiency is very limited, at these low temperature conditions. The general agreement with major species is satisfactory. Hydrogen peroxide and formaldehyde are under-predicted by a factor of 2-3, similar deviations were also observed by Cord et al. [227]. The detail of measured intermediate products was very useful to further validate the low temperature oxidation mechanism, and also to include in the kinetic scheme the new reaction paths of hydroperoxides, previously neglected. Particularly, the formation of several intermediate oxygenated species in the very low temperature region is well explained by adding to the previous mechanism H-abstraction and molecular reactions of hydroperoxides. As a matter of clarity, Figure **77** also compares model predictions with and without these new reactions. The reduction of propane conversion is here less evident in comparison with n-butane results reported in *Figure 72*. Nevertheless, the new reactions improve the predictions of acetic acid and propyl-hydroperoxide and introduce new reaction channels to form oxirane, acetone, propanal, propanols, and C_3 components with two carbonyl groups, previously neglected.

Methyl-oxirane and oxetane are lumped into a single equivalent species (C_3–Cyclic ether), which is directly formed through the decomposition of C_3-hydroperoxy radicals (see *Figure 70*) and agrees well with the experimental data. Similar agreement is also observed for methane, acetaldehyde, and propene, with an overestimation of ethylene in the NTC region. Methanol, properly predicted, is mostly obtained through the H-abstraction reactions of methoxy radicals on propane and different reaction products, such as formaldehyde and hydrogen peroxide. As already mentioned, an important source of acetic acid is the

recombination reaction of peracetyl and methyl-peroxy radicals. The Korcek mechanism, i.e. the reaction pathways of carbonylhydroperoxide ($C_3H_6O_3$) forming the cyclic peroxide, which decomposes into acetic acid and formaldehyde [249]:

$$C_3H_6O_3 \rightarrow CH_2O + CH_3COOH$$
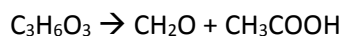
is included and it accounts for its remaining amount. The rate constant for this reaction channel was discussed in Section 3, and reported in Table S2 of the Supplemental Material.

The two C_3-hydroperoxides, lumped in the single equivalent component (C_3H_7OOH), are properly predicted with the complete model, while they are overestimated disregarding the H-abstraction reactions. As already shown in Figure **73**, the H-abstraction reactions on these hydroperoxides, with the successive fast decomposition of the intermediate radicals, are the effective paths to form acetone and propanal, at low temperatures. As far as the $C_3H_6O_3$ are concerned, 2-formyl-ethyl-hydroperoxide ($CHOCH_2CH_2OOH$) is the prevailing one, due to the fast isomerization of the corresponding peroxy-hydroperoxy radical. It accounts for more than 90% of the lumped component $C_3H_6O_3$ considered in the POLIMI kinetic scheme. Thus, the following reactions, with the corresponding kinetic parameters of the H-abstraction by OH radicals, have been included in the mechanism:

$\bullet OH + C_3H_6O_3 \rightarrow H_2O + C_3\text{-dicarbonyls} + \bullet OH$	$3.5 \cdot 10^9 \exp(-630/RT)$ [m^3/kmol/s]
$\bullet OH + C_3H_6O_3 \rightarrow H_2O + \text{Acrolein} + HOO\bullet$	$1.75 \cdot 10^9 \exp(-630/RT)$ [m^3/kmol/s]
$\bullet OH + C_3H_6O_3 \rightarrow H_2O + CO + \text{Oxirane} + \bullet OH$	$5.9 \cdot 10^9 \exp(-630/RT)$ [m^3/kmol/s]
$\bullet OH + C_3H_6O_3 \rightarrow H_2O + CH_2CO + CH_2O + \bullet OH$	$4.8 \cdot 10^9 \exp(-630/RT)$ [m^3/kmol/s]
$\bullet OH + C_3H_6O_3 \rightarrow H_2O + CO + CH_3CHO + \bullet OH$	$1.2 \cdot 10^9 \exp(-630/RT)$ [m^3/kmol/s]
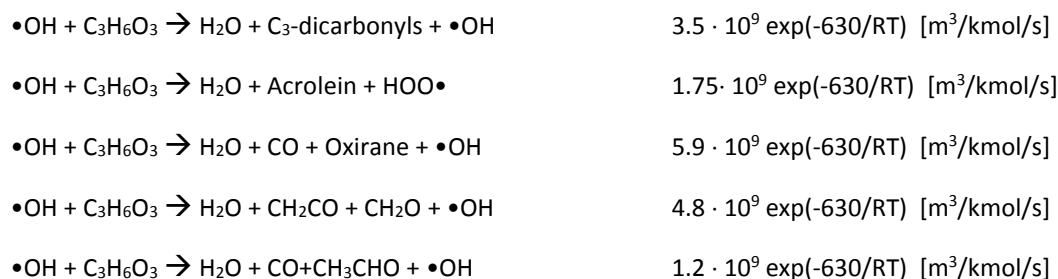
Kinetic parameters for the other H-abstracting radicals are obtained by applying the usual similarity and analogy rules [52]. Propandial ($CHOCH_2CHO$) is obtained via H-abstraction on 2-formyl-ethyl-hydroperoxide, while acetyl-methyl-hydroperoxide (CH_3COCH_2OOH) forms 2-oxopropanal (CH_3COCHO):

$$\bullet OH + CHOCH_2CH_2OOH \rightarrow H_2O + CHOCH_2CHO + \bullet OH$$
$$\bullet OH + CH_3COCH_2OOH \rightarrow H_2O + CH_3COCHO + \bullet OH$$
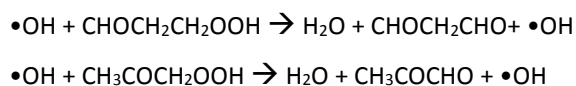
both these C_3-dicarbonyl species are grouped into the lumped component ($C_3H_4O_2$).

The mole fraction profile of oxirane (C_2H_4O) shows a very sharp peak at the lowest temperatures, again suggesting its formation via H-abstraction reactions on $C_3H_6O_3$ and a fast decomposition of the intermediate radical ($\bullet COCH_2CH_2OOH$).

The formation of 1- and 2-propanol involves the recombination and disproportionation of propyl-peroxy radicals. While 1-propanol and propanal are obtained from the recombination of 1-propyl-peroxy radicals, 2-propanol and acetone are obtained from the recombination of two 2-propyl-peroxy radicals. Similarly, the formation of molecules with one hydroperoxy and one alcohol function can be explained with the recombination and disproportionation reactions of peroxy-hydroperoxy radicals.

Finally, Figure **77** also shows the expected mole fractions of C_3-molecules including two carbonyl groups ($C_3H_4O_2$) not measured by Cord et al. [227]. In similar low temperature experiments, Herbinet et al. [226] mentioned relative errors of carbon balances up to 20%, mainly due to the non-quantification of some oxygenated species in the very low temperature conditions.
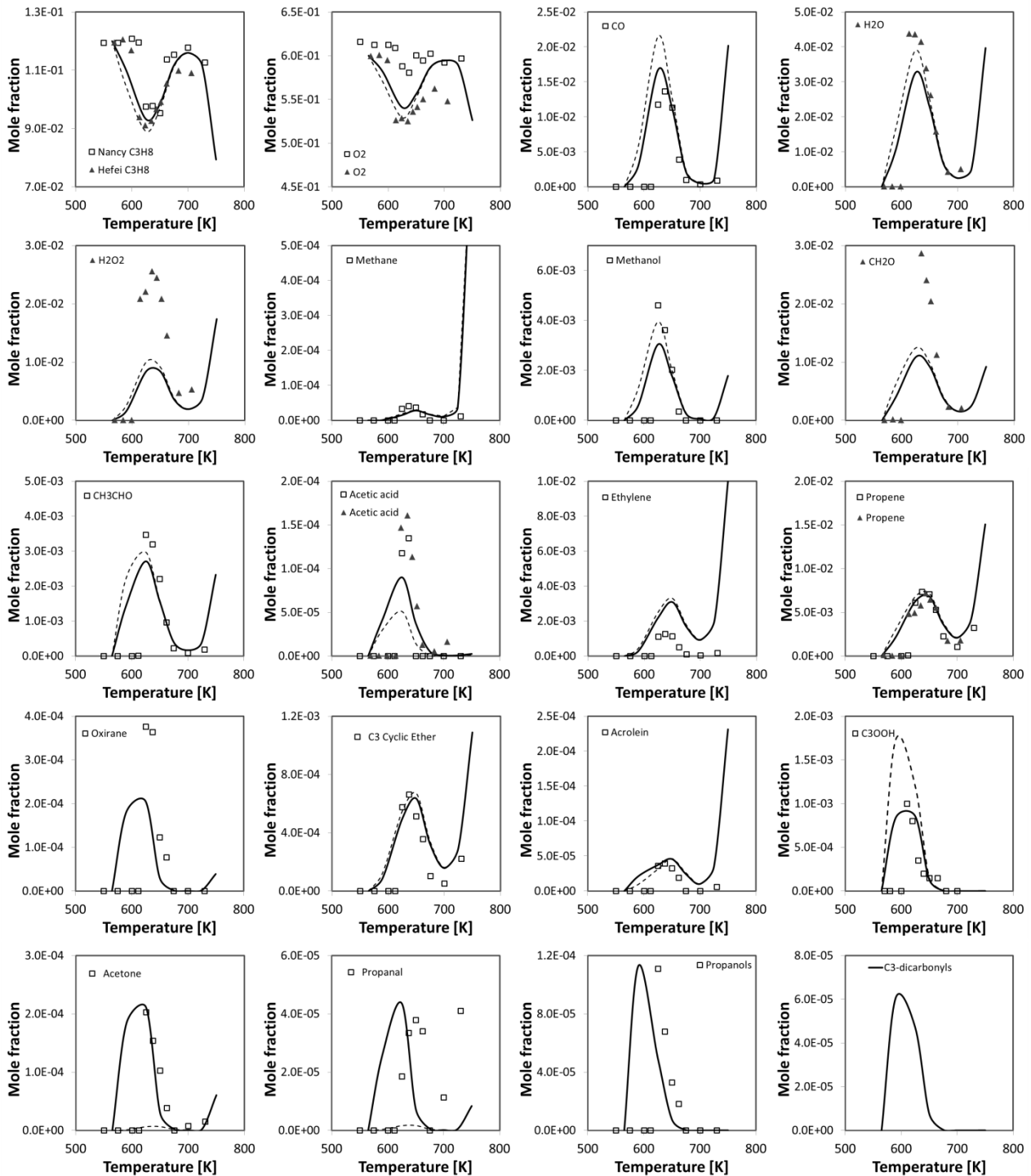
Figure 77: *Stoichiometric propane oxidation in a jet stirred reactor (12% C₃H₈; 1 atm; residence time 6 s) [227]. Mole fractions of major species and relevant intermediates at different reactor temperatures. Comparison of experimental measurements of Nancy [squares] and Hefei [triangles] with model predictions with [solid lines] and without [dashed lines] the new reactions.*

4.2 Oxidation of n-butane in Nancy and Hefei stirred reactor [225, 228]

As already partially shown in Figure 72, the low-temperature oxidation of n-butane in a jet-stirred reactor was presented and discussed by Herbinet et al. [225] and Cord et al. [228]. Experiments were performed at 1.06 [225] and 1.0 [228] atm, for temperatures between 550 and 800 K, at a mean residence time of 6 s and

with a stoichiometric n-butane/oxygen/argon mixture (4/26/70 in mol%). Similar experiments with a stoichiometric n-butane/O$_2$/helium mixture (2.3/15/82.7 in mol%) were also presented by Bahrini et al. [229, 230]. A detailed kinetic model [224] was able to reproduce the global reactivity and the major oxidation products, while the predictions of alcohols, ketones, diones, and acetic acid were not completely satisfactory [228, 245].

While the formation of organic acids can be explained with the Korcek mechanism [249], the H-abstraction reactions on the most favored C$_4$-carbonyl-hydroperoxides reported in *Figure 78* show simple channels to form not only C$_4$-dicarbonyl species, but also ketene, acetaldehyde, methyl-vinyl-ketone, and 1- and 2-butenal. Figure 80 reports detailed comparisons between experimental data [225, 228, 256] and predictions of the POLIMI kinetic scheme, with and without the new reactions.

The reactivity of the system, oxygen consumption, and the NTC region are well reproduced by the model together with major oxidation products. As far as the differences in acetaldehyde measurements of Nancy and Hefei are concerned, the model better agrees with Nancy measurements. Model over-predictions of ethylene, propene and butenes are present, mainly at 700-800 K in the NTC zone, and they are mainly due to the decomposition of the alkyl-hydroperoxy radicals. This decomposition is also responsible for the over-prediction of cyclic ethers with 4 carbon atoms (methyl-oxetane, dimethyl-oxirane, ethyl-oxirane, and tetrahydro-furan) grouped in a single lumped component. As already mentioned, the differences between the two model predictions are limited to the temperature range 550-650 K. More than the different reactivity, it is important to underline that the new reactions allow to predict several species that were previously completely neglected (butanol, hydroxypropanone, and C4-dicarbonyl compounds) and also to improve the predictions of other components strongly underestimated (acetic acid, ethanol, and acetone). The experimental mole fraction of several species show a very sharp onset when reaction starts, while the model shows a smoother behavior. These model deviations on the order of 20-30 K could be also due to the effect of wall reactions on the onset of system reactivity. While the wall reactions are proved to have influence mainly at higher temperatures [225], we suspect a possible effect also in these conditions.

The measured mole fraction of acetic acid exceeds 1000 ppm and it is more than three times the amount observed in propane oxidation, despite the higher dilution. The previous radical path, via peracetyl radicals gives here only a contribution of ~30%, while the Korcek reaction route plays a major role. The decomposition products of the two C$_4$-ketohydroperoxide isomers through the Korcek mechanism can be either acetic acid and acetaldehyde [249] or acetone and formic acid, through the formic conformer of the cyclic peroxide. Details on rate parameters and mechanistic aspects were discussed in Section 3 and are reported in Table S2 of the Supplemental Material.

Butanone or methyl-ethyl-ketone (MEK) is largely under-predicted. It is mainly formed via the recombination/disproportionation of peroxy-hydroperoxy and methylperoxy radicals, while the contribution of the H-abstraction reactions on C_4-hydroperoxide is in the order of 10%.
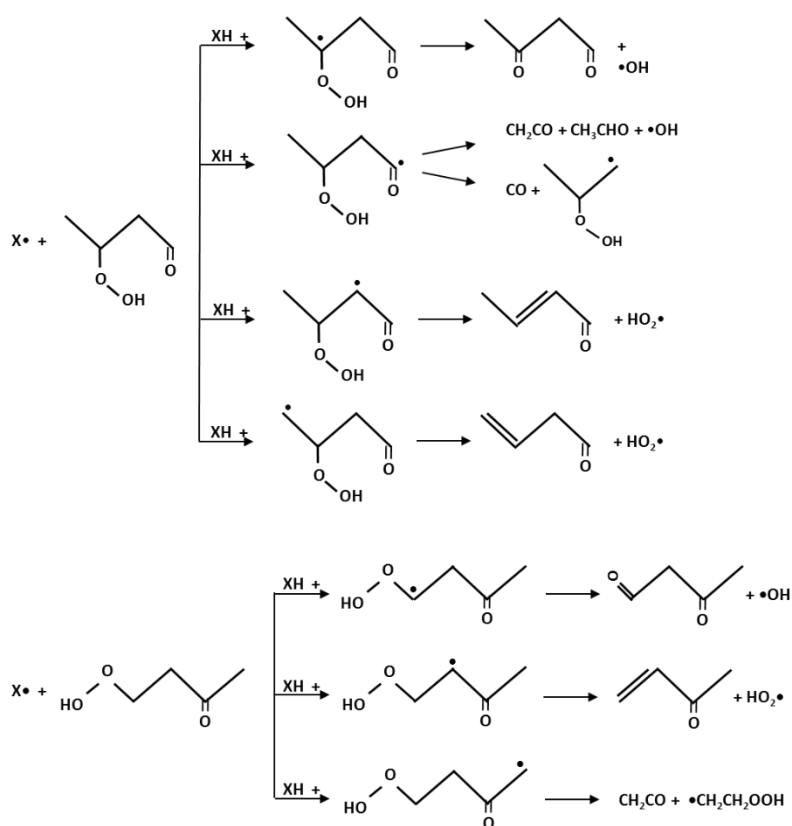
Figure 78: H-abstraction reactions on the most favored C_4-carbonyl-hydroperoxides.

Further possible reactions to explain the significant formation of ethanol, acetol and acrolein are shown in **Errore. L'origine riferimento non è stata trovata.**. While acrolein and formaldehyde can be obtained through the fast decomposition of an intermediate radical of H-abstraction reactions on 1-formyl-3-propyl-hydroperoxide, acetol (hydroxypropanone) and formaldehyde are the possible products of a four center reaction of 2-acetyl-ethyl-hydroperoxide. Finally, another four center molecular reaction of 1-formyl-1-propyl-hydroperoxide can explain ethanol formation. The feasibility of the molecular reaction pathways reported in **Errore. L'origine riferimento non è stata trovata.** was discussed in Section 3, while the rate constants of the H-abstraction reactions are estimated through the similarity rules [52] and are not further theoretically investigated.

Figure 81 shows a comparison between model predictions and experimental measurements of hydroperoxide species. While the comparisons are reasonable for C_2- and C_4-hydroperoxides, large differences are observed for H_2O_2, CH_3OOH, and C_4CHP. For this reason, scaling factors are applied to the experimental data of Figure 81. Large deviations were also observed by Herbinet et al. [225], and there are

critical uncertainties on these difficult experimental measurements [256]. It is indeed surprising to have this large over-prediction of H_2O_2, while there was an under-prediction in Figure 77 for propane oxidation.
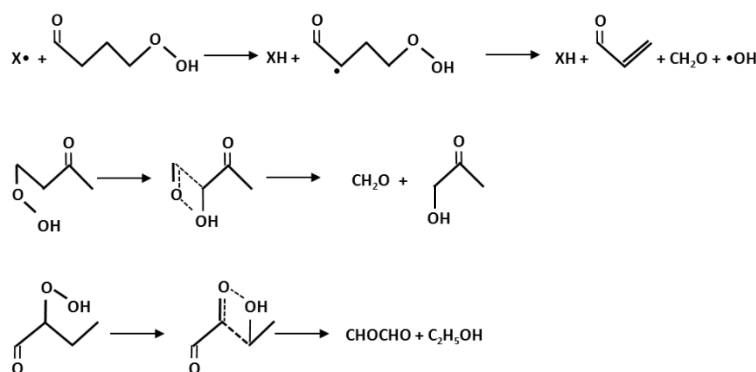
Figure 79: Reaction paths to form acrolein, acetol, glyoxal and ethanol.

Bahrini et al. [229, 230] have quantified H_2O_2 during n-butane oxidation in a jet-stirred reactor under conditions very close to those used by Herbinet et al. [225] using continuous wave cavity ring-down spectroscopy (cw–CRDS) in the near-infrared. This analytical system is expected to give accurate measurements of hydroperoxides, and relative uncertainties for different species are also discussed [229, 230]. Moreover, accepting a scarce influence of the inert gas, the two independent sets of experimental data on propane and n-butane give further indication of experimental uncertainties in these measurements. Figure 82 shows a few comparisons between experimental measurements [229, 230] and predictions obtained with both the POLIMI and the Nancy kinetic schemes [229, 230]. Both the models give satisfactory agreement with these major species, including H_2O_2. The NTC region predicted by POLIMI is slightly wider with respect to the experimental data, while the reverse is observed with the Nancy model. Nevertheless, the better agreement with H_2O_2 mole fractions supports the uncertainty of the previous H_2O_2 measurements (Figure 81). A more complete comparison between these experimental measurements [229, 230] and the predictions of the POLIMI kinetic scheme is reported in the Supplemental Material of this paper.
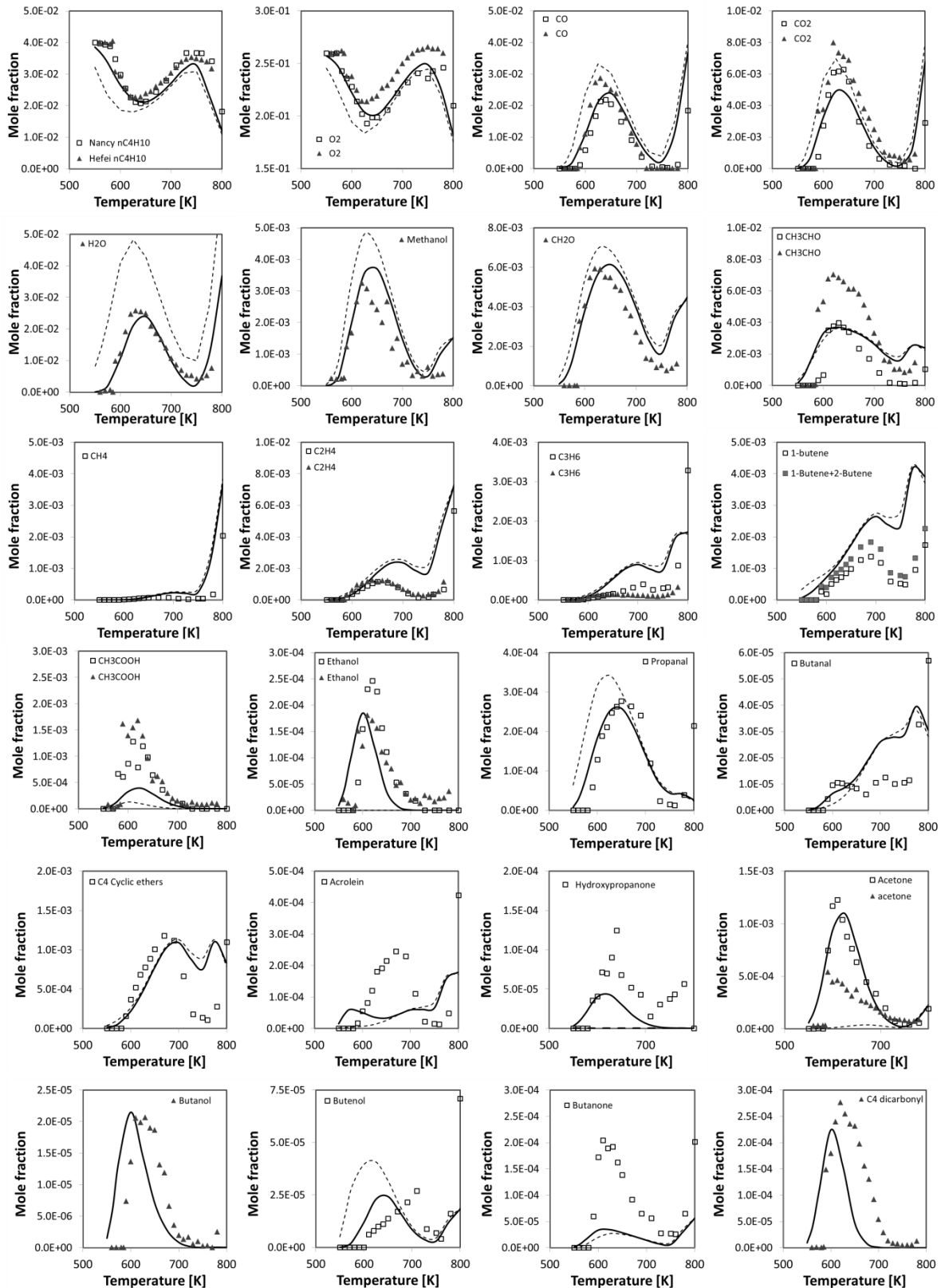
Figure 80: Oxidation of n-butane in jet stirred reactor (n-butane/O_2/Ar = 4/26/70 mol%; 1 atm; residence time 6 s) [225, 228]. Mole fractions of relevant intermediates at different reactor temperatures. Comparison of experimental measurements of Nancy [squares] and Hefei [triangles] with model predictions with [solid lines] and without [dashed lines] the new reactions. Note that butanol predictions are compared with the signal of mass 74 amu profile [256].
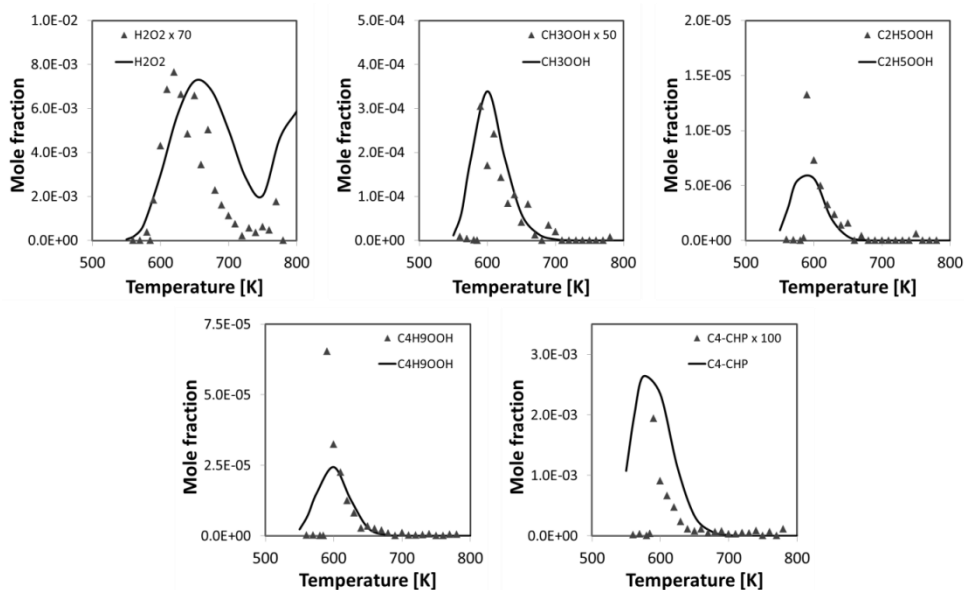
Figure 81: Oxidation of n-butane in jet stirred reactor (n-butane/O₂/Ar = 4/26/70 mol%; 1 atm; residence time 6 s) [225, 228]. Mole fractions of hydrogen peroxide, alkyl-hydroperoxides, and carbonyl-hydroperoxides at different reactor temperatures. Comparison of experimental measurements of Hefei [triangles] with model predictions [lines].
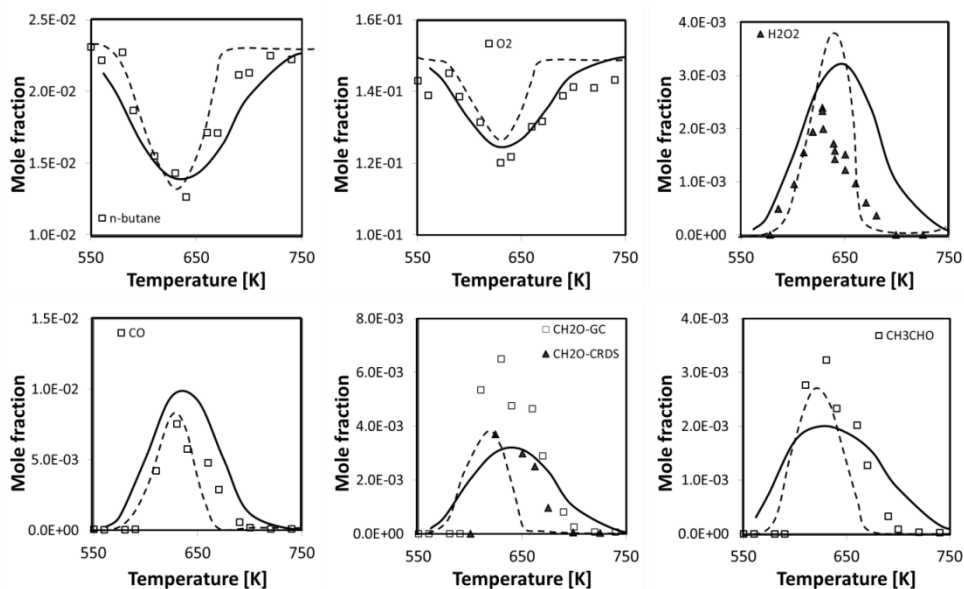
Figure 82: Oxidation of n-butane in jet stirred reactor (n-butane/O₂/He = 2.3/15/82.7 mol%; p= 1 atm; residence time 6 s) [229, 230]. Mole fractions of n-butane, oxygen and relevant products. Comparison between experimental data [GC: squares and CRDS: triangles]and predictions of POLIMI [solid lines] and Nancy [dashed lines] kinetic schemes.

5. Conclusions

After twenty years since the first kinetic mechanism of propane and butane oxidation [239], the careful kinetic analysis of recent detailed data highlights the importance of three new reaction classes, previously

neglected in the low temperature mechanisms. Particularly, the following reaction classes should be added to these mechanisms:

1-   H-abstraction reactions on hydroperoxides and carbonyl-hydroperoxides, to form carbonyl and dicarbonyl components.

2-   Molecular reactions of carbonyl-hydroperoxides (Korcek mechanism [249]), to form organic acids.

3-   Recombination/disproportionation reactions of peroxy radicals, to form alcohols, ketones and species containing two oxygenated groups.

It is important to underline that these reactions are effective only at very low temperatures (550-650 K), reducing the overall reactivity of the system, and mainly explaining the important formation of organic acids and minor oxygenated species. The extension of the overall kinetic mechanism, with the addition of these new reaction classes for heavier hydrocarbon fuels, already allows satisfactory comparisons also with the reaction products of the low temperature oxidation of n-heptane [226]. Finally, preliminary theoretical calculations already show the reliability of these reaction paths in justifying the formation of these species and point out the need for further research activities in the investigation of successive reactions of hydroperoxide species. Similar conclusions on this topic were also very recently drawn by Herbinet and Battin Leclerc [245].

5.1.2 Improved Kinetic Model of the Low Temperature Oxidation of n-heptane [73]

1.   Introduction

n-heptane is a primary reference fuel commonly used, together with iso-octane, for the octane rating of gasoline as well as a surrogate to represent linear alkanes in diesel fuels. In the attempt to better understand the knocking tendency and auto-ignition behavior of interest at engine relevant conditions, both the high and low temperature oxidation mechanisms of n-heptane were extensively studied and reported in the literature [233, 238, 257, 258]. In the last decades the experimental characterization of n-heptane oxidation focused on several laboratory devices such as shock tubes [259-265], rapid compression machines [232, 266-270], jet-stirred reactors [226, 257], flow reactors [30, 271, 272] and laminar premixed flames [273-277], as well as in engines [278]. Due to the importance of auto-ignition phenomena in the prevention of engine knock or backfire in prevaporized-premixed combustors, Tanabe et al. [279] and Schnaubelt et al. [280] experimentally investigated the oxidation of heptane droplets in air. Most of the studies in ideal reactors were carried out at conditions of interest in conventional SI engines, thus at relatively high temperatures (>800 K). The investigation of the low-temperature oxidation is of concern to understand combustion and auto-ignition phenomena such as cool flames and negative temperature coefficient (NTC behavior). Furthermore, the recent interest in the improvement of diesel engine efficiency and in the development of

new engine technologies such as HCCI, highlighted the need for a better characterization of the low temperature combustion of reference fuels such as n-heptane, at temperatures below those commonly studied (500-800 K).

Very recently, the importance of H-abstractions and new successive reactions of hydroperoxides and carbonyl hydroperoxides (CHP) was highlighted [281] to explain the formation of several intermediate species in the low temperature oxidation of propane and n-butane [224, 225, 227, 228, 230]. Furthermore, preliminary theoretical calculations were carried out to determine rate constants for relevant reaction channels [281]. Always at very low temperatures, Herbinet et al. [226] investigated the stoichiometric oxidation of n-heptane diluted in an inert gas using a jet-stirred reactor and two different analytical methods: gas chromatography (GC) and synchrotron vacuum ultraviolet photoionization mass spectrometry (SVUV-PIMS). The use of SVUV-PIMS in Hefei, with direct sampling through a molecular jet, allowed the identification of a large set of oxygenated products, such as molecules with hydroperoxy functions, not stable enough to be detected using GC.

The first purpose of this paper is to extend, with the usual systematic approach, the new reaction classes already investigated and successfully applied to the low temperature oxidation mechanism of propane and butane [281] up to n-heptane. These successive reactions of carbonyl-hydroperoxides (CHP) explain the formation of oxygenated species, such as organic acids and diones, experimentally detected [225-227] and previously neglected in detailed kinetic models of hydrocarbon fuels [18, 233, 258].

The work is organized as reported in the following. We first discuss the kinetic mechanism, with particular emphasis on successive reactions of hydroperoxide species and the formation of oxygenated components, such as organic acids, ketones, alcohols, diones and molecules including two oxygenated groups. Then, an extensive validation of the new kinetic mechanisms is reported in Section 3. Finally, Section 4 discusses a couple of more complex applications of the kinetic model to the auto-ignition of n-heptane droplets in microgravity conditions and to the auto-ignition of n-heptane/air mixtures in the homogeneous charge compression ignition (HCCI) engine.

2. Kinetic mechanism and successive reactions of hydroperoxide species

The kinetic mechanism of n-heptane oxidation was already discussed in previous publications [258], together with the automatic generation of the kinetic scheme as well as with the extension towards heavier n-alkanes [64]. Figure 83 schematically shows the overall reaction mechanism of n-heptane oxidation. At low temperatures, the n-heptyl radicals add to molecular oxygen and form the corresponding peroxy-heptyl radicals. These radicals then isomerize to hydroperoxy-heptyl radicals by internal H transfer [258]. A second oxygen addition forms peroxy-heptylhydroperoxy radicals, which then isomerize and decompose into

carbonyl-hydroperoxides and OH. Due to the very low O–O bond energy of the hydroperoxy function, carbonyl-hydroperoxides are responsible for the low-temperature chain branching reactions.
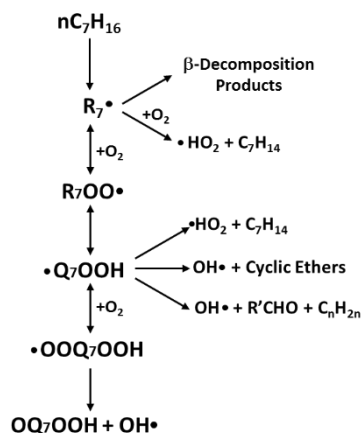
Figure 83: Reaction path diagram of n-heptane oxidation.

As already mentioned, the low temperature oxidation of n-heptane, as well as those of propane and n-butane, has been recently further investigated by measuring several intermediate species with advanced analytical techniques [224-228, 230]. This new experimental information already allowed to extend propane and n-butane oxidation mechanisms by including new reaction classes in order to explain the formation of oxygenated species previously neglected [281]. In fact, successive reactions of hydroperoxide species, such as H-abstraction reactions to form ketones and diones, as well as molecular reactions to form organic acids through the Korcek mechanism [249], constitute relevant low temperature reaction channels [281]. Thus, in addition to the 25 reaction classes usually considered in the low and high temperature oxidation schemes of alkanes [233, 242], the following new reaction classes can conveniently complete the low temperature oxidation mechanism:

1- H-abstraction reactions on hydroperoxides, to form ketones
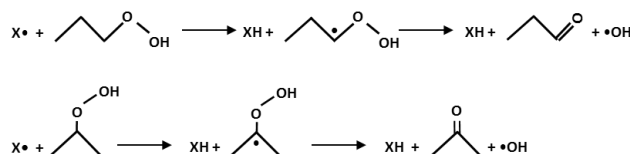
2- H-abstraction reactions on carbonyl-hydroperoxides, to form diones

3- Molecular reactions of carbonyl-hydroperoxides (Korcek mechanism), to form organic acids

4- Recombination/disproportionation reactions of peroxy and hydroperoxy-alkylperoxy radicals to form alcohols and different oxygenated species.

Figure 84 and Figure 85 show the measured mole fractions of heptadiones, heptanones, and acetic and propanoic acids, at different temperatures in a JSR at atmospheric pressure [226]. These experimental data clearly highlight the abundance of these species at low temperatures. In fact at 550 K, with n-heptane

conversion of ~15-20%, very high selectivities towards heptadiones and especially acids can be easily estimated.
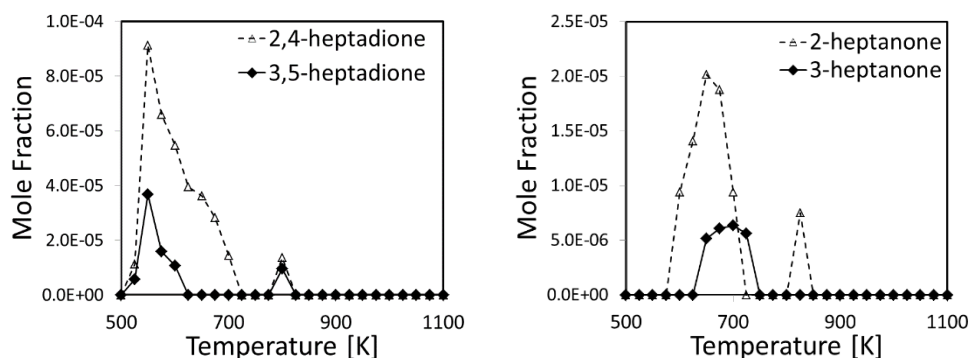
Figure 84: Stoichiometric oxidation of n-heptane in a jet stirred reactor (fuel initial mole fraction 0.005) [226]. GC measured mole fractions of heptadione and heptanone isomers at different reactor temperatures.
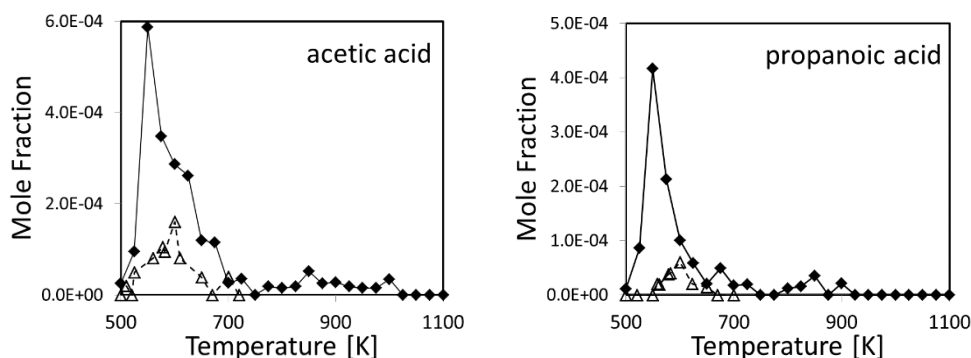
Figure 85: Stoichiometric oxidation of n-heptane in a jet stirred reactor (fuel initial mole fraction 0.005)[226]. Measured mole fractions of acetic and propanoic acids at different reactor temperatures (diamonds-GC; triangles-PIMS).

The low temperature oxidation mechanism of n-heptane involves 4 different alkyl and peroxy radicals with the corresponding 4 C_7-hydroperoxides. Moreover, after the second O_2 addition and the internal isomerization, 15 hydroperoxy-alkylperoxy radicals, together with 15 carbonyl-hydroperoxides (CHP), are obtained [258]. Due to the prevailing role of the internal six membered ring isomerization, the 5 γ–CHP (shown in Figure 86) are the favored ones among the 15 isomers. This fact is well confirmed by the experimental observations reported in Figure 84. In fact, as already discussed for propane and n-butane oxidation [281], diones ($C_7H_{12}O_2$) are directly formed via H-abstractions on the corresponding carbonyl-hydroperoxides ($C_7H_{14}O_3$):

$$R + C_7H_{14}O_3\ (i,j) \rightarrow RH + C_7H_{12}O_2\ (i,j) + \bullet OH$$
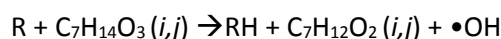
where i and j refer to the position of carbonyl and hydroperoxide groups, respectively. Thus, the 2,4 and 3,5 are the favored heptadiones, as expected from the internal distribution of carbonyl-hydroperoxides. Among the five γ–CHP, there are four γ-ketohydroperoxides (1,3 is the only hydroperoxy-aldehyde). 2,4-heptadione is the most abundant dione because it can be obtained both from 2,4 and 4,2–CHP. Similarly, the abundance of 2- and 3-heptanones in Figure 84 marks the relative presence of the corresponding heptyl-hydroperoxides, and further confirms the prevailing role of the secondary alkyl and peroxy radicals. As a matter of fact, H-abstraction reactions on hydroperoxides are the relevant source of the corresponding heptanones ($C_7H_{14}O$):

$$R + C_7H_{15}OOH(j) \rightarrow RH + C_7H_{14}O(j) + \bullet OH$$

where j again refers to the position of the hydroperoxide group.

The experimental data of Figure 84 are fully consistent with the low temperature oxidation mechanism of n-alkanes, once we include the successive H-abstraction reactions of hydroperoxide species. Kinetic parameters for the H-abstraction reactions are obtained by applying the usual similarity and analogy rules[52].

Figure 86 shows the major H-abstraction reactions on the 5 γ-carbonyl-hydroperoxides. The successive decomposition reactions of the intermediate radicals are also schematically reported. It is very important to observe that, as already discussed in the previous study on propane and butane oxidation [281], the successive decomposition reactions of carbonyl-hydroperoxy-alkyl radicals are very fast, also at 550-600 K. For this reason, diones are the most relevant products expected from H-abstraction reactions, while other more stable radicals are less effective in the chain propagation reactions. An important feature of the unimolecular decomposition reactions of γ-carbonyl-hydroperoxides, shown in Figure 87, is the significant formation of several γ-diones, from C_3 up to C_6. Thus, the extension of the detailed kinetic model requires also the addition of all these new radical and molecular species.
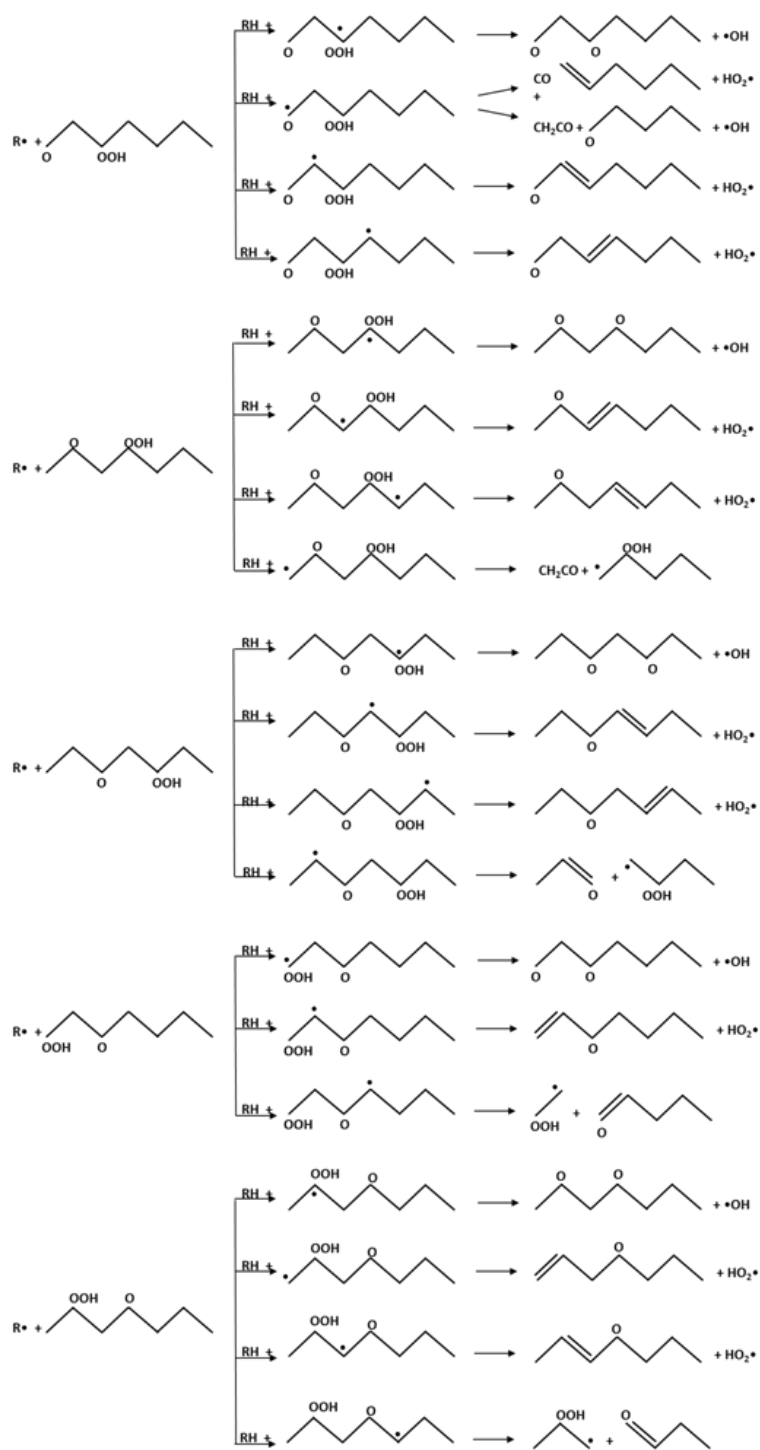
Figure 86: H-abstraction reactions of γ-carbonyl-hydroperoxides
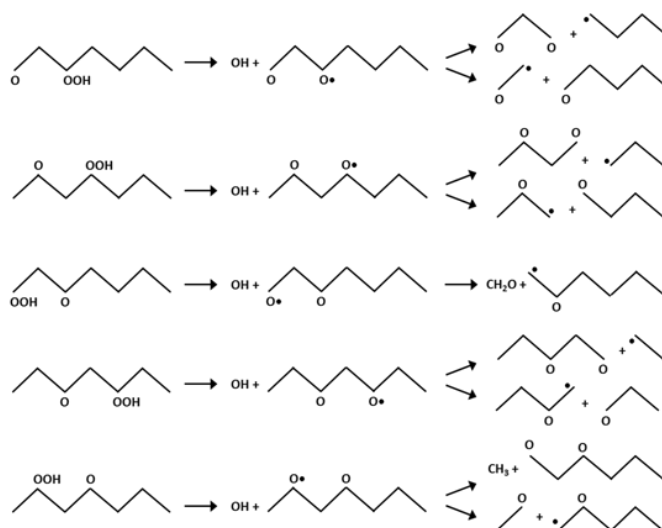
Figure 87: Unimolecular decomposition reactions of γ-carbonyl-hydroperoxides

As shown in Figure 85, significant amounts of acetic and propanoic acids were also measured at low temperatures. Data obtained with GC and PIMS analyses are different, mainly at very low temperatures. While GC data exhibit a sharp maximum located at 550 K, the PIMS data peak at ~600 K. As already discussed by Herbinet et al. [226], the higher acid concentrations could result from carbonyl-hydroperoxide decomposition in the transfer line between the reactor and the GC. The formation of organic acids, rarely observed in combustion experiments, was already detected in the low temperature oxidation of propane and n-butane in a jet-stirred reactor [225] and also of n-dodecane in a flow reactor [282].

The formation of an organic acid together with the corresponding carbonyl product can be explained through an exothermic concerted reaction of C_7–CHP (Korcek mechanism), previously discussed by Jalan et al. [249] and already included in the extended low temperature kinetic mechanism of propane and n-butane [281]. According to this reaction channel, the 5 γ–CHP can decompose to form an organic acid (from formic up to pentanoic) and a carbonyl component (from C_6 down to acetaldehyde) as shown in Figure 88. The kinetic parameters $3.37x10^5$ $T^{1.126}$ exp(-26068/RT) [s^{-1}], already calculated for C_4–CHP [281], are also used as a reference for this class of molecular reactions of C_7–CHP.
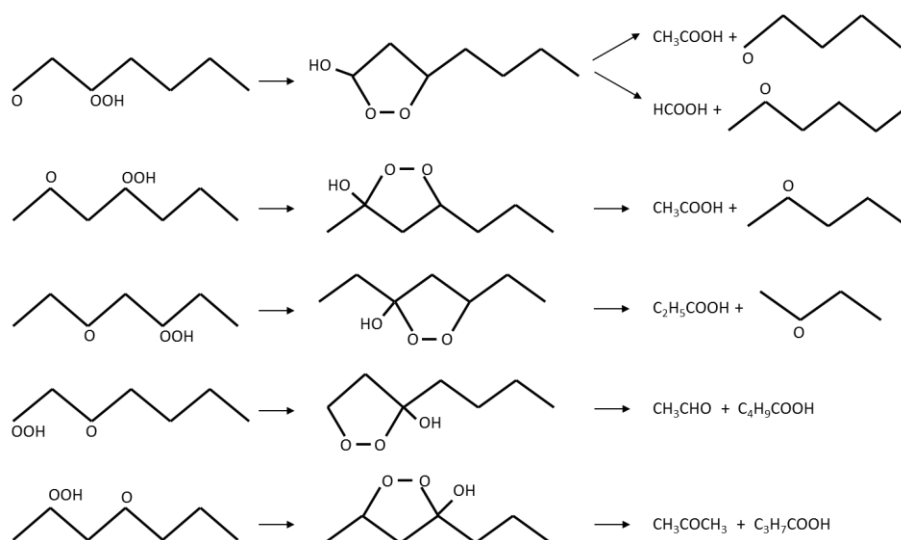
Figure 88: Decomposition of C_7–CHP through the formation of a cyclic peroxide isomer intermediate to a C_n organic acid and C_m carbonyl compound (n+m=7), according to the Korcek mechanism [249].

The fourth reaction class to be considered is the recombination/disproportionation of peroxy and hydroperoxy-alkylperoxy radicals to form oxygenated species with alcohol functions. The recombination of peroxy radicals explains the formation of alcohols and carbonyl components:
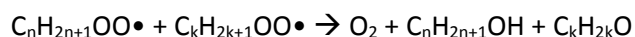
$$C_nH_{2n+1}OO\bullet + C_kH_{2k+1}OO\bullet \rightarrow O_2 + C_nH_{2n+1}OH + C_kH_{2k}O$$

Similarly, the recombination/disproportionation of peroxy and hydroperoxy-alkylperoxy radicals can form also two oxygenated groups (e.g. one hydroperoxy and one carbonyl or alcohol function) [225]:

$$C_nH_{2n+1}OO\bullet + \bullet OOC_kH_{2k}OOH \rightarrow O_2 + C_nH_{2n+1}OH + OC_kH_{2k-1}OOH$$

$$C_nH_{2n+1}OO\bullet + \bullet OOC_kH_{2k}OOH \rightarrow O_2 + C_nH_{2n}O + HOC_kH_{2k}OOH$$
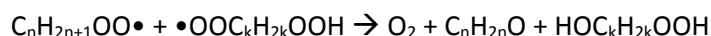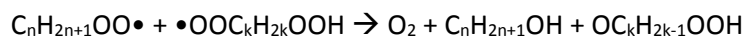
Figure 89 schematically shows a couple of examples of this reaction class. Reference kinetic parameters for this reaction class are similar to the ones already used for Reaction Class 15 ($RO_2 + CH_3O_2 = RO + CH_3O + O_2$) and 16 ($RO_2 + RO_2 = RO + RO + O_2$) by Curran et al. [233, 240] and by Westbrook et al. [242].
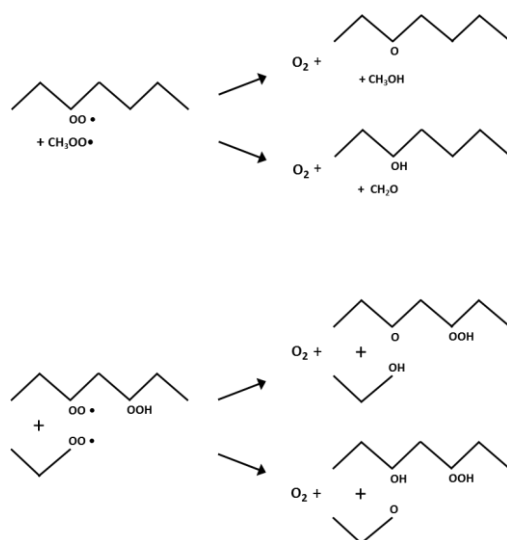
Figure 89: Recombination/disproportionation reactions of peroxy radicals

Due to the lumped approach, we include only one lumped C_7–CHP, whose successive reactions are obtained with a proper average of the successive reactions of the individual isomers. As already mentioned, the 2,4- and the 4,2–CHPs are the prevailing ones, together with the 3,5. The successive lumped H-abstraction and decomposition reactions of C_7–CHP are properly weighted on this relative abundance. Similarly, single lumped species are also assumed for the different C_7-dione and C_7-ketone isomers. Moreover, in order to preserve a full consistency within the overall kinetic scheme, these new reaction classes and relative lumped species have been also included to extend the low temperature oxidation mechanism not only of n-heptane but also of n-pentane. Figure 90 shows the effect of these new reactions on the stoichiometric oxidation of n-pentane with air in a JSR with 0.4 s residence time, at 1 and 10 atm. The successive reactions of hydroperoxide species, together with the new disproportionation reactions of peroxy radicals, clearly reduce the fuel conversion and CO formation, in the temperature range 550-700 K. This effect is more pronounced and persistent at higher pressures. Model predictions in the high temperature conditions remain evidently unchanged.
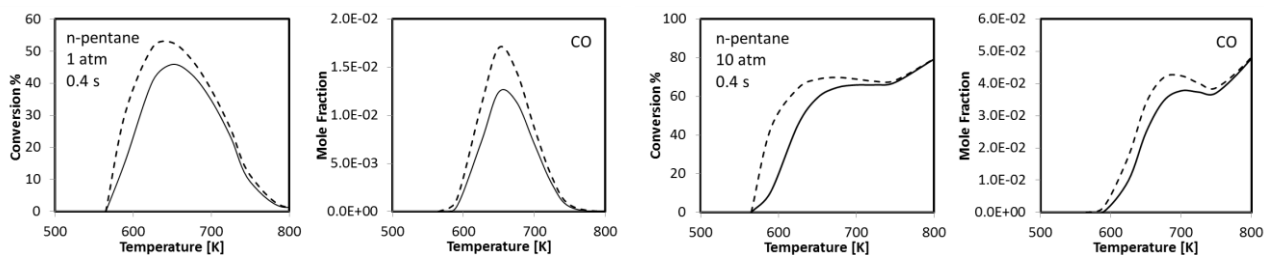
Figure 90: Stoichiometric oxidation of 2560 ppm of n-pentane with air in a JSR at 1 and 10 atm, with 0.4 s residence time. Model predictions without (dashed lines) and with (solid lines) the new successive reactions of peroxide species.

3. Mechanism validation

Mechanism validation mainly refers to the detailed measurements of the recent low temperature oxidation of n-heptane in jet stirred reactors [226]. To extend this kinetic analysis also to different operating conditions, further comparisons between model predictions and experimental measurements relevant to the oxidation of n-heptane in the Orléans JSR at 10 and 40 atm [231, 283]. n-heptane oxidation in Princeton [272], and Drexel flow reactors [30] complement this validation. Finally, shock tube [259, 260], rapid compression machine [232, 270] experiments and laminar flame velocity [273, 274, 277] are also analyzed. The effect of the new reactions is limited to the very low temperatures, but the comparisons at high temperature conditions are made to update the overall validation of the kinetic mechanism of n-heptane oxidation.

All simulations were performed with the OpenSMOKE++ code [66], adopting the kinetic scheme POLIMI_1407 available, in Chemkin format with thermo and transport properties, on the CreckModeling web site (http://creckmodeling.chem.polimi.it), and also reported as Supplemental Material to this paper. Moreover, the governing equations of the reactor models adopted for the different simulations are also reported in the Supplemental material.

Thus, the comparisons refer to the following systems:

> 3.1- Jet Stirred Reactors
> > 3.1.a- Nancy and Hefei [226]
> > 3.1.b- Orléans [231, 283]
> 3.2- Pressurized Flow Reactors
> > 3.2.a- Princeton flow reactor [272]
> > 3.2.b- Drexel flow reactor [30]
> 3.3- Shock tube experiments [259, 260]
>
> 3.4- Low temperature ignition of n-heptane in a Rapid Compression Facility [232, 270]
>
> 3.5- Laminar flame velocity [273, 274, 277]

3.1- Jet Stirred Reactors

3.1.a- Jet Stirred Reactor at Nancy and Hefei [226]

As already mentioned, the low-temperature oxidation of n-heptane was experimentally investigated by Herbinet et al. [226] in a jet-stirred reactor, using two analytical methods (GC and SVUV-PIMS). Mole fractions of reactants, intermediates and reaction products were measured in the temperature range 500–1100 K, at a residence time of 2 s, at near atmospheric pressure (800 Torr), under stoichiometric conditions, with n-heptane mole fraction of 0.005 diluted in an inert gas (helium in Nancy and argon in Hefei). Species involved in the low-temperature oxidation, such as olefins, cyclic ethers, aldehydes, ketones, diones and

hydroperoxides were carefully analyzed. Figure 91 shows comparisons of experimental mole fractions versus reactor temperature together with model predictions for a large number of compounds and the general agreement with major and minor species is very satisfactory, both in the low and high temperature conditions. Despite a slight deviation in the prediction of oxygen in the NTC region, n-heptane overall reactivity is well captured. The model over-predicts the low temperature formaldehyde peak by about a factor of 2 and this deviation will be further discussed later in this section. Anyway, formaldehyde formation is not directly related to n-heptane specific reactions nor to the new low temperature reactions. Instead, the main sources of formaldehyde are inside the C_0–C_4 sub-mechanism. Major low temperature intermediate products, such as cyclic ethers and heptenes are properly predicted, while the low temperature overpredictions of alkenes, and mainly butadiene, are not dependent on the new reaction classes. As already discussed and shown in Figure 88, organic acids are mostly formed via the Korcek mechanism. The recombination/disproportionation reaction:

$$CH_3CO_3\bullet + CH_3OO\bullet \rightarrow O_2 + CH_3COOH + CH_2O$$
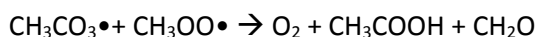
only contributes less than 10% of acetic acid formation, in these conditions. Reasonable comparisons for acetic and propanoic acids are obtained by increasing by a factor of 3 the reference kinetic parameters of the Korcek mechanism. The 'Nancy' mechanism, via recombination/disproportionation of $CH_3CO_3\bullet$ and $HO_2\bullet$, useful for predicting acetic acid in n-butane and n-heptane oxidation [226] failed in predicting acetic acid in propane oxidation and it required a further analysis and confirmation [227]. The Korcek reaction channel is also the major path to form not only acetone, correctly estimated, but also butanoic acid, not experimentally determined. Relative errors in carbon balances of up to 20% are mentioned by Herbinet et al. [226], mainly due to the non-quantification of some oxygenated species in the very low temperature conditions. About 80% of 2-butanone (methyl-ethyl-ketone) is again formed via the Korcek mechanism. The lumped heptanones and heptadiones are compared with the sum of the relative isomers reported in Figure 84. While C_7-diones are mainly produced via the H-abstraction on C_7–CHP already reported in Figure 86, the H-abstraction reactions on C_7-hydroperoxides simply contribute to 20-30% of the formation of heptanones. The recombination/disproportionation reactions of peroxy radicals are responsible for their remaining amount. It is important to observe that the model well captures the shape of the profile of C_7–CHPs even if the experimental points for NC_7-OQOOH correspond to a signal in arbitrary units and not to quantitative information. Therefore this is only a qualitative agreement. Finally, the sharp peaks of the predicted heptanone and heptadione profiles occur at a lower temperature than that experimentally observed.
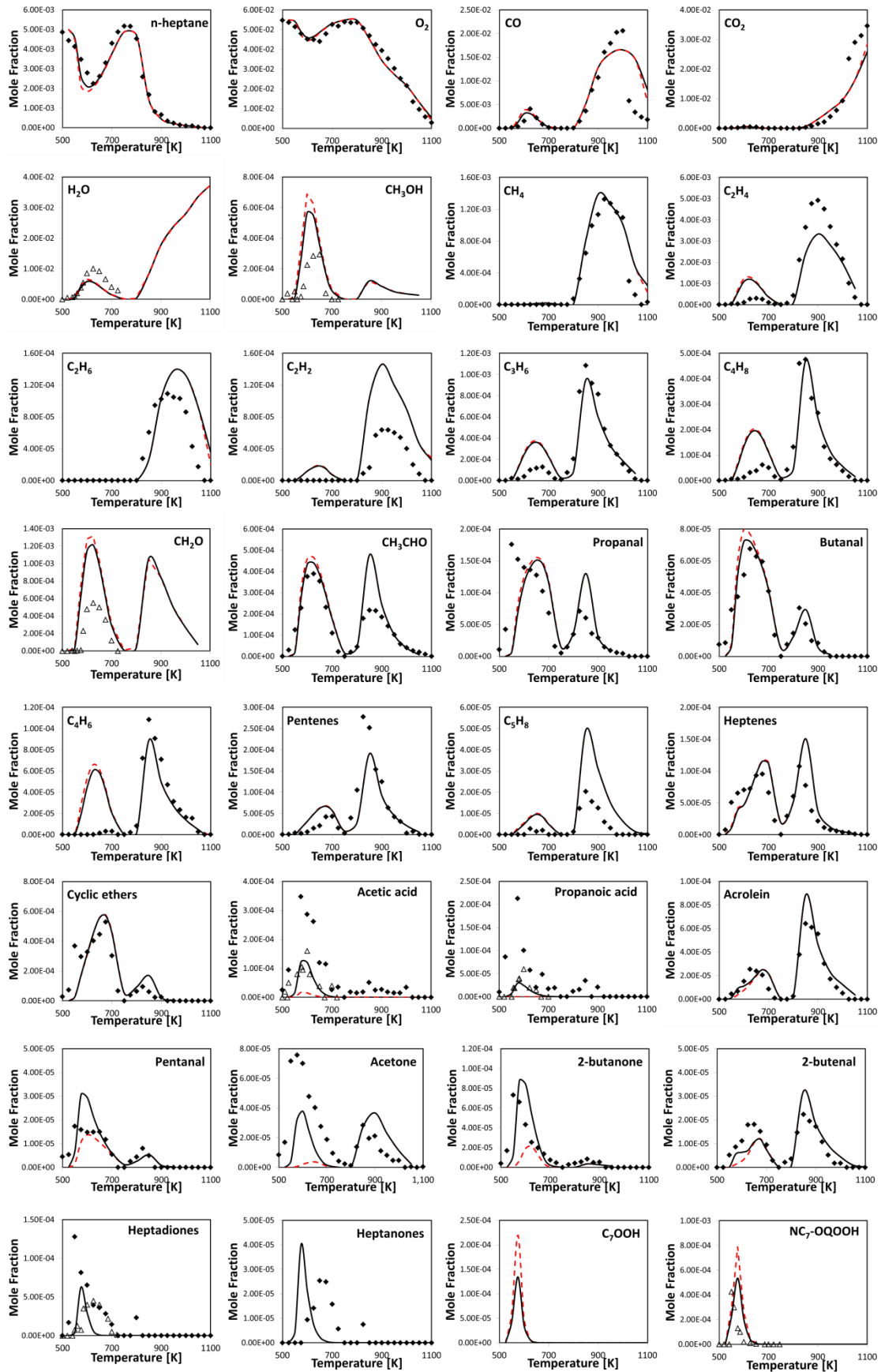
Figure 91: Stoichiometric oxidation of n-heptane in a jet stirred reactor [226] (0.5 mole % fuel, 1 atm, and 2 s). Mole fractions of major and intermediate species at different reactor temperatures. Comparison of experimental data (Symbols: diamonds-GC;

triangles-PIMS) with model predictions with (solid lines) and without (dashed lines) the new reaction classes. The experimental points for NC7-OQOOH correspond to a signal in arbitrary units and not to quantitative information.

The effect of the new reaction classes is limited to very low temperatures and these reactions are mainly useful to explain the formation of organic acids as well as heptanones and diones. The high temperature mechanism remains unchanged. For this reason, Figure 92 further compares experimental data with model predictions, with and without the new reactions, for a few selected species, only at low temperatures. The new reactions slightly reduce n-heptane reactivity and CO formation. The effect on acetic acid is well evident. As already mentioned, the limited formation of acetic acid, without the Korcek mechanism, is simply due to the recombination disproportionation reaction of methyl peroxy and peracetyl radicals. Propanoic acid is not reanalyzed because it is only formed with the new reaction classes. As already shown in Figure 88, 2-butanone (methyl ethyl ketone) is mainly formed together with propanoic acid, via the Korcek mechanism. The lower peaks of hydroperoxide species are due to their successive reactions. Heptadiones and heptanones are only formed through the new reaction classes, and therefore are not reported.
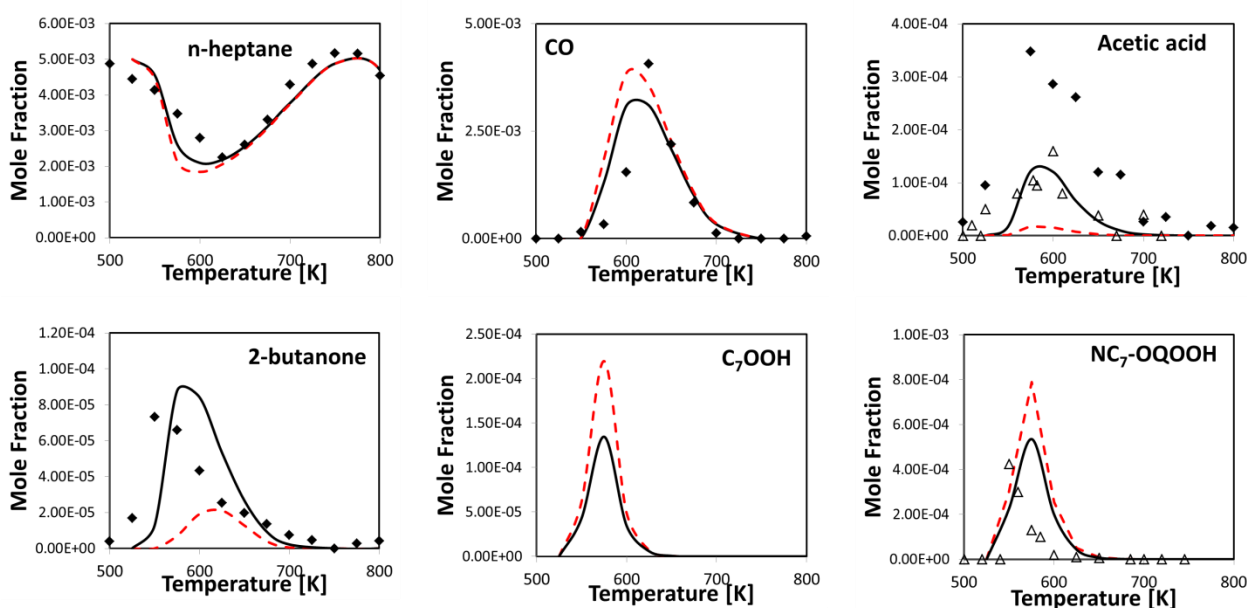
Figure 92: Stoichiometric oxidation of n-heptane in a jet stirred reactor [226] (0.5 mole % fuel, 1 atm, and 2 s). Mole fractions of selected species at different reactor temperatures. Comparison of experimental data (Symbols: diamonds-GC; triangles-PIMS) with model predictions with (solid lines) and without the new reaction classes (dashed lines).

To further clarify the effect of these reactions, Figure 93 reports the comparison of the overall rate constants (panel a) for unimolecular decomposition, Korcek mechanism, and H-abstraction reactions of C_7-carbonyl hydroperoxides. We used the predicted OH concentration, which increases from 5×10^{-12} kmol/m^3 at 550 K to a maximum value of $\sim 7 \times 10^{-11}$ kmol/m^3 at 600 K and then decreases to 1×10^{-11} kmol/m^3 at 700 K, to calculate the apparent first order rate constants of H-abstractions. The relative importance of the different reaction paths is shown in panel b) at 550 K and 650 K and clearly highlights the large difference of their activation

energies. At these temperatures, the formation of heptadiones is the prevailing channel for the H-abstraction reactions.
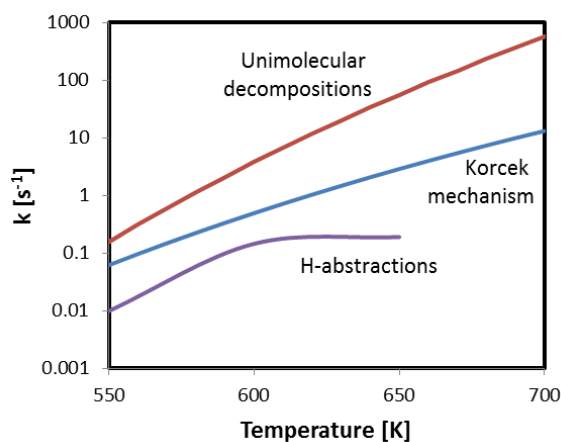
Panel a)
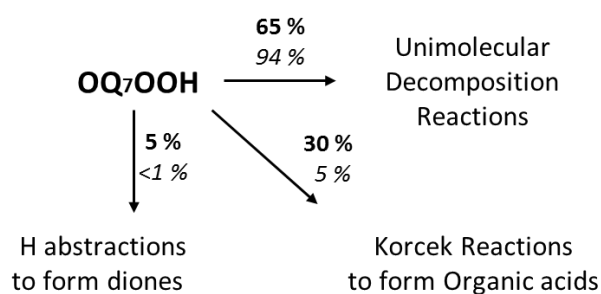
Panel b)

Figure 93: Stoichiometric oxidation of n-heptane in a jet stirred reactor (0.5 mole % fuel, 1 atm, and 2 s).Panel a): rate constants versus temperature for decomposition, Korcek mechanism, and H-abstraction reactions (k=C$_{OH}$*k$_{abs}$) of C$_7$-carbonyl hydroperoxides; panel b): relative importance of the three reaction channels at 550 K (bold) and 650 K (italic).

3.1.b- Jet Stirred Reactor at Orléans [231, 283]

n-heptane oxidation in the Orléans high-pressure JSR was experimentally investigated at 10 and 40 atm in a wide range of conditions covering the low and high temperature regimes [231, 283]. Figure 94 and Figure 95 show the comparisons between model predictions and experimental measurements for stoichiometric mixtures, at both operating pressures. Again, there is generally satisfactory agreement in n-heptane conversion and major products, thus confirming the model ability to properly account for the pressure effects. In particular, it is possible to highlight a clear reduction of the NTC zone with pressure increase, ranging from 630-780 K at 1 atm [226], and from 630-700 K at 40 atm [43]. This trend is more evident in the experimental data and it is reasonably predicted by the model. In contrast with the previous formaldehyde over-predictions at atmospheric pressure, model predictions agree well with experimental data at 10 bar, whilst slight underpredictions are observed at 40 atm. As already mentioned, n-heptane specific reactions are only marginally responsible for formaldehyde formation. Reasons for these possibly systematic deviations at the different pressures need to be better investigated in the C$_0$–C$_4$ mechanism.
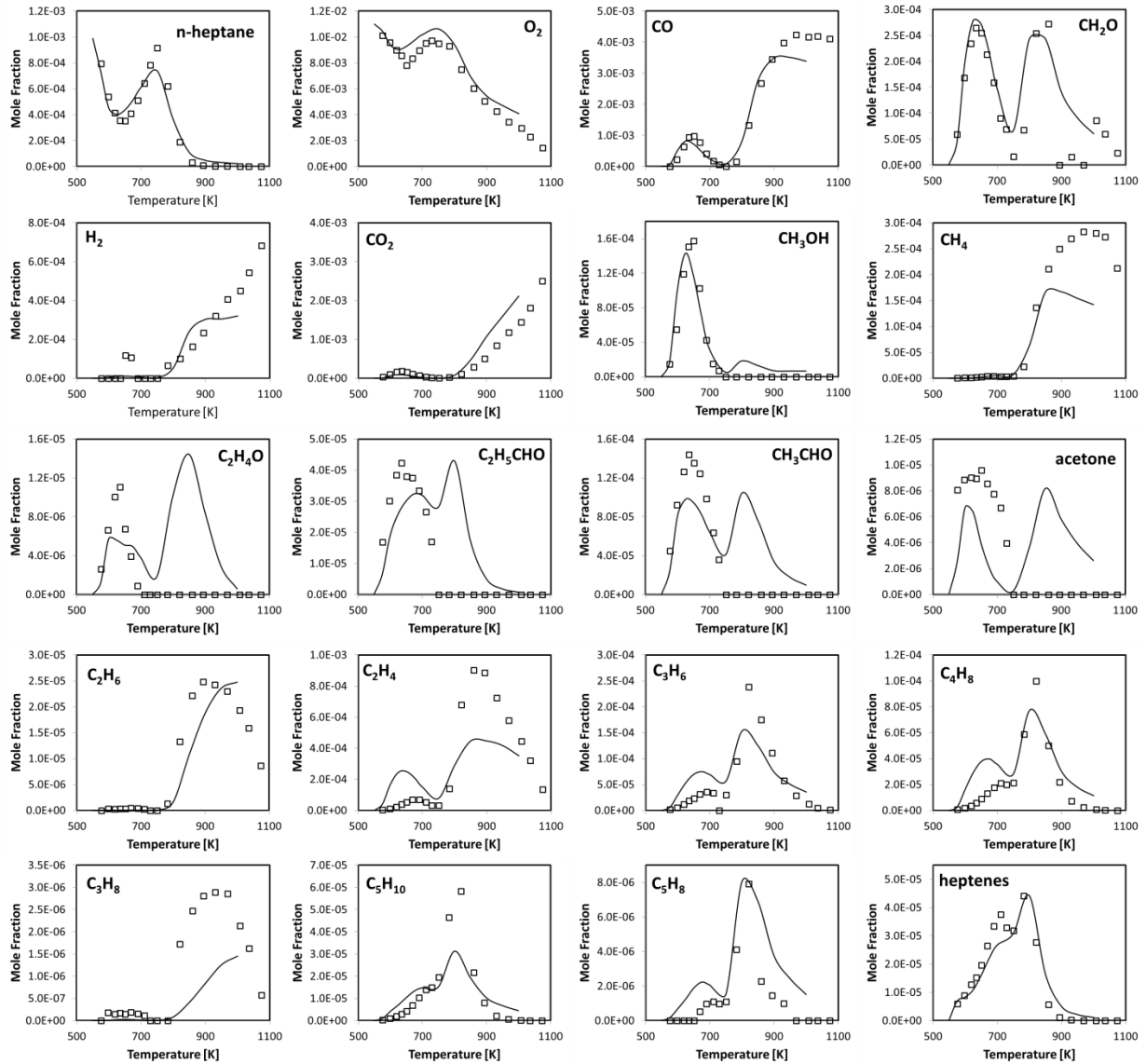
Figure 94: Stoichiometric oxidation of n-heptane in a jet stirred reactor [283] (0.1 mole % fuel, 10 atm, and 1 s). Mole fractions of major and intermediate species at different reactor temperatures. Comparison of experimental data (symbols) with model predictions (lines).
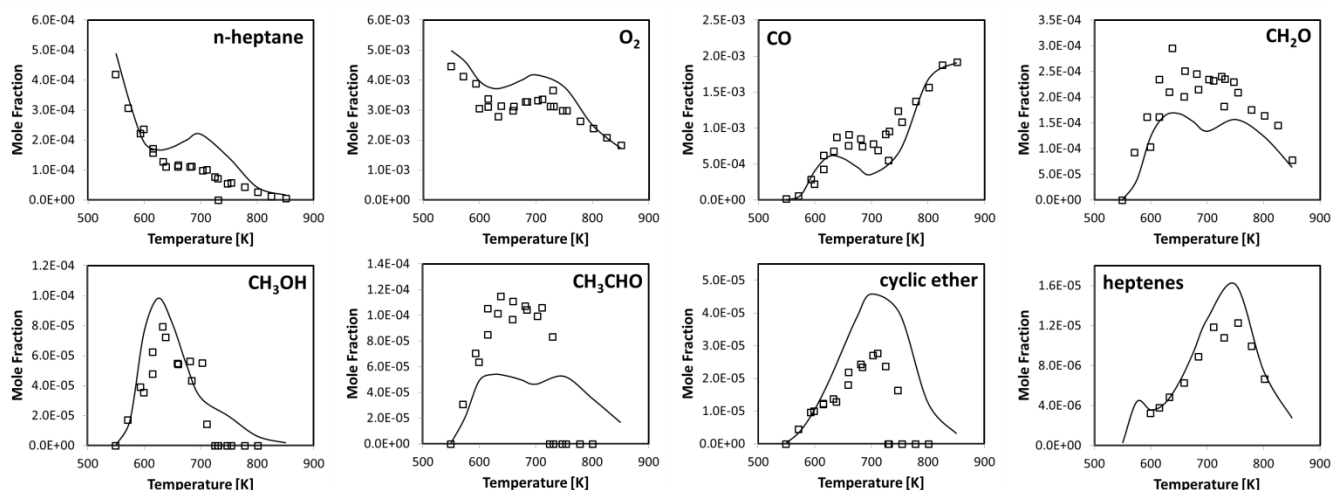
Figure 95: Stoichiometric oxidation of n-heptane in jet stirred reactor [231] (0.05 mole% fuel, 40 atm, and 2 s). Mole fractions of major and intermediate species at different reactor temperatures. Comparison of experimental data (symbols) with model predictions (lines).

3.2 - Pressurized flow reactors

3.2.a- Princeton flow reactor [272]

Veloo et al. [272] studied the stoichiometric oxidation of an n-heptane/oxygen mixture diluted with nitrogen in the Princeton Variable Pressure Flow Reactor at temperatures of 500-1000 K, 8 atm and 1 s residence time. Figure 96 reports the comparison between the measured [272] and predicted mole fraction profiles of selected species. The agreement with experimental data is quite satisfactory, especially in the low-temperature region, also in this case. The slight O_2 deviation in the NTC region seems the opposite of the one previously observed in Figure 91. These comparisons indicate an over-prediction of formaldehyde at low temperatures, despite the relatively high pressure. Again, the analysis of the relevant contributions to formaldehyde shows that only 10% of this production is due to specific reactions of n-heptane, while remaining contributions belong to the interactions of O_2 with small C_1–C_3 species.
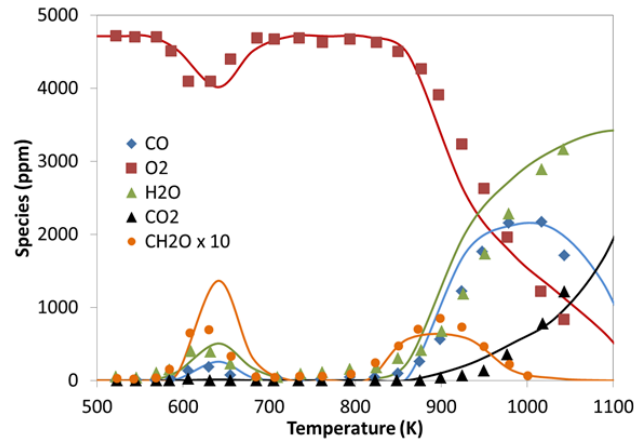
Figure 96: n-heptane oxidation in the Princeton flow reactor (8 atm, 0.3 % mol carbon, Φ=1, 1 s residence time). Comparison between measured [272] (symbols) and predicted (lines) mole fraction at different reactor temperatures.

3.2.b- Drexel Pressurized Flow Reactor (PFR) [30]

Lenhert et al. [30] investigated the pre-ignition reactivity behavior of a gasoline surrogate in a pressurized flow reactor over the low and intermediate temperature regime at 8 atm. The PFR was operated in a controlled cool down mode to examine the reactivity in the temperature range 600-780 K at a fixed residence time of 0.1 s, creating a reactivity map of the fuel. The fuel and oxidizer were diluted with nitrogen to limit the rise in temperature. Each of the surrogate components were also examined individually. n-heptane started to react at 630 K and exhibited a strong negative temperature coefficient (NTC) behavior between 700 and 800 K. Figure 97 shows the satisfactory comparisons between model predictions and experimental measurements. The model properly captures the range of fuel reactivity between 630 and 780 K, the production of CO and CO_2, and also the temperature rise.
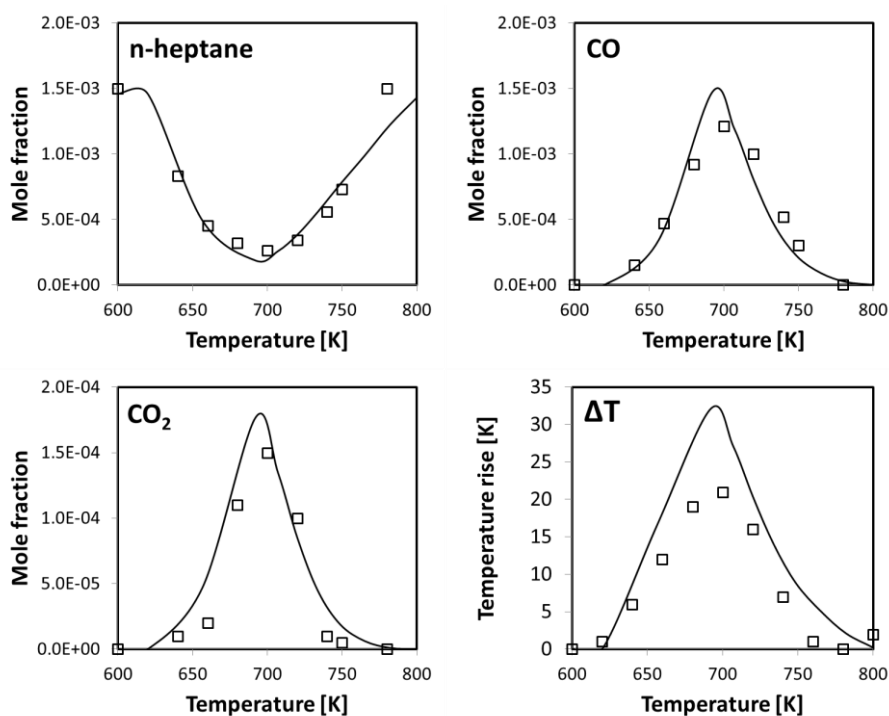
Figure 97: Species profiles (n-heptane, CO, and CO$_2$) and temperature rise as a function of reactor temperature for n-heptane (1469 ppm, φ = 0.51, 100 ms, and 8 atm). Symbols are experimental results [30]; lines are model predictions.

3.3- Ignition Delay Time experiments [14, 259, 260]

Figure 98 and *Figure 99* show comparisons between experimental and computed ignition delay times for n-heptane/air mixtures [14, 259, 260]. Measurements carried out by Shen et al. [260] at three different equivalence ratios conditions have been scaled to 48 and 12.5 atm pressure respectively and are presented in Figure 98. While the mechanism, compared to Shen data [260], correctly reproduces both pressure and dilution effects, at 12.5 atm and stoichiometric conditions it is up to a factor of 2 slower in the temperature range 850–1000 K. At 48 atm pressure the NTC region is well captured for φ=1.0 and φ=0.5 conditions, while deviations within a factor of 2 are still observed, particularly for very lean conditions and higher temperatures. *Figure 99* shows further comparisons between experimental *[14, 259]* and predicted ignition delay times of stoichiometric n-heptane/air mixtures. Measurements were carried out by Ciezki et al. [259] in shock tubes and by Mehl et al. [14] in a rapid compression facility. The mechanism is able to closely reproduce the experimental auto-ignition behavior.

The comparisons shown in Figure 98 and *Figure 99* confirm that the kinetic model properly accounts for both the low and high temperature oxidation regimes. The deviations between experimental data and model predictions are within the experimental uncertainties. Once again, the kinetic model could take advantage

from the experimental data, but it can also become a useful guideline to compare and to evaluate the consistency of experimental measurements involving similar conditions from different sources and facilities.
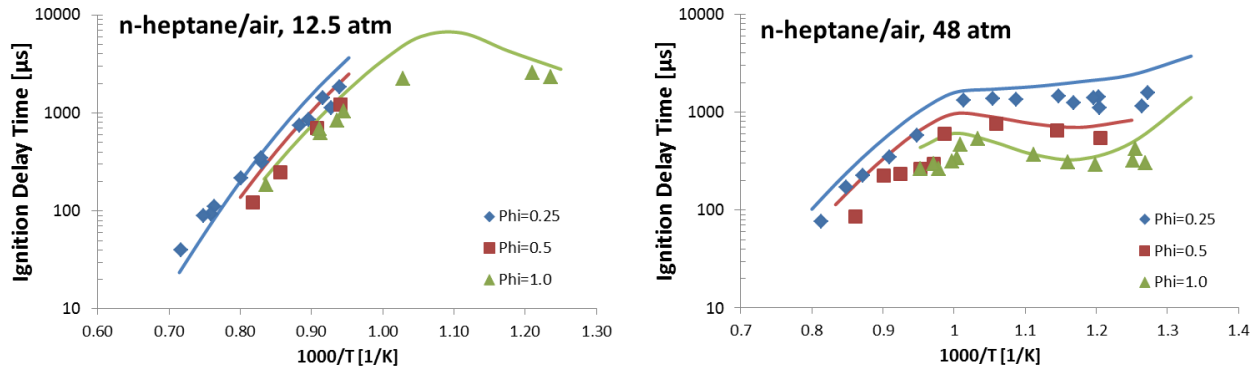
Figure 98: Comparison of predicted (lines) and measured [260] (symbols) ignition delay times for n-heptane/air mixtures at 12.5 and 48 atm and different equivalence ratios.
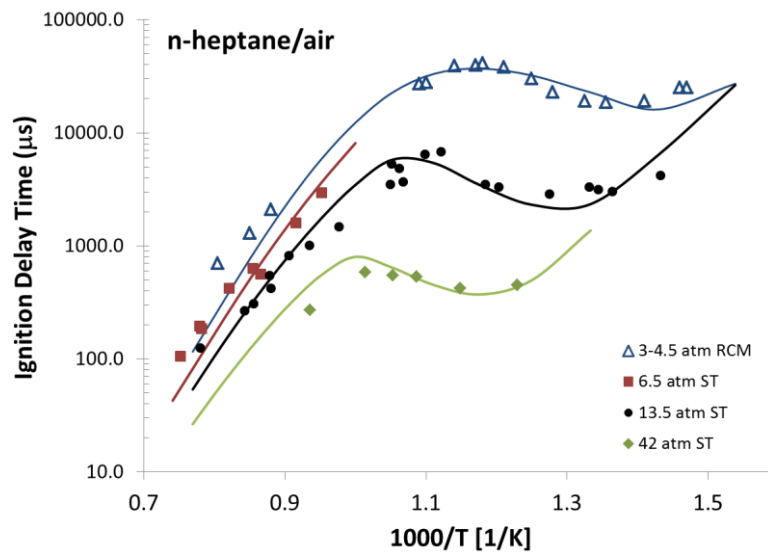
Figure 99: Comparison of predicted (lines) and measured (symbols) ignition delay times for n-heptane/air stoichiometric mixtures at 6.5, 13.5, and 42 atm in a shock tube [259] and 3–4.5 atm in a rapid compression machine.

3.4-Low temperature ignition of n-heptane in a Rapid Compression Facility[270]

These further comparisons refer to new ignition and speciation data from n-heptane oxidation in diluted conditions at 9 atm, low temperatures (660–710 K), obtained in the University of Michigan Rapid Compression Facility (UM-RCF)[270]. The detailed time-histories of n-heptane and several species, including large alkenes, aldehydes, and carbon monoxide were quantified using gas chromatography. Figure 100 shows a comparison of model predictions with these ignition delay experiments [270], and also with the previous data of Minetti et al. [232] in a Rapid Compression Machine. At the initial temperature of 700 K and 9 atm, a low temperature ignition at 8.49 ms is followed by the high temperature ignition, occurring at 14.53 ms. The model predictions, based on a constant volume, adiabatic simulation, agree well with these measurements especially in terms of the low temperature ignition delay time. Moreover, the heat release (pressure increase) is properly characterized in the two distinct ignition phases. The different behavior of the high temperature ignition is possibly due to the simulation assumptions. The final peaks of both CO and CH_4 clearly identify the high temperature ignition. Figure 100 also shows that the kinetic model overestimates the fuel consumption during the low temperature ignition. A similar deviation between experiments and model predictions was also observed by Karwat et al. [270] and might be related to the adiabatic assumption.
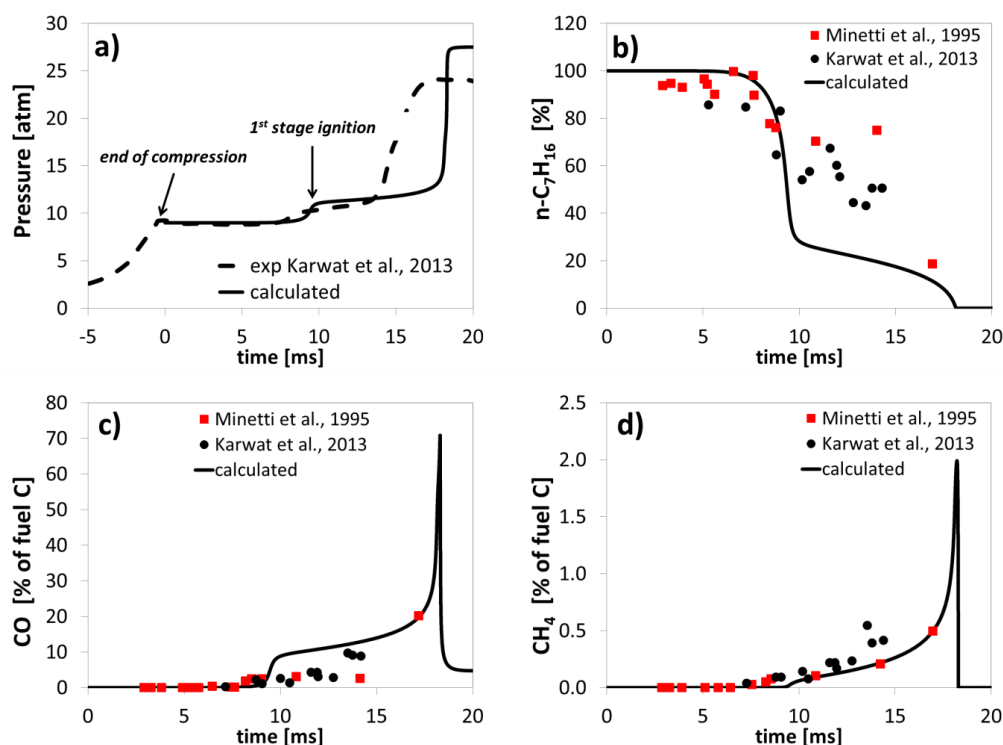
Figure 100: n-heptane ignition delay time and speciation at initial temperature 700 K and 9 atm. Panel a) Comparison of experimental [270] and predicted pressure time-histories. Panel b-d) Species concentration time-histories: UM-RCF experiments (solid circles) [270]; Minetti et al. [232] (squares). Data are presented as normalized to the % of fuel carbon in the initial reactant mixture (n–C_7H_{16}=0.0134, O_2 = 0.149, N_2 = 0.2336, and CO_2 = 0.604).

3.5- Laminar flame velocity
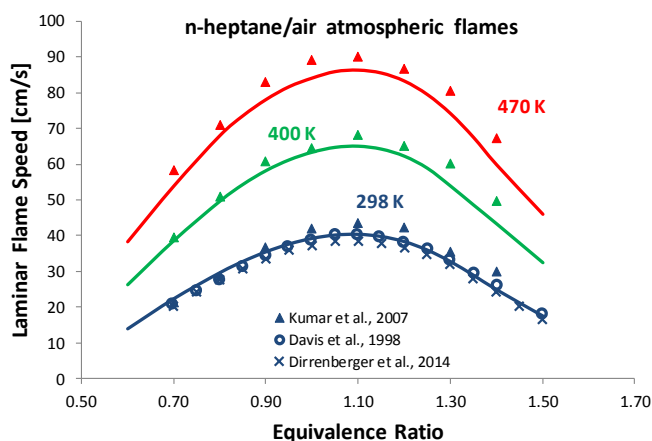
Figure 101: *Laminar flame speeds of n-heptane/air mixtures at atmospheric pressure. Comparison between experimental data [22, 23, 26] (symbols) and model predictions (lines) at different initial temperatures.*

Figure 101 shows the comparison between measured [22, 23, 26] and predicted laminar flame speeds of atmospheric n-heptane/air flames as a function of the equivalence ratio, at three different initial temperatures: 298 K, 400 K and 470 K. Model predictions agree better with the experiments of Davis and Law [22] and those of Dirrenberger et al. [277]. While it is clear that the laminar flame speed is not affected by the low temperature oxidation mechanism, this further comparison is useful to complete the validation of the kinetic mechanism over the wider set of conditions.

4. Auto-ignition behavior of n-heptane

This Section analyzes two more complex applications of the low temperature oxidation mechanism of n-heptane: the auto-ignition of n-heptane droplets in microgravity conditions and in the homogeneous charge compression ignition (HCCI) engine. Due to the typical sensitivity feature of ignition processes, the possible effect of these new reaction classes is worth analyzing.

4.1- Auto-ignition of n-heptane droplets in microgravity conditions.

Tanabe et al. [279] and Schnaubelt et al. [280] experimentally investigated the spontaneous ignition of isolated fuel droplets of n-heptane in microgravity conditions. In their experiments the suspended fuel droplets (initial diameter of 0.7-0.8 mm) were suddenly inserted into a pre-heated furnace in a pressurized chamber. Ignition delay times were measured in a wide range of operating conditions, with air at an initial pressure of 1–20 bar and uniform temperature of 500–1100 K. Ignition regions were mapped on temperature-pressure planes, as reported in Figure 102. Different types of ignition regimes can be recognized, similarly to what is usually observed in premixed gas explosion diagrams: no-ignition (NI), cool flame ignition (CF), single-stage (SI) and two-stage (2SI) ignition. The differences can be better analyzed from

Figure 103, where the maximum temperature in the gas-phase is reported versus the time for selected initial ambient pressures and temperatures. At low ambient temperatures, the droplet vaporizes before chemical reactions can lead to ignition (curve V). If the ambient temperature is sufficiently high for promoting the low-temperature reactions, the formation of dumped cool flames (CF) can be observed, with a successive temperature *plateau* at relatively low-temperature (curve IV). The hot-ignition occurs only when the ambient temperature is high enough so that the high-temperature reactions becomes dominant (curve I). When the ambient temperature and/or the pressure are high enough to make the oxidation reactions competitive with heat transfer, a multi-stage ignition phenomenon can be observed, i.e. a first maximum of temperature, associated to a cool flame, is followed by a *plateau* temperature and then by a hot flame ignition (curves II and III).

The map reported in Figure 102 is quite complex, suggesting that the chemistry plays a fundamental role in controlling the auto-ignition process. In particular, as explained in Cuoci et al. [116, 284], the competition between the low- and high-temperature mechanisms is the main reason behind the different types of auto-ignition phenomena. Therefore, the auto-ignition experiments of Tanabe et al. [279] and Schnaubelt et al. [280] appear as a further interesting system for the validation of the kinetic mechanism developed in the present work.

The mathematical model of Cuoci et al. [116, 284] was used for the numerical simulations of experiments reported in Figure 102. The model assumes spherical symmetry, because of the microgravity conditions. The conservation equations of energy and mass are solved both for the liquid and gas phases. In addition, the conservation equations of species are solved for the gas phase. Only the ordinary mass diffusion is taken into account in the species equations. Chemical reactions in the gas phase are described using the POLIMI_1407 kinetic mechanism. The radiative heat fluxes were estimated by adopting the approach proposed by Kazakov et al. [285]. The Planck mean absorption coefficients were derived from polynomial expressions for CO, CO_2, and H_2O [286]. Symmetry conditions are imposed at the center of the droplet. At the liquid/gas interface the continuity of fluxes of heat and species is considered. The resulting system includes partial differential equations and non-linear, algebraic equations. The partial differential equations are discretized using the finite-difference method, using an adaptive grid fixed on the droplet surface. The resulting DAE system is solved in a fully-coupled approach using the BzzDae solver [287].

The numerical predictions are compared with the experimental data (maps and lines) in Figure 102. The numerical calculations recognize the different experimental auto-ignition behaviors, especially at low temperature, where only a negligible effect of the new reaction classes is observed.

Figure 104 shows the very satisfactory comparisons between predicted and measured first and total ignition times, at different pressures. The total induction time τ_t is defined as the sum of the first (τ_1) and the second (τ_2) induction times (see Figure 103). The induction times decrease with increasing the ambient temperature, due to the enhanced vaporization of the fuel droplet. At low temperatures, the difference between the total and the first induction times is very small. At intermediate pressure (4 bar), there is a Zero Temperature Coefficient (ZTC) region between 700 K and 750 K. In this region, the second induction time (τ_2), which is the time to activate the high-temperature mechanism, is controlled by the cool flame temperature, and it does not depend on the ambient temperature. The total induction time decreases with increasing the pressure, due to the higher reactivity of the system. In contrast, since the ambient pressure tends to reduce the vaporization rate, the first induction time, which is mainly influenced by the physical processes, increases with increasing pressure. These results further confirm that the low-temperature chemistry plays a crucial role in the auto-ignition process. In particular, the transition between low- and high-temperature mechanisms explains the different auto-ignition behaviors, experimentally observed. Further details on this example can be found in Cuoci et al. [116, 284].
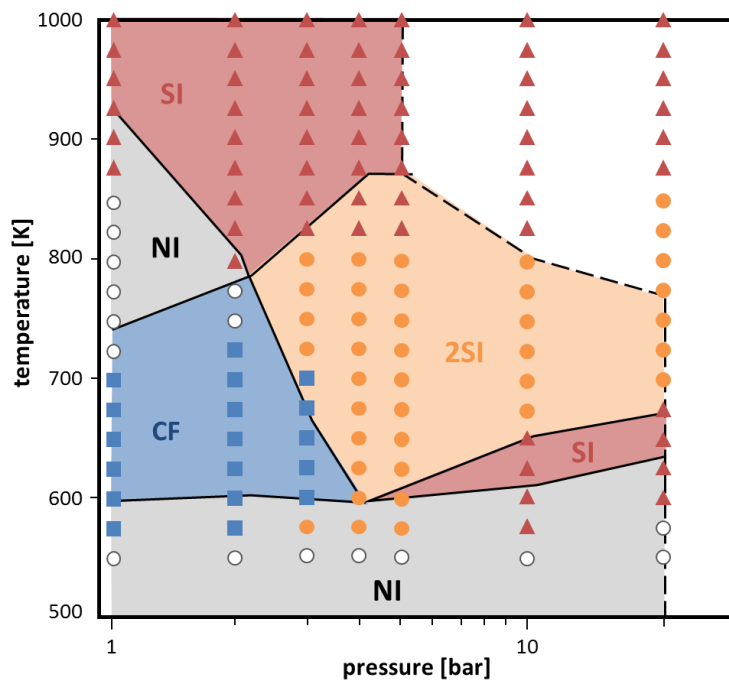
Figure 102. Ignition regions of n-heptane droplets (with initial diameter d0=0.70 mm) in air at different pressures and initial temperatures. Comparison between experiments (colored maps) [28] and numerical predictions (symbols: ○ no ignition, ■ cool-flames, ● 2-stage ignition, ▲ single-stage ignition). In the white regions no experimental data are available.
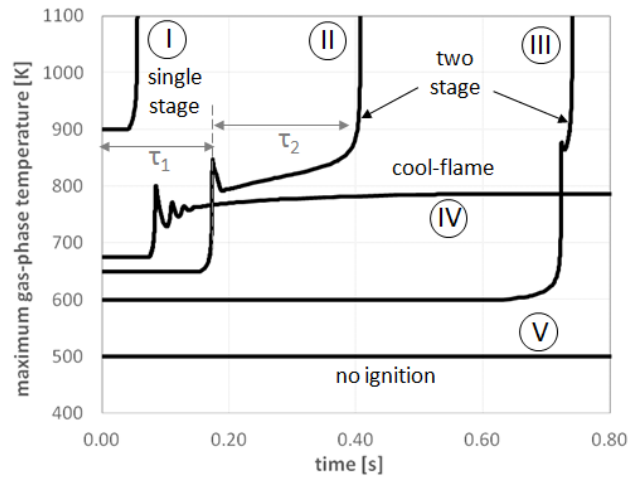
Figure 103. Maximum gas-phase temperature versus time for n-heptane droplets (numerical simulations). Line I: 4 bar, 900 K; Line II: 4 bar, 650 K; Line III: 4 bar, 600K; Line IV: 2 bar, 675 K; Line V: 1 bar, 500 K. The total induction time τt is defined as the sum of the first ($\tau 1$) and the second ($\tau 2$) induction times.
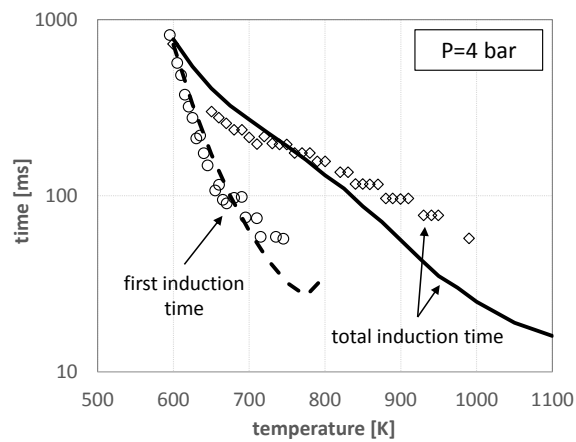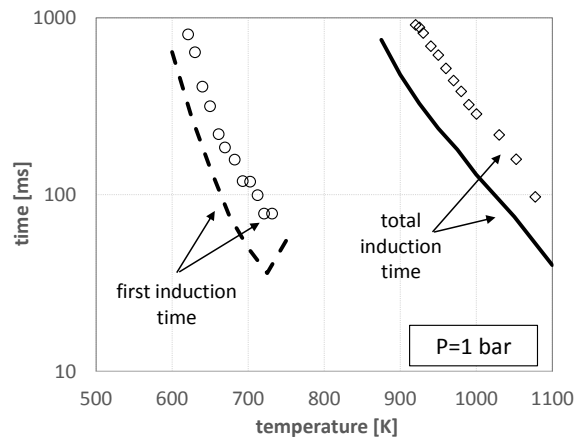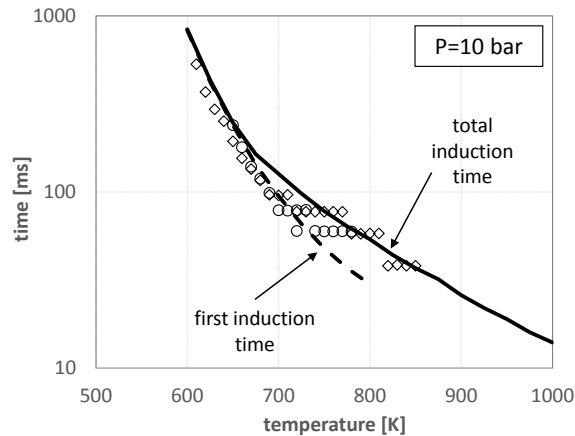
Figure 104: Auto-ignition of n-heptane droplets (with initial diameter d0=0.70 mm): comparison between experiments (symbols) [279] and simulations (lines). For each pressure the first (○ and dashed lines) and total (◊ and continuous lines) induction times are reported.

4.2-Auto-ignition of n-heptane/air mixtures in HCCI engines.

Since several years, the stringent emissions standards and the promises of improving fuel efficiency, led car and especially heavy duty vehicle manufacturers to look at the Homogeneous Charge Compression Ignition (HCCI) as one of the future technologies for transportation engines. HCCI is characterized by the fact that fuel and air are mixed before combustion starts and the mixture auto-ignites as a result of the temperature increase in the compression stroke [288]. In an ideal HCCI engine cycle, premixed gaseous fuel and air are introduced into the combustion chamber of a conventional piston engine at a very lean equivalence ratio and then uniformly ignited upon compression, so that no flame propagation is possible. The very low temperatures and the homogeneous conditions significantly decrease NOx and soot formation. Moreover, good thermodynamic efficiency is achieved, because of the large compression ratios [289]. Since no external means are utilized to activate ignition, chemical kinetics play a very crucial role in HCCI combustion. Ignition uniformly starts where the thermodynamic conditions of pressure, temperature and species concentration are favorable [290].

Szybist et al. [278] investigated the auto-ignition differences between n-heptane and diesel fuels with a series of motored engine experiments. Particularly, they used a CFR octane rating engine to analyze the auto-ignition behavior of n-heptane, at compression ratios from 4.0 to 13.75, at 900 rpm. Recently, Bissoli et al. [291] developed a mathematical model for the simulation of HCCI engines. The model discretizes the reacting volume into several concentric zones, each of which is considered as a well-mixed reactor with time-variable volume. Heat and mass diffusion exchanges between neighboring zones, both laminar and turbulent, are described, as well as the effects of the residual burned gases. These data constitute the final application and validation example of the kinetic model. The main characteristics of the CFR engine used in these simulations

are reported in Table 13, while Figure 105 and Figure 106 show the temperature and pressure profiles during the cycle, at equivalence ratios of 0.5 and 0.25. For both these stoichiometries, three different Compression Ratios (CR) are analyzed in order to highlight the different effect of the low and high temperature ignitions. While the low temperature peak always occurs at ~800 K, the maximum temperature of the hot ignition moves from ~1250 to ~1900 K due to the different dilutions. For this reason, the critical compression ratio required to reach the complete combustion is ~6.7 at φ=0.5 and ~9 at φ=0.25. The transition between low and high temperature ignition highlights the interest in kinetic data in the pressure range 10–15 atm.

Engine Speed [RPM]	900
Bore [mm]	82.6
Stroke [mm]	114.4
Displacement [cm^3]	613
CR	4.0-13.75
Intake valve closing [°CA BTDC]	166
Exhaust valve opening [°CA ATDC]	153
Inlet Pressure [bar]	1
Equivalence Ratio (φ)	0.25-0.50

Table 13: Main characteristics of the CFR engine[278].
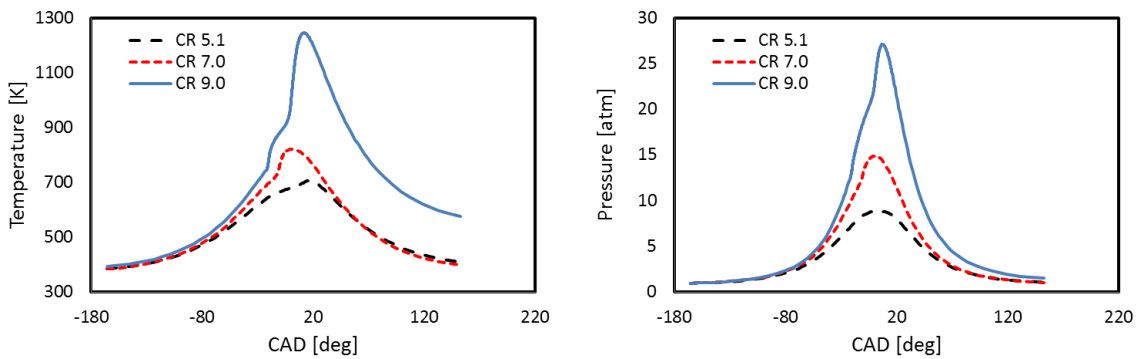
Figure 105: n-heptane oxidation in a HCCI engine at φ=0.25. Predicted temperature and pressure profiles during the cycle at different CR. Operating conditions are reported in Table 1.
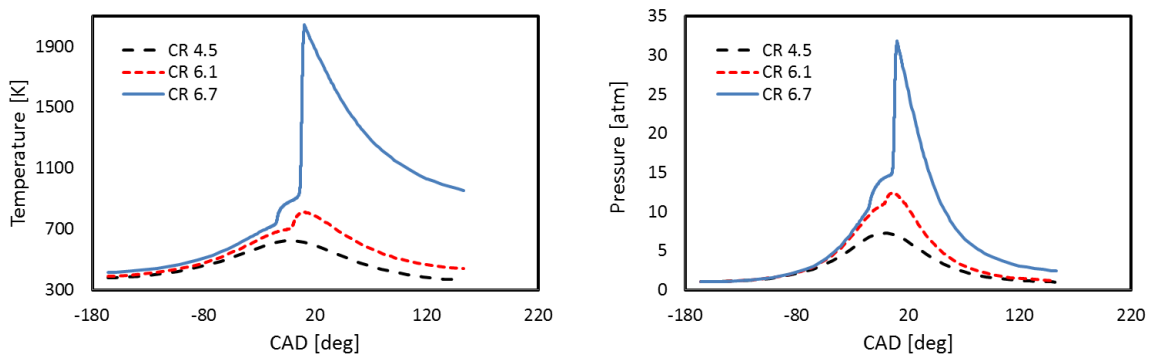
Figure 106: n-heptane oxidation in a HCCI engine at φ=0.50. Predicted temperature and pressure profiles during the cycle at different CR. Operating conditions are reported in Table 1.

Figure 107 shows a comparison between experimental data and model predictions. CO and CO_2 profiles refer to their concentration in the exhaust tail gas, as obtained at different compression ratios. The model properly predicts the critical compression ratios for both the analyzed conditions. The low temperature ignition occurs at CR=4.5 for both conditions. At ϕ=0.25 the high temperature ignition starts only at Compression Ratios ~8.5-9, due to the lower temperatures as shown in Figure 105. Thus, the kinetic model properly captures the effect of the different equivalence ratios in HCCI conditions.
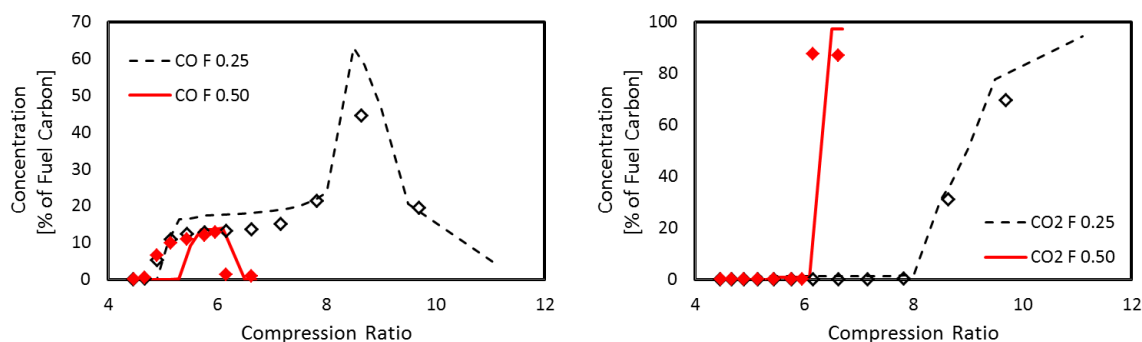
Figure 107: n-heptane oxidation in a HCCI engine. CO and CO_2 profiles vs the compression ratio, at equivalence ratios 0.25 and 0.50. Comparison between experimental data (symbols) [278] and model predictions (lines).

5. Conclusions

Based on new experimental measurements of organic acids and other oxygenated species in the low temperature oxidation of alkanes [225-227, 230], four new classes have been added to the 25 reaction classes usually considered in the oxidation mechanism of n-alkanes [233, 242]. Particularly, the POLIMI kinetic scheme has been improved by adding the following reaction classes:

1- H-abstraction reactions on hydroperoxides, to form ketones

2- H-abstraction reactions on carbonyl-hydroperoxides, to form diones

3- Molecular reactions of carbonyl-hydroperoxides (Korcek mechanism[249]), to form organic acids

4- Recombination/disproportionation reactions of peroxy and hydroperoxy-alkylperoxy radicals to form alcohols, ketones and oxygenated species containing two oxygenated groups.

The same extension has been recently investigated for the low temperature oxidation of propane and n-butane [281]. The lumped approach allows to handle the complex oxidation mechanism with a limited number of equivalent species, still maintaining an accurate reliability in model predictions. The extension of the mechanism to include these minor, but relevant, oxygenated species permits to better understand the low temperature mechanism of hydrocarbon fuel combustion.

The improved kinetic model POLIMI_1407 has then been validated over a wide range of conditions (jet stirred and plug flow reactors, shock tubes, rapid compression machines and premixed laminar flames) confirming the reliability of the mechanism both in the low and in the high temperature oxidation regimes.

The kinetic model was also used in two more complex applications of n-heptane auto-ignition. Comparisons with experimental data for the auto-ignition of n-heptane droplets in microgravity conditions and the auto-ignition of n-heptane/air mixtures in an HCCI engine further prove the reliability of the overall oxidation mechanism.

5.2 Kinetic Modeling of the Pyrolysis and Oxidation of Toluene

The motivation behind this portion of research arises from the necessity of better understand toluene combustion, controversially described in the literature [218, 219]. *Figure **108*** summarizes this observation.
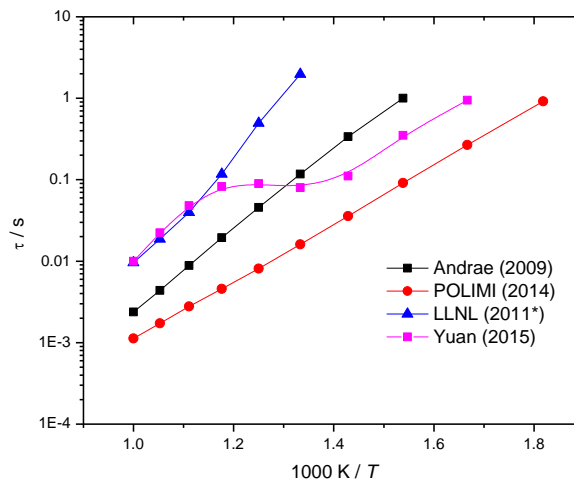
Figure 108: Ignition delay time of stoichiometric toluene/air mixtures at p=20 atm according to different kinetic mechanisms [14, 292-295]. Adapted from Zhang et al. [218] and Somers et al. [219].

Recent experimental studies [218, 294, 295] also allow for a more comprehensive validation of the kinetic mechanism.

5.2.1 Ab Initio and Kinetic Modeling Study of Toluene Oxidation: H-abstraction Reactions by $\dot{O}H$, $H\dot{O}_2$, $\ddot{O}$ and O_2

1. Introduction

Figure 109 shows the sensitivity coefficients of ignition delay times to reaction rate constants for toluene/air stoichiometric mixtures at p=12 atm and T=1200 K. Such representation highlights the important reaction

steps in toluene oxidation. Clearly H-abstraction reactions play a major role, thus their correct assessment is necessary to accurately describe toluene oxidation. Four different abstraction sites are available in toluene.
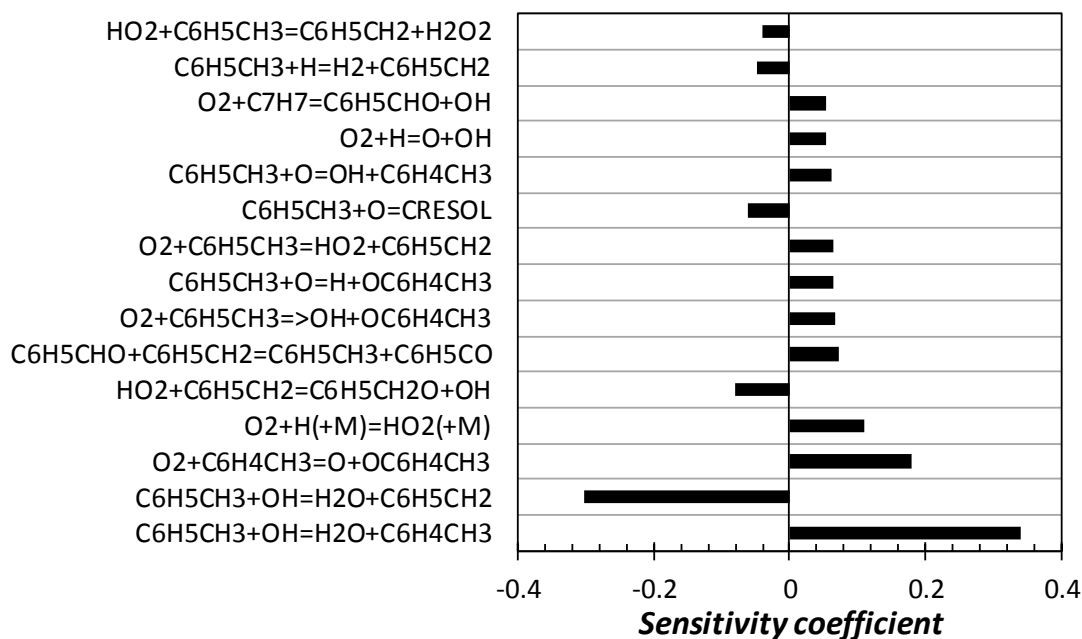
Figure 109: Sensitivity coefficients of ignition delay times to reaction rate coefficients for stoichiometric toluene/air mixtures at p=12 atm and T=1200 K. A positive coefficient stands for a reaction enhancing reactivity.

Figure 110 shows bond dissociation energies calculated from the generic reactions R-H→R+H. The bond dissociation energy is defined as the difference in energy between the products (R+H), and the compound (R−H) whose C–H bond undergoes simple fission. The C–H bond in the methyl group is ~22 kcal/mol weaker than those located at the ring and abstraction from this site produces resonance-stabilized benzyl radical ($C_6H_5CH_2$). The three ring positions (*ortho-*, *meta-*, *para-*) have very similar BDEs, with the formation of *para*-methylphenyl radical being slightly unfavored.

Figure 111 shows the four different radicals derived from H-abstraction on toluene with the nomenclature used in the following discussion. Referring back to Figure 109, the pathways producing methylphenyl radicals usually enhance reactivity, while the production of benzyl radical reduces reactivity. Benzyl radical interactions with oxygen are discussed in Section 5.2.3. Other key reactions are those involving benzyl radical and $H\dot{O}_2$ [296-298]. For this reason, a correct assessment of the branching ratios between the competing pathways plays a major role.

This section describes the investigation of H-abstraction reactions by $\dot{O}H$, $H\dot{O}_2$, $\ddot{O}$ and O_2, providing rate constants for direct use in existing kinetic mechanisms.
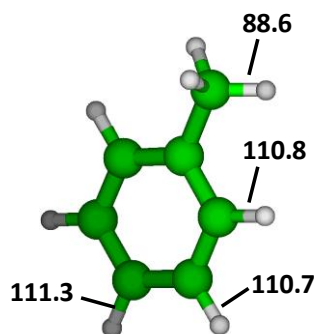
Figure 110: Toluene bond dissociation energies in kcal/mol. $E=E_{CCSD(T)-F12/VTZ-F12} + E_{MP2-F12/VQZ-F12} - E_{MP2-F12/VTZ-F12}$.

| $C_6H_5CH_2$ | o–$C_6H_4CH_3$ | m–$C_6H_4CH_3$ | p–$C_6H_4CH_3$ |
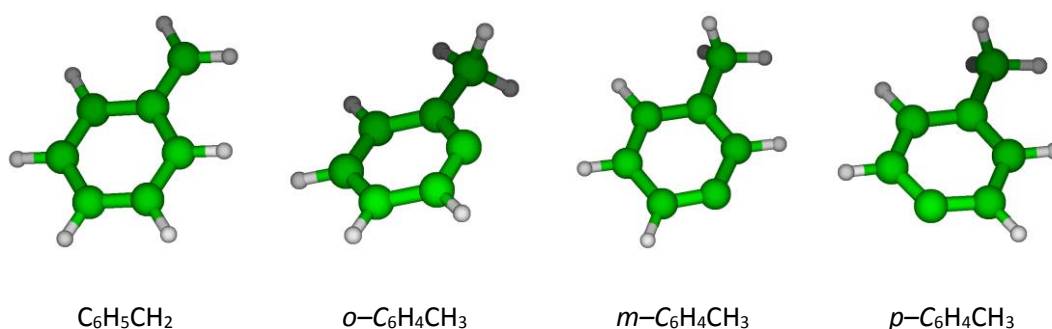
Figure 111: Structure and names of toluene radicals.

Despite the importance of toluene as a reference component in surrogate mixtures representing real fuels, some of its key reaction pathways, including H-abstractions, have not been systematically investigated in the literature.

Several experimental investigations exist for OH+$C_6H_5CH_3$ both at very low temperatures (T<400 K) [299-301] and at higher temperatures (400 K<T<1500 K) [302-304]. Within these studies it is worth highlighting the systematic study of Seta et al. [304] that obtained rate constants for H-abstractions, addition and H/OH substitution reactions through an effective coupling of TST and experiments. Single point energies were calculated at the G3(MP2)//B3LYP [305] and at the CBS-QB3 [171] level. The height of the TS barriers were adjusted to reproduce the high temperature measurements, providing a reliable set of rate constants adopted in the more recent toluene kinetic mechanisms of Zhang et al. [218] and Yuan et al. [294, 295].

O(^{3}P) + $C_6H_5CH_3$ has been measured by Hoffmann et al. [306] behind incident shock waves in a quite narrow temperature range (1100–1350 K).

Eng et al. [307] and more recently Oehlschlaeger and co-workers [308], measured H-abstraction by O_2 behind reflected shock waves between 1050 and 1400 K.

Very recently Li et al. [309] systematically investigated H-abstractions by $\dot{O}H$, $\dot{H}$, $\ddot{O}$, $\dot{C}H_3$, and $H\dot{O}_2$ with the G4 composite method [172]. As discussed in Section 4.1 geometries and frequencies of reactants, transition states and products are calculated at the B3LYP/6-31G(2df,p) level. The potential energy surface was investigated using the composite G4 method [172].

The need of identifying the most accurate method at an affordable computational cost for quite large systems (9 heavy atoms), the scarcity, or lack, of experimental measurements at conditions of interest for combustion application, and the dearth of theoretical studies of key H-abstraction reactions motivated this study.

2. Computational Methods

Geometry optimizations and frequency calculations for reactants, wells, transition states and products have been carried out at the M062x/6-311+g(d,p) level [168] as implemented in Gaussian [46]. After a first PES investigation at the same level of theory, higher level single point energies are obtained at CCSD(T)/aug-cc-pVTZ [159, 160], DF-MP2/aug-cc-pVTZ, DF-MP2/aug-cc-pVQZ level [310] using Molpro [47]. Final single point energies are calculated according to the expression $E=E_{CCSD(T)/aug-cc-pVTZ} + E_{DF-MP2/aug-cc-pVQZ} - E_{DF-MP2/aug-cc-pVTZ}$.

Potentials for internal rotations and coupled internal rotations were obtained from relaxed scans at 20° intervals at the M062x/6-311+g(d,p) level. Low-frequency torsional motions were taken into account in the partition function calculation according to the one-dimensional hindered rotor method. 2-dimensional hindered rotor effects were considered for the reaction $O_2+C_6H_5CH_3 \rightarrow HO_2+C_6H_5CH_2$.

Internal reaction coordinate (IRC) calculations were performed with a step size of ~0.016 Å. For every reaction investigated, 30 steps toward the products and 30 toward the reactants confirmed the existence of the single imaginary frequency saddle point and allowed the location of product-like van der Waals complexes in the case of H-abstraction by $H\dot{O}_2$ and $\ddot{O}$.

The one-dimensional tunneling correction, of importance mainly at low temperatures, was applied to the canonical TST rate constants according to the Eckart model [186].

3. Results and discussion

$\dot{O}H$+C$_6$H$_5$CH$_3$

Figure 112 shows the potential energy surface for H-abstraction reactions by OH. In contrast with the work of Seta et al. [304] and Li et al. [309], the H-abstractions by OH are characterized by an entrance well (W$_{R-METHYL}$) which is ~3 kcal/mol more stable than the reactants. More precisely Seta et al. [304] only considered the formation of the van der Waals complex in the case of submerged barrier addition reactions. Very similar configurations have been found for the four complexes, therefore the similar energies (±0.1 kcal/mol). In the

case of abstraction from the methyl group, the transition state lies 0.6 kcal/mol above the reactants and thus 3.6 kcal/mol above the entrance well. H-abstractions from the different ring positions have comparable barriers (6.5-7.0 kcal/mol) with respect to the reactant complexes, but a much lower exothermicity compared to the abstraction from the methyl group. Resonance-stabilized benzyl radical is, in fact, ~22 kcal/mol more stable than its methylphenyl isomers.
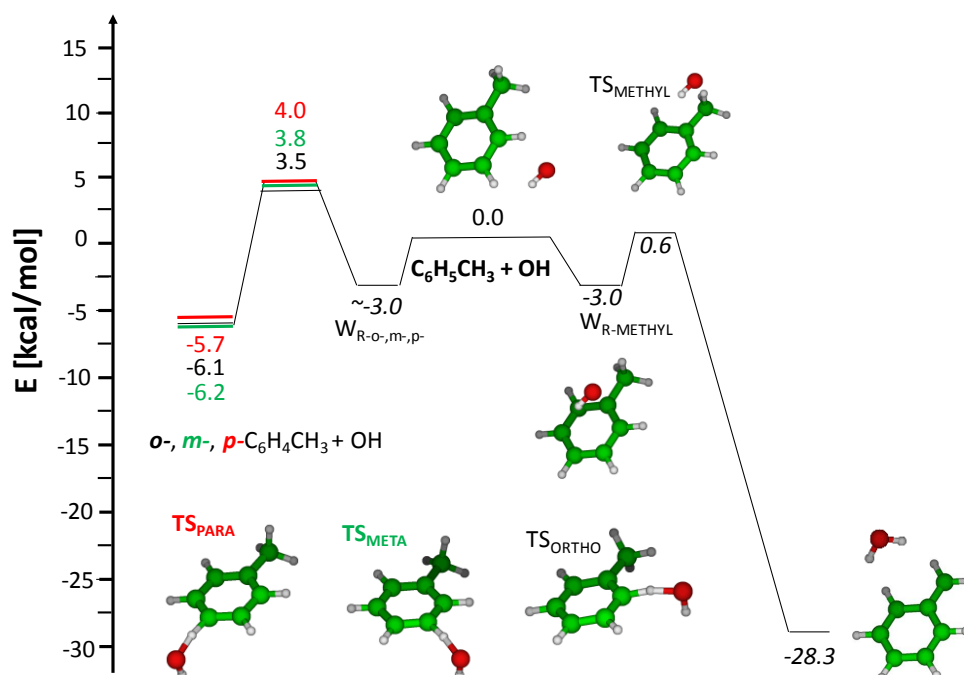
Figure 112: Potential energy surface for the reaction OH+toluene. Energies are in kcal/mol relative to the reactants.

Table 14 compares the relative energies of the PES in Figure 112 with those from previous studies. Good agreement is found between the three studies ($\pm$1.3 kcal/mol), with the only major difference being the neglect of the reactants complex.

Transition State	This work	Li et al.	Seta et al.	Products	This work	Li et al.	Seta et al.
TS$_{METHYL}$	0.6*	1.2	0.6	**C$_6$H$_5$CH$_2$+H$_2$O**	-28.3	-28.5	-29.3
TS$_{ORTHO}$	3.5	3.2	2.4	**o–C$_6$H$_4$CH$_3$+H$_2$O**	-6.2	-6.2	-6.3
TS$_{META}$	3.8	3.5	3.1	**m–C$_6$H$_4$CH$_3$+H$_2$O**	-6.1	-6.1	-6.4
TS$_{PARA}$	4.0	3.6	2.7	**p–C$_6$H$_4$CH$_3$+H$_2$O**	-5.7	-5.6	-5.2

Table 14: Relative energies of transition states and products. Units are kcal/mol. * Considers the reactants complex.

Figure 113 compares the total H-abstraction rate constant from this study with measurements and theoretical studies from the literature. The calculation agrees with the experimental data to within a factor

of 2. Moreover, the agreement with the rate constant of Seta et al. [304] is within a factor of ~1.35. The right panel of Figure 113 shows the branching ratio between abstraction on the ring leading to the formation of methylphenyl radicals ($C_6H_4CH_3$) and benzyl radical ($C_6H_5CH_2$). Benzyl radical formation dominates up to ~900 K where a crossover is observed. This observation is consistent with the study of Li et al. [309], while Seta et al. [304] found that the formation of benzyl radical covers a branching ratio of 0.9-0.6 moving from 300 K to 2000 K.
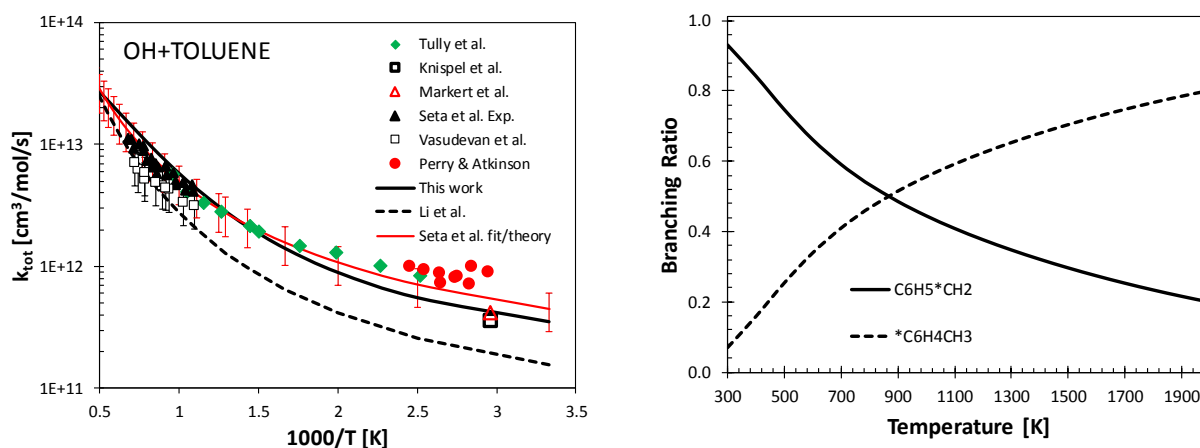
Figure 113: Left panel: comparison of the total rate constant of OH+toluene with other studies [304, 309] and with experimental measurements)[299-304]. Right panel: branching ratio between benzyl radical and methylphenyl radicals.

Figure 114a shows the effect of neglecting the four Van der Waals complexes on the total rate constant between 1000 and 2000 K. Deviations up to a factor of ~2.7 can be observed for such low barrier channels. Clearly the most of the deviation (~90%) is related to lowest energy barrier channel forming benzyl radical, as reported in Figure 114b.
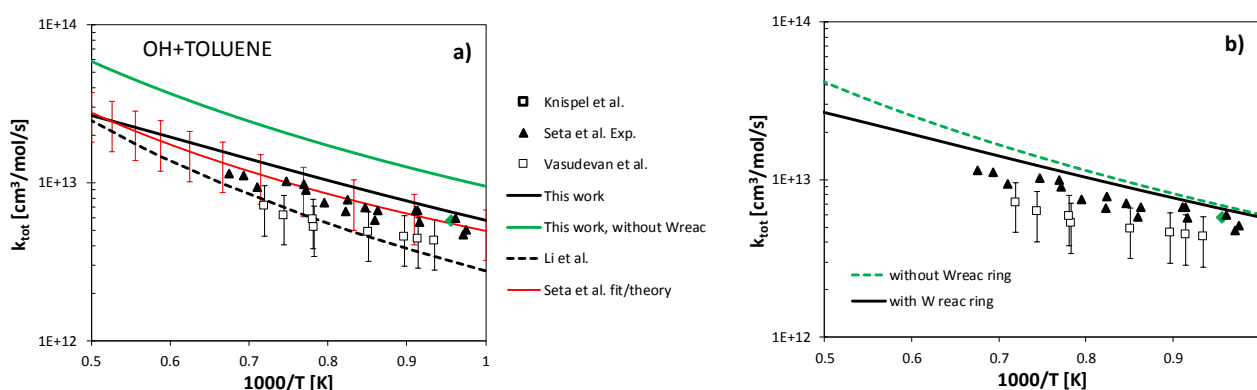
Figure 114: Panel a: effect of neglecting the formation of Van der Waals complexes. Green line: rate constant without accounting for VdW complexes, black line: effect of including VdW complexes. Panel b: relative effect of VdW complexes for ring H-abstractions.

Following the discussion in the introduction to this Section, the ratio between the formation of benzyl or methylphenyl significantly impacts toluene reactivity, therefore the update of such rate constants might

sensibly impact mechanism performance. An example is given in *Figure 115*, the inclusion of the rate constants from Seta et al. (dashed lines) results in a factor of ~1.6-2.1 decrease in ignition delay times at these conditions.
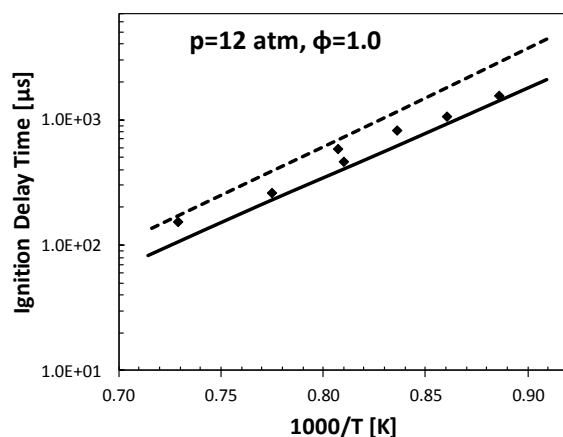
Figure 115: Ignition delay time of stoichiometric mixtures of toluene/air at p=12 atm. Symbols: experimental data [311], solid lines: POLIMI mechanism OH+toluene from this study, dashed line: POLIMI mechanism with OH+toluene from Seta et al. [304].

$H\dot{O}_2$+C$_6$H$_5$CH$_3$

The correct theoretical assessment of $H\dot{O}_2$+fuel reactions is of particular importance because they are difficult to measure experimentally [48]. *Figure 116* shows the potential energy surface for toluene H-abstraction reactions by $H\dot{O}_2$.
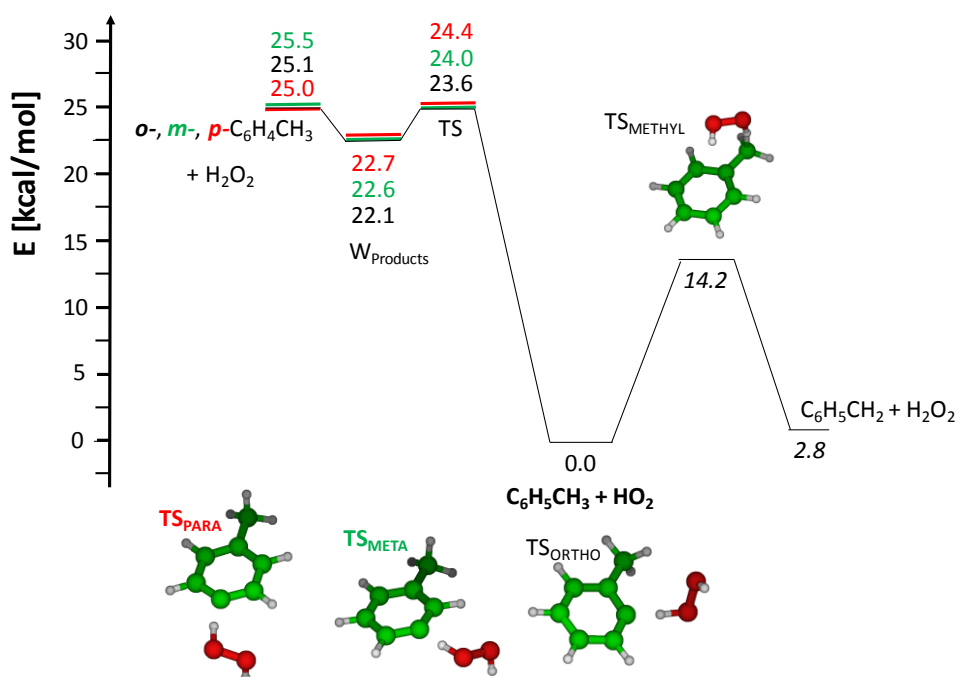
Figure 116: Potential energy surface for the reaction $H\dot{O}_2$+toluene. Energies are in kcal/mol relative to the reactants.

Beside the rate constants recommended by Baulch et al. [312], H-abstractions by $H\dot{O}_2$ from toluene have been investigated theoretically only by Altarawneh et al. [313] and very recently by Li et al. [309]. The former used the density functional method BB1K/6-311+G(d,p) [314] for the analysis of this reaction pathways. Consistently with the observations of Li et al. [309], product-like van der Waals complexes slightly more stable than the products (~1.5 kcal/mol) exist for abstractions from the ring. Such complexes were neglected by Li et al. in the calculation of the rate constant, assuming a direct dissociation to methylphenyl radicals.

Transition State	This work	Li et al.	Complexes	This work	Li et al.	Products	This work	Li et al.
TS$_{METHYL}$	14.2	13.5				$C_6H_5CH_2+H_2O_2$	2.8	2.8
TS$_{ORTHO}$	23.6	22.7	o-, HO$_2$	22.1	21.3	o-$C_6H_4CH_3+H_2O_2$	25.1	25.1
TS$_{META}$	24.0	23.3	m-, HO$_2$	22.6	21.4	m-$C_6H_4CH_3+H_2O_2$	25.5	25.2
TS$_{PARA}$	24.4	23.7	p-, HO$_2$	22.7	22.1	p-$C_6H_4CH_3+H_2O_2$	25.0	25.7

Table 15: Relative energies of transition states and products. Units are kcal/mol.

Figure 113 compares the total H-abstraction rate constant from this study with other studies from the literature. Additional comparison with rate constants from Zador et al. [315] for propene and iso-butene are also reported. The rate constant calculated in this study agrees within a factor of ~2 with the calculations of Li et al. [309] and Zador et al. [315] for iso-butene. Larger deviations are observed with respect to Baulch et al. and propene+$H\dot{O}_2$ from Zador et al. [315]. In terms of branching ratio, the formation of benzyl radical dominates up to ~1400 K. It is worth mentioning that $H\dot{O}_2$ plays an important role in fuel consumption mainly at intermediate temperatures (~900–1100 K) and high pressure, where its concentration builds up due to the reaction H+O$_2$+M=HO$_2$+M and, in the case of mixtures with alkanes, due to the rise of pathways characteristic of the NTC region (see Section 3.2).
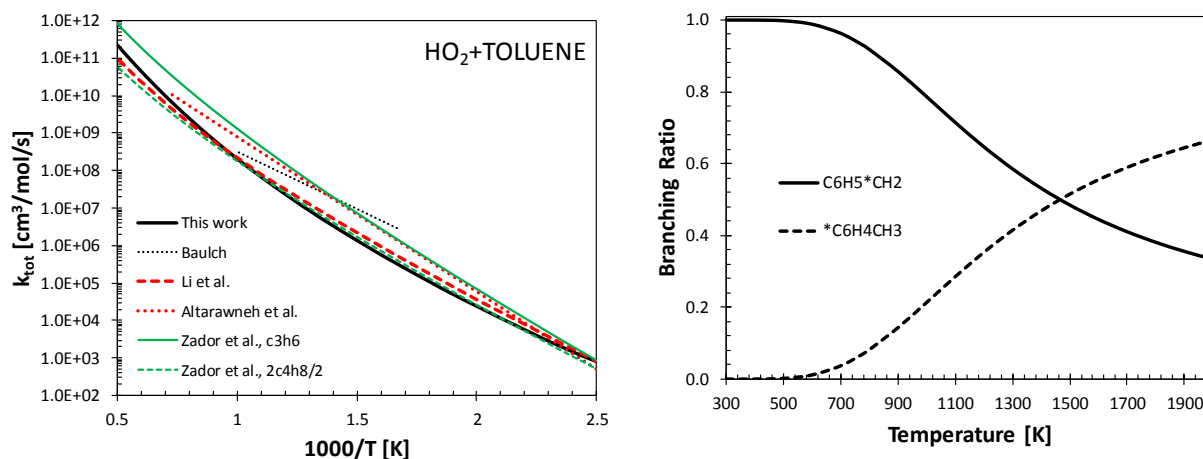
Figure 117: Left panel: comparison of the total rate constant of $H\dot{O}_2$+toluene with other studies [309, 312, 313, 315]. Right panel: branching ratio between benzyl radical and methylphenyl radicals.

$\ddot{O}$+C$_6$H$_5$CH$_3$

*Figure **118*** shows the triplet potential energy surface for toluene H-abstraction reactions by O. The three different electronic energy levels, together with their multiplicity (5, 3, 1) have been considered in the reactant configuration. A triplet transition state has been considered, i.e the ground state, and the excited states have been neglected. The H-abstraction from the methyl group has a barrier of ~5.2 kcal/mol, and is ~4.3-4.8 kcal/mol lower than the abstraction from the ring. In contrast with Li et al. [309] more stable product-like complexes were also identified. An additional barrier of ~5 kcal/mol has to be overcome to reach the product configuration. The phenomenological rate coefficients for such multiple-well multiple transition state PES have been obtained using the master equation code of Georgievskii et al. [203]. Rate coefficients are obtained according to the chemically significant eigenstate approach of Klippenstein and Miller [316, 317].
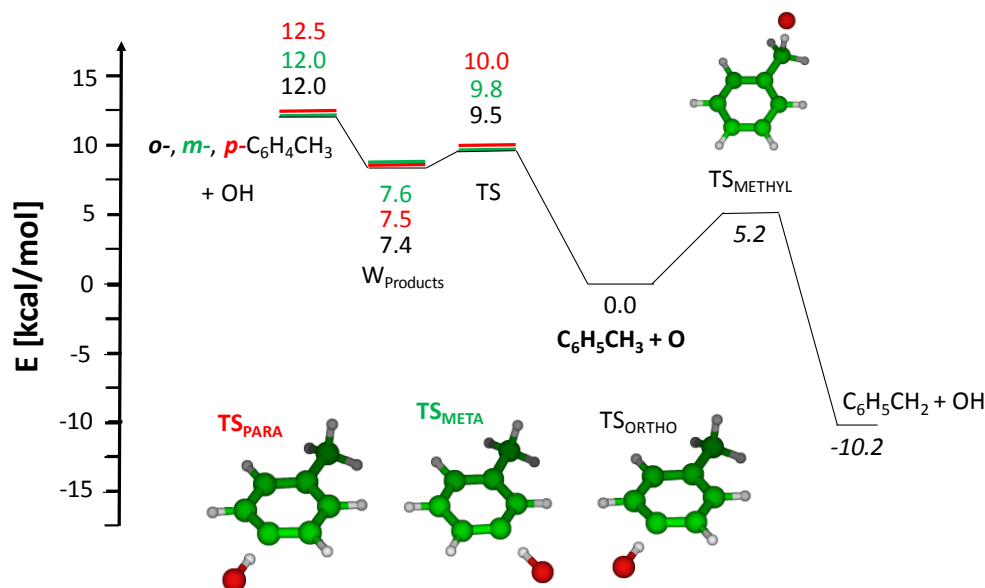
Figure 118: Potential energy surface for the reaction $\ddot{O}$+toluene. Energies are in kcal/mol are relative to the reactants.

H-abstraction by $\ddot{O}$ was investigated experimentally by Hoffmann et al. [306] in shock tubes in a very narrow temperature range (1150–1300 K). Other than this study, the only theoretical investigation in the literature is from Li et al. [309]. Some inconsistency is found in the results of Li et al. [309] as the relative energies of the products are much more similar to the relative energies of the complexes rather than the products identified in *this study*. This is somewhat incoherent with previous comparisons, where the energies of the products were found to be in very good agreement.

Transition State	This work	Li et al.	Complexes	This work	Products	This work	Li et al.
TS$_{METHYL}$	5.2	4.2			$C_6H_5CH_2$+OH	-10.2	-13.6
TS$_{ORTHO}$	9.5	9.6	o-, O	7.4	o-$C_6H_4CH_3$+OH	12.0	8.7
TS$_{META}$	9.8	9.7	m-, O	7.6	m-$C_6H_4CH_3$+OH	12.0	8.8
TS$_{PARA}$	10.0	10.0	p-, O	7.5	p-$C_6H_4CH_3$+OH	12.5	9.3

Table 16: Relative energies of Transition States and Products. Units are kcal/mol.

The lack of the additional barrier connecting the van der Waals complexes to the products results in the factor of ~3 differences between our results and those from Li et al. [309] as observed in *Figure 119*. The calculated rate constant agrees well with the one proposed in the kinetic mechanism of Narayanaswamy et al. [318] for T> 700 K. The experimental results of Hoffmann et al. [306] are overestimated by a factor larger than 2. The branching ratio is once again dominated by the formation of benzyl radical for temperatures up to ~1600 K. According to Li et al. [309], neglecting the additional barrier connecting the product-like complex

($W_{Products}$) and the final products, the H-abstraction from the ring is more and the formation of benzyl radical dominates only up to ~1150 K.
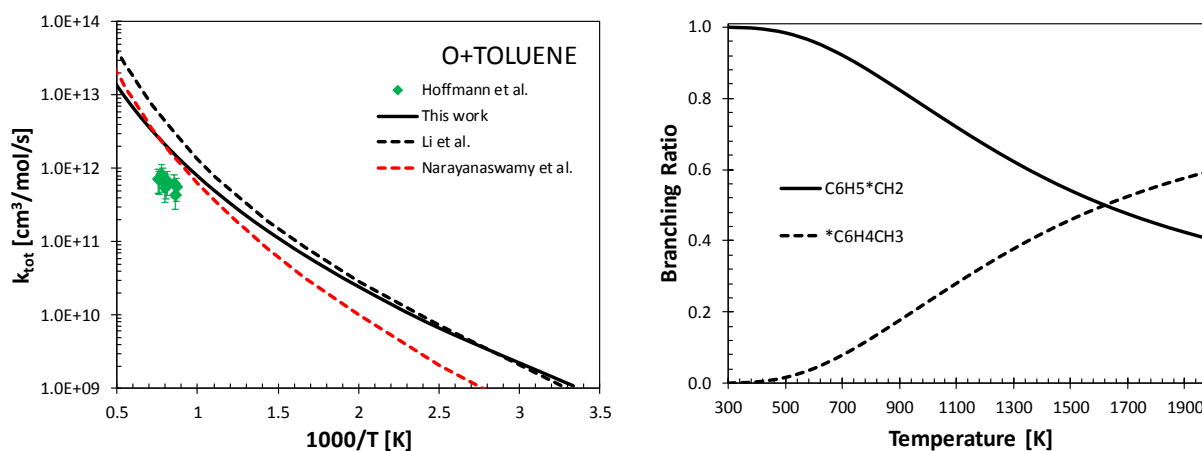
Figure 119: Left panel: comparison of the total rate constant of $\ddot{O}$+toluene with other studies [306, 309, 318]. Right panel: branching ratio between benzyl radical and methylphenyl radicals.

$O_2+C_6H_5CH_3$

The recent interest in better understanding the oxidation of alkenes and aromatics [319-322] as component of real fuel surrogates highlighted H-abstraction reactions by O_2 as highly sensitive reactions. Differently from other H-abstraction reactions, those by molecular oxygen are initiation reactions, converting two stable molecules into two radicals. Therefore, they are of great importance in correctly describing the reactivity of an unsaturated fuel. To the authors knowledge no theoretical studies have directly addressed this class of reactions for toluene.

Figure 120 shows the triplet potential energy surface of the $O_2+C_6H_5CH_3$ system. As expected from the reverse barrierless radical-radical recombination reactions, no evidence of a clear maximum in the potential energy surface is found. The benzyl radical + $H\dot{O}_2$ products lie ~37 kcal/mol above the reactants, while a barrier of ~60 kcal/mol is found for the methylphenyl isomers. The transition state configuration is found ~0.7 kcal/mol and ~6.7-7 kcal/mol below the corresponding products, respectively. These values are consistent with those calculated by Altarawneh et al. [323] for the same reaction in ethylbenzene.

Figure 121 compares the rate constant from this study with the experimental measurements of Eng et al. [307] and from Oehlschlaeger [308] showing large discrepancies (factor of ~10). Ingham et al. [324] also proposed a rate constant that largely deviates from the experimental values. An indirect experimental study by Ingham and co-workers [324] proposed a rate constant which deviates from our estimate as much as a factor of ~10, showing a significantly different activation energy. For comparison purposes we also report in

Figure 121 the rate constant calculated by Chen and Bozzelli [325] for iso-C_4H_8+O_2. Reasons for such deviations are still under investigation.
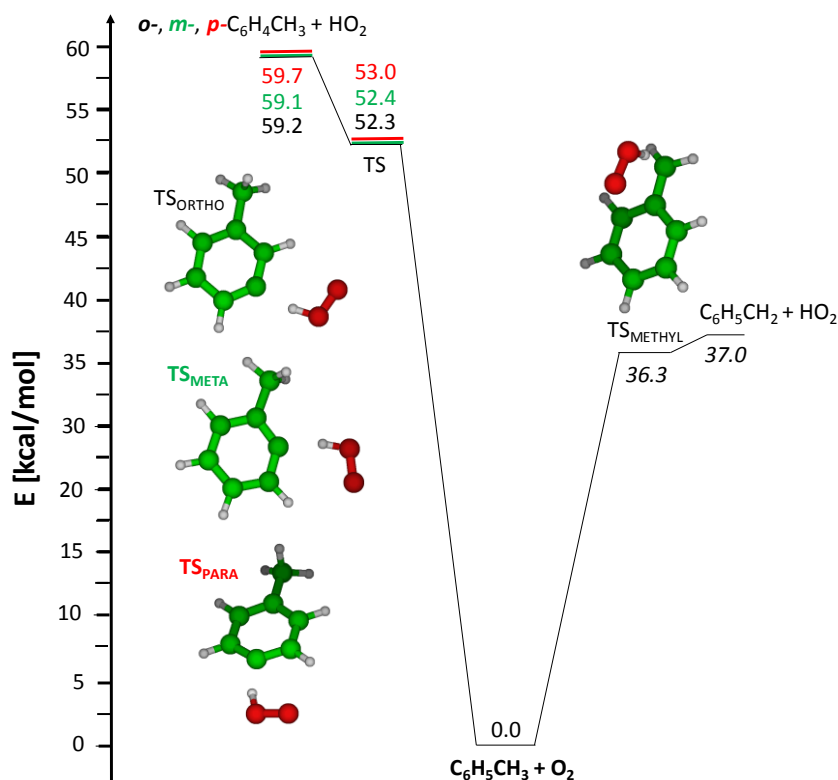
Figure 120: Potential energy surface for the reaction O_2+toluene. Energies are in kcal/mol relative to the reactants.
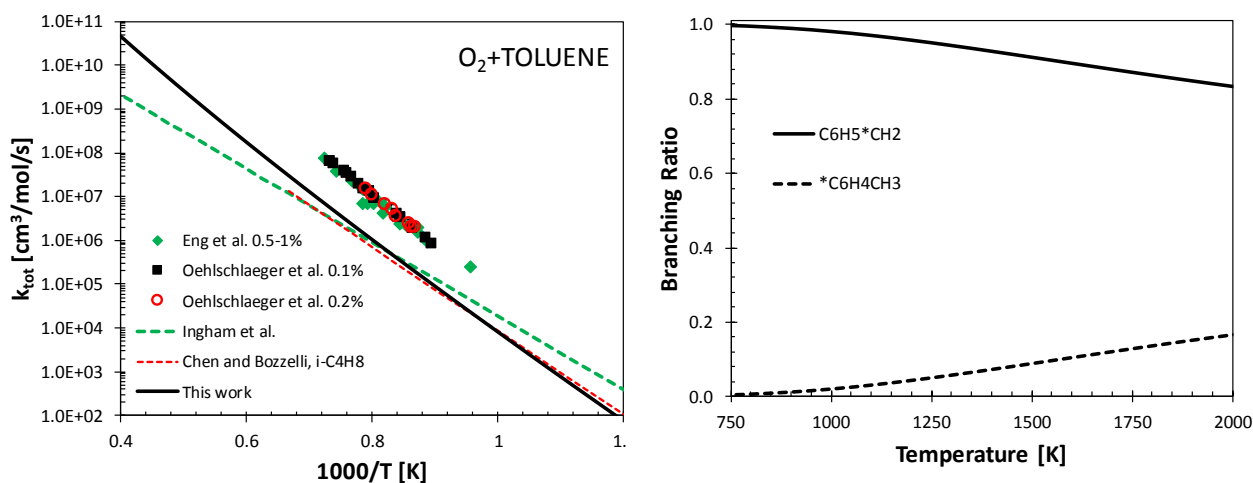
Figure 121: Left panel: comparison of the total rate constant of O_2+toluene with other studies. Right panel: branching ratio between benzyl radical and methylphenyl radicals.

4. Conclusions

Table 17 summarizes the rate constants for the H-abstraction reactions calculated in this study and discussed in this section. Despite some open questions, in particular for the case of O_2+toluene showing large deviations from the experimental data, these parameters are, to the authors knowledge, the most accurate parameters available in the literature. The calculated rate constants have been introduced in the revised POLIMI mechanism, allowing satisfactory agreement with a large set of experimental targets. The validation of the POLIMI mechanism is reported in Section 5.2.3.

Reaction	A	n	Ea
$OH+C_6H_5CH_3 \leftrightarrow C_6H_5CH_2+H_2O$	6.80E+07	1.547	288.4
$OH+C_6H_5CH_3 \leftrightarrow C_6H_4CH_3+H_2O$	1.68E+04	2.858	1289.4
$O_2+C_6H_5CH_3 \leftrightarrow C_6H_5CH_2+HO_2$	2.72E+00	3.996	39107.9
$O_2+C_6H_5CH_3 \leftrightarrow C_6H_4CH_3+HO_2$	7.53E+07	1.989	53168.7
$O+C_6H_5CH_3 \leftrightarrow C_6H_5CH_2+OH$	3.30E+06	2.000	3414.5
$O+C_6H_5CH_3 \leftrightarrow C_6H_4CH_3+OH$	6.47E+06	2.153	9205.6
$HO_2+C_6H_5CH_3 \leftrightarrow C_6H_5CH_2+H_2O_2$	2.72E+00	3.527	12149.0
$HO_2+C_6H_5CH_3 \leftrightarrow C_6H_4CH_3+H_2O_2$	3.53E+01	3.650	22217.3

Table 17: Rate constant for the H-abstraction reactions of toluene calculated in this study.

Referring back to Figure 109, O and OH addition reactions to form cresol and its successive chemistry also play an important role and deserve further attention. Moreover, toluene kinetic models would benefit from further investigations of the pressure dependency of the complex $C_6H_5CH_2+HO_2$ system, already studied partially by da Silva and Bozzelli [296, 297]. In support to this, recent comprehensive validation of the NUIG toluene kinetic mechanism [218] required cost effective assessment of the pressure dependency carried out using QRRK theory. The level of theory adopted in *this study* coupled with a rigorous RRKM/ME treatment should allow higher fidelity toluene models and a better understanding of aromatic oxidation kinetics.

5.2.2 Ab Initio and Kinetic Modeling Study of Toluene Oxidation: O_2+C_7H_7 Potential Energy Surface

1. Introduction

As recently pointed out by Zhang et al. [218], the most recent kinetic mechanism for toluene pyrolysis and oxidation [294, 295] showed a negative temperature coefficient (NTC) region below 900 K. This observation is not consistent with the general thinking that high octane number fuels such as toluene (RON=120, MON=109) do not show the NTC typical of linear alkanes such as n-heptane (RON=MON=0). The lack of measurements for pure toluene oxidation at T < 900 K drives the need for further investigating reaction

pathways derived from benzyl radical addition to O_2, in analogy with alkane oxidation where $R+O_2$ reactions activate the low temperature chemistry.

2. Previous theoretical studies and benzyl radical oxidation chemistry

Murakami et al. [326] investigated the potential energy surface of benzyl + O_2 at the CBS-QB3 [171] level of theory. The rate constant for the dissociation reaction $C_6H_5CH_2OO = C_6H_5CH_2 + O_2$ was calculated and used to obtain the reverse addition reaction rate constant from thermochemistry. Three different dissociation channels were found for benzyl-peroxy radical. The first one leading to the formation of benzaldehyde and $\dot{O}H$, the second one giving phenoxy radical and formaldehyde and a third one producing hydroxyphenyl radical and, again, formaldehyde. A single well master equation analysis was performed at various pressures and temperatures for the backward dissociation and the remaining isomerization channels. Uncertainties in the calculated energies and in the hindered rotation treatment were identified as possible reasons for the observed deviations from experimental measurements of the $C_6H_5CH_2 + O_2 = C_6H_5CH_2OO$ rate constant (see Figure 124 and Figure 125). An overall branching ratio of 0.7 was calculated for the benzaldehyde + OH channel in agreement with previous suggestions of Clothier et al. [327].

Canneaux et al. [328] studied the isomerization channel leading to benzaldehyde and OH. After testing 54 different levels of theory, coupling different methods with different basis sets, they identified CASPT2/ANO-L-VDZP//B3LYP/cc-pVDZ as the best method in reproducing the indirect experimental measurements of Ellis et al. [329] at 773 K, claiming a strong multi-reference character of the transition state (TS1 of Figure 124). The CASPT2 calculations were carried out using a minimal 3 electrons 3 orbitals active space.

Da Silva, Bozzelli and co-workers focused on the recombination of benzyl radical with $H\dot{O}_2$ to form benzyl hydroperoxide ($C_6H_5CH_2 + HO_2 = C_6H_5CH_2OOH$) [296] and on its decomposition channels [298]. Another study from the same authors provided rate constants for the bimolecular reaction $C_6H_5CH_2 + HO_2$ to directly form benzoxyl radical ($C_6H_5CH_2O$) and $\dot{O}H$ [297]. In the recent study by Zhang et al. [218] both the recombination and the formation of benzoxyl and $\dot{O}H$ were highlighted as highly sensitive for ignition delay times.

3. Rate prediction methodology

Geometries, frequencies and zero point energies for reactants, wells (W), products and transition states (TS) were obtained with the B2PLYP-D3 [169, 170] density functional theory method (DFT), employing the cc-pVTZ basis set. The DFT calculations were performed with the Gaussian program [46]. Energy calculations were computed at the CCSD(T)-F12/VTZ-F12 [159, 160, 330, 331], MP2-F12/VTZ-F12 [332] and MP2-F12/VQZ-F12 levels, using Molpro [47]. The highest level single point energies, as reported in black in Figure 125, were finally calculated as $E = E_{CCSD(T)-F12/VTZ-F12} + E_{MP2-F12/VQZ-F12} - E_{MP2-F12/VTZ-F12}$. The barrierless entrance

channel (R+O$_2$=RO$_2$) has been treated according to the VRC-TST approach developed by Georgievskii and Klippenstein [205], as discussed recently in the work of Zhang et al. [333]. Overall, an exothermicity of ~20.8 kcal/mol was obtained, in good agreement with the experimental value of Elmaimouni [334] (20.0 kcal/mol) and Fenter et al. [335] (21.8 kcal/mol). The strongly coupled rotations of the -CH$_2$OO group of W1 (Figure 122), were treated as a 2-dimensional rotor determining the 2D rotational PES at the B3LYP/CBSB7 level. Potential energy scans are reported in Figure 123.
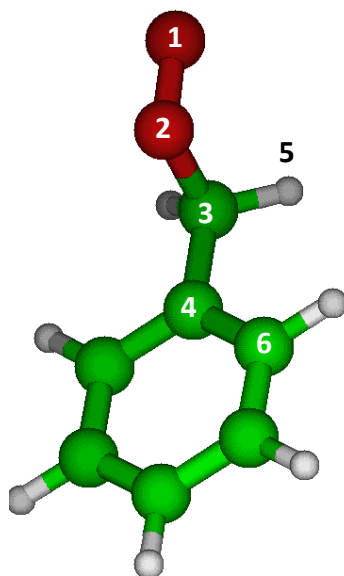
Figure 122: W1 minimum energy structure at B3LYP/CBSB7 level
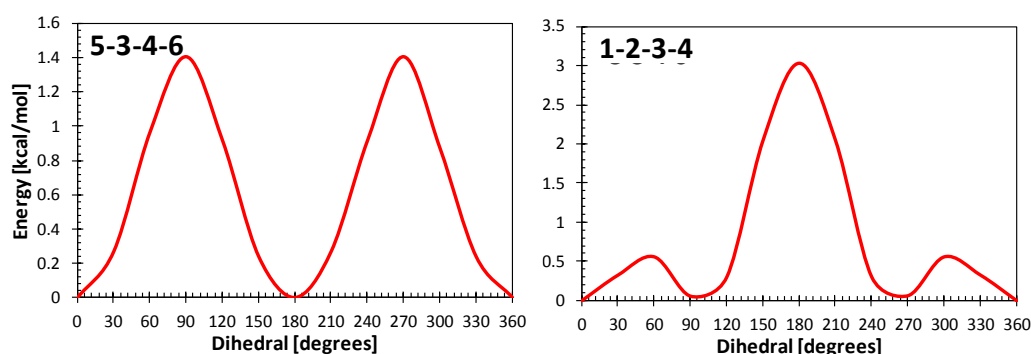
Figure 123: Dihedral scan of the coupled rotations of CH$_2$-OO at B3LYP/CBSB7 level.

Rate coefficients were calculated for a range of temperature (300–2500 K) and pressure (0.1–1000 atm), by solving the master equation with the MESS code [203]. The collisional energy transfer probability was described by the exponential down model, with ΔE_{down} = 260 (T/300)$^{0.875}$ (cm^{-1}) assuming an argon bath gas. Quantum tunneling contributions to the rate constant were determined using the Eckart model [186]. *Figure 124* shows the reaction channels considered in this study. The corresponding potential energy surface is reported in *Figure 125*.
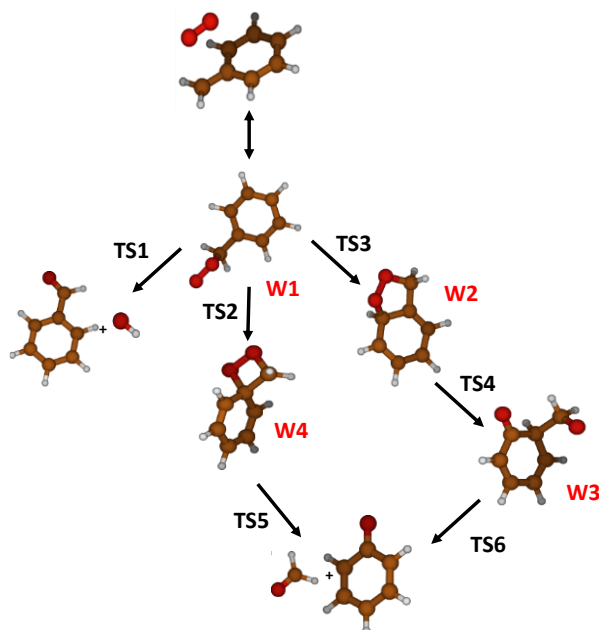
Figure 124: Investigated reaction pathways on the potential energy surface for the C$_6$H$_5$CH$_2$+O$_2$ system.

Figure 125 also shows results obtained by Murakami et al. [326] at the CBS-QB3 level highlighting the impact of the level of theory on computed energies. Deviations between 1 and 3 kcal/mol are observed for transition states according to the two different levels. With respect to the work of Murakami et al. [326] an additional pathway involving the cyclization of W1 to form W2 through TS3 and finally forming C$_6$H$_5$ and CH$_2$O.
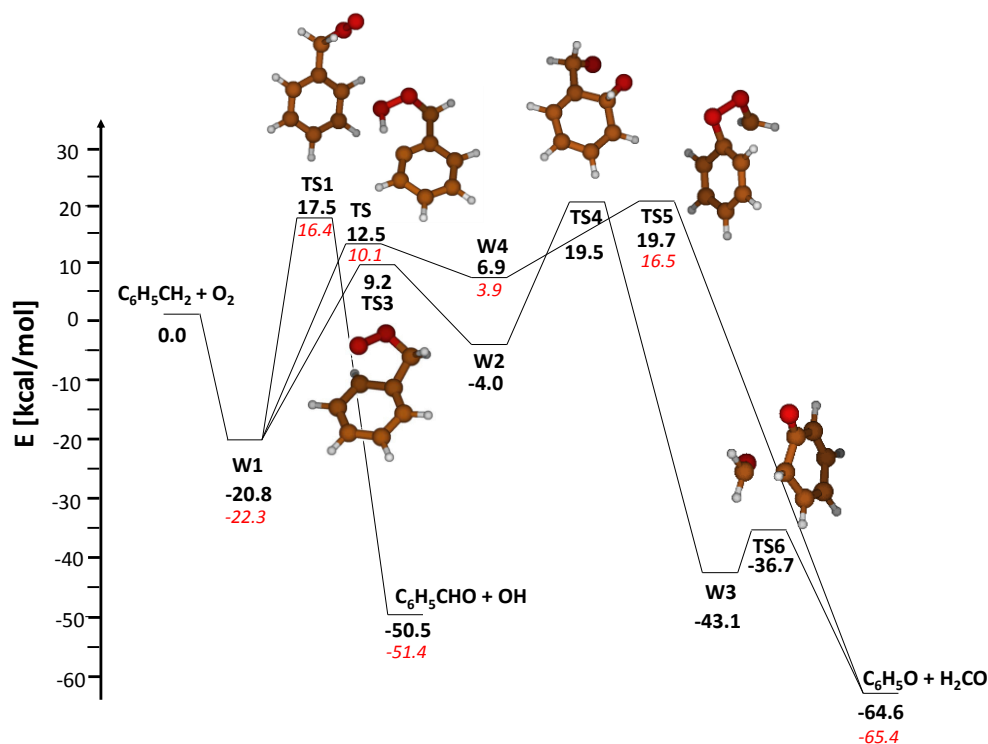
Figure 125: Potential energy surface for the C$_6$H$_5$CH$_2$+O$_2$ reaction. Numbers in red are CBS-QB3 calculated energies from Murakami et al. [326]. Numbers in black are energies computed in this study. Molecular structures represent transition states.

For many radical-radical recombination reactions and, radical addition to oxygen, not only the ground state electronic configuration has to be accounted for in the wave function, but also that of excited states. In a Coupled Cluster calculation, it is possible to obtain information about the multireference character of the wave function through the calculation of the T1-diagnostic. If this parameter is lower than 0.02-0.03, then the CCSD(T) wave function is expected to give results close to the full-CI limit. For the cases where T1>0.02-0.03 it is necessary to employ a multi-reference method such as CASPT2 (second-order multireference perturbation theory) [336]. **Table 18** shows T1-diagnostics for the transition states of **Figure 124** and **Figure 125**. TS4 and the subsequent TS6 show a strong multireference character, and their treatment with single reference methods leads to uncertainties in the order of ~4 kcal/mol.

Table 18: T1 diagnostics calculated at CCSD(T)-F12/VTZ-F12 level.

	TS1	TS2	TS3	TS4	TS5	TS6
T1-diagnostic	0.024	0.019	0.020	0.034	0.017	0.038

CASPT2/cc-pVDZ saddle point searches were performed with a 3e3o active space along the M06-2X/6-311++G(d,p) intrinsic reaction coordinate (IRC) without success. As reported in **Figure 126**, calculations performed at CCSD(T) and RHF levels starting from the reactants and from the products side produced very different potential energy surfaces, confirming the strong multireference character of the investigated transition state.
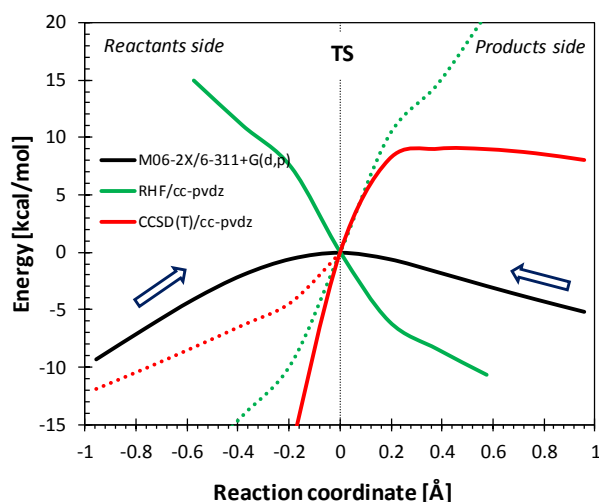
Figure 126: Electronic energy profiles along the M06-2X/6-311+ +G(d,p) IRC around the TS4 structure. The energy profiles are normalized defining the zero at the M06-2X saddle point.

4. Master equation results: entrance channel $R+O_2=RO_2$

*Figure 127*a shows calculated rate constants for the entrance channel ($C_6H_5CH_2+O_2=C_6H_5CH_2OO$) as a function of temperature and pressure. The calculated high pressure limit (solid black line) shows a slightly positive temperature dependence, in contrast with that reported by Murakami [326] where two trends are observed: a positive dependence for T<550 K and a negative non-monotonic dependence for T>550 K. Between 300 and 400 K the high pressure limit calculated in this study is a factor of ~4 higher than that of Murakami et al. [326], and correctly reproduces the experimental measurements within their uncertainties.

Benzyl peroxy radical decomposition rate constants are plotted in *Figure 127*b. As an example, a typical decomposition rate constant of an alkyl-peroxy radical is also reported (green line). While in alkanes the peroxy-radicals can easily undergo successive isomerizations and low temperature branching pathways, the relatively unstable benzyl-peroxy radical more likely decomposes back to the reactants, partially explaining the high anti-knocking properties of toluene.

*Figure 127*c shows the equilibrium constant calculated in this study (black line) and that reported by Murakami et al. [326] (red line). Despite a factor of ~5 deviation from the experimental measurements of Fenter et al. [335], K_{eq} calculated in this study better reproduces the temperature dependence, highlighting a lower stability of $C_6H_5–CH_2OO·$ compared to Murakami et al. [326].
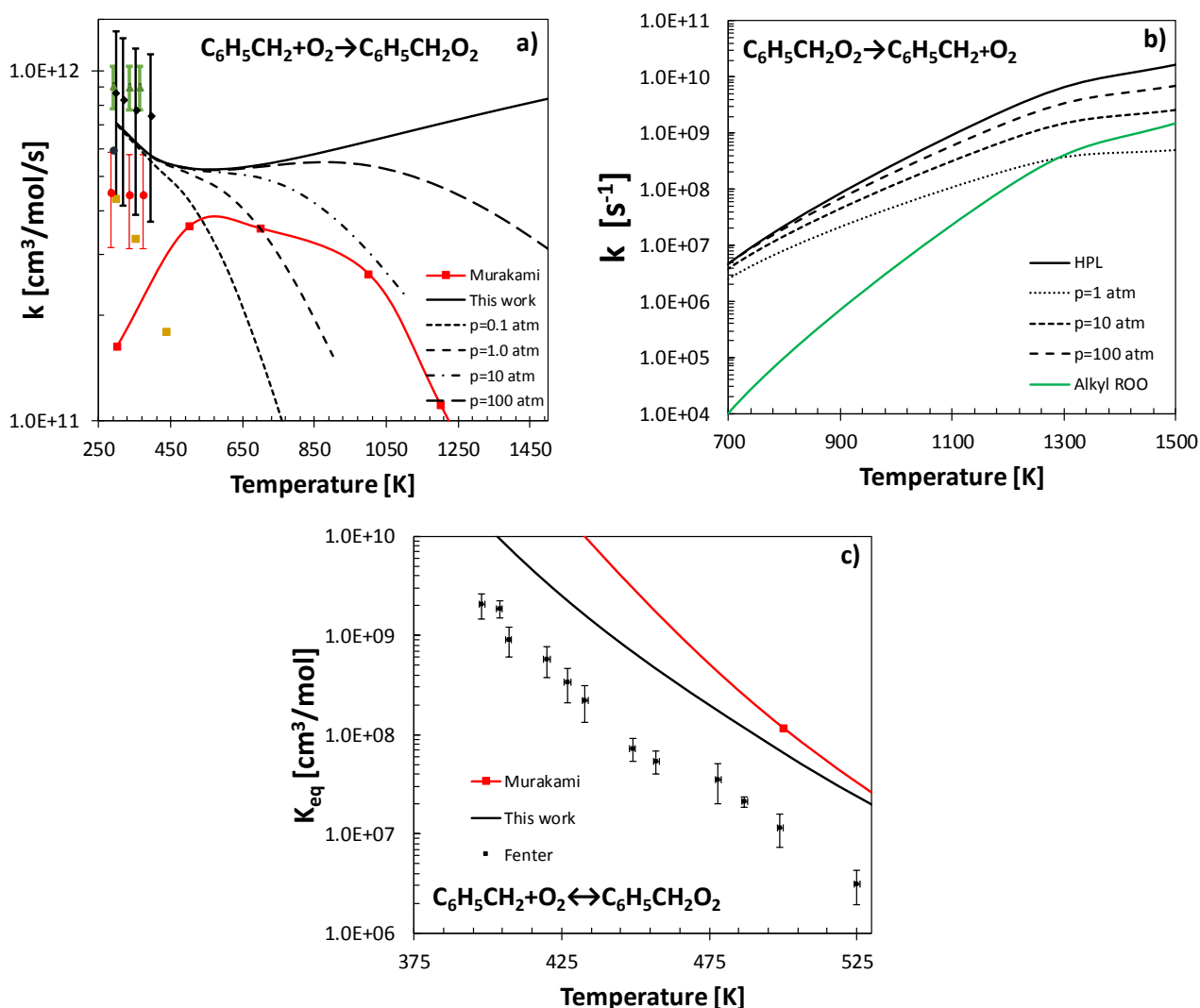
Figure 127: a) Calculated k(T,p) rate constants for benzyl addition to O_2 from this study (black lines), HPL from Murakami et al. [9] (red line) and comparison with experimental data [334, 335, 337, 338]. b) Calculated k(T,p) rate constants for benzyl-peroxy radical decomposition: black lines: this study, green line: typical decomposition rate constant of an alkyl peroxy radical. c) Comparison of calculated equilibrium constant with experimental data of Fenter et al. [335] and Murakami et al. [326](red line).

5. Master equation results: decomposition products

The rate constants for the decomposition channels of C_6H_5–$CH_2OO\cdot$ are orders of magnitude lower than that for the backward dissociation to reactants. For this reason, the bimolecular well-skipping reaction between O_2 and benzyl forming benzaldehyde and $\cdot OH$ can play an important role in increasing toluene reactivity, converting a resonantly stabilized radical (benzyl) and molecular oxygen into reactive $\cdot OH$.

Table 19 reports the calculated rate constant for direct use in chemical kinetic mechanisms for toluene oxidation.

Reaction	A	n	Ea

$C_6H_5CH_2+O_2 \leftrightarrow C_6H_5CH_2O_2$			
0.1 atm	8.60E+33	-7.457	4998.0
1 atm	4.20E+23	-3.967	2719.8
10 atm	1.62E+17	-1.817	1234.2
100 atm	7.64E+13	-0.703	472.4
1000 atm	8.88E+10	0.251	-317.6
$C_6H_5CH_2+O_2 \leftrightarrow C_6H_5CHO+OH$			
0.1 atm	1.51E+05	1.859	15376.7
1 atm	4.70E+07	1.17	17355.2
10 atm	1.64E+13	-0.343	22290.3
100 atm	5.57E+14	-0.678	26153.9
1000 atm	1.31E+04	2.378	23001.3
$C_6H_5CH_2O_2 \leftrightarrow C_6H_5CHO+OH$			
0.1 atm	2.72E+00	1.897	24945.04
1 atm	2.72E+00	2.602	27453.09
10 atm	2.72E+00	3.022	29085.89
100 atm	2.72E+00	3.249	30050.4
1000 atm	2.72E+00	3.371	30626.56
$C_6H_5CH_2+O_2 \leftrightarrow C_6H_5+CH_2O$			
0.1 atm	1.58E+09	0.474	20508.8
1 atm	6.40E+09	0.306	21017.6
10 atm	7.15E+14	-1.072	25488.2
100 atm	1.76E+12	-0.267	25983.6
1000 atm	1.53E+19	-2.044	37559.4

$C_6H_5CH_2O_2 \leftrightarrow C_6H_5 + CH_2O$			
1 atm	1.99E+19	-3.633	36399.4
10 atm	1.18E+07	0.464	30767.1
100 atm	1.78E+35	-7.147	51748.1
1000 atm	1.42E+23	-3.279	48917.7

Table 19: Kinetic rate constants in CHEMKIN format for direct use in kinetic mechanisms.

6. Conclusions

This study presents an accurate theoretical investigation of the potential energy surface of $C_6H_5CH_2 + O_2$. Electronic structure and energy calculations for reactants, wells, transition states and products have been performed at possibly the most accurate level of theory affordable for a 9 heavy atoms system. The master equation analysis provided rate constants as a function of temperature and pressure for direct use in existing chemical kinetic mechanisms. Results for the entrance channel have been compared with experimental measurements showing satisfactory agreement. The dominant reaction channel is the direct bimolecular formation of benzaldehyde and $\dot{O}H$, contributing to enhanced toluene reactivity. The uncertainty of the rate constants provided here is estimated to be a factor of ~2-3, due primarily to an uncertainty of ~1-2 kcal/mol in the computed energies. A larger uncertainty (up to ~4 kcal/mol) is associated with TS4 energy, due to its strong multireference character. This could slightly affect the overall branching ratio to phenoxy radical (C_6H_5) and CH_2O but the formation of benzaldehyde and ·OH would still be the dominant pathway.

The calculated rate constants have been introduced in the revised POLIMI mechanism, allowing satisfactory agreement with a large set of experimental targets. The validation of the POLIMI mechanism is reported in the next Section.

5.2.3 Update of POLIMI Toluene Kinetic Mechanism

The POLIMI toluene kinetic mechanism, formerly based on Andrae et al. [292] was updated based on the calculation described in Section 5.2.1 and 5.2.2, and other quantum chemical calculations and modelling studies from the literature. The references to these studies are reported as comments in the CHEMKIN format mechanism attached to *this thesis*.

Table 20 lists the validation targets for the updated POLIMI toluene mechanism.

Reactor	Reference	T (K)	P	φ
		Pyrolysis		
Plug Flow	[294, 295]	1100–1730	5–760 Torr	∞
Shock Tube	[339]	1550–2145	0.2-0.5 atm	∞
	[340]	1300–1800	1.5–7.8 bar	∞
	[341]	1705,1602	0.1,1.6 bar	∞
	[342]	1200–1850	10 atm	∞
	[343]	1200–1900	27,45 bar	∞
		Oxidation		
Plug Flow	[344]	1173	1 atm	0.76
Jet Stirred Reactor	[345]	873,893,923	1 atm	0.45,0.9
	[346]	1000–1400	1 atm	0.5,1.0,1.5
	[295]	950–1200	10 atm	0.5,1.0,1.5
Laminar Flame Speed	[273] [347, 348] [349] [350] [351]	298–470	1-3 atm	0.7–1.4
Shock Tube (IDT)	[352]	1330–1820	2.27,6.81 atm	0.33,1.0
Shock Tube (IDT)	[346]	1430–1950	1.1 atm	0.5,1.5
Shock Tube (IDT)	[353]	1430–1820	1 atm	1
Shock Tube (IDT)	[311]	1021–1400	12,50 atm	0.25,0.5,1.0
Shock Tube (IDT)	[354]	1000–1300	50 atm	0.5,1.0
Shock Tube (IDT)	[355]	1210–1480	22,50,550 bar	1.0,5.0
Shock Tube (IDT)	[218]	900–1459	20, 40 atm	0.5,1.0,2.0
Rapid	[356]	920–1100	50 atm	0.5–1.0

Table 20: Validation targets for toluene kinetic mechanisms.

Pyrolysis

Recent detailed measurements of toluene pyrolysis in flow reactors at 5-760 torr [294] provided further insights into the "vertical" decomposition pathways of benzyl radical ($C_6H_5CH_2$). The secondary mechanism of benzyl radical decomposition has been controversial for many years. Kinetic simulations of the overall decomposition process showed that it was possible to obtain good agreement with experimental data by assuming a direct unimolecular decomposition step $C_6H_5CH_2=cyC_5H_5+C_2H_2$. Beside the difficulties in justifying such an elementary step, the work of Cavallotti et al. [357] highlighted the "vertical" decomposition pathway of benzyl radical to fulvenallene (C_7H_6) as the main consumption pathway of benzyl radical. However, due to the poor predictions of acetylene and cyC_5H_5 yields, it was necessary to include a very rapid reaction of $\dot{H}$ with fulvenallene to form the same products. Despite the physical meaning of such channel, a rate constant about a factor of 50 higher than the one calculated from theory had to be assumed to obtain reasonable predictions. C_7H_6 decomposition was investigated further by Polino et al. [358]. Two main channels were highlighted: the direct H-elimination to form fulvenallenyl radical ($C_7H_6=C_7H_5+H$) and decomposition to cyclopentadienylidene and C_2H_2 ($C_7H_6=cyC_5H_4+C_2H_2$). The introduction of such channels was beneficial for the performance of the updated POLIMI mechanism, with the exception of cyclopentadienyl radical (cyC_5H_5), which is consistently underestimated. A new channel is proposed in this work which involves the addition of $\dot{H}$ to the fulvenallenyl radical ring, with subsequent elimination of acetylene and cyclopentadienylidene ($H+C_7H_5=cyC_5H_4+C_2H_2$). cyC_5H_4 is highly reactive and can abstract H-atoms to form cyC_5H_5. This second channel to the formation of cyC_5H_4 and cyC_5H_5 correctly explains recent detailed measurements by Yuan et al. [294], as reported in Figure 128. Preliminary calculations at the M062x/6-311+G(d,p) level of theory suggest rate constants for $H+C_7H_5=cyC_5H_4+C_2H_2$ on the order of $1-2 \cdot 10^{13}$ in the temperature range 1400–1700 K. Arrhenius rate expressions for the H-abstraction channels $cyC_5H_4+H_2=cyC_5H_5+H$ and $cyC_5H_4+CH_4=cyC_5H_5+CH_3$ are respectively $k_{H2} = 1.76 \ 10^{5.0} \ T^{2.18} \exp(\frac{5760}{RT})$ and $k_{H2} = 1.22 \ 10^{10.0} \ T^{1.46} \exp(\frac{10490}{RT})$ cm³/mol/s. CH_4 and H_2 were selected because of their relatively high concentrations in environments typical of pyrolysis, in order to test the actual relevance of the proposed channels. The rate constant for the H-abstraction from toluene was adopted from Derudi et al. [359].
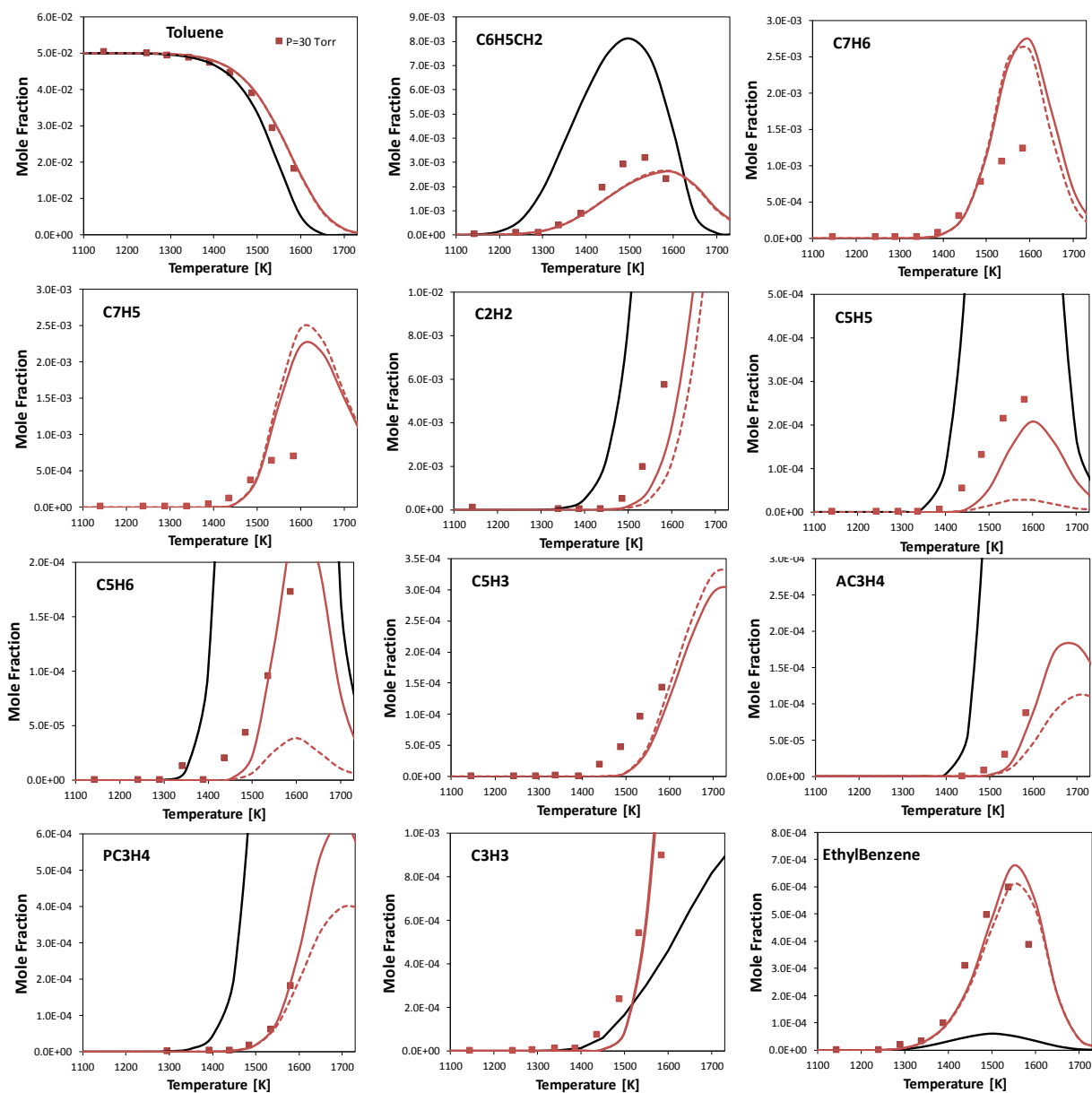
Figure 128: Toluene/Ar pyrolysis in plug flow reactors at p=30 torr. Comparison between POLIMI1412 (black lines), updated POLIMI mechanism from this study (solid red lines) and the POLIMI mechanism without the additional pathways (H+C₇H₅=CyC₅H₄+C₂H₂ and cyC₅H₄+H₂/CH₄) (dashed red lines). Experimental data from Yuan et al. [294].

As clear from Figure 128 the proposed pathways allow the accurate prediction of cyC$_5$H$_5$ and cyC$_5$H$_6$, and improved acetylene yields. Other pressure cases from Yuan et al. [294] are reported in *Figure 129*.
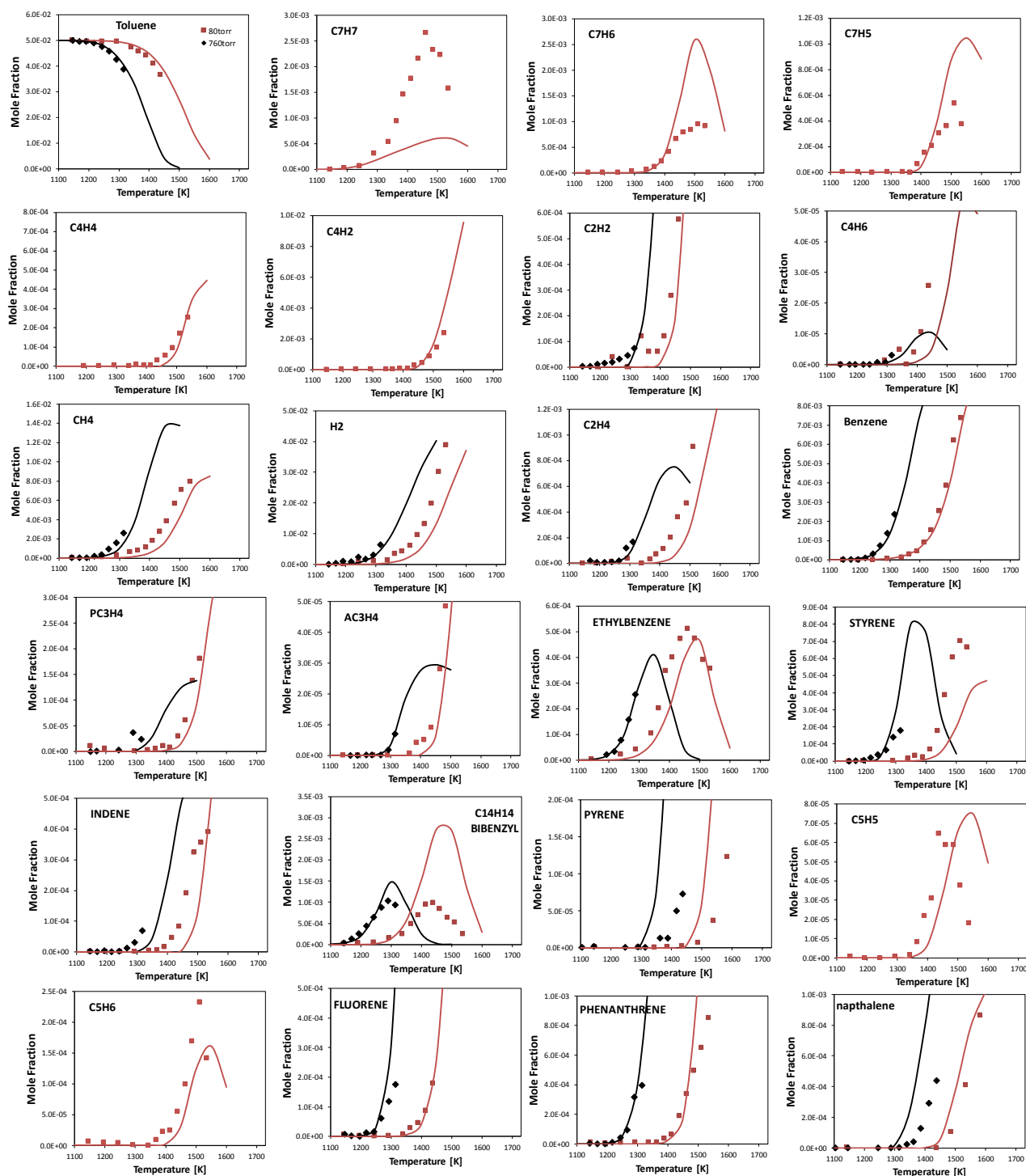
Figure 129: Toluene/Ar pyrolysis in plug flow reactors at p=80 (red) and 760 torr (black). Comparison between the updated POLIMI mechanism from this study and experimental data from Yuan et al. [294] (symbols).

Colket et al. [342] investigated toluene pyrolysis in shock tubes at p=10 atm. *Figure **130*** compares results from the POLIMI mechanism and experimental data.
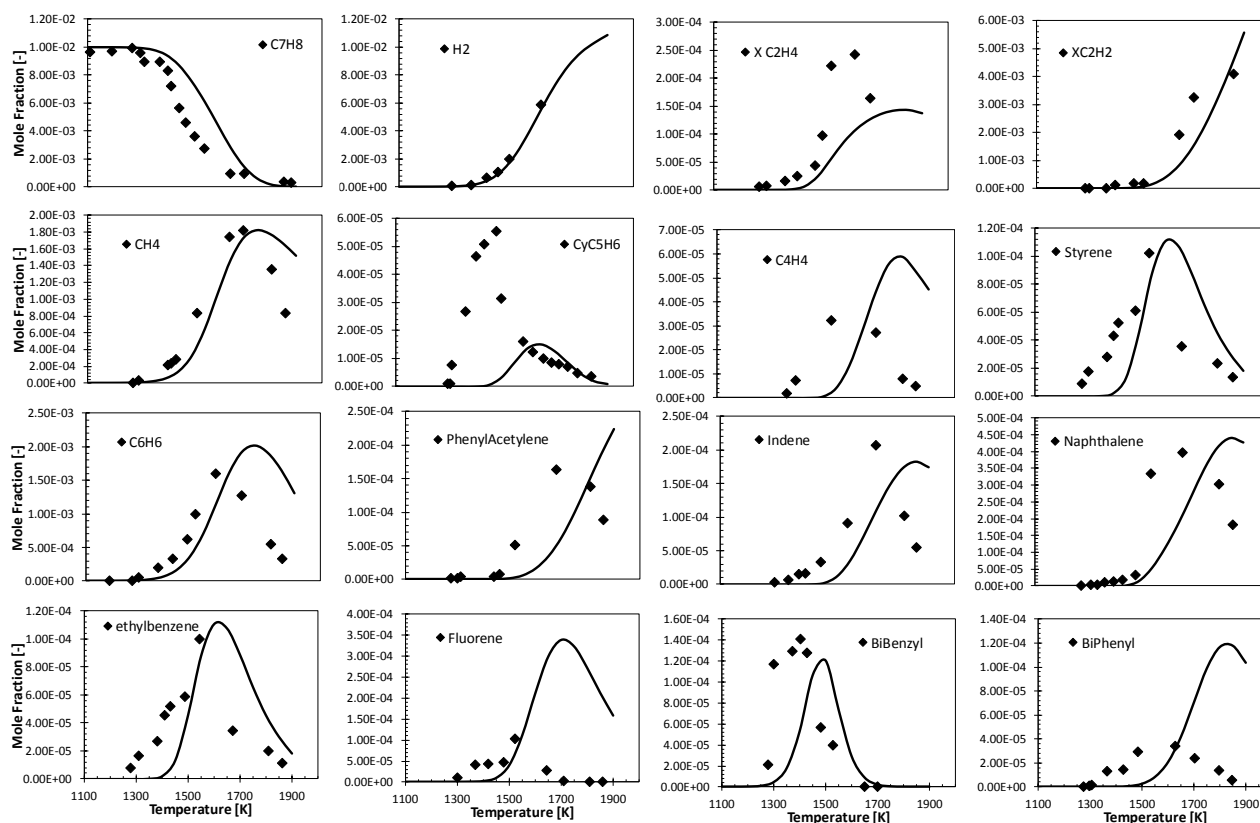
Figure 130: 1% toluene/Ar shock tube speciation at p=10 atm [342]. Lines: POLIMI mechanism, Symbols: experimental data.

Overall the mechanism accurately captures toluene consumption and the main decomposition products. Larger deviations are observed for the case of *Figure **130*** where a ~70 K delay is observed in fuel conversion and therefore in decompostion products. Similar discrepancies were observed by Yuan et al. [294]. *Figure **131*** and *Figure **132*** shows rate of production analyses carried out at ~20 % fuel consumption at T=1400 K and p=0.5, 1.0 and 10 atm. *Figure **131*** clearly shows the expected increasing contribution of the unimolecular initiation reaction $C_6H_5CH_3+M \leftrightarrow C_6H_5CH_2+H+M$ for increasing pressure. Rate coefficients for this channel are from Klippenstein et al. [360]. H-abstractions by $\dot{H}$ and $\dot{C}H_3$ to form benzyl radical are the main consumption channels and the rate constants are from Narayanaswamy et al. [318]. The fate of benzyl radical reported in *Figure **132*** is strongly pressure dependent. At lower pressure the vertical decomposition pathway previously discussed producing fulveneallene (C_7H_6) accounts for up to ~60%. For increasing pressure the recombination of benzyl radicals to form bibenzyl ($C_6H_5C_2H_4C_6H_5$) becomes the dominant pathway, followed by the recombination with methyl radical to form ethyl benzene ($C_6H_5C_2H_5$). Other minor pathways lead to the formation of phenyl radical (C_6H_5) benzyne (C_6H_4) and diphenylmethane ($C_6H_5CH_2C_6H_5$).
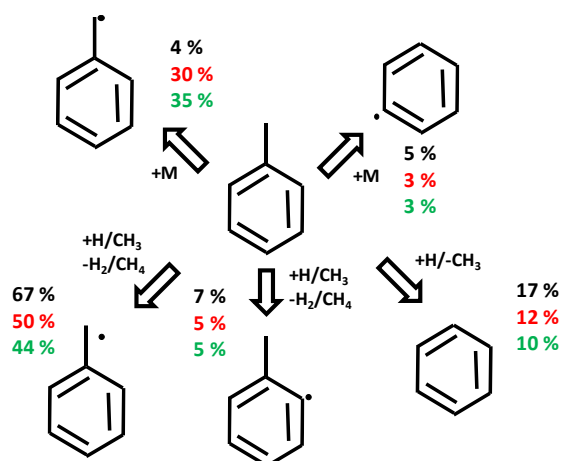
Figure 131:Toluene consumption pathways for a 1% toluene/Ar mixture in a shock tube at T=1400 K and p=0.5, 1.0 and 10.0 atm.
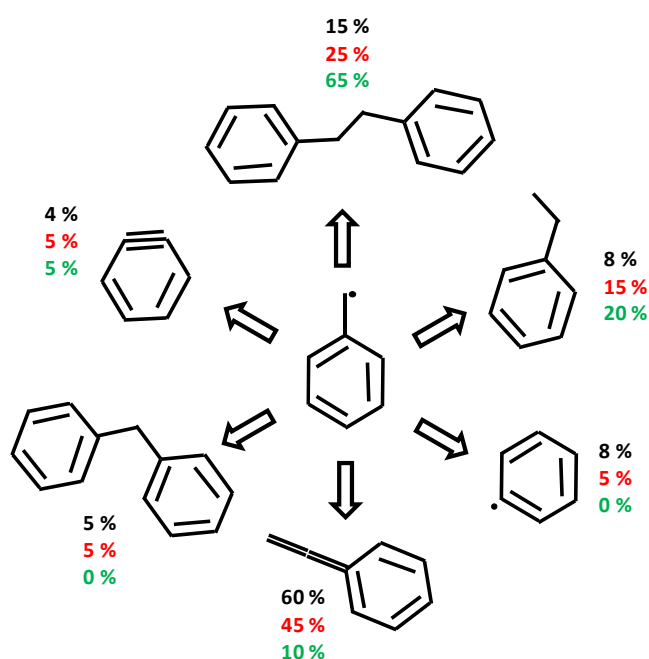
Figure 132: Benzyl radical consumption pathways for a 1% toluene/Ar mixture in shock tube at T=1400 K and p=0.5, 1.0 and 10.0 atm.

Sensitivity coefficients of toluene consumption to rate constants at the same conditions of *Figure 131* and *Figure 132* in a shock tube reactor are reported in *Figure 133*. The results show the increasing importance of initiation reactions for increasing pressure and the relevance of the ipso-substitution reaction $C_6H_5CH_3+H \leftrightarrow C_6H_6+CH_3$ converting $\dot{H}$ into less reactive methyl radical at lower pressures. This reaction has been poorly investigated in the literature, the values adopted in this study agree within a factor of ~2 with the experimental value of Ellis et al. at 773 K [329] and with the recommendation of Narayanaswamy et al. [318]. Further investigations are necessary as an even bigger impact of this reaction is expected in laminar flames.
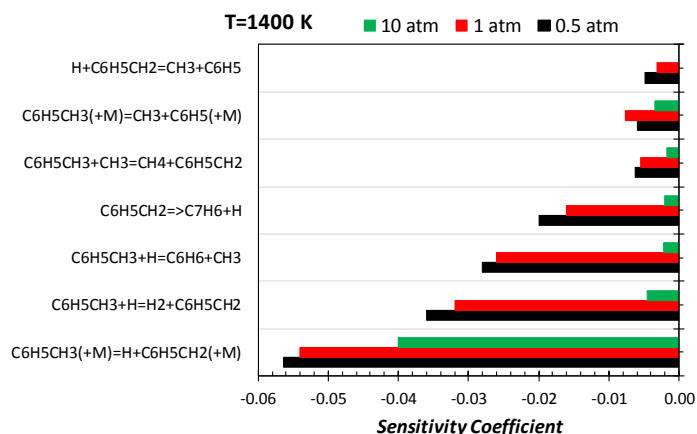
Figure 133: Sensitivity coefficients of toluene consumption to reaction rate constants for a 1% fuel/Ar mixture in a shock tube at T=1400 K and p=0.5, 1.0 and 10.0 atm.

Oxidation

Sivaramakrishnan et al. [355] investigated the high pressure (20, 50 and 550 bar) and high temperature oxidation of toluene in shock tubes. Results for the 50 bar, φ=1.0 case are reported in *Figure 134*. Modification to the kinetic mechanism allow improved agreement although significant deviations are still observed for CO_2 and ethylene.
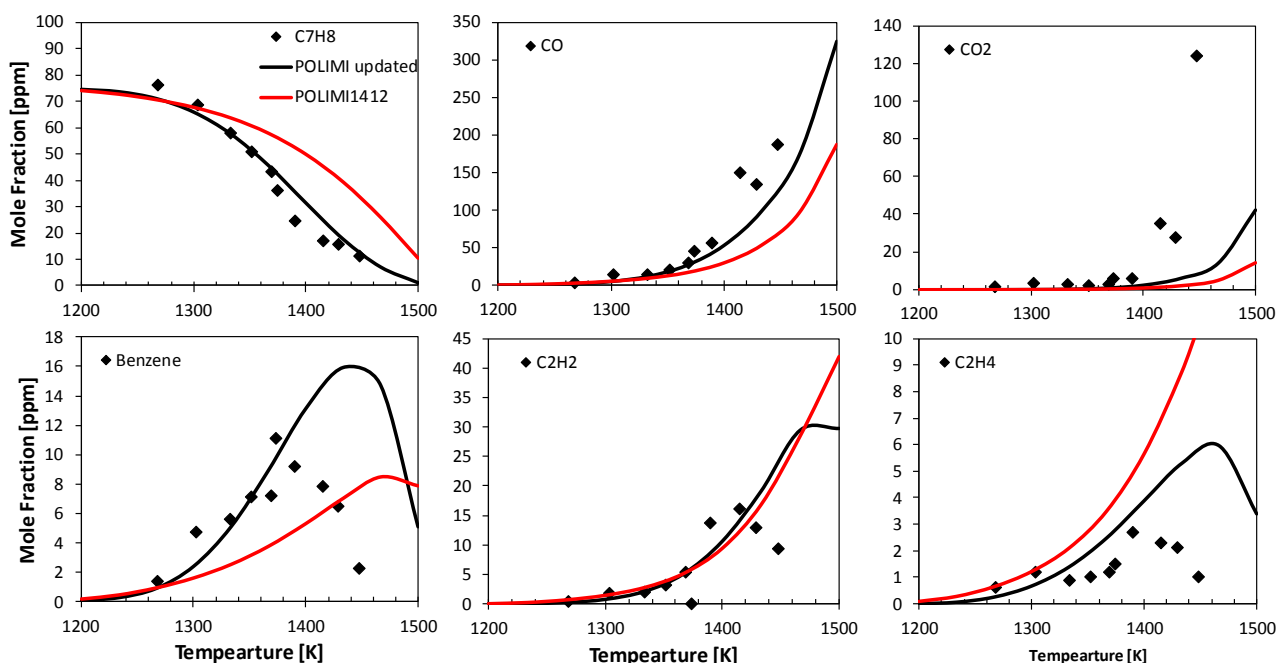
Figure 134: Oxidation of 75 ppm of toluene in O_2/Ar at φ~1.0 and p=50 bar. Symbols: experimental measurements, lines: model.

Dagaut et al. [346] investigated the oxidation of toluene in jet stirred reactors at p=1 atm in the temperature range 1100–1400 K. A comparison between these data, the previous version and the updated version of the POLIMI mechanism is reported in *Figure 135* for the case at φ~1.0.
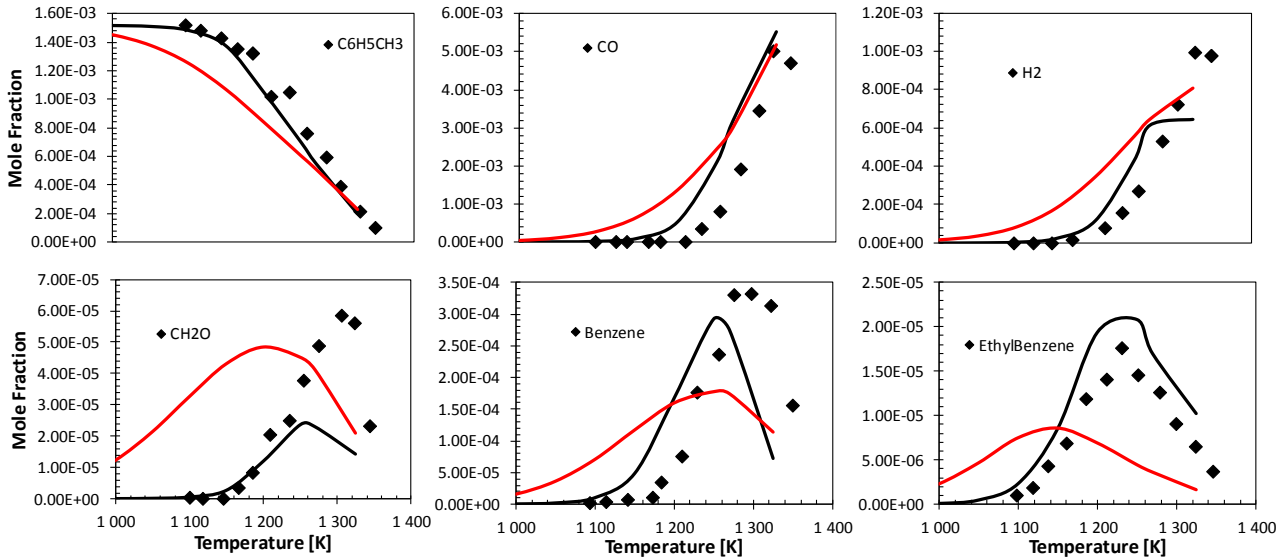
Figure 135: Speciation in an isothermal jet stirred reactor. 0.15% toluene/O_2/N_2, φ=1.0, p=1 atm, τ=1.0 s. Symbols: experimental [346], red lines: POLIMI1412, black lines: updated POLIMI.

Yuan et al. [295] recently extended the available experimental measurements in JSR at p=10 atm. *Figure 136* compares these measurements with POLIMI mechanism, highlighting the improved performances of the updated version.
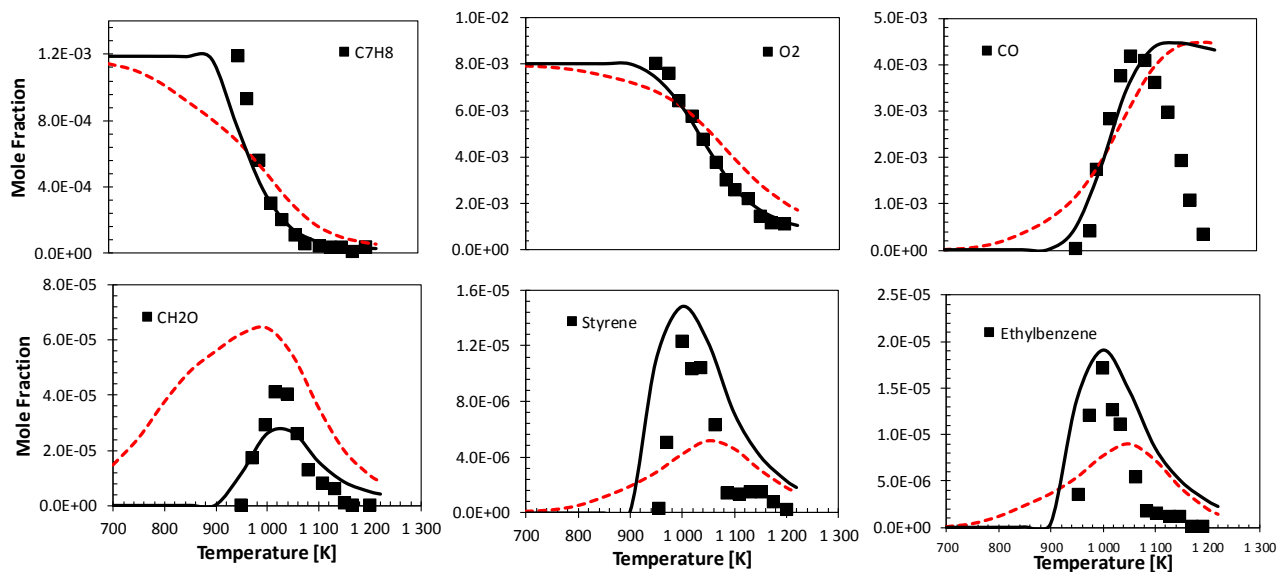
Figure 136: Speciation in an isothermal jet stirred reactor. 0.12% toluene/O_2/N_2, φ=1.0, p=10 atm, τ=0.5 s. Symbols: experimental data [295], red lines: POLIMI1412, black lines: updated POLIMI.

The main differences in terms of global reactivity between the POLIMI1412 version and the updated mechanism are summarized in the sensitivity analysis of *Figure 137*. One of the most significant differences relates to the empirical reaction proposed by Andrae et al. [293] $C_6H_5CH_2+O_2 \leftrightarrow C_6H_5+CH_2O+O$ enhancing production of OH *via* $O+ C_6H_5CH_3 \leftrightarrow C_6H_5CH_2+OH$. This reaction has been removed and the interactions of benzyl radical and molecular oxygen are described according to the calculation of Section 5.2.1. These updated rate constants should be included in the kinetic mechanisms published in the literature [218, 294, 295].
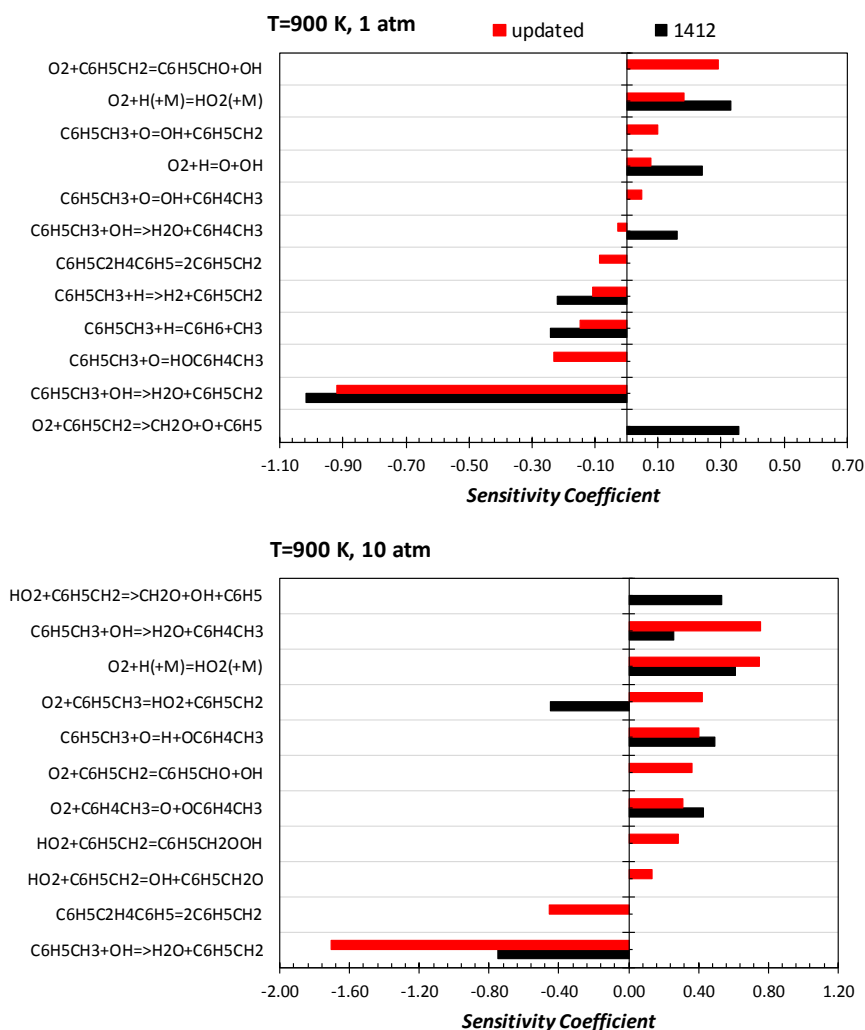
Figure 137: Sensitivity coefficient of OH formation to reaction rate constants. Isothermal jet stirred reactor simulations at φ=1.0, p=1 atm (top), and p=10 atm (bottom). Mixture compositions as in Figure 135 and Figure 136.

The updated thermochemistry of benzyl radical [98, 298] and the inclusion of the pressure dependent rate constant for $C_6H_5CH_2+C_6H_5CH_2 \leftrightarrow C_6H_5C_2H_4C_6H_5$ estimated by Yuan et al. [294, 295] had a significant impact on the reactivity. The large amount of bibenzyl formed in the presence of oxygen and mostly at high pressure might require an accurate treatment of its formation at first, and eventually its low temperature reactivity. A lumped submechanism based on the alkyl-benzenes low temperature chemistry already included in the

POLIMI mechanism [40] has been considered for bibenzyl oxidation. The modifications to the branching ratio of H-abstractions by OH also affected significantly the predicted reactivity. The $HO_2+C_6H_5CH_2$ system investigated by da Silva and Bozzelli [296-298] plays a major role and its further refinement might lead to higher fidelity toluene mechanisms.

Relevant channels deserving further investigations are O and OH addition/substitution reactions leading to cresol ($HOC_6H_4CH_3$) and parent radicals ($OC_6H_4CH_3$, $HOC_6H_4CH_2$) chemistry.

Figure 138 shows an additional comparison with the JSR data of Dagaut et al. [346] and Yuan et al. [295] at φ~1.5.
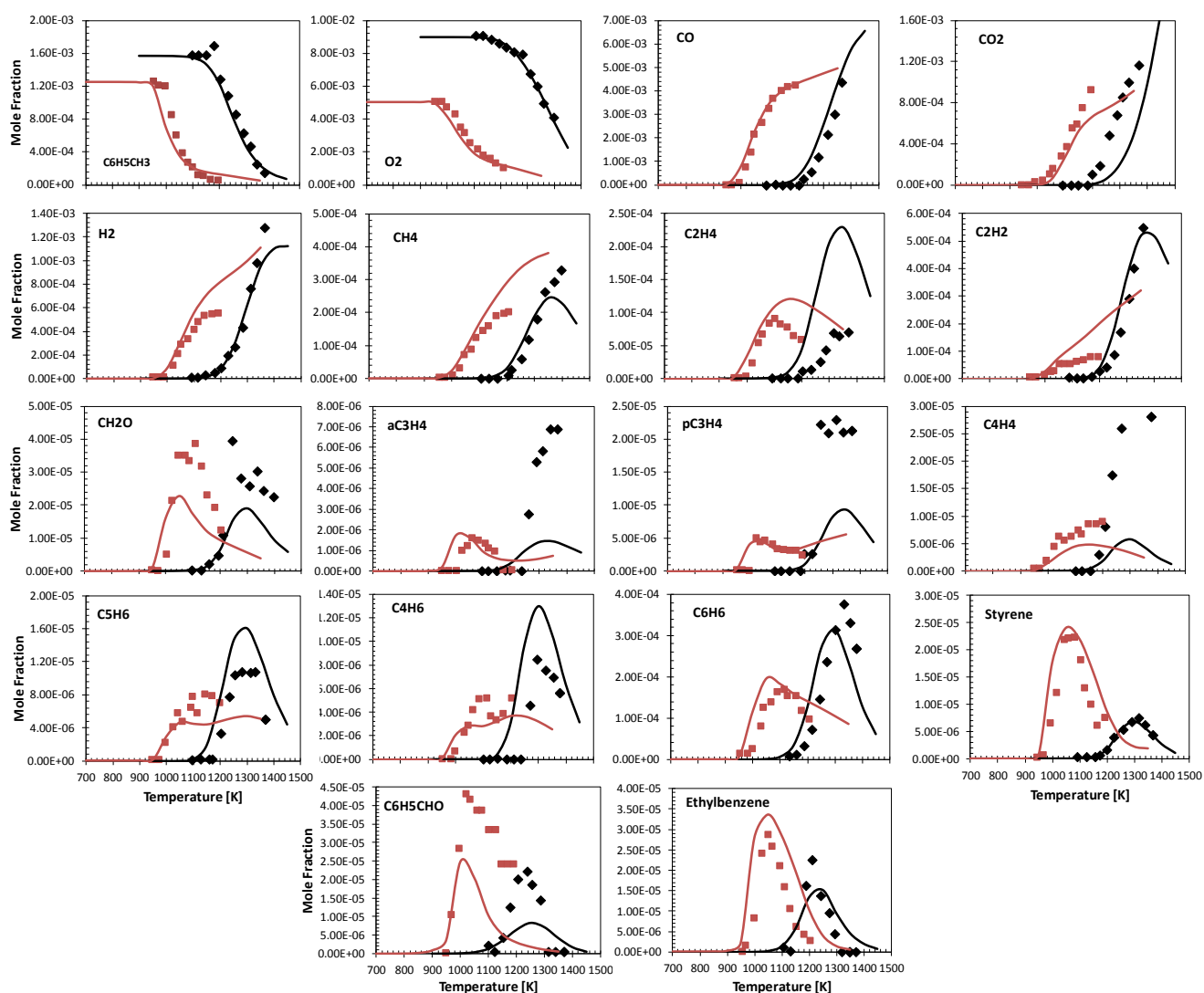
Figure 138: Speciation in an isothermal jet stirred reactor. 0.15% toluene/O_2/N_2, φ=1.5, p=1 atm, τ=1.0 s (black). 0.12% toluene/O_2/N_2, φ=1.5, p=10 atm, τ=0.5 s (red). Symbols: experimental data [295, 346], lines: updated POLIMI.

Ignition delay time measurements at low (1-6.81 atm) and high (12-50 atm) pressure from the literature are compared with model predictions in *Figure 139* and *Figure 140* respectively. Refer to *Table 20* for references to the experimental studies.
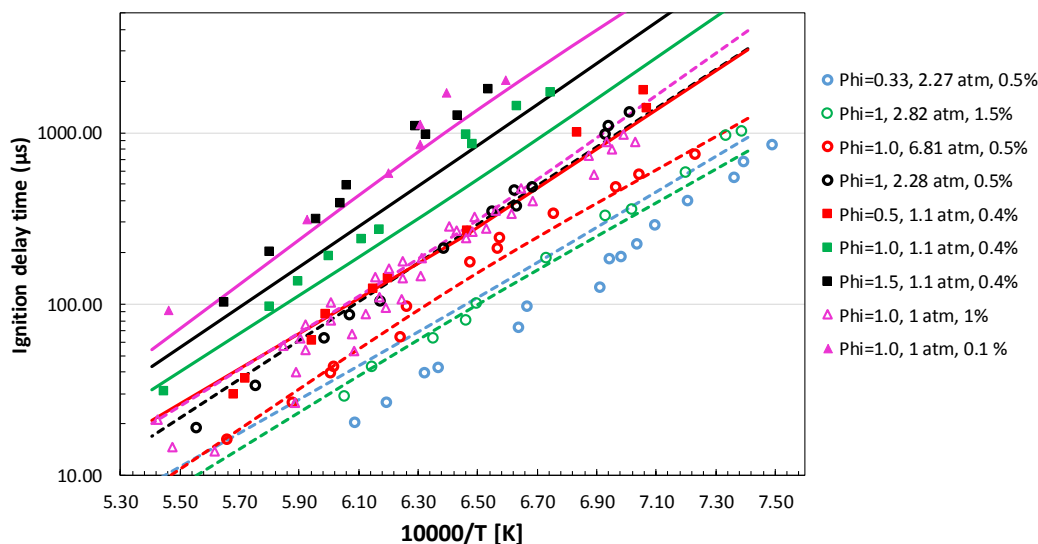
Figure 139: Ignition delay times for toluene/O₂/Ar mixtures at 1-6.81 atm pressure and φ=0.33–1.5.
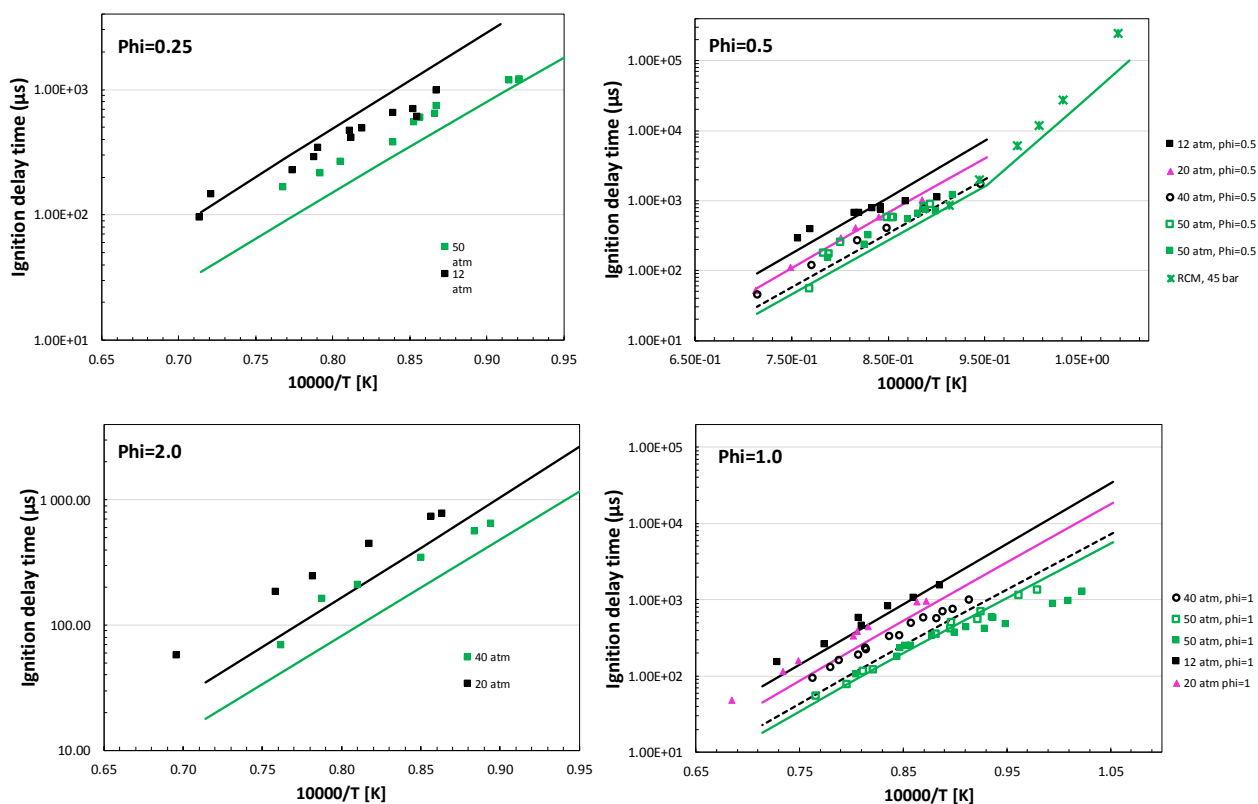
Figure 140: Ignition delay times for toluene/air mixtures at 12-50 atm pressure and φ=0.25-2.0.

Higher pressure ignition delay times are reported in *Figure 140* for fuel/air mixtures at φ=0.25, 0.5, 1.0 and 2.0. Except for the case at φ=2.0, the agreement is mostly within the experimental uncertainty (~1.2–1.4).

Results from sensitivity analysis highlighting the influence of temperature, pressure and equivalence ratio on key reaction channels are reported in *Figure 141*. The most important reactions are once again H-abstractions by OH where the production of benzyl inhibits reactivity while the H-abstraction from the ring enhances reactivity. The most sensitive reactions are the H-abstraction by $O_2+C_6H_5CH_3=HO_2+C_6H_5CH_2$ previously discussed and the following interactions of $H\dot{O}_2$ and benzyl.
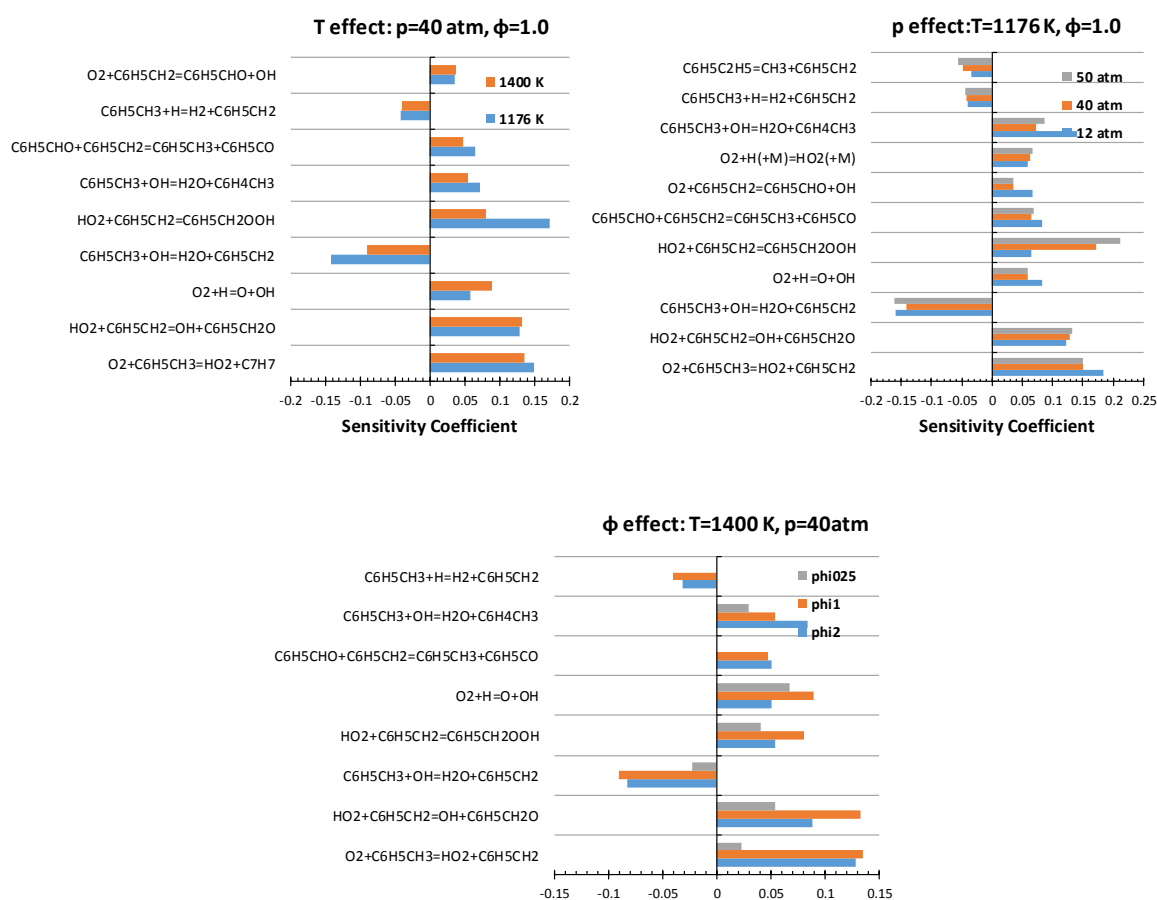
Figure 141: Sensitivity coefficients of ignition delay times to rate constant for toluene/air mixtures.

Figure 142 shows a rate of production analysis for toluene/air stoichiometric mixtures at p=12 atm and T=1175 and 1400 K. At higher temperatures H-abstractions from the ring dominates over benzyl radical formation. Successive interactions of methylphenyl radicals with molecular oxygen lead to an increase in reactivity as reported in Figure 141. At lower temperatures benzyl radical mostly undergoes self-recombination to form bibenzyl or interacts directly with oxygen to form benzaldehyde and OH. The

importance of $HO_2+C_6H_5CH_2$ increases for increasing temperature and pressure as also observed by Zhang et al. [218].
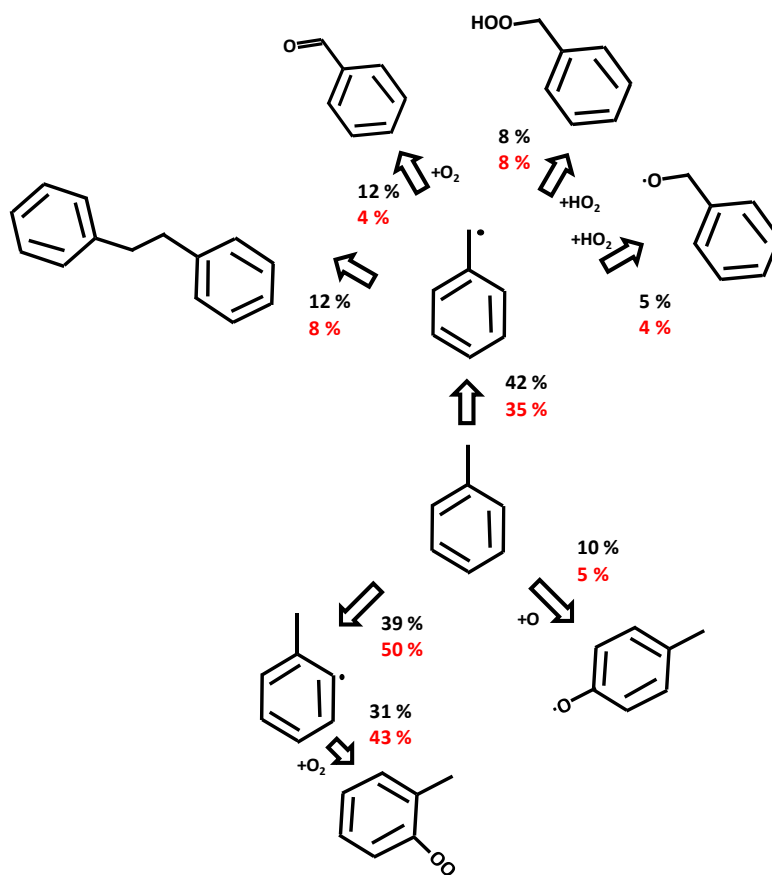
Figure 142: Rate of production analysis at 20% fuel consumption for toluene/air mixtures at φ=1.0, p=12 atm and T=1175 (black) and 1400 K (red). Adiabatic constant volume simulation.

*Figure **143*** compares experimental laminar flame speeds of toluene/air mixtures at 298 K and 1 atm with predictions from the POLIMI1412 mechanism and from the updated version whose performance is significantly improved.
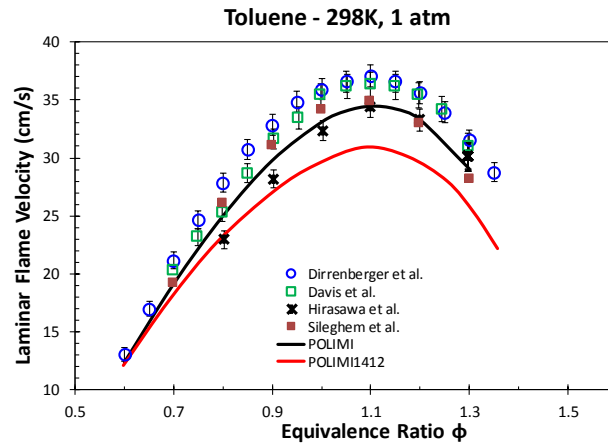
Figure 143: Laminar flame speed of toluene/air mixtures at T_u=298 K and p=1 atm. Symbols: experimental data [273, 277, 348, 350], black line: updated POLIMI mechanism, red line: POLIMI1412.

Chapter 6 – Kinetic Modeling of Oxygenated Biofuels Combustion: Alcohols and Aldehydes.

This Chapter reports results from the research activity carried out on oxygenated fuels pyrolysis and oxidation. The first part described in Section 6.1 is devoted to alcohol oxidation. The revision and extension of propanol and butanol isomers high temperature oxidation to pentanol isomers is described in Section 6.1.1, while the development of a lumped low temperature mechanism for n-butanol is discussed in Section 6.1.2. The systematic extension to n-pentanol and n-hexanol generally provides good agreement with high pressure ignition delay time data and speciation measurements. Some inconsistencies are highlighted between n-hexanol unpublished model predictions and new experimental data [361] at low temperatures and atmospheric pressure. Results suggest the systematic revision of alcohols low temperature oxidation starting from ethanol. This investigation coupled with a better theoretical assessment of key reaction pathways [4, 77] can allow a complete definition of the role of the hydroxyl moiety at low temperatures, characterizing the ignition propensity of alcohols.

Section 6.2 focuses on aldehydes high and low temperature oxidation in Section 6.2.1 [78] and 6.2.2, respectively [77]. Aldehydes are known to be dangerous compounds released from the combustion of transport fossil and bio-fuels. In particular aldehydes are primary decomposition products of alcohols oxidation and pyrolysis. The hierarchical development of alcohols kinetics requires the implementation of an accurate sub-mechanism for the parent aldehyde. Extension to recent experimental data on n-hexanal [362] proves the reliability of the proposed approach and rules to the kinetic modeling of aldehydes.

The last Section 6.3 compares and highlights the main reaction pathways characterizing the combustion behavior of oxygenated fuels: alcohols, aldehydes, ketones, methyl esters [77]. Starting from a consistent assessment of C–H and C–C bond dissociation energies (BDEs), their impact on the selectivity of the different H-abstraction reactions and their relative reactivity are analyzed.

Section 6.4 compares the global POLIMI mechanism thus obtained with recent experimental data on TRFs and TRFs/butanol blends [35] and PRFs/butanol blends [34].

6.1 Alcohols

6.1.1 Laminar Flame Speeds of Pentanol Isomers: an Experimental and Modeling Study [75].

1. Introduction

In order to decrease green-house gases and increase energy independence, new combustion modes are currently being developed that will likely require fuel reformulation. Furthermore, regulations impose blending petroleum-based fuels with biofuels up to 20%. Consequently, it is mandatory to study the impact of biofuel addition on fundamental combustion parameters and especially on pollutant emissions. Ethanol for example is widely used alone or blended with gasoline. However, ethanol is problematic due to both its supply source and its pollutant emissions. Indeed, ethanol-gasoline and diesel blend engine-out emissions showed high concentration of carbonyl species (e.g., acetaldehyde). These compounds present an air quality concern since they are toxic and irritating, as well as being precursors of urban smog (e.g., free radicals, ozone. and peroxyacetyl nitrates) [4]. To overcome these two aspects, heavier alcohols, such as 1-pentanol and iso-pentanol, are foreseen as a suitable replacement for ethanol, constituting the next generation of biofuels. Moreover, pentanol isomers have several advantages compared to ethanol such as a higher energy density, a higher boiling point and a lower hygroscopicity [363]. Up to now, only few experimental studies were reported in the literature. Togbé et al. [364] studied 1-pentanol oxidation in a Jet Stirred Reactor (JSR) and in a 23.32 L combustion bomb. Flame speed results were presented and the unstretched laminar flame speed was derived using a non-linear relation. They also proposed a detailed chemical kinetic mechanism. Li et al. [363] measured laminar flame speeds of three pentanol isomers in a 5.35 L cylindrical vessel and used a linear relation to extrapolate the unstretched laminar flame speed. In a very recent work, Li et al. [363] have revised these data using the non-linear method. More recently, Heufer et al. [365] presented a detailed kinetic model for 1-pentanol oxidation validated against ignition delay time, speciation in JSR and laminar flame speed data. For iso-pentanol, a detailed kinetic model was presented by Dayma et al. [366] and validated against speciation data from JSR. Recently, Sarathy et al. [367] developed another detailed chemical kinetic model validated against shock tube and rapid compression machine ignition delay times, speciation from JSR and counterflow premixed flame speed data.

The primary objective of the present work is to obtain new experimental laminar flame speed data, with the best accuracy possible for iso-pentanol and 1-pentanol. Laminar flame speeds of iso-pentanol and 1-pentanol in air were measured, in a 56 L spherical bomb, at three initial temperatures 353, 433

and 473 K. The initial pressure was fixed at 1 bar and the equivalence ratios varied from 0.7 to 1.5. For details on the experimental facility, uncertainty quantification and a comparison with other experimental data from the literature the reader is referred to the original paper of Nativel et al. [75].

The updated mechanism for alcohol combustion from CRECK group at Politecnico di Milano (POLIMI) is discussed in Section 2 and comparisons with experimental data are reported in Section 3. The high temperature mechanism is based on previous studies of alcohol fuels [368-370].

2. High temperature kinetic mechanism

Figure 144 and Figure 145 show simplified primary decomposition mechanisms of *1-pentanol* and *iso*-pentanol respectively. A radical chain initiates at high temperature via unimolecular initiation reactions leading to the formation of two radical species. Both C–C and C–H bond breakings (not reported in Figure 15 and 16) are included in the mechanism here discussed. Molecular dehydration and dehydrogenation reactions involving a four center cyclic transition state lead to the formation of the corresponding alkene or aldehyde respectively. Six different radicals are generated via H-abstraction reactions from *1-pentanol*. Only five radicals are considered for *iso*-pentanol due to the symmetry of the primary δ positions (6 primary hydrogen available for H-abstraction). These radicals can isomerize via 5-, 6- or 7-member ring intermediates or decompose via β-decomposition reactions to smaller radicals and unsaturated species. Beside the fuel specific reactions, consumption pathways for important intermediates have been included. For the unsaturated alcohols (*1-* and iso-pentenol) kinetic parameters are based on smaller enols already included in the mechanism. It has to be noticed that a single species representative of all the possible isomers is considered for *1-* and iso-pentenol. Aldehyde specific reactions are from a recent study of the high temperature oxidation of n-C$_3$–C$_5$ aldehydes [78]. While high temperature kinetics for n-pentanal were already included in the mechanism, rate parameters for *iso*-pentanal were derived based on analogy rules.

Unimolecular intitiation reactions

CBS-QB3 calculations were carried out by Zhao et al. [371] to systematically investigate the dominant reaction channels of the thermal decomposition of three pentanol isomers: *1-pentanol* (*1*-pentanol), 2-methyl-1-butanol, 3 methyl-1-butanol (*iso*-pentanol in this study). Subsequently the same authors computed temperature and pressure dependent rate constants by RRKM/ME. Figure 146 shows a comparison of the high pressure limit rate constants as calculated by Zhao et al. [371] and those included in the kinetic mechanism of POLIMI discussed here. Activation energies are consistent with the previous study on butanol isomers by Grana et al. [369], frequency factors have been updated to improve agreement with values from Zhao et al. [371]. An average factor of ~2 is observed between

proposed rate constant values and those adopted in this study. Relative selectivities to the different channels involving a C–C bond breaking at 1500 K are also reported in the graph, showing good agreement between the two sets of rate constants.

Similar deviations, still within kinetic uncertainty, are also observed for *iso*-pentanol decomposition reactions. A recent study by Sarathy et al. [367] highlighted the need to increase the A factor (10 times) for the reaction leading to the formation of a methyl radical and γ-hydroxybutyl radical to improve agreement with the experimental data. Considering this large uncertainty, the rate constant proposed by Grana et al. [369] for the analogous channel of *iso*-butanol has been increased by a more careful factor of 3.5, as detailed in Figure 147. Moreover, also shown in Figure 147, a correct activation energy of ~88 kcal/mol was proposed by Grana et al. prior to any detailed calculation was available in literature. The total decomposition rate constant is also reported at the bottom right of Figure 146.

Concerning C–H bonds the presence of the hydroxyl moiety weakens the adjacent C_α-H (~95 kcal/mol) with respect to a secondary C–H in alkanes (~99 kcal/mol). As a consequence C_β-H bonds are slightly stronger than the corresponding bond in alkanes of (~1-2 kcal/mol) [4], while C_γ-H are not strongly influenced by the presence of the OH group. The O-H Bond Dissociation Energies (BDE) are high for every alcohol fuel (~105 kcal/mol), therefore unimolecular reactions involving the scission of this bond do not significantly contribute to fuel decomposition. Although unimolecular reactions involving the breaking of a C–H bond are less important, they are all included in the mechanism because of the possible influence on flame propagation. The same reference kinetic parameters for the reverse recombination reaction

H+R' = R'H $k = 5.0 \times 10^{13} \, [cm^3 \, mol^{-1} \, s^{-1}]$
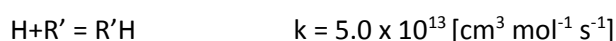
is adopted, where R'H is the fuel molecule and R' is the fuel radical derived from the C–H fission. Harding and coworkers [372] systematically analyzed H+R' reactions for a set of hydrocarbon radicals suggesting values ranging between $3.6 \cdot 10^{13}$ and $1.6 \cdot 10^{14}$ at T= 1000 K for $H+C_2H_5$, $H+i-C_3H_7$ and H+tert-C_4H_9, respectively.
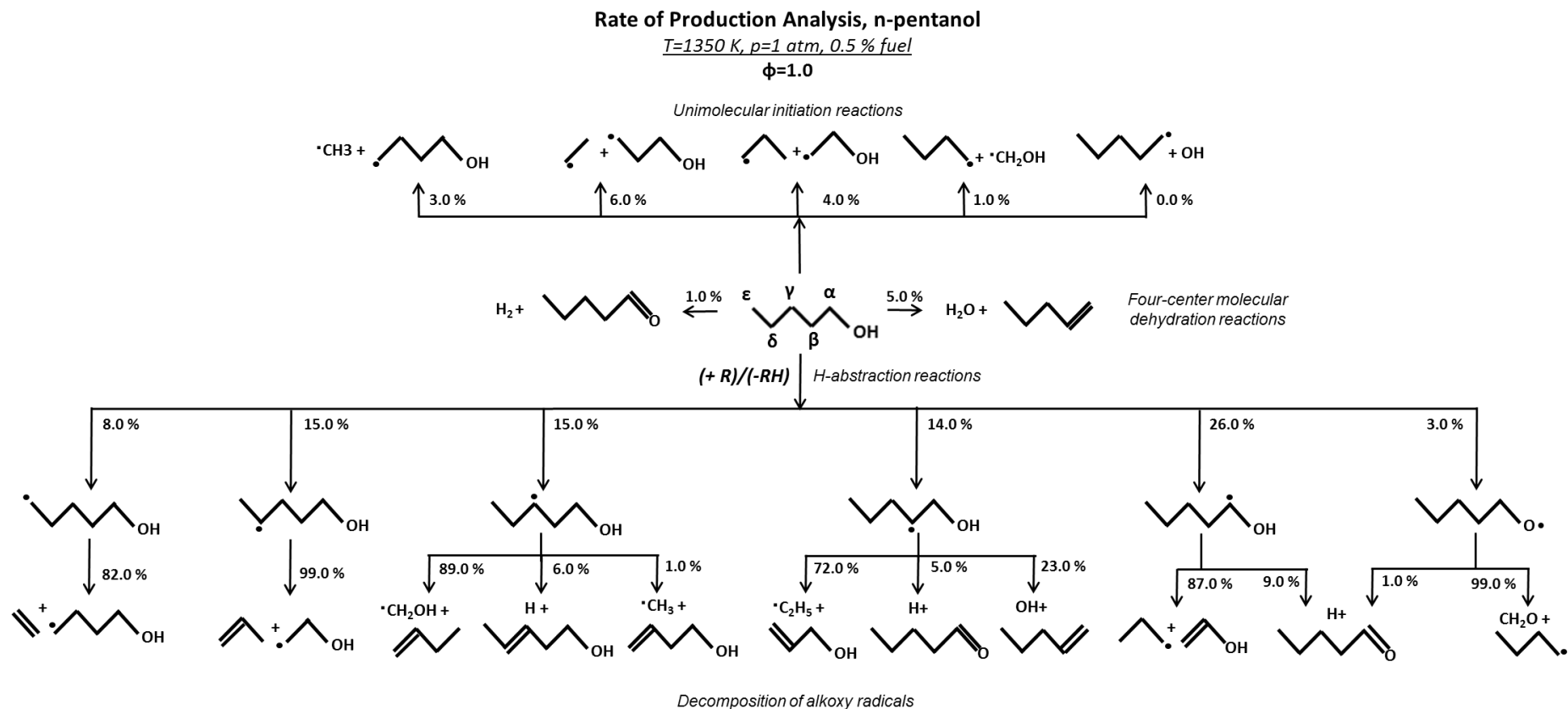
Figure 144: Primary decomposition reactions of 1-pentanol. Unimolecular initiation reactions involving C–H bond breakings and isomerization channels have been omitted for clarity. Global reaction path analysis for 1-pentanol at 1350 K, 1 atm, φ=1.0. Isomerization contributions can be deduced by closing the balance of individual radical decomposition channels to 100%.
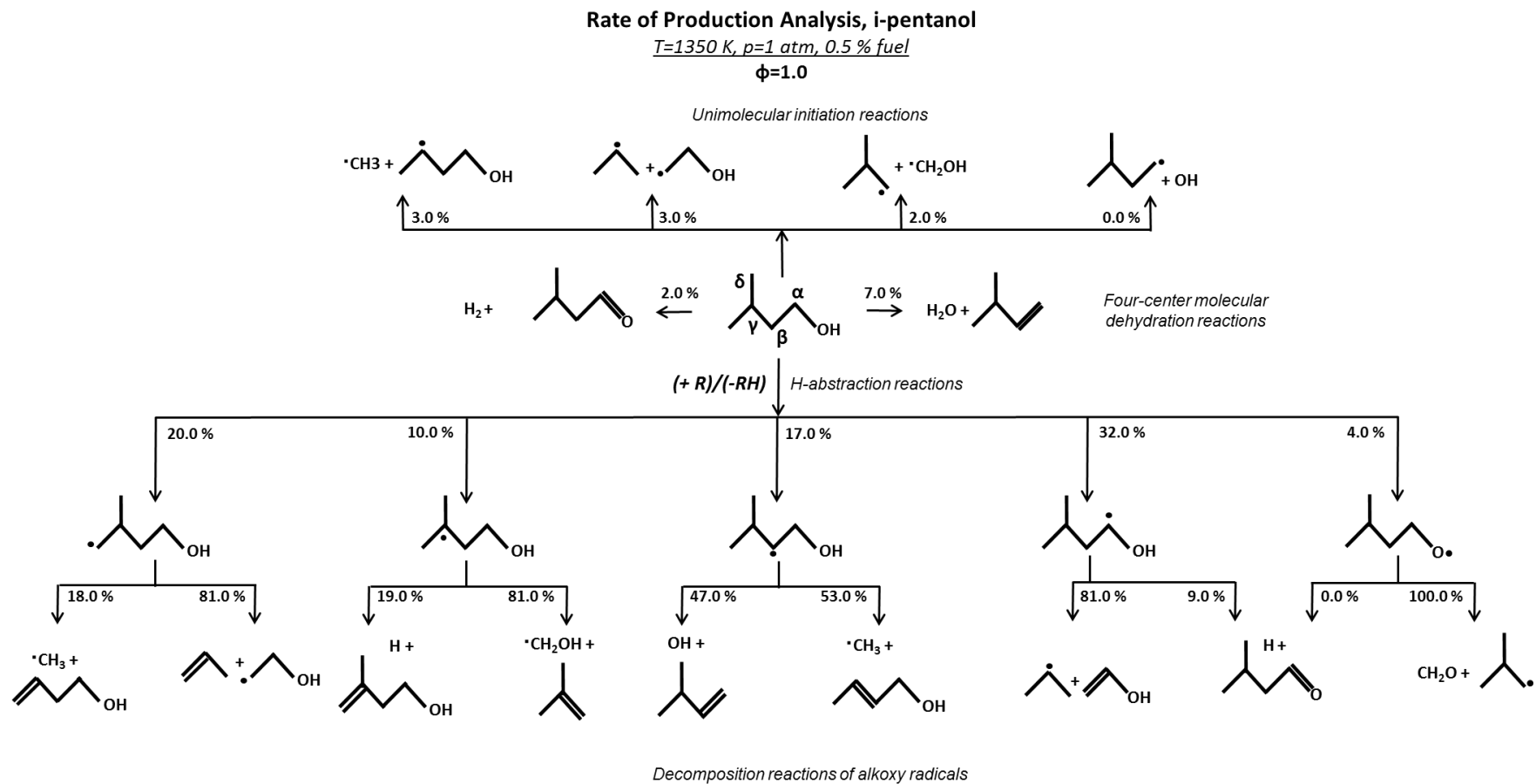
Figure 145: Primary decomposition reactions of iso-pentanol. Unimolecular initiation reactions involving C–H bond breakings and isomerization channels have been omitted for claritity. Global reaction path analysis for iso-pentanol at 1350 K, 1 atm, φ=1.0. Isomerization contributions can be deduced by closing the balance of individual radical decomposition channels to 100%.
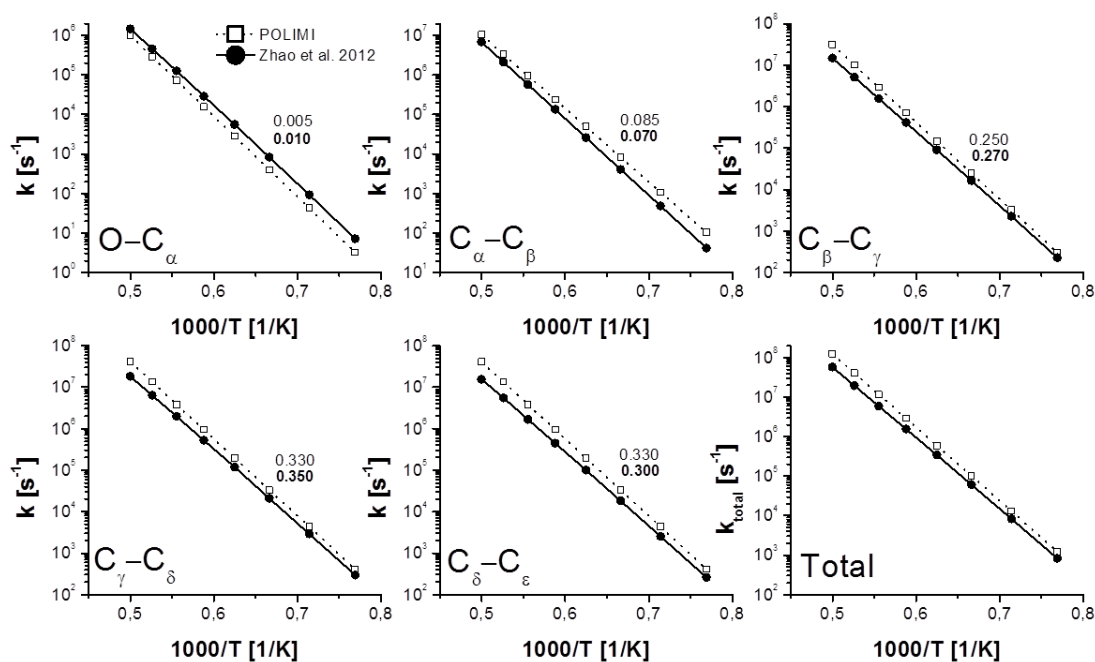
Figure 146: High pressure limit rate constants (s⁻¹) for 1-pentanol decomposition channels, and total decomposition rate constant. Comparison between values from Zhao et al. [371] and those adopted in this study. Values reported inside graphs represent relative selectivities of the different C–C unimolecular channels at 1500 K: this study (plain), Zhao et al. (bold).
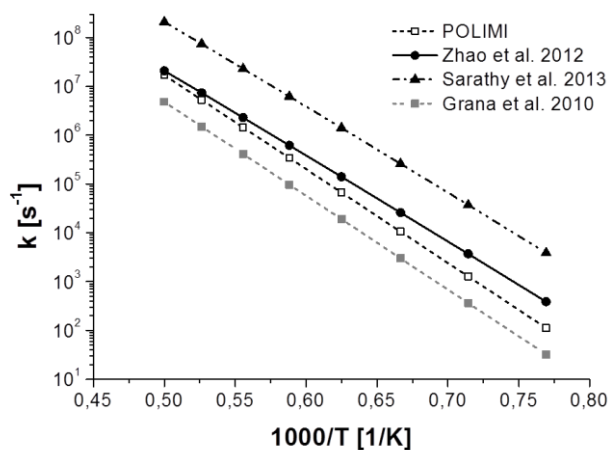
Figure 147: Rate constant [s⁻¹] of the decomposition of iso-pentanol to methyl radical and γ-hydroxybutyl radical. Comparison between values from Zhao et al. [371], Sarathy et al. [367], Grana et al. [369] (iso-butanol) and that adopted in this study.

H-abstraction reactions

Rate parameters of H-abstraction reactions are based on the systematic approach described elsewhere [52]. As reported in Grana et al. [369], the kinetic parameters for the H-abstraction from the hydroxyl group are assumed to be equal to those of a primary H atom from a methyl group. To account for the weakened C_α-H bond discussed in the previous section, the reference kinetics for a secondary site in alkanes have been increased by 50%. Remaining primary, secondary and tertiary sites are treated according to alkane rules in their general form of R+R'H=RH+R', where R'H is the fuel molecule and R is the generic abstracting radical.

H-abstractions by $\dot{H}$, $\dot{O}H$ and $H\dot{O}_2$ have been carefully considered, being dominant paths over the conditions explored in this study. Figure 148 shows relative selectivities of metathesis reactions by $\dot{H}$, $\dot{O}H$ and $H\dot{O}_2$ as adopted in this study (panel a and b) and those from similar studies of 1- and iso-pentanol (panel c and d) [365, 367]. Consistent with the C–H BDEs discussed in the previous section, abstraction from the α-site dominates for both fuels, β-sites are slightly less selective than an alkane-like secondary H-atom abstraction (i.e. γ-site and δ-site for 1-pentanol) and more selective than the single tertiary H-atom available at the γ-site for iso-pentanol. Lower contributions to the fuel decomposition through H-abstraction are those coming from the O-H group. Selectivities on primary ε (1-pentanol) and δ (iso-pentanol) are respectively ~3 times and ~6 times higher than that of the primary H-atom of the hydroxyl moiety.

According to Heufer et al. [365] 70% of the abstracting $H\dot{O}_2$ reacts at the α-site for *1-pentanol* resulting in a much lower selectivity on secondary β and γ sites. In general, a more homogeneous distribution between secondary sites is observed in *1-pentanol* selectivities from this study compared to those of Heufer [365]. Good agreement between the two studies is found for δ and ε positions.
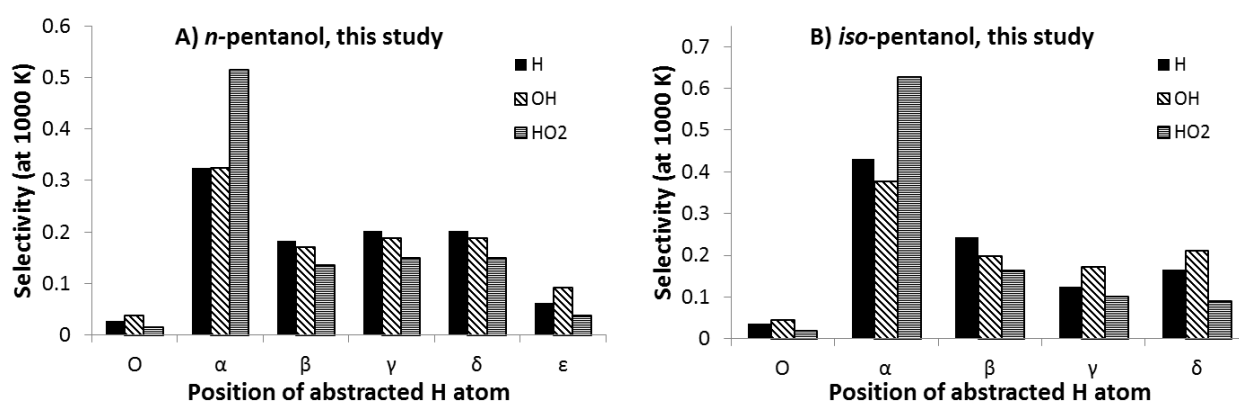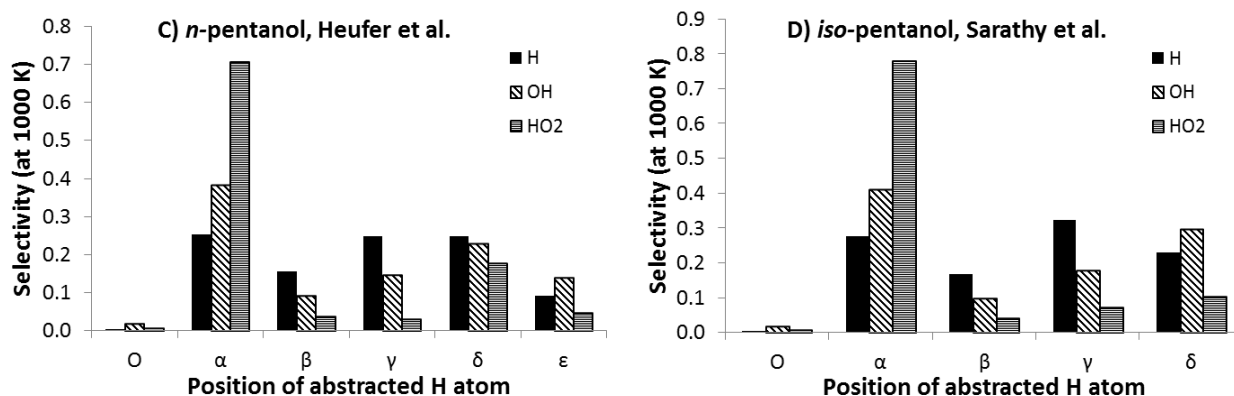
Figure 148: Selectivity of the abstracted H-atom to form primary $C_5H_{11}O$ radicals from H-abstraction reactions by $\dot{H}$, $\dot{O}H$ and $H\dot{O}_2$ at T=1000 K. 1-pentanol (panel a) and iso-pentanol (panel b) from this study, and previous works from Heufer et al. [365] and from Sarathy et al. [367].

Similar trends are observed for the analogous α-abstraction reaction in *iso*-pentanol. According to Sarathy et al. [367], up to 80% of abstraction by $H\dot{O}_2$ occurs at the weakened α secondary site resulting in a decreased selectivity to β. Selectivity of H-abstraction by $\dot{H}$ on tertiary γ is about twice that proposed in this study. Good agreement is found for the 6 primary hydrogens available at the primary δ position.

Table S3 in the Supplemental Material reports rate constants for hydrogen abstractions for *1*- and *iso*- C_4 and C_5 alcohol fuels, highlighting the internal consistency existing between alcohol fuels in the POLIMI mechanism.

Decomposition reactions of alkoxy radicals

Kinetic parameters of alkoxy radicals decomposition have been discussed previously by Frassoldati et al. [368]. Alkoxy radicals from primary alcohols with n carbon atoms can decompose to form a C_{n-1} alkyl radical and formaldehyde or dehydrogenate to give the corresponding C_n aldehyde. The first channel prevails over the dehydrogenation channel in the whole temperature range of interest to this study. Dehydrogenation of α-alkyl radicals leads to the formation of the corresponding aldehyde, while its decomposition produces vinyl alcohol, assumed to be instantaneously transformed into acetaldehyde via keto-enol tautomerism, and an alkyl radical. Based on analogy, reference kinetic parameters already adopted in previous studies for smaller alcohols have been adopted [368, 369]. Kinetic data for other alkyl-hydroxy radical decompositions and isomerization are the same as those for alkanes [17, 90, 152]. Kinetic parameters for this class of reaction are reported in the Supplemental Material (Table S3).

Isomerization reactions

1-4, 1-5 and 1-6 H-transfer reactions, via 5-, 6- or 7- membered rings play a significant role at low-intermediate temperatures (700–1100 K). The number of atoms in the transition state ring structure and the type of sites involved allows estimation of rate parameters according to rules proposed by Dente et al. [152]. To account for the differences between BDEs of a standard C–H primary bond and that of an O-H bond, an extra 1.5 kcal/mol energy is added when an oxygen atom is incorporated in the cyclic intermediate. The same rule was applied in the previous work on butanol isomers by Grana et al. [369]. Table S3 in the Supplemental Material reports rate constants for isomerization reactions. The largest contribution to *1*-pentanol isomerization channels comes from the primary ε radical, turning into α secondary radical through a 6-membered ring transition state, followed by the 5-membered isomerization leading from α to δ. δ-radical also undergoes isomerization to form the alkoxy radical, via a 6-membered ring. The net result at ~1000 K is that about 70% of the ε-radical turns into the alkoxy radical and partially into the α radical. Concerning *iso*-pentanol oxidation, at ~1000 K about 20% of the α-radical is consumed through the internal H-abstraction reaction (5-membered cyclic intermediate) from the 6 primary hydrogen atoms sited in δ positions. This constitutes the most important isomerization channel. A non-negligible contribution also comes from the 6-membered ring isomerization turning delta into the alkoxy radical.

Four-center molecular dehydration and dehydrogenation reactions

Dehydration reactions (Figure 149) are the main source of pentene isomers in *1*- and *iso*-pentanol combustion at temperatures higher than ~1200 K. Only those proceeding via a four-center transition state ring are generally considered in alcohol kinetic models being both thermodynamically and kinetically favored according to calculations by Moc et al. [373]. Reference kinetic parameters were defined by Grana et al. [369] for reactions involving a primary OH group and a single primary H atom

$k = 5.0 \times 10^{13} \exp[-68600/(RT)] \, [s^{-1}]$

Corrections need to be applied to the reference rate constant to account for the secondary H-atom involved (-1000 cal/mol to the activation energy, factor of 2 increase to the frequency factor).
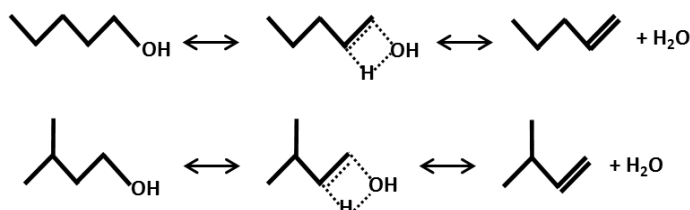
Figure 149:Dehydration reactions of 1- and iso- pentanol to form 1-pentene and 3-methyl-1butene respectively.

The mechanism also includes a similar class of four-center dehydrogenation reactions leading to the formation of hydrogen and a carbonyl compound in alcohol combustion (Figure 150). In the case analyzed here dehydrogenation reactions constitute a major path to the formation of *iso*-pentanal and *n*-pentanal respectively for *1*- and *iso*-pentanol. The interest of this reaction class at high temperatures (> 1300 K) and low pressure was already discussed in the C_4 alcohols mechanism by Grana et al. [369]. Despite its important contribution to the formation of acyl compounds (aldehydes from primary alcohols and ketones from secondary alcohols) this reaction was neglected in the previous comprehensive studies on pentanol isomers by Heufer [365] and Sarathy [367]. Due to the analogous transition state configuration (see Figure 21) the same kinetic parameters are assumed for both *1*- and *iso*-pentanol.

$$k = 5.0 \times 10^{13} \exp[-69500/(RT)] \; [s^{-1}]$$
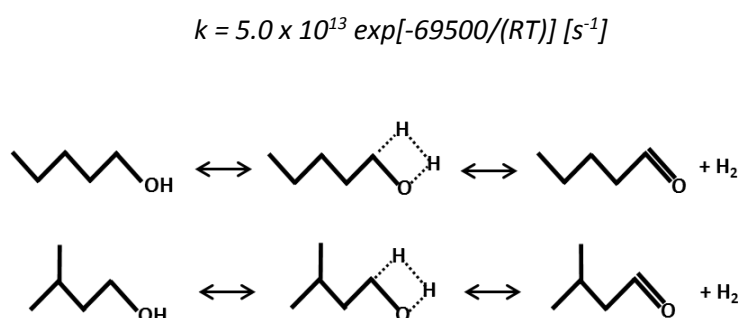
Figure 150: Dehydrogenation reactions of 1- and iso- pentanol to form n- and iso-pentanal.

3. Results and discussion

The oxidation mechanism used to describe the high temperature oxidation of pentanol isomers, consisting of 230 species and 7885 reactions, is available with thermo and transport properties in the Supplemental Material attached to this study and online (http://creckmodeling.chem.polimi.it). Thermochemical and transport parameters for the two isomers and related radicals were adopted from Heufer et al. [365] (1-pentanol) and from Sarathy et al. [367](iso-pentanol).

Details on the approach to the solution of the steady, freely propagating, adiabatic flames are reported in the original paper [75].

Laminar Flame Speeds

Figure 151 shows a comparison between the experimental data from this study and calculated atmospheric laminar flame speed for *1*-pentanol/air mixtures at three different initial temperatures. Not surprisingly, sensitivity coefficients reported in Figure 152 do not highlight any fuel specific reaction to be of importance, limiting the kinetics governing laminar flame propagation to the hydrogen-syngas-methane sub-mechanism.
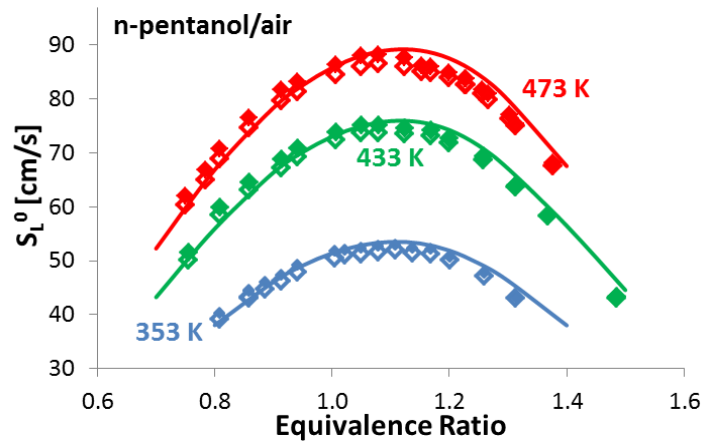
Figure 151: Laminar flame speeds of 1-pentanol/air mixtures, at p=1 bar, and T_u=353 K, 433 K, 473 K. Experimental data from this study. Open symbols: non-linear stretch correction, full symbols: linear stretch correction, lines: simulations.
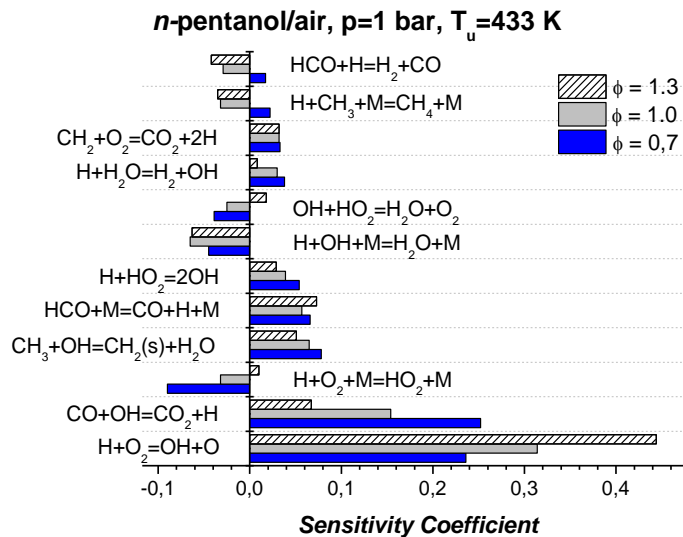
Figure 152: Sensitivity coefficients of laminar flame speed to reaction rate coefficients, for rich (φ=1.3), stoichiometric (φ=1.0) and lean (φ=0.7) 1-pentanol/air flames at p=1 bar and T_u=433 K.

In Figure 153, the calculated laminar flame speeds have also been compared with previous experimental measurements from Togbè et al. [364] and Li et al. [363]. Following the discussion of Section 3.2 in the original paper [75], the model is compared also with Togbè et al. [364] data at 423 K (air composition 20.5% O_2, 79.5% N_2). While good agreement is found for lean to stoichiometric conditions, the model starts to deviate for φ>1.0, predicting a flame speed up to ~11 cm/s higher than the measured value at φ=1.4. A similar behavior is observed in the case of Li et al. [363] at 433 K.
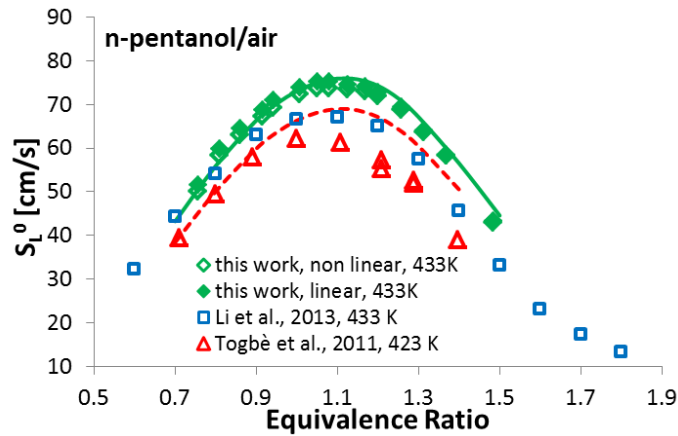
Figure 153: Laminar flame speeds of 1-pentanol/air mixtures, p=1 atm, T_u=433 K. Experimental data from this study (diamonds) and from previous studies [363, 364]. Open diamonds: non-linear stretch correction (this work), full diamonds: linear stretch correction (this work), open squares: Li et al. [363], open triangles: Togbè et al. [364] (T_u=423 K). Solid line: simulation at T_u=433 K, dashed line: simulation at T_u=423 K. Simulations of Togbè et al. have been performed in 20.5%O_2-79.5%N_2 air.

Figure 154 shows a comparison between measurements of Li et al. [363] at T_u=433 K and varying pressure [0.1-0.75 MPa] for both *1*-pentanol (left panel) and *iso*-pentanol (right panel). Despite the observed deviations whose possible reasons have been discussed in Section 3.2 [75], the model is able to accurately reproduce the pressure effect on laminar flame speeds of both fuels. Once again good agreement is found from lean up to stoichiometric conditions. Comparisons with other data from Li et al. [363] at 0.1 MPa and different initial temperatures (393 K, 433 K, 473 K) are reported in the Supplementary Material attached to this study (Figure S5).
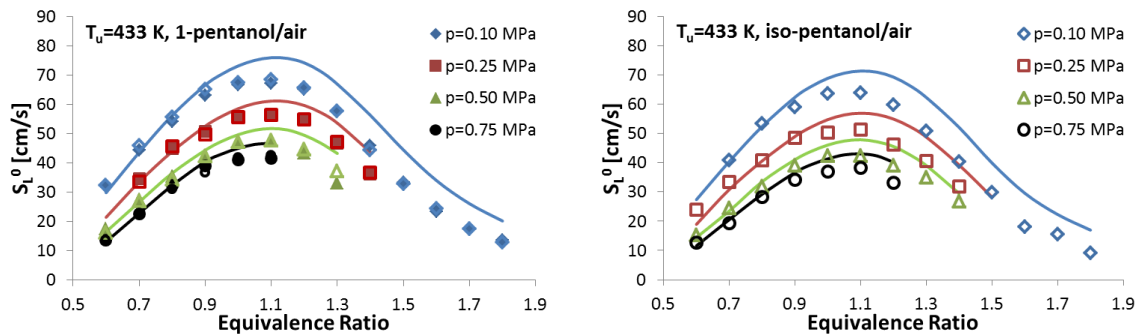
Figure 154: Laminar flame speeds of 1-pentanol/air (left panel) and iso-pentanol/air (right panel) at T_u=433 K and different pressures. Full symbols: experimental data by Li et al. [363], open symbols: experimental data by Li et al. [363], lines: simulations.

Calculated laminar flame speeds for *iso*-pentanol/air mixtures are compared to the experimental data from this work at three different initial temperatures and 1 bar pressure in Figure 155 showing satisfactory agreement. Data from Sarathy et al. [367] obtained in a counterflow configuration at 353 K are also reported in *Figure 155*. As previously observed (Section 3.2 in [75]), despite an overall reasonable agreement between the two different measurements at 353 K, data from Sarathy appears to be shifted towards leaner regions, resulting in a ~8 cm/s difference between model predictions and experimental measurements at ϕ=1.5.
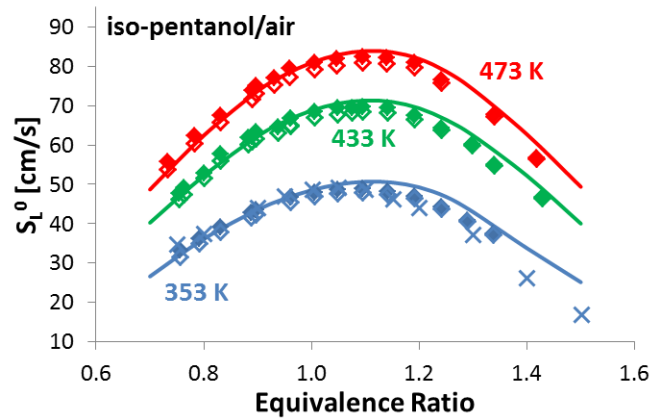
Figure 155: Laminar flame speeds of iso-pentanol/air mixtures, at p=1 atm, and T_u=353 K, 433 K, 473 K. Experimental data from this study (diamonds) and from Sarathy et al. [374] (crosses). Open symbols: non-linear stretch correction, full symbols: linear stretch correction, lines: simulations.

The same reactions previously highlighted as sensitive for *1*-pentanol flames are found to govern iso-pentanol flame propagation, as reported in the sensitivity coefficients of Figure 156. Nevertheless, comparing *1*- and *iso*-pentanol flame speeds at the same initial temperature conditions (433 K) in Figure 157, it can be noticed that *iso*-pentanol is clearly less reactive. In fact, *iso*-pentanol flame speeds are 3.9-5.5 cm/s slower than those of *1*-pentanol over the equivalence ratio range analyzed. This trend is satisfactorily reproduced by the numerical simulations as reported.
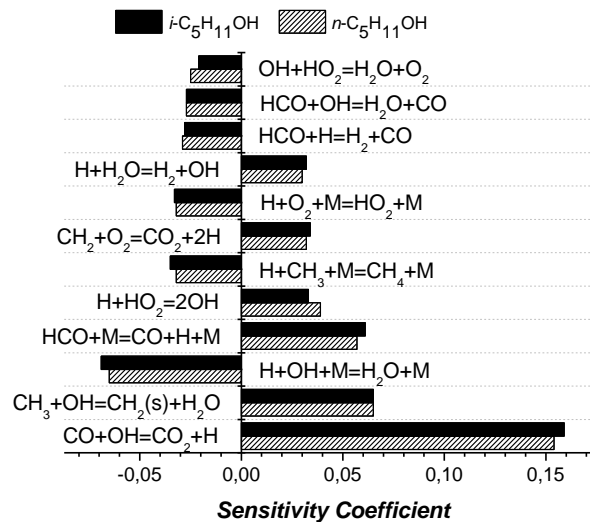
Figure 156: Sensitivity coefficients of laminar flame speed to reaction rate coefficients, for φ=1.0 1- and iso-pentanol/air flame at p=1 atm and T_u=433 K. The most sensitive reaction H+O$_2$=OH+O has been omitted for clarity.
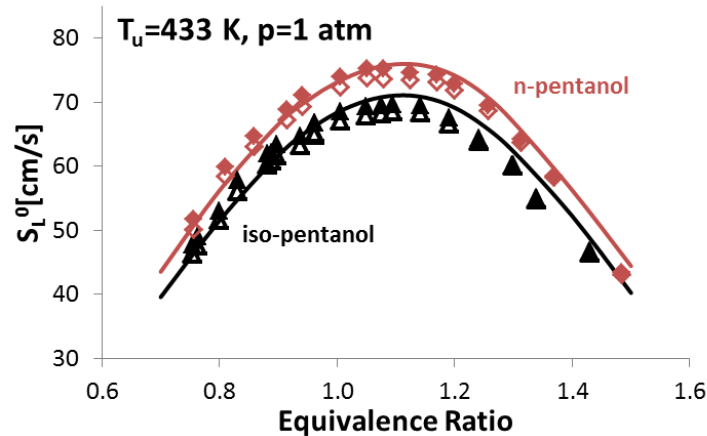
Figure 157:Laminar flame speeds of 1- and iso-pentanol/air mixtures, at p=1 atm, and T$_u$=433 K. Experimental data from this study. Diamonds: 1-pentanol, triangles: iso-pentanol. Open symbols: non-linear stretch correction, full symbols: linear stretch correction.

Since the adiabatic flame temperatures at φ=1.1 for *1-* and *iso-*pentanol/air flames are very similar (~2336 K and ~2330 K at 433 K initial temperature), reasons for the different reactivity have to be found in the kinetics of the two systems. Important intermediate species profile versus the axial position in a φ=1.1 atmospheric flame are reported in Figure 158 for both fuels. While *1-*pentanol mainly proceeds towards the formation of ethylene (see Figure 144), large amounts of propylene are formed in the *iso-*pentanol flame through the primary reactions shown in Figure 145.
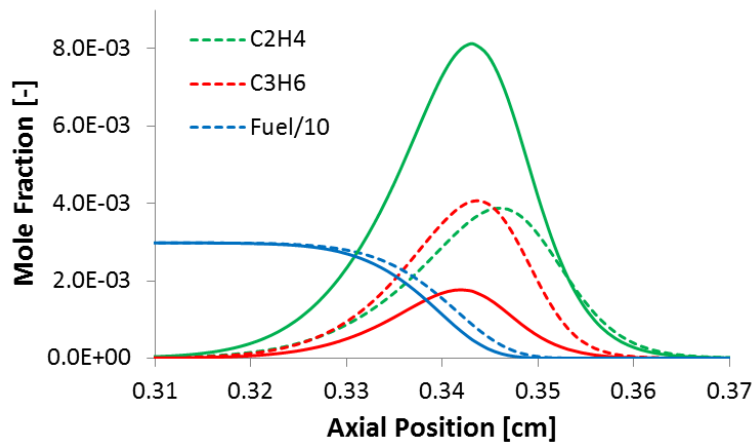
Figure 158: Species profile in a φ=1.1 atmospheric fuel/air flame at 433 K. Dashed lines: iso-pentanol, Solid lines: 1-pentanol.

Similarly to what was discussed by Ranzi et al. [101] in comparing pure ethylene and propylene/air flames, H-abstractions by $\dot{H}$ and $\dot{O}H$ on propylene mainly produce resonantly stabilized allyl radical (aC$_3$H$_5$), resulting in a reduced flame speed. Ethylene instead is mainly converted to vinyl radical (C$_2$H$_3$) via H-abstraction. The subsequent interaction of vinyl radical with molecular oxygen (O$_2$+C$_2$H$_3$=O+CH$_2$CHO) is known to largely promote flame propagation. Figure 159 reports a comparison of vinyl and allyl radical profiles in *1-* and *iso-*pentanol flames.
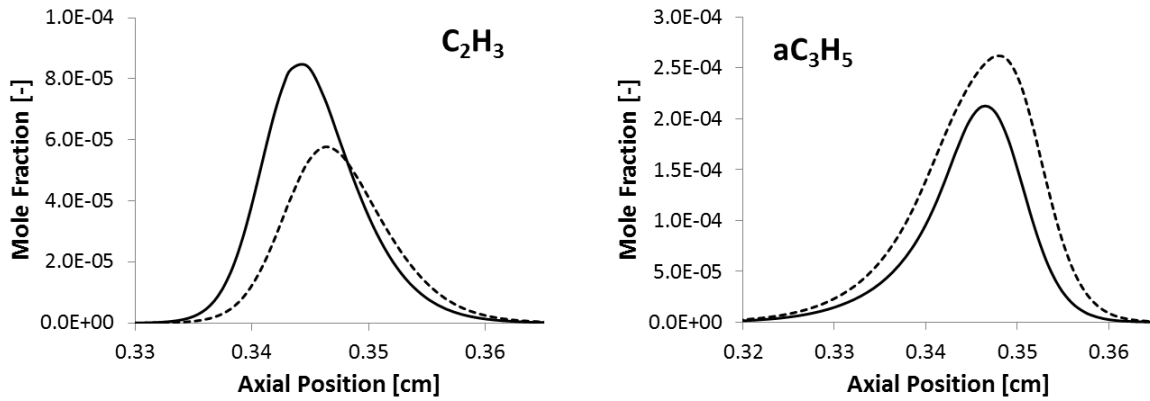
Figure 159:Radical species profile in a φ=1.1 atmospheric fuel/air flame at 433 K. Dashed lines: iso-pentanol, Solid lines: 1-pentanol.

To further validate *1-* and *iso*-pentanol high temperature chemistry, model predictions have been compared with the high temperature shock tube data presented by Tang et al. [375]. Results for 0.5% fuel/O_2/Ar mixtures at 1 atm reflected pressure are shown in Figure 160. Mixture composition in mole fractions and temperature conditions after the reflected shock [375] are reported in Table 21.

Table 21: Mixture composition in mole fractions and temperature conditions after the reflected shock as measured by Tang et al. and reported in Figure 31.

1-pentanol	x_{fuel}	x_{O2}	x_{Ar}	T [K]
ɸ=0.25	0.005	0.15	0.845	1222–1415
ɸ=0.50	0.005	0.0750	0.920	1202–1464
ɸ=1.00	0.005	0.0375	0.9575	1267–1482
iso-pentanol	x_{fuel}	x_{O2}	x_{Ar}	T [K]
ɸ=0.25	0.005	0.15	0.845	1203–1465
ɸ=0.50	0.005	0.0750	0.920	1214–1481
ɸ=1.00	0.005	0.0375	0.9575	1306–1570

The lower reactivity of *iso*-pentanol is once again confirmed by both experimental measurements and model predictions. Particularly the different reactivity of the two isomers is evident at stoichiometric conditions, while for leaner conditions (ɸ=0.5 and ɸ=0.25) the ignition delay times become closer. The model is able to

reasonably reproduce both the measured ignition delay times at any stoichimetry conditions, and the relative reactivity of *1*- and *iso*-pentanol.
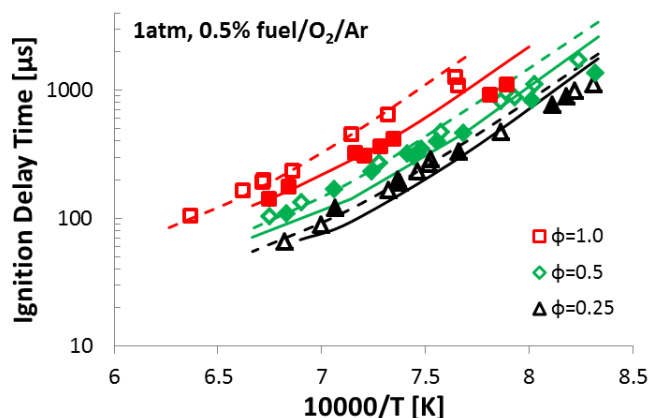
Figure 160: Ignition delay times for 1-pentanol and iso-pentanol at 1 atm. Experimental data by Tang et al. [375]. Open symbols/dashed lines: iso-pentanol, full symbols/solid lines: 1-pentanol.

Figure 144 and Figure 145 of Section 2 also present rate of production analyses at 1350 K and 1 atm pressure, for *1*- and *iso*-pentanol/O_2/Ar stoichiometric mixtures.

Unimolecular decomposition reactions are responsible for ˜15 % of *1*-pentanol consumption (Figure 144), mainly occurring through the cleavage of the C_γ–C_δ bond to form ethyl radical and γ-hydroxypropyl radical (·$CH_2CH_2CH_2OH$). A non-negligible contribution is given by the dehydration reaction to form *1*-pentene. Most of the fuel undergoes H-abstraction, mainly by $\dot{H}$ and $\dot{O}H$. The dominant channel corresponds to abstraction at the α site, followed by the secondary positions β, γ and δ. β-decomposition reactions of fuel radicals lead to the formation of smaller radicals and unsaturated species (olefins, aldehydes and enols). Isomerization contributions, of small magnitude under the flux analysis conditions, have not been reported for clarity. However, their relative importance can be deduced by closing the balance of fuel radical decompositions up to 100%.

Referring to Figure 145, unimolecular pathways in *iso*-pentanol oxidation are of even lower significance, compared to *1*-pentanol. A slightly larger contribution is observed for the dehydration channel, leading to the formation of *iso*-pentene. H-abstraction is largely dominated by the alpha channel, closely followed by the primary δ positions.

As already observed by Sarathy et al. [367] for *iso*-pentanol, the importance of the different reaction pathways is not sensitive to the equivalence ratio for both *1*-pentanol and *iso*-pentanol.

Following the observations of Figure 158 and Figure 159, predicted species profiles for the oxidation of stoichiometric fuel/O$_2$/Ar mixture at 1 atm and 1350 K analyzed at shock tube conditions are reported in Figure 161. Also in this case, *1*-pentanol oxidation directly proceeds through the formation of ethylene. On the contrary larger amounts of less reactive propylene are formed in *iso*-pentanol oxidation. Ethylene peaks later and is consumed correspondingly to ignition (represented by OH profile).
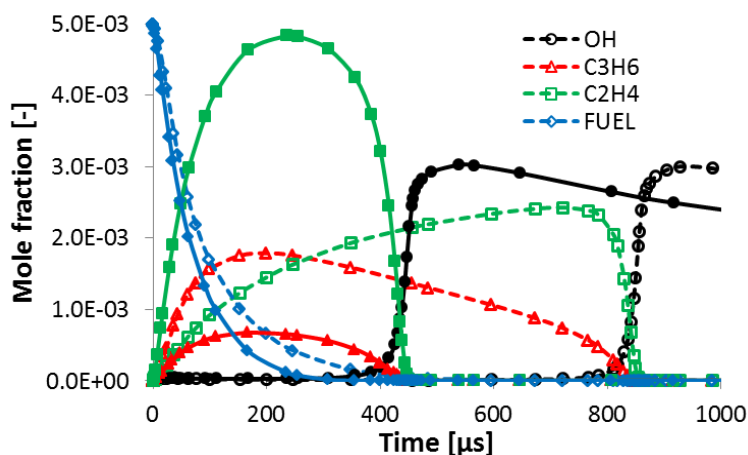
Figure 161: Predicted mole fractions of fuel and intermediate species as a function of time for the oxidation of a stoichiometric fuel/O$_2$/Ar mixture at 1 atm and 1350 K. Open symbols/dashed lines: iso-pentanol, Full symbols/solid lines: 1-pentanol.

These considerations are also supported by the flux analyses of Figure 144 and Figure 145. In fact, both the dominating H-abstraction channels in *iso*-pentanol oxidation (α and γ) lead to the formation of propylene, either directly (δ-radical decomposition) or through the formation of *iso*-propyl radical (α-radical decomposition). Moreover, as reported in Figure 162a, sensitivity analyses carried out at the same conditions of Figure 144 and Figure 145, highlight how propylene specific reactions increase of importance moving from *1*-pentanol to *iso*-pentanol. Conversely *1*-pentanol is more sensitive to reactions involving ethylene, and mainly to the H-abstraction by OH reaction leading to the formation of reactive vinyl radical.

Finally, Figure 162b shows the most sensitive fuel specific reactions. The importance of H-abstractions by $\dot{H}$ and $\dot{O}H$ on δ and α sites is highlighted for both fuels. H-abstraction reactions contribute to a decreased reactivity (longer ignition delay times) by subtracting reactive radicals from the system. It is of interest to notice the opposite effect of dehydration reactions enhancing reactivity in the case of *iso*-pentanol and inhibiting reactivity for *1*-pentanol, and the positive contributions of unimolecular initiation reactions.
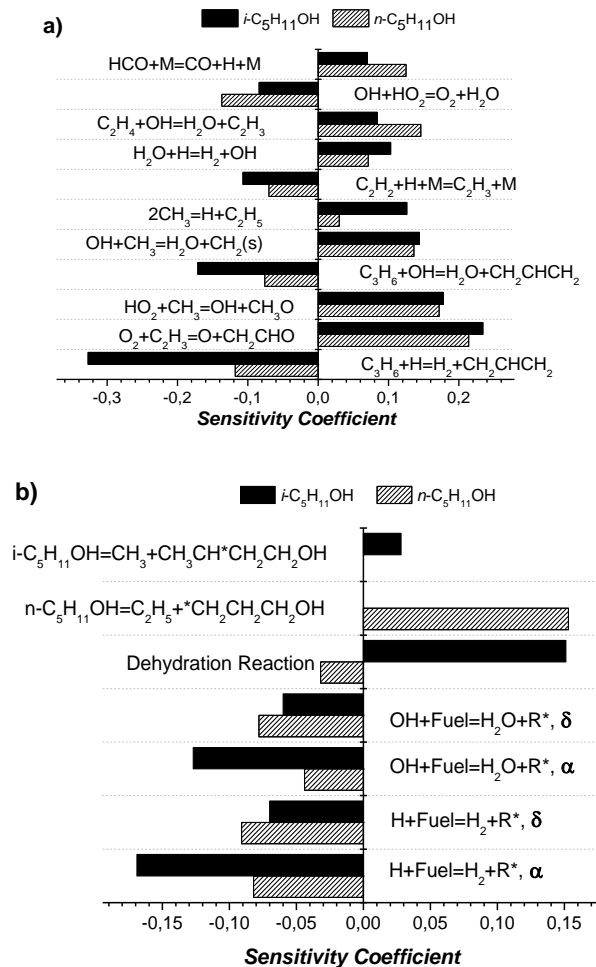
Figure 162: Sensitivity coefficients of ignition delay times to reaction rate coefficients, for 0.5% fuel/O_2/Ar stoichiometric mixtures at T=1350 K, p=1 atm. a) Most sensitive reactions belonging to the C0─C4 submechanism, b) most sensitive fuel specific reactions. A positive sensitivity coefficient stands for a reaction enhancing reactivity (shorter ignition delay time) and viceversa.

4. Conclusions

In the present work, laminar burning velocities of two pentanol isomers (*1*- and *iso*-pentanol) were rigorously obtained using the spherical bomb method. Three initial temperature were investigated for each fuel (353, 433 and 473 K) for equivalence ratio mixtures ranging from 0.7 to 1.5, at initial pressure of 1 bar. New experimental results were compared with previous data from the literature. An overall good agreement was found for *iso*-pentanol flame speeds compared to the measurements of Sarathy et al. [367] but larger discrepancies were observed for *1*-pentanol flame speeds compared with those from Li et al. [363] and Togbé et al. [364]. These discrepancies were extensively analyzed and discussed. It was shown that laminar flame speeds for kinetic modeling evaluation are useful only if the initial conditions are well documented, especially the initial temperature corresponding to each run and more importantly the air composition. Only then may a fair comparison between model and experiments be made. A kinetic mechanism that describes the high

temperature oxidation was developed and validated for both *1-* and *iso*-pentanol against laminar flame speeds from the present study. The mechanism consists of 230 species and 7885 reactions. The model was also tested with flame speeds from the literature. Larger deviations were observed for both *1-* and *iso*-pentanol for equivalence ratios > 1.0 when considering these data [364, 367]. For a more complete validation, the mechanism was also tested with high temperature shock tube ignition data from Tang et al. [375]. Sensitivity analyses were performed highlighting important kinetic features. On the whole, a lower reactivity of *iso*-pentanol was observed both in the experimental measurements and in model predictions.

6.1.2 Lumped Low Temperature Oxidation Mechanism of n- and iso- butanols and pentanols

The approach to the development of the low temperature mechanism for alcohols starts from the assumption, recently supported by the systematic evaluation of BDEs by Pelucchi et al. [77] (Section 6.3), that the hydroxyl moiety only influences bond strength up to the β position. Similar assumptions were made by Heufer et al. [365] when developing the low temperature oxidation mechanism for n-pentanol. This assumption, summarized in *Figure 163*, leads to the H-abstraction selectivities discussed in the previous Section and in Section 6.3 on high temperature oxidation, and is conserved when dealing with internal H-abstraction typical of low temperature oxidation pathways.
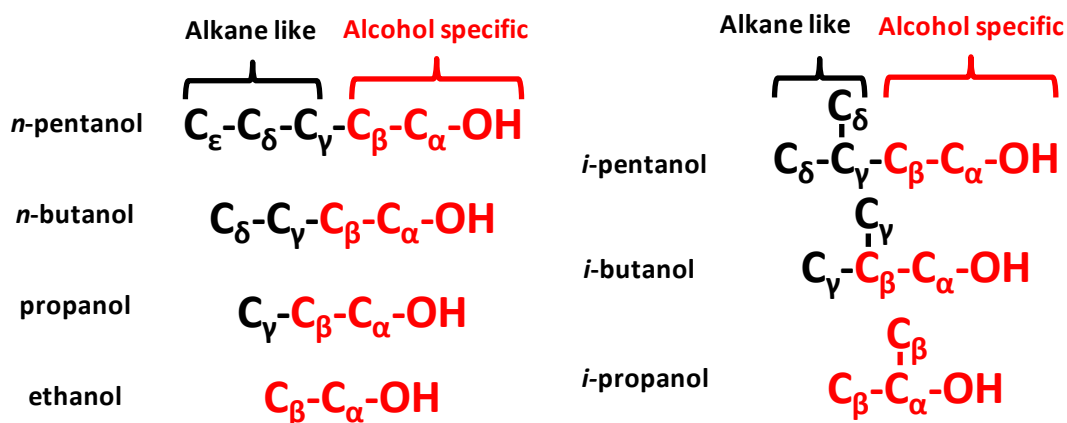
Figure 163: Treatment of the different carbon positions in alcohols. Adapted from [365].

The same corrections previously applied for the definition of the reference kinetic parameters for H-abstraction reactions are considered in the estimation of the rate constants for steps involving an isomerization, whose rate constant are estimated as explained in Section 3.2.7.

The peculiarity of alcohols oxidation at low temperatures is that the α-hydroxyalkylradical (R-·CH-OH) reacts with O_2 to rapidly form $H\dot{O}_2$ and the parent aldehyde or ketone without forming stable peroxy radicals contributing to the low temperature branching pathways. This reaction pathway is the major motivation for the relatively high RON and MON indices of alcohol fuels (ethanol, propanol and butanol isomers), making

them suitable for gasoline engines. Of course, the influence of such pathway decreases with increasing chain length, making longer alcohols (pentanol, hexanol, octanol) more suitable for diesel and avio engines due to relatively high cetane numbers. As pointed out by Sarathy et al. [4], despite the known importance of this reaction pathway, there is very little information at combustion relevant temperatures. The only available studies are from Zádor et al. [376] and da Silva et al. [377] on the α-hydroxyethyl + O$_2$ reaction system in ethanol. Both studies agree on the formation of an activated α-hydroxy-ethylperoxy adduct that rapidly decomposes to acetaldehyde and $H\dot{O}_2$. A single step apparent rate constant is assumed in the POLIMI mechanism, similarly to what was wasdiscussed in Section 3.2.5 for R+O$_2$→HO$_2$+olefin reactions. This rate constant is compared with that from da Silva et al. [377] in *Figure 164*.
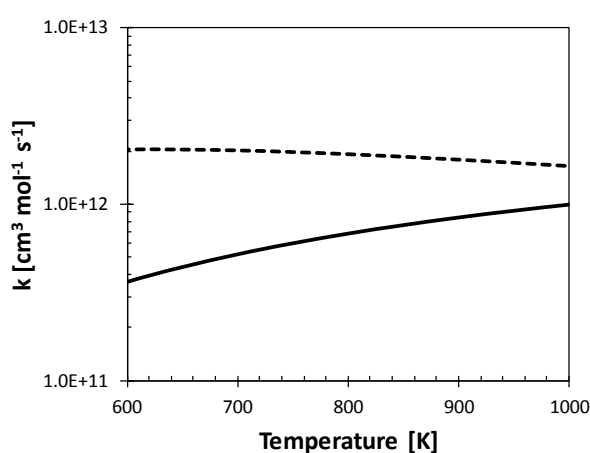
Figure 164: Comparison between the single step rate constant from rate rules in POLIMI alcohols mechanism (solid line) and that obtained from da Silva et al. [377] (dashed line).

The formation of a carbonyl compound and $H\dot{O}_2$ is also considered in successive steps when internal isomerization reactions lead to the formation of an α-hydroxy-hydroperoxyalkyl radicals as reported in *Figure 165*
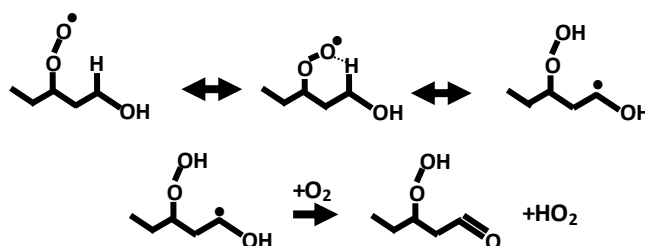
Figure 165: formation of α-hydroxy-hydroperoxyalkyl radical and its interactions with O$_2$ to form hydroperoxy pentanal and $H\dot{O}_2$.

The lumped kinetic mechanism to describe the oxidation of n-butanol and n- and iso-pentanol is reported in *Table 22*.

Lumped reactions	*n*-butanol		*iso*-pentanol		*n*-pentanol	
	A	Ea	A	Ea	A	Ea
$R+O_2 \rightarrow RO_2$	2.50E+12	0	2.50E+12	0	2.50E+12	0
$RO_2 \rightarrow R + O_2$	3.00E+13	30000	3.00E+13	30000	3.00E+13	30000
$RO_2 \rightarrow QOOH$	4.50E+12	24000	4.50E+12	27000	2.00E+11	19500
$QOOH \rightarrow RO_2$	5.00E+11	20000	3.00E+10	19000	2.50E+10	15000
$\beta\text{-}QOOH \rightarrow H\dot{O}_2 + Unsat\ Alcohols$	2.00E+13	24000	7.00E+12	24000	5.00E+12	24000
$\gamma/\delta\text{-}QOOH \rightarrow OH + Olefins$	3.00E+13	24000	2.00E+13	24000	3.00E+13	24000
$QOOH \rightarrow Cyclic\ Ether + OH$	1.00E+11	17000	1.00E+11	17000	1.00E+11	17000
$QOOH + O_2 \rightarrow OOQOOH$	2.50E+12	0	2.50E+12	0	2.50E+12	0
$OOQOOH \rightarrow QOOH + O_2$	3.00E+13	30000	3.00E+13	30000	3.00E+13	30000
$OOQOOH \rightarrow OQOOH + OH$	4.50E+12	24000	4.50E+12	27000	2.00E+11	19500
$OQOOH \rightarrow OH + Products$	3.00E+15	42000	3.00E+15	42000	3.00E+15	42000
$RO_2 \rightarrow OH+CH_2O+C_{n-1}aldehyde\ (Waddington)$	1.00E+10	22000	1.00E+10	22000	1.00E+10	22000

Table 22: Kinetic parameters of the lumped oxidation reactions of alcohols (units are mol, cm, s, cal).

The following part compares the mechanism predictions with a number of experimental targets such as ignition delay times in shock tubes and rapid compression machines (RCMs) and jet stirred reactor concentration profiles.

6.1.2.1 n-butanol

Figure 166 compares concentration profiles measurements with model predictions for n-butanol in a jet stirred reactor. The addition of the low temperature sub-mechanism to the model of Grana et al. [369] provides good agreement with the experimental measurements. Figure 167 highlights model capability of reproducing the pressure effect on ignition delay times in shock tubes and RCMs. The deviations observed for the lower temperature case at 15 bar [378] is partially due to a slight overestimation of the reactivity and largely to the constant volume adiabatic core assumption used for the ignition delay time simulations [66]. A more detailed discussion of these ignition data will be presented in Section 6.3. It is important to emphasize that the systematic approach applied to low temperature alcohol oxidation (Table 22) is easily generalized to longer or branched alcohols.
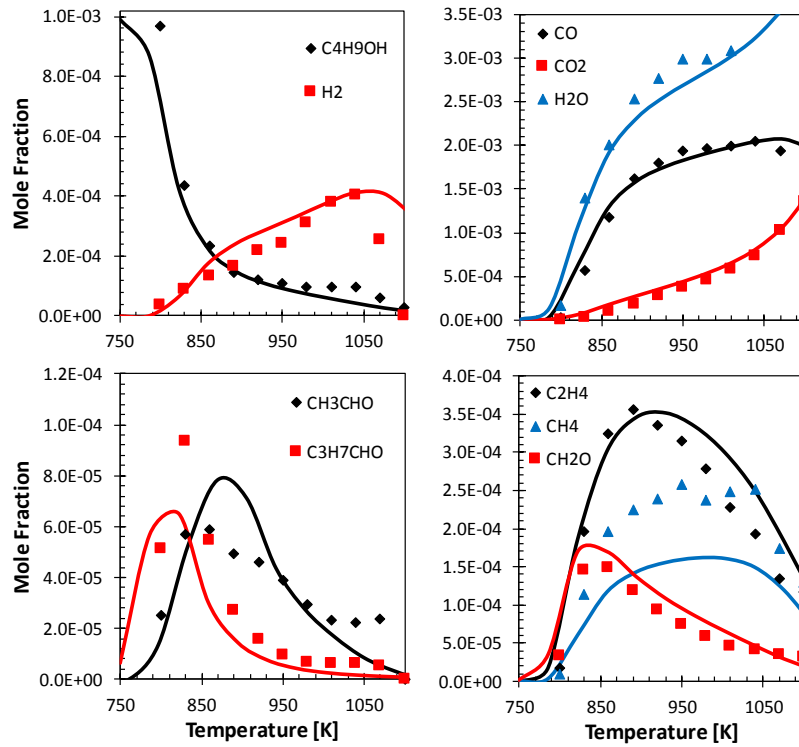
Figure 166: 0.1% n-butanol/O_2/N_2 oxidation in a JSR at φ=1.0, p=10 atm, τ=0.7 s. Symbols: experimental data [379], lines: model predictions.
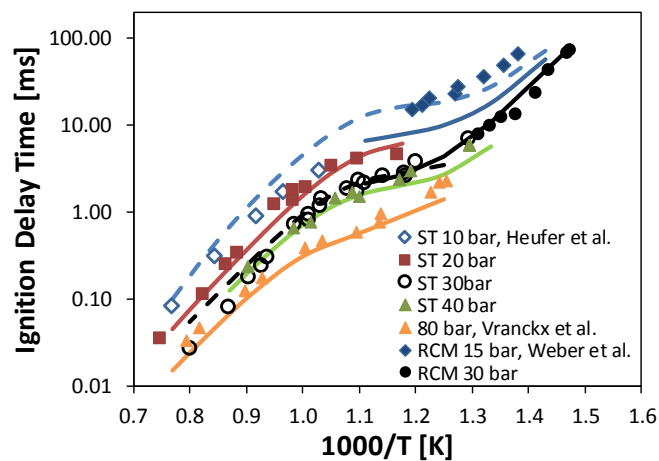
Figure 167: Ignition delay times of stoichiometrich n-butanol/air mixtures. Symbols: experimental data [378, 380, 381], lines: model predictions. Adiabatic constant volume simulations.

6.1.2.2 n-pentanol

Jet stirred reactor speciation and ignition delay times for n-pentanol are reported in Figure 168 and Figure 169, respectively. Once again the model shows reasonable agreement for both cases.
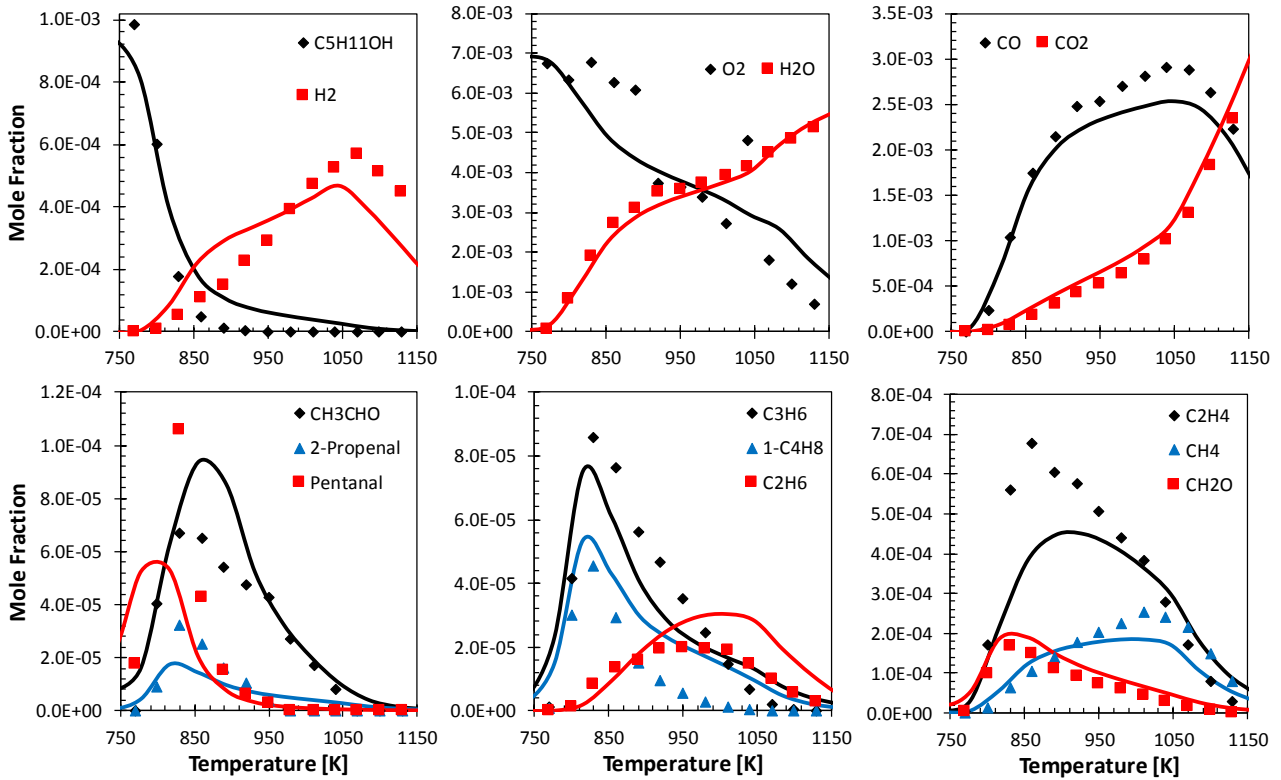
Figure 168: 0.1% n-pentanol/O₂/N₂ oxidation in a JSR at φ=1.0, p=10 atm, τ=0.7 s. Symbols: experimental data [364], lines: model predictions.
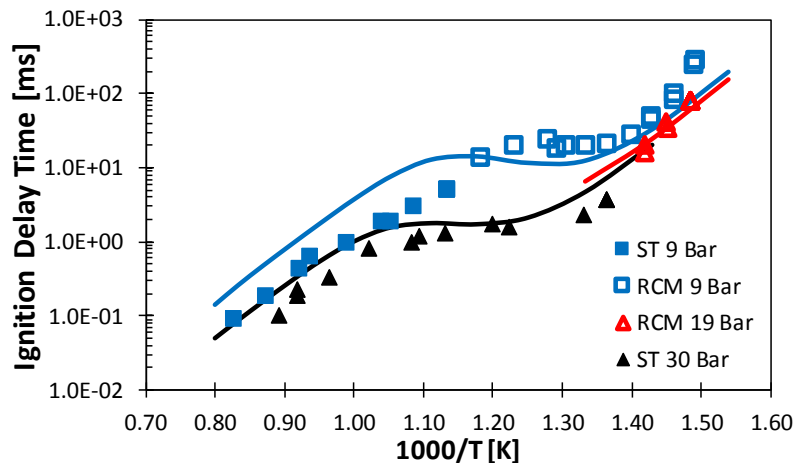
Figure 169: Ignition delay times of stoichiometric n-pentanol/air mixtures. Symbols: experimental data [382], lines: model predictions. Adiabatic constant volume simulations.

6.1.2.3 iso-butanol

Figure 170 reports jet stirred reactor measurements and model predictions for iso-butanol. Quite large deviations can be observed for T > 850 K, while the onset of reactivity is correctly captured. It is worth mentioning that information on molecular oxygen concentration is lacking from the original experimental paper [383] and the actual stoichiometry might deviate significantly from φ=1.0, causing part of the observed

deviations. No fuel/air ignition delay times over broad ranges of pressures and temperatures are reported in the literature at present.
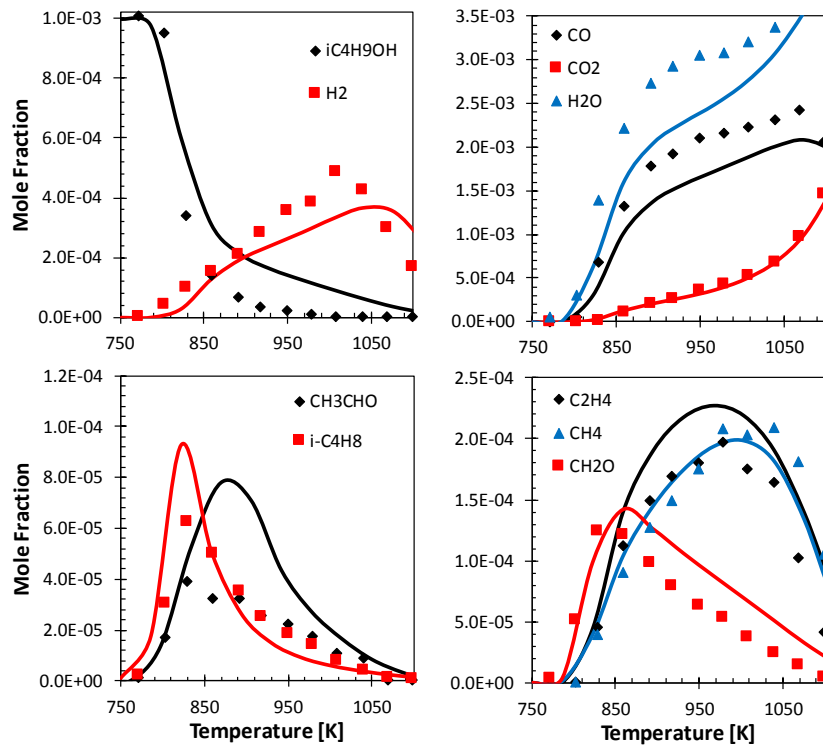
Figure 170: 0.1% iso-butanol/O₂/N₂ oxidation in a JSR at φ=1.0, p=10 atm, τ=0.7 s. Symbols: experimental data [383], lines: model predictions.

6.1.2.4 iso-pentanol

The present mechanism is compared with speciation and ignition delay times measurements at high pressures in Figure 171 and Figure 172, respectively, showing good agreement. Figure 172 highlights the capability of the model to capture the influence of the equivalence ratio on the ignition propensity of iso-pentanol, despite deviations within experimental uncertainty which may be due to the adiabatic constant volume treatment of the RCM simulations.
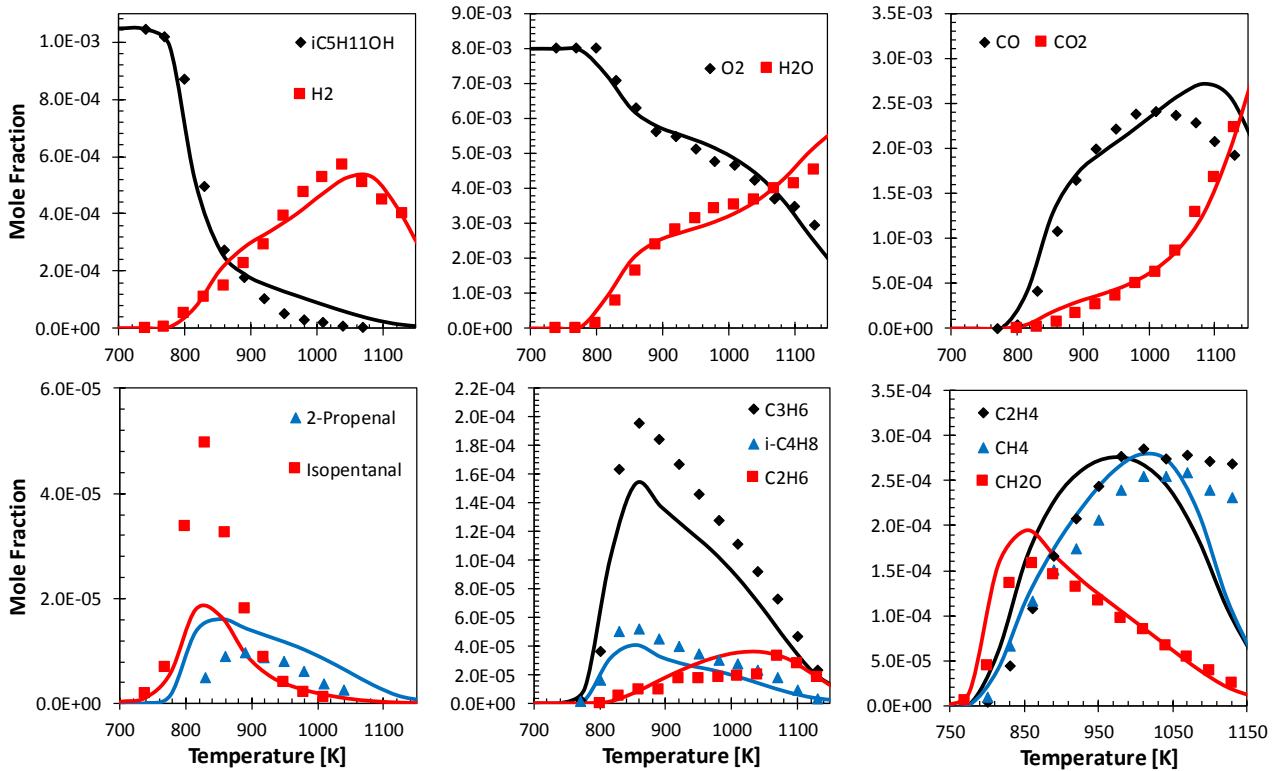
Figure 171: 0.1% iso-pentanol/O_2/N_2 oxidation in a JSR at φ=1.0, p=10 atm, τ=0.7 s. Symbols: experimental data [366], lines: model predictions.
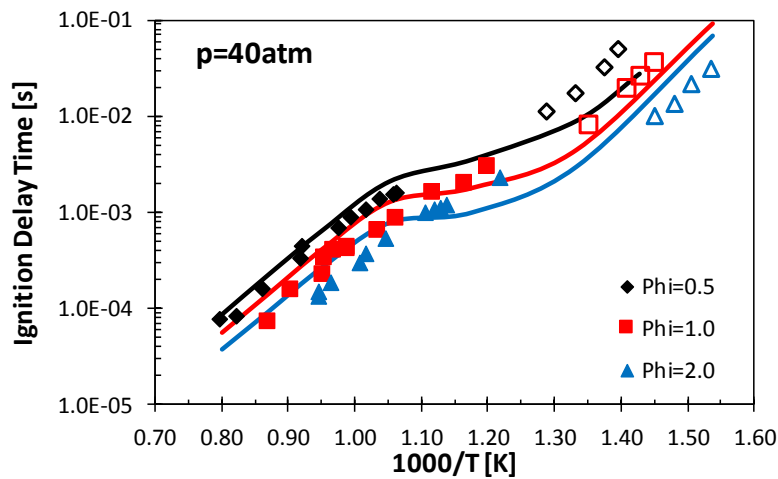
Figure 172: Ignition delay times of stoichiometric iso-pentanol/air mixtures. Symbols: experimental data [367], lines: model predictions.

6.1.2.5 n-hexanol

Recently, the mechanism was systematically extended to describe the oxidation of n-hexanol. *Figure 173* shows a comparison between fuel profiles in an isothermal jet stirred reactor at φ=0.5 and 1.0, p=10 atm and low temperatures [384]. The mechanism is able to predict the low temperature reactivity for the leaner case,

while it greatly overestimates fuel conversion for the stoichiometric condition. Experiments at the same conditions were recently presented for n-pentane [128], whose conversion is compared to that obtained for n-hexanol in the center and right panel of *Figure 173*. The significant assumption behind this comparison is that, like in n-pentane, five carbon atoms out of six will fully contribute to the low temperature branching of hexanol. As expected, the low temperature reactivity of hexanol is inhibited from the formation of $H\dot{O}_2$ and the parent aldehyde (i.e. hexanal) competing with the alkane-like low temperature branching pathway. A similar effect would be expected also for the φ=1.0 case (red), where, surprisingly, no low temperature reactivity is observed for n-hexanol.
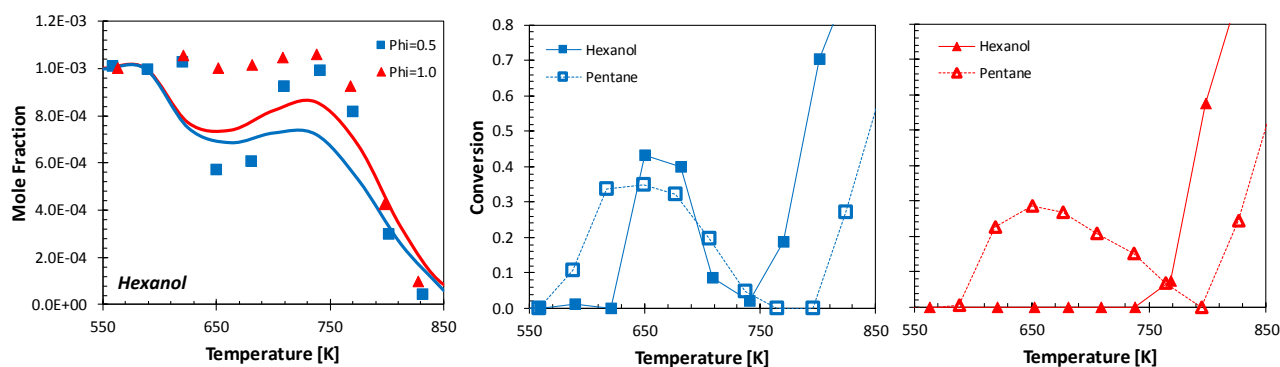
Figure 173: 0.1% n-hexanol/O$_2$/N$_2$ oxidation in a JSR at p=10 atm, τ=0.7 s. Symbols: experimental data [384], lines: model predictions. Comparison of experimental conversions of n-hexanol and n-pentane [128] at equal conditions.

Similar questionable trends are observed when considering lower pressure speciation measurements. *Figure 174* compares model predictions with recent unpublished experimental measurements [361] of n-hexanol oxidation in a JSR. While the mechanism predicts low temperature reactivity and a clear NTC region, the experiments only show very limited conversion for T<700 K.
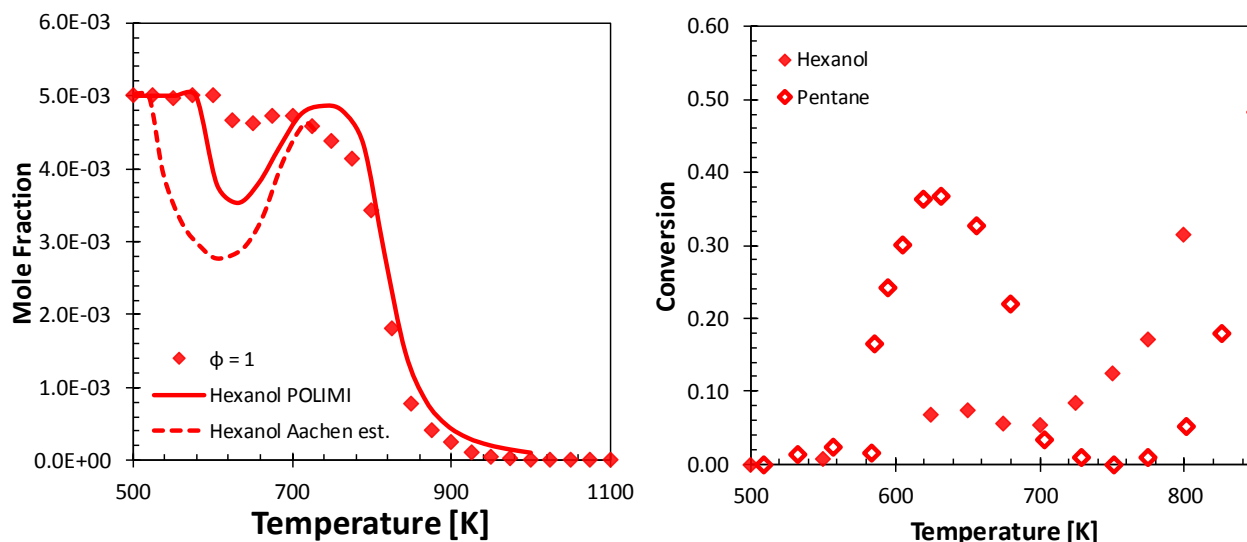
Figure 174: left panel: 0.5% n-hexanol/O₂/He oxidation in a JSR at φ=1.0, p=1 atm, τ=2.0 s. Symbols: experimental data [361], solid lines: POLIMI model predictions, dashed lines: Aachen mechanism(67% n-pentanol/33%n-octanol) [385]. Right panel: comparison of experimental conversion of n-hexanol [361] and n-pentane [128] at comparable conditions.

To investigate possible reasons for such deviations, the recent n-octanol mechanism of Cai et al. [385], systematically developed from the n-pentanol mechanism of Heufer [365] has been used to simulate the n-hexanol data, assuming the lever rule discussed in Section 3.3.3. The stoichiometric mixture of 67% n-pentanol and 33% n-octanol overestimates the fuel conversion even more significantly.

On the other hand, the mechanism reproduces the ignition delay time measurements of Heufer et al. [382] although some margin for improvement (Figure 175) exists. It is interesting to notice how the deviations in the ignition delay times highlight a lack of reactivity at low temperatures (T < 750 K) and an excessive reactivity at intermediate temperatures (T=750–900 K). These observations are not consistent with those from the JSR experiments of *Figure 173* and *Figure 174*.
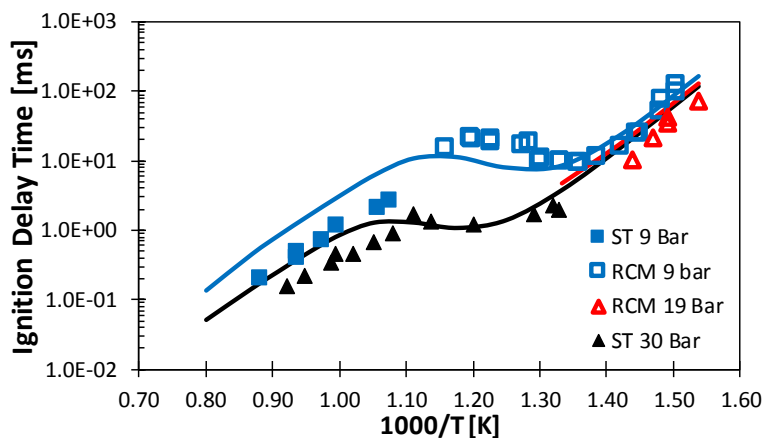
Figure 175: Ignition delay times of stoichiometric n-hexanol/air mixtures. Symbols: experimental data [382], lines: model predictions.

6.1.2.6 Summary

A mechanism to describe the low temperature oxidation of n-butanol has been developed and extended to iso-butanol and higher alcohols such as n- and iso-pentanol and n-hexanol. In general, the mechanism agrees with available experimental data in shock tubes, rapid compression machines and jet stirred reactors. Deviations are observed for JSR speciation data of n-hexanol both for 10 atm published data and unpublished data at atmospheric pressure. Reasons for such discrepancies are still under investigation.

Figure 176 compares the ignition delay times of stoichiometric fuel in air mixtures for the alcohols discussed above. The reactivity increases with increasing chain length and the branched isomers are consistently slower to ignite than the linear alcohols.

A clearer explanation of such trends is reported in *Figure 177*, showing radical species (RO_2, QOOH, OOQOOH) and ketohydroperoxides (KHYP) mole fraction profiles for n-butanol, n-pentanol and iso-pentanol at 850 K and 10 atm. As expected, the more pronounced low temperature reactivity of heavier and linear alcohols is justified by higher concentration of radical species typical of the low temperature oxidation paths, finally resulting in higher yields of ketohydroperoxides whose decomposition gives chain branching.
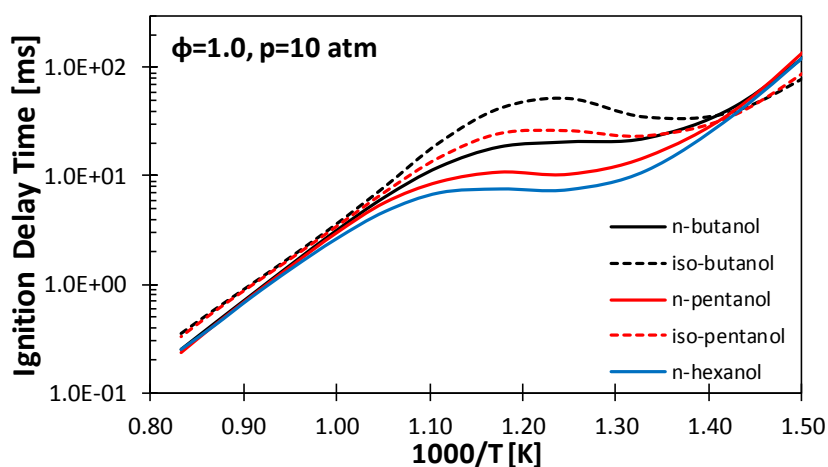
Figure 176: Ignition delay time of alcohol/air mixtures at p=10 atm. Adiabatic constant volume simulations.
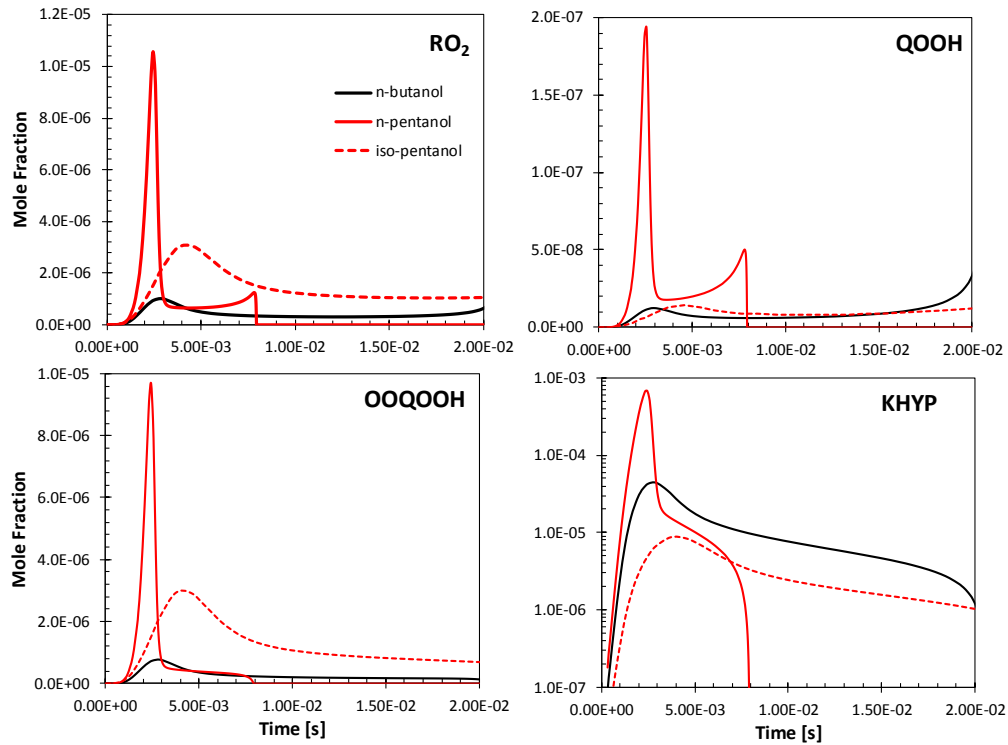
Figure 177: Low temperature radical species (RO2, QOOH, OOQOOH) and ketohydroperoxides (KHYP) profiles in n- and iso-pentanol and n-butanol oxidation at T=800 K, p=10 atm and φ=1.0.

The recent review of Sarathy et al. [4] on alcohol combustion chemistry already highlighted the need for consistent higher pressure (10–100 bar) lower temperature (550–950 K) measurements for alcohols. The experimental uncertainty highlighted here (e.g. n-hexanol) further emphasizes this necessity for systematically re-developing low temperature kinetic mechanisms for alcohols. Further constraints in model parameters are also needed and this Section highlighted a few of extreme importance (see also Section 6.3), mostly related to the fate of the α-secondary radical (R-·CH-OH) at low temperatures. Theoretical studies of alcohols have been quite limited despite the global interest in their exploitation as renewable fuels. Similarly to what has been done on alkanes, the coupling of theory and experiments should allow kinetic modelers to reduce the large uncertainties still existing in alcohols low temperature combustion kinetics. Only then would a better understanding of the impact on NOx and Soot emission of alcohol/commercial fuel blends be possible.

In this regard a joint research activity with the Combustion Chemistry Group at National University of Ireland Galway is in progress.

6.2 Aldehydes

This section describes the chemistry involved in aldehydes pyrolysis, high and low temperature oxidation by means of two recent papers of Pelucchi et al. [77, 78]. The experimental activity performed for the high

temperature study [78] was the subject of the Master Thesis of Pelucchi and won't be reiterated any further herein.

6.2.1 An experimental and Kinetic Modelling Study of the Pyrolysis and Oxidation of n-C$_3$–C$_5$ Aldehydes [78].

1. Introduction

The depletion of fossil fuel reserves and the stringent targets for air pollution reduction have greatly increased the focus on gaseous, liquid and solid biofuels as a sustainable source of energy for transport, domestic and industrial applications. Biomass can be used to produce either liquid or gaseous biofuels for transportation purposes (hydrogen, methane, ethanol and long chain alcohol, dimethyl ether, diesel) through different processes such as Biomass-To-Liquid (BTL) or as a side product of Gas-To-Liquid (GTL) processes in Fischer-Tropsch synthesis. Similarly, municipal solid waste (MSW), agricultural and forest residues can also be converted to feedstock for energy production through gasification or combustion, followed by conventional power generation cycles.

Within this scenario, low and high molecular weight aldehydes are known to be toxic, some of them carcinogenic, and precursors of free radicals leading to the formation of ozone and urban smog [386]. C$_4$ and C$_5$ aldehydes belong to the class of non-regulated pollutants and they are classified as mobile source air toxic (MSAT) compounds. Recent fundamental studies of biofuel combustion have addressed the strong belief that long-chain alcohols (propanol, butanol, pentanol and related isomers) are likely to be used either as an alternative to conventional gasoline (n-butanol and iso-pentanol mainly) or as additives in order to reduce pollution in terms of PAH, particulates and soot formation. Fundamental studies on the oxidation of alcohols identified the presence of aldehydes as intermediate products derived from radical as well as molecular dehydrogenation reactions [364, 365, 368-370, 374, 387-393].

Aldehydes are products of partial or incomplete combustion and they are released into the atmosphere from conventional spark ignition (SI) gasoline and compression ignition (CI) diesel engines, and also from biomass gasification or aerobic treatments [394]. Grosjean et al. [395] studied carbonyl emissions from light-duty and heavy-duty vehicles on a motorway tunnel, detecting emissions of saturated, unsaturated and aromatic aldehydes. Zervas [396] analyzed the exhaust gases from a diesel engine recording high emission of carbonyl compounds, particularly when synthetic fuels were tested compared to a commercial fuel. Karavalakis et al. [397] highlighted how the use of a Euro4 diesel engine increases the emissions (aldehydes and ketones) compared to a Euro3 engine identifying linear aldehydes from formaldehyde up to C$_5$–C$_6$ and aromatic aldehydes. De Abrantes and co-workers focused on formaldehyde and acetaldehyde emissions from diesel engines [398], highlighting higher concentrations than those observed in spark ignition engines. Gasoline and

diesel engine emissions of aldehydes were also compared by Roy [399] through high performance liquid chromatography. Significant and comparable amounts of formaldehyde, acetaldehyde and propanal were detected from SI and CI engines investigating different injection technologies. Schauer [400] measured the emissions of aldehydes from a gasoline-powered vehicle, detecting concentrations on the order of those measured for diesel engines. Other works in recent years focused on the influence of diesel-biodiesel blended fuels on carbonyl emissions, agreeing that alternative fuel blending increases the release of aldehydes and that the engine technology influences the phenomena as much as the kind of fuel blend itself [401-405].

From a pure chemical kinetics perspective aldehydes are primary stable intermediate products of biofuel oxidation and pyrolysis, influencing reaction pathways and important combustion properties [406]. Therefore their combustion behavior is non-negligible with respect to designing more efficient and environmentally friendly combustion systems. For all of these reasons, the understanding of combustion kinetics of aldehydes and furthermore developing a deeper understanding of the reactivity of the carbonyl side of the molecule (R–CH=O) under combustion or pyrolytic conditions, plays a crucial role in the capability of kinetic mechanisms to better predict pollutant release from both conventional and renewable fuels.

Since the pioneering work of Dean and co-workers [407] and of Hochgreb and Dryer [408], several kinetic studies on the pyrolysis and oxidation of formaldehyde at low- and high-temperature were undertaken [409-416].

Similarly, acetaldehyde oxidation has been described in detail by different authors. Dating back to the early 1970s Halstead et al. [417] discussed cool flames phenomena and low-temperature oxidation. Oscillatory ignitions in the low-temperature regime were studied in the early 80s by Gray and co-workers [418], and in the 90s by Cavanagh et al. [419] and by Di Maio et al. [420]. Kaiser et al. proposed a model to describe the negative temperature coefficient (NTC) behavior of acetaldehyde [421]. The high-temperature oxidation of acetaldehyde was investigated by Dagaut et al. [422] in a jet-stirred reactor and in a shock tube, while Hidaka and co-workers studied its pyrolysis in a single-pulse shock tube [423], and Yasunaga et al. [424] suggested a mechanism describing the oxidation and pyrolysis for the high-temperature regime.

Da Silva and Bozzelli [425] calculated the enthalpies of formation of C_2 to C_7 n-aldehydes through quantum chemical calculations and determined bond dissociation energies (BDE) for all C–C and C–H bonds in the molecules. Their study revealed that the R–CH2CH=O bond is the weakest bond in all the aldehydes larger than acetaldehyde, due to the formation of the resonantly stabilized vinoxy radical. Kaiser [426] developed a chemical kinetic model to describe propanal oxidation in the temperature range 400–700 K. An experimental and modeling study at higher temperatures was carried out by Lifshitz and co-workers [427]. They investigated the thermal decomposition of propanal in a single pulse shock-tube under pyrolysis

conditions. A sub-mechanism of 52 elementary reaction steps and 22 species was developed, and the kinetic analysis emphasized the importance of unimolecular initiation reactions involving a C–C bond breaking in predicting the intermediate and product species. Furthermore, the species profile predictions were found to be sensitive to the ratio between abstraction by ethyl radical on the fuel molecule and ethyl radical decomposition to form ethylene and a hydrogen atom. Kasper et al. [428] studied the combustion chemistry of propanal in a stoichiometric flame at low pressures with molecular beam mass spectrometry, highlighting, under the investigated conditions, the importance of alkyl radical addition to the fuel molecule and the need of more detailed kinetic studies to assess the relative importance of available reaction pathways. Akih-Kumgeh and Bergthorson [429] studied the ignition of propanal in a shock tube and developed a mechanisms underlining the importance of the initiation reaction forming $\dot{C}2H5$ and $H\dot{C}O$ and the H-atom abstraction reactions from the alpha-carbonyl site in predicting ignition delay times. Laminar flame speeds were measured by Veloo et al. [430] together with jet-stirred reactor experiments to quantify reactant, intermediate and product concentrations. A model to describe the low- and high-temperature oxidation of propanal was then developed and validated.

Veloo and co-workers also studied n-butanal and iso-butanal oxidation in laminar flames and in a jet-stirred reactor proposing a comprehensive mechanism for low- and high-temperature combustion consisting of 244 species and 1198 elementary reaction steps [431]. The authors highlighted the importance of $\dot{C}_3H_5$ radical and other key reaction subsets of the mechanism. An interesting comparison between n- and iso-butanal and propanal is also shown for flame speed data, with an emphasis on radical species profiles such as $H\dot{C}O$ and $\dot{O}H$ of high importance in flame propagation phenomena. Davidson and co-workers investigated the ignition behavior of n-butanal [432] as part of an update to the Dooley et al. methyl butanoate mechanism [433]. Zhang measured ignition delay times for n-butanal [434] and i-butanal [435] over a wide range of equivalence ratios, pressures and temperatures, and developed kinetic sub-models for both of the C4 aldehydes based on a literature review and validated them against the measured data.

To the best of our knowledge, no experimental measurements currently exist for n-butanal pyrolysis and n-pentanal pyrolysis and oxidation. Furthermore, despite C_3–C_5 aldehydes being included in many hydrocarbon and bio-fuels kinetic models, no studies have specifically addressed the development and validation of an oxidation mechanism for n-pentanal. There have clearly been significant efforts focused on understanding the combustion behavior of aldehydes. Yet a consistent and detailed summary of their combustion behavior is still somewhat lacking in the literature.

Two important goals support and justify the present work. Firstly, it provides new experimental data on the pyrolysis and the auto-ignition behavior of C_3–C_5 aldehydes, in order to extend the database available for high-temperature combustion conditions. Secondly, the experimental data, both from the current study and

from the literature, have been used to develop and validate the sub-mechanism of C_3–C_5 aldehydes, with the objective of better characterizing the role of the acyl group. This validation has been performed by coupling a newly developed aldehyde sub-mechanism with the C_0–C_4 mechanism of NUIG [436-441] and the one of POLIMI [442].

This joint paper between the two research groups is also a first step toward a unified mechanism. The two C_0–C_4 mechanisms present several differences in the rate constants (within their accuracy) and for both of them it is necessary to preserve internal consistency. Internal consistency means that the branching ratio between competitive reactions is more important than the values of kinetic parameters of single reactions. For this reason, reactions within the C_0–C_4 mechanism (including C_1–C_2 aldehydes) have forced some differences between the implementation of the aldehyde sub-mechanism within the two kinetic frameworks. As a matter of fact, the concentration of $\dot{H}$, $\dot{O}H$ and other radicals are mainly controlled by two different C_0–C_4 mechanisms. More than the same kinetic constants (k) it is important to have the same rate parameters (k [R] s^{-1}), that is the reason why there are differences between the two mechanisms. The unification process would need to start from the C_0–C_4 mechanism, which is beyond the aim of this study, and would require more time and effort. Moreover, the POLIMI kinetic mechanism is systematically reduced by using a lumping approach; this is not considered nor applied in the NUIG mechanism.

Both the mechanisms were previously validated for formaldehyde and acetaldehyde. Figure 178 shows a first comparison with experimental data. Figure 178a shows the oxidation of formaldehyde in an atmospheric pressure flow reactor at 1095 K and ϕ = 1.08 [409], while Figure 178b shows the high-temperature pyrolysis of acetaldehyde in a shock tube [424]. Figure 179 compares the ignition delay times of formaldehyde [412] and acetaldehyde [424] (1% fuel in oxygen-argon) at lean conditions (ϕ = 0.5). The higher reactivity of formaldehyde is evident in this figure, mainly at lower temperatures. The apparent activation energies are significantly different, on the order of 40 kcal mol^{-1} for formaldehyde and close to 60 kcal mol^{-1} for acetaldehyde. At temperatures higher than 1600 K, both aldehydes have similar reactivity. These comparisons show that both of the models agree with the experimental data, providing a solid basis for the development of kinetic mechanisms for heavier aldehydes.
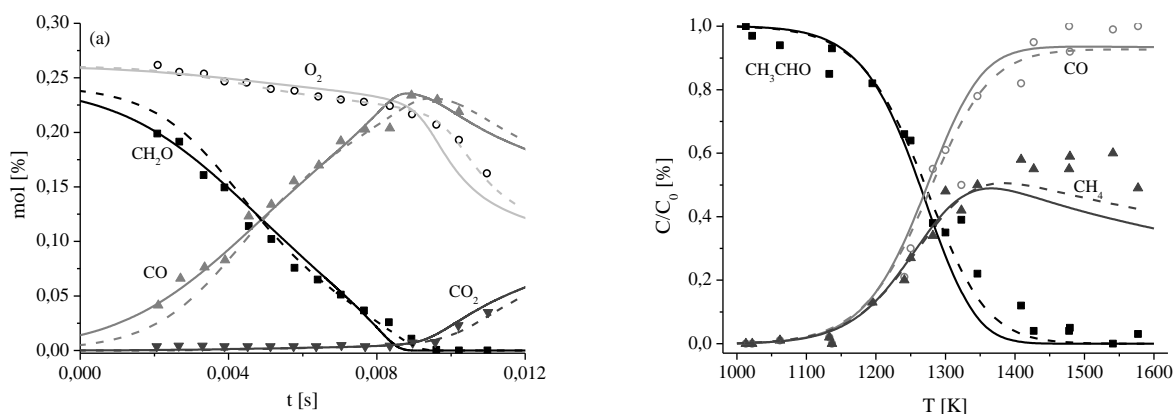
Figure 178: a) Oxidation of formaldehyde at 1 atm and 1095 K [409]. b) Pyrolysis of acetaldehyde at 2 atm and 2 ms residence time [424]. Comparison of experimental data (symbols) and predictions of NUIG (dashed lines) and POLIMI (solid lines) kinetic schemes.
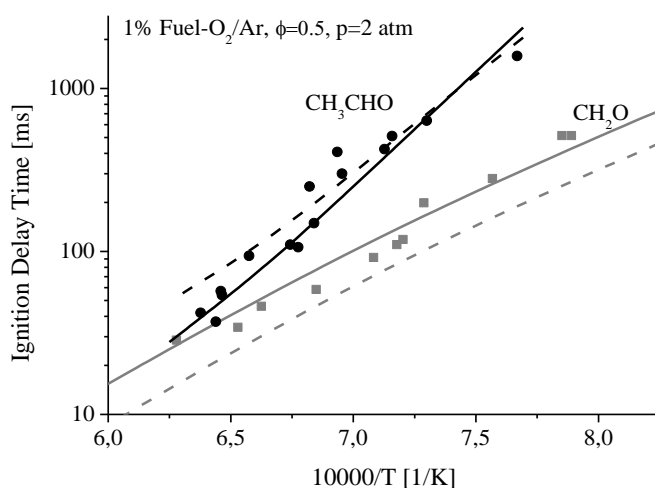
Figure 179: Ignition delay times of formaldehyde [412] and acetaldehyde [424] oxidation. Comparison of experimental data (symbols) and predictions of NUIG (dashed lines) and POLIMI (solid lines) kinetic schemes.

1. Kinetic mechanism

1.1 *Thermochemistry*

The thermodynamic data for the three aldehydes (Figure 180) and related radicals, were calculated using the THERM program from Ritter and Bozzelli [91], based on group additivity methods developed by Benson [50] and further optimized by Burke [100] at NUIG. The computed values of enthalpies, entropies of formation and heat capacities for aldehydes and primary radicals are shown in Table 23, together with enthalpies of formation computed by da Silva and Bozzelli [425], and the nomenclature used in this study. Good agreement between the group additivity rules and the theoretical computations is shown in Table 23, with maximum

deviations being 1.5–2.0 kcal mol^{-1} for the enthalpies of formation. The bond dissociation energies (BDE) for the three aldehydes will be analyzed in the next paragraph when discussing chain initiation reactions.
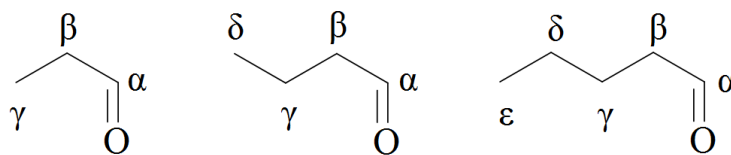
Figure 180: propanal, n-butanal and n-pentanal chemical structure and named carbon sites

Species	Name	$\Delta H°_f$ (298.15 K) [425]	$\Delta H°_f$ (298.15 K) *	$S°$(298.15 K) *	C_P (cal mol^{-1} K^{-1}) *				
		kcal mol^{-1}	kcal mol^{-1}	cal mol^{-1}K^{-1}	300	500	800	1000	1500
Propanal	C$_2$H$_5$CHO	−45.18	−45.35	72.86	19.38	26.94	36.90	42.12	49.83
α	C$_2$H$_5$ĊO	−8.00	−8.45	73.98	18.55	24.98	33.74	38.39	45.19
β	Ċ$_2$H$_4$CHO-1	−7.10	−5.55	70.49	18.02	25.21	34.24	39.01	46.33
γ	Ċ$_2$H$_4$CHO-2	5.10	3.73	76.20	18.85	25.19	33.53	38.03	44.79
***n*-butanal**	n-C$_3$H$_7$CHO	−50.00	−50.31	82.28	24.82	35.26	48.21	54.29	64.57
α	n-C$_3$H$_7$ĊO	−13.00	−13.41	83.40	23.99	33.30	45.05	50.56	59.93
β	Ċ$_3$H$_6$CHO-1	−11.50	−10.51	79.91	23.46	33.53	45.55	51.18	61.07
γ	Ċ$_3$H$_6$CHO-2	−2.50	−4.48	86.29	23.29	32.26	44.04	49.65	59.28
δ	Ċ$_3$H$_6$CHO-3	0.10	−1.23	85.62	24.29	33.51	44.84	50.20	59.53
***n*-pentanal**	n-C$_4$H$_9$CHO	−54.61	−55.27	91.70	30.26	43.58	59.52	66.46	79.31
α	n-C$_4$H$_9$ĊO	−18.30	−18.37	92.82	29.43	41.62	56.36	62.73	74.67
β	*Ċ$_4$H$_8$CHO-1*	*−17.20*	*−15.47*	*89.33*	*28.90*	*41.85*	*56.86*	*63.35*	*75.81*
γ	*Ċ$_4$H$_8$CHO-2*	*−8.10*	*−9.44*	*95.71*	*28.73*	*40.58*	*55.35*	*61.82*	*74.02*

δ	*$\dot{C}_4H_8CHO$-3*	*−7.60*	*−9.44*	*95.71*	*28.73*	*40.58*	*55.35*	*61.82*	*74.02*
ε	*$\dot{C}_4H_8CHO$-4*	*−5.20*	*−6.19*	*95.04*	*29.73*	*41.83*	*56.15*	*62.37*	*74.27*

*Table 23: Thermochemical data and nomenclature of aldehydes and related primary radicals (*group additivity).*

1.2 *Primary reactions of aldehydes*

Figure 181, *Figure **182*** and Figure ***183*** show simplified primary chain initiation and propagation reactions of the three aldehydes, in terms of initiation, H-atom abstraction, and radical decomposition reactions. The chain initiation reactions occur *via* unimolecular decompositions with a C–C bond cleavage, forming an alkyl radical and an oxygenated radical ($H\dot{C}O$, $\dot{C}H_2CHO$, $\dot{C}_2H_4CHO$-2, $\dot{C}_3H_6CHO$-3). In flame conditions, the chain initiation and the reverse recombination reactions involving the C–H bonds can become significant. H-atom abstraction reactions are reported in their general form with $\dot{R}$ being the generic H-atom abstracting radical. These reactions lead to three, four and five primary fuel radicals, respectively, for propanal, *n*-butanal and *n*-pentanal. Radical decomposition reactions proceed to form either an alkene and an oxygenated radical or an unsaturated oxygenated species (CO, ketene, acrolein, methylketene, or 1-butenal) and a small alkyl radical. For instance, the α-radical derived from the C_n aldehyde could, in principle, decompose via β-scission to form either ketene and a C_{n-2} alkyl radical or, more likely, CO and a C_{n-1} alkyl radical. Radicals can also isomerize mainly to form the thermodynamically favored α-radical. For the sake of clarity, isomerization pathways are not reported in Figure 181, *Figure **182*** and Figure ***183***.
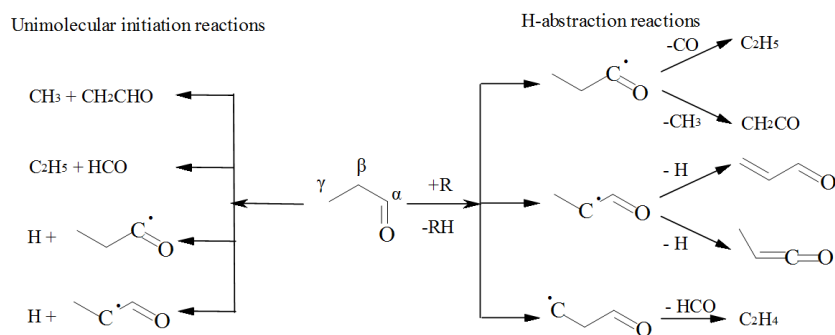
Figure 181: Primary decomposition reactions of propanal.
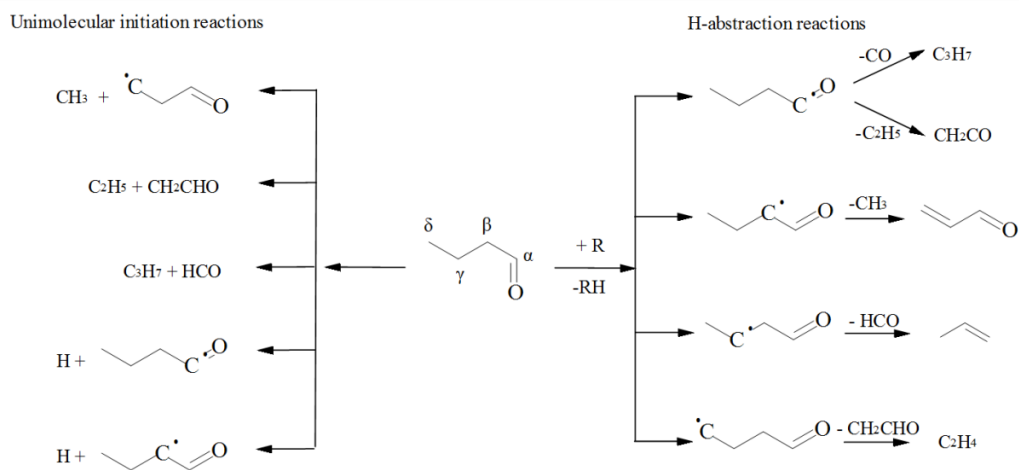
Figure 182: Primary decomposition reactions of n-butanal.
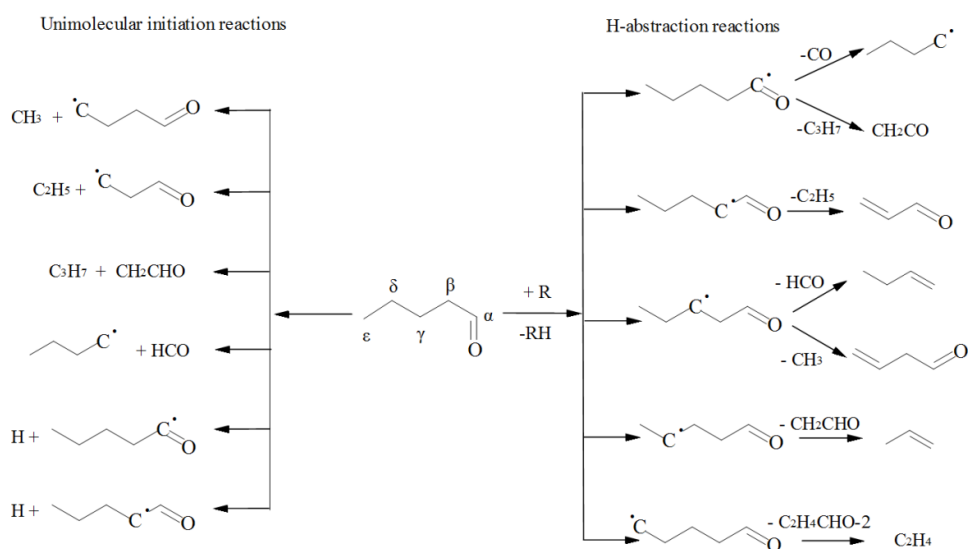
Figure 183: Primary decomposition reactions of n-pentanal.

1.3 *Unimolecular Decomposition Reactions*

A three-frequency version of Quantum-Rice-Ramsperger-Kassel theory (QRRK/MSC) [443-445] was used to calculate the temperature and pressure dependency of unimolecular decomposition reactions involving the three aldehydes. Collisional stabilization was calculated using a modified strong collision approximation. The high-pressure limiting rate constants were calculated through microscopic reversibility using estimates for radical-radical recombination reactions. Table 24 shows the BDEs derived from the updated thermochemistry compared to those evaluated by G. da Silva and J.W. Bozzelli [425]. The C_β–C_γ is the weakest bond, as would be expected from the proximity to the electron withdrawing carbonyl group, followed by C_α–C_β. The weakest

C–H bond is the C_α–H, followed by C_β–H. Once again group additivity methods show good agreement with theoretical computations.

Bond	propanal		n-butanal		n-pentanal	
	This work	[425]	This work	[425]	This work	[425]
C_α–C_β	84.4	83.8	84.6	84.1	84.5	83.4
C_β–C_γ	83.5	83.7	82.3	82.5	82.5	82.3
C_γ–C_δ			89.1	90.1	87.9	88.5
C_δ–C_ε					89.1	89.4
C_α–H	89.0	89.3	89.0	89.1	89.0	88.8
C_β–H	91.9	90.2	91.9	90.6	91.9	89.5

Table 24: Calculated bond dissociation energies (kcal mol^{-1}) of C–C and C–H bonds and comparison to ab initio computed values by G. da Silva and J.W. Bozzelli [425].

Table 25 reports the high-pressure limit rate parameters of initiation reactions in the modified-Arrhenius form $A\,T^n \exp[-E_a/RT]$, where A is the frequency factor, E_a is the activation energy, and R is the gas constant. Units are: cm^3, mol, s, cal, K. Relative branching ratios at four different temperatures of 1000, 1500, 2000 and 2500 K are also shown. Whilst for propanal the decomposition is mainly initiated by C_α–C_β breaking throughout the temperature range explored, for $T < 1500$ K, the chain initiation for n-butanal and n-pentanal mainly occurs via the breakage of the C_β–C_γ bond to form the $\dot{C}H_2CHO$ radical. As already mentioned, the C_α–H bond cleavage contributes to the chain initiation only at high temperatures, and even then, it is still negligible due to its high activation energy.

Reactions	k_i [s^{-1}]			Branching Ratios [%]			
	A_i	n_i	E_{ai}	1000 K	1500 K	2000 K	2500 K
propanal							
$C_2H_5CHO \leftrightarrow \dot{C}H_3 + \dot{C}H_2CHO$	1.16E+25	−2.80	85718.	32.9	31.4	29.7	27.1
$C_2H_5CHO \leftrightarrow \dot{C}_2H_5 + H\dot{C}O$	1.34E+26	−3.00	86406.	66.5	65.6	62.1	56.0
$C_2H_5CHO \leftrightarrow C_2H_5\dot{C}O + \dot{H}$	9.42E+16	−0.43	89167.	0.6	2.7	6.6	12.2
$C_2H_5CHO \leftrightarrow \dot{C}_2H_4CHO\text{-}1 + \dot{H}$	1.22E+15	−0.08	91694.	0.0	0.2	0.7	1.5
$C_2H_5CHO \leftrightarrow \dot{C}_2H_4CHO\text{-}2 + \dot{H}$	5.80E+17	−0.52	101476.	0.0	0.1	0.9	3.2
n-butanal							

n-C$_3$H$_7$CHO$\leftrightarrow$ĊH$_3$+Ċ$_2$H$_4$CHO-2	1.09E+24	−2.25	90369.	4.1	14.4	26.2	36.2
n-C$_3$H$_7$CHO$\leftrightarrow$Ċ$_2$H$_5$+ĊH$_2$CHO	5.04E+27	−3.50	84479.	67.3	52.3	40.5	31.5
n-C$_3$H$_7$CHO$\leftrightarrow$$n$Ċ$_3H_7$+HĊO	7.49E+27	−3.51	86758.	28.4	32.1	30.0	26.1
n-C$_3$H$_7$CHO$\leftrightarrow$ n-C$_3$H$_7$ĊO+ Ḣ	2.72E+17	−0.58	88995.	0.2	1.1	3.0	5.5
n-C$_3$H$_7$CHO$\leftrightarrow$Ċ$_3$H$_6$CHO-1+ Ḣ	3.62E+15	−0.23	91529.	0.0	0.1	0.3	0.7
n-pentanal							
n-C$_4$H$_9$CHO$\leftrightarrow$ĊH$_3$+Ċ$_3$H$_6$CHO-3	1.18E+22	−1.61	90120.	3.3	9.9	16.5	22.0
n-C$_4$H$_9$CHO$\leftrightarrow$Ċ$_2$H$_5$+Ċ$_2$H$_4$CHO-2	2.84E+24	−2.24	89004.	17.1	33.4	42.1	45.8
n-C$_4$H$_9$CHO$\leftrightarrow$$n$Ċ$_3H_7$+ĊH$_2$CHO	1.70E+27	−3.31	84704.	57.9	35.6	23.1	16.0
n-C$_4$H$_9$CHO$\leftrightarrow$$n$Ċ$_4H_9$+HĊO	1.20E+26	−2.94	86380.	21.6	20.4	16.8	13.7
n-C$_4$H$_9$CHO$\leftrightarrow$ n-C$_4$H$_9$ĊO+ Ḣ	1.64E+17	−0.50	89262.	0.1	0.6	1.3	2.1
n-C$_4$H$_9$CHO$\leftrightarrow$ Ċ$_4$H$_8$CHO-1+ Ḣ	4.06E+14	0.11	91691.	0.0	0.1	0.2	0.4

Table 25: High-pressure limit rate parameters of initiation reactions and relative branching ratios at different temperatures [units are: cm^3, mol, s, cal].

In order to support the QRRK/MSC approach, a direct comparison between QRRK/MSC and RRKM/ME approaches for propanal dominant unimolecular decomposition channels (C$_\alpha$–C$_\beta$ and C$_\beta$–C$_\gamma$ breaking) is presented in Figure 184. A complete description of the quantum chemical, RRKM/ME and QRRK/MSC methods and results is provided in Supplementary Material. Quantum chemical calculations were carried out using the Gaussian 09 application [253], with the B3LYP functional [167, 446] and the CBSB7 basis set used to optimize geometries, to determine frequencies (scaled by 0.99), and to carry out relaxed scans of internal rotors for use in a 1-D hindered rotor approximation. The average energy transferred in a deactivating collision was estimated as $<\Delta E_d>(T) = 200(T/300)^{0.85}$ cm^{-1} which is in line with recent RRKM/ME calculations carried out on the potential energy surfaces of propoxy [447] and butoxy [448] radicals. All calculations were carried out in an argon bath gas with Lennard-Jones parameters of σ = 3.53Å and ε/k_B = 162 K assumed. Lennard-Jones parameters for all three aldehydes were estimated from their critical constants [449] and the empirical correlations recommended by Kee and co-workers [208]. RRKM/ME computations for the two dominant unimolecular fission reactions were carried out using the the MultiWell code [178, 450] using the inverse Laplace transform method to compute $k(E)$. Identical high-pressure limiting rate constants and energy

transfer parameters were assumed in QRRK/MSC and RRKM/ME computations. QRRK/MSC results are shown to agree with the more rigorous RRKM/ME computations to within 80% under the conditions tested. Both approaches highlight that above 1 atm, fall-off in the primary unimolecular decomposition pathways of propanal is limited below 1500 K. Above this temperature, the kinetic model showed little sensitivity to the inclusion of fall-off. As part of *this work*, the QRRK/MSC approach was also validated against RRKM/ME and experimental measurements of analogous alkane decompositions from Oehlschlaeger *et al*. [451, 452] where a factor of 2—3 agreement in *k*(*T*,*p*) was observed when the QRRK/MSC and RRKM/ME/experimental recommendations were compared. Detailed results together with a detailed quantification of the fall-off behavior of aldehydes are reported in the Supplementary Material attached to this study. The above results re-enforce the applicability of the QRRK/MSC method as a means to include a cost-effective assessment of the influence of fall-off in the kinetic modelling of our high-temperature experiments.
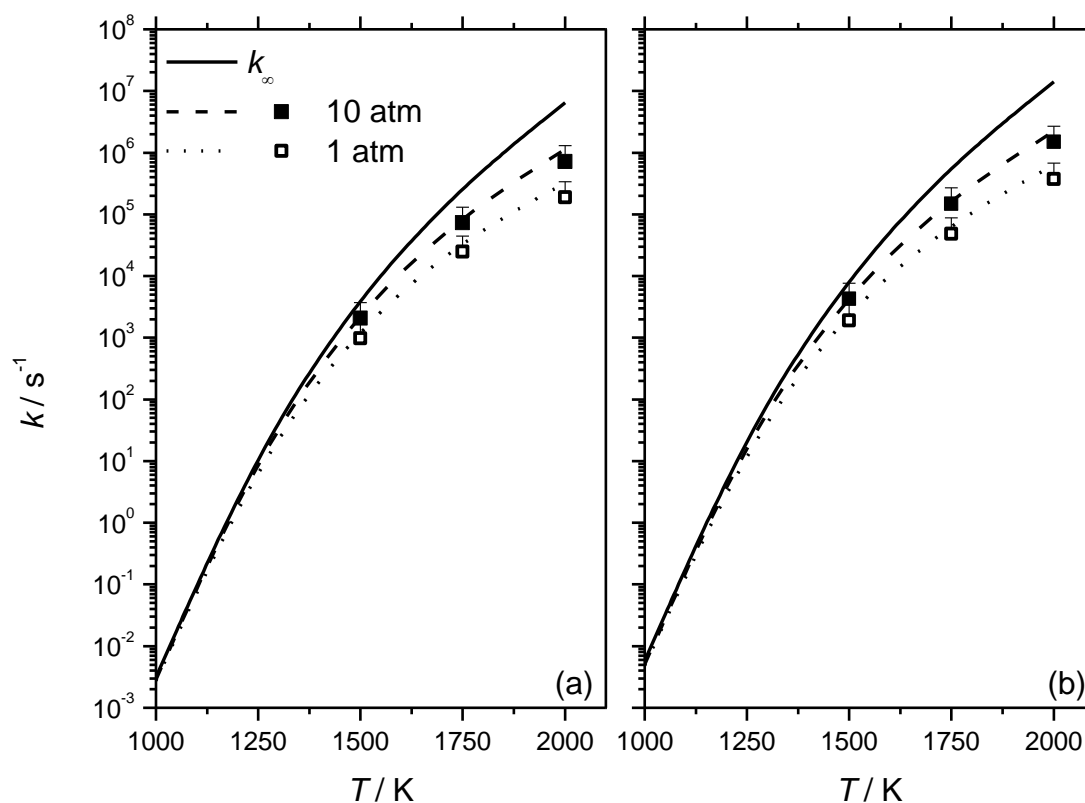
Figure 184: Comparison of RRKM/ME (symbols) and QRRK/MSC (dashed lines) derived k(T,p) for propanal thermal decomposition to (a) CH$_3$ and CH$_2$CHO, and (b) HCO+C$_2$H$_5$. 80% uncertainty bars illustrate the agreement between the two methods.

1.4 *H-abstraction reactions*

Rate constant for abstraction of the acyl H-atom at the α position were estimated by analogy with the same site in formaldehyde and acetaldehyde. The presence of the H–C=O groups leads to the formation of resonantly stabilized radicals and the reactivity of the H-atoms in the β site is slightly enhanced with respect to secondary H-atoms in alkanes. This fact is also evident observing the enthalpy of formation in **Table 23** and it is further supported by the kinetic study of 3-pentanone oxidation by Serinyel *et al.* [453]. Rate constants for abstractions from the remaining secondary and primary H-atoms were adopted according to their values used for *n*-alkanes [454, 455].

Rate constants for this class of reactions need to be defined for all the H-atom abstracting radicals. To maintain an internal consistency inside NUIG and POLIMI mechanisms, rate parameters for H-atom abstraction reactions are defined in two different ways, but still within their kinetic uncertainty, as will be discussed in part 2.1 and 2.2.

1.5 *Radical Decomposition Reactions*

Arrhenius parameters for the decomposition of α-radicals to form CO were taken from the evaluation by Simmie [456] for 1-oxo-butyl radical (*n*-$C_3H_7\dot{C}O$) decomposition to *n*-propyl radical and CO. β-scission to form ketene and C_{n-2} alkyl radical has also been included in the kinetic scheme, based on the following rationale. Methyl radical addition to ketene to form 1-oxo-propyl radical ($C_2H_5\dot{C}O$) was taken as a reference and the kinetic parameters were estimated by analogy with methyl radical addition to propylene [457]. Rate constants for the analogous β-scission of 1-oxo-butyl and 1-oxo-pentyl radical (*n*-$C_4H_9\dot{C}O$) were based on the *ab initio* calculations of Huynh and Violi [458].

For the β-radical decomposition to form acrolein (C_2H_3CHO, 1-propenal) and an alkyl radical the recommended values of Curran [457] for the reverse addition reaction are used. Rate parameters for the dehydrogenation reactions of $\dot{C}_2H_4CHO$-1 radical to form acrolein or methylketene are derived from the kinetic values of the reverse $\dot{H}$-atom addition to propylene to give *iso*-propyl radical. Methyl and ethyl radical addition to propylene to form the secondary radicals were used to derive the corresponding decomposition of β-radicals of *n*-butanal and *n*-pentanal, forming acrolein and a methyl or an ethyl radical, respectively.

β-scission of γ-radicals to produce formyl radicals and alkenes, were based on computations of *n*-butanal radical decomposition by Huynh and Violi [458]. The rate constant for the decomposition of propanal γ-radical to form H$\dot{C}$O and ethylene was obtained by analogy from a study of H$\dot{C}$O addition to propylene [458] accounting for the symmetry effect. The γ-radical of pentanal ($\dot{C}_4H_8CHO$-2) can also form a methyl radical and 1-butenal. Similarly to the estimate for methyl radical addition to acrolein in butanal, methyl radical addition to propylene was used as a reference reaction [457].

Again, the *n*-butanal calculations by Simmie [456] were adopted for the decomposition of δ-radicals to form ethylene (or propylene) and $\dot{C}H_2CHO$ radical.

Finally, the decomposition of the ε-radical ($\dot{C}_4H_8CHO$-4) of *n*-pentanal to produce ethylene and the γ-radical of propanal were based on analogy with the addition of alkyl radicals to ethylene, as suggested by Orme *et al.* [454].

Table 26 summarizes the decomposition reactions and related kinetic parameters, together with literature references.

1.6 *Radical Isomerization Reactions*

Radical isomerization reactions, i.e. internal H-atom shift through 3-, 4-, 5- and 6- membered ring intermediates, were also considered. Reaction rate constants were estimated according to general rules [459-461]. The activation energy was estimated through Evans-Polanyi correlations accounting for reaction enthalpy of the H-atom shift reaction and the ring strain energy associated with ring formation in the transition state. Frequency factors were estimated on the basis of hindered rotor effects. As the ring intermediate gets bigger, the reactions become energetically more favored due to lower ring strain energies, but conversely are entropically inhibited due to the loss of internal rotors. Isomerization reactions of the different radicals and kinetic parameters are reported in Table 26.

Reaction

propanal radicals	A	n	Ea	*[ref]*
$\dot{C}_2H_4CHO$-2 <=> $C_2H_5\dot{C}O$	3.80E+10	0.67	30200.0	*[459]*
$\dot{C}_2H_4CHO$-1 <=> $C_2H_5\dot{C}O$	3.56E+10	0.88	37300.0	"
$C_2H_5\dot{C}O$ <=> CO + $\dot{C}_2H_5$	5.78E+14	0.00	16843.5	*[456]*
$\dot{C}H_3 + CH_2CO$ <=> $C_2H_5\dot{C}O$	1.76E+04	2.48	6130.0	*[457]*
$\dot{H} + C_2H_3CHO$ <=> $\dot{C}_2H_4CHO$-1	4.24E+11	0.51	1230.0	*[457]*
$\dot{H} + CH_3CHCO$ <=> $\dot{C}_2H_4CHO$-1	4.24E+11	0.51	1230.0	*[457]*
$H\dot{C}O + C_2H_4$ <=> $\dot{C}_2H_4CHO$-2	2.56E+02	2.89	6728.4	*[458]*
n-butanal radicals				
$\dot{C}_3H_6CHO$-3 <=> $nC_3H_7\dot{C}O$	7.73E+11	0.00	15464.4	*[459]*

$\dot{C}_3H_6CHO\text{-}2 \Leftrightarrow nC_3H_7\dot{C}O$	3.80E+10	0.67	32100.0	"
$\dot{C}_3H_6CHO\text{-}1 \Leftrightarrow nC_3H_7\dot{C}O$	3.56E+10	0.88	37300.0	"
$nC_3H_7\dot{C}O \Leftrightarrow n\dot{C}_3H_7+CO$	5.78E+14	0.00	16843.5	[456]
$\dot{C}_2H_5 + CH_2CO \Leftrightarrow nC_3H_7\dot{C}O$	3.33E+02	2.73	13953.9	[458]
$\dot{C}H_3 + C_2H_3CHO \Leftrightarrow \dot{C}_3H_6CHO\text{-}1$	1.76E+04	2.48	6130.0	*[457]
$H\dot{C}O + C_3H_6 \Leftrightarrow \dot{C}_3H_6CHO\text{-}2$	1.28E+02	2.89	6728.4	[458]
$\dot{C}_3H_6CHO\text{-}3 \Leftrightarrow \dot{C}H_2CHO + C_2H_4$	3.95E+13	0.00	22316.3	[456]

n-pentanal radicals

$\dot{C}_4H_8CHO\text{-}4 \Leftrightarrow nC_4H_9\dot{C}O$	3.67E+12	−0.60	7090.0	[459]
$\dot{C}_4H_8CHO\text{-}3 \Leftrightarrow nC_4H_9\dot{C}O$	7.85E+11	−0.12	16800.0	"
$\dot{C}_4H_8CHO\text{-}2 \Leftrightarrow nC_4H_9\dot{C}O$	3.80E+10	0.67	32100.0	"
$\dot{C}_4H_8CHO\text{-}1 \Leftrightarrow nC_4H_9\dot{C}O$	3.56E+10	0.88	37300.0	"
$nC_4H_9\dot{C}O \Leftrightarrow p\dot{C}_4H_9 + CO$	5.78E+14	0.00	16843.5	*[456]
$n\dot{C}_3H_7 + ch2co \Leftrightarrow nC_4H_9\dot{C}O$	3.33E+02	2.73	13953.9	*[458]
$\dot{C}_2H_5 + C_2H_3CHO \Leftrightarrow \dot{C}_4H_8CHO\text{-}1$	8.80E+03	2.48	6130.0	*[457]
$H\dot{C}O + C_4H_8\text{-}1 \Leftrightarrow \dot{C}_4H_8CHO\text{-}2$	1.28E+02	2.89	6728.4	[458]
$\dot{C}H_3 + C_3H_5CHO \Leftrightarrow \dot{C}_4H_8CHO\text{-}2$	1.76E+04	2.48	6130.0	*[457]
$\dot{C}H_2CHO + C_3H_6 \Leftrightarrow \dot{C}_4H_8CHO\text{-}3$	1.88E+02	3.11	3660.0	*[456]
$\dot{C}_2H_4CHO\text{-}2 + C_2H_4 \Leftrightarrow \dot{C}_4H_8CHO\text{-}4$	1.32E+04	2.48	6130.0	*[454]

Table 26: Rate constant parameters of decomposition and isomerization reactions of aldehydes radicals [units are: cm³, mol, s, cal] and references (* extended analogy as discussed in this paper).

Due to their possible competing effect, a comparison of decomposition and isomerization rate constants of each radical is relevant. Figure 185 shows this comparison for *n*-pentanal radicals in the temperature range 1000–2500 K. Figure 185d shows the 1-5 isomerization reaction of the ε-radical, occurring through the energetically favored six membered ring intermediate, which prevails over the decomposition channel at

temperatures lower than ~1430 K. The remaining figures show that generally, the decomposition paths dominate. Moreover, Figure 185b shows that for *n*-pentanal γ-radical ($\dot{C}_4H_8CHO$-2) the decomposition reaction to form 3-butenal and a methyl radical prevails over the alternate channel generating 1-butene and a formyl radical. Decomposition of the α-radical (1-oxo-pentyl radical, *n*-$C_4H_9\dot{C}O$) to form CO and an *n*-butyl radical largely prevails over the 1-5 isomerization reaction in the complete range of temperature. For this reason isomerization rate constants for the α-radical are not reported in Figure 185. A similar analysis for propanal and *n*-butanal radicals is reported in the Supplementary Material.
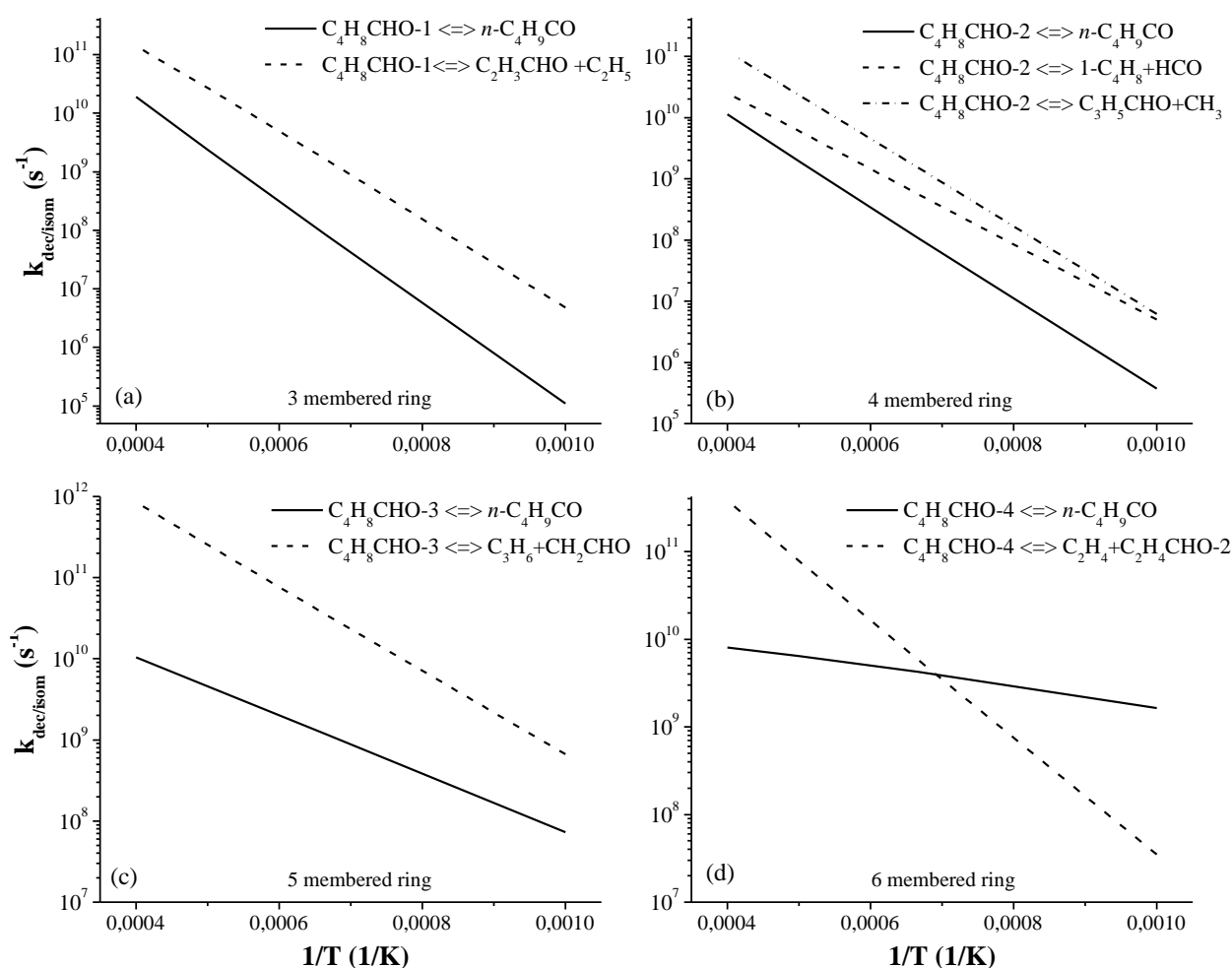
Figure 185: Isomerization (solid lines) and decomposition (dashed lines) reactions of n-pentanal radicals a) β-radical (C_4H_8CHO-1), b) γ-radical (C_4H_8CHO-2), c) δ-radical (C_4H_8CHO-3), d) ε-radical (C_4H_8CHO-4).

2. Overall kinetic mechanism

The Transport Data Estimator package of the Reaction Mechanism Generator software of Green and co-workers has been used to provide relevant transport properties [58].

2.1 *NUIG Kinetic Mechanism*

The aldehyde mechanism was coupled with the NUIG C_0–C_4 sub-mechanism, recently revised and validated as reported in several recent studies [436-438, 440, 441, 462].

H-atom abstraction rates at the β secondary site forming $\dot{C}_4H_8CHO$-1 radicals were based on those for secondary H-atom abstractions in ketones. Rate constants for H-abstractions by $\dot{O}H$ and $H\dot{O}_2$ radicals were taken from the *ab initio* calculations for ethylmethyl ketone by Zhou *et al.* [463] and by Mendes *et al.* [464] respectively.

Before coupling the aldehyde sub-mechanism with the NUIG kinetic scheme, some modifications were made.

The total initiation rate constant for *n*-butanal has been increased of a factor of 1.5 with respect to the calculated reaction rates previously discussed. This correction factor, well within the kinetic uncertainty, has been also applied to POLIMI mechanism. H-atom abstraction from the α carbonyl site has been decreased by about 20% with respect to the reference abstraction from acetaldehyde. Rate constants for abstraction reactions by $\dot{H}$, $\dot{O}H$, $\dot{C}H_3$ and $H\dot{O}_2$ radicals are listed in the Supplementary Material. Moreover, overall rate constants of H-abstraction by $\dot{O}H$ radical for C_1–C_4 aldehydes were studied in shock tubes very recently by Wang *et al.* [465], further supporting the kinetic parameters proposed here.

The overall kinetic model, with thermodynamic and transport properties, consisting of 2,011 reactions and 329 species is available as part of the Supplementary Material.

2.2 POLIMI kinetic mechanism

Metathesis reactions are treated according to the systematic approach described by Ranzi *et al.* [52]. The reactivity of primary and secondary H-atoms are considered to be the same as those for alkanes. Similar to the acyl H-atoms of formaldehyde and acetaldehyde, H-atom abstraction on the α site requires a correction of –4500 cal mol^{-1} to be applied to the activation energy for H-atom abstraction of a primary H-atom from a methyl group. Moreover, a greater selectivity of $\dot{H}$ and $H\dot{O}_2$ radicals relative to the corresponding one of $\dot{O}H$ and $\dot{C}H_3$ radicals is also accounted for. With regards to abstraction from the β-site, leading to resonantly stabilized radicals, a correction factor of about 1.25 has been applied to increase the frequency factor of the secondary H-atom abstraction in alkanes. Rate constants for abstraction reactions by $\dot{H}$, $\dot{O}H$, $\dot{C}H_3$ and $H\dot{O}_2$ radicals are listed in the Supplementary Material. Again, the kinetic parameters proposed here for H-abstractions by $\dot{O}H$ radical are further supported by the recent study by Wang *et al.* [465].

Figure 185 shows that the lifetime of large radicals is so short at high temperatures that they decompose and isomerize without significant interactions with the remaining mixture. When parallel competing reactions are absent or not strongly dependent on temperature, larger radicals can be conveniently and directly substituted by their reaction products. Therefore, it is possible to assume them as being directly transformed

into their products which are already part to the C_0–C_4 mechanism [17]. This is the advantage of a lumped approach: it leads to a reduction of the total number of species needed to describe the overall oxidation process. The analysis of Figure 9 highlights that only the ε-radical ($\dot{C}_4H_8CHO$-4) of pentanal shows a temperature dependent competition between isomerization and decomposition rates at high-temperatures. Therefore, it is convenient to keep the ε-radical inside the scheme. The four remaining radicals have been assumed to directly transform into their final products. The same assumption has been also applied to the intermediate radicals of *n*-butanal and propanal. The effect of these simplifications has proven to be of very limited importance in the high-temperature range of the analyzed conditions. At low-temperatures, interactions with oxygen forming peroxyl radicals will precede the decomposition of primary radicals; therefore, it would be necessary to increase the detail of the involved species.

The oxidation mechanism adopted here [101] consists of over 10,000 reactions and more than 350 species and was developed based on hierarchical modularity. It covers from hydrogen and oxygenated species, up to diesel and biodiesel fuels. The thermochemical data for most species in the global mechanism were obtained from the CHEMKIN thermodynamic database [466, 467]. For those species whose thermodynamic data are not available in the literature, the group additivity method was used to estimate these properties [468].

The overall kinetic model, with thermo and transport properties, is available in CHEMKIN format from: http://creckmodeling.chem.polimi.it and in the Supplementary Material.

3. Model predictions and comparison with experimental data

The new experimental data on pyrolysis speciation and ignition delay times for the three aldehydes were used to validate the aldehyde sub-mechanism in both the kinetic models. Furthermore, propanal pyrolysis data by Lifshitz *et al.* [427] and ignition delay times by Akih-Kumgeh and Bergthorson [429] were also used. Similarly, *n*-butanal ignition delay times measured by Davidson *et al.* [432] and by Zhang *et al.* [434] were also compared with model predictions. Finally, comparisons with premixed laminar flame speeds of propanal and *n*-butanal by Veloo *et al.* [430, 431] complete this kinetic study. The current study, therefore considers all relevant experimental data which exist at present for long chain aldehydes, thus providing a comprehensive evaluation of mechanism performance. A summary of the experimental data at which the aldehydes mechanisms were validated in this study is reported in Table 27.

Aldehyde	*Reactor/Facility*		*T* (K)	*p* (atm)	ϕ	*Ref*
Formaldehyde	Shock Tube	Pyrolysis	1160–1890	1.4–2.5	/	Hidaka et al. [412]
	"	"	1200–2000	1.3–3.0	/	Hidaka et al. [414]
	"	"	1560–2276	0.9–2.5	/	Eiteneer et al. [411]
	"	Oxidation	1600–3000	1.0–2.0	0.54, 0.63	Dean et al. [415]
	"	"	1160–1618	1.4–2.5	0.25, 0.5, 1.0, 2.0, 4.0	Hidaka et al. [412]
	"	"	1334–1974	0.8–2.3	0.16, 0.25, 1.0, 1.7, 5.9	Eiteneer et al. [411]
	Plug Flow Reactor	"	945	1.0	1.56	Li et al. [416]
	"	"	1095	1.0	0.93	"
Acetaldehyde	Shock Tube	Pyrolysis	1013–1577	1.2-2.8	/	Yasunaga et al. [424]
	Jet Stirred Reactor	Oxidation	900–1300	1,10	0.09, 0.43, 0.82, 1.0, 1.61	Dagaut et al. [422]
	Shock Tube	"	1276–1703	1.7–2.6	0.2, 0.4, 1	Yasunaga et al. [424]
Propanal	Shock Tube	Pyrolysis	970–1300	2.0–2.7	/	Lifshitz et al. [427]
	"	"	972–1372	1.4–2.8	**/**	**This work**
	"	Oxidation	1170–1750	1.0, 3.0	0.5, 1.0, 2.0	**This work**
	"	"	1150–1560	1.0, 12.0	0.5, 1.0	Akih-Kumgeh [429]
	Premixed Flat Flame	"	314–2000	0.05	1.0	Kasper et al. [428]
	Laminar Premixed Flames	"	343–2320	1.0	0.75–1.6	Veloo et al. [430]
n-butanal	Shock Tube	Pyrolysis	1096-1368	1.1–2.8	/	**This work**
	"	Oxidation	1190–1550	1.7	1.0, 2.0	Davidson et al. [432]
	"	"	1180–1580	1.3, 5, 10	0.5, 1.0, 2.0	Zhang et al. [434]
	"	"	1224–1634	1.0, 3.0	0.5, 1.0, 2.0	**This work**
	Laminar Premixed Flames	"	343–2320	1.0	0.75–1.6	Veloo et al. [431]
n-pentanal	Shock Tube	Pyrolysis	970–1370	1.4–2.8	/	**This work**
	"	Oxidation	1167–1850	1.0, 3.0	0.5, 1.0, 2.0	**This work**

Table 27: Experimental data used for the validation of the aldehydes mechanisms.

3.1 *Pyrolysis in shock tubes*

Propanal pyrolysis of a 1% fuel mixture in argon was studied in a single-pulse shock tube by Lifshitz *et al.* [427] over the temperature range 1000–1300 K. Experimental data and modeling predictions are shown in Figure 186 for the NUIG and POLIMI mechanisms. Furthermore, Figure 187 compares experimental data from this work and predicted concentration profiles for propanal (3%) decomposition in argon. Propanal undergoes decomposition at ~1050 K according to both the experimental data sets and the mechanisms slightly under-predict fuel conversion: an overall good agreement is observed for the main products (CO and C_2H_4), as well as for the minor hydrocarbon species, particularly in terms of their relative concentrations. Analysis of the mechanisms shows that chain radical initiation occurs via unimolecular decomposition reactions involving a C–C bond cleavage, and propanal decomposition mainly occurs via H-atom abstraction reactions by $\dot{H}$ atoms and $\dot{C}H_3$ radicals.
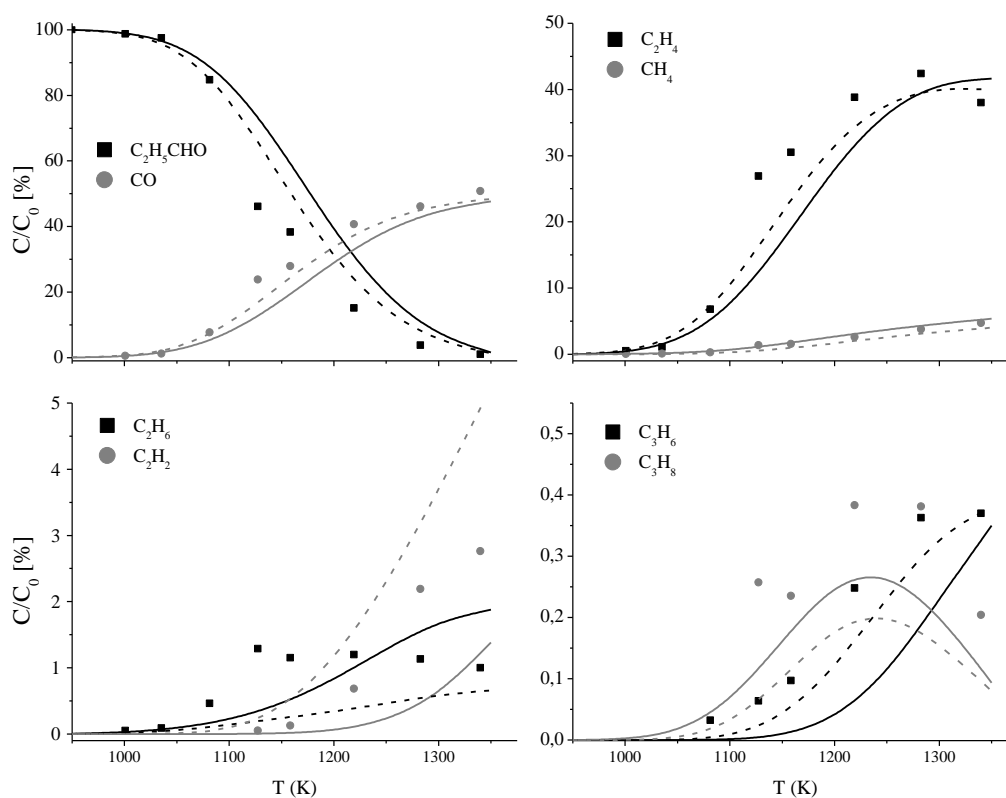
Figure 186: Predicted and experimental concentration profiles from shock tube pyrolysis of 1% propanal in argon [427] (τ=2.5 ms). Experimental (symbols), POLIMI mechanism (solid lines) and NUIG mechanism (dashed lines).
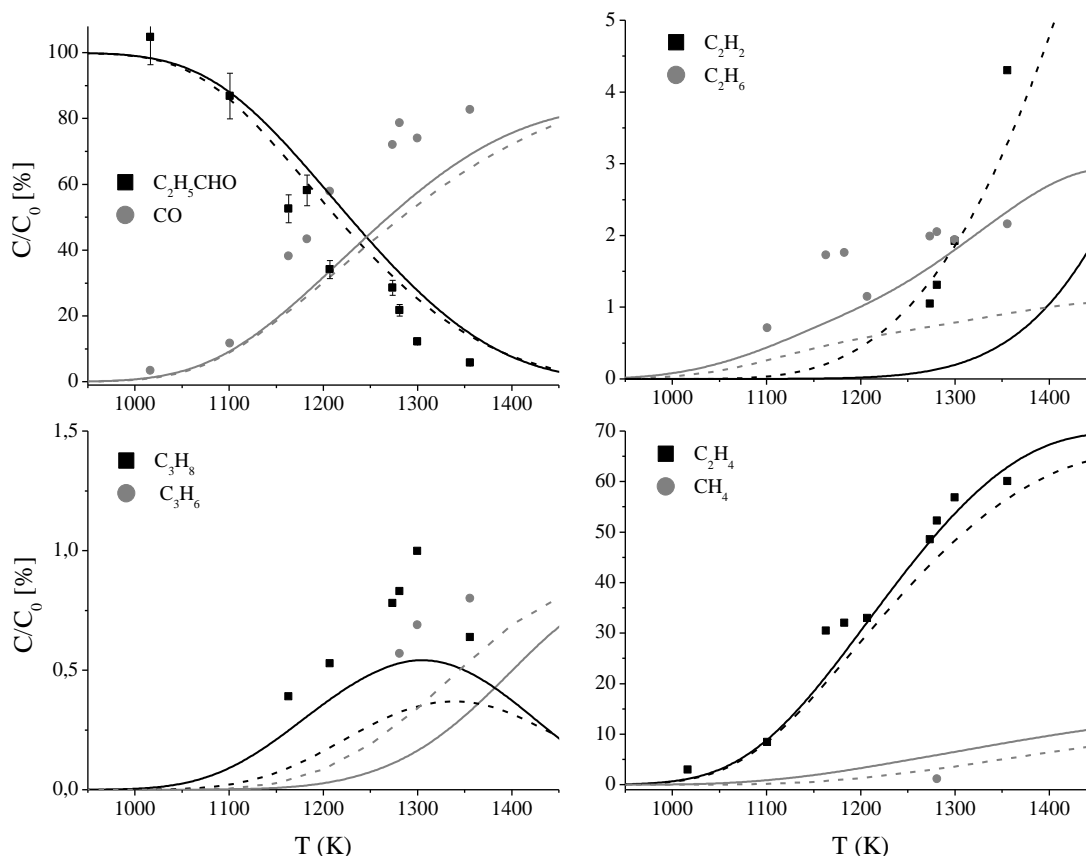
Figure 187: Predicted and experimental concentration profiles from shock tube pyrolysis of 3% propanal in argon (τ=2.5 ms). Experiments (symbols), POLIMI mechanism (solid lines) and NUIG mechanism (dashed lines).

The POLIMI mechanism under-predicts C_2H_2 formation reported in Figure 186 by ~40% at temperatures higher than 1200 K and even larger deviations are observed in Figure 187. The chemistry of the vinyl radical ($\dot{C}_2H_3$) is responsible for this under-prediction. H-atom abstractions from acrolein (C_2H_3CHO) are the main pathways generating acetylene, either through the vinyl radical formed by the CO elimination of the α radical, or via the β-scission of the γ radical to give formyl radical. The same chemistry is responsible for the over-prediction of acetylene observed for the NUIG mechanism in Figure 186, while good agreement is observed in Figure 187. The under-predictions of propane and propylene can be attributed to a low methyl radical concentration, i.e. a relatively low importance of the chain initiation reactions. The results shown in Figure 186 and Figure 187 are considered to be well within the expected experimental uncertainties.

Figure 188 compares experimental and predicted concentration profiles for *n*-butanal (3%) decomposition in argon. Predictions of fuel conversion as well as the major products, such as CO and ethylene, are in very good agreement with the experimental observations. Smaller hydrocarbons detected in the measurements (CH$_4$, C_2H_2, C_2H_6, C_3H_6 and C_3H_8), are also very well captured by both models. The main relative deviations are

observed in the trace amount of propane; this under-prediction is due to methyl and ethyl radical recombination. In analogy with the direct formation of methane and CO from acetaldehyde [424], molecular reactions to form CO or ketene and the corresponding C_{n-1} or C_{n-2} alkane are considered, and they play only a limited role under the investigated conditions.

Figure 189 shows a global rate of production analysis performed at 1200 K, for both the NUIG and POLIMI mechanisms. The chain initiation occurs *via* unimolecular decomposition reactions, the successive decomposition of formyl, ethyl and propyl radical intermediates leads to the generation of $\dot{H}$ atoms and $\dot{C}H_3$ radicals, which are responsible, via H-atom abstraction, for ~90% of fuel consumption, at 1200 K.
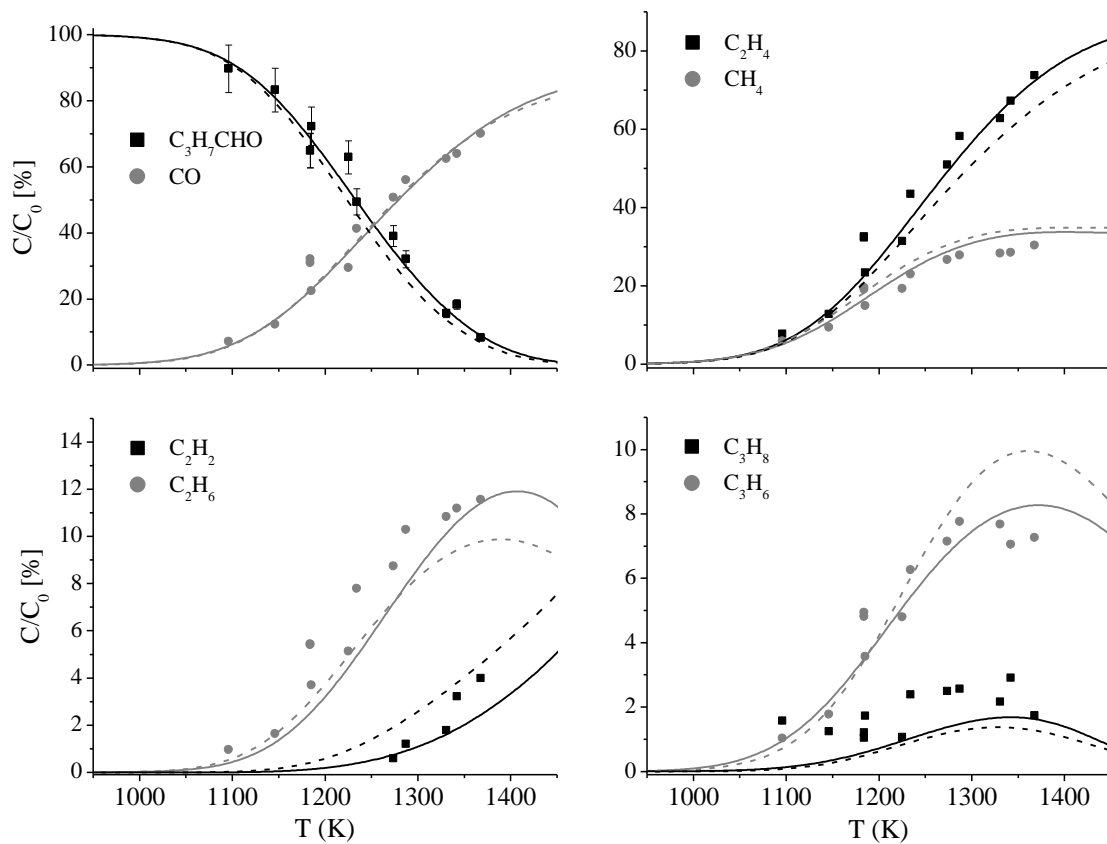
Figure 188: Predicted and experimental concentration profiles from shock tube pyrolysis of 3% n-butanal in argon (τ=2.0 ms). Experiments (symbols), POLIMI mechanism (solid lines) and NUIG mechanism (dashed lines).
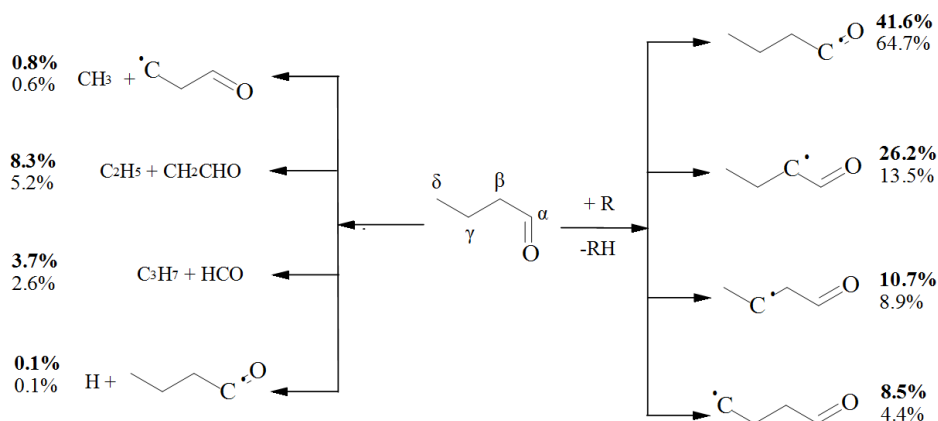
Figure 189: Global rate of production analysis carried out at 1200 K under the same pyrolysis conditions of Figure 188, NUIG mechanism (bold) and POLIMI mechanism (standard).
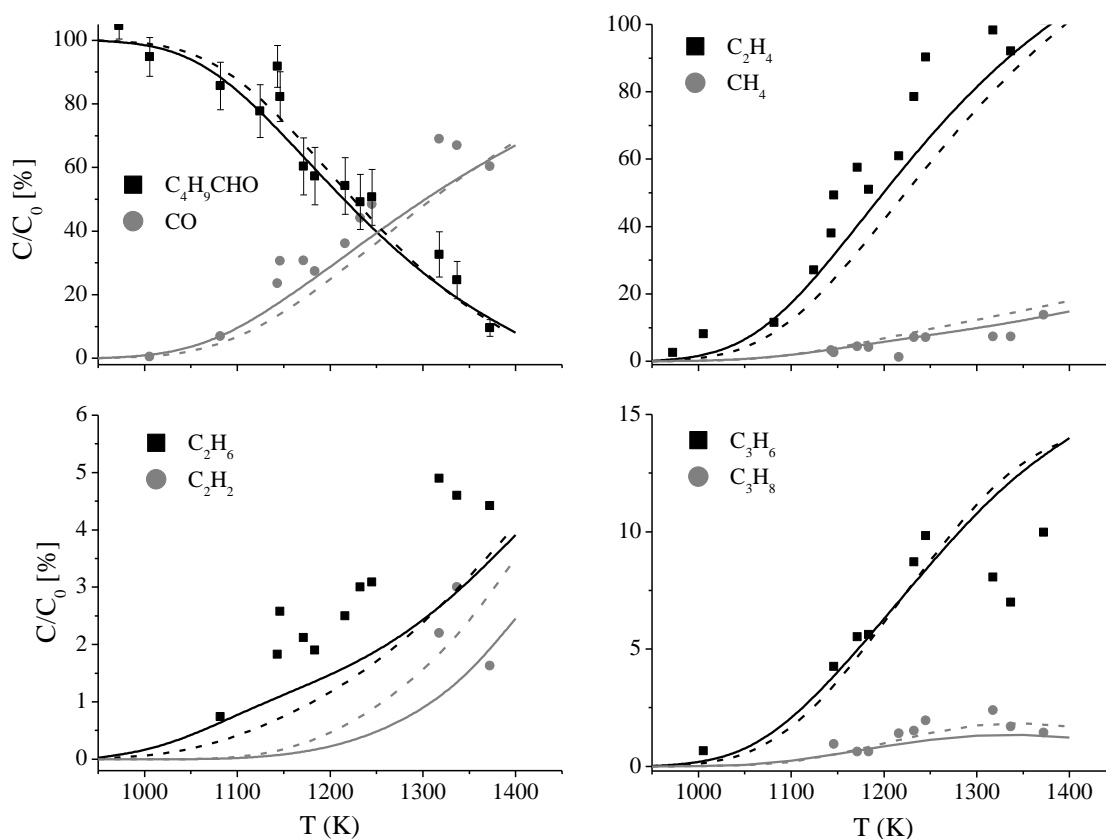
Figure 190: Predicted and experimental concentration profiles from shock tube pyrolysis of 3% n-pentanal in argon (τ=2.3 ms). Experiments (symbols), POLIMI mechanism (solid lines) and NUIG mechanism (dashed lines).

Figure 190 compares the species predictions by both mechanisms to experimental data for 3% *n*-pentanal pyrolysis in argon. Both of the models are able to reproduce the fuel conversion, indicating that *n*-pentanal starts to decompose at temperatures of ~1000–1050 K. Both of the mechanisms reproduce the relative

importance of all species. Within the experimental uncertainty, the two kinetic schemes satisfactorily reproduce the minor hydrocarbon species.

Experimentally, the three aldehydes seem to behave very closely for temperatures up to ~1200 K. Propanal shows the highest conversion rate for T>1200 K, while no big differences are highlighted between n-pentanal and n-butanal. As schematically shown in Figure 181, this can be justified by the fact that the H-abstraction from the highly reactive α and β positions of propanal results in a very high production of H· radical, via β-scission reactions. Both the mechanisms predict very similar reactivity up to ~1200 K, with butanal showing the highest conversion rate for higher temperatures.

Both mechanisms agree with the pyrolytic experiments, indicating that the core pyrolytic kinetics and thermodynamics are of reasonable accuracy. Particularly, both the models satisfactorily reproduce fuel and methane profiles for the three aldehydes, indicating that rate constants for unimolecular decomposition (initiation step), abstraction by hydrogen and methyl radical (propagation steps), and methyl-methyl radical recombination (termination step) are well-constrained.

3.2 *Ignition delay times in shock tubes*

3.2.1 Propanal

Ignition delay time measurements at 1 and 3 atm reflected pressures made in this study are shown in Figure 191 together with modeling predictions. Experiments were carried out using 1% fuel in O_2/argon as described in the original paper. While the mechanisms are in good or reasonable agreement with the experimental data at 3 atm under all investigated conditions, larger deviations are observed at atmospheric pressure. In this case, both of the mechanisms predict higher apparent activation energies, particularly at stoichiometric and fuel-lean conditions.
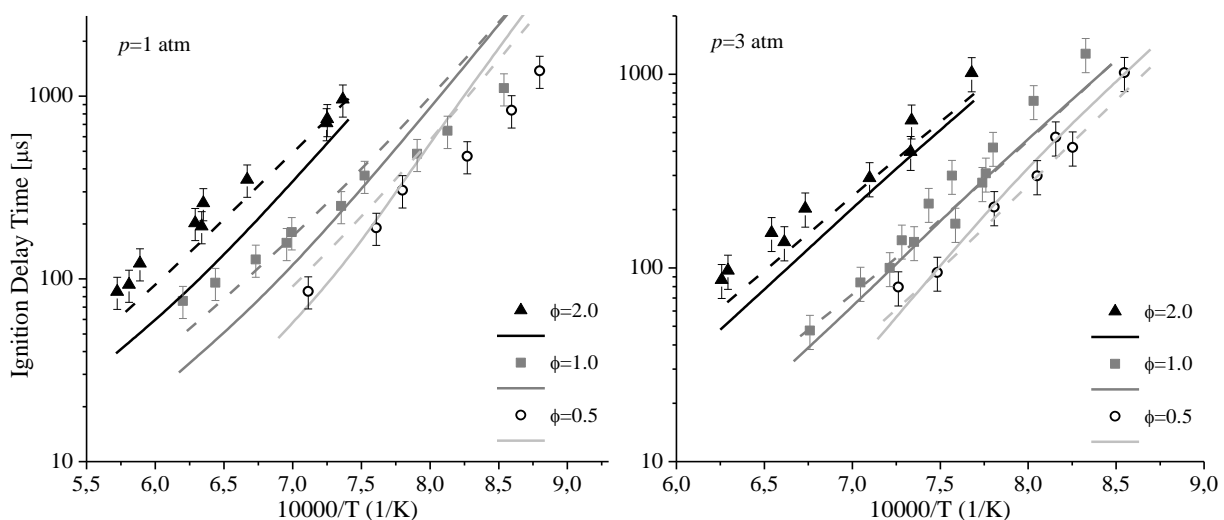
Figure 191: Predicted and experimental ignition delay times of 1 % propanal in O₂/Ar mixtures. Experiments (symbols), POLIMI mechanism (solid lines) and NUIG mechanism (dashed lines).

Figure 192 compares model predictions and ignition delay times measured by Akih-Kumgeh and Bergthorson [429]. In line with the previous observations of Figure 191, while good agreement is obtained at 12 atm pressure, at atmospheric pressure the activation energy is over-predicted by both mechanisms. The NUIG mechanism shows better agreement with the data of Akih-Kumgeh, primarily for stoichiometric atmospheric conditions.
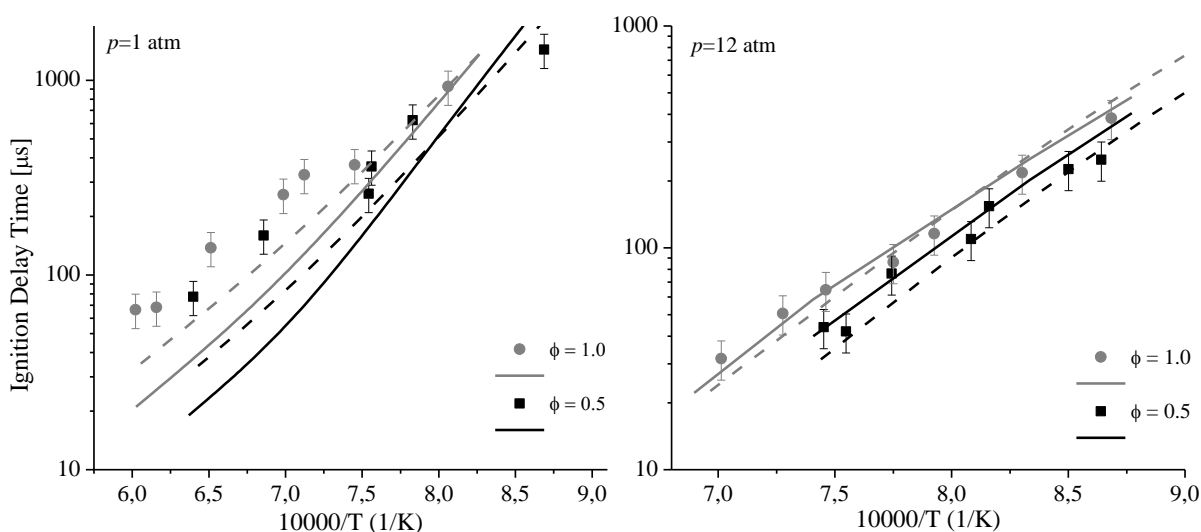
Figure 192: Predicted and experimental ignition delay times of O₂/Ar mixtures containing 1.25% propanal [429]. Experiments (symbols), POLIMI mechanism (solid lines) and NUIG mechanism (dashed lines).
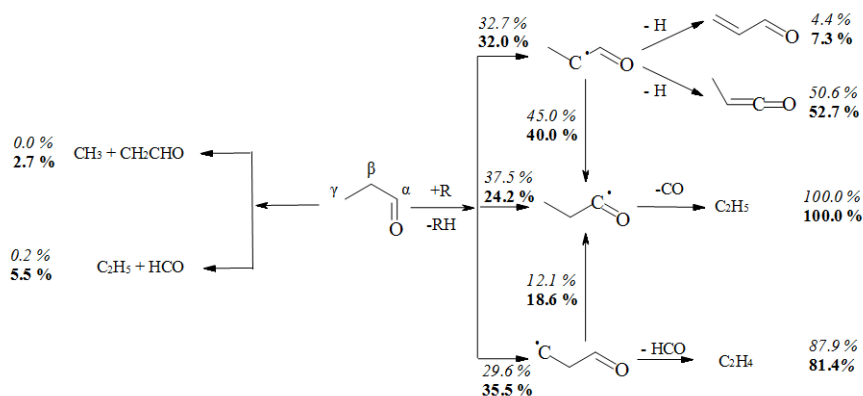
Figure 193: Rate of production analysis for 1% propanal in O₂/Ar mixtures at φ = 1.0, p = 1 atm. NUIG mechanism, T = 1150 K (italic) and 1620 K (bold).

Figure 193 shows a global rate of production analysis at stoichiometric conditions, atmospheric pressure, and at temperatures of 1150 K and 1620 K for the NUIG mechanism. At 1620 K, the unimolecular decomposition pathways contribute ~8% to fuel consumption, being negligible at 1150 K. The fuel decomposition mostly occurs through the α channel, either via direct H-atom abstractions or due to isomerization of β and γ radicals, with a relevant formation of $\dot{C}_2H_5$ radicals. At 1620 K ethyl radicals mostly decompose to ethylene and $\dot{H}$ atoms promoting reactivity, while at 1150 K ethyl radicals can also react with molecular oxygen producing $H\dot{O}_2$ radicals, thus inhibiting the system.

Figure 194 shows the sensitivity coefficients of ignition delay times to rate constants in the NUIG mechanism. Sensitivity coefficients were calculated for each reaction via a brute force method, where a negative coefficient indicates a reaction promoting reactivity, i.e. decreases ignition delay times. Increasing the rates of H-atom abstraction reactions by $\dot{H}$ atoms decreases reactivity making ignition delay times longer. This is because by reacting with any species but O_2 a $\dot{H}$ atom is removed from the system to form H_2, rather than reacting with O_2 to generate $\ddot{O}$ atoms and $\dot{O}H$ radicals which is the predominant chain-branching process for high temperature combustion. H-atom abstraction by $H\dot{O}_2$ radicals on the α site appears as a sensitive parameter at 1150 K, due to the subsequent decomposition of H_2O_2 to generate two $\dot{O}H$ radicals, which is highlighted as a promoting reaction. The importance of radical species such as formyl, methyl, vinyl and ethyl radicals is also highlighted, confirming the influence of reactions involving β-scission products such as ethylene and acrolein in the correct determination of propanal ignition. It is also of interest to observe the strong competition between vinyl radical decomposition through the third body reaction forming acetylene and $\dot{H}$ atom, enhancing reactivity, and the bimolecular disproportionation reaction to form acetylene and H_2, inhibiting reactivity.
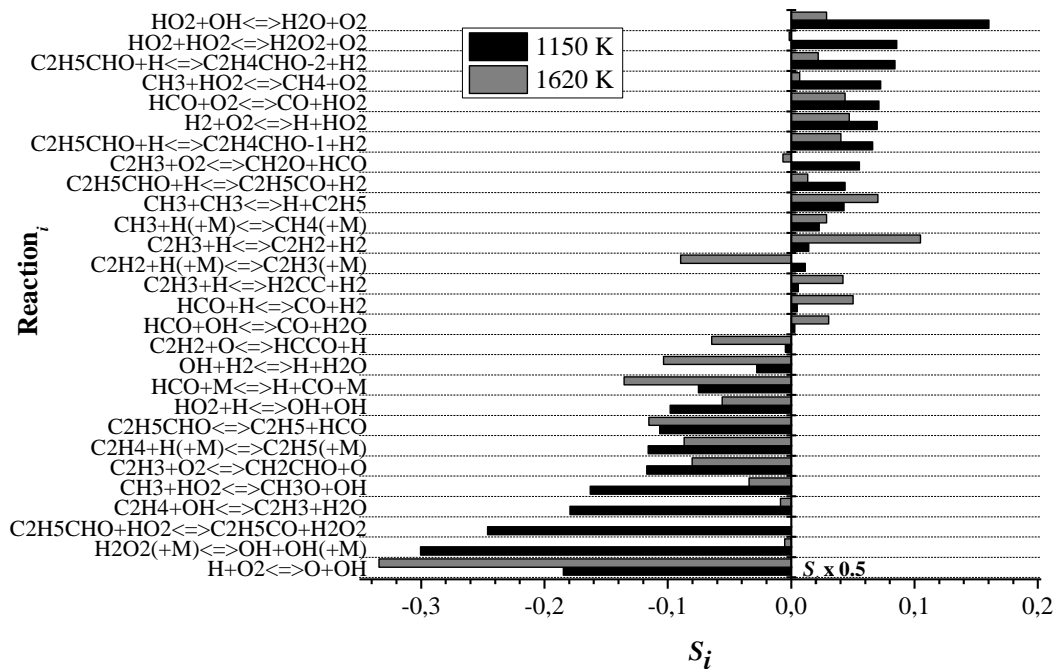
Figure 194: Sensitivity coefficients of ignition delay times to rate constants for 1% propanal in O_2/Ar mixtures at φ = 1.0, p = 1 atm, 1150 K (black bars) and 1620 K (grey bars). NUIG mechanism.

3.2.2   *n*-butanal

Figure 195 shows a comparison between experimental and calculated ignition delay times for mixture of 1% *n*-butanal in O_2/argon. Both of the mechanisms agree with the experimental data at the conditions tested, with the NUIG mechanism being consistently slower compared to the POLIMI mechanism, particularly at atmospheric and fuel rich conditions. The larger deviations from the experimental observations, mainly in terms of apparent activation energies, can be observed for the POLIMI and NUIG mechanisms at 1 atm and φ = 0.5.

Figure 196 compares the mechanisms predictions with the experimental measurements of Davidson et al. [432], at two different stoichiometries. The NUIG mechanism reproduces the apparent activation energy in both cases, while the POLIMI mechanism, slightly faster than NUIG, over-predicts the activation energies, but is still in reasonable agreement with experiments.
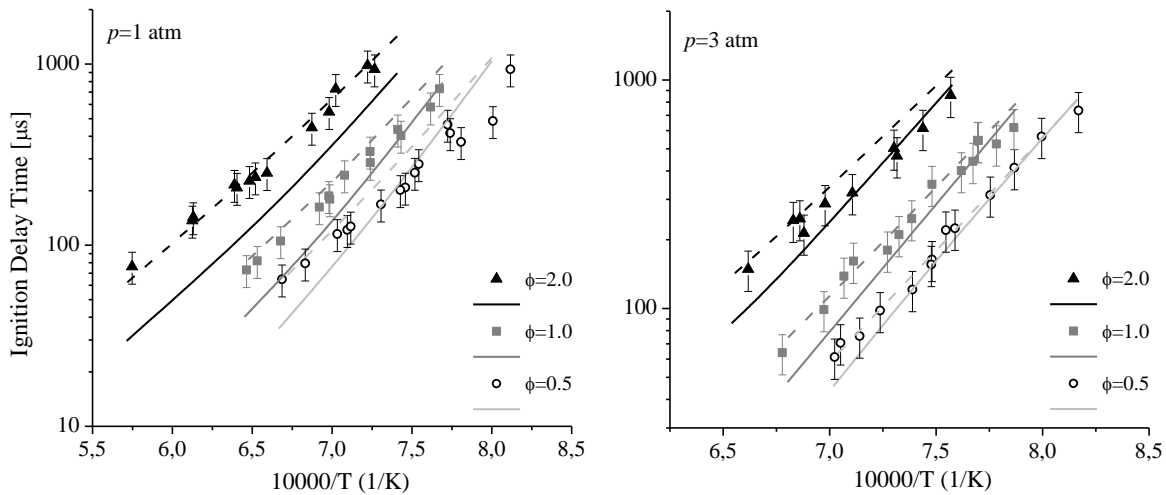
Figure 195: Predicted and experimental ignition delay times of O_2/Ar mixtures containing 1% n-butanal. Experiments (symbols), POLIMI mechanism (solid lines) and NUIG mechanism (dashed lines).
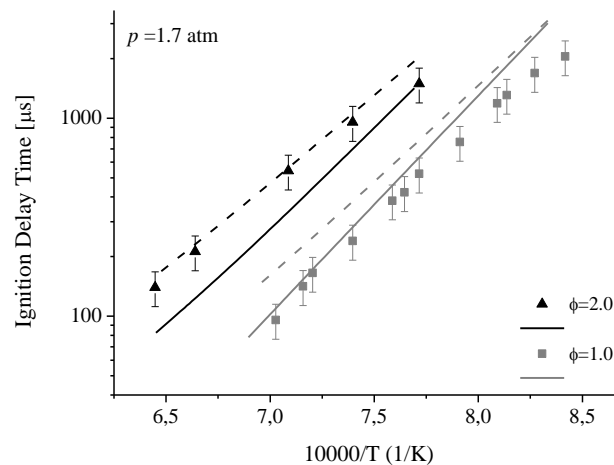
Figure 196: Predicted and experimental ignition delay times of O_2/Ar mixtures containing 1% n-butanal [432]. Experiments (symbols), POLIMI mechanism (solid lines) and NUIG mechanism (dashed lines).

Figure 197 compares all three sets of experimental data (our experiments at 1 atm, Zhang *et al.* [434] at 1.3 atm and Davidson *et al.* [432] at 1.7 atm). Following the approach of Davidson *et al.* [432], all of the data have been scaled to 1.7 atm, assuming a scaling factor of $p_{exp}/1.7^{-0.52}$. Reasons for the choice of this particular scaling factor are reported in the study of Davidson et al. [432]. The experimental data agree under stoichiometric conditions, while the measurements of Zhang are notably faster under fuel-rich conditions. Figure 198 compares the experimental data from Zhang *et al.* [434] with model predictions. Both of the mechanisms tend to over-predict ignition delay times, particularly at 1.3 atm. The POLIMI mechanism reproduces these experiments more closely than the NUIG mechanism, which over-predicts the ignition

delay times, particularly at atmospheric pressure. However, on the basis of the observations of Figure 197, the performances of the two mechanisms are considered to be in satisfactory agreement with the experimental data.
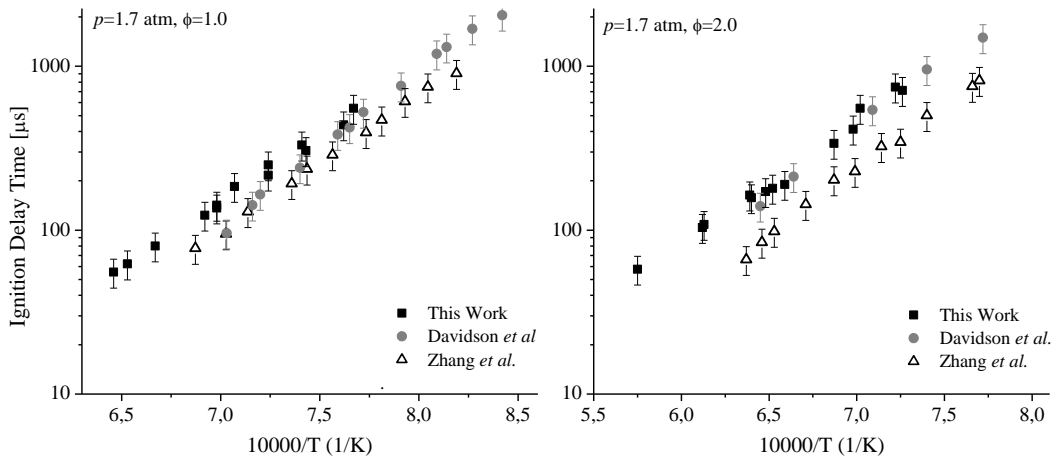
Figure 197: Comparison amongst experimental ignition delay times for n-butanal-O₂/Ar mixtures, scaled at 1.7 atm. This work: 1% fuel at 1 atm (squares); Zhang et al [434]: 1.2% fuel at 1.3 atm (triangles); Davidson et al. (circles) [432]: 1% fuel at 1.7 atm.
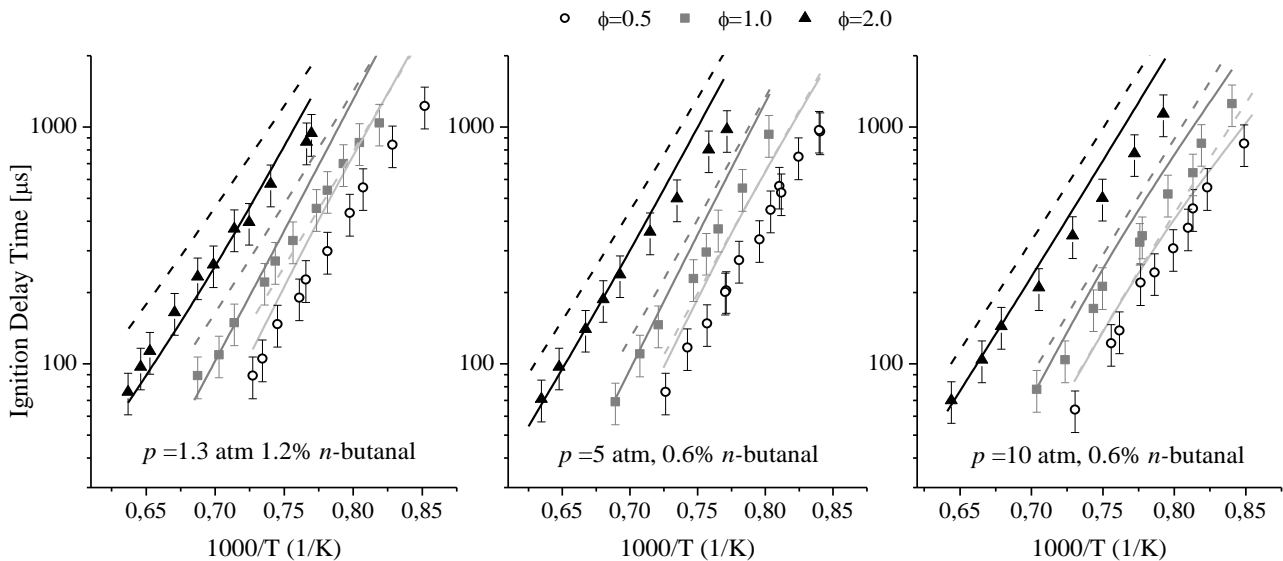
Figure 198: Predicted and experimental ignition delay times of n-butanal in O₂/Ar mixtures [434]. Experiments (symbols), POLIMI mechanism (solid lines) and NUIG mechanism (dashed lines).

Figure 199 shows a reaction path analysis carried out for fuel-lean (ϕ = 0.5) and fuel-rich (ϕ = 2.0) mixtures at 3 atm and 1320 K, with the NUIG mechanism. The unimolecular decomposition reactions account for 12.6% and 7.5% of fuel consumption under fuel-rich and fuel-lean conditions, respectively. H-atom abstraction from

the α site is an important decomposition channel (~27.0 %). The β and γ sites show similar selectivities (20–30%), with β favored at fuel-rich conditions and γ at fuel-lean conditions. This can be explained on the basis of a higher production of $\dot{O}H$ radicals through the chain-branching reaction $\dot{H}+O_2 \leftrightarrow \ddot{O}+\dot{O}H$, due to the higher concentration of oxygen in the system. $\dot{O}H$ radicals are then more likely to abstract on the γ site relative to the β site.

Figure 200 presents sensitivity coefficients of ignition delay times to rate constants for the NUIG mechanism at the same conditions shown in Figure 199, in order to identify the reactions controlling the auto-ignition behavior. Chain initiation reactions generating highly reactive radicals promote the system's reactivity at both conditions. Particularly, the breaking of the weak $C_β–C_γ$ bond producing an ethyl radical and the breaking of the $C_α–C_β$ bond producing a formyl radical exhibit some sensitivity. Decreasing the oxygen concentration largely enhances the importance of small unsaturated species such as acetylene, ethylene, propylene and the parent radicals. H-atom abstraction reaction by $\dot{H}$ atoms reduces the reactivity due to the competition with the branching reaction $\dot{H}+O_2 \leftrightarrow \ddot{O}+\dot{O}H$. Furthermore, H-atom abstractions from the α site increase the ignition delay times due to the formation of 1-propyl radical, which mainly decomposes to produce methyl radicals. Analyses carried out for the POLIMI mechanism highlighted the same classes of fuel specific reactions as sensitive for the ignition delay time determination.
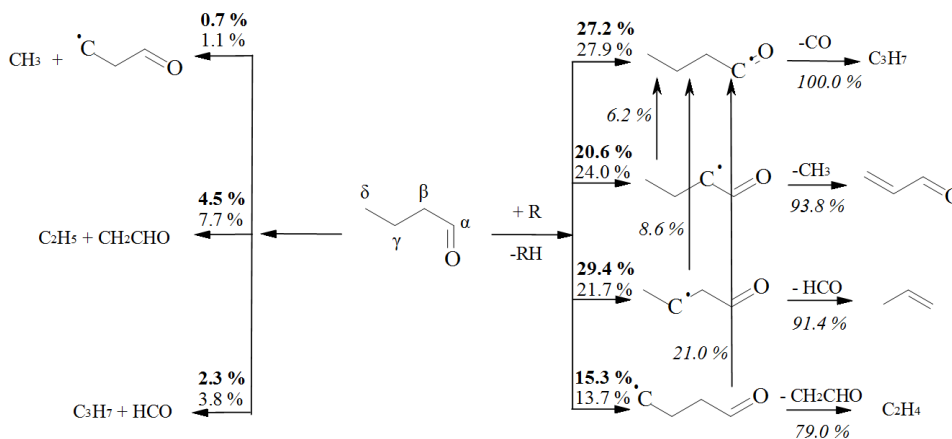
Figure 199: Rate of production analysis for 1 % n-butanal in O_2/Ar mixtures at p=3 atm, T=1320 K at φ = 0.5 (bold) and φ = 2.0 (standard).
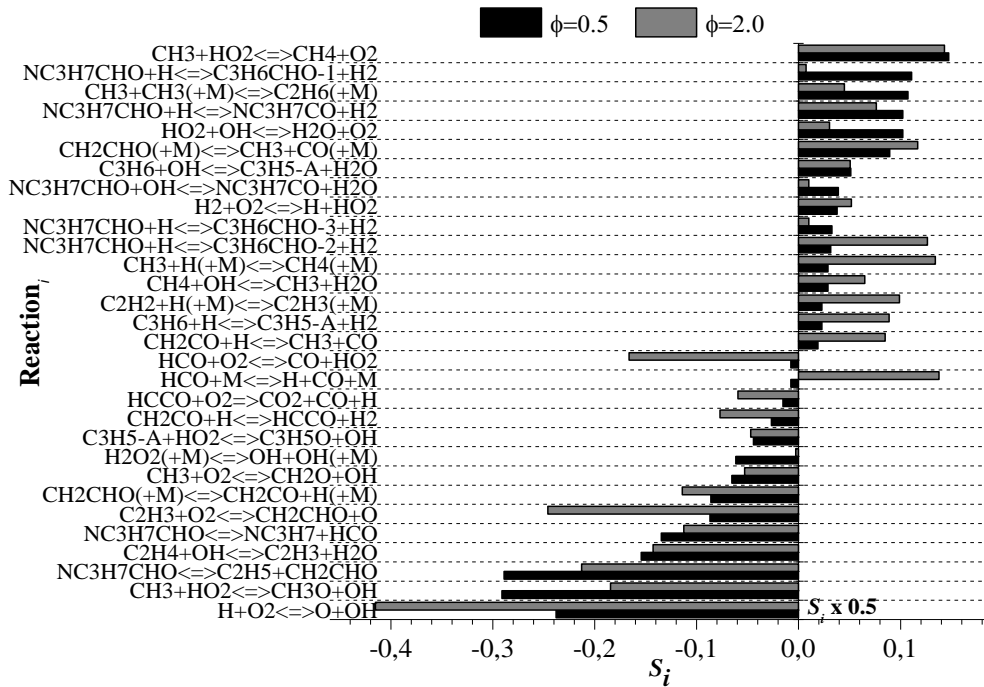
Figure 200: Sensitivity coefficients of ignition delay times to rate constants for 1 % n-butanal in O_2/Ar mixtures at p = 3 atm, T =
1320 K at φ = 0.5 (black bars) and φ =2.0 (grey bars).

3.2.3   *n*-pentanal

Experimental and calculated ignition delay times for 1% *n*-pentanal mixtures in O_2/Ar are reported in Figure 201. The NUIG mechanism captures the experimental data at every condition tested. The POLIMI mechanism tends to predict shorter ignition delay times for fuel-rich conditions particularly at atmospheric pressure. At 1850 K, the ignition delay time is under-predicted by a factor of three. Again, the model over-predicts the apparent activation energy. At 3 atm both of the models over-estimate the ignition delay time at fuel-lean conditions for temperatures below 1100 K. Lower temperature $H\dot{O}_2$ chemistry, outside the scope of this work, might have an effect at these conditions.
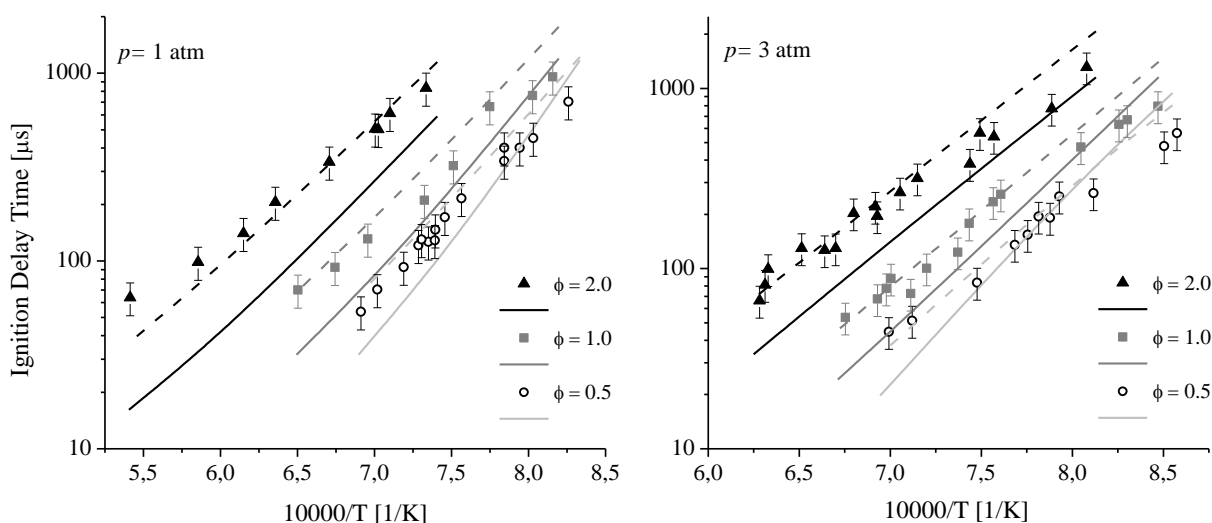
Figure 201: Predicted and experimental ignition delay times of O₂/Ar mixtures containing 1 % n-pentanal. Experiments (symbols), POLIMI mechanism (solid lines) and NUIG mechanism (dashed lines).

Figure 202 presents a rate of production analysis carried out for the POLIMI mechanism at intermediate conditions (ϕ =1.0, p = 2 atm, T = 1300 K). Unimolecular decomposition reactions account for less than 3.0% of n-pentanal consumption. Decomposition occurs mainly via H-atom abstraction from the α position (~54%), followed by abstraction from the γ and δ (~15%) positions. At the conditions investigated ~75% of the ε-radical ($\dot{C}_4H_8CHO$-4) isomerizes to the α-radical (n-C₄H₉$\dot{C}O$), which is assumed to eliminate CO (90%) and/or decompose to n-propyl and ketene (10%). As already discussed in Section 4.2, the POLIMI lumped mechanism only accounts for the ε-radical, the rate of production is simply obtained through a *de-lumping* procedure.
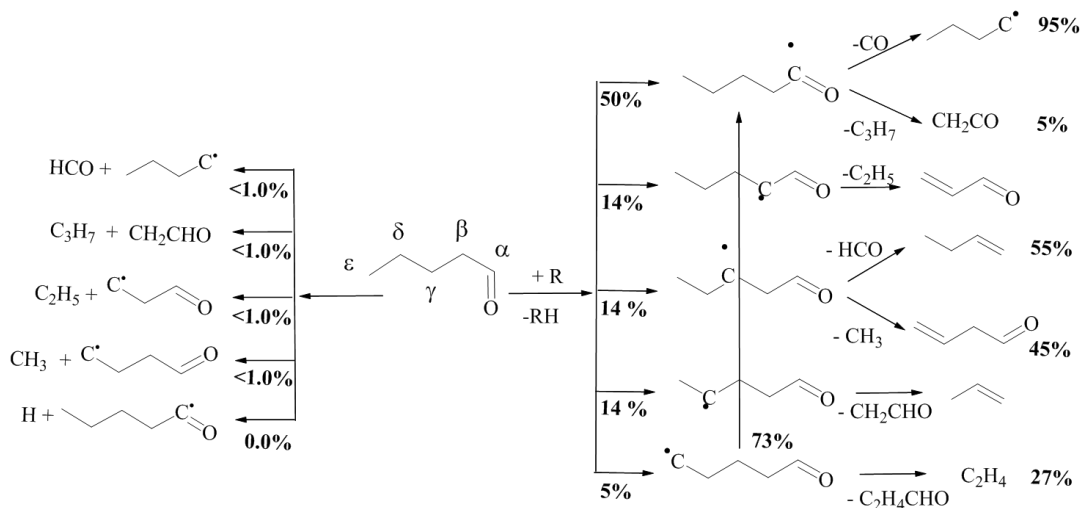
Figure 202: Rate of production analysis for 1 % n-pentanal in O₂/Ar mixtures at φ =1.0, p = 2 atm, T = 1300 K, POLIMI mechanism.

Figure 203 shows the sensitivity analyses of ignition delay times to rate constants for the NUIG and POLIMI mechanisms, at ϕ = 1.0, p = 2 atm, and T = 1300 K. With regards to fuel specific reactions, both of the

mechanisms show that H-atom abstraction rates from the γ and δ positions have positive coefficients, i.e. they decrease reactivity (longer ignition delay times). Unimolecular initiation reactions enhance reactivity in the NUIG mechanism, whilst they are not highlighted as sensitive for the POLIMI mechanism. H-atom abstractions from the α position contribute to shortened ignition delay times for the POLIMI mechanism. Once again, the great importance of the C_0–C_4 sub-mechanism is highlighted. To make the comparison more clear, the most sensitive branching reaction $\dot{H}+O_2 \leftrightarrow \ddot{O}+\dot{O}H$, normalized to −1 for both the mechanisms, is not reported in Figure 203.
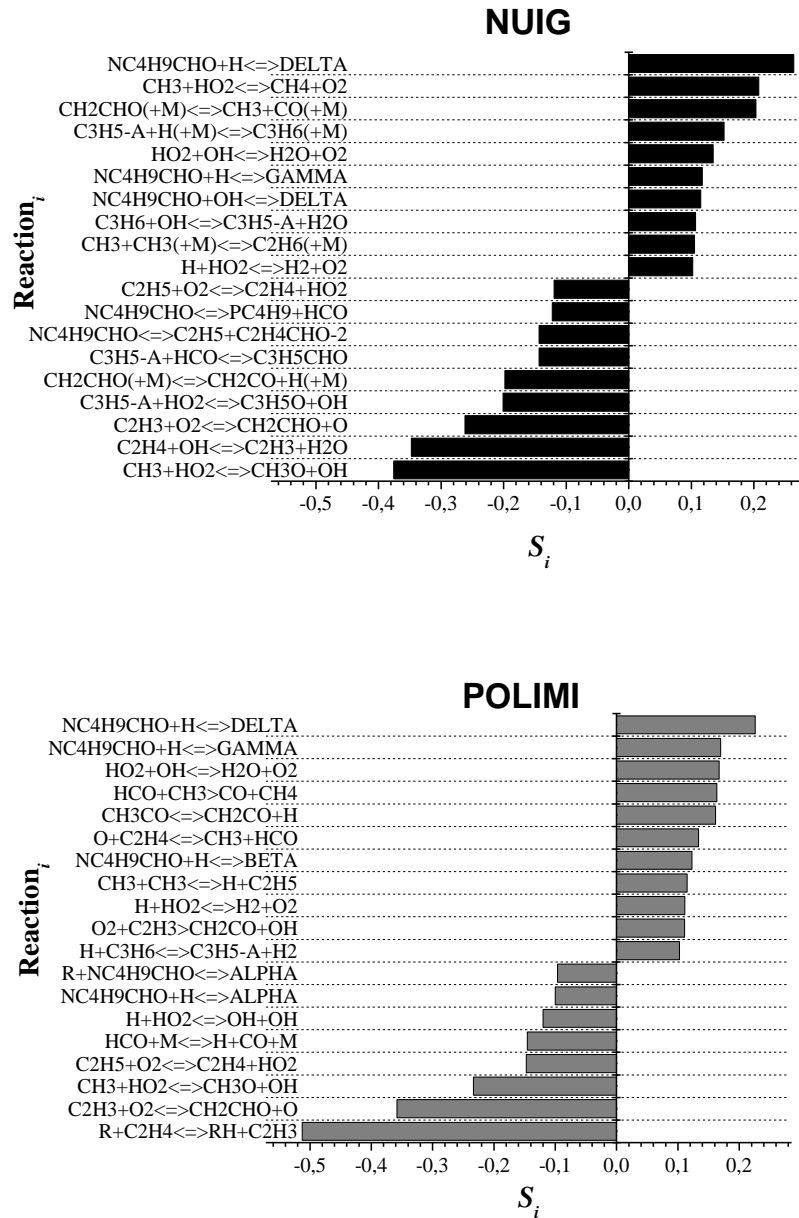
Figure 203: Sensitivity coefficients of ignition delay times to rate constants for 1 % n-pentanal in O₂/Ar mixtures at φ = 1.0, p = 2 atm, T = 1300 K. NUIG mechanism (black bars), POLIMI mechanism (grey bars).

3.3 *Apparent activation energy of ignition delay times*
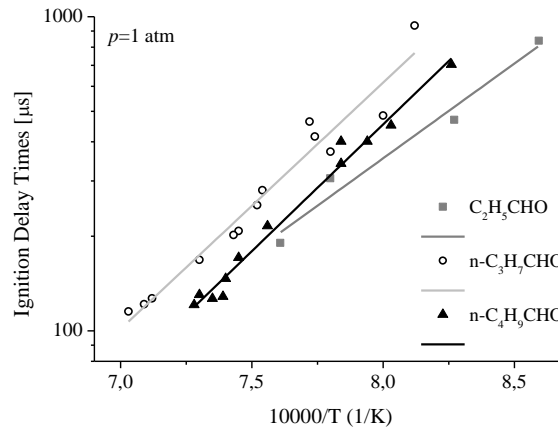
Figure 204: 1% fuel–O₂/Ar mixtures; φ = 0.5, p = 1 atm, experimental data from present work (symbols) and linear fit (lines).

Figure 204 compares the experimental ignition delay times at 1 atm and lean conditions for the three aldehydes. Propanal tends to be the faster to ignite, followed by *n*-pentanal and *n*-butanal. At 1% fuel concentration, due to the larger amount of oxygen, one would expect *n*-pentanal to be the fastest to ignite followed by *n*-butanal and propanal. In contrast propanal is the most reactive and this trend is correctly reproduced by both of the mechanisms. In fact, a greater amount of $\dot{H}$ atoms are produced by primary propagation reactions during propanal oxidation, while methyl radicals are formed via the decomposition of β and γ radicals in *n*-butanal and *n*-pentanal, respectively. This figure also highlights a lower apparent activation energy for propanal (~25 kcal mol^{-1}) relative to C_4 and C_5 aldehydes (~35-40 kcal mol^{-1}). The average of the experimental values from Akih-Kumgeh and Bergthorson [429], Zhang et al. [434], and Davidson et al. [432] confirm this trend. As far as the predicted activation energies are concerned, the averages of previous simulations show that the NUIG mechanism over-estimates the activation energy by ~5 kcal mol^{-1}, while the POLIMI mechanism exceeds by ~10 kcal mol^{-1}. The largest deviations are observed in both cases for fuel-lean conditions. While these deviations need to be better investigated, it is important to observe that they are largely due to the C_0–C_4 mechanism.

3.4 *Laminar flame speeds*

3.4.1 Propanal

Figure 205 shows a comparison of experimental [430] and predicted laminar flame speeds for propanal/air mixtures at atmospheric pressure. Experimental (53 cm s^{-1}) and predicted peaks (52.7 cm s^{-1} and 56.7 cm s^{-1} respectively for POLIMI and NUIG mechanism) are correctly placed at ϕ = 1.1–1.15. The NUIG mechanism over-predicts the laminar flame speed at stoichiometric and fuel-rich conditions by 2–4 cm s^{-1}. The POLIMI mechanism well reproduces the flame speed over the full equivalence ratio range explored. Accounting for

the experimental uncertainty represented in Figure 205 by the error bars (3.5–12.5%), the overall agreement of the mechanisms seems quite satisfactory.
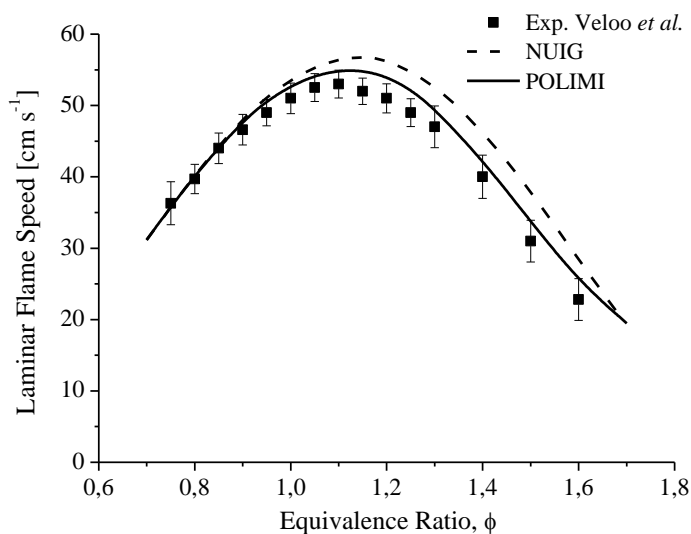
Figure 205: Experimental and computed laminar flame speeds of propanal/air flames at T_u = 343 K and p = 1 atm. Experimental data (symbols) by Veloo et al. [430], POLIMI mechanism (solid lines) and NUIG mechanism (dashed lines).

Figure 206 reports the sensitivity coefficients of the laminar flame speed to rate constants for propanal/air flames at ф = 1.3, T_u = 343 K, using both mechanisms. H-atom abstraction reaction from the α site is sensitive in reducing the flame speed for both mechanisms. H-atom abstraction from the γ site has a positive sensitivity coefficient (flame propagation enhancer) in the NUIG mechanism. This is due to the fact that, while the γ radical forms $\dot{H}$ and CO from H$\dot{C}$O, ethyl radical can also react with an $\dot{H}$ atom forming two methyl radicals. Results confirm that the chemistry of propanal at flame temperatures is dominated by the C_0–C_2 portion of the mechanisms.
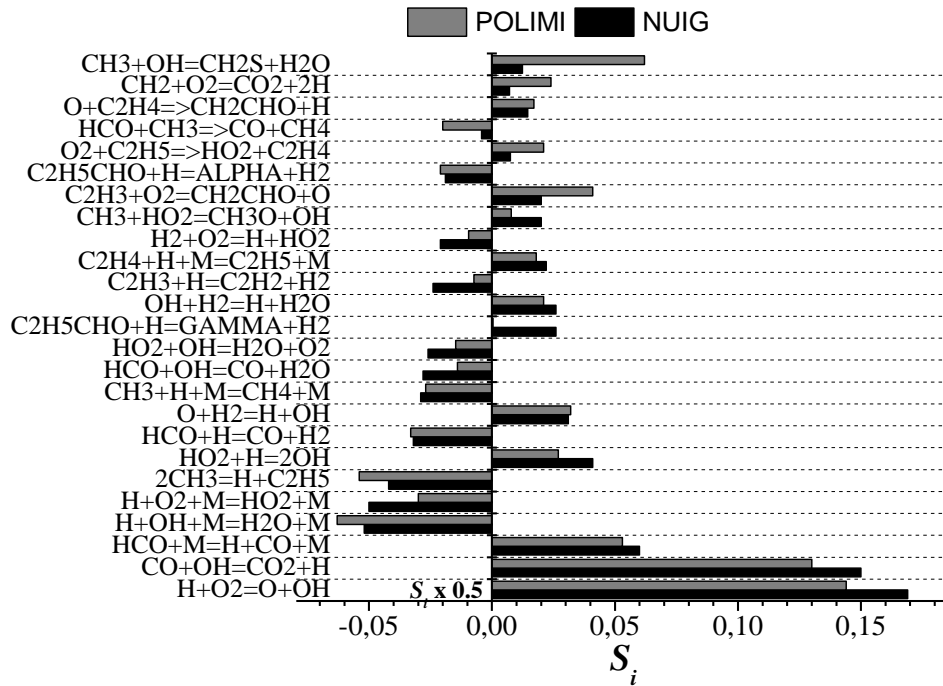
Figure 206: Sensitivity coefficients of laminar flame speed to rate constants for propanal/air flames at φ = 1.3, T$_u$ = 343 K [430]. NUIG mechanism (black bars) and POLIMI mechanism (grey bars).

3.4.2   *n*-butanal

Experimental [431] and calculated laminar flame speeds for *n*-butanal/air mixtures at atmospheric pressure are reported in Figure 207. Both the mechanisms are able to well reproduce the experimental measurements for any stoichiometry. Sensitivity analyses of flame speeds to rate constants have been carried out for both mechanisms at stoichiometric conditions, the results of which are reported in Figure 208. Again, the chemistry is mainly controlled by the C$_0$–C$_4$ sub-mechanism. Apart from the highly sensitive reactions involving $\dot{H}$, $\dot{C}H_3$, $H\dot{C}O$ and $\dot{O}H$ radicals, also vinyl radical and ethylene chemistry controls the flame speed predictions.
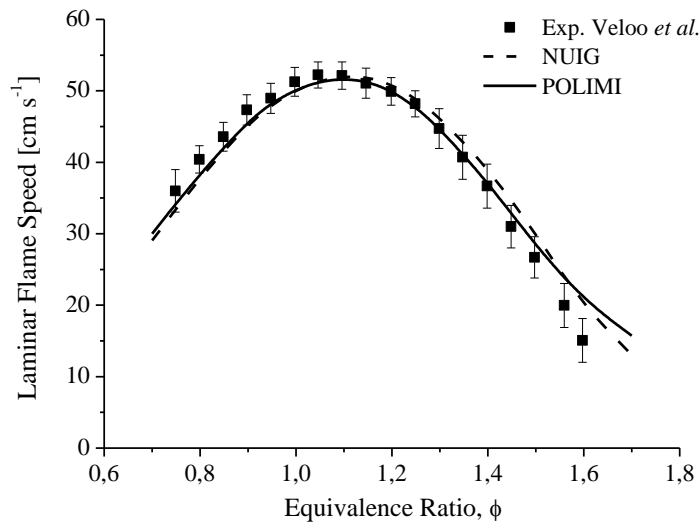
Figure 207: Experimental and computed laminar flame speeds of n-butanal/air flames at T_u = 343 K and p = 1 atm [431].

Experimental data (symbols) by Veloo et al. [431], POLIMI mechanism (solid lines) and NUIG mechanism (dashed lines).
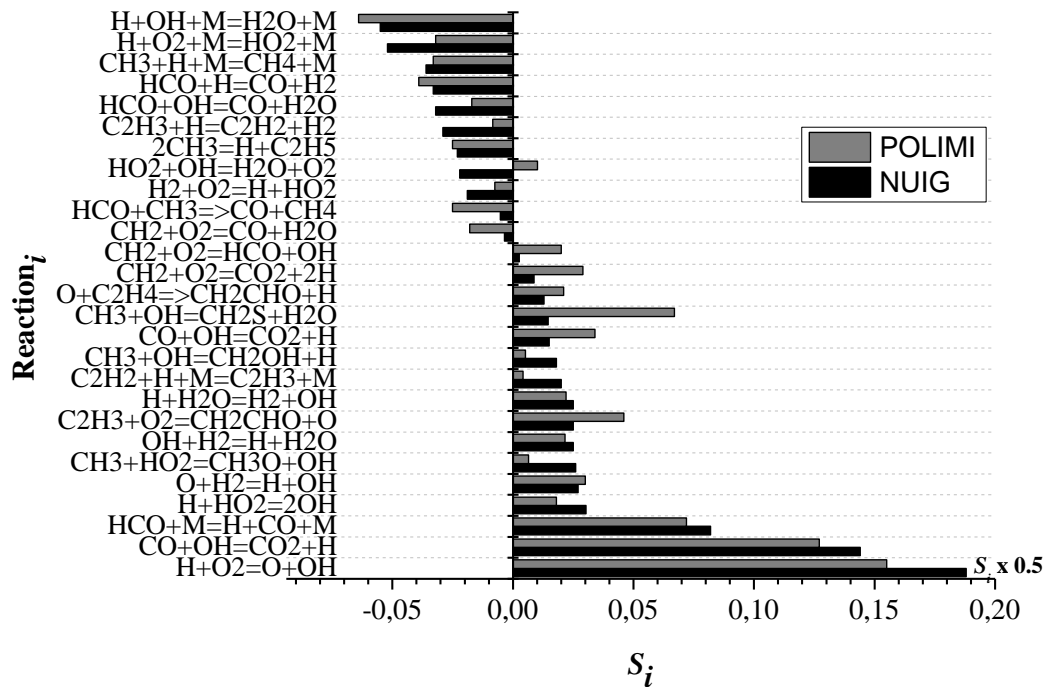
Figure 208: Sensitivity coefficients of laminar flame speed to rate constants for n-butanal/air flames at φ = 1.0 T_u = 343 K [431].

NUIG mechanism (black bars) and POLIMI mechanism (grey bars).

NUIG mechanism is slightly faster than POLIMI in flame speeds predictions, with maximum deviations of ~2 cm s^{-1} on the rich side. This is in contrast with the previous comments on ignition delay times. This fact

supports the key role played by the C_0–C_4 sub-mechanisms, but also shows that key reactions for ignition delay times are different from those more sensitive for laminar flame speeds.

3.4.3 Comparisons of aldehydes/air laminar flame speeds

Figure 209 compares predicted laminar flame speeds of C_1–C_5 aldehydes/air mixtures at T_u = 343 K and atmospheric pressure. Formaldehyde flame speed peaks at ~115 cm s^{-1} and equivalence ratio ϕ of ~1.5. This behavior can be justified on the basis of both the higher production of Ḣ and the absence of ĊH$_3$ radicals, with respect to the other aldehydes, as clearly highlighted by Figure 210. The oxidation of formaldehyde at high temperatures completely occurs through the formation of HĊO, which is rapidly decomposed to Ḣ + CO through a third body reaction. Experimental measurements of formaldehyde laminar flame speed were not available in the literature when this study was firstly submitted for publication. During the revision process laminar flame speed data of trioxane were published and a comparison with model predictions is reported in the Supporting Information available in the online version of this study. Remaining aldehydes show peaks of 50 ± 2 cm s^{-1}, at equivalence ratios of ~1.1–1.15. The higher concentration of methyl radical shown by acetaldehyde (Figure 210b) justifies its lower flame speed, with respect to propanal. Experimentally [430, 431], propanal flames propagate slightly faster relative to *n*-butanal flames, particularly at rich conditions. This trend is well captured by both NUIG and POLIMI mechanisms. Once again, Figure 210a supports this observation showing a slightly higher Ḣ concentration in the propanal flame with respect to those of *n*-butanal and *n*-pentanal.
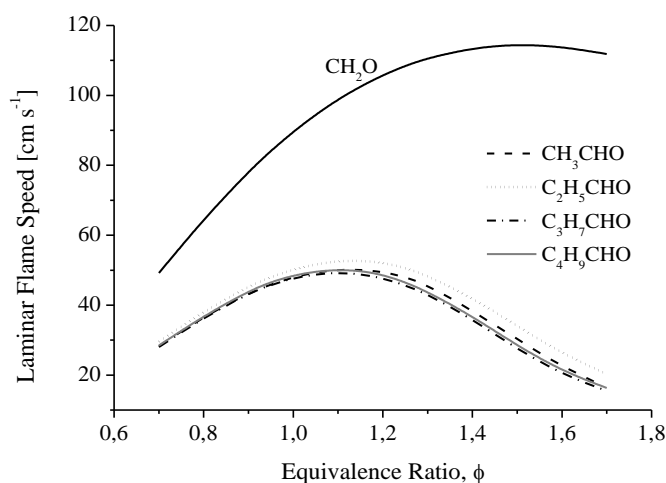
Figure 209: Comparisons of computed laminar flame speeds (POLIMI mechanism) of aldehyde/air at T_u=343 K and p=1 atm.
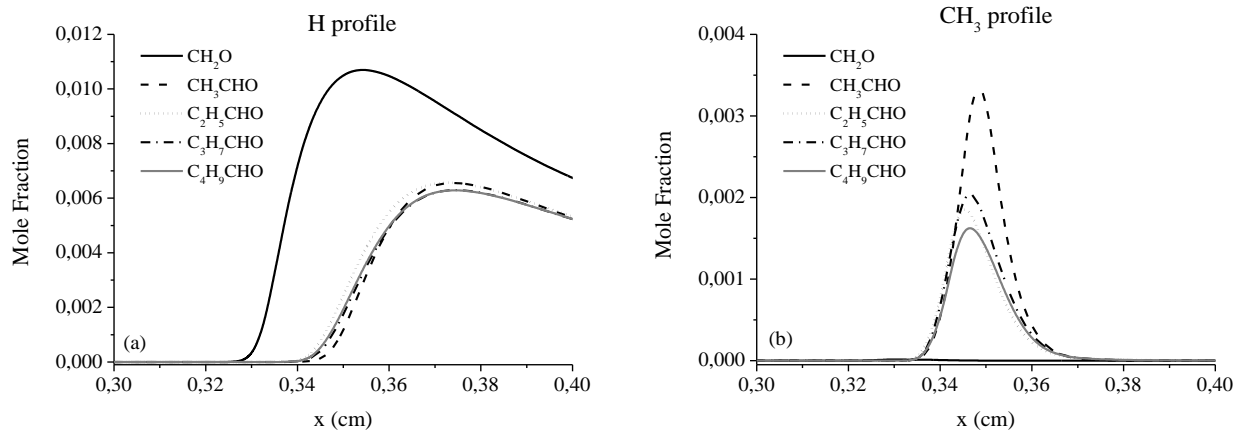
Figure 210: Computed (POLIMI mechanism) $\dot{H}$ (a) and $\dot{C}H_3$ (b) profiles for aldehyde/air flames at φ=1.0, T_u=343 K and p=1 atm.

4. Conclusions

An experimental and kinetic modeling study of the high temperature pyrolysis and oxidation of C_3–C_5 *n*-aldehydes is presented in this work.

New experimental data have been provided for both pyrolysis and oxidation in shock tubes. Species profile measurements were carried out for the three aldehydes in a single pulse shock tube under pyrolytic conditions. Ignition delay times were measured for 1% fuel O_2/Ar mixtures at 1 and 3 atm in a UV emission shock tube for propanal, *n*-butanal and *n*-pentanal. In both oxidative and pyrolytic environments, propanal showed higher or at least comparable reactivity with that of *n*-pentanal, with *n*-butanal being the less reactive aldehyde.

For the first time the homologous series of C_3–C_5 has been analyzed in detail. Based on previously developed C_1 and C_2 aldehydes mechanisms, a detailed mechanism for the pyrolysis and oxidation of aldehydes was developed and discussed. The mechanism has been coupled with the C_0–C_4 kinetic mechanism of NUIG and of POLIMI, requiring adjustments of H-abstraction reactions within the uncertainties of theoretical calculations, which depend on each specific kinetic environment and approach. Both of the resulting mechanisms were then validated and compared with the complete set of experimental data. Both mechanisms were able to closely reproduce the pyrolysis data, including major and minor species, within the experimental uncertainty. Ignition delay times were also satisfactorily captured by both mechanisms, with the NUIG mechanism being systematically less reactive than the POLIMI one, particularly at low pressures.

Laminar flame speeds of propanal and *n*-butanal were also quite satisfactorily compared with experimental measurements. A comparison of calculated C_1–C_5 aldehydes/air flames allowed insights on important reactions and radical species governing aldehydes flame propagation. Laminar flame speed measurements

for formaldehyde and acetaldehyde, missing from the literature at present, could be useful to completely characterize the high temperature oxidation behavior of aldehydes.

Despite the different H-abstraction reaction rates in the two mechanisms, the kinetic analysis highlighted the same fuel specific reactions as being sensitive in the investigated conditions and, furthermore, the relevant role of the two different C_0–C_4 sub-mechanisms. The major differences between the models and the experiments have to be attributed to the chemistry of the smaller species, more than to aldehyde specific reactions (including H-abstractions). This observation further supports the need of an highly accurate C_0–C_4 sub-mechanism, well validated over the wider range of conditions possible as discussed in previous works by Metcalfe et al. [440], Naik et al. [469] and by Ranzi et al. [101].

5. Supplementary material

For the Supplementary Material associated with this study the reader is referred to the web version of the present paper [78]. The Supplementary Material contains:

- NUIG kinetic mechanism with thermodynamic and transport properties
- POLIMI mechanism with thermodynamic and transport properties
- Comparison between NUIG and POLIMI rate of abstraction and radical decomposition
- Comparison between the QRRK/MSC and RRKM/ME calculations for the unimolecular initiation reactions.

6.2.2 Alkyl Radicals Rule the Low Temperature Oxidation of Aldehydes [77]

1. Introduction

Long chain alcohols (C_3–C_6) are considered amongst the most promising alternative fuels for transport due to their high energy density and to the compatibility of their physical-chemical properties with existing infrastructures [4]. While the use of alcohols has been largely proven to reduce CO, nitrogen oxides, and particulate matter emissions, an increased release of harmful carbonyl compounds such as aldehydes and ketones is observed [8]. As clearly summarized in a recent review paper by Sarathy et al. [4], the presence of the hydroxyl moiety in alcohol molecules, causes the reactive path proceeding towards aldehydes formation to be of key importance both at high and low temperatures. For these reasons, a detailed knowledge of aldehyde oxidation kinetics is needed for exploring the viability of alcohol fuels in terms of combustion properties and pollutant emissions. Pelucchi et al. [78] recently reported a comprehensive kinetic study of the high temperature pyrolysis and oxidation of n-C_3–C_5 aldehydes in shock tubes. Based on the low

temperature oxidation of acetaldehyde, the global POLIMI kinetic mechanism [40] has been extended to describe propanal, *n-* and *iso-*butanal oxidation at low temperatures. The experimental data of Veloo et al. [430, 431] in an isothermal jet stirred reactor (JSR) are very useful for this goal. In the same studies an interpretative kinetic model was also reported. This low temperature mechanism [430, 431] constitutes the only one proposed in the literature at present. Moving from these data, the aim of this study is to provide a general and simple approach for the characterization of the low temperature kinetics of C_3–C_4 and heavier aldehydes (R_nCHO). The main oxidation pathway arising from the H-abstraction at the aldehydic site forms the carbonyl radical R_n–CO. Due to its fast decomposition to the corresponding alkyl radical (R_n) and CO, the low temperature mechanism of aldehydes is mainly ruled by the successive and well established low temperature reactions of alkyl radicals. The oxidation pathways of the remaining primary radicals again follow the rate rules of alkanes.

2. Kinetic Mechanism

2.1 H-abstraction reactions

At low temperatures (T<1000 K), aldehydes are mainly consumed via H-abstraction from the weakly bound aldehydic R_n(CO)-H site by $\dot{O}H$ and $H\dot{O}_2$ radicals. Mendes et al. [470] systematically investigated the H-abstractions by $\dot{H}$, $\dot{O}H$, $H\dot{O}_2$ and $\dot{C}H_3$ from aldehydes (C_1–C_3 and *iso-*butanal) between 500 K and 2000 K, using conventional transition state theory. Wang et al. [471] presented direct measurements of the total H-abstraction rate constant by OH for C_1–C_4 aldehydes in shock tubes, in the temperature range of 950–1400 K. *Figure 211* shows a comparison among different abstraction rate constants from the carbonyl site of propanal, by $\dot{O}H$ (a) and $H\dot{O}_2$ (b), according to different authors [78, 430, 431, 470]. The rate constants discussed by Pelucchi et al. [78] (POLIMI) and adopted in this work were estimated by reducing the activation energy of the reference H-abstraction of a primary H-atom of alkanes by 4.5 kcal/mol [52]. As a further comparison, Figure 211 also reports the total rate of abstraction by OH on propanal as measured by Wang et al. [471].
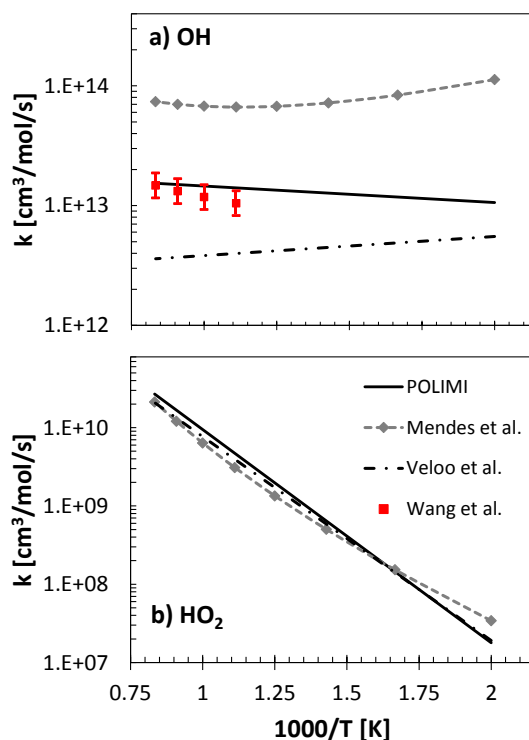
Figure 211: Rate constant of H-abstraction of the aldehydic H-atom by $\dot{O}H$ (a) and $H\dot{O}_2$ (b) [78, 430, 431, 470]. Experimental rate constant for OH+propanal: symbols [471].

Figure 212 shows the relative selectivities of H-abstraction reactions by OH on the different H-sites for propanal (a) and butanal (b), at T=650 K. The weakly bound H-atom at the carbonyl site is much more likely to be abstracted. In propanal, it accounts for ~70-80%, and even up to ~99% according to Mendes [7]. Despite the reported uncertainty of ~2.5 in the calculations [7], the selectivity of the aldehydic H-site seems excessive. Referring to *n*-butanal, the aldehydic hydrogen accounts for ~60-70% of the selectivity and, of course, it is expected to decrease for larger aldehydes. This predominance becomes even larger for abstractions by $H\dot{O}_2$, not reported in Figure 212.
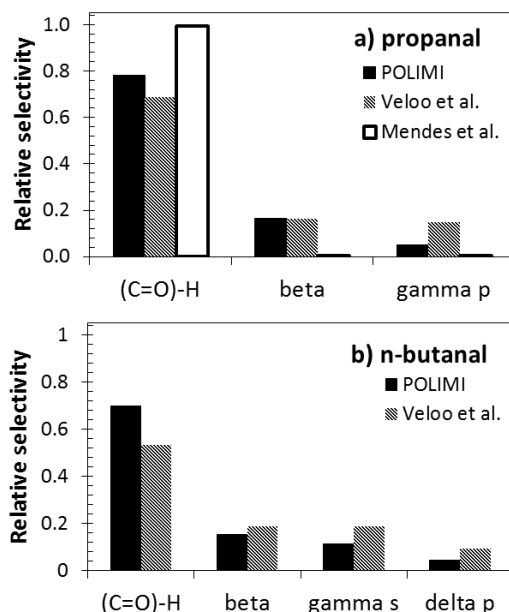
Figure 212: Comparison between relative selectivities to the different H-abstraction positions by OH in propanal (a) and n-butanal (b). Present study and literature values [430, 431, 470].

The influence of the carbonyl group on the adjacent β-site results in a correction factor of 1.25, with respect to the corresponding H-atoms in alkanes [52, 78]. This influence is assumed to be negligible after the β-site.

2.2 Carbonyl (R$_n$–CO) radical decarbonylation versus addition to O$_2$

The transition between the high and the low temperature oxidation mechanisms in alkanes, as well as in oxygenated fuels, strongly depends on the competition between alkyl radical (R) decomposition and their addition to O$_2$ to form peroxy radicals (RO$_2$) [17, 233]. At high temperatures, carbonyl radicals (R$_n$-(CO)) preferentially undergo decarbonylation forming CO and the corresponding R$_n$ alkyl radical [78]. The remaining primary alkyl radicals can isomerize and decompose through β-scission according to standard alkane rules [17, 90, 123]. At low temperatures, mechanisms are different between acetaldehyde and heavier aldehydes. The competition between acetyl radical decomposition (CH$_3$CO+M=CH$_3$+CO+M) and addition to O$_2$ to form acetyl-peroxy radical (CH$_3$CO+O$_2$+M=CH$_3$CO$_3$+M) is important in atmospheric chemistry. Therefore, many theoretical studies at atmospheric pressure and ~298 K (conditions of marginal interest for combustion systems) are reported in the literature [472-474]. Moreover, the relative rate values of the competing reaction channels in low temperature acetaldehyde combustion were already discussed in previous studies [250, 418, 475]. Particularly, these features were highlighted by Gray et al. [418] when studying the cool flame behavior of acetaldehyde in a continuous well stirred flow reactor at T=450-625 K and very low pressures. More recently, an accurate assessment of acetyl radical decomposition has been carried out by Senosiain et al. [476], using the master equation and variational transition state theory. The addition to O$_2$ to form acetyl-peroxy radical was investigated through QRRK theory by Lee et al. [477] and

through multichannel RRKM by Hou et al. [478]. At very low temperatures (<600 K), where the addition to O_2 is relevant, the subsequent interaction with $H\dot{O}_2$ produces peracetic acid (CH_3CO_3H) giving rise to the low temperature reactivity summarized in Figure 213 (black arrows). Overall, this path consumes $H\dot{O}_2$ radicals forming one more reactive $\dot{O}H$, thus enhancing reactivity.
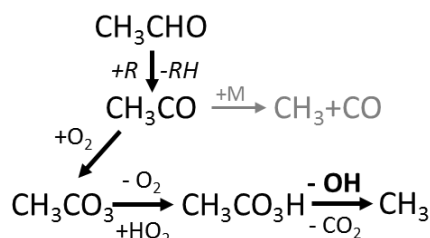
Figure 213: Low temperature reactivity of acetaldehyde.

Experimentally investigating the cool flame behavior of acetaldehyde, Gray et al. [418] highlighted nine different stable modes, strongly dependent on the competition between acetyl radical decomposition and the low temperature path of Figure 213. These modes were summarized into five regimes:

1) Slow combustion: steady reaction without light emission.

2) Stable oscillatory ignition with simple waveform.

3) Stable oscillatory ignition with complex waveforms (five different types observed).

4) Stable oscillatory cool flames.

5) Steady rapid reaction accompanied by light emission.

Figure 214 shows experimental results (lines) together with model simulations (symbols) obtained with the POLIMI kinetic mechanism [40]. Figure 214 also shows typical temperature profiles as function of time for the 5 different regimes. All the simulations presented in this work, including sensitivity and flux analyses, were performed with the OpenSMOKE++ code [66]. The energy balance of the non-adiabatic Perfectly Stirred Reactor (PSR) accounts for the usual heat exchange term ($Q=U\ S\ (T-T_{amb})$). The heat transfer coefficient U, strongly affects the transition between the different regimes. The qualitative agreement observed in Figure 214 was obtained by adopting the U values suggested by Lignola et al. [420], i.e. 11–18 $W/m^2/K$ depending on the pressure. To the authors knowledge, this work [420] constitutes the most useful experimental study of the low temperature oxidation of acetaldehyde. The calculated T profiles showed deviations from the experimental of at most ~40 K for the experimental peak values [418]. However, considering the uncertainty in the determination of the heat exchange coefficient, the obtained agreement allows insights to the different kinetic phenomena as discussed below.
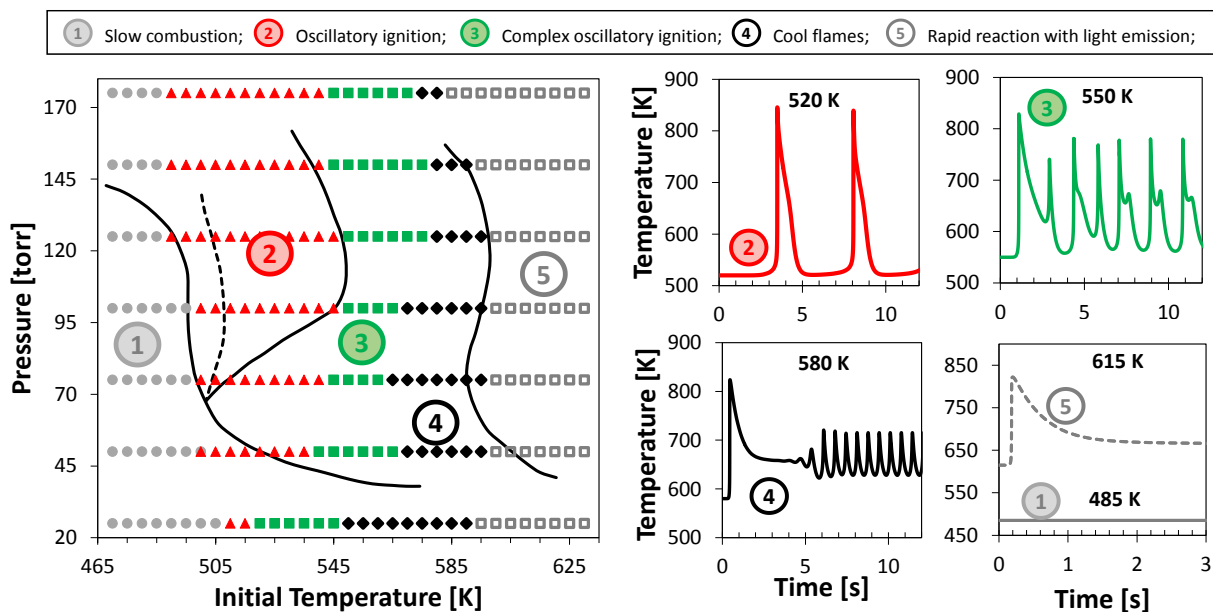
Figure 214: Ignition diagram of CH₃CHO/O₂/N₂ (33%/33%/34%), τ=3.0 s in a continuous well stirred reactor. Experimental (lines) [17] and calculated regimes (symbols). Temperature versus time profiles of periodic cool flames at p=100 torr and varying initial temperatures.

Moving towards heavier aldehydes, Simmie [456] calculated the high pressure limit rate constant for the thermal decomposition of the carbonyl radical of *n*-butanal (1-oxo-butyl radical) to *n*-propyl and CO ($C_3H_7CO=C_3H_7+CO$). In agreement with previous studies [473, 479], an energy barrier of ~15 kcal/mol was obtained. The same kinetic parameters are here assumed for propionyl radical decomposition ($C_2H_5CO=CO+C_2H_5$) [78]. The kinetic parameters of the addition reaction $CH_3CO+O_2=CH_3CO_3$ were also adopted for the analogous reaction ($R_n-CO+O_2=R_n-CO_3$) of heavier carbonyl radicals, due to the lack of targeted studies.

Further calculations were carried out at higher levels of theory in this study. Energy barriers are reported in Figure 215 for CH_3CO, C_2H_5CO and C_3H_7CO decomposition reactions. The results are consistent with the literature and support the rapid decomposition of carbonyl radicals.
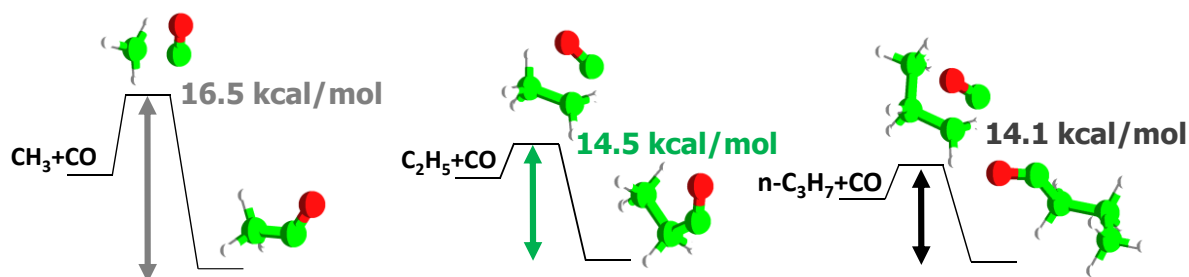
Figure 215: Energy barrier for the decarbonylation reactions of different carbonyl radicals. Geometries and frequencies: M062x/6-311+G(d,p), energies: CCSD(T)-F12/VTZ-F12, MP2 extrapolation to complete basis set.

Figure 216 shows the pseudo first order high pressure limit of carbonyl radical addition to O_2 [477], together with acetyl [476], carbonyl [456], and alkyl radical decomposition [17]. With regards to the bimolecular addition reaction, the pseudo first order rate constant ($k_{app}=k_{add}[O_2]$) is based on the oxygen concentrations reported by Gray et al. [418] (50–150 torr, 33% O_2) and by Veloo et al. [430, 431] (10 atm, 0.3%-2.75% O_2), with the grey band of Figure 216 covering the full range of oxygen concentration considered in these studies [418, 430, 431]. Due to the lower activation energy required for the decarbonylation (~15–16 kcal/mol) compared to that of the β-decomposition of alkyl radicals (~30 kcal/mol), the addition to O_2, activating the peracid channel, plays a role only at very low temperatures. Particularly, a non-negligible contribution of the addition is obtained only up to 600 K for acetyl radical and only up to ~500 K for propionyl, and heavier carbonyl radicals. Of course, these ceiling temperatures would increase in internal combustion engines due to higher O_2 concentrations. Nevertheless, only acetyl-peroxy formation is expected to play a significant role at such conditions.
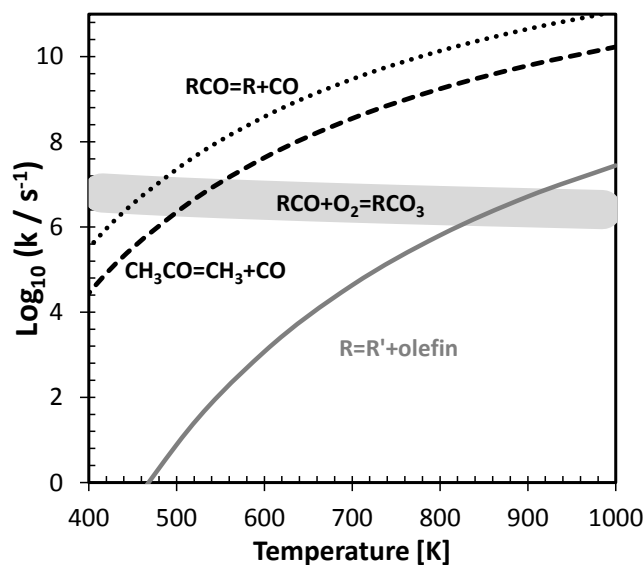
Figure 216: Rate constant plot of carbonyl and alkyl radical decompositions versus apparent rate of addition to O_2 ($k_{app}=k_{add} [O_2]$).

For these reasons, in the present study carbonyl radicals heavier than acetyl do not add to oxygen and are considered directly decomposed to CO and the corresponding alkyl radicals (see grey arrows of Figure 217), whose low temperature branching pathways largely dominate aldehydes reactivity. Similarly, Veloo et al. [430] in propanal oxidation observed a significant formation of ethyl radical from the decarbonylation reaction of propionyl. Thus, they concluded that the low temperature reactivity (T<700 K) was mainly ruled by ethyl radical addition to O_2 and ethyl hydro-peroxide (C_2H_5OOH) formation. On the contrary, in the low temperature oxidation of *n*-butanal [431], they assumed a significant contribution of C_3H_7CO addition to O_2 to form the carbonyl-peroxy radical ($C_3H_7CO_3$). But, instead of observing a peracid channel (*Figure 213*), they assumed a preferential channel leading to C_3H_6.

2.3 Low temperature oxidation of aldehyde alkyl moiety

The usual reaction classes with established rate rules of alkanes [17, 233] are considered in the description of the low temperature oxidation of the alkyl moiety. As an example, Figure 217 shows the low temperature oxidation of the β-radical of propanal. At 650 K, H-abstractions at the β position contribute to ~18% of the overall consumption. The peroxy radical obtained from its addition to O_2 mostly undergo a 5 member ring isomerization (13:16,~80%), abstracting the weak aldehydic H-atom to produce a carbonyl-hydroperoxide radical. According to the previous discussion, this carbonyl radical is also assumed to directly decompose to CO and an ethyl hydroperoxide radical ($CH_3 \cdot CHOOH$).
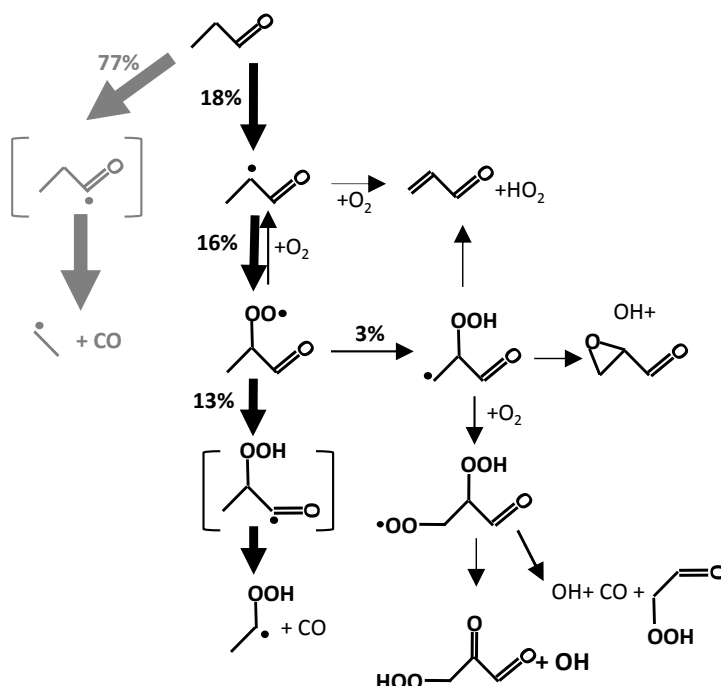
Figure 217: Reaction path analysis of propanal β-radical in a JSR (T=650 K, Φ=0.5, p=10 atm, and τ=0.7 s). The size of the arrows is indicative of the relative importance of a reaction channel and the percentages are absolute values.

2.4 Relative reactivity of alkanes and aldehydes

Figure 218 compares the reactivity of propanal and *n*-butanal with that of ethane and propane, respectively. At low and intermediate temperatures, the ignition of aldehydes in shock tubes is up to 50 times faster, while at high temperatures the ignition behaviors become similar. The conversion of alkanes in a JSR is delayed by more than 70 K. Moreover, alkanes do not express low temperature reactivity in these selected operating conditions (0.15% fuel, Φ=1.0, p=10 atm, residence time τ=0.7 s).
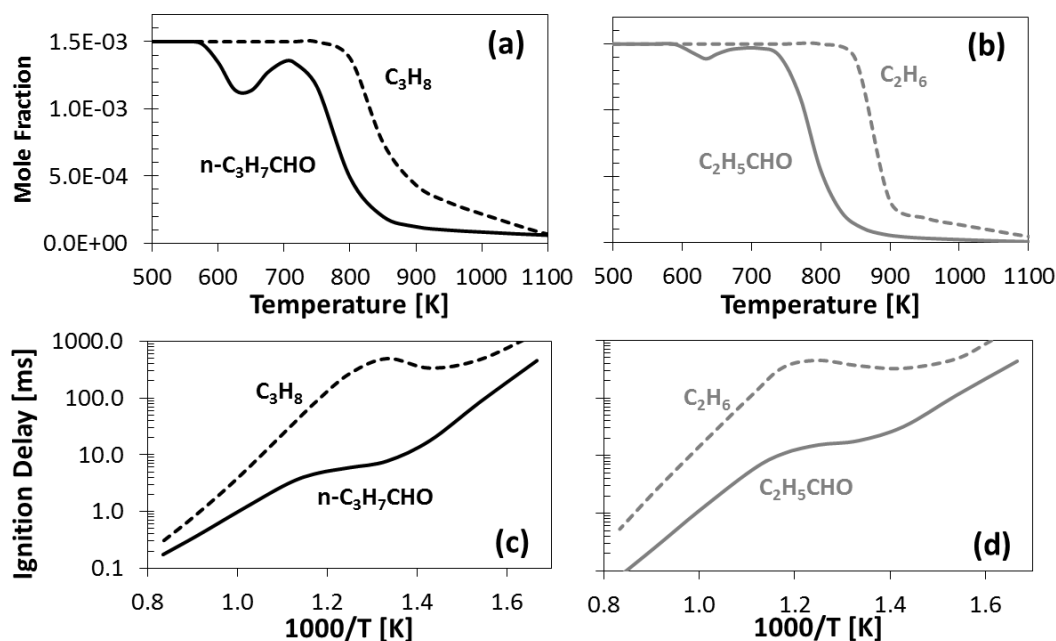
Figure 218: Relative reactivity of alkanes and aldehydes at stoichiometric conditions. a) and b): JSR, 0.15% fuel in nitrogen, p=10 atm, τ=0.7 s. c) and d): ignition delay times of fuel/air mixtures at 10 atm.

The faster rate of H-abstraction from the aldehydic site relative to the primary and/or secondary H atoms from the alkane justifies this much higher reactivity with respect to the corresponding alkanes, both at high and especially low temperatures. Note that the low temperature mechanism of propane in the POLIMI kinetic scheme was recently updated [72] and validated in comparison also with the latest experimental data of Cord et al. [227]. As mentioned above, the selectivity of the H-abstraction from the aldehydic site is expected to gradually decrease with increasing length of the alkyl moiety (~60% for *n*-pentanal, and ~50% for *n*-hexanal according to our rate rules [78]). Consequently, the differences in ignition delay times between longer *n*-aldehydes (C_n) and C_{n-1} *n*-alkanes would gradually decrease.

3 Comparison with experimental data

This Section compares model predictions with isothermal JSR species measurements in the oxidation of propanal, *n*- and *iso*-butanal from Veloo et al. [430, 431]. The kinetic mechanism, together with thermodynamic properties and a glossary of the species is attached as Supplemental Material. The Supplemental Material also reports comparisons of the experimental data with the Veloo et al. mechanism [430, 431]. The global POLIMI mechanism [40] reported here includes the recent updates of aldehyde high temperature kinetics [78] and alkane low temperature kinetics [72]. Thermodynamic properties for aldehyde specific species were taken from Veloo et al. [430, 431].

3.1. Propanal

Figure 219 shows experimental and calculated species profiles as a function of reactor temperature for 0.15% propanal/O_2/N_2 mixtures at Φ=0.5, p=10 atm and τ=0.7 s. The model accurately reproduces global reactivity, major and minor species. Similar agreement is also obtained for other stoichiometries as reported in the Supplemental Material.
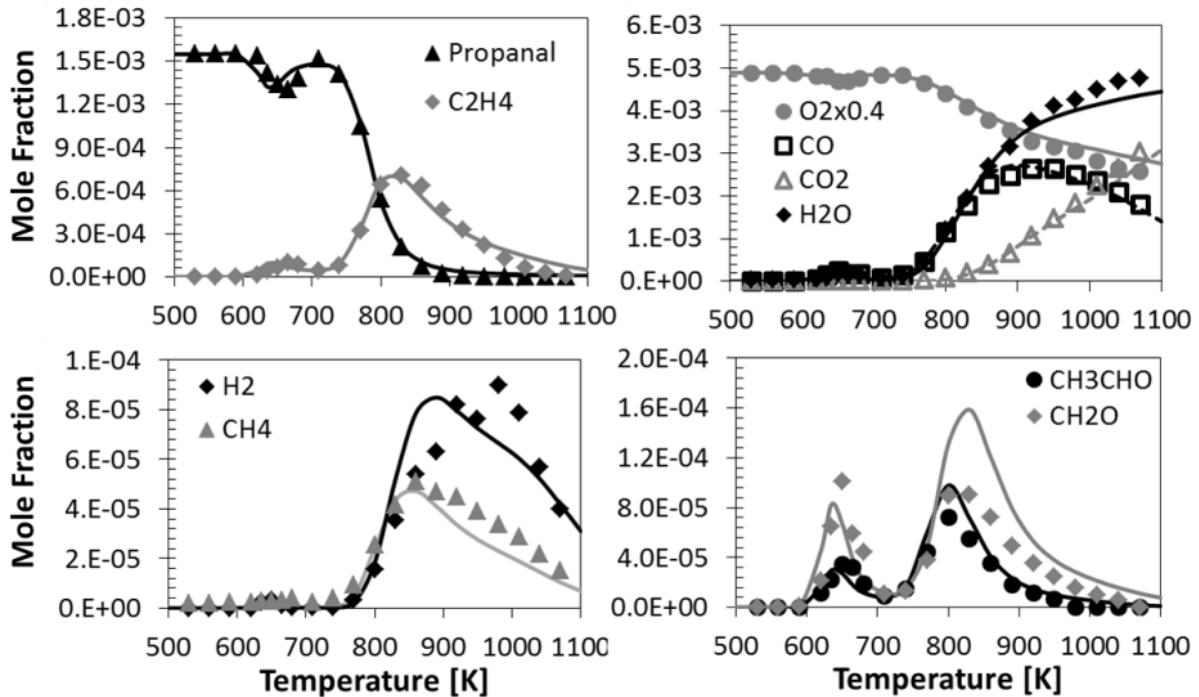
Figure 219: Propanal oxidation in a JSR at 10 atm, τ=0.7 s and Φ~0.5. Initial fuel mole fraction is ~0.15%. Experimental data (symbols) [430] and model predictions (lines).

Figure 220 shows sensitivity coefficients to fuel concentration at 650 K, where the low temperature conversion reaches its maximum. As previously discussed (Section 2.2), the reactivity is dominated by the low temperature oxidation of ethyl radical. Particularly, the isomerization of the ethyl peroxy radical to ethyl-hydroperoxy radical contributes greatly to fuel consumption activating the low temperature branching path. As expected, ethyl radical reaction with O_2 to directly produce ethylene and $H\dot{O}_2$ reduces reactivity. Within the fuel specific reactions, H-abstraction of the aldehydic H-atom by $H\dot{O}_2$ is highlighted as the most sensitive.

Propanal, T=650 K, ϕ=0.5, 10 atm
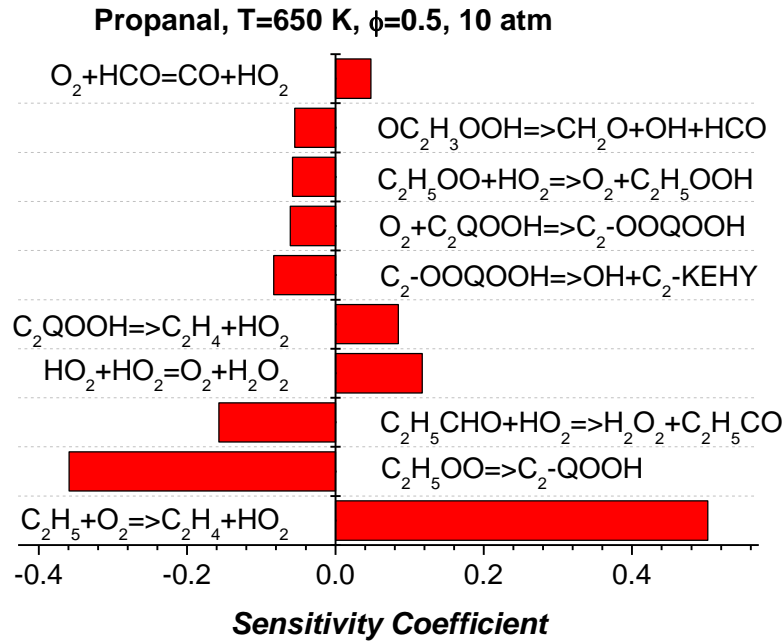
Figure 220: Sensitivity of propanal concentration to rate constants for the mixture of Figure 219.

3.2. *n*-Butanal

Recently, Veloo et al. [431] investigated the oxidation of *n*-butanal mixtures between 500 and 1100 K in a JSR at 10 atm, τ=0.7 s. Figure 221 compares experimental conversion of *n*-butanal at different equivalence ratios and species profiles at Φ~0.5 with model predictions. Despite a lower reactivity at low temperatures, POLIMI mechanism correctly predicts the extent of the negative temperature coefficient (NTC) region and the reactivity at high temperatures. The underestimation of the reactivity in the NTC region leads to a corresponding under-prediction of propylene between 700 and 800 K. At higher temperatures (T>800 K), the largest deviations are observed for methane, mainly formed via H-abstraction by $\dot{C}H_3$, and ethylene, produced from the decomposition of *n*-propyl-hydroperoxide radical and partially from β-decomposition of *n*-C_3H_7. Even formaldehyde and acetaldehyde profiles, clearly representative of the low and high temperature regimes, are quite well predicted.
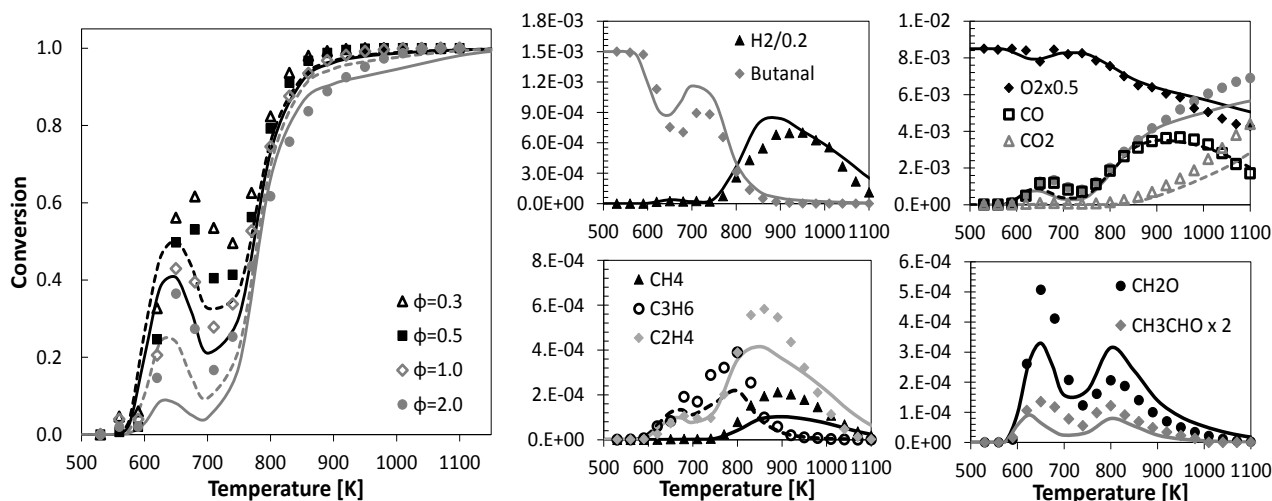
Figure 221: n-butanal (0.15%) oxidation in a JSR at 10 atm, τ=0.7 s. Fuel conversion for varying Φ and species profiles at Φ~0.5. Experimental data [431] (symbols) and mechanism predictions.

Again, Figure 222 shows the most sensitive reactions to *n*-butanal concentration at 650 K. The reactivity is dominated by the low temperature reactions of *n*-propyl radical. In particular, the major role is played by the competition between the branching path of *n*-propyl-hydroperoxide radical and the decomposition reaction to form C_3H_6 and $H\dot{O}_2$. Moreover, the H-abstractions by OH of the aldehydic and the secondary H-atoms in β show a negative sensitivity, contributing to fuel conversion.
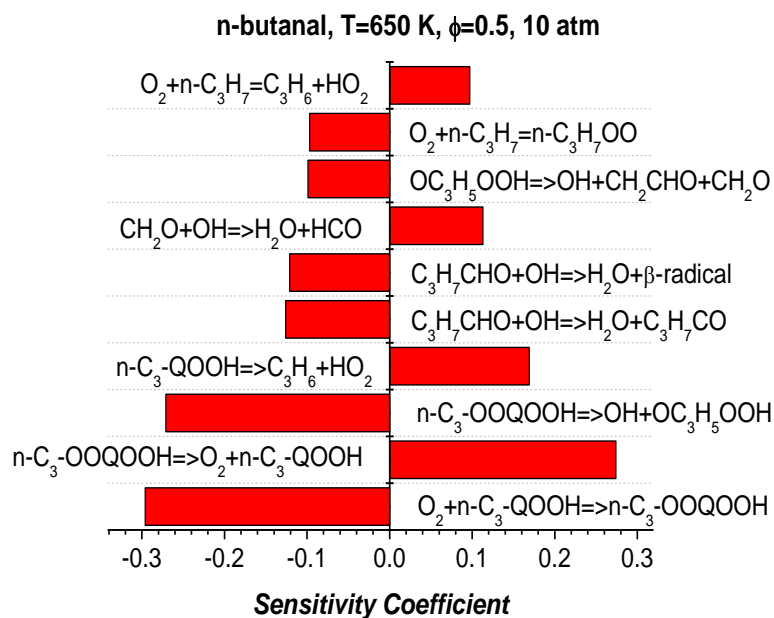
Figure 222: Sensitivity of n-butanal concentration to rate constants for the mixture of Figure 221.

3.3. *iso*-Butanal

As an effective generalization of the previous kinetic assumptions and of the rate rules adopted for aldehydes [78], the low and high temperature oxidation mechanism of *iso*-butanal (2-methyl-propanal) was developed. The carbonyl radical produced via the H-abstractions from the aldehydic site is assumed to directly form CO and *iso*-propyl radical. Figure 12 shows experimental [431] and predicted major species profiles at Φ=0.3 (Figure 223a) and Φ=2.0 (Figure 223b).

The stable *iso*-C_3H_7 formed via the decomposition of the carbonyl radical explains the much less pronounced low temperature reactivity of *iso*-butanal with respect to *n*-butanal.

In fact, a very limited conversion (~4%) is observed only at Φ=0.3, within 600 and 700 K.
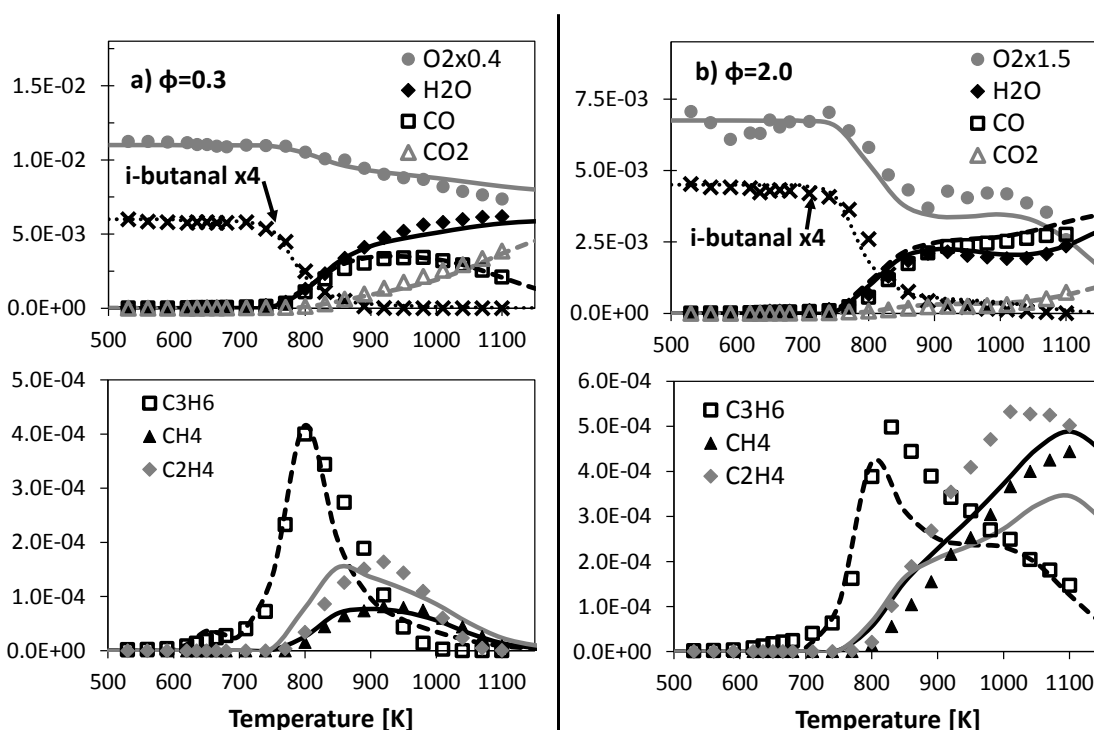
Figure 223: iso-butanal (0.15%) oxidation in a JSR at 10 atm, τ=0.7 s, Φ~0.3 (a) and Φ~2.0 (b). Experimental data [431] (symbols) and mechanism predictions (lines).

4. Conclusions

This paper presents and discusses a general kinetic model of the low temperature oxidation of aldehydes. The proposed rules allow successive easy extension to heavier normal and branched aldehydes. In fact, H-abstractions preferentially form unstable carbonyl radicals, rapidly decomposed to alkyl radicals whose low temperature kinetics rule aldehydes reactivity. The remaining alkyl radicals derived from H-abstractions are treated according to the consolidated reaction classes and rate rules of alkanes, still considering the high

reactivity of the aldehydic H-atom. A comprehensive kinetic analysis of the low temperature oxidation data (including cool flames of acetaldehyde, oxidation of propanal, *n*-butanal, and *iso*-butanal in JSR) validates and supports not only the kinetic model, but also the assumption of the direct decomposition of heavy carbonyl radicals. Additional validation targets are reported in the Supplementary Material of the original paper [77].

6.2.2.1 Lumped low temperature oxidation of aldehydes and extension to n-hexanal oxidation

As mentioned above, the accurate description of alcohol oxidation requires an accurate description of the derived aldehydes, which are primary products in alcohol oxidation that strongly impact low temperature ignition phenomena. This thesis discussed in many instances the need and the effectiveness of balancing the accuracy of the kinetic mechanism and its complexity, through the lumping approach. *Figure 224* reports the minimum number of species to include in the kinetic model for a detailed description of aldehyde oxidation. It is clear that if one wants to describe n-hexanol oxidation, in addition to the species typical of the fuel oxidation another ~60 species have to be accounted for in the n-hexanal submechanism. In the case of n-octanol and n-octanal this number would rapidly increase to ~95. At this point it should be also clear that including such a large number of species in the POLIMI kinetic framework, which is able to describe fuel oxidation up to heavy diesel fuels with only ~500 species, would not be acceptable. For this reason, a lumped version of the low temperature mechanism of propanal and n-butanal has been obtained and systematically extended to n-hexanal.
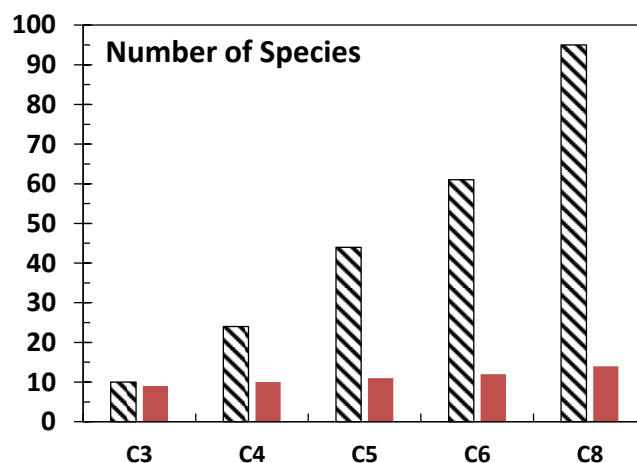
Figure 224: Number of species in the detailed (black striped bars) and lumped (red bars) kinetic mechanism of C$_n$ aldehydes.

Table 28 lists the lumped low temperature rate coefficients for the n-hexanal sub-mechanism. The assumption of rapid decomposition of the R-CO radicals is also applied to low temperature species. For this reason, some isomerization reactions (RO$_2$=QOOH) involving the abstraction of the H-atom at the carbonyl site (R-(C=O)-H) are written directly accounting for the decomposition of the carbonyl radical.

Lumped Reactions	n-hexanal		
	A	n	Ea
O_2+RALD6X=>HEXENAL+ $H\dot{O}_2$	3.00E+11	0.0	3000
O_2+RALD6X=>RALD6XOO	4.00E+12	0.0	0.0
RALD6XOO=>O_2+RALD6X	1.00E+13	0.0	31500
RALD6XOO=>QA6X	3.00E+12	0.0	25000
QA6X=>RALD6XOO	3.00E+10	0.0	15000
RALD6XOO=>CO+OH+products	6.00E+11	0.0	25000
RALD6XOO=>CO+OH+products	3.00E+10	0.0	19000
RALD6XOO=>CO+ $H\dot{O}_2$+products	3.00E+10	0.0	19000
O_2+QA6X=>ZA6X	4.00E+12	0.0	0.0
QA6X=>OH+ETALD6	1.00E+12	0.0	18000
QA6X=>HEXENAL+ $H\dot{O}_2$	1.00E+14	0.0	23000
QA6X=>OH+products	4.50E+13	0.0	23000
ZA6X=>O_2+QA6X	1.00E+13	0.0	31000
ZA6X=>OH+KEA6X	1.00E+11	0.0	18000
ZA6X=>CO+OH+products	1.00E+11	0.0	18000
KEA6X=>OH+products	3.50E+15	0.0	41000

Table 28: Lumped reactions of the low temperature oxidation of n-hexanal.

Figure 225 compares recent species measurements in jet stirred reactors [362] with predictions from the mechanism discussed above.
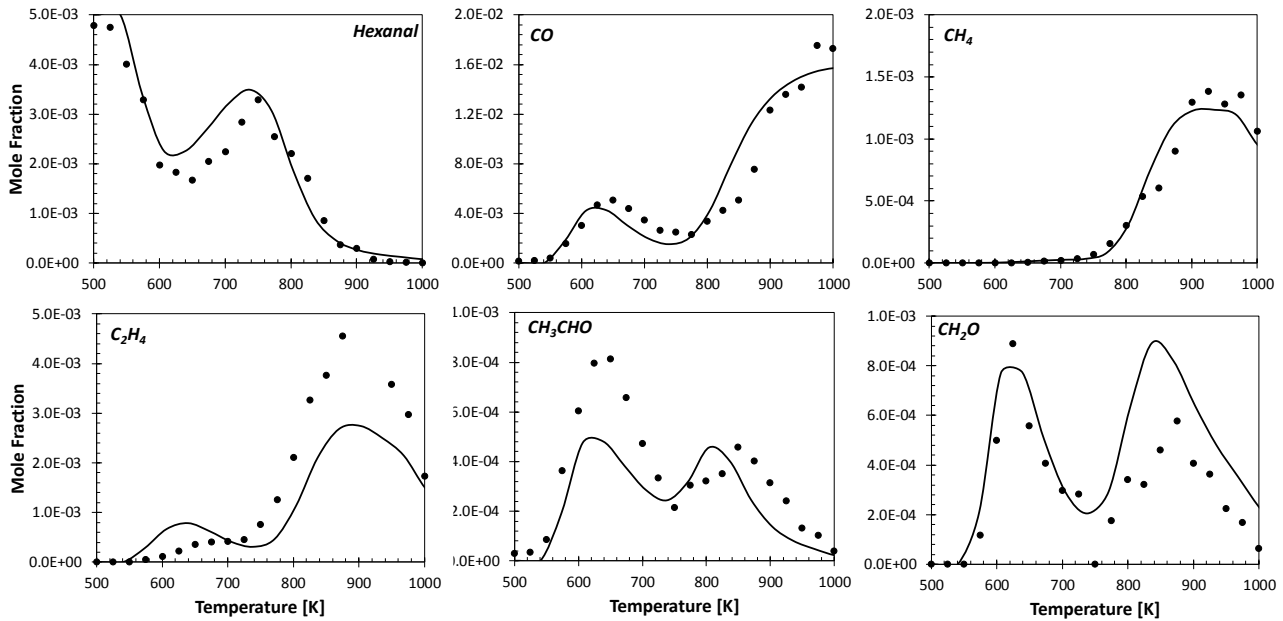
Figure 225: 0.5% n-hexanal/O_2/He oxidation in a JSR at φ=1.0, p=1 atm, τ=2.0 s. Symbols: experimental data [362], lines: model predictions.

6.3 Relative Reactivity of Oxygenated Fuels: Alcohols, Aldehydes, Ketones, and Methyl Esters [76]

Over the next few decades, population and income growth are expected to create new demands for energy. Particularly, rising prosperity will drive increased energy demand for transportation (~40% by 2040 [1]) Despite the decreasing trend of fossil fuel price, government incentive programs, environmental issues (e.g. greenhouse gas emissions) and the need to lower import dependency from political unstable countries [480], drive the exploitation of biofuels (e.g. alcohols) and biodiesels (e.g. methyl esters) for transport. In this context, as recently reported by Bergthorson and Thomson [11], fundamental combustion properties (i.e. chemical-kinetics) rule engine performance and exhaust pollutant emissions of advanced biofuels. Kinetic modeling advances the understanding of the influence of specific chemical compounds allowing the tailoring of a fuel, or fuel blend, for an existing engine technology or the tuning of an engine for a desired blend. As recently reviewed by Sarathy et al. [4], alcohols with different carbon number and substitution can be used in modern internal combustion engines with minor modifications to the engine design. Besides ethanol, which is nowadays conveniently produced from corn and sugar cane and widely used as a biofuel, other linear and branched alcohol species are foreseen as viable biofuels for road, air and sea transport. Some concern exists regarding pollution from alcohol fueled engines. Sadeghinezhad et al. [8] presented a statistical analysis of biofuel performance in terms of power, fuel economy and pollutant emissions. While particulate matter (PM), CO and unburned hydrocarbons (HC) emissions generally improve when a biofuel is used, a large increase in the release of carbonyl compounds is observed (aldehydes and ketones). Although aldehyde formation pathways during alcohol oxidation at low (~500–1000 K) and high temperatures (~1000-2500 K)

are quite well understood, very few kinetic modeling studies specifically addressing aldehydes exist in the literature [77, 78, 430, 431].

The Cluster of Excellence "Tailored Made Fuels from Biomass" (TMFB) recently identified methyl ethyl ketone, together with 2-methylfuran, as promising future biofuels through an effective interdisciplinary approach [481]. Part of the activity in the TMFB was devoted to a better assessment of MEK anti-knocking properties from a kinetics perspective. New experimental data in a rapid compression machine were measured and a kinetic mechanism covering also the low temperature conditions was developed [482].

Biodiesels are complex mixtures of multi-component alkyl esters of long-chain fatty acids, generally produced by transesterification of soy and rapeseed oil with methanol [483]. Many kinetic studies have addressed the kinetic features of methyl esters in the last 10 years [484, 485]. The kinetic characterization of methyl esters conveniently started from methyl-butanoate (MB) which, due to its small size, allowed a better understanding of the influence of the ester moiety by introducing a relatively small number of species in detailed kinetic mechanisms.

Despite the large number of kinetic studies on oxygenated species, a systematic characterization of the influence of the oxygenated functional group on their relative reactivity is still lacking in the literature.

The complexity of gas phase kinetics, together with the high level of accuracy required, led to a steep increase in kinetic mechanism size, both in terms of reactions and species [37]. As emphasized by Carstensen and Dean [486] the manual creation of gas-phase reaction mechanisms is not only a tedious and time-consuming procedure, but it is also prone to errors and incompleteness. In the last 25 years, many algorithms have been developed to automatically generate reaction mechanisms [38, 51, 58, 59, 92]. To allow the implementation of a consistent set of reaction pathways and include physically meaningful kinetic parameters, reaction classes need to be clearly defined [53, 54] and rate rules needs to be established and revised based on fundamental properties [17, 55], obtained from experiments and/or theory. Once rate rules are defined the extension to heavier species becomes relatively simple [64]. As widely known and first generalized to complex kinetic mechanisms by Dente et al. [43, 51], H-abstraction reactions play a key role in determining the reactivity of a fuel both during pyrolysis and oxidation. As discussed by Ranzi et al. [52], the evaluation of the rate constant for the generic

R·+R'-H=R-H+R'·
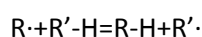
reaction, depends on the properties of the abstracting radical (R) and on the type of hydrogen to be abstracted. As an example, the activation energy required by an alkyl radical for a secondary H-atom abstraction in an alkane is lowered by ~2.5 kcal/mol with respect to the reference primary H-atom. Again, a

tertiary H-atom abstraction is favored by ~4 kcal/mol. Whenever direct and more accurate kinetic parameters are not available, the automatic generation of H-abstraction reactions included in the global POLIMI mechanism [40] is based on these rules and energy corrections. The same approach is applied to oxygenated species where the presence of the oxygen atom largely influences the adjacent C–H and C–C bonds lowering their BDEs compared to alkane fuels.

This paper aims at providing a description of the main reaction pathways that characterize the reactivity of oxygenated fuels, as well as at identifying a rational interpretation of the kinetic motivations determining differences and similarities in the kinetic behavior of each fuels. In many cases, it is sufficient to refer to some key bond dissociation energies, which relate to a few specific reaction channels. Despite the abundant recent literature on biofuels, this is the first attempt, to our knowledge, to investigate and rationalize the effect of the hetero $\ddot{O}$ atom on the closest bond dissociation energies and, consequently, on the reactivity of straight chain fuels. Sudholt et al. [487] presented an analogous approach for furanic species emerging as promising biofuels from the TMFB project. The goal of this previous study was to correlate the BDEs of saturated and unsaturated furans to their derived cetane number (DCN). Dominant H-abstraction channels were identified for every class of compounds, and the kinetic discussion was limited to the identification of successive decomposition or ring-opening reactions of the derived radicals. Insights on specific kinetic pathways were referred by analogy to previous studies for the high temperature oxidation of such compounds [456, 487, 488].

This study complements and differs from the previous approach [487] *i)* by analyzing the effect of four different functional groups (R-OH, R-(C=O)-H, R-(C=O)-R, R-(C=O)-O-CH₃) on BDEs and on fuel specific reaction pathways; *ii)* by providing a single kinetic mechanism able to quantify and reproduce the features of the different fuels; *iii)* by focusing the kinetic discussion on low temperature oxidation, where the fuels most strongly differ in their reactivity.

The discussion presented in this paper is mostly based on the general, hierarchical and lumped kinetic mechanism developed at Politecnico di Milano over the last 30 years, effectively serving the final goal of characterizing the different reactivity of oxygenated species. To this goal, the mechanism is extended to characterize the low temperature reactivity of n-butanol together with the low and high temperature reactivity of 2-butanone.

Section 2 of this paper provides a consistent assessment of the bond dissociation energies (BDEs) of the C–H and C–C bonds in *n*-butane, *n*-butanol, *n*-butanal, methyl-ethyl ketone and methyl butanoate (MB). The differences in BDEs justify the relative rate parameters of the H-abstraction reactions and their relative selectivity for oxygenated species, as included in the POLIMI mechanism (Section 3). An updated and

extended validation of *n*-butane and oxygenated species in the whole temperature range is presented in Section 4. Lastly, Section 5 summarizes and discusses the impact of different oxygenated functional groups on the reactivity (i.e. ignition delay time), from low to high temperature.

1. Bond Dissociation Energies

The G4 computational method developed by Curtiss et al. [172] and implemented in the Gaussian-09 suite of programs [46] was used to calculate C–H and C–C bond dissociation energies. The G4 method has been shown to be one of the more reliable methods for calculating thermochemistry and therefore BDEs [94].

According to the following reactions

R-H→R·+H· (for C–H bonds)

and

R-R'→R·+R' (for C–C bonds)
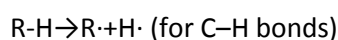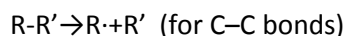
the BDEs are determined as the difference in the 298 K G4-energy between the corresponding radical (·R) and H· (or ·R') and the parent compound (R-H or R-R'). All energies were computed with reference to the minimum energy structure using the rigid rotor harmonic oscillator approximation. To determine the minimum energy structure potential energy curves for internal rotation of single bonds for the parent and radical species were determined using the B3LYP/6-31+G(d,p) level of theory performing relaxed scans at 20° intervals. Figure 226 shows BDEs obtained in this study for *n*-butane, *n*-butanol, *n*-butanal, MEK and methyl butanoate at the G4 level and 298 K. Figure 226 also reports a Δ_{BDE} (parentheses) assuming the BDE of the primary C–H bond of butane as a reference. Calculated BDEs are in good agreement with those estimated with the MRACPF2 method by Oyeyemi et al. [489-491] with maximum deviations of ~2 kcal/mol as reported in Table S1 of the Supplemental Material. The calculated values are also compared with experimental values (brackets of Figure 226) when available [99, 492]. Maximum deviations from experimental values are ~1 kcal/mol. As the aim of this study is to provide a consistent set of BDEs to discuss the relative reactivity of oxygenated species with different functional groups, the obtained agreement is considered satisfactory.
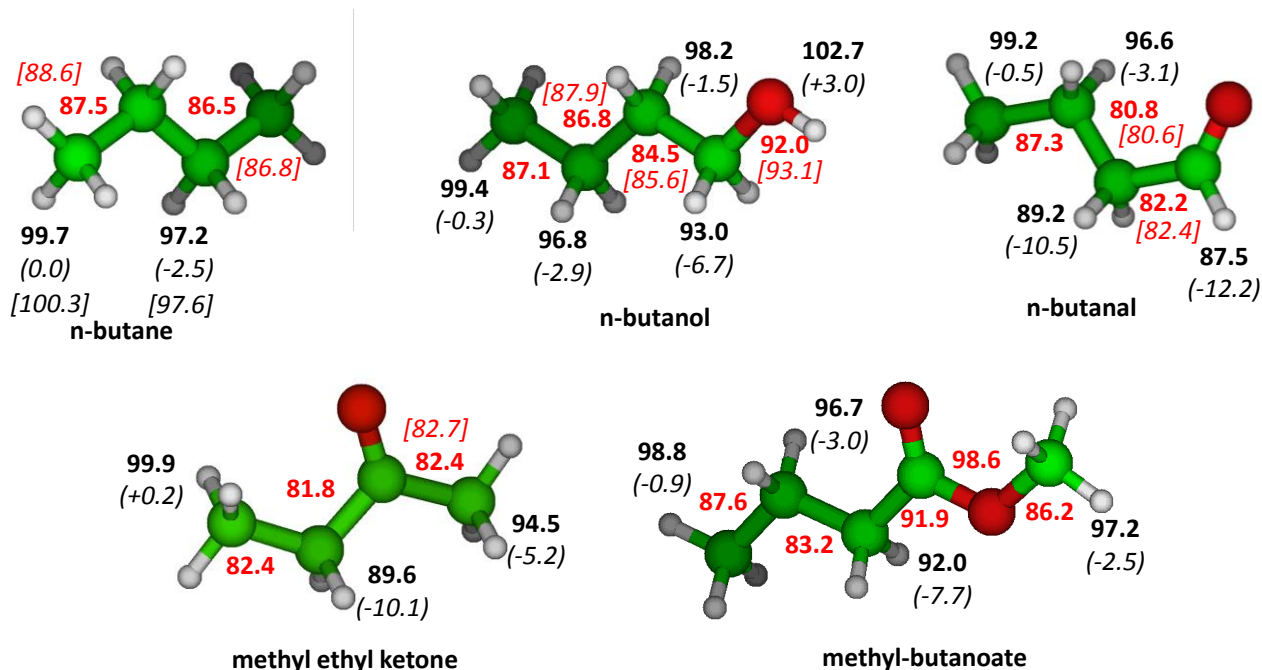
Figure 226: C–H (black) and C–C (red) bond dissociation energies (kcal mol⁻¹) for butane, n-butanol, n-butanal, methyl ethyl ketone and methyl butanoate calculated at the G4 level (298 K) [172]. Numbers in parentheses represent the difference in BDEs (ΔBDE) with respect to a primary C–H bond. Numbers in brackets ( ) are experimental values [99, 492].

The electronegativity of the oxygen atom typically reduces the strength of the closest bonds. *n*-butanol and especially *n*-butanal and methyl ethyl ketone (MEK) show a reduced energy of both the alpha C–C bond and the beta C–H bond. In contrast, the substituted carboxyl group of methyl-butanoate makes the molecule more stable. The mesomeric structures of unshared pair of electrons in the oxygen singly bonded to the carbonyl carbon, allow the formation of the ester resonance, which stabilizes the molecule. Consequently, the closest C–C bond is stronger with a higher dissociation energy (~92 kcal/mol).

2. Selectivities of H-abstraction reactions

According to the relative bond strengths discussed in Section 1, previous kinetic studies have adopted specific rate constants reflecting the effect of the presence of the oxygen atom in different functional groups. Beside the C–C bond dissociation energies, whose values mainly affects the rate of radical chain initiation reactions, H-abstraction reactions dominate fuel consumption in the whole temperature range of interest for combustion systems (500-2000 K). While at low temperatures the abstracting radicals are typically OH and, to a lesser extent $H\dot{O}_2$, at higher temperatures and particularly under pyrolysis or fuel rich conditions, also $\dot{H}$ and $\dot{C}H_3$ become important H-abstracting radicals. Assuming that the rate of abstraction largely depends on the nature of the H-atom to be abstracted, it is clear how intrinsic bond dissociation energies directly affect the rate values, and, more importantly, the relative selectivities of the available abstraction sites.

Figure 227 shows the H-abstraction rates of primary, secondary, and tertiary H-atoms by $\dot{H}$, $\dot{O}H$ and $\dot{C}H_3$ radicals on a per H-atom basis, according to the generic rate rules (19). Considering H-abstractions on *n*-butane by $\dot{O}H$ at 1000 K, the four available secondary H-atoms contribute to ~60% of the total rate constant, while ~40% undergoes an H-abstraction on the terminal methyl groups. According to Benson [50] and Carstensen and Dean [89], only short range forces affect the reaction rates, therefore the effect of the functional group vanishes after the β positions. This assumption is further confirmed by the values reported in Figure 226. Thus, the rate of H-abstractions from the terminal CH₃ group is taken as that for alkanes, with the exception of MEK.
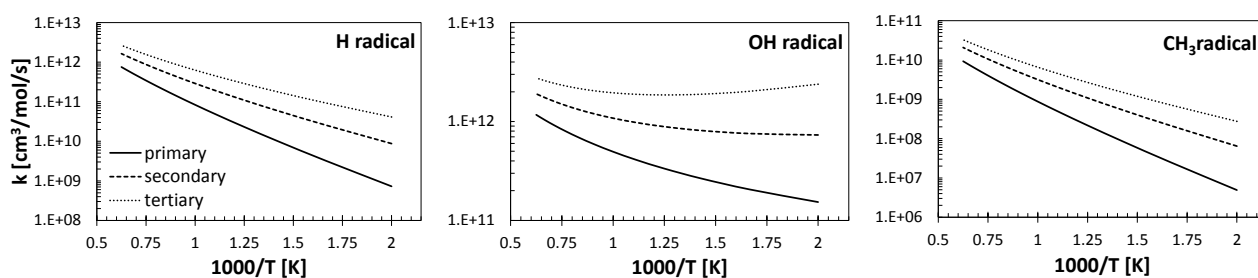
Figure 227: H-abstraction reactions. Calculated rate constants (per H-atom) for simple primary, secondary, tertiary H-atoms.

3.1 *n*-butanol

Figure 228 shows the relative selectivities of the H-abstraction reactions by $\dot{O}H$ radical of *n*-butanol at T=1000 K, as evaluated and discussed by Frassoldati et al. [370]. In agreement with the BDEs of Figure 226, the α position is the dominant one (~45%), followed by the alkane-like secondary position γ (~25 %). β position only contributes ~15%, due to its higher BDE (98.2 kcal/mol) compared to the one of the γ site.

According to the low temperature study of da Silva et al. [377] on the kinetics of the α-hydroxyethyl radical addition to O₂, R-·CH-OH radicals are assumed to interact with O₂ mainly producing $H\dot{O}_2$ and the parent aldehyde (e.g. R-·CH-OH+O₂=HO₂+R-CHO). Thus, the formation of peroxy radicals from the predominant α radicals is a negligible low temperature branching pathway for alcohol fuels. This feature partially justifies the anti-knocking properties of alcohols up to butanol isomers (Research Octane Number=98–117, Motor Octane Number=85-95 [4]), making them useful for use in spark ignition engines.
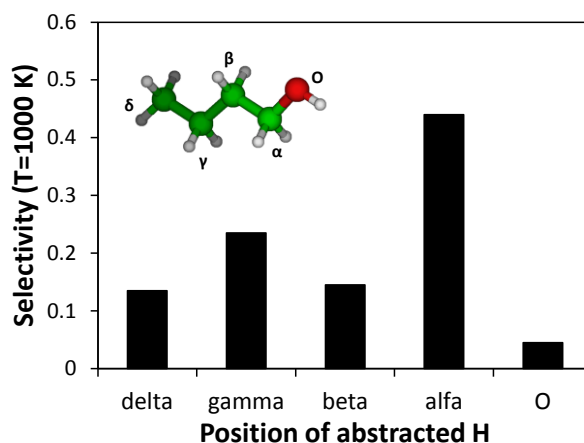
Figure 228: Selectivity of n-butanol radicals from H-abstraction reactions (44) by $\dot{O}H$ at T=1000 K.

3.2 *n*-butanal

Figure 229 shows the relative selectivities for the different positions in *n*-butanal oxidation according to the kinetic mechanism of Pelucchi et al. [77, 78] and of Veloo et al. [431].
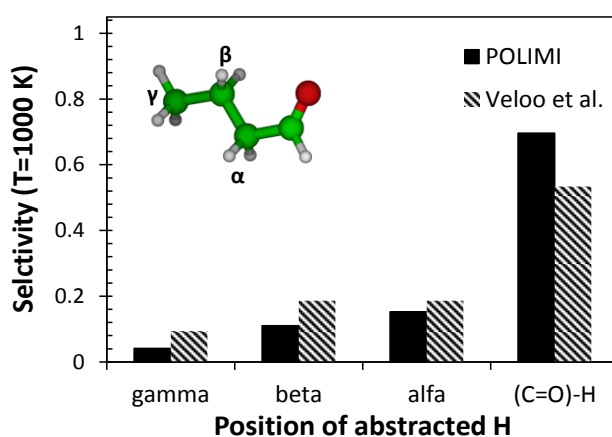
Figure 229: Selectivity of n-butanal radicals from H-abstraction reactions by $\dot{O}H$ at T=1000 K according to Pelucchi et al. [77, 78] (black bars), and Veloo et al. (striped bars) [431].

Despite some quantitative differences, both the mechanisms describe *n*-butanal oxidation as largely dominated (~50-70%) by H-abstraction at the weak C–H bond of the aldehydic site forming a carbonyl radical R_n-CO (i.e. C_3H_7CO). As recently discussed [77], carbonyl radicals heavier than acetyl do not add to oxygen, rapidly decomposing to CO and the corresponding alkyl radicals, whose low temperature branching pathways largely dominate aldehyde reactivity. Table 29 reports the branching ratios of the pseudo first order high pressure limit of C_3H_7CO addition to O_2 to form a carbonyl-peroxy radical, together with C_3H_7CO decomposition to CO and *n*-propyl radical. With regards to the bimolecular addition reaction, the pseudo

first order rate constant ($k_{app}=k_{add}(O_2)$) is based on the oxygen concentration of a stoichiometric *n*-butanal/air mixture (3.67% n-butanal/20.23% O_2/76.1% N_2) at 10 atm.

Because of the lower activation energy required for the decarbonylation (~15–16 kcal/mol) compared to that of the β-decomposition of alkyl radicals (~30 kcal/mol), the addition to O_2, activating the peracid channel, plays a role only at very low temperatures (T < 600 K).

Table 29: Branching ratios of C_3H_7CO addition to O_2 and its decomposition to CO and n-C_3H_7.

T (K)	C3H7·CO+O₂= C₃H₇CO-OO·	C3H7·CO=CO+·C₃H₇
400	1.00	0.00
500	0.85	0.15
600	0.22	0.78
700	0.03	0.97
800	0.01	0.99
900	0.00	1.00
1000	0.00	1.00

According to the BDEs of Figure 226, a significant selectivity of H-abstraction is expected for the secondary α position. With respect to the standard secondary H-atom in alkanes [52] a limited enhancing factor ~1.25 is applied, because of the resonantly stabilized nature of this radical, which inhibits reactivity from this channel.

3.3 methyl ethyl ketone

Figure 230 shows the relative selectivity of the three available abstraction channels in MEK, according to the rate constants proposed by Burke et al. [482] and to those adopted in this study (see the upcoming Section 4.4). The weakened secondary and primary C–H bonds, explain the predominant selectivity to α_s and α_p, accounting for ~50% and ~30% respectively.
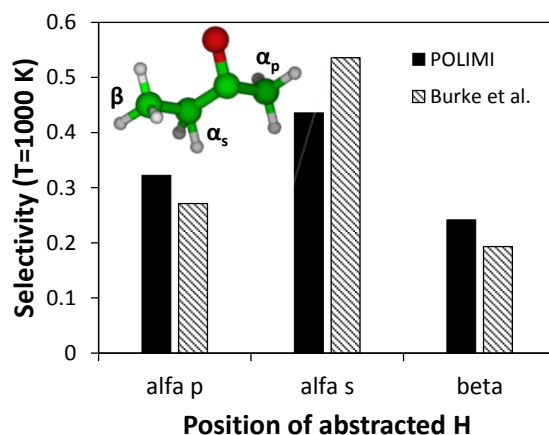
Figure 230: Selectivity of MEK radicals from H-abstraction reactions by $\dot{O}H$ at T=1000 K according to Burke et al. [482] and this study (POLIMI).

3.4 methyl butanoate

Grana et al. [493] already presented the high temperature oxidation mechanism of methyl butanoate (MB), together with a lumped low temperature mechanism derived from the detailed mechanism of Hakka et al. [494]. In a more recent study, Mendes et al. [495] calculated H-abstraction reactions by $\dot{O}H$ for a series of methyl esters (from methyl-ethanoate to methyl-butanoate). Figure 231 shows the relative importance of H-abstraction channels according to the detailed mechanism of Hakka et al. [494], adopted in the mechanism, and according to the theoretical calculations [495].
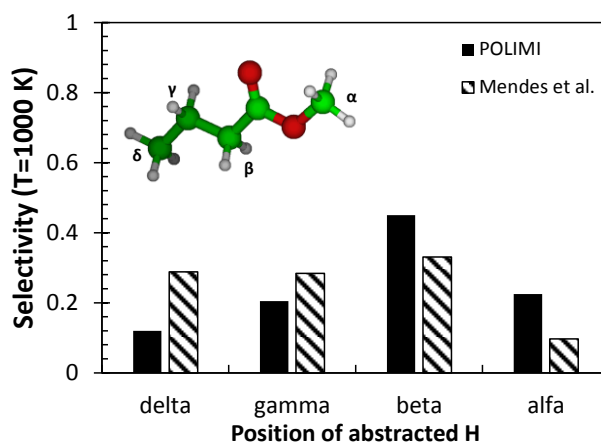
Figure 231: Selectivity of methyl butanoate radicals from H-abstraction reactions by $\dot{O}H$ at T=1000 K according to Hakka et al. [494] and Mendes et al. [495].

Again, Tan et al. [496] calculated H-abstraction reactions by important radicals ($\dot{H}$, $\dot{C}H_3$, $\dot{O}H$, $\ddot{O}$, $H\dot{O}_2$) for methyl-propanoate (MP). Figure 232 compares the experimental results for the total H-abstraction rate constant by $\dot{O}H$ as measured by Lam et al. [497], with rate constants from recent theoretical studies [495, 496] and that included in the lumped POLIMI mechanism for methyl butanoate [493].
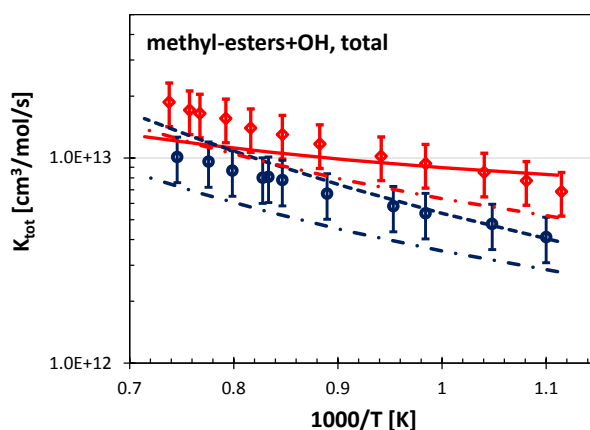
Figure 232: total rate constant for $\dot{O}H$ +MP (blue) and $\dot{O}H$ +MB (red). Symbols: experimental data by Lam et al. [497], solid line: POLIMI mechanism (MB) [493], dashed-dot line: Mendes et al. [495] (MP and MB), dashed line: Tan et al. [496](MP).

Despite the overall agreement between rate constant estimates and/or calculation and experiments (factor of ~1.5), Figure 233 shows some incoherent trends. In fact, according to the rate constants calculated by Tan et al. [496], the relative importance of the H-abstraction channels in MP at 1000 K, does not reflect the hierarchy in BDEs. Despite the surprising trend, it has to be mentioned that the same rate constants were recently found to have a positive effect on MP laminar flames prediction [498].

The C–H secondary bond in the β position is the weakest and, giving rise to the formation of a resonantly allylic-like radical, is expected to be the favored channel for H-abstractions, accounting for 45% of the selectivity in MB. According to the calculations of Mendes et al., this value is expected to increase to up to 60~% for MP. A BDE based approach in this case also provides useful guidance to critically interpret theoretical calculations.
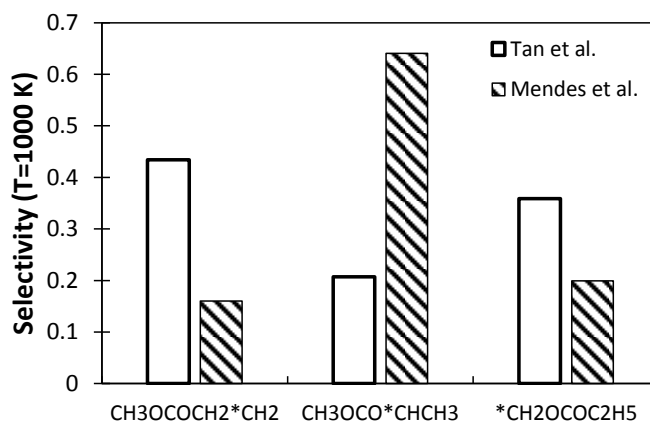
Figure 233: Selectivity of methyl propanoate radicals from H-abstraction reactions by $\dot{O}H$ at T=1000 K according to Tan et al. [496] and Mendes et al. [495].

Considering the low temperature oxidation, based on the length of the hydrocarbon chain in methyl butanoate and on the predominance of the H-abstraction from the central carbon β, typical negative temperature coefficient behavior is expected to be very limited, in agreement with observations of Gail et al. [499] and Walton et al. [500]. However, the analysis of the recent literature and the scarcity of data at temperatures lower than 800 K emphasize the uncertainty still existing in kinetic parameters for methyl esters.

3. Validation of the kinetic mechanisms of n-butane and oxygenated species

Before a kinetic analysis and discussion on the relative reactivity of n-butane and oxygenated fuels, a short validation of the updated kinetic mechanism POLIMI_1605 is presented. Moreover, the new lumped low temperature mechanisms of n-butanol and methyl ethyl ketone oxidation are also discussed. The global POLIMI mechanism includes ~500 species and ~20000 reactions, and is provided in the Supplemental Material attached to this study and on the website http://creckmodeling.chem.polimi.it/.

3.1 Lumped low temperature reactions

Due to the lack of symmetry in the molecular structure of oxygenated molecules, the size of the detailed kinetic scheme of pyrolysis and oxidation largely increases with respect to linear alkanes. Lumped or simplified approaches are therefore necessary to minimize the number of species and to allow easier extensions to longer species with the same functional group. An effective example of this systematic generalization to heavier molecular weight compounds belonging to the same class, can be found in the sequential studies of Grana et al. [493, 501], recently successfully extended by Rodriguez et al. [502]. In the case of methyl-butanoate (see Section 4.6), a single alkyl-like radical was included to avoid exponential increase in the number of species when extending the kinetic mechanism to longer methyl-esters (C_{11}–C_{19}

[501, 502]). For such fuels, detailed kinetic mechanisms from the literature can include up to ~5000 species, an order of magnitude more than the complete POLIMI mechanism.

Concerning the other oxygenated species analyzed in this study the detail of the different fuel radicals is maintained, allowing a more effective definition of site-specific reaction channels at high and low temperatures.

When generalizing this approach to oxidation reactions at low temperatures, it is necessary to include interactions of these radicals with O_2. Therefore, it is necessary to enlarge the kinetic scheme to include the intermediate lumped radicals RO_2, QOOH and its decomposition products (heterocyclic components and unsaturated species), OOQOOH, ketohydroperoxides, each one representing all the possible different isomers.

Following the validated and consolidated procedure proposed more than 20 years by Ranzi et al. [38], the mechanism refers to only three intermediate lumped radicals (RO_2, QOOH, OOQOOH) and four stable species derived from the low temperature oxidation (cyclic component, unsaturated alcohol, aldehyde or ketone, ketohydroperoxide). Kinetic parameters of the lumped reactions (see Table 30 and Table 31) are derived by fitting the selectivities obtained with the lumped mechanism with those obtained with the detailed kinetic scheme defined upstream. The detailed kinetic scheme is implemented based on rate rules for standard low temperature reaction classes [17], taking into account site specific BDEs and fuel specific reaction classes for oxygenated fuels.

3.2 *n*-butane

The *n*-butane kinetic mechanism [239] was recently revised with the inclusion of new reaction classes justifying the formation of organic acids and other minor oxygenated species at low temperatures [72]. Experiments were performed in a Jet Stirred Reactor (JSR) by Herbinet et al. [225] at ~1.0 atm, for temperatures between 550 and 800 K, at a mean residence time of 6 s for a stoichiometric *n*-butane/oxygen/argon mixture (4/26/70 in mol%). Figure 234 shows a comparison of experimental data with model predictions.
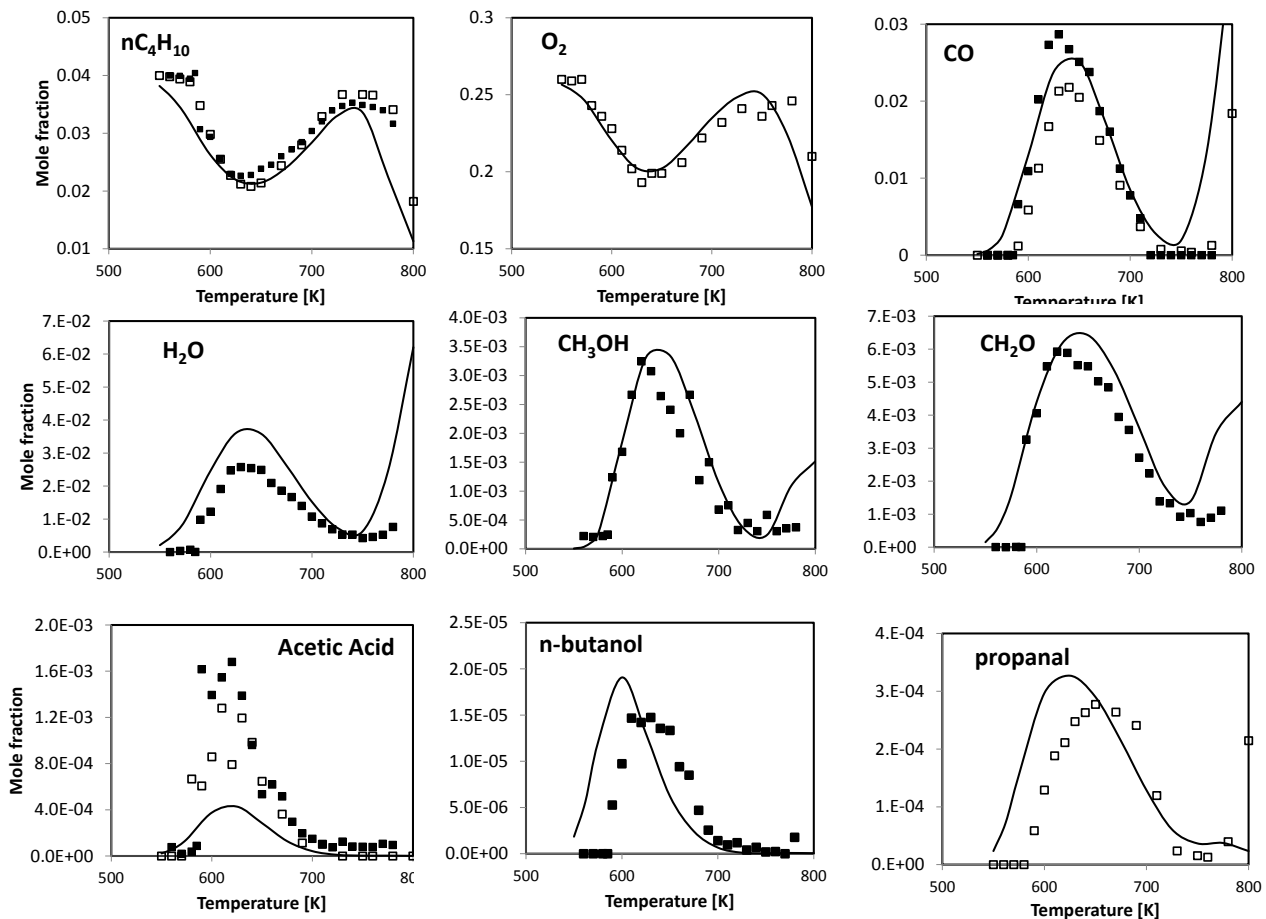
Figure 234: Oxidation of n-butane in a jet stirred reactor (n-butane/O₂/Ar = 4/26/70 mol%; 1 atm; residence time 6 s). Comparison of experimental measurements of Nancy (open symbols) and Hefei (full symbols) [225] with model predictions.

Predicted ignition delay times in shock tubes and rapid compression machines (RCMs) were measured by Healy et al. [436], between 1 and 40 atm. A comparison with mechanism predictions is given in Figure 235. To better highlight kinetic effects discussed in Section 5, RCM simulations were performed assuming an adiabatic constant volume reactor, not including heat losses. This simplification partially explains the observed deviations, as discussed in Cuoci et al. [66].
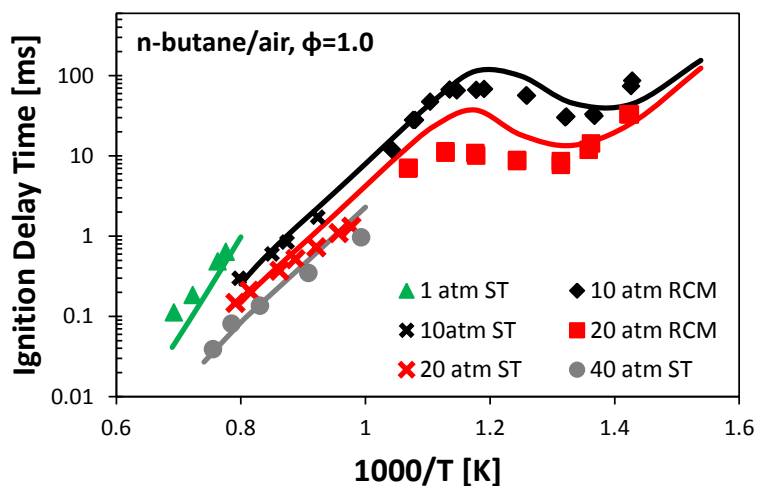
Figure 235: Ignition delay times of stoichiometric n-butane/air mixtures. Experimental data by Healy et al. [436] (symbols) and model predictions.

3.3 *n*-butanol

The kinetic mechanism for butanol isomers was developed and extensively validated by Grana et al. [369] and partially revised later by Frassoldati et al. [370]. A lumped low temperature oxidation mechanism of n-butanol has been developed in this study and is reported in Table 30. Details of the lumped species representing the different isomers are reported in Table S2 of the Supplemental Material. Rate parameters are based on the low temperature rate rules by Ranzi et al. [17].

Table 30: Lumped low temperature reactions of n-butanol. Species: CH3CH2·CHCH2OH (β, secondary radical), CH3·CHCH2CH2OH (γ, secondary radical), ·CH2CH2CH2CH2OH (δ, primary radical) as in Figure 228. Lumped species: RBU1OOX (peroxy radicals), QBU1OOX (hydroperoxyalkyl radicals), ZBU1OOX (hydroperoxyalkyl peroxy radicals), KEHYBU1 (ketohydroperoxides), HCE-BU1 (hydroxyl cyclic ether). Units are cm³, mol, s.

Reaction	A	E_a (cal/mol)
$CH_3CH_2·CHCH_2OH+O_2 \rightarrow RBU1OOX$	2.50E+12	0
$CH_3·CHCH_2CH_2OH+O_2 \rightarrow RBU1OOX$	2.50E+12	0
$·CH_2CH_2CH_2CH_2OH+O_2 \rightarrow RBU1OOX$	2.50E+12	0
$RBU1OOX \rightarrow .3CH_3CH_2·CHCH_2OH+.5$ $CH_3·CHCH_2CH_2OH+.2·CH_2CH_2CH_2CH_2OH +O_2$	3.00E+13	30000
$RBU1OOX \rightarrow QBU1OOX$	4.50E+12	24000

QBU1OOX → RBU1OOX	5.00E+11	20000
QBU1OOX → $H\dot{O}_2$ + unsat alcohol	2.00E+13	24000
QBU1OOX →OH+carbonyl+olefin/unsat alcohol	3.00E+13	24000
QBU1OOX →OH+HCE-BU1	1.00E+11	17000
O_2+ QBU1OOX → ZBU1OOX	2.50E+12	0
ZBU1OOX →O_2+ QBU1OOX	3.00E+13	30000
ZBU1OOX →OH+KEHYBU1	4.50E+12	24000
KEHYBU1→OH+OHCH$_2$CHO+CH$_2$CHO	5.00E+15	42000
RBU1OOX →OH+CH$_2$O+C$_{n-1}$aldehyde (Waddington)	1.00E+10	22000

Several experimental data allowed to validate this lumped mechanism. Ignition delay times were measured between 770–1250 K by Heufer et al. [380] and Vranckx et al. [381] at high pressure (10-80 bar). Rapid compression machine measurements were also presented by Weber et al. [378]. Figure 236 shows some comparisons between experimental data and results from adiabatic constant volume simulations. The kinetic mechanism, already extensively validated for high temperature conditions, provides reliable results also at low temperatures and high pressures.
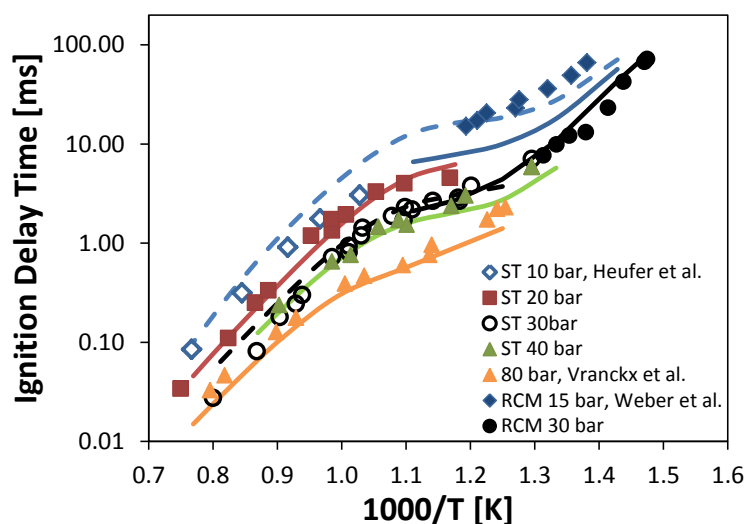
Figure 236: Ignition delay times of stoichiometric n-butanol/air mixtures. Experimental data (symbols) and kinetic mechanism predictions (lines) (adiabatic constant volume simulations).

3.4 *n*-butanal

Pelucchi et al. [78] developed a kinetic mechanism for *n*-C$_3$–C$_5$ aldehyde pyrolysis and oxidation at high temperatures. The model was recently extended to describe low temperature oxidation [77]. Figure 237 shows a comparison with the speciation data of Veloo et al. [431] in a jet stirred reactor at 10 atm, in the temperature range of 500–1100 K. Despite the slight underestimation of fuel conversion at low temperatures, the kinetic mechanism correctly predicts the effect of oxygen concentration and the extension of the NTC region. For the case at φ=0.5 a detailed comparison is reported, confirming the assumptions of the predominance of alkyl radical low temperature chemistry, as discussed in Pelucchi et al. [77].
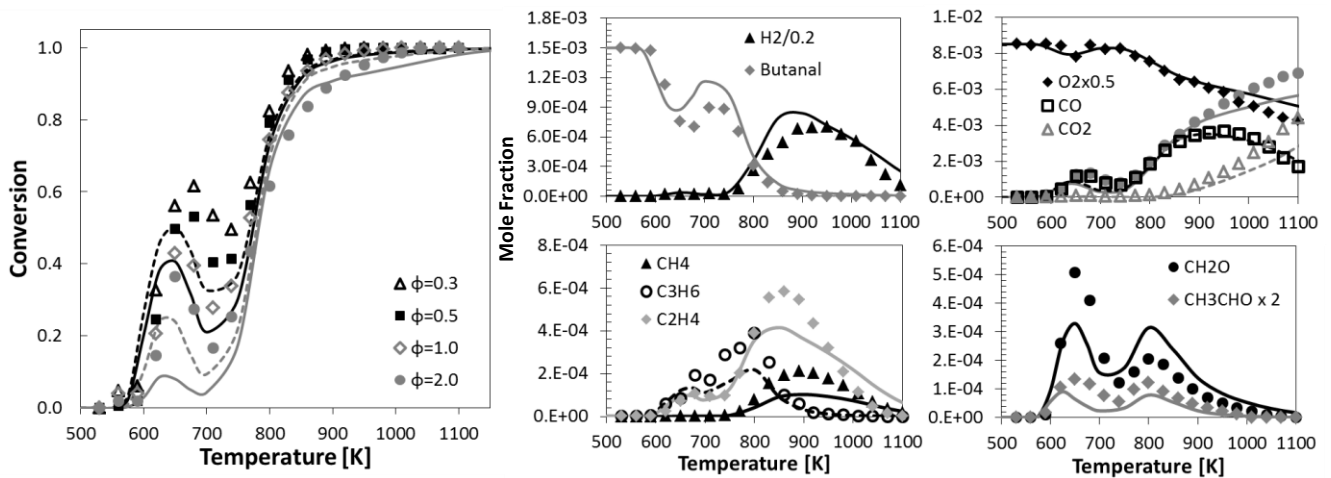
Figure 237: n-butanal (0.15%) oxidation in a JSR at 10 atm, τ=0.7 s. Fuel conversion for varying Φ and species profiles at Φ~0.5. Experimental data [431] (symbols) and mechanism predictions.

3.5 Methyl ethyl ketone

Methyl ethyl ketone (MEK) kinetics received large attention not only as an intermediate in hydrocarbon fuel combustion, but also for its role in the combustion of bio-oil from fast biomass pyrolysis. The more recent work of Hoppe et al. [481] and Burke et al. [482] directly focused on its potential as a biofuel. In particular Burke et a. [482] recently extended the available experimental data to conditions of interest for engines, measuring ignition delay times of MEK/air stoichiometric mixtures in a rapid compression machine, between 850–1280 K, at 20 and 40 bar. Moreover, a kinetic mechanism including also the low temperature chemistry was developed and validated [482]. New experimental measurements were also carried out at the same conditions for a series of ketones [503] (acetone, 2-pentanone, 3-pentanone) at high temperatures (1028–1399 K) and high pressures (20 and 40 bar). Ignition delay time correlations were derived and the reactivity trend was explained based on BDEs, H-abstraction and radical decomposition reactions.

The high temperature pyrolysis and combustion mechanism of MEK is simply limited to the three main initiation reactions

$CH_3CH_2COCH_3 = CH_3CH_2\bullet + \bullet COCH_3$
$$k = 2. \cdot 10^{16} \cdot \exp\left(-\frac{82500}{RT}\right) \quad [s^{-1}]$$

$CH_3CH_2COCH_3 = CH_3\bullet + \bullet CH_2COCH_3$
$$k = 2. \cdot 10^{16} \cdot \exp\left(-\frac{84000}{RT}\right) \quad (s^{-1})$$

$CH_3CH_2COCH3 = CH_3CH_2CO\bullet + \bullet CH_3$
$$k = 2. \cdot 10^{16} \cdot \exp\left(-\frac{84000}{RT}\right) \quad (s^{-1})$$

together with three possible H-abstraction channels:

$R\bullet + CH_3CH_2COCH_3 = RH + CH_3\bullet CHCOCH_3$
$$k^{OH} = 8.8 \cdot 10^5 \cdot T^2 \cdot \exp\left(\frac{2260}{RT}\right) \quad \left[\frac{cm^3}{mol \cdot s}\right]$$

$R\bullet + CH_3CH_2COCH_3 = RH + CH_3CH_2CO\bullet CH_2$
$$k^{OH} = 1.6 \cdot 10^6 \cdot T^2 \cdot \exp\left(\frac{474}{RT}\right) \quad \left[\frac{cm^3}{mol \cdot s}\right]$$

$R\bullet + CH_3CH_2COCH_3 = RH + \bullet CH_2CH_2COCH_3$
$$k^{OH} = 1.2 \cdot 10^6 \cdot T^2 \cdot \exp\left(\frac{474}{RT}\right) \quad \left[\frac{cm^3}{mol \cdot s}\right]$$

While the H-abstraction reactions are written in their generic form for all the H-abstracting radicals (R•), rate parameters reported above specifically refer to $\dot{O}H$ as the abstracting radical. The first H-abstraction reaction (referred to as α_s in Figure 230 of Section 3.3) is the dominant one also at low and intermediate temperatures accounting for slightly more than the 50% of the total propagation rate and MEK depletion.

Burke et al. [482] adopted rate constants for H-abstraction by $\dot{O}H$ as calculated by Zhou et al. [463]. According to the authors, the overall uncertainty of these theoretical calculation is a factor of ~3, due to uncertainty in energy calculations, tunneling effects and hindered rotors treatment. Figure 238a shows a comparison between the total H-abstraction rate constant by $\dot{O}H$ in the POLIMI mechanism, the experimental values of Lam et al. [504], and the total rate constant as calculated by Zhou et al. [463]. Panels b to d, show a detailed comparison of the site-specific rate constants showing good agreement between the values adopted in the POLIMI mechanism and theoretical calculations [463].
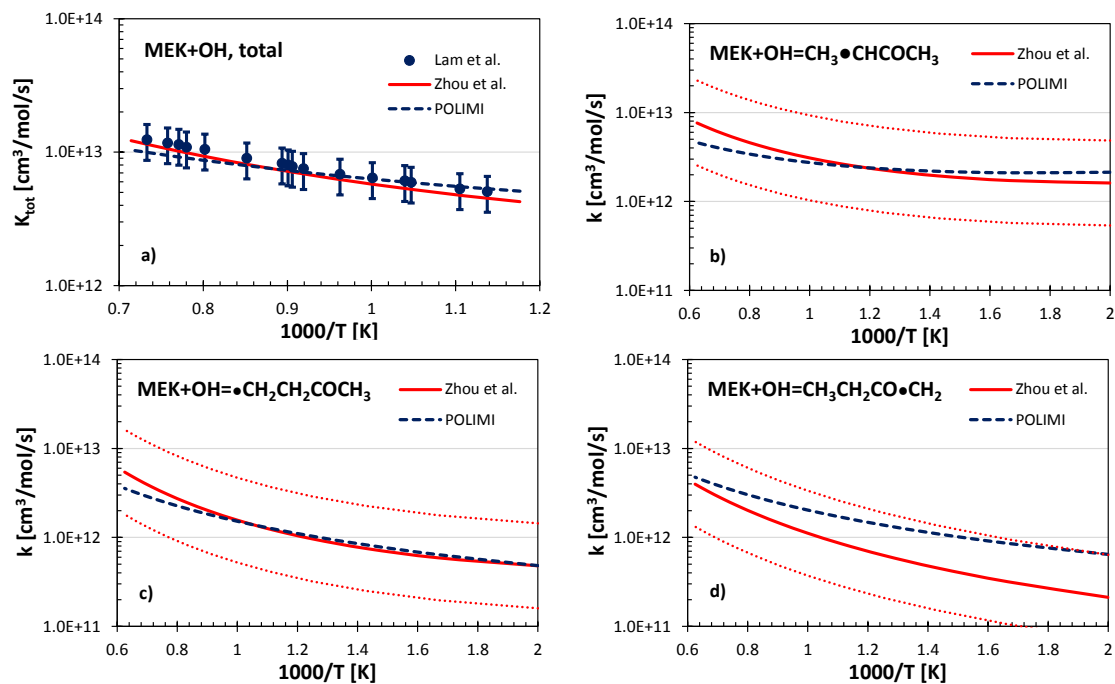
Figure 238: a) Total rate constant of $\dot{O}H$ +MEK. b-d) Site specific rate constant for H-abstraction by $\dot{O}H$. Symbols: experimental data [504] red solid lines [463], red dotted lines: uncertainty (~2.5 as in [463]), black lines: POLIMI.

Lam et al. [505] studied the high-temperature pyrolysis of MEK behind reflected shock waves by using several species time-history measurements. Figure 239 shows comparisons between experimental data and model predictions.
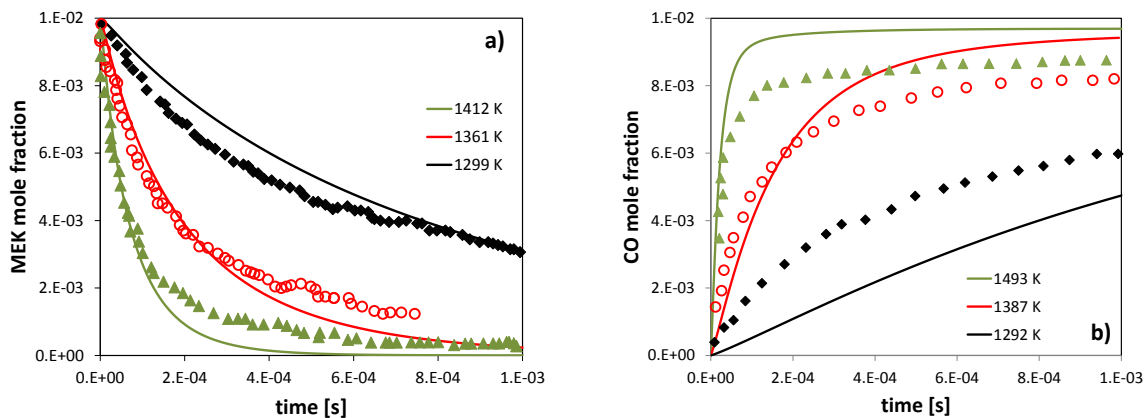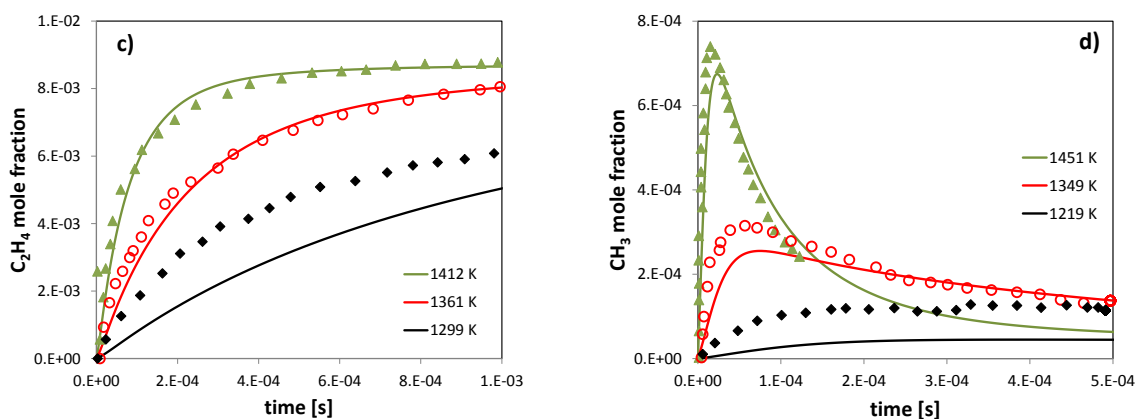
Figure 239: Pyrolysis of MEK. Panel a) Time-history of 1% MEK in Ar. Panel b) and c) time-histories of CO and C_2H_4 for 1% MEK in Ar. Panel d) time-history of methyl radical for 0.25% MEK in Ar. Comparisons of experimental data (symbols) [505] and model predictions (lines).

Recently, Badra et al. [506] presented shock tube ignition delay times of MEK ($C_2H_5COCH_3$) over temperatures of 1100–1400 K, pressures of 3–6.5 atm, at equivalence ratios of 0.5 and 1. They also modified the chemical kinetic mechanism of Serinyel et al. [507] improving MEK reactivity, because of systematic over-predictions of the ignition delay times, with respect to their experimental data. Figure 240 shows the satisfactory agreement of POLIMI mechanism predictions with these data, both in terms of pressure and stoichiometry dependence. In contrast, the model systematically under-predicts the ignition delay times of Serinyel et al. [507] by at least a factor of two.
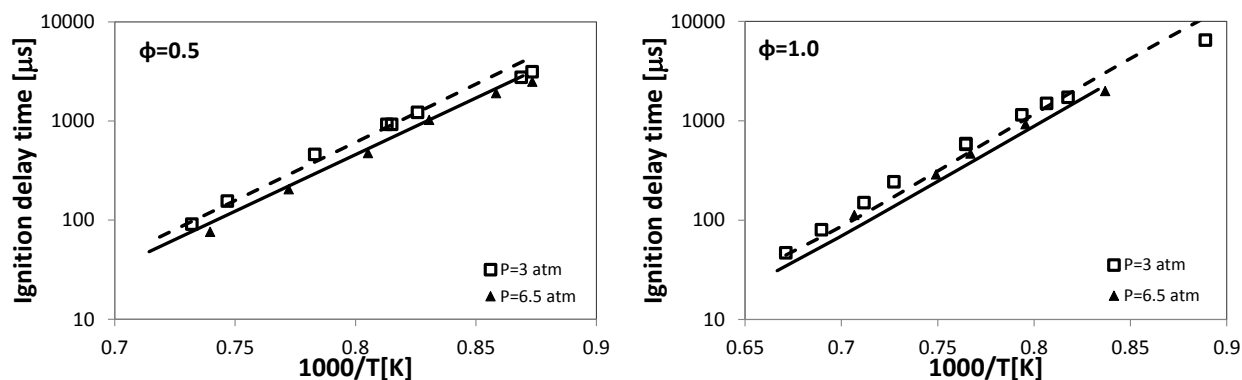
Figure 240: Ignition delay times for MEK/O_2/Ar mixtures at 3 and 6.5 atm (Φ= 0.5 and Φ= 1.0). Experimental data from Badra et al. [506].

The recent works of Hoppe et al. [481] and Burke et al. [482] highlighted the anti-knocking property and the lower reactivity of MEK with respect to commercial gasoline, in the temperature range 850–1000 K. From a kinetic perspective, the presence of the carbonyl group weakens the adjacent C–H bonds, and stabilizes both

the alkyl radical and the peroxy radical formed via addition to O_2. The high rate of $H\dot{O}_2$ elimination (mainly RMEKOO=>HO₂+CH3COCHCH2) largely explains the observed lower reactivity.

Burke et al. [482] reported a detailed discussion on RMEKOO=>HO₂+CH3COCHCH2 (methyl vinyl ketone), based on previous studies [508, 509]. These literature values were found to differ greatly from each other (i.e. a factor of ~7). Figure 241 shows a comparison of the rate constant adopted in the lumped mechanism, and those adopted in previous studies on MEK [482] and diisopropyl ketone (DIPK) [509], weighted on the relative abundance of α_s and β radicals in each mechanism. The lumped rate constant is respectively ~1.6 and ~2.0 times faster than the literature values. As in the lumped approach RMEKOO represents all of the peroxy radical isomers in MEK oxidation, the comparison is carried out by weighing the rate constants in the detailed mechanisms by the relative abundance of the two radicals (α_s and β) leading to this pathway, i.e. the selectivity to their formation as a function of temperature.
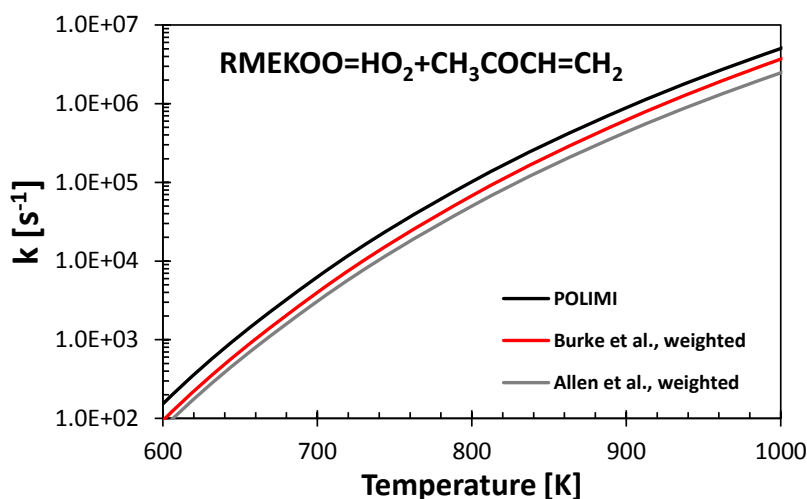
Figure 241: Comparison between the lumped rate constant for RMEKOO=>HO₂+CH₃COCHCH₂ and the rate constants adopted in previous detailed kinetic mechanism [482, 509].

Beside the above reaction, the total number of available H-atoms for the internal isomerization to form the lumped hydroperoxy alkyl radical (RMEKOO=>QOOH-MEK) is lower than in *n*-butane. The coupling of the two effects leads to a prevalence of chain propagating reactions with respect to chain branching reactions typical of the low temperature oxidation of alkanes.

The lumped low temperature oxidation mechanism of MEK, as developed in this study, is reported in Table 31. Details of the lumped species representing the different isomers are reported in Table S2 of the Supplemental Material. Figure 242 compares constant volume simulations with the recent experimental data of Burke et al. [482] and shows the weak effect of the low temperature reactions, in these conditions.

Reaction	A	E_a (cal/mol)
RMEKAS+O_2→RMEKOO	2.00E+12	0
RMEKAP+O_2→RMEKOO	2.00E+12	0
RMEKB+O_2→RMEKOO	2.00E+12	0
RMEKOO→.5RMEKAS+.3RMEKAP+.2RMEKAB+O_2	2.00E+13	28000
RMEK+O_2↔ $H\dot{O}_2$+$CH_3COCH=CH_2$	2.50E+12	6000
RMEKOO→ $H\dot{O}_2$+$CH_3COCH=CH_2$	3.00E+13	31000
RMEKOO→QOOH-MEK	1.00E+12	26000
QOOH-MEK→RMEKOO	1.00E+10	16000
QOOH-MEK→ $H\dot{O}_2$+$CH_3COCH=CH_2$	2.00E+11	21000
QOOH-MEK→OH+CH_2CO+CH_3CHO	5.00E+13	22500
QOOH-MEK→OH+CCE-MEK	2.00E+11	16700
O_2+QOOH-MEK →OOQOOH-MEK	5.00E+12	0
OOQOOH-MEK→O_2+QOOH-MEK	2.00E+13	28000
OOQOOH-MEK→OH+KHYMEK	1.00E+12	26000
KHYMEK→OH+CH_2O+CO+CH_3CO	3.00E+15	43000
KHYMEK→OH+CH_2O+CH_2CO+HCO	2.00E+15	43000

Table 31: Lumped low temperature reactions of methyl ethyl ketone. Species: RMEKAS (α, secondary radical), RMEKAP (α, primary radical), RMEKB (β, primary radical) as in Figure 230. Lumped species: RMEKOO (peroxy radicals), QOOH-MEK (hydroperoxyalkyl radicals), OOQOOH-MEK (hydroperoxyalkyl peroxy radicals), KHYMEK (ketohydroperoxides), CCE-MEK (carbonyl cyclic ether). Units are cm³, mol, s.
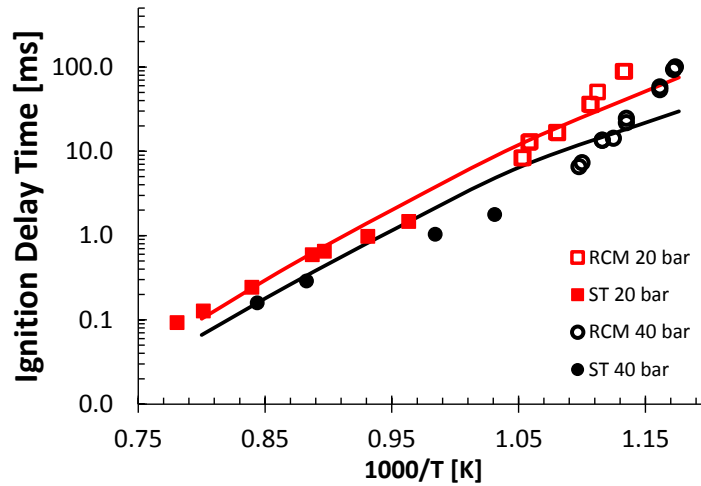
Figure 242: Ignition delay times of stoichiometrich MEK/air mixtures. Experimental data [482] (symbols) and kinetic mechanism predictions (lines) (adiabatic constant volume simulations).

3.6 Methyl butanoate

Grana et al. [493] extensively investigated the oxidation of methyl butanoate in shock tubes, plug flow reactors, jet stirred reactors, rapid compression machines and premixed laminar flames. For the low temperature oxidation a lumped kinetic mechanism mostly based on the work of Hakka et al. [494] was developed. Model predictions are compared to the ignition delay time measurements of HadjAli et al. [510] at T=815 K, Φ=1.0 and varying compressed pressure in a RCM in Figure 243.
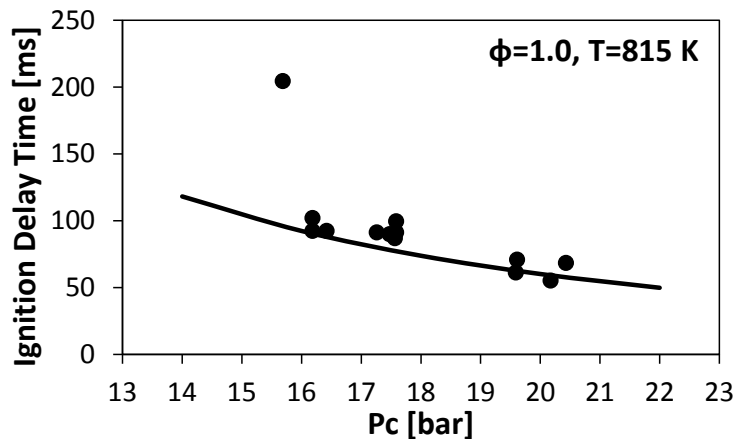
Figure 243: Ignition delay times of stoichiometric methyl butanoate/air mixtures at T=815 K and varying compressed pressure. Experimental data [510] (symbols) and model predictions (lines) [493].

As a further comparison, Figure 244 shows species profiles measured by Gail et al. [511] in an atmospheric JSR, in the temperature range of 850–1400 K, at Φ=0.75 and residence time of 0.07 s.
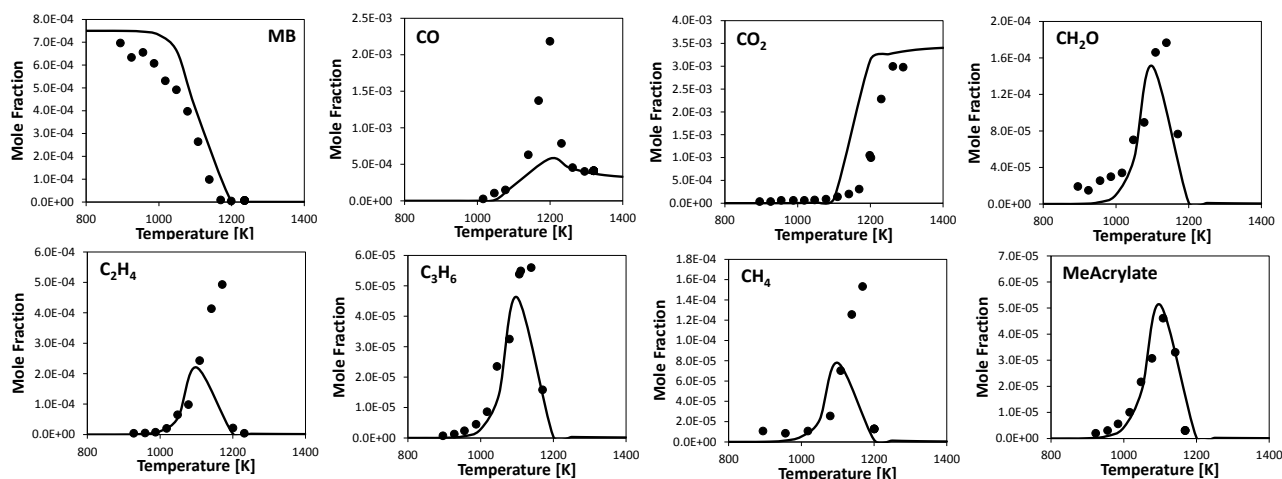
Figure 244: Experimental results [511] and model predictions of major products from methyl butanoate oxidation in the JSR at φ=0.75, atmospheric pressure and 0.07 s.

4. Relative reactivity of oxygenated fuels and the influence of the oxygenated moiety

Figure 245 compares the reactivity of *n*-butane, *n*-butanol, *n*-butanal, methyl ethyl ketone and methyl butanoate in terms of ignition delay times of stoichiometric fuel/air mixtures at 10 (a) and 30 atm (b and c). Considering that the relative reactivity of the fuels is very consistent at both pressures, the discussion will focus on the 10 atm case, where the differences at lower temperatures are clearer. In fact, as the pressure increases, the peroxy radical (RO_2) can better stabilize allowing more efficient isomerization reactions to form hydroperoxyalkyl radicals (QOOH). However, the fuel specific reaction pathways discussed in the following, directly derived from the effect of the different functional group on BDEs, still play a major role and explain the consistent trend observed in panel c of Figure 245.
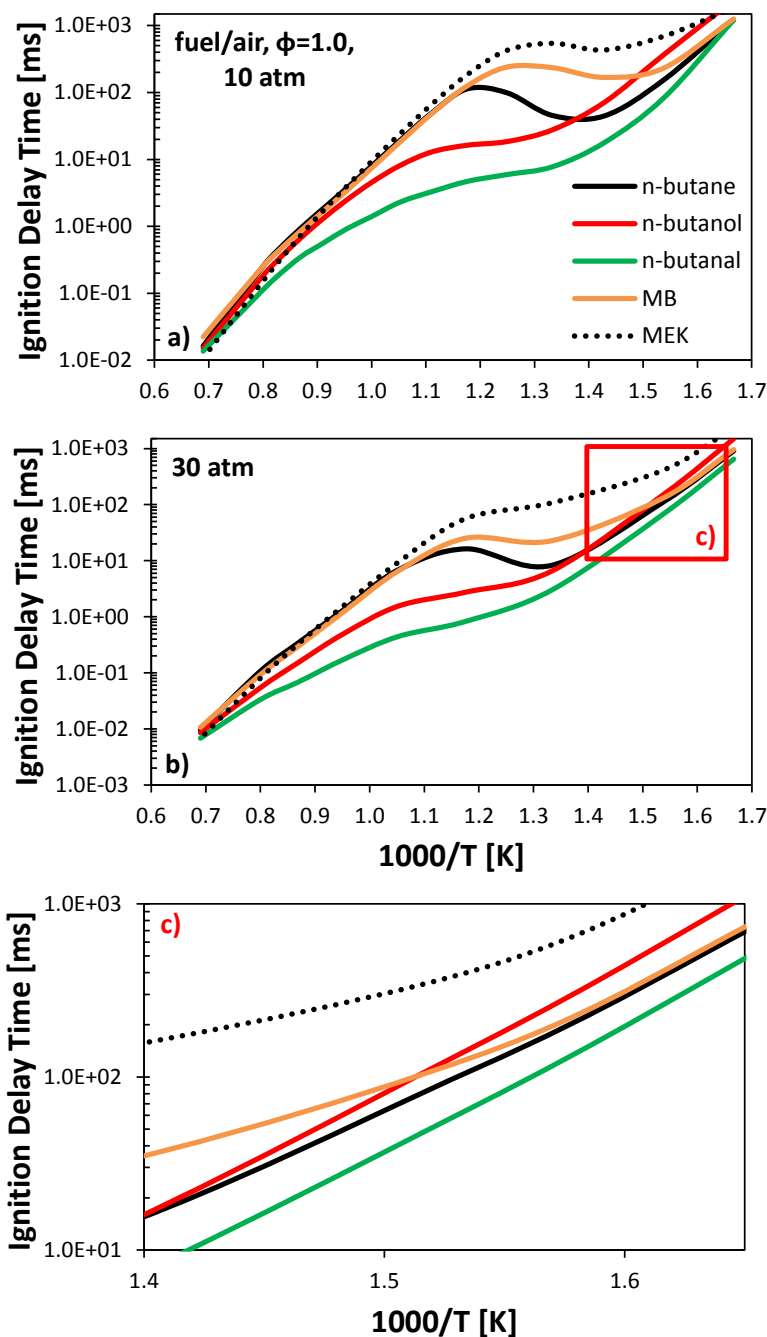
Figure 245: Relative reactivity of alkanes and oxygenated species. Ignition delay times of stoichiometric fuel/air mixtures at 10 atm (a) and 30 atm (b and c).

At high temperatures, the fuel pyrolysis controls the reacting process. The fast molecule decomposition forms components of lower molecular weight, which in turn oxidize. Thus, fuels behave quite similarly at these conditions. The initiation reactions play a significant role and this explains the slightly higher reactivity of *n*-butanol and especially of *n*-butanal. As shown in *Figure 226*, the oxygen atom weakens the closest C–C bonds, reducing their BDEs. In particular, the carbonyl group of *n*-butanal decreases the energies of both the nearest C–C bonds by about 5.5 kcal/mol, with respect to the corresponding bonds in *n*-butane. The hydroxyl

group of *n*-butanol shows a lower weakening effect and affects the closest C–C bond only, reducing its energy by about 3.6 kcal/mol, compared to the analogous bond between a primary and a secondary C atom of a linear alkane.

At low and very low temperatures (< 650 K), the typical branching decomposition reactions, via successive oxygen additions to radicals, and isomerization reactions leading to ketohydroperoxides are the prevalent pathways. Therefore, the induction times of *n*-butane, *n*-butanal and MB converge.

In contrast, the low reactivity of *n*-butanol, that is its longer induction time, is due to the favored formation (~45% of fuel consumption) of the alpha radical (CH$_3$CH$_2$CH$_2$·CHOH), because of the reduced BDE of the alpha C–H bond induced by the OH group (Figure 246). Once formed, the alpha radical does not undergo the typical low temperature branching mechanism, but it mostly produces *n*-butanal and $H\dot{O}_2$ (O$_2$+CH$_3$CH$_2$CH$_2$·CHOH=C$_3$H$_7$CHO+HO$_2$·). Heufer et al. [382] obtained similar trends when comparing *n*-C$_4$–C$_5$ alcohols and alkanes reactivity at low temperatures.
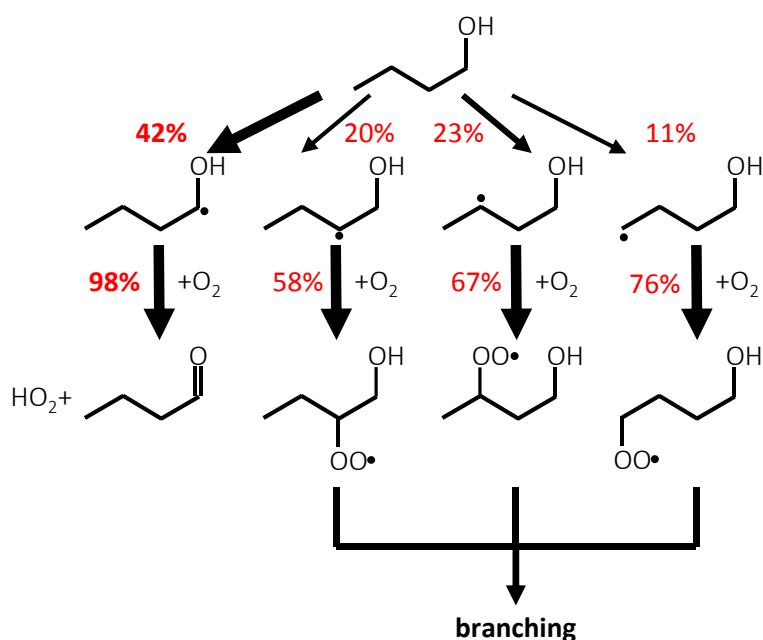
Figure 246: Sketch of the low T mechanism of n-butanol at 650 K and 10 atm. Pathways involving the butoxy radical (RO·), accounting for ~4% of n-butanol consumption and not contributing to the low temperature branching, have been omitted for clarity.

MEK is also slow to ignite at T<800 K. Although the $H\dot{O}_2$ elimination from the peroxy radical could explain this behavior, additional experimental data in that specific temperature regime are needed for a better assessment of MEK low temperature reactivity.

The largest differences among the different fuels are observed at intermediate temperatures (750-950 K). Figure 247 shows the sensitivity analysis of the ignition delay times performed for the different fuels at stoichiometric conditions at 850 K and 10 atm. H-abstraction reactions, mainly by $H\dot{O}_2$, are the activating reactions, together with the low/intermediate temperature mechanism, involving in particular additions to oxygen (R+O₂) and the peroxy radical isomerizations (RO₂=QOOH). Hydroperoxyalkyl radical (QOOH) decomposition to form $H\dot{O}_2$ and the conjugate unsaturated species shows the most inhibiting effect, because of the relative stability of the hydroperoxy radical ($H\dot{O}_2$).

n-butanal shows the lowest ignition delay times. The faster rate of H-abstraction from the aldehydic site, caused by the low BDE of the C–H bond (see Figure 226), justifies this higher reactivity with respect to the corresponding alkanes, alcohols and esters. Due to the fast decomposition of the carbonyl radical previously discussed, *n*-propyl radical low temperature oxidation dominates the reactivity of the aldehyde.

The second fastest fuel to ignite in these conditions is *n*-butanol. The low BDE of the alpha hydrogen results in a reduction of the reactivity, as reported in the sensitivity analysis of Figure 247. The formed radical (CH₃CH₂CH₂·CHOH) does not undergo the conventional low temperature branching pathway, but interacts with O₂ forming the parent aldehyde and the less reactive $H\dot{O}_2$ radical. All the other H-abstractions in β, γ and δ positions promote *n*-butanol reactivity, with γ being the most favored position (see Figure 228).
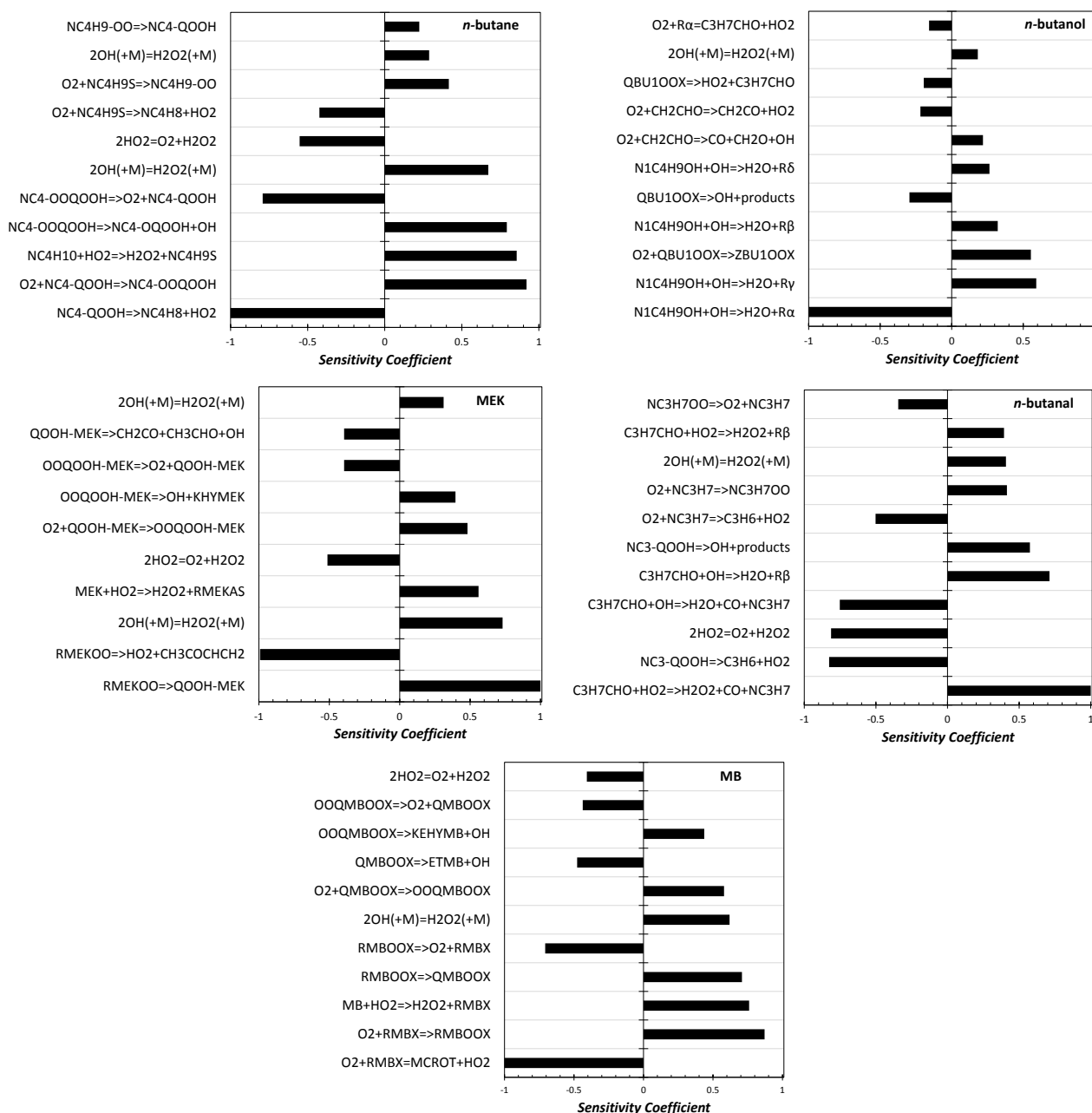
Figure 247: Sensitivity of ignition delay times to rate constants at 10 atm and 850 K, for stoichiometric fuel/air mixtures. A positive sensitivity coefficient stands for a reaction increasing reactivity (i.e. decreasing ignition delay time). Sensitivity coefficients are normalized to +1/-1. For lumped species representing the different isomers refer to Table S2 in the supplementary material.

At intermediate temperatures, Figure 247 clearly shows that MEK limited reactivity is controlled by the very sensitive decomposition reaction of the peroxy radical RMEKOO to form $H\dot{O}_2$ and methyl-vinyl-ketone.

The high production of $H\dot{O}_2$ radical enhances its importance as abstracting radical from the weak C–H in α_s, giving rise to H₂O₂. The subsequent dissociation of hydrogen peroxide (H₂O₂+M=$\dot{O}H$ +$\dot{O}H$ +M) partly explains the positive sensitivity coefficient of H-abstraction by $H\dot{O}_2$. It is clear that a correct assessment of $H\dot{O}_2$ production via RO₂=>HO₂+unsaturated ketones and $H\dot{O}_2$ consumption via H-abstraction is key in properly predicting MEK reactivity at these conditions. Figure 248 shows the main reaction pathway of MEK oxidation at 850 K and 10 atm.
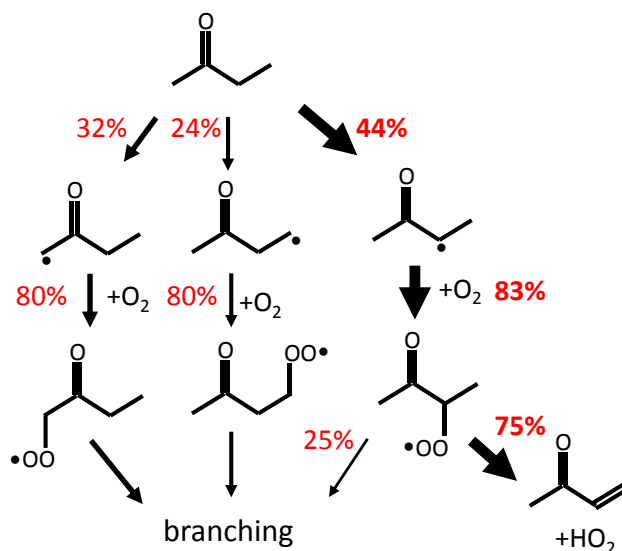
Figure 248: Relative importance of reaction pathways in methyl ethyl ketone (MEK) oxidation at 850 K and 10 atm.

Methyl butanoate (MB) lacks a pronounced NTC and shows the second lowest reactivity in the intermediate temperature range. Its alpha C–H bond is weaker than those of *n*-butanol and *n*-butane, contributing positively to the reaction propagation. The resonance stabilization of the formed radical inhibits the successive oxygen addition. Moreover, the corresponding α-peroxy-methyl-butanoate radical can only isomerize, either through a seven membered ring or through a five membered ring (Figure 249). Both these paths are less favored, one for entropic reasons (too many rotors to block in the larger ring) and the other for energy reasons (extra strain of the 5-atom ring). Thus, as the sensitivity analysis of Figure 247 shows, the most effective reaction between oxygen and the alpha resonant radical is not the addition, but mainly the formation of $H\dot{O}_2$ and the unsaturated methyl-crotonate (O₂+RMBX=HO₂+MCROT), with the consequent decrease in reactivity.
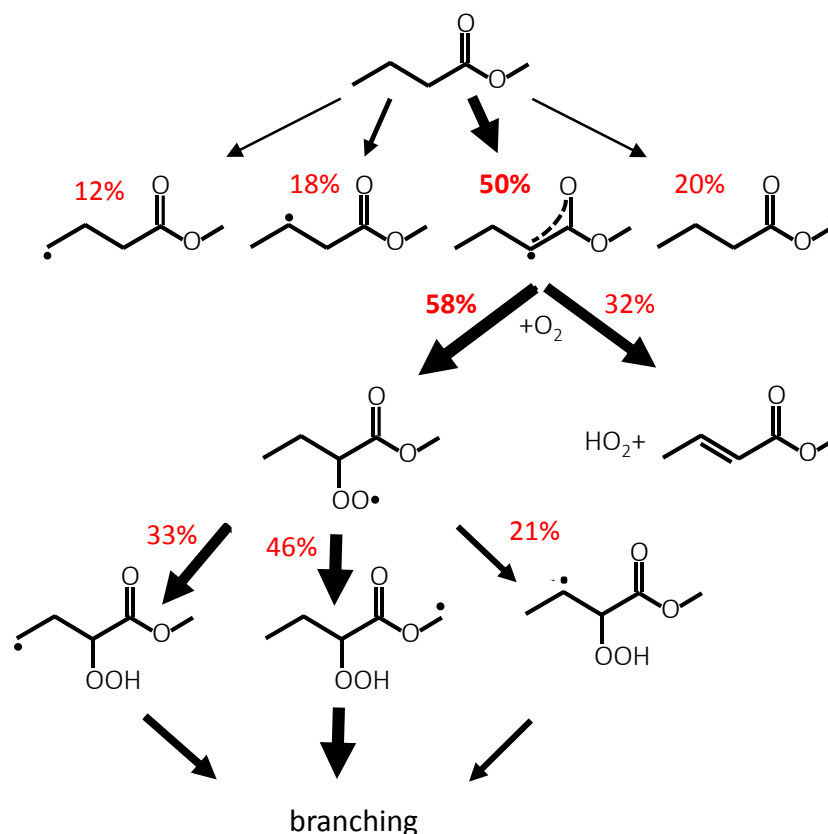
Figure 249: Sketch of main reactions in the low T mechanism of methyl-butanoate (MB) at 850 K and 10 atm.

5.   Conclusions

This work allowed the first comparative analysis of the reactivity of oxygenated fuels with different functional groups (R-OH, R-CHO, R-(C=O)-O-CH$_3$, R-(C=O)-R).

A consistent assessment of C–H and C–C BDEs in *n*-butane and oxygenated species such as *n*-butanol, *n*-butanal, methyl ethyl ketone (MEK) and methyl butanoate (MB) has been provided, and they clearly reflect the effect of the oxygen atom in different functional groups on the neighboring bonds.

Rate parameters of H-abstraction and initiation reactions implemented in the POLIMI mechanism, take into account these BDEs. The relative reactivity and selectivity of the H sites in the different fuels are also discussed. The upgraded POLIMI kinetic mechanism, here extended to the low temperature mechanisms of n-butanol and to the high and low temperature oxidation of MEK, is applied to support this kinetic analysis of relative reactivity of oxygenated species in the whole temperature range 600–1450 K.

In general, the reactivity scales as:

n-butanal > *n*-butanol > *n*-butane > MB > MEK.

The extreme reactivity of the aldehydic moiety leading to the formation of the carbonyl radical (C_3H_7CO) largely explains *n*-butanal ignition properties. Although some secondary products from rather unknown and challenging reaction channels have been identified for longer aldehydes, it is quite understood that the major role at low temperatures is played by *n*-C_3H_7 branching pathways. Ignition measurements for aldehydes at low temperatures would be useful to support such analysis.

At low temperatures (T<675 K) *n*-butanol shows the lowest reactivity, because the favored α-radical mainly interacts with O_2 producing $H\dot{O}_2$ and *n*-butanal, thus inhibiting the low temperature paths. As already pointed out by Sarathy et al. [4], very little information exists for the rate coefficient of this key reaction channel for linear alcohols longer than ethanol. A systematic theoretical analysis of this reaction class for a series of linear alcohols would be useful in defining an accurate rate rule.

Between 750 K and 850 K MEK and MB are the slowest to ignite. These results are consistent with those reported by Lin et al. (80) for MB. The lower reactivity is due to the sensitive peroxy radicals decomposition reactions to form $H\dot{O}_2$ and, in the case of MB, mainly for the direct bimolecular reaction to form methyl crotonate (RMBX+O2=HO2+MCROT). Only one theoretical study focused on RMEKOO=HO2+CH3COCH=CH2 (67), while no study addressed $H\dot{O}_2$ formation in MB from these two channels. Despite recent extension of the MEK experimental database [482], data below 850 K are still missing.

Above 1000 K, *n*-butanol ignition behaves similar to that of n-butane, MEK, and MB, whereas only at higher temperatures does the fast ignition of *n*-butanal approach the common asymptotic behavior.

Sensitivity and flux analyses clarify how the presence of the oxygen atom, influencing closest bonds dissociation energies, activates specific reaction pathways, explaining the observed trends. Although the relative importance of H-abstraction sites seems quite understood and shared, the combustion kinetics community should systematically tackle the correct evaluation of the specific rate constants here highlighted. Although theoretical methods are now viable at affordable costs for relatively small molecules [48] (5-7 heavy atoms), these rate constants still carry relatively high uncertainties.

6.4 PRFs/butanol and TRFs/butanol Mixtures

This section compares the model obtained from the union of the different portions discussed in this thesis with recent ignition delay time data of PRFs and TRFs mixed with butanol. The present mechanism is attached as Supplementary Material.

Kumar et al. [34] recently investigated the ignition delay times of butanol/n-heptane/iso-octane blends using a rapid compression machine. The experiments were performed at equivalence ratios of 0.4 and 1.0, for a compressed pressure of 20 bar, and temperature ranging from 613 K to 979 K. Results are reported in *Figure 250*.
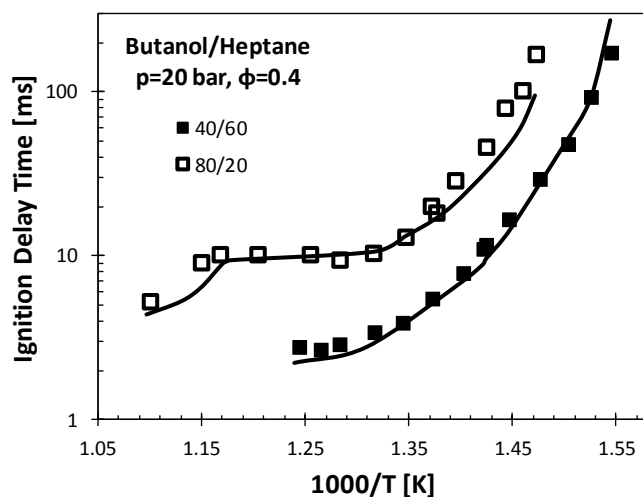
Figure 250: Ignition delay times for n-butanol/heptane blends at p=20 bar and φ=0.4. Symbols: experimental data [34], lines: POLIMI mechanism.

Dagaut et al. [512] investigated the oxidation of 20/80 and 50/50 (in moles) n-butanol/n-heptane mixtures at φ=1.0 and 10 atm in a jet stirred reactor in the temperature range of 530–1100 K. Comparison between experimental data and model predictions is reported in Figure 251.
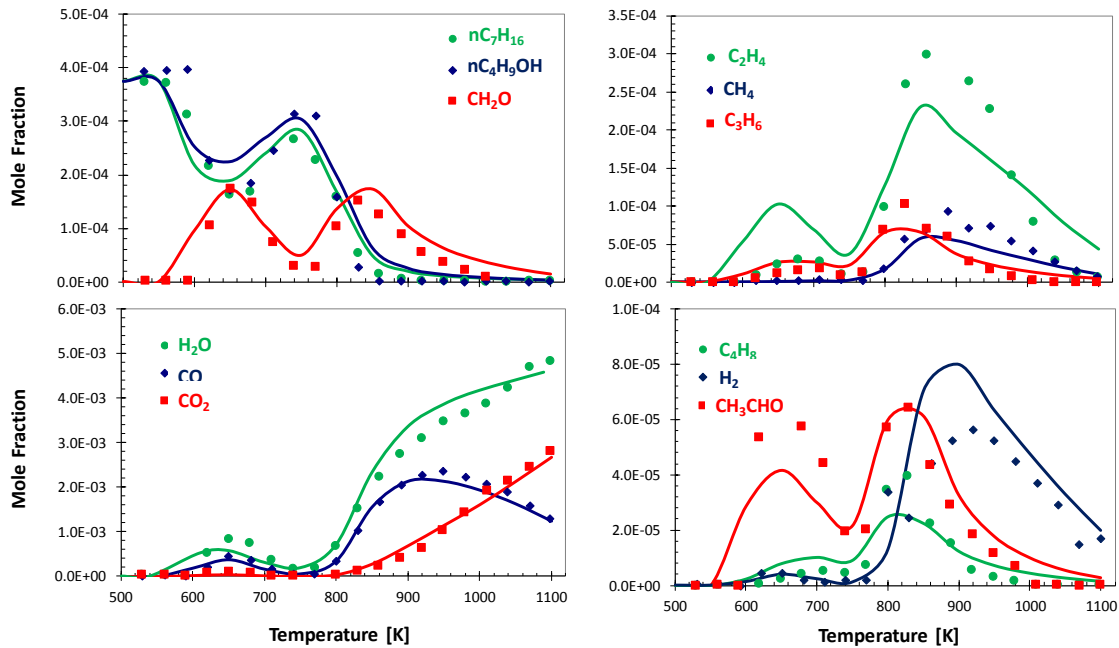
Figure 251: Oxidation of a 1-butanol/heptane 50/50 mol % fuel mixture in a JSR at 10 atm, 700 ms, and φ=1. Symbols: experimental results [512], lines: POLIMI mechanism.

Agbro et al. [35] recently investigated the influence of blending n-butanol at 20% by volume on the ignition delay times for a reference gasoline in a rapid compression machine for stoichiometric fuel/air mixtures at 20 bar and in the temperature range of 678–858 K. The TRFs/butanol mixtures consists of 41.2/8.1/22.4/28.3 of iso-octane/n-heptane/toluene/n-butanol in moles.
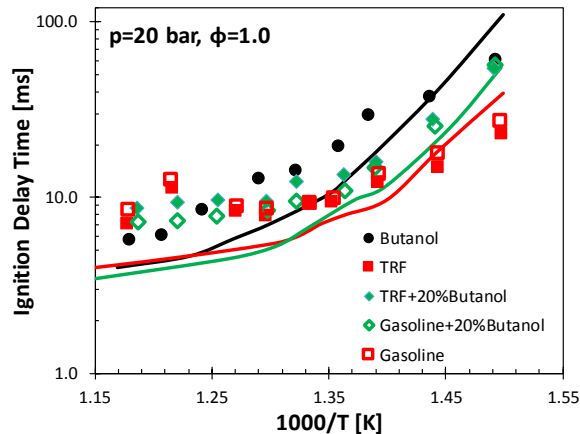
Figure 252: Ignition delays for TRF on blending with 20% n-butanol, stoichiometric TRF and n-butanol mixtures at p = 20 bar in Rapid Compression Machine. Symbols: experimental data [35], lines: POLIMI mechanism.

The implementation of the different portions that have been the topic of *this thesis* allows satisfactory agreement with experimental ignition delay times of real fuel surrogates. Future refinements should address key reactions pathways in toluene oxidation and include a systematic revision of key reaction steps in alcohols low temperature oxidation (e.g. R-CH-OH+O_2↔HO_2+R-CHO).

Chapter 7 – Evaluation of Combustion Kinetic Mechanisms

7.1 Curve Matching, a Generalized Framework for Model/Experiment Comparison: An Application to n-heptane Combustion Kinetic Mechanisms [74]

The following section directly derived from the reference paper [74] is organized as follows. For details on the application examples, the reader is referred to the Supplementary Material available in the web version of the present paper

1. Introduction
2. Numerical Assessment of Experiments and Models: previous example of model experiments comparisons
3. Functional Data Analysis for Curve Matching models

    3.1 Summary of the Method

    3.2 Functional Estimation for the Experimental Data and the Models

    3.3 Computation of Dissimilarity Measures between Model and Experimental Data

    3.4 Comparison Between Models

    3.5 Normalization of the Dissimilarity Measures

    3.6 Choice of the Relevant $\hat{d}$ for the Conditions of interest: the case of Plug Flow Reactor Simulations

    3.7 Computation of an Overall Integrated Index Based on Experimental Uncertainty

    3.8 Identification of Critical Experimental Conditions

4   Case Study: *n*-heptane oxidation

    4.1 Experimental Database and Kinetic Mechanisms

    4.2 Numerical Simulations

    4.3 Ignition Delay Times in Shock Tube

        4.3.1   Application of Curve Matching for Model Improvement

    4.4 Speciation in Jet Stirred Reactor

    4.5 Laminar Flame Speed

    4.6 Identification of Critical Experimental Conditions

    4.7 Final Remarks

5   Conclusions

1. **Introduction**

Recent years have seen an increase of the experimental and theoretical data of combustion processes. The new experimental techniques, together with the increase of the measurement accuracy, produced wider and more valuable sets of experimental data. Photoionization mass spectrometry, fluorescence or incandescence spectroscopy, high resolution transmission electron microscopy and fast repetition rate imaging diagnostic are just a few examples of nowadays possibilities to increase the knowledge of the chemistry and the physics in laminar and turbulent flames.

On the other side, the continuous and fast growth of computer performance enhanced the development of modeling activity. The availability of computational power extended the use of quantum chemistry to large molecules, thus increasing the number of reactions with well estimated rate constants. The easy accessibility to fast and cheap PCs has also contributed to the development of a large number of kinetic mechanisms for different fuels of different complexity, also thanks to the computer-aided automatic mechanism generation. Lu and Law [37] already showed that, starting from the year 2000, the number of available mechanisms has significantly augmented and their dimension, in terms of species and reactions, has exponentially increased.

In this scenario, the validation of highly complex mechanisms through comparison with a large number of experimental data has become of outstanding importance in assessing their overall predictive capabilities. Moreover, the rapid evolution and modification of the energy scenario, international regulations, and fuel specification targets force the combustion community to systematically update, revise, or extend existing kinetic mechanisms to focus on different targets (new fuels, new pollutants, etc.). Last, but equally important, when extending combustion modeling to large-scale computations (i.e. computational fluid dynamics or CFD) through mechanism reduction, the choice of the most appropriate mechanism for given operating conditions is of primary importance.

A further requirement of comparisons among kinetic mechanisms refers to the update of a kinetic mechanism. As an example, a kinetic mechanism for the pyrolysis and oxidation of fuels from hydrogen, methane, ethane, etc., up to jet fuels and diesel, including bio-fuels such as alcohols and methyl-esters, has been developed and continuously updated at Politecnico di Milano (POLIMI) in the last 20 years [40]. The kinetic model can simultaneously describe the formation of pollutants, like Nitrogen Oxides (NOx), Polycyclic Aromatic Hydrocarbons (PAH) or soot (http://creckmodeling.chem.polimi.it/). A peculiarity of the approach at POLIMI is its generality [111]. Thanks to a reduced number of species resulting from the lumping approach [17], the same kinetic mechanism can be used to model the combustion of any fuel, in the range of operating conditions at which it is validated (T, P, equivalence ratio φ), including the formation of pollutants. When new experimental data, more accurate thermodynamic properties or rate constant estimates induce

modifications in the mechanism to improve its performance, it is necessary to systematically check that the updates have not perturbed the system in its entirety. In fact, due to the nature of combustion, detailed mechanisms are implemented hierarchically from the smallest to the heaviest molecules. It is clear that, when a modification is introduced at the lowest level of the hierarchy, possible effects on the chemistry of larger molecules might be significant.

For instance, new experimental evidences in Nancy and Hefei's Jet Stirred Reactors (JSR) recently led to the introduction of new reaction classes to describe the formation of oxygenated species such as diones, ketones, organic acids, alkyl- and carbonyl-hydroperoxides in the low temperature oxidation of alkanes [72]. The new reaction channels were then systematically extended up to n-heptane [73], to reproduce analogous measurements [149]. Given the importance of n-heptane as a Primary Reference Fuel for gasoline, a complete verification of the mechanism performance according to standard targets was then necessary. Similarly, new reaction pathways were proposed for dimethyl ether oxidation at low temperatures according to detailed molecular-beam measurements of keto-hydroperoxide and other oxygenated species in JSRs [513].

Finally, during the reduction procedures, it is important to verify how the performance of the generated reduced mechanism compares to the original mechanism, with respect to different targets. In most cases, ignition delay times are checked and this is a relatively easy task. In other cases, it may arise the need that the reduced mechanisms are able to reproduce not only the global reactivity, but also a trend, like the laminar flame speed at different equivalence ratios, or a species profile, generally when pollutant formation is of interest (NOx, soot precursors etc. [514]).

All these comparisons are usually performed using plots in which the experimental data and the calculated curves are plotted together. This is a very effective approach, which has been used since the dawn of science, whenever a model had to be compared with empirical observations. In some cases, as those previously mentioned, the qualitative result is not sufficient. Moreover, when a very large number of comparisons have to be made, the procedure could result in impractical times [515]. An agreement evaluated on a quantitative basis can better highlight measurements or models limits, but it becomes strictly necessary if an automatic procedure of comparison is required.

The first step in this complex process of assessing model validity is the definition of a standardized and quantitative approach to estimate the agreement between models and experimental data, and especially to compare the performance of different model in reproducing the same set of measurements. To pursue this goal, a novel framework named Curve Matching (CM), is presented and applied in this work.

Section 2 provides a brief state of the art on the numerical assessment of models and experiments. A previous example of model/experiment comparisons from the literature, together with its limitations, is also discussed. The features of CM are described in detail in Section 3. Section 4 reports several applications of CM to the comparison of kinetic mechanisms describing the combustion of n-heptane. Finally, conclusions are drawn in the last Section.

2. Numerical assessment of experiments and models: previous example of model experiments comparisons

As recently discussed by Wang and Sheen [67], model validation is a "poorly posed" problem. In fact, both model and experimental uncertainties would need to be precisely quantified to overcome usual "agree-disagree" statements, mostly based on subjective assumptions. The rigorous quantification of complex kinetic mechanisms uncertainty has been largely reported in the literature and constitutes one of nowadays most challenging topics in combustion [68, 516, 517]. In a certain way, the aforementioned increase in the number of kinetic mechanisms for a given fuel [37] already maps the underlying uncertainty of kinetic parameters [67]. Moreover, the increasing knowledge of combustion kinetics can be directly related to a progressive reduction of model uncertainties, obtained by exploiting new theoretical and experimental tools.

Recently, Olm *et al.* [70, 518] published the first extensive comparisons of hydrogen and syngas combustion mechanisms, well emphasizing the needs and outcomes of such comparisons. The experimental data, collected in different facilities (laminar flames and ideal reactors such as shock tubes, rapid compression machines, plug flow reactors, and jet stirred reactors) from different research groups worldwide, intrinsically have different uncertainties and can show systematic errors. The kinetic mechanisms can provide a guide to compare the measurements and to highlight the presence of misleading data. Kinetic mechanisms can show very good performance in some experimental conditions, but they can fail in others. Some problematic regions can be shared by most of the mechanisms, indicating where specific attention and efforts should be focused on experimental activities. On the other hand, the deviation between kinetic mechanisms and experiments, in some specific conditions, may also be due to the lack of knowledge to be addressed with particular focus by combustion kinetics modelers (i.e. missing reaction channels, inaccurate rate constants to be revised, etc.).

Up to now, the agreement between models and experiments has been evaluated by adopting error functions, weighted on the experimental uncertainties. In the already mentioned works of Olm *et al.* [70, 518], both the Error Function Value (EFV) and the absolute deviation (D) are used:

$$(1) \quad \text{EFV} = \frac{1}{N} \sum_{i=1}^{N} \left[\frac{1}{n_i} \sum_{j=1}^{n_i} \left(\frac{Y_{ij}^{sim} - Y_{ij}^{exp}}{\sigma\left(Y_{ij}^{exp}\right)} \right)^2 \right]$$

$$(2) \quad \text{D} = \frac{1}{N} \sum_{i=1}^{N} \left[\frac{1}{n_i} \sum_{j=1}^{n_i} \frac{Y_{ij}^{sim} - Y_{ij}^{exp}}{\sigma\left(Y_{ij}^{exp}\right)} \right]$$

being

$$(3) \quad Y_{ij} = \begin{cases} Y_{ij} \text{ if } \sigma\left(Y_{ij}^{exp}\right) \cong \text{constant} \\ \ln\left(Y_{ij}\right) \text{ if } \sigma\left(\ln\left(Y_{ij}^{exp}\right)\right) \cong \text{constant} \end{cases}$$

where N and n_i are the number of datasets and the number of data inside each $i-th$ dataset, respectively. Y_{ij}^{exp} is the $j-th$ experimental observation of the $i-th$ dataset and $\sigma\left(Y_{ij}^{exp}\right)$ is its standard deviation, better explained in the Supplementary Material of the referred paper [70]. Y_{ij}^{sim} is the corresponding value obtained from the numerical simulation using a kinetic mechanism. A large set of experimental data in laminar flames and ideal reactors was collected and simulations for every $X_{ij}^{sim} = X_{ij}^{exp}$ were carried out using the CHEMKIN-II package [466] with the different kinetic mechanisms. EFV and D were then calculated as reported in equations (1) and (2) for every type of experiment considered. Taking into account all the experimental data, an overall error function value of the tested mechanism was calculated, thus finding the most reliable hydrogen [70] and syngas [518] mechanisms available in the literature. Sensitivity analyses were also performed to highlight relationships among different mechanisms and reactions needing a revision to improve agreement with experimental data.

Despite the important outcomes, reliability, robustness, and simplicity of such an approach, the main limit is that it does not account for the shape of the curves. An example can better explain the problem. *Figure 253* shows the comparison between the experimental ignition delay times of stoichiometric $H_2/O_2/Ar/N_2$ oxidation in a Rapid Compression Machine [519] and three plausible different models.
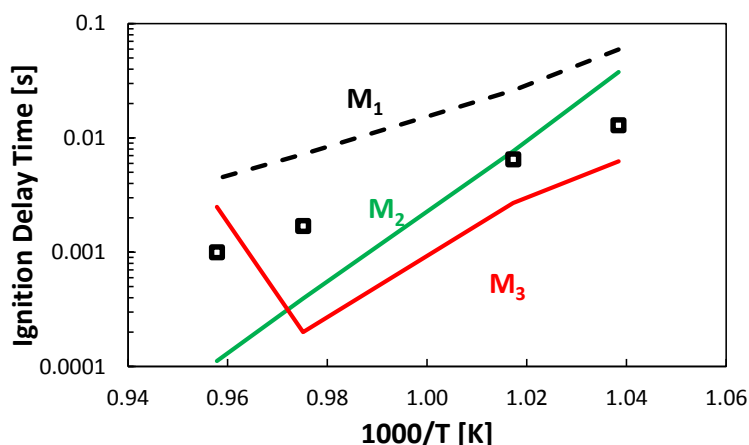
Figure 253: Ignition delay times of a stoichiometric hydrogen mixture at 50 bar. Experiments (symbols) [519] and plausible models (lines) aiming at reproducing the experimental measurement.

The Error Function Values (EFV) for the three models (M$_1$, M$_2$ and M$_3$) are 213, 203, and 168, respectively, while the absolute deviations are 13, -6, and -16.

From these errors, model M$_3$ seems to better agree with the measurements, followed by M$_2$, with M$_1$ showing the worst performances. It could be argued, based on a graphical criterion, that the ranking is the exact opposite of that suggested by the EFV, with M$_3$ showing an unreasonable trend, M$_2$ more closely capturing the ignition values with the wrong slope (i.e. apparent activation energy of the ignition process), and M$_1$ overestimating the induction times of a factor ~3 but correctly reproducing the apparent activation energy. Moreover, the overall EFV does not provide an exhaustive information of use for kinetic modelers, aiming at improving the mechanism performances.

A further example of the limitations of approaches based on the Sum of Square Error (SSE) is given in *Figure 254*. While from the plot it is clear that M$_1$ gives a better performance if compared to M$_2$ despite a 10–15 K delay in the global reactivity (see Section 3.3, *Figure 257*), calculating the Error Function Value would lead to the opposite conclusion. Indeed, the calculated Error Function Values are ~8400 and ~7400 for M$_1$ and M$_2$ respectively.
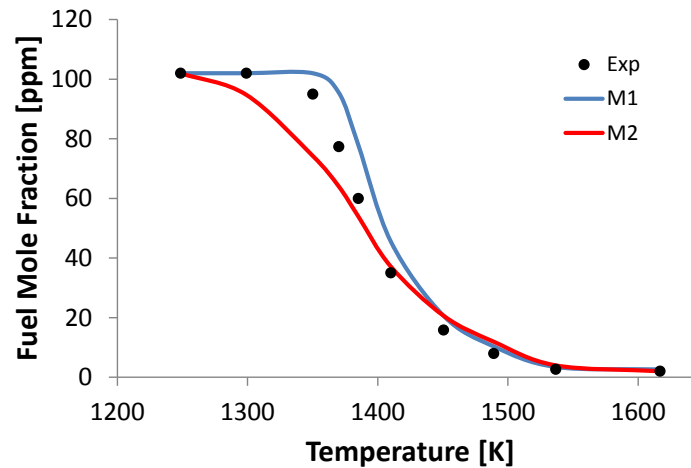
Figure 254: Typical fuel mole fraction profile in isothermal reactor versus reactor temperature. Plausible experiments (symbols) and models (lines).

3. Functional data analysis for Curve Matching models

Quantifying the capability of a kinetic mechanism to reproduce real behaviors is not a straightforward task. In addition, ranking kinetic models through a single, characterizing index is even more difficult. In this work, a mathematical methodology is presented, based on functional analysis for the values obtained in both experiments and models. Their comparison is then carried out through the creation of a series of characterizing indices, the starting points for the desired model assessment as described in the following. The whole approach is summarized in Section 3.1, and a flow diagram of the overall procedure is provided in *Figure **255***. The next sub-sections give a deeper insight into the conceptual features of the methodology: Section 3.2 and 3.3 describe the development of dissimilarity indices between data and models, while Section 3.4 is dedicated to the quantification of dissimilarities between models. The formulation of an averaged index is then introduced in Section 3.5, with an application to plug flow reactor experiments as a case study (Section 3.6). Finally, Section 3.7 describes an overall index to rank each model, while Section 3.8 shows an application of the methodology to identify critical experimental conditions.

3.1 Summary of the method

The core of the method is the computation of dissimilarity measures between the output of each model and the experimental data. A schematic of the procedure is reported in *Figure **255*** and will be better explained in this upcoming section.

The experimental data are discrete measurements of the quantity of interest. The assumption is that the data are noisy point-wise evaluations of an underlying smooth functional process, whose realization is estimated from the data as a preprocessing step. The same technique is applied to the models, since only point-wise evaluations of them are available for the analysis.

In order to better describe the performances of the models, four dissimilarity measures are computed. Each of them gives a different information allowing a precise interpretation of the model capability in reproducing the experimental measurements.

Moreover, since some experimental data are gathered in comparable experimental settings, their dissimilarity measures can be grouped. Finally, the statistical analysis of the groups of dissimilarity measures allows to identify the positive or negative outliers in the population of models describing the same experiments or group of experiments.
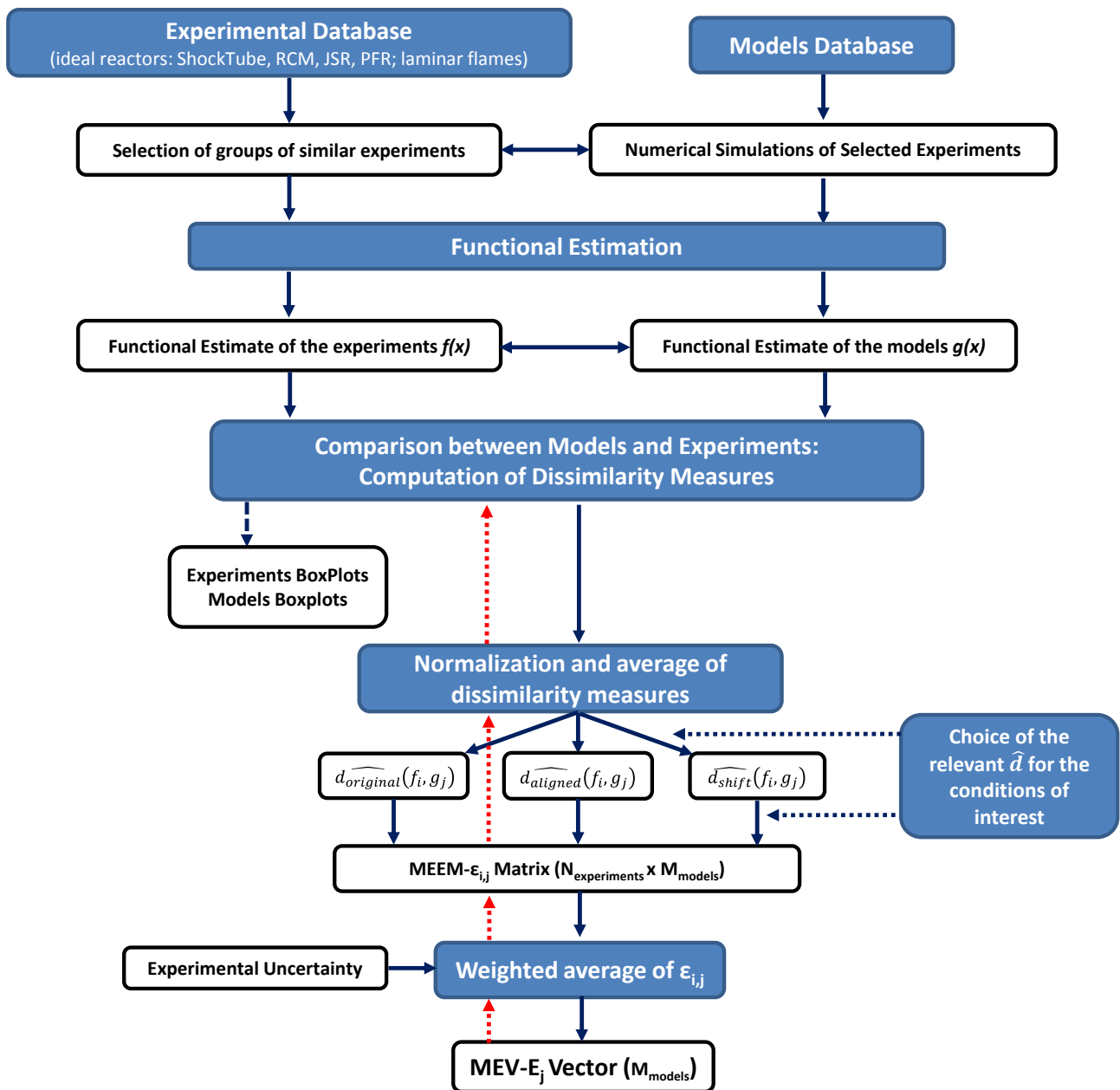
Figure 255: Schematic of the CM framework. Dashed-red arrows represent the methodology for results analysis and interpretation as discussed in Section 4.

3.2 Functional estimation for the experimental data and the models

The method assumes the regularity of the processes involved (both the model and the process generating experimental measurements). Indeed, the computation of the dissimilarity measures requires the curves to be square integrable and have square integrable first derivatives.

As shown in Figure 255, the first step of the process is the estimation of the functional representative for both the experimental data ($f(x)$) and the models ($g(x)$). In this study, the functional estimation is achieved by spline smoothing with a roughness penalty, but other interpolation approaches can be also conveniently applied. Details on the method are reported in the Supplementary Material (S1). Further insights in the mathematical details are provided in Ramsay and Silverman [520].

3.3 Computation of dissimilarity measures between model and experimental data

Let

$$(4) \quad \|f\| = \sqrt{\int_a^b f(x)^2 dx}$$

and

$$(5) \quad \langle f, g \rangle = \sqrt{\int_a^b f(x)g(x)dx}$$

be the norm and the scalar product in the L^2-space of the functions $f(x)$ and $g(x)$. The extremes a and b of the domain of the integration are, respectively, the minimum and the maximum of the abscissa of the experimental data.

In order to evaluate the differences between two curves f and g (where f is the curve estimated from the experimental data, or in general the reference curve and g is the curve obtained from the model), four dissimilarity measures are computed [521, 522]:

$$(6) \quad d_{L^2}^0(f, g) = \frac{\|f - g\|}{|D|} \in (0, +\infty)$$

$$(7) \quad d_{L^2}^1(f, g) = \frac{\|f' - g'\|}{|D|} \in (0, +\infty)$$

$$(8) \quad d_{Pearson}^0(f, g) = \frac{1}{2}\left\|\frac{f}{\|f\|} - \frac{g}{\|g\|}\right\| \in (0,1)$$

$$(9) \quad d_{Pearson}^1(f, g) = \frac{1}{2}\left\|\frac{f'}{\|f'\|} - \frac{g'}{\|g'\|}\right\| \in (0,1)$$

where D is the intersection between the domains of the two functions.

For each dissimilarity measure, the minimum value is zero, indicating minimal dissimilarity between f and g.

$d_{L^2}^0(f,g)$ and $d_{L^2}^1(f,g)$ are the L^2-norm of the difference between the two functions and the two first derivatives of the functions, respectively. The curves are rescaled before computing these two dissimilarity measures dividing f and g by the maximum value of the experimental curve f and f' and g' by the maximum value of the first derivative of the experimental curve f', so that the maximum value of the experimental curve and of its derivative is 1.

The dissimilarity measure $d_{L^2}^0$ is the generalization to the continuous case of the Sum of Square Errors, used for instance by Olm *et al.* [70, 518] (eq. 1). Particularly, the integration of eq. 4 allows to compute an difference in terms of areas instead of a sum of punctual differences.

$d_{L^2}^1$ considers as perfectly similar two functions that differ only by a vertical translation, such as those shown in panel A of Figure 256:

$$(10) \quad d_{L^2}^1(f, f + a) = 0 \qquad \forall a \in \mathbb{R}$$

The last two dissimilarity measures ($d_{Pearson}^0(f,g)$ and $d_{Pearson}^1(f,g)$) are obtained from the following similarities:

$$(11) \quad \rho_{Pearson}^0(f,g) = \frac{\langle f,g \rangle}{\|f\|\|g\|}$$

$$(12) \quad \rho_{Pearson}^1(f,g) = \frac{\langle f',g' \rangle}{\|f'\|\|g'\|}$$

Since $\rho_{Pearson}$ measures the cosine of the angle between the two functions, it is an index of the correlation between the two functions, measuring their similarity in shape. The correspondence between the similarities and the dissimilarity measures is the following:

$$(13) \quad d_{Pearson} = \sqrt{\frac{1 - \rho_{Pearson}}{2}}$$

$d_{Pearson}^0$ considers as perfectly similar two functions that differ only by a vertical dilation, such as those shown in panel B of Figure 256:

$$(14) \quad d_{Pearson}^0(f, f \times a) = 0 \qquad \forall a \in \mathbb{R}$$

$d_{Pearson}^1$ considers as perfectly similar two functions that differ only by a vertical affine transformation (translation and dilation), such as those shown in panel C of Figure 256:

$$(15) \quad d^1_{Pearson}(f, f \times a + b) = 0 \qquad \forall a \in \mathbb{R} \quad \forall b \in \mathbb{R}$$
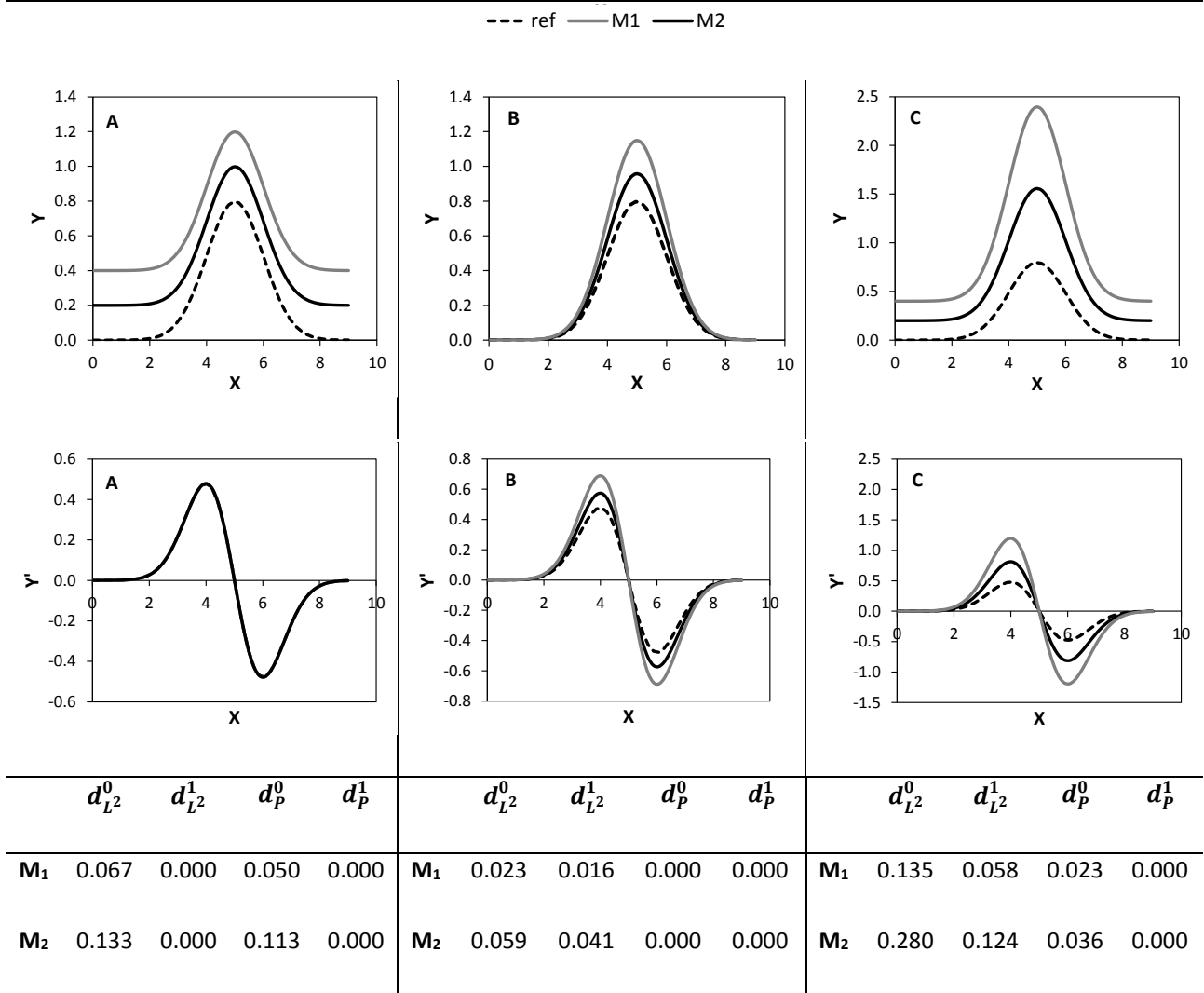
Figure 256: Panel A: M_1 and M_2 differ only by a vertical translation; panel B: M_1 and M_2 differ only by a vertical dilation; panel C: M_1 and M_2 differ by a linear affine transformation of the y-axis. Respective dissimilarity values are reported below each panel.

The four dissimilarity measures take into account the differences between the functions along the "vertical direction". To evaluate the differences along the "horizontal direction", an alignment between the functions has to be carried out. The optimal horizontal shift δ_{opt} between the functions f and g is calculated by means of the following minimization:

$$(16) \quad \delta_{opt} = \text{argmin}_\delta \, d\big(f(x + \delta), g(x)\big)$$

where d is one of the four indices previously defined. The maximum shift allowed in the algorithm is 50% of the range of the experimental data. The shift value is expressed as a percentage of the range of the experimental data. After the alignment, the dissimilarity measure between the aligned functions are newly calculated.

Summarizing, for each index a value of the dissimilarity measure between the functions, an optimal shift, and a value of the dissimilarity measure after the alignment are obtained. The first index provides an overall evaluation of the difference between the functions, while the other two indices explain whether the dissimilarity measure between the functions is due to a horizontal shift or not.

As a further explanation of the meaning of the dissimilarity indices, the original values calculated for the test models of Figure 253 (Section 1) are reported in Table 32. The Error Function Value (EFV) and $d^0_{L^2,orig}$ index yield the same relative ranking of the three models, with M$_3$ resulting the most accurate to reproduce the experimental measurements shown in Figure 253. The first derivative index $d^1_{L^2,orig}$ clearly recognizes the better performances of M$_1$ ($d^1_{L^2,orig} = 0.13$) in reproducing the slope of the experimental data (i.e. the apparent activation energy). While the Pearson dissimilarity index ($d^0_{P,orig}$) does not highlight large differences among the models, the anomalous trend of M$_3$ is clearly highlighted by the corresponding index for the first derivative ($d^1_{P,orig} = 0.39$), which is the highest among the models.

original	$d^0_{L^2,orig}$	$d^1_{L^2,orig}$	$d^0_{P,orig}$	$d^1_{P,orig}$	EFV [70, 518]
M$_1$	0.54	0.13	0.01	0.02	213
M$_2$	0.42	4.30	0.07	0.00	203
M$_3$	0.37	2.60	0.02	0.39	168

Table 32: Original dissimilarity indices for the example shown in Figure 253 as calculated through the CM approach.

Table 33 reports the original and aligned dissimilarity indices, together with the shift values, calculated for the test models M$_1$ and M$_2$ of Figure 254 (Section 2). While the performances of the two mechanisms are quite comparable if only the original values are considered, a significant change in the interpretation of their performances is observed when analyzing the aligned dissimilarities. In fact, consistent with what was observed in Figure 254, a very small alignment of M$_1$ ($\delta^0_{L^2}, \delta^1_{L^2}, \delta^0_P, \delta^1_P \sim 3.7\%$) would lead to much lower aligned dissimilarity values. Conversely, M$_2$ does not significantly benefit from a horizontal shift (~2%), due to larger differences in shape. Thus, it can be concluded that, despite a ~10–15 K delay in the reactivity (corresponding to a 3-4% shift in the considered experimental domain of Figure 254 and *Figure 257*), M$_1$ better reproduces the experimental measurements. Although the aim of *Figure 257* is to highlight the meaning of alignment values and to guide their interpretation, it has to be mentioned that also uncertainties in the vertical direction need to be taken into account (see Section 3.7).

original	$d_{L2,orig}^0$	$d_{L2,orig}^1$	$d_{P,orig}^0$	$d_{P,orig}^1$
M₁	0.0035	0.0080	0.0442	0.1517
M₂	0.0036	0.0083	0.0405	0.1676
shift	$\delta_{L^2}^0$	$\delta_{L^2}^1$	δ_P^0	δ_P^1
M₁	0.0405	0.0345	0.0365	0.0365
M₂	0.0265	0.0225	0.0025	0.0305
aligned	$d_{L2,align}^0$	$d_{L2,align}^1$	$d_{P,align}^0$	$d_{P,align}^1$
M₁	0.0013	0.0055	0.0188	0.0928
M₂	0.0032	0.0080	0.0404	0.1543

Table 33: original dissimilarity indices, shift values and aligned dissimilarity indices for the example shown in Figure 254 and recalled in Figure 257, as calculated through the CM approach.
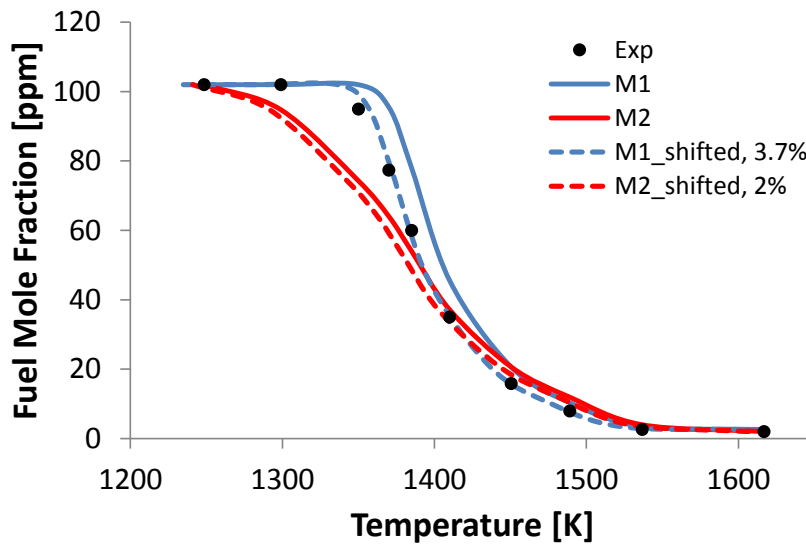
Figure 257: Original (solid lines) and shifted (dashed lines) fuel mole fractions of M1 and M2 of Figure 254 (Section 2.1). Shift percentages (3.7% for M₁ and 2% for M₂) refer to the experimental domain of ~368 K ($T_{min,exp}$=1248 K, $T_{max,exp}$=1616 K).

3.4 Comparison between models

Considering a group of N experimental datasets gathered in comparable settings and M models, the dissimilarity measures before the alignment are $4 \times N \times M$:

$$d^0_{L^2,orig}(f_i,g_j) , d^1_{L^2,orig}(f_i,g_j) , d^0_{P,orig}(f_i,g_j) , d^1_{P,orig}(f_i,g_j)$$

$$i = 1, \dots, N \quad j = 1, \dots, M$$

together with $4 \times N \times M$ shifts:

$$\delta^0_{L^2}(f_i,g_j) , \delta^1_{L^2}(f_i,g_j) , \delta^0_{P}(f_i,g_j) , \delta^1_{P}(f_i,g_j) \quad i = 1, \dots, N \quad j = 1, \dots, M$$

and $4 \times N \times M$ dissimilarity measures after the alignment:

$$d^0_{L^2,align}(f_i,g_j) , d^1_{L^2,align}(f_i,g_j) , d^0_{P,align}(f_i,g_j) , d^1_{P,align}(f_i,g_j)$$

$$i = 1, \dots, N \quad j = 1, \dots, M$$

Figure 258 shows a visualization technique based on boxplots, a standard tool of descriptive statistics that represents the position and the dispersion of a set of numerical data, useful to assess the relative performances of the models, as quantified by the dissimilarity measures and by the shifts.

The box of the boxplot is delimited by the first and third quartiles of the data and the median is represented by the black dash inside the box, while the two whiskers have at most length 1.5 times the length of the box and their actual extreme is the value of the datum which is farthest from the box; the data which lie outside the extremes of the whiskers are marked with dots.

The boxplots of *Figure 258* refer to the group of experiments "ignition delay time, rapid compression machines, Ar/N₂" as identified by Olm *et al.* [70]. The group is composed of $N = 12$ datasets of experimental ignition delay times of H₂/O₂/Ar/N₂ mixtures in a rapid compression machine from the literature. $M = 19$ models were considered in this example; those already reported in Olm *et al.* [70] and the optimized mechanism from Varga *et al.* [523] (M₁₉).

Within the 4×3 panels, the four rows represent the four dissimilarity measures, while the first column represents the dissimilarity measures before the alignment, the second column the shifts and the third column the dissimilarity measures computed after the alignment. In each panel, for each of the 19 models, a boxplot representing the 12 values $d(f_i,g_j)$ for $i \in \{1, \dots, 12\}$ is drawn.

The visual comparison of boxplots of the different models allows for an evaluation of the performance of the models and to rank them. In particular, considering the indices $d^0_{L^2,orig}$ and $d^0_{P,orig}$, M₁₆, M₁₇, M₁₈ are ranked as the worst performing. Moreover, M₁₈ presents high dissimilarity values also in terms of first derivatives ($d^1_{L^2,orig}$, $d^1_{P,orig}$). Despite the high shift values for the three models (second column), the aligned dissimilarity indices do not improve their ranking. Therefore, the "bad" performances are both due to a

horizontal misalignment and a vertical distance. A detailed analysis of the case of *Figure 258* is reported in the Supplementary Material.

Figure 259 reports a qualitative comparison between the Error Function Value computed by Olm *et al.* [70] and the $d^0_{L^2,orig}$ dissimilarity measure. As already mentioned, $d^0_{L^2}$ is the generalization to the continuous case of the Sum of Squares index (i.e. Error Function Value [70]), thus the very good qualitative agreement observed between the two measures in *Figure 258*. As already stressed in Section 2, due to the limitations of the Sum of Squared Error (SSE) based approach, the CM methodology allows a much larger amount of information to be used in the model assessment.
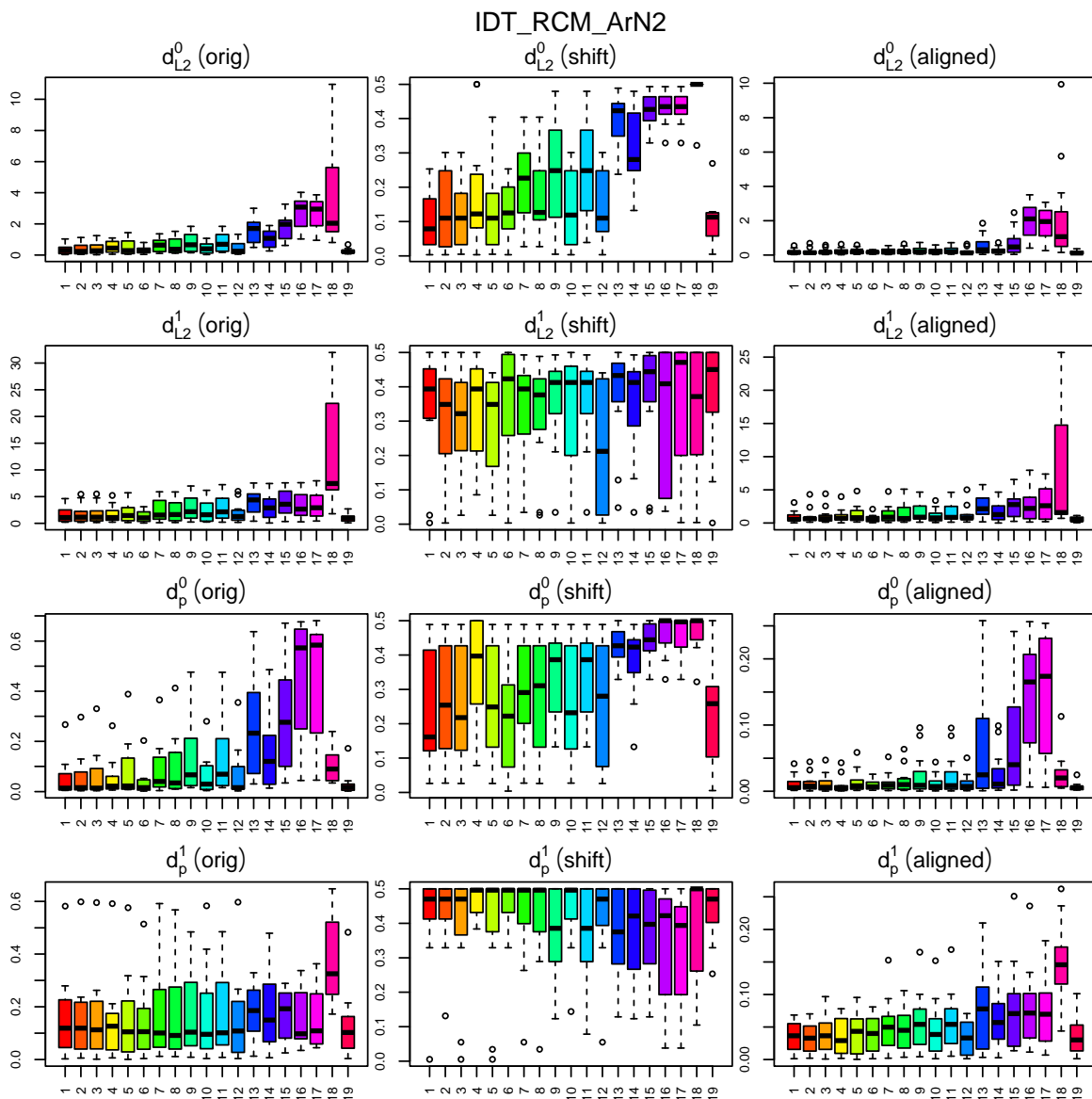
Figure 258: Boxplot visualization of M models ($M = 19$) for the group of experiments "Ignition delay time, rapid compression machines, Ar/N₂" [70], composed of $N = 12$ experimental datasets.
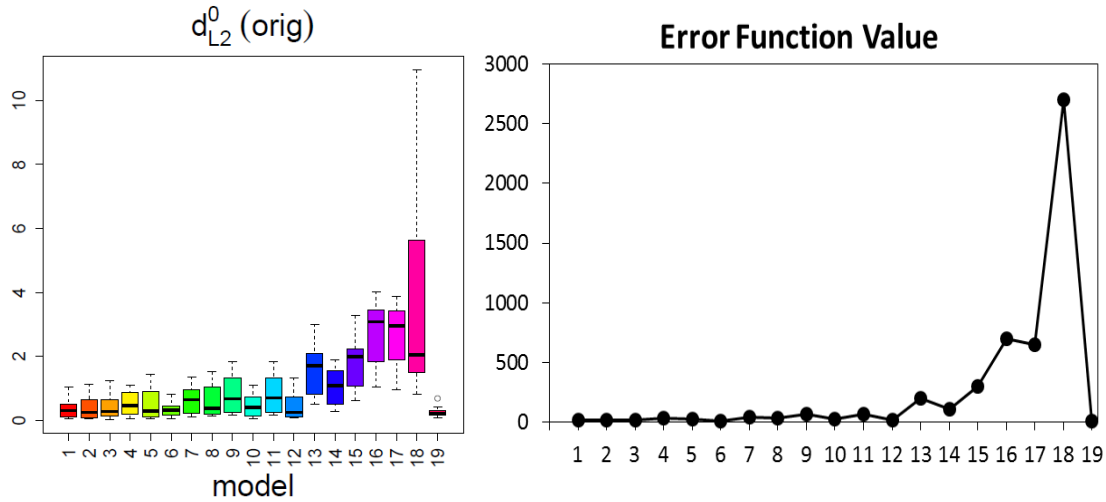
*Figure 259: Qualitative agreement between $d_{L^2}^0$ boxplot evaluations of hydrogen combustion models (left) and **EFV** ranking reported by Olm et al. [70] (right) for the experimental group "Ignition delay time, rapid compression machines, Ar/N₂".*

3.5 Normalization of the dissimilarity measures

It is now useful to obtain an integrated index, summarizing all the aspects highlighted by the four dissimilarity measures. However, their values are not comparable between each other, since they refer to different quantities and are dimensionally not homogeneous. Therefore, the indices need to be normalized to be directly comparable. The dimensionless index is obtained as described below.

Let us consider for simplicity only the four dissimilarity measures computed before the alignment for a fixed experiment i for the M models. For a fixed dissimilarity measure, here denoted as d, the median m and the interquartile range (IQR) over the M dissimilarity measures of the models with respect to the experimental data are computed. For each model j, it is possible to calculate the difference between its dissimilarity measure and the median in terms of the interquartile range:

$$(17) \quad \frac{d(f_i, g_j) - m}{IQR/2}$$

The dimensionless index obtained is a measure of the relative goodness of model j in describing the experimental data i with respect to the population of models considered, as quantified by the dissimilarity index d. A negative number means a good performance of the model (distance closer to zero with respect to the population of models considered), while a positive number means a bad performance (distance farther from zero with respect to the population of models considered). Interpretatively, it is reasonable to establish that values between -1 and 1 represent average performances, values in the range [-2, -1] (resp. [1, 2]) represent good (resp. bad) performances and values below -2 (resp. above 2) represent especially good (resp. bad) performances.

In order to take into account all four dissimilarity measures, it is possible to average the four dimensionless indices obtained for the four dissimilarity measures:

$$(18) \quad \hat{d}(f_i, g_j) = \frac{1}{4}\left(\frac{d^0_{L^2}(f_i, g_j) - m^0_{L^2}}{IQR^0_{L^2}/2} + \frac{d^1_{L^2}(f_i, g_j) - m^1_{L^2}}{IQR^1_{L^2}/2} + \frac{d^0_P(f_i, g_j) - m^0_P}{IQR^0_P/2} + \frac{d^1_P(f_i, g_j) - m^1_P}{IQR^1_P/2} \right)$$

where, for example, $m^0_{L^2}$ and $IQR^0_{L^2}$ are the median and the interquartile range computed over the M dissimilarity measures $d^0_{L^2}$ of the models and an analogous notation denote those computed over the other three dissimilarity measures.

3.6 Choice of the relevant $\widehat{d}$ for the conditions of interest: the case of Plug Flow Reactor simulations

The index $\hat{d}(f_i, g_j)$ defined above can be computed by averaging all the dimensionless indices obtained for the four dissimilarity measures (as reported in the formula above) or averaging only some of them. The choice depends on the type of experimental data under investigation. For example, in some cases it may be required to take into account only the dissimilarity measures computed on the first derivative, since vertical translations should not be considered in the evaluation of the goodness of the model.

The same procedure can be applied to the four dissimilarity measures computed before the alignment, to the four shift, and to the four dissimilarity measures computed after the alignment, thus obtaining three indices:

$$\hat{d}_{orig}(f_i, g_j), \ \hat{d}_{shift}(f_i, g_j), \ \hat{d}_{align}(f_i, g_j).$$

The evaluation of the adherence of the model j to the experimental data i can be based on an index $\varepsilon_{i,j}$, which can be equal to one of the $\hat{d}_{orig}$, $\hat{d}_{shift}$, $\hat{d}_{align}$ indices, or can be computed as the average of two or all three indices $\hat{d}_{orig}$, $\hat{d}_{shift}$, $\hat{d}_{align}$, depending on the selected experimental data. For example, in the case of plug flow reactors, $\varepsilon_{i,j} = \hat{d}_{align}$, since the dissimilarity measures $\hat{d}_{orig}$, $\hat{d}_{shift}$ should not be taken into account. This is due to the fact that, when performing ideal plug flow reactors simulations with detailed kinetics, possible mixing effects at the inlet of the reactor [524] cannot be modeled by the one-dimensional approximation commonly adopted [66, 466, 525]. Kinetic modelers usually apply a time (or length) shift of the calculated profiles. The time shift is usually equal to that between the experimental and the calculated 50% fuel conversion (η) as graphically explained in *Figure **260***.
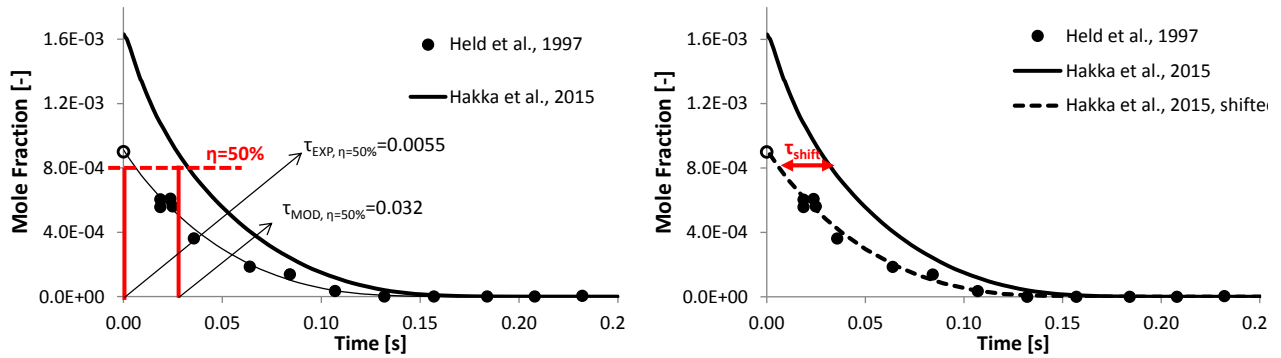
Figure 260: Example of time shift of a plug flow reactor simulation. Experimental data for n-heptane (0.163%) /O_2/N_2 mixture, φ=2.27, P=3 atm pressure and T_{inlet}=1075 K [271]. Adiabatic simulations were carried out using the recent mechanism from Hakka et al. [119]. Panel a: original results of numerical simulation. Panel b: time-shifted numerical simulations ($τ_{shift}$=0.0265 s).

As shown in *Figure 261*, it is necessary to take into account the time-shift of calculated profiles in plug flow reactor simulations, to avoid misleading conclusions on model performances. Indeed, while the "Test Model" of *Figure 261* shows a lower reactivity compared to the model of Hakka *et al.* [119], once both model are shifted at 50% of fuel conversion (η), their performances become undistinguishable. For a more significant comparison, it is important to both compute a parameter giving information of the shift value and to consider only aligned dissimilarity values when evaluating the model performances.

As clearly discussed in the recent review paper of Dryer et al. [25], the use of plug flow reactors for kinetic model validation requires a proper initialization method to correctly interpret non-idealities of the specific experimental facility. Coordinate shifting is, within all the possibilities, the easiest to implement, but not always the most reliable. An accurate evaluation of the fluid mechanics at the injection point should be carried out for each case individually, to figure out reasonable and physically meaningful shift values. Once the maximum shift value is obtained based on such analyses, its inclusion in the curve matching procedure allows a better evaluation of the kinetic mechanism performance.

Table 34 report the dissimilarity indices as calculated through the CM approach. As expected the Hakka *et al.* [119] mechanism gives lower original dissimilarity values and lower shift values. Once aligned, the two mechanisms become undistinguishable.
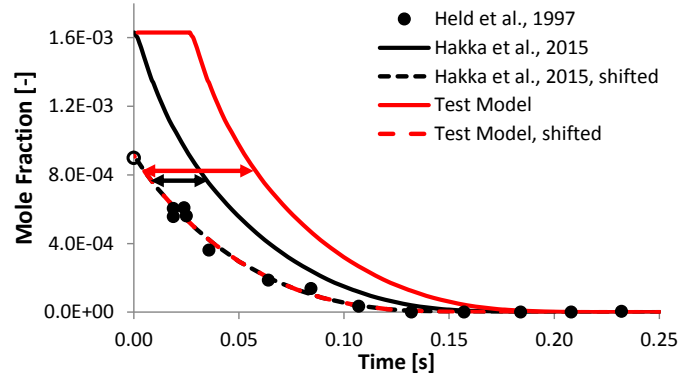
Figure 261: Example of time-shift influence on model evaluations. Solid lines: original models, dashed lines: time-shifted models. Dissimilarity indices ad shift values are reported in Table 34.

original	$d^0_{L^2,orig}$	$d^1_{L^2,orig}$	$d^0_{P,orig}$	$d^1_{P,orig}$
Hakka *et al.*, 2015 [119]	0.31	0.64	0.04	0.12
Test Model	0.67	0.86	0.09	0.36
shift	$\delta^0_{L^2}$	$\delta^1_{L^2}$	δ^0_P	δ^1_P
Hakka *et al.*, 2015 [119]	0.06	0.09	0.03	0.05
Test Model	0.13	0.15	0.11	0.13
aligned	$d^0_{L^2,align}$	$d^1_{L^2,align}$	$d^0_{P,align}$	$d^1_{P,align}$
Hakka *et al.*, 2015 [119]	0.03	0.12	0.04	0.10
Test Model	0.03	0.12	0.04	0.10

Table 34: Original dissimilarity indices, shift values and aligned dissimilarity indices (as calculated through the CM approach) for the example shown in Figure 261.

We point out that, when the value of the shift is high, but the decrease of dissimilarity produced by the alignment is negligible, the inclusion of $\hat{d}_{shift}$ in the computation of $\varepsilon_{i,j}$ may distort the final evaluation and ranking of the model. In these cases, the alignment should not be performed, nor considered in the analysis.

In our analysis we partially avoid this problem by choosing $\varepsilon_{i,j} = \hat{d}_{orig}(f_i, g_j)$ in the cases where the computed shift reached the maximum value allowed by the algorithm (50% of the experimental domain) for all the models g_j. Indeed, this condition refers to cases in which the alignment should not be performed.

3.7 Computation of an overall integrated index based on experimental uncertainty

In order to obtain an overall integrated index for model j (E_j) considering all the N experimental data, it is possible to average the dimensionless indices $\varepsilon_{i,j}$ for $i = 1, \ldots, N$ weighting each value with a measure of uncertainty of the experimental data as in eq. 18.

$$(18) \; E_j = \frac{1}{\left(\sum_{i=1}^{N} \frac{1}{\sigma_i}\right)} \sum_{i=1}^{N} \frac{\varepsilon_{ij}}{\sigma_i}$$

The measure of uncertainty of the *i*-th experimental data (σ_i) can be the standard deviation of the experimental data, if available, or a proper estimation from the data. The way we include the measure of uncertainty of the experimental data in our methodology is comparable to that used by Olm *et al.* [70, 518] for the computation of the Error Function Value (eq. 1) and of the absolute deviation (eq. 2): errors from experiments with larger uncertainty have less influence in the computation of the final index with respect to those with smaller uncertainty.

As already pointed out by Olm and co-workers [70] computing the standard deviation as a function of the differences between the experimental data and the smoothing function often results in unrealistically low error values. Therefore, as proposed in the same study, in cases where the standard deviation is not available, a minimal standard deviation is assumed. In the present work, the following errors were chosen according to Olm *et al.* [70]:

- 10% relative error for ignition delay times;
- 2 cm/s for flame velocities;
- the lowest measured concentration or 1% of the highest measured concentration for measured JSR, flow reactor and laminar flame concentrations.

It is clear that this assumption largely affects the weighted integrated index. It has to be noted that, despite several efforts in recent years to obtain accurate quantifications of experimental errors [526], such information remains scarce for most of the fuels studied by kinetic modelers.

As shown in Figure 255, we define Model/Experiment Error Matrix ($MEEM$) the matrix whose elements are the $\varepsilon_{i,j}$ indices, and Model Error Vector (MEV) the vector whose elements are the E_j indices.

3.8 Identification of critical experimental conditions

Another useful tool is the visualization of the N boxplots of the dissimilarity measures grouped by experiment. This visualization allows the identification of experimental data on which the models are performing significantly worse than in other experiments. *Figure 262* represents the group of "laminar flame speed" experiments for *n*-heptane/air mixtures composed of $N = 20$ laminar flame speed experiments, simulated according to $M = 8$ models. Laminar flame speeds were calculated for the steady, freely propagating, adiabatic flames in the doubly infinite domain, allowing for Soret diffusion effects as described by Cuoci *et al.* [527]. The picture shows how two experimental datasets (Case23 [528] and Case29 [529] of Table 35) are described worse than the others by the models considered. This evidence indicates that either all the models present a lack of understanding for these conditions, or the experiments show a systematic and significant error. As an example, Case 23 will be further discussed in Section 4.6.
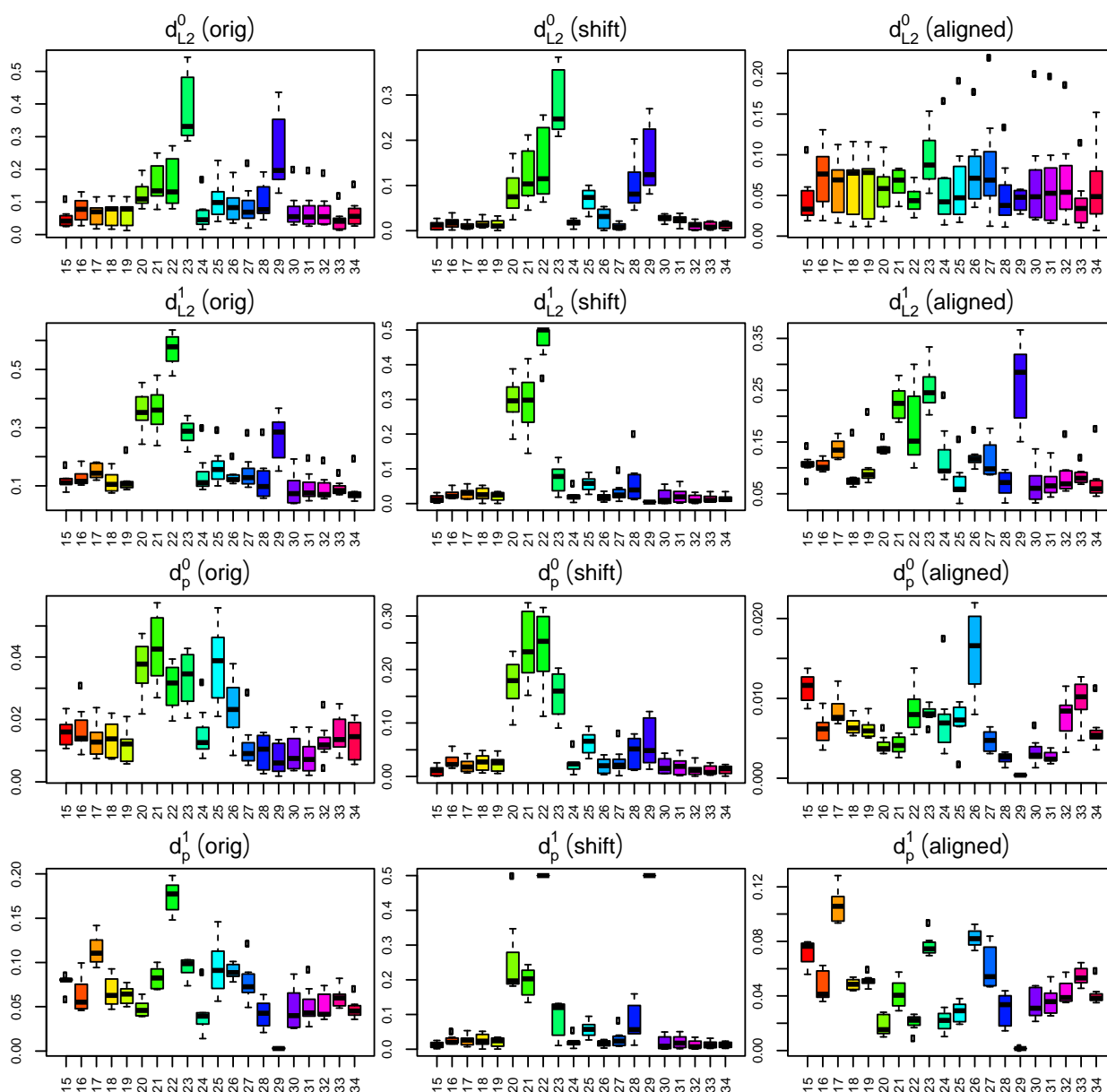
Figure 262: Boxplots grouped by experiment for the "laminar flame speed" group (see Table 35 in Section 4.1) for n-heptane/air mixtures.

4. Case study: n-heptane oxidation

4.1. Experimental Database and Kinetic Mechanisms

The CM approach was applied to a selected experimental database referring to *n*-heptane oxidation. As already mentioned *n*-heptane is a primary reference fuel commonly used, together with iso-octane and toluene, for the octane rating of gasoline as well as a surrogate to represent linear alkanes in diesel and jet fuels. In the last decades, the experimental characterization of *n*-heptane oxidation has been carried out in several laboratory devices such as:

1. shock tubes and rapid compression machines [26, 146, 260, 262, 266, 530-532] to study its auto-ignition properties;

2. intermediate and product species formation in jet-stirred [119, 149, 257, 283] and plug flow reactors [30, 271, 533];

3. laminar flames [107, 120, 274, 275, 277, 350, 528, 529, 534, 535].

Table 35 summarizes the experimental datasets considered in this study. The complete database is available in usable format in the Supplementary Material attached to this study.

	Jet Stirred Reactor						Plug Flow Reactor				
#	T [K]	P [atm]	φ	τ [s]	Ref.	#	T [K]	P [atm]	φ	τ [s]	Ref.
1	550–1150	10	1	1	[257]	10	500–1100	8	1	1	[533]
2	550–850	10	1	0.5	[257]	11	940	3	0.79	-	[271]
3	550–850	40	1	2	[257]	12	1075	3	2.27	-	[271]
4	550–950	10	0.3	1	[283]	13	1085	3	∞	-	[271]
5	550–1100	10	0.5	1	[283]	14	600-800	8	0.51	0.1	[30]
6	550–1150	10	1.5	1	[283]		Premixed Laminar Flame Speciation				
7	550–1100	1	3	2	[119]	#	T_u [K]	P [atm]	φ	notes	Ref.
8	550–1100	1	3	1	[119]	35	567–1630	1	1.9	-	[535]
9	500–1100	1.05	1	2	[149]	36	400–2200	0.04	1.69	-	[120]

	Laminar Flame Speed						Ignition Delay Time				
#	T_u [K]	P [atm]	φ	notes	Ref.	#	T [K]	P [atm]	φ	dP/dt	Ref.
15	298	1	0.7–1.7	-	[534]	37	700–1250	3–4.5	1	-	[146, 530]
16	298	1	0.7–1.4	-	[274]	38	1050–1300	6.5	1	-	[146]
17	360	1	0.7–1.4	-	[274]	39	700–1300	13	1	-	[146]
18	400	1	0.7–1.4	-	[274]	40	800–1100	42	1	-	[146]

19	470	1	0.7–1.4	-	*[274]*	*41*	1300–1700	1	1	-	*[531]*
20	373	10	0.7–1.2	20.5% O_2	*[528]*	*42*	1300–1700	2	1	-	*[531]*
21	373	15	0.7–1.2	20.5% O_2	*[528]*	*43*	1300–1700	4	1	-	*[531]*
22	373	20	0.7–1.2	20.5% O_2	*[528]*	*44*	1300–1700	6	1	-	*[531]*
23	373	25	0.7–1.2	20.5% O_2	*[528]*	*45*	1300–1700	1	0.5	-	*[531]*
24	298	1	0.7–1.4	-	*[275]*	*46*	1300–1700	1	0.9	-	*[531]*
25	353	1	0.7–1.5	-	*[107]*	*47*	1300–1700	1	2	-	*[531]*
26	353	1	0.7–1.7	-	*[529]*	*48*	1250–1380	2	1	-	*[26]*
27	353	2	0.7–1.3	-	*[529]*	*49*	1230–1350	10/12	1	-	*[26]*
28	353	5	0.7–1.1	-	*[529]*	*50*	800–1050	15/25	1	-	*[26]*
29	353	10	0.6–0.8	-	*[529]*	*51*	900–1120	45/60	1	-	*[26]*
30	298	1	0.7–1.3	-	*[350]*	*52*	1150–1650	1	0.5	-	*[262]*
31	358	1	0.7–1.3	-	*[350]*	*53*	1150–1650	1	1	-	*[262]*
32	298	1	0.6–1.7	-	*[277]*	*54*	1150–1650	1	2	-	*[262]*
33	358	1	0.6–1.8	-	*[277]*	*55*	640–960	10	1	-	*[266]*
34	398	1	0.6–1.9	-	*[277]*	*56*	640–960	20	1	-	*[266]*
						57	720–1100	50	0.1	-	*[532]*
						58	720–1101	50	0.2	-	*[532]*
						59	720–1102	50	0.3	-	*[532]*
						60	720–1103	50	0.4	-	*[532]*
						61	786–1400	12	0.25	*2%/ms*	*[260]*
						62	786–1400	45	0.25	*2%/ms*	*[260]*
						63	786–1400	13	0.5	*2%/ms*	*[260]*
						64	786–1400	45	0.5	*2%/ms*	*[260]*

65	786–1400	12	1	*2%/ms*	*[260]*
66	786–1400	50	1	*2%/ms*	*[260]*

Table 35: Summary of the experimental investigations of heptane pyrolysis and oxidation analyzed in this work. Experimental data are available in the supplementary material.

Since the early 90s, in the attempt to better understand the knocking tendency and auto-ignition behavior of interest at engine relevant conditions, both the high and low temperature oxidation mechanisms of *n*-heptane have been extensively investigated [53, 233]. $M = 12$ models were selected as a case study for the CM as reported in Table 36.

Kinetic Mechanisms		
Model_j	**Name**	**Refs**
M1	POLIMI_2008	*[536]*
M2	POLIMI_2010	*[536]*
M3	POLIMI_2012	*[101, 536]*
M4	POLIMI_2014	*[73, 536]*
M5	POLIMI_REDUCED_98	*[537]*
M6	LLNL_3.1	*[14, 538]*
M7	LLNL_2.0	*[233, 240]*
M8	LLNL_RED_159	*[539]*
M9	AACHEN_OPTIMIZED	*[118]*
M10	SANDIEGO_2015	*[540]*
M11	COTTBUS_2015	*[120]*
M12	Hakka_2015	*[119]*

Table 36: n-heptane kinetic mechanisms analyzed in this study

Following the CM procedure, all the models were used to simulate the whole set of experimental data. The measurements and the model results were properly organized in a database, according to the type of

reactors and of measurements. Once all the information is collected, the different dissimilarity indices are evaluated, averaged, and stored. Finally, both the $\varepsilon_{i,j}$ matrix and the E_j vector are built. The complete analysis of the $N = 66$ datasets with the $M = 12$ models is reported in the Supplementary Material, together with figures for each individual models-experiment comparison, dissimilarity measures, boxplots, matrix of dimensionless $\varepsilon_{i,j}$ indexes, E_j vectors for groups of experiments, functional estimates of both the curve and its first derivative, and experimental uncertainties for each single case.

Some examples of the application of the method described in the previous Sections are discussed in the following:

- o Ignition Delay Times in Shock Tubes (Section 4.3)
- o Speciation in Jet Stirred Reactors (Section 4.4)
- o Laminar Flame Speed (Section 4.5)
- o Identification of critical experimental conditions (Section 4.6)

The discussion of these examples will be carried out as identified by the red dashed arrows in Figure 255, starting from the end of the flow chart (i.e. the Model Error Vector (MEV) of E_j values for M models in the selected group of experiments) backward. The reason for such a presentation is that, starting from highlighting negative outliers in the vector of models E_j value, it is possible to better identify the dataset where the model fails in predicting the experimental observations in the $N \times M$ Model/Experiment Error Matrix ($MEEM$). Once the specific case (or more cases) is identified, it is possible to get back to the dissimilarity values identifying possible reasons for the observed behavior.

4.2 Numerical simulations of ideal reactors and laminar flames

Numerical simulations were performed with the OpenSMOKE++ framework [66]. Isothermal jet stirred reactor and adiabatic plug flow reactor simulations were performed in this study. Shock tube and rapid compression machine experiments were simulated assuming adiabatic constant volume conditions. Ignition delay times were determined according to the definition reported in the referenced publications (OH, OH*, CH, CH* profiles or pressure increase). Low-temperature experiments should include non-ideal effects of the facilities ($\frac{dP}{dt}$, i.e. pressure increase due to boundary conditions effect in shock tubes [541, 542] and pressure decrease caused by heat losses in rapid compression machines [543]). With the exception of the experimental data by Shen *et al.* [260], neither pressure correction due to shock attenuation nor pressure time histories in rapid compression machine were discussed in the considered publications [26, 146, 262, 266, 530-532]. Therefore, they have not been accounted for in numerical simulations. Laminar flame velocity and species simulations were carried out using the 1-D flame solver [527] included in the OpenSMOKE++

package. Due to numerical issues caused by both the large number of species in the mechanism and the presence of highly negative activation energies for a few reverse reaction rate constants (up to ~-30, ~-40 kcal/mol), M_6 [14, 538], M_7 [233, 240], M_{11} [120] were not always able to provide a solution for laminar flame velocity calculations. The same problem was encountered for M_{10} [540] despite the very limited number of species.

4.3 Ignition Delay Times in Shock Tubes

From the vector visualization of the "Ignition Delay Times" group of experiments, as reported in Table 37, it is possible to identify one negative outlier, M_{12} [119].

$Model_j$	E_j	$Model_j$	E_j
M_1	0.15	M_7	0.02
M_2	1.34	M_8	-0.17
M_3	0.01	M_9	-0.93
M_4	0.43	M_{10}	1.38
M_5	0.66	M_{11}	0.30
M_6	-1.08	M_{12}	2.43

Table 37: Model Error Vector (MEV) of E_j values of the models for the group of experiments "Ignition Delay Times". The E_j values here reported account for the three dimensionless indices $\widehat{d}_{orig}$, $\widehat{d}_{shift}$, $\widehat{d}_{align}$

From the corresponding $MEEM\ N \times M$ matrix partially reported in Table 38, it is possible to identify one experimental case where the deviation of M_{12} is particularly relevant: Case 65 [29] where $\varepsilon_{65,M12}$ =6.22. Together with M_{12}, also M_{10} ($\varepsilon_{65,M10}$=3.23) [540], M_9 [52] and M_{11} [42] ($\varepsilon_{65,M9}$ =-0.54 and $\varepsilon_{65,M11}$=-2.91) are discussed in the following. Despite its global accuracy in predicting the experimental ignition delay times, M_6 shows average performance for Case 65 ($\varepsilon_{65,M6}$=-0.7).

Experiment$_i$

	….	**49**	**50**	**51**	**52**	**53**	**54**	**55**	**56**	**57**	**58**	**59**	**60**	**61**	**62**	**63**	**64**	**65**	**66**
M$_1$	…	0.7	0.16	−0.61	0.37	−0.75	0.32	−0.45	−0.42	−0.52	−0.54	0.23	0.08	−0.19	−0.45	−1.37	−0.35	−0.07	0.74
M$_2$	…	0.23	−0.09	−0.56	1.32	1.08	0.83	−0.73	−0.43	−0.75	−0.42	0.03	0.07	−0.85	−0.42	−0.2	−0.16	−0.47	0.67
M$_3$	…	0.55	−0.37	−1.15	1.18	0.9	0.32	−0.75	−0.29	−0.53	−0.58	−0.22	−0.43	−0.46	−0.71	−0.33	−0.89	−0.38	−0.17
M$_4$	…	−0.02	0.13	0.94	1.6	1.6	4.52	0.74	0.16	−0.36	−0.57	−0.63	−0.53	−0.47	−0.42	−0.35	−0.2	0.16	−0.48
M$_5$	…	0.02	0.57	1.41	1.53	2.06	5.22	0.78	0.14	−0.32	−0.56	−0.48	−0.19	−0.47	0.06	−0.38	0.37	0.37	0.02
M$_6$	…	−1.52	−1.46	−2.6	−1.04	−0.71	−0.76	0.21	−0.01	−0.09	0.91	−0.35	−0.04	−1.96	−1.35	0.84	−3.15	−0.7	−1.98
M$_7$	…	−0.55	0.88	0.49	−0.44	−0.66	−0.06	−0.65	0.93	3.8	−0.69	0.02	−0.14	0.11	0.59	1.53	0.67	1.19	0.26
M$_8$	…	−1.12	0.84	0.33	−1.06	−1.26	−0.59	−0.61	0.45	1.91	0.02	0.13	−0.25	0.26	1	−0.87	0.87	0.9	0.86
M$_9$	…	−1.39	−1.88	−1.73	−0.79	−0.51	−0.77	0.6	0.09	0.38	1.04	0.71	1.3	−2.49	−0.33	2.93	−1.99	−0.54	−2.57
M$_{10}$	…	0.59	2.89	2.17	0.15	−0.46	−1.94	1.03	1.18	0.02	1.35	3.47	3.8	2.18	6.67	−1.16	5.5	3.23	2.1
M$_{11}$	…	−0.46	−3.7	−0.51	−1.42	−1.51	−0.25	1.37	−0.81	3.3	12.65	−0.7	−0.56	0.15	1.41	1.18	−1.69	−2.91	−1.72
M$_{12}$	…	−0.8	1.37	6.63	−0.48	−0.68	−0.13	8.46	5.64	1.52	5.61	5.3	8.71	2.79	2.18	0.41	5.22	6.22	19.16

Model$_j$ (row label, left side)

Table 38. $\varepsilon_{i,j}$ Model/Experiment Error Matrix (MEEM) for the group of experiments "Ignition Delay Times" (see Table 35). Complete MEEM is available in the Supplementary Material.

It has to be noted that for the computation of dissimilarity indices for ignition delay times $Y = \ln(y)$ is assumed. This choice is based on the commonly used logarithmic scale plot versus inverse temperature for ignition delay times.

*Figure **265*** shows the experimental ignition delay time measurements from Shen et al. [260] for *n*-heptane/air stoichiometric mixtures at 12 atm reflected pressure, together with model predictions. As reported by Shen and co-workers [260] the influence of gasdynamic pressure changes on the measured ignition times was small. Therefore, it is not considered in the numerical simulations.

n-heptane/air, 12 atm
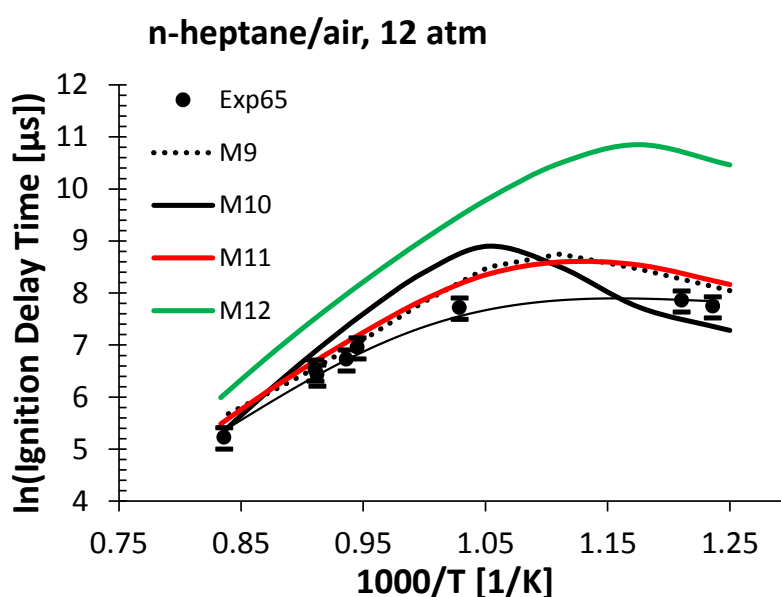
Figure 263: Experimental ignition delay times as measured by Shen et al. [260] (Case 65) and predictions from different kinetic mechanisms (M₉, M₁₀, M₁₁, M₁₂). Note that $Y = ln(y\,[\mu s])$. 20% error bars are reported. Thin black line is the functional representative of the experimental data $f(x)$.

As reported in Table 39a, from a $d^0_{L^2,orig}$ perspective, M₉, M₁₀ and M₁₁ are quite comparable, but they differ in first derivative index $d^1_{L^2,orig}$, highlighting larger deviations especially for M₁₀. In fact, although the ignition delay times are reproduced quite well, the transition from the high to the intermediate temperature regime (relative maximum in ignition delay time) is anticipated by about ~70 K, resulting in high first derivative indices $d^1_{L^2,orig}$ and $d^1_{P,orig}$. Further insights to first derivative trends are given in *Figure **264***.
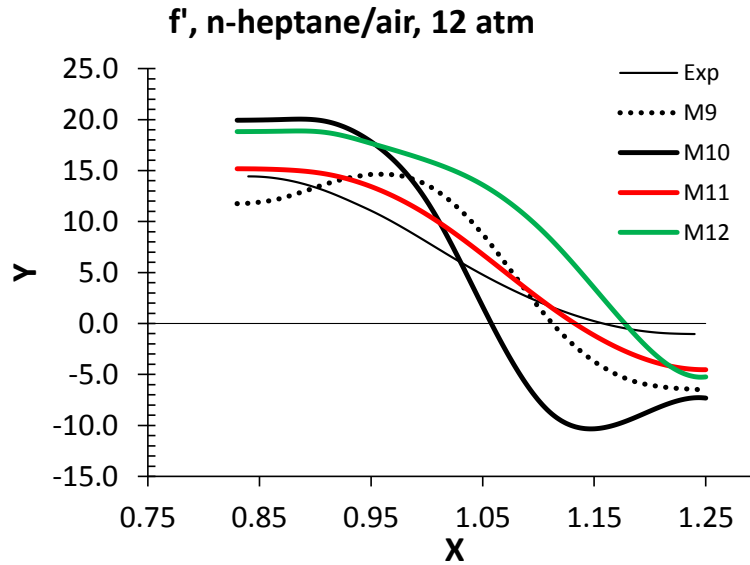
Figure 264: First derivatives of functional estimate for experimental data and models of Case 65 [260]. Note that $Y = \ln(y\ [\mu s])$. Thin black line is the functional representative of the first derivative of the experimental data $f'(x)$.

As previously discussed, Pearson indices refer to the shape of the curve (or to its first derivative). Thus, the high values computed for M_{10} and M_{12} ($d^0_{P,orig} = 0.031$ and $d^0_{P,orig} = 0.029$ respectively, Table 39b) are evident.

The minimization of the dissimilarity index through the horizontal shift δ does not affect too much the aligned dissimilarities for M_9, M_{10} and M_{11} (Table 39c). On the other hand, M_{12} performances would be largely improved from a shift towards higher temperatures (i.e. factor of ~2 decrease in the aligned dissimilarity values), but still showing the highest $d^0_{L^2,orig}$, due to the large overestimation of ignition delay times.

a)	$Model_j$	$d^0_{L^2,orig}$	$d^1_{L^2,orig}$	$d^0_{P,orig}$	$d^1_{P,orig}$
	M_9	0.113	0.418	0.013	0.181
	M_{10}	0.139	0.788	0.031	0.247
	M_{11}	0.107	0.225	0.007	0.080
	M_{12}	0.426	0.673	0.029	0.142

b)	$Model_j$	$\delta^0_{L^2}$	$\delta^1_{L^2}$	δ^0_P	δ^1_P
	M_9	0.055	0.045	0.040	0.043

M$_{10}$	0.093	0.018	0.064	0.198
M$_{11}$	0.075	0.048	0.028	0.006
M$_{12}$	**0.500**	0.236	0.164	0.144

c)	$Model_j$	$d^0_{L^2,align}$	$d^1_{L^2,align}$	$d^0_{P,align}$	$d^1_{P,align}$
	M$_9$	0.105	0.406	0.011	0.180
	M$_{10}$	0.118	0.787	0.027	0.182
	M$_{11}$	0.094	0.204	0.005	0.079
	M$_{12}$	0.282	0.398	0.004	0.086

Table 39: Dissimilarity values for the experimental dataset 65 shown in Figure 265. Panel a) original values, panel b) shift values, panel c) aligned values.

4.3.1 Application of Curve Matching for model improvement

A sample application of Curve Matching for the improvement of the current kinetic mechanism [73] is here reported. *Figure 265*a shows a comparison of the results from the recently revised *n*-heptane mechanism [73] (solid line, M$_4$) with the data of Case 65 [260].
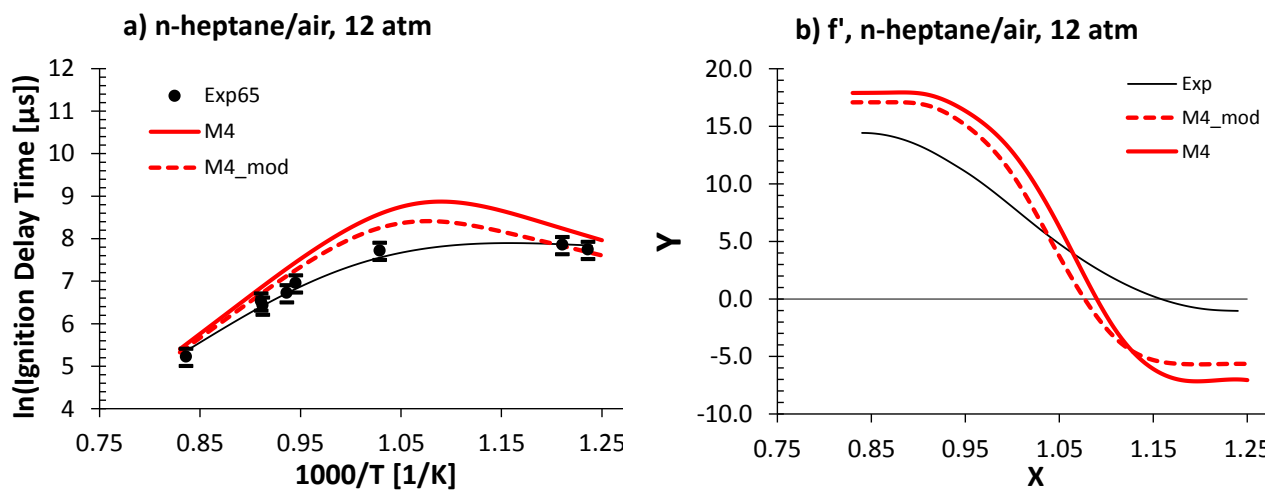
Figure 265: Experimental ignition delay times as measured by Shen et al. [260] and predictions from M$_4$ and M$_4$ modified mechanisms. Thin black line is the functional representative of the experimental data $f(x)$.

A sensitivity analysis was carried out for the same heptane/air mixture, at 900 K and 12 atm. As reported in *Figure 266*, the rate constant of heptyl radical and hydroperoxy-heptyl radical addition to O_2, and the H-abstraction by $H\dot{O}_2$ increases reactivity (i.e. decrease ignition delay times). In the aim of testing the impact of modifying such reaction rates on the dissimilarity values of M_4, the rate constant were multiplied by 1.2 in the test model $M_{4,mod}$. Predictions of this test mechanism, together with its first derivative, are reported as dashed lines in *Figure 265*a and *Figure 265*b, respectively. Table 40 shows the impact of a slight increase of these rate constants on the dissimilarity values of M_4. While a consistent reduction of $d^0_{L^2,orig}$ (~40%) and of $d^1_{L^2,orig}$ (~20%) is observed, Pearson indices are not sensitive to such modifications.
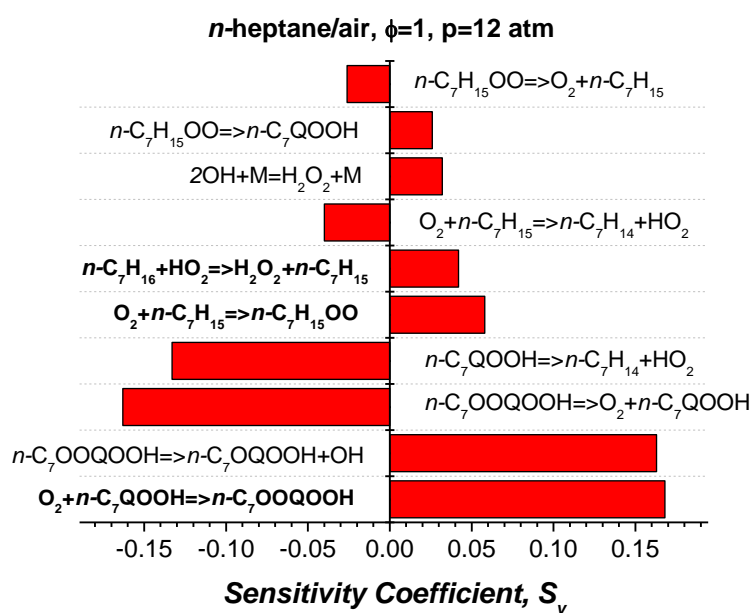
Figure 266: Sensitivity of Ignition Delay Times to rate constants in M_4 [73]. n-heptane/air, Φ=1.0, T=900 K, p=12 atm.

$Model_j$	$d^0_{L^2,orig}$	$d^1_{L^2,orig}$	$d^0_{P,orig}$	$d^1_{P,orig}$
M_4	0.149	0.529	0.016	0.161
$M_{4,mod}$	0.088	0.437	0.016	0.160

Table 40. Original dissimilarity values for the experimental dataset 65 shown in Figure 265, for the original M_4 [73] and its modified version $M_{4,mod}$.

4.4 Speciation in Jet Stirred Reactors

From the vector reported in Table 41, it is possible to identify two negative outliers, M_{10} [540] and M_8 [539], and two positive outliers M_6 [14, 538] and M_{12} [119] for the group of experiments "Speciation in Jet Stirred Reactors".

$Model_j$	E_j	$Model_j$	E_j
M_1	0.45	M_7	−0.82
M_2	−0.17	M_8	2.02
M_3	0.25	M_9	0.34
M_4	−0.56	M_{10}	*4.63*
M_5	−0.36	M_{11}	0.57
M_6	−1.10	M_{12}	−1.16

Table 41: Model Error Vector ($\mathbf{MEV}$) of E_j values of the models for the group of experiments "Speciation in Jet Stirred Reactors". The E_j values here reported account for the three dimensionless indices $\widehat{d}_{orig}$, $\widehat{d}_{shift}$, $\widehat{d}_{align}$

According to the corresponding $MEEM$ partially reported in Table 42 one of the largest deviation is obtained in the experimental Case 5 (0.1% *n*-heptane/O_2/N_2 mixture, ɸ=0.5, T=550–1100 K, p=10 atm) [283].

		Experiments_i										
	…	5a	5b	5c	5d	5e	5f	5g	5h	5i	5l	…
M_1	…	−0.14	−0.33	−0.21	1.33	0.26	−0.14	0.74	2.06	1.39	1.06	…
M_2	…	0.07	−0.19	0.01	−0.39	1.27	−0.43	0.51	−0.02	0.14	1.23	…
M_3	…	−0.46	−0.29	0.07	0.45	0.47	−0.27	0.92	1.48	0.5	0.17	…
M_4	…	−2.18	−0.61	−1.12	−0.42	−0.41	−0.28	−0.54	0.23	−0.89	0.18	…
M_5	…	−2.29	−0.6	−1.1	−0.18	−1.53	−0.4	−0.03	0.04	−0.42	0.32	…
M_6	…	0.58	−0.72	1.61	3.99	0.63	−2.48	0.23	−1.5	1.15	0.54	…

M₇	…	−0.16	−0.02	−0.7	−3.35	−1.2	0.1	−1.35	−1.14	−2.12	−1.91	…
M₈	…	1.52	1.18	0.9	0.88	0.45	−0.36	−0.85	−0.1	0.11	−1.28	…
M₉	…	2.07	3.04	0.95	1.18	1.46	−1.94	−0.64	−0.1	2.34	−1.03	…
M₁₀	…	9.91	4.2	5.77	−0.44	0.54	1.01	4.1	3.76	11.99	0.34	…
M₁₁	…	0.71	0.47	0.6	−0.47	1.11	1.49	1.7	−1.36	−1.66	4.89	…
M₁₂	…	−1.97	−1.21	−1.56	−4.19	2.31	1.27	−1.72	−1.7	−0.53	−0.37	…

*Table 42. $\varepsilon_{i,j}$ Model/Experiment Error Matrix (**MEEM**) for the group of experiments "Speciation in JSR" (see Table 35). Complete **MEEM** is available in the Supplementary Material.*

It should be noted that larger deviations are obtained in many other cases, but it is of interest to firstly focus on the global reactivity of the fuel (Case 5a) largely contributing to the disagreement between M_{10} and experiments observed for minor species (e.g. 5i, C_3H_6 profile). Particularly in this example M_{10} [540] and M_9 [118] ($\varepsilon_{5a,M10}$=9.91 and $\varepsilon_{5a,M9}$=2.07 respectively) are considered, together with M_4 [5, 10], M_5 [4] and M_{12} showing the best agreement with the experimental data ($\varepsilon_{5a,M4}$ =-2.29, $\varepsilon_{5a,M5}$ =-2.18 and $\varepsilon_{5a,M12}$ =-1.97 respectively).

According to the MEV of Table 41, M_8 and M_6 are, globally, a bad mechanism ($E_8 = 2.02$) and a quite accurate mechanism ($E_6 = -1.10$) respectively. Despite their global performance for the "Speciation in Jet Stirred Reactors" group of experiments, they do not show highly negative (or highly positive) performances when considering the single Case 5a here discussed.

*Figure **267*** reports the comparison between selected models and experimental data.
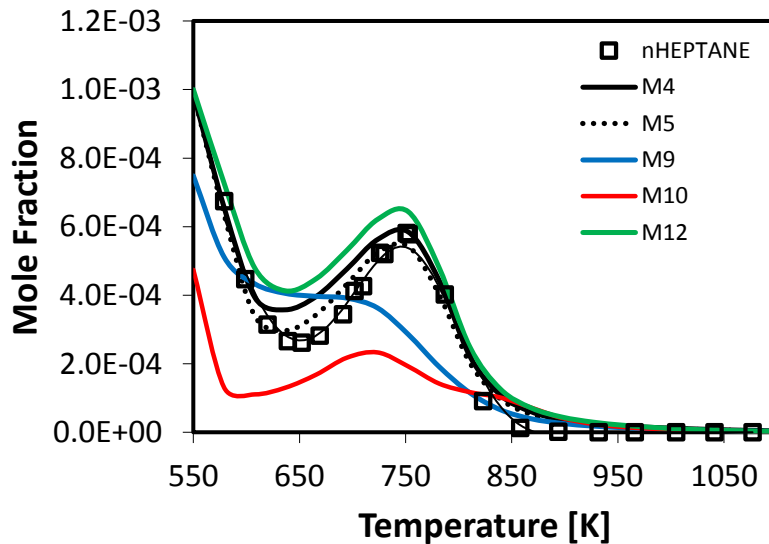
Figure 267: Experimental mole fraction of n-heptane as measured by Dagaut et al. [283] and predictions from different kinetic mechanisms (M$_4$, M$_5$, M$_9$, M$_{10}$, M$_{12}$). The thin black line represents the functional estimate of the experiments of Case5a (symbols).

From the original values of dissimilarities reported in Table 43a it clearly appears that model M$_{10}$ shows the largest deviation in terms $d^0_{L^2,orig}$. Referring to M$_9$, although from a Sum of Squared Errors (SSE) point of view it could be concluded that the disagreement is comparable to that of M$_{12}$ ($d^0_{L^2,orig} = 0.007$ and $d^0_{L^2,orig} = 0.006$ respectively), looking at the first derivative index $d^1_{L^2,orig}$ the presence of a high $\varepsilon_{5a,j}$ value ($\varepsilon_{5a,M9}$=2.07) is clear. In fact, both M$_9$ and M$_{10}$ have $d^1_{L^2,orig}$ values a factor of ~3 higher than those of the better performing M$_4$, M$_5$ and M$_{12}$. Figure 267 shows the functional estimates for the experimental data and models f discussed in this Section. *Figure 268* shows their first derivatives functional estimates f' clarifying the meaning of calculated dissimilarities indices of selected models: while M$_4$, M$_5$ and M$_{12}$ closely reproduce the experimental first derivative, large deviations are observed for M$_9$ and M$_{10}$.
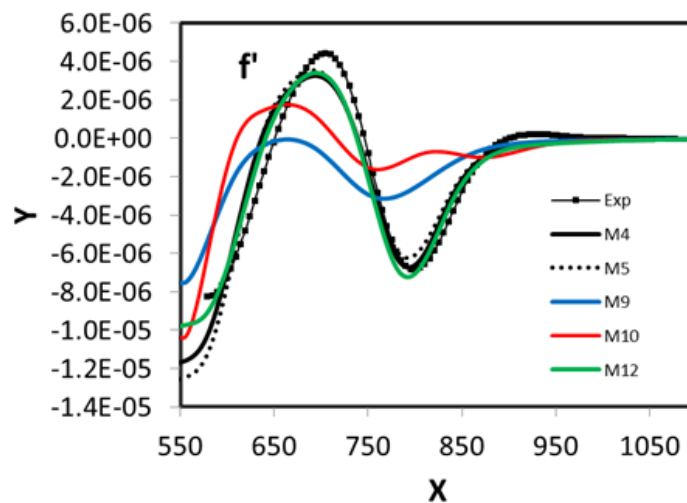
Figure 268: First derivatives of functional estimate for experimental data and models of Figure 267.

Moving toward the Pearson index the same disagreement is found between "good" and "bad" models. As reported in Table 43b, M_9 and in particular M_{10}, show the highest shift values. Nevertheless, no sensible improvements are observed in the aligned dissimilarity values (Table 43c), suggesting that the deviations are not due to a horizontal shift, but to the shape of curves and first derivatives ($d_{L^2,orig}^1$).

a) $Model_j$	$d_{L^2,orig}^0$	$d_{L^2,orig}^1$	$d_{P,orig}^0$	$d_{P,orig}^1$
M_4	0.004	0.005	0.059	0.125
M_5	0.002	0.005	0.051	0.137
M_9	0.007	0.014	0.178	0.388
M_{10}	0.013	0.016	0.174	0.432
M_{12}	0.006	0.004	0.063	0.108

b) $Model_j$	$\delta_{L^2}^0$	$\delta_{L^2}^1$	δ_P^0	δ_P^1
M_4	0.002	0.014	0.013	0.015
M_5	0.009	0.012	0.011	0.015
M_9	0.048	0.063	0.053	0.059
M_{10}	0.079	0.500	0.037	0.500
M_{12}	0.009	0.015	0.012	0.015

c) $Model_j$	$d_{L^2,align}^0$	$d_{L^2,align}^1$	$d_{P,align}^0$	$d_{P,align}^1$
M_4	0.004	0.003	0.049	0.093
M_5	0.002	0.004	0.042	0.112
M_9	0.006	0.011	0.151	0.273
M_{10}	0.011	0.011	0.146	0.213
M_{12}	0.006	0.002	0.057	0.065

Table 43: Dissimilarity values for the experimental dataset 5a shown in Figure 267. Panel a) original values, panel b) shift values, panel c) aligned values.

4.5 Laminar Flame Speed

The Model Error Vector shown in Table 44 highlights the existence of a single undesirable outlier, M_8 [539]. As previously discussed it is possible to state that all of the other tested mechanisms belong to the [-1, 1] range of normalized dissimilarity index previously defined as "average performances". No outstanding performances are identified.

$Model_j$	E_j
M_1	−0.13
M_2	1.05
M_3	−0.06
M_4	−0.6
M_5	−0.05
M_8	2.64
M_9	−0.38
M_{12}	0.2

*Table 44: Model Error Vector (**MEV**) of E_j values of the models for the group of experiments "Laminar Flame Speed". The E_j values here reported account for the three dimensionless indices $\hat{d}_{orig}$, $\hat{d}_{shift}$, $\hat{d}_{align}$*

By looking at the detail in the $MEEM\ N \times M$ matrix partially reported in Table 45, it is possible to observe that the largest deviation of M8 from the experimental data is obtained for Case 24. Despite showing the lowest E_j value in Table 44 ($E_4 = -0.6$), M_4 shows average capability to predict the experimental data for this particular case ($\varepsilon_{24,M4} = 0.09$).

$Model_j$		Experiments$_i$						
	…	22	23	24	25	26	27	…
M_1	…	0.5	1.26	0.32	0.26	−0.09	1.1	…

M_2	...	1.53	0.66	−1	−1.36	0.24	0.13	...
M_3	...	1.27	0.69	−2.28	−0.2	−0.29	−0.76	...
M_4	...	−1.09	−0.93	0.09	0.54	0.25	−0.27	...
M_5	...	−1.84	−1.36	0.09	1.23	1.47	0.73	...
M_8	...	−1.3	0.68	6.77	2.65	2.93	5.17	...
M_9	...	0.01	−0.54	−0.91	−0.67	−1.75	−1.17	...
M_{12}	...	0.4	−0.24	2.14	−1.38	−1.09	0.75	...

Table 45. $\varepsilon_{i,j}$ Model/Experiment Error Matrix ($\boldsymbol{MEEM}$) for the group of experiments "Laminar Flame Speed" (see Table 35). Complete $\boldsymbol{MEEM}$ is available in the Supplementary Material.

In the following M_3 [101, 536], M_8 [539] and M_{12} [119] are discussed. Calculated ε values for these models are -2.28, 6.77 and 2.14 respectively. Laminar flame speeds of *n*-heptane/air mixtures at atmospheric pressure and 298 K unburned gas temperature were measured by Huang *et al.* [275] in a counterflow configuration. Experimental data and modeling results are compared in *Figure 269*a. Functional estimates for experimental and models first derivative are reported in *Figure 269*b.

As reported in Table 46a, M_3 presents the lowest values among the four original dissimilarity indices being able to accurately reproduce the experimental observations, both in terms of laminar flame speed and its first derivative ($\frac{dS_L}{d\varphi}$). As mentioned above, M_8 is clearly highlighted as the least accurate in reproducing the measured values. It can also be observed from Table 46b that horizontal shift values for the three models are very limited, resulting in very similar aligned dissimilarity values (see Table 46c).
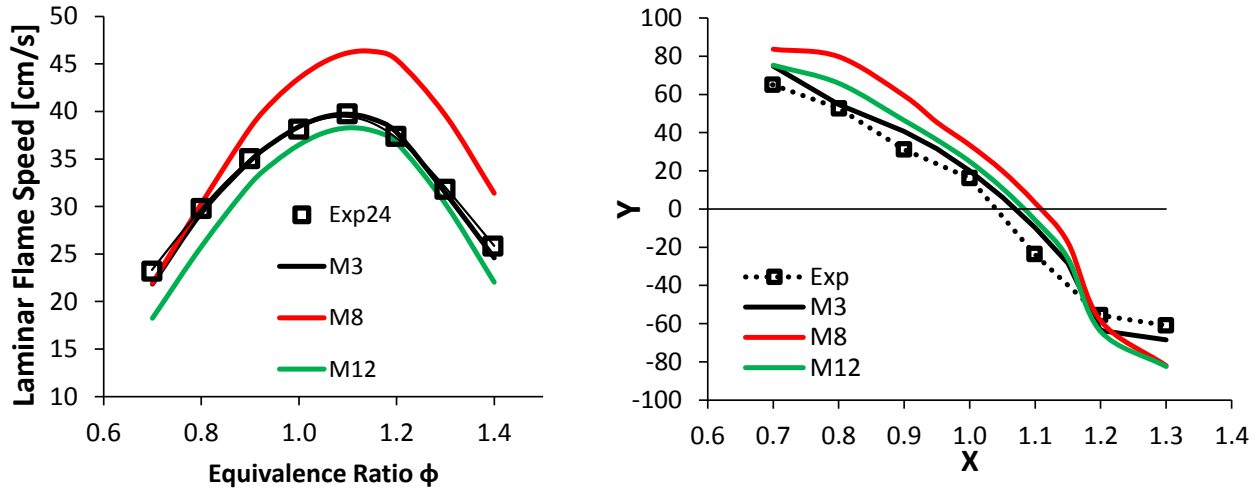
Figure 269: Left panel: experimental laminar flame speed of n-heptane/air mixtures as measured by Huang et al. [275] and predictions from different kinetic mechanisms (M3, M8, M12). T_u=298 K, p=1 atm. Right panel: experimental and model functional estimates for the first derivatives. Experimental error (~2% [275]) is already included in the size of symbols.

a)	$Model_j$	$d^0_{L^2,orig}$	$d^1_{L^2,orig}$	$d^0_{P,orig}$	$d^1_{P,orig}$
	M_3	0.016	0.099	0.008	0.014
	M_8	0.170	0.300	0.032	0.089
	M_{12}	0.077	0.179	0.022	0.035

b)	$Model_j$	$\delta^0_{L^2}$	$\delta^1_{L^2}$	δ^0_P	δ^1_P
	M_3	0.004	0.004	0.004	0.003
	M_8	0.027	0.059	0.062	0.056
	M_{12}	0.028	0.018	0.026	0.018

c)	$Model_j$	$d^0_{L^2,align}$	$d^1_{L^2,align}$	$d^0_{P,align}$	$d^1_{P,align}$
	M_3	0.016	0.099	0.007	0.014
	M_8	0.167	0.241	0.007	0.019

M$_{12}$	0.072	0.171	0.018	0.022

Table 46: Dissimilarity values for the experimental dataset 24 shown in Figure 15. Panel a) original values, panel b) shift values, panel c) aligned values.

4.6 Identification of critical experimental conditions

Referring to Figure 262 of Section 3.8 the detailed view of the $d^0_{L^2,orig}$ is reported in *Figure **270***. To better explain the potential of boxplot visualization of experiments Case 23 of the "Laminar Flame Speed" group is discussed in the following. Experimental data were measured by Jerzembeck *et al.* [528] in a constant volume bomb configuration for *n*-heptane/air lean-stoichiometric mixtures at 25 bar and unburned gas temperature of 373 K. As shown in *Figure **270*** and *Figure **271***, every mechanism poorly predicts the experimental measurements. In particular, M$_1$ [536], M$_2$ [536] and M$_3$ [101, 536] show deviations up to ~7 cm/s. The best predictions are those of M$_4$ [73] and M$_9$ [118], with maximum over-predictions of ~5 cm/s. In both cases the detected deviations are higher than the experimental uncertainty (2-2.5 cm/s) provided by the authors.
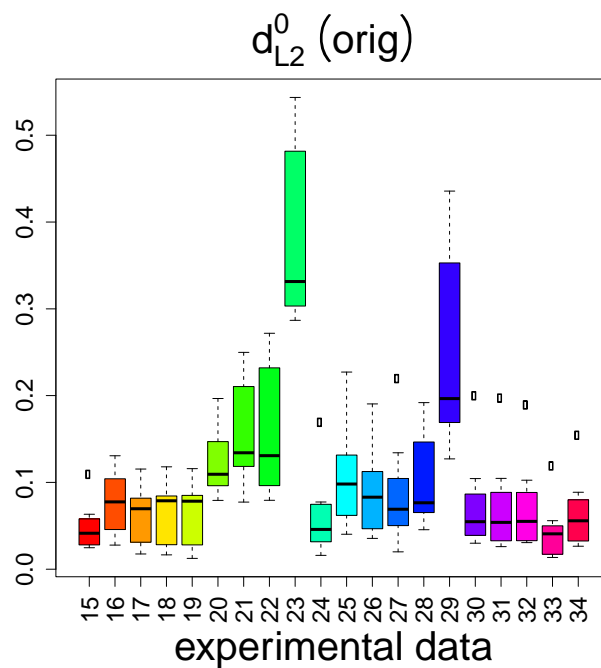
Figure 270: Detail of the boxplot for the group of experiments "Laminar Flame Speed" reported in Figure 262 of Section 3.8.
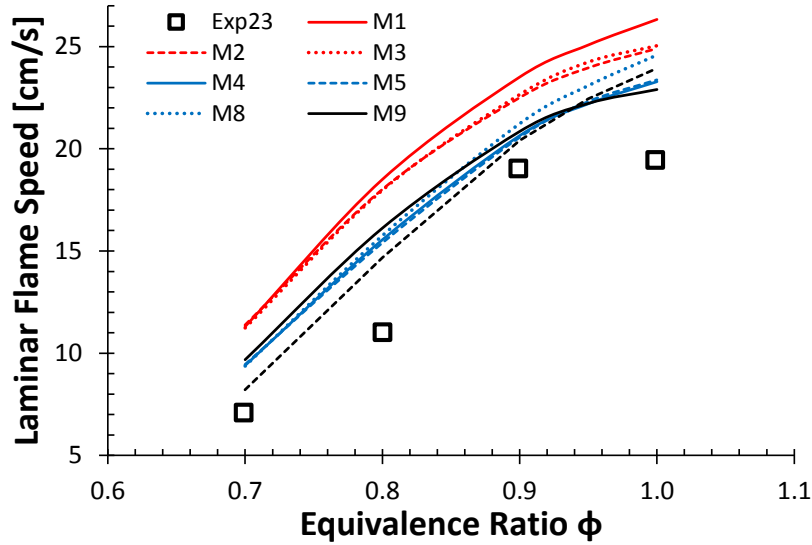
Figure 271: Experimental laminar flame speed of n-heptane/air mixtures as measured by Jerzembeck et al. [528] and predictions from different kinetic mechanisms. T_u= 373 K, P=25 bar. Experimental error is 2-2.5 cm/s.

Table 47 reports the computed $d^0_{L^2,orig}$, $\delta^0_{L^2}$, and $d^0_{L^2,align}$ indices for the models considered, further confirming the large discrepancies existing between models and experiments. Moreover it clearly appears that horizontal shifts in the order of 30% of the experimental domain (φ=0.7–1.0) towards richer regions ($\Delta\varphi\approx+0.1$) would be needed to improve model performances, at least in terms of Sum of Square Errors ($d^0_{L^2,orig}$).

Model	$d^0_{L^2,orig}$	$\delta^0_{L^2}$	$d^0_{L^2,align}$
M_1	0.544	0.384	0.154
M_2	0.479	0.357	0.113
M_3	0.484	0.355	0.122
M_4	0.291	0.216	0.070
M_5	0.287	0.209	0.074
M_8	0.335	0.233	0.100
M_9	0.315	0.238	0.071
M_{12}	0.327	0.257	0.053

Table 47: Original shift and aligned values of $d_{L^2}^0$ index for Case 23 [528] reported in Figure 271..

4.7 Final remarks

Notwithstanding the experimental uncertainty, the three datasets investigated in Sections 4.2, 4.3 and 4.4, complemented by the available Supplemental Material, pointed out that quantifying the goodness of a kinetic model is not a straightforward task, and the ranking resulting from different datasets may be different, too.

In spite of it, such an approach may provide important guidelines towards the improvement of a kinetic mechanism, as discussed in Section 4.3.1. As a representative example, the assessment of the different POLIMI mechanisms (M_1 to M_4), summarized into the integrated indices, highlighted significant overall improvements in the laminar flame speed predictions and species formation. On the other hand, a slight worsening in the prediction of ignition delay times was observed. Although very short, such an information is very useful to the kinetic modelers, who can then investigate the indices provided in the single datasets in more detail, and act accordingly. To this purpose, the indices distribution in the boxplot form is the successive step, in order to identify critical predictions, and work towards their improvement.

As a second advantage, the CM framework can be of great importance in making sure that skeletal mechanisms have kept the desired accuracy with respect to the original model. With reference to the M_5 model, it is worth noticing that for the first two datasets, the integrated indices are very close to the parent mechanism. If it was somewhat expectable for the ignition delay subset, since it was the target property of the reduction approach [537], the similar behavior in Jet stirred reactors is a positive (and not guaranteed) outcome for the reduction approach. Slightly worse performances are observed for the laminar flame speed predictions, but accuracy is still comparable to the other kinetic mechanisms. This does not happen, for example, for the LLNL model M_8, obtained from M_7, whose development had been explicitly targeted at matching autoignition properties.

5. Conclusions

So far, the application of functional data analysis to chemical kinetic analysis has been an uncharted territory, with qualitative approaches being the dominant methodology for mechanism development and validation. In this background, this work has presented an innovative framework, named CM, whose development was conceived around two main tasks:

- assess the capability of a kinetic model in reproducing experimental measurements

- compare and rank different models

The introduction of dissimilarity indices, and their framing into a more general methodology, were able to accomplish both of them. A quantitative estimation of the capability of kinetic models was made possible through a multi-faceted analysis of the profiles obtained from both models and experiments.

In the field of chemical kinetics, such a framework is a powerful tool in the hand of the kinetic modeler, who can use it for verifying, updating, and troubleshooting his own mechanism. Moreover, the comparison of different models on the same dataset may also help to identify possible systematic errors, which might be due to either a shared lack of knowledge of all the models, or to issues with experimental data.

As an explicative application, different kinetic mechanisms available for n-heptane (Primary Reference Fuel for gasoline engines) have been compared over a wide set of experimental data of different nature (ideal reactors and laminar flame speeds). As a result, the strengths and weaknesses of the different kinetic mechanisms have been identified, as well as the actual improvements due to mechanism update and the loss of accuracy resulting from mechanism reduction.

The applications of such a methodology are manifold, and not limited to combustion model validation. In principle, it could be applied in any situation where at least one of the two mentioned tasks is involved. As a direct one, the development of a species-targeted skeletal reduction approach, described in detail in a separate work [537], is a clear example. Here, through an error-controlled procedure, the authors showed how it is possible to create skeletal kinetic models with the desired degree of accuracy for pre-defined targets, e.g. the dynamics of formation of a given species. In this way, compact and reliable kinetic models can be used for more demanding applications like CFD.

Chapter 8 – Conclusions and Future Perspectives

Formulation of new fuels, engine optimization and the exploration of new engine technologies strongly relies on an accurate description of combustion chemistry over a broad range of operating conditions and regimes. Due to the complexity of real fuels in terms of the number of components, it is standard practice to refer to surrogate mixtures of a limited number of compounds representative of the families of species found in commercial gasoline, diesel and jet fuels. The addition to the most common Primary Reference fuels (n-heptane, iso-octane) of toluene at first, and successively the need to model the effects of oxygenated fuels blending on fundamental combustion properties (ignition delay times, laminar flame speed, species formation) requires the development of accurate kinetic mechanisms for single components or the progressive revision of existing modules, in light of more accurate parameters from theory or due to the availability of wider validation targets.

This thesis focused on many aspects such as the formulation of new reaction classes for the low temperature oxidation of alkanes, on the theory driven revision of toluene pyrolysis and oxidation chemistry, on the development of comprehensive kinetic mechanisms for C_4–C_5 alcohols and C_3–C_5 aldehydes high and low temperature oxidation. Extension of the proposed rate rules to heavier species of the same family allows satisfactory comparison with experimental data and highlights possibilities of further refinement. An extensive comparison of rate rules for alkane oxidation with the recent study of Bugler et al. [55] also highlights some deviations deserving further attention.

Advances in experimental measurements coupled with theoretical calculation of rate constants highlighted missing reaction pathways for alkanes oxidation at low temperature. The extension through analogy of these channels and their kinetic parameters to n-heptane resulted in a revised mechanism, validated in standard ideal reactors and in more complex applications such as HCCI engines and droplets combustion.

Recent experimental and kinetic modelling studies highlighted a quite controversial and inconsistent literature on toluene oxidation. A thorough review of rate constants from the literature, together with high level theoretical calculations of important reaction channels such as the interactions of O_2 with benzyl radical and the H-abstractions by $\dot{O}H$, $\ddot{O}$, $H\dot{O}_2$ and O_2 led to a reliable mechanism able to describe toluene oxidation over a wide range of temperature and pressure. Preliminary investigations of additional pathways in benzyl radical pyrolytic "vertical decomposition" involving fulvenallenyl and cyclopentadienylide radicals are well supported by recent measurements in plug flow reactors [294]. Some deviations are highlighted between theoretical predictions and experimental measurements of O_2+toluene H-abstraction. Other important channels deserving more accurate investigations involve $\dot{H}$, $\ddot{O}$ and $\dot{O}H$ addition to the ring and ipso-

substitution reactions. A better assessment of both the high pressure limit rate constants for HO_2+benzyl channels and their pressure dependence is also strongly encouraged.

The low temperature mechanism of n- and iso-C_4 and C_5 alcohols has been developed starting from a revision of the high temperature chemistry already implemented in the POLIMI mechanism. Although key pathways in the low temperature ignition chemistry of alcohols such as R-CH-OH+O_2↔HO_2+R-CHO (i.e. aldehyde) still lack a theoretical assessment, the model satisfactorily reproduces experimental measurements over a broad range of pressure and temperatures. Extension to n-hexanol oxidation points out some large inconsistencies in some experimental measurements and the need for systematically revisiting alcohols low temperature/high pressure oxidation both at an experimental and theoretical/modelling level.

Aldehydes are primary products of alcohol decomposition and oxidation. Moreover, they are carcinogenic and harmful pollutants and the use of biofuels has been associated with a clear increase of aldehydes concentration in the atmosphere. The accurate treatment of aldehyde chemistry is crucial to correctly model alcohols ignition propensity and to explore ways to limit their emissions. An experimental and kinetic modelling study of C_3–C_5 aldehydes pyrolysis and oxidation at high temperatures and the following extension at low temperatures conditions provided guidelines for the implementation of heavier aldehydes chemistry in existing mechanisms. The extension of such rules to n-hexanal confirms their reliability.

Overall, the union of the different parts (heptane, toluene, alcohols and aldehydes) allowed to accurately reproduce recent ignition delay time and speciation measurements of PRFs/butanol and TRFs/butanol blends.

A systematic investigation of the influence of the oxygenated functional groups on different fuels reactivity has been carried out considering alcohols, aldehydes, ketones and methyl esters. The influence of the oxygen atom on the adjacent bond strengths determines H-abstraction reaction selectivities and activates peculiar pathways, characterizing the ignition propensity of the different oxygenated fuels. These important pathways still lack systematic theoretical evaluations or the clear definition of rate rules. Moreover, the limited number of experimental measurements available at engine relevant conditions partly prevent a deeper knowledge of the impact of such fuels on engine performances.

Inputs from theoretical calculations and extended validation targets drives a continuous refinement of kinetic models of increasing complexity. As implicit in the hierarchical nature of combustion, variations to the lower molecular weight portions of kinetic mechanisms (e.g. H_2/O_2, C_1–C_4 species) propagate to heavier fuels, positively or negatively perturbing their capability of reproducing experimental measurements. The development of a method named Curve Matching to automatically evaluate the performances of a kinetic

mechanism was also discussed in *this thesis*. This method advances the state of the art sum of squared errors based methods, considering also the first derivatives and shape evaluation indices.

The implementation of such method in a fully automated system for the development, validation and evaluation of kinetic mechanisms is in progress at POLIMI. A schematic representation of the final goal is reported in *Figure 272*, summarizing some of the biggest challenges in modern chemical kinetic modelling.
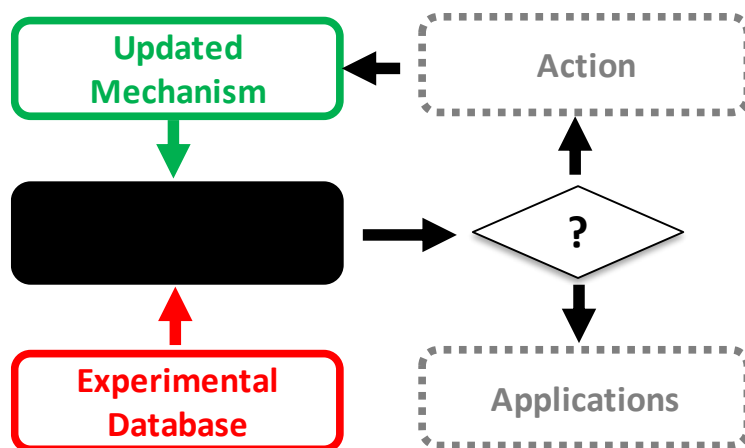
Figure 272: Schematic representation of an "automatic modelling system" for the development, validation and evaluation of a kinetic mechanism.

Kinetic mechanisms are often updated with more accurate parameters, or extended to include new fuels and new pollutants, or re-validated due to an increasing amount of experimental data. This suggests the need for an automatic tool able to manage experimental information, compare them with numerical predictions and make decisions based on model performances. If the model does not reproduce the experimental data within a defined threshold, standard kinetic analyses can highlight reasons for deviation and drive a more accurate evaluation of key parameters. Once the mechanism is updated the procedure is reiterated.

The first critical aspect concern the definition of a database. Different approaches to data storage and exchange are available in the literature (ReSpecTh database at ELTE Budapest University, Hungary; CloudFlame at KAUST University, Saudi Arabia; PriME kinetics at Berkley University, USA). Many EU founded programs within the combustion community started to face the challenges involved in the definition of a common standard to store data and in making them always directly available to kinetic modelers (COST Action CM1404, Smartcats).

Once a dataset is stored in the database, all information needed to execute the corresponding numerical simulation is also saved. Results from kinetic simulations carried out with OpenSMOKE++ are compared with experimental data through Curve Matching. Many open questions still remain for mechanism evaluation:

how to deal with a limited number of models (e.g. 2 models)? How to select the best coupling of mechanisms from different sources to represent a fuel mixture?

Increased theoretical knowledge and increasing computational capabilities allow to automatically explore potential energy surfaces and calculate rate constants for primary reactions of a given fuel. The abundant literature on theoretical gas-phase kinetics already maps the best methods and approaches to calculate accurate rate constants for a given reaction class (H-abstractions, unimolecular initiation or radical recombination, isomerization, addition or β-decomposition). The automatic execution of these standard procedures has the potential of extensively integrating theoretical kinetics into mechanism development. For example, given a number of compounds belonging to the same class (e.g. alcohols) it is possible to systematically and efficiently calculate the rate constant for a specific reaction class (e.g. R-CH-OH+O_2↔HO_2+R-CHO) and extrapolate a rate rule. Again, given a new fuel of interest, it is possible to generate its primary oxidation mechanism completely from fundamental calculations. *Figure **273*** summarizes the procedure implemented in EStoKTP, a tool under development in collaboration with the theoretical kinetics group at Argonne National Laboratory [544].

Stochastic search of absolute minima
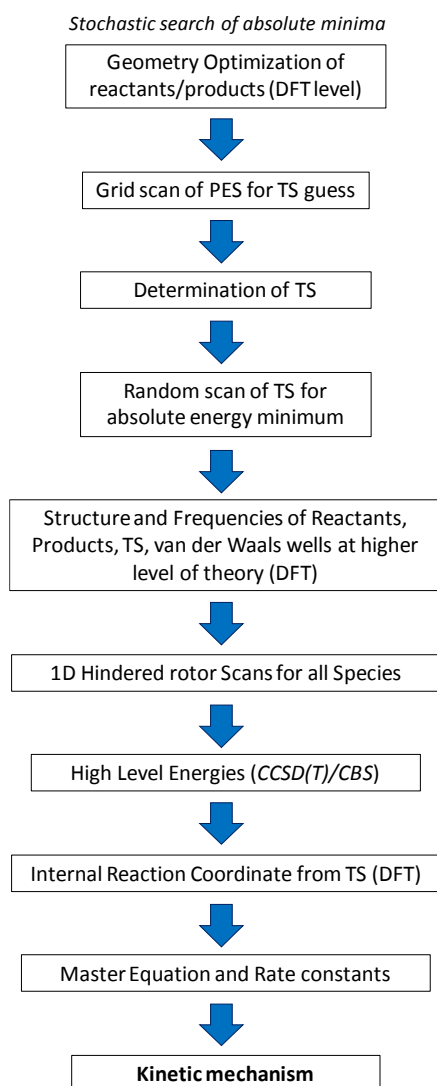
Figure 273: Schematic of EStoKTP structure [544], adapted from [545].

Appendix – Additional Studies

This Section provides references to other studies published during the course of the PhD programme [546, 547] and one study rejected for publication in the Proceedings of The Combustion Institute 2016 [192] in preparation for re-submission.

A1 – High-Temperature Chemistry of HCl and Cl₂.

High-temperature chemistry of HCl and Cl₂

CrossMark

Matteo Pelucchi [a], Alessio Frassoldati [a], Tiziano Faravelli [a,*], Branko Ruscic [b,c], Peter Glarborg [d]

[a] *Dipartimento di Chimica, Materiali e Ingegneria Chimica "G. Natta", Politecnico di Milano, P.zza Leonardo da Vinci 32, 20133 Milano, Italy*
[b] *Chemical Sciences and Engineering Division, Argonne National Laboratory, Argonne, IL 60439, USA*
[c] *Computation Institute, University of Chicago, Chicago, IL 60637, USA*
[d] *DTU Chemical Engineering, Technical University of Denmark, 2800 Lyngby, Denmark*

A R T I C L E   I N F O

A B S T R A C T

The high temperature chlorine chemistry was updated and the inhibition mechanisms involving HCl and Cl₂ were re-examined. The thermochemistry was obtained using the Active Thermochemical Tables (ATcT) approach, resulting in improved data for chlorine-containing species of interest. The HCl/Cl₂ chemistry discussed in the paper was based on reference and experimental measurements of rate constants available in the literature. By coupling the new HCl/Cl₂ subset with the Politecnico di Milano (POLIMI) syngas mechanism a kinetic mechanism consisting of 25 species and 102 reactions was obtained. The validation was carried out on selected experimental data from laminar flames, shock tubes and plug flow reactors. Systems containing Cl₂ showed high sensitivity to $Cl_2 + M \rightleftharpoons Cl + Cl + M$; the rate constant for this reaction has a significant uncertainty and there is a need for an accurate high-temperature determination. The importance of the chain propagating steps such as $Cl + H_2 \rightleftharpoons HCl + H$ and $Cl_2 + H \rightleftharpoons HCl + Cl$ competing with the branching reaction $H + O_2 \rightleftharpoons OH + O$ and the termination reaction $H + Cl + M \rightleftharpoons HCl + M$ is also pointed out by the kinetic analysis. Other relevant reactions in HCl containing systems are the chain propagation reactions $HCl + O \rightleftharpoons Cl + OH$, $HCl + OH \rightleftharpoons Cl + H_2O$ and $Cl + HO_2 \rightleftharpoons ClO + OH$, together with the termination reaction $Cl + HO_2 \rightleftharpoons HCl + O_2$. With the present thermochemistry and rate constants, reaction cycles involving HOCl and ClCO were found not to be important under the investigated conditions.

Figure 274: High temperature chemistry of HCl and Cl2 [547].

A2 – Detailed Kinetic Mechanism of Gas-Phase Reactions of Volatiles Released from Biomass Pyrolysis

Research paper

Detailed kinetic mechanism of gas-phase reactions of volatiles released from biomass pyrolysis

CrossMark

Paulo Eduardo Amaral Debiagi, Giancarlo Gentile, Matteo Pelucchi, Alessio Frassoldati, Alberto Cuoci, Tiziano Faravelli, Eliseo Ranzi[*]

Dipartimento di Chimica Materiali ed Ingegneria Chimica "G. Natta", Politecnico di Milano, Piazza Leonardo da Vinci 32, 20133 Milano, Italy

ABSTRACT

Comprehensive chemical models to describe the behavior of biomass pyrolysis, gasification and combustion are crucial for the simulation and design of thermochemical processes of ligno-cellulosic materials. Despite this importance, reliable and predictive models are still not well known. The original aspect of this work is to present a comprehensive and predictive model of pyrolysis, gasification, and combustion, starting from biomass characterization, through the description of released volatiles at the particle scale, until the effect of the secondary gas-phase reactions at the reactor scale. All these aspects can play a relevant role in the biomass thermo-valorization processes. Most of released species from biomass devolatilization are oxygenated hydrocarbons. This study aims at identifying some reference rate parameters, based on analogy and thermochemistry rules, for the different reaction classes. Once rate rules are defined, they allow an easy extension to analogous compounds. In this way, the kinetic mechanism already developed for jet and diesel fuels is extended to the new tar species released by biomasses. Despite unavoidable approximations when the interest is also at the reactor scale, this model is the only one, to our knowledge, able to describe the whole process from biomass to final products, in a predictive and satisfactory way.

Figure 275: Detailed kinetic mechanism of gas-phase reactions of volatiles released from biomass pyrolysis [546].

A3 - Theoretical Calculation of the Rate Coefficient for CH₃Cl+M=CH₃+Cl+M and Kinetic Modeling of Chloromethane Pyrolysis and Oxidation

Matteo Pelucchi, Carlo Cavallotti, Alessio Frassoldati, Eliseo Ranzi, Tiziano Faravelli*

Department of Chemistry, Materials and Chemical Engineering "G. Natta", Politecnico di Milano, P.zza

Leonardo da Vinci 32, 20133 Milano, Italy

Abstract

The high temperature chemistry of chloromethane was updated. Results from theoretical calculations of the decomposition reaction $CH_3Cl+M=CH_3+Cl+M$ were compared with previous experimental measurements at high temperatures and with evaluations of the reverse recombination reaction at lower temperatures. A CH_3Cl pyrolysis and oxidation sub-mechanism was then developed. The rate parameters for primary reactions of CH_3Cl were derived from experimental or theoretical estimates from the literature. By coupling the new CH_3Cl sub-mechanism with the previously developed HCl/Cl_2 sub-set and with the POLIMI C_1–C_3 mechanism, a kinetic mechanism consisting of 118 species and 2394 reactions was obtained. The validation was performed through comparison with pyrolysis and oxidation measurements available for pure CH_3Cl and its mixtures with CH_4, H_2 and CO/H_2O. $Cl+CH_3Cl=\cdot CH_2Cl+HCl$ was highlighted as a key reaction step in the whole temperature range investigated here. $\cdot CH_2Cl+O_2=CH_2O+ClO\cdot$, for which the need for a better assessment is highlighted, played a major role during oxidation. The key CH_3Cl initiation reaction also showed particular importance as a promoting step at high temperatures for CH_4/CH_3Cl mixtures, due to the low energy of the C–Cl bond (~82 kcal/mol).

Keywords

Chloromethane

Kinetic modeling

Master equation

Spin-orbit

Flame inhibition

References

1.   Exxonmobil, in: *The Outlook for Energy: A View to 2040*, Exxonmobil, (Ed.) 2015.

2.   UN Kyoto protocol to the united nations framework convention on climate change http://unfccc.int/resource/docs/convkp/kpeng.pdf

3.   C2ES Outcomes of the UN climate change conference in Paris. http://www.c2es.org/docUploads/cop-21-paris-summary-02-2016-final.pdf

4.   S. M. Sarathy; P. Oßwald; N. Hansen; K. Kohse-Höinghaus, *Alcohol combustion chemistry*, Progress in Energy and Combustion Science 44 (2014) 40-102

5.   EPA, in: *Environmental Protection Agency Federal Register*, 2012; Vol. 77

6.   M. Gautam; D. Martin, *Combustion characteristics of higher-alcohol/gasoline blends*, Proceedings of the Institution of Mechanical Engineers, Part A: Journal of Power and Energy 214 (5) (2000) 497-511

7.   L. Starck; N. Jeuland; M. Braun-Unkoff; P. Leclerq; P. Bogers; O. Salvi, *ALFA-BIRD-Alternative Fuels and Biofuels for Aircraft Development*, International association for stability, handling and use of liquid fuels (42) (2010)

8.   E. Sadeghinezhad; S. Kazi; F. Sadeghinejad; A. Badarudin; M. Mehrali; R. Sadri; M. R. Safaei, *A comprehensive literature review of bio-fuel performance in internal combustion engine and relevant costs involvement*, Renewable and Sustainable Energy Reviews 30 (2014) 29-44

9.   W. E. Tyner, *Policy Update: Why the push for drop-in biofuels?*, Biofuels 1 (6) (2010) 813-814

10.   S. Karatzos; J. D. McMillan; J. N. Saddler, *The potential and challenges of drop-in biofuels*, Report for IEA Bioenergy Task 39 (2014)

11.   J. M. Bergthorson; M. J. Thomson, *A review of the combustion and emissions properties of advanced transportation biofuels and their impact on existing and future engines*, Renewable and Sustainable Energy Reviews 42 (2015) 1393-1417

12.   G. Kalghatgi, *Fuel/engine interactions*, Training 1998 (2014) 09-21

13.   G. T. Kalghatgi, *The outlook for fuels for internal combustion engines*, International Journal of Engine Research   (2014) 1468087414526189

14.   M. Mehl; W. J. Pitz; C. K. Westbrook; H. J. Curran, *Kinetic modeling of gasoline surrogate components and mixtures under engine conditions*, Proceedings of the Combustion Institute 33 (1) (2011) 193-200

15.   P. Gaffuri; T. Faravelli; E. Ranzi; N. P. Cernansky; D. Miller; A. d'Anna; A. Ciajolo, *Comprehensive kinetic model for the low temperature oxidation of hydrocarbons*, AIChE journal 43 (5) (1997) 1278-1286

16.   C. K. Westbrook, *Chemical kinetics of hydrocarbon ignition in practical combustion systems*, Proceedings of the Combustion Institute 28 (2) (2000) 1563-1577

17.   E. Ranzi; M. Dente; A. Goldaniga; G. Bozzano; T. Faravelli, *Lumping procedures in detailed kinetic modeling of gasification, pyrolysis, partial oxidation and combustion of hydrocarbon mixtures*, Progress in Energy and Combustion Science 27 (1) (2001) 99-139

18.   F. Battin-Leclerc, *Detailed chemical kinetic models for the low-temperature combustion of hydrocarbons with application to gasoline and diesel fuel surrogates*, Progress in Energy and Combustion Science 34 (4) (2008) 440-498

19.   C. K. Westbrook; M. Mehl; W. J. Pitz; M. Sjöberg, *Chemical kinetics of octane sensitivity in a spark-ignition engine*, Combustion and Flame   (2016)

20.   S. Kokjohn; R. Hanson; D. Splitter; R. Reitz, *Fuel reactivity controlled compression ignition (RCCI): a pathway to controlled high-efficiency clean combustion*, International Journal of Engine Research 12 (3) (2011) 209-226

21.   E. Ranzi, *A wide-range kinetic modeling study of oxidation and combustion of transportation fuels and surrogate mixtures*, Energy & fuels 20 (3) (2006) 1024-1032

22.   W. J. Pitz; N. P. Cernansky; F. L. Dryer; F. Egolfopoulos; J. Farrell; D. Friend; H. Pitsch, in: SAE Technical Paper: 2007.

23.   K. V. Puduppakkam; C. V. Naik; C. Wang; E. Meeks, in: SAE Technical Paper: 2010.

24.   S. Dooley; S. H. Won; M. Chaos; J. Heyne; Y. Ju; F. L. Dryer; K. Kumar; C.-J. Sung; H. Wang; M. A. Oehlschlaeger, *A jet fuel surrogate formulated by real fuel properties*, Combustion and Flame 157 (12) (2010) 2333-2339

25.   A. Violi; S. Yan; E. G. Eddings; A. Sarofim; S. Granata; T. Faravelli; E. Ranzi, *Experimental formulation and kinetic model for JP-8 surrogate mixtures*, Combustion Science and Technology 174 (11-12) (2002) 399-417

26.   B. Gauthier; D. Davidson; R. Hanson, *Shock tube determination of ignition delay times in full-blend and surrogate fuel mixtures*, Combustion and Flame 139 (4) (2004) 300-311

27.   C. V. Naik; W. J. Pitz; C. K. Westbrook; M. Sjöberg; J. E. Dec; J. Orme; H. J. Curran; J. M. Simmie, in: SAE Technical Paper: 2005.

28.   G. Vanhove; G. Petit; R. Minetti, *Experimental study of the kinetic interactions in the low-temperature autoignition of hydrocarbon binary mixtures and a surrogate fuel*, Combustion and Flame 145 (3) (2006) 521-532

29.   F. M. Haas; M. Chaos; F. L. Dryer, *Low and intermediate temperature oxidation of ethanol and ethanol–PRF blends: An experimental and modeling study*, Combustion and flame 156 (12) (2009) 2346-2350

30.   D. B. Lenhert; D. L. Miller; N. P. Cernansky; K. G. Owens, *The oxidation of a gasoline surrogate in the negative temperature coefficient region*, Combustion and flame 156 (3) (2009) 549-564

31.   L. Sileghem; V. Alekseev; J. Vancoillie; E. Nilsson; S. Verhelst; A. Konnov, *Laminar burning velocities of primary reference fuels and simple alcohols*, Fuel 115 (2014) 32-40

32.   M. Fikri; J. Herzler; R. Starke; C. Schulz; P. Roth; G. Kalghatgi, *Autoignition of gasoline surrogates mixtures at intermediate temperatures and high pressures*, Combustion and flame 152 (1) (2008) 276-281

33.   P. Saisirirat; C. Togbé; S. Chanchaona; F. Foucher; C. Mounaim-Rousselle; P. Dagaut, *Auto-ignition and combustion characteristics in HCCI and JSR using 1-butanol/n-heptane and ethanol/n-heptane blends*, Proceedings of the Combustion Institute 33 (2) (2011) 3007-3014

34.   K. Kumar; Y. Zhang; C.-J. Sung; W. J. Pitz, *Autoignition response of n-butanol and its blends with primary reference fuel constituents of gasoline*, Combustion and Flame 162 (6) (2015) 2466-2479

35.   E. Agbro; A. S. Tomlin; M. Lawes; S. Park; S. M. Sarathy, *The influence of n-butanol blending on the ignition delay times of gasoline and its surrogate at high pressures*, Fuel 187 (2017) 211-219

36.   C. K. Westbrook; C. V. Naik; O. Herbinet; W. J. Pitz; M. Mehl; S. M. Sarathy; H. J. Curran, *Detailed chemical kinetic reaction mechanisms for soy and rapeseed biodiesel fuels*, Combustion and Flame 158 (4) (2011) 742-755

37.   T. Lu; C. K. Law, *Toward accommodating realistic fuel chemistry in large-scale computations*, Progress in Energy and Combustion Science 35 (2) (2009) 192-215

38.   E. Ranzi; T. Faravelli; P. Gaffuri; A. Sogaro, *Low-temperature combustion: automatic generation of primary oxidation reactions and lumping procedures*, Combustion and flame 102 (1) (1995) 179-192

39.   A. Stagni. Implementation of detailed chemistry in large-scale combustion computations. PhD Thesis, Politecnico di Milano, 2016.

40.   E. Ranzi; A. Frassoldati; A. Stagni; M. Pelucchi; A. Cuoci; T. Faravelli, *Reduced kinetic schemes of complex reaction systems: fossil and biomass-derived transportation fuels*, International Journal of Chemical Kinetics 46 (9) (2014) 512-542

41.   A. Stagni; A. Cuoci; A. Frassoldati; T. Faravelli; E. Ranzi, *Lumping and reduction of detailed kinetic schemes: an effective coupling*, Industrial & Engineering Chemistry Research 53 (22) (2013) 9004-9016

42.   R. D. Reitz, *Directions in internal combustion engine research*, Combustion and Flame 1 (160) (2013) 1-8

43.   M. Dente; E. Ranzi; A. Goossens, *Detailed prediction of olefin yields from hydrocarbon pyrolysis through a fundamental simulation model (SPYRO)*, Computers & Chemical Engineering 3 (1-4) (1979) 61-75

44.   E. Ranzi; M. Dente; S. Pierucci; G. Biardi, *Initial product distributions from pyrolysis of normal and branched paraffins*, Industrial & Engineering Chemistry Fundamentals 22 (1) (1983) 132-139

45.   P. A. Dirac in: *Quantum mechanics of many-electron systems*, Proceedings of the Royal Society of London A: Mathematical, Physical and Engineering Sciences, 1929; The Royal Society: 1929; pp 714-733.

46. M. Frisch; G. Trucks; H. B. Schlegel; G. Scuseria; M. Robb; J. Cheeseman; G. Scalmani; V. Barone; B. Mennucci; G. Petersson, *Gaussian 09, Revision A. 02, Gaussian*, Inc., Wallingford, CT 200 (2009)

47. H.-J. Werner; P. Knowles; G. Knizia; F. Manby; M. Schütz; P. Celani; T. Korona; R. Lindh; A. Mitrushenkov; G. Rauhut, *MOLPRO, version 2010.1, a package of ab initio programs*, See http://www. molpro. net (2010)

48. S. J. Klippenstein, *From Theoretical Reaction Dynamics to Chemical Modeling of Combustion*, Proceedings of the Combustion Institute in press (2016)

49. S. W. Benson; J. H. Buss, *Additivity rules for the estimation of molecular properties. Thermodynamic properties*, The Journal of Chemical Physics 29 (3) (1958) 546-572

50. S. W. Benson, Thermochemical kinetics, Wiley, 1976, p.^pp.

51. M. Dente; S. Pierucci; E. Ranzi; G. Bussani, *New improvements in modeling kinetic schemes for hydrocarbons pyrolysis reactors*, Chemical engineering science 47 (9) (1992) 2629-2634

52. E. Ranzi; M. Dente; T. Faravelli; G. Pennati, *Prediction of kinetic parameters for hydrogen abstraction reactions*, Combustion science and technology 95 (1-6) (1993) 1-50

53. E. Ranzi; P. Gaffuri; T. Faravelli; P. Dagaut, *A wide-range modeling study of n-heptane oxidation*, Combustion and Flame 103 (1) (1995) 91-106

54. H. J. Curran; P. Gaffuri; W. J. Pitz; C. K. Westbrook, *A comprehensive modeling study of n-heptane oxidation*, Combustion and flame 114 (1) (1998) 149-177

55. J. Bugler; K. P. Somers; E. J. Silke; H. J. Curran, *Revisiting the kinetics and thermodynamics of the low-temperature oxidation pathways of alkanes: a case study of the three pentane isomers*, The Journal of Physical Chemistry A 119 (28) (2015) 7510-7527

56. A. S. Tomlin; T. Turányi; M. J. Pilling, *Mathematical tools for the construction, investigation and reduction of combustion mechanisms*, Comprehensive chemical kinetics 35 (1997) 293-437

57. F. Di Maio; P. Lignola, *KING, a kinetic network generator*, Chemical engineering science 47 (9-11) (1992) 2713-2718

58. W. H. A. Green, Joshua W.; Buesser, Beat A.; Ashcraft, Robert W.; Beran, Gregory J.; Class, Caleb A.; Gao, Connie; Goldsmith, C. Franklin; Harper, Michael R.; Jalan, Amrit; Keceli, Murat; Magoon, Gregory R.; Matheu, David M.; Merchant, Shamel S.; Mo, Jeffrey D.; Petway, Sarah; Raman, Sumathy; Sharma, Sandeep; Song, Jing; Suleymanov, Yury; Van Geem, Kevin M.; Wen, John; West, Richard H.; Wong, Andrew; Yelvington, Paul E.; Yee, Nathan; Yu, Joanna;, in: *http://rmg.sourceforge.net/*, 2013.

59. V. Warth; F. Battin-Leclerc; R. Fournet; P.-A. Glaude; G.-M. Côme; G. Scacchi, *Computer based generation of reaction mechanisms for gas-phase oxidation*, Computers & chemistry 24 (5) (2000) 541-560

60. E. S. Blurock, *Detailed mechanism generation. 2. Aldehydes, ketones, and olefins*, Journal of chemical information and computer sciences 44 (4) (2004) 1348-1357

61. L. J. Broadbelt; S. M. Stark; M. T. Klein, *Computer generated pyrolysis modeling: on-the-fly generation of species, reactions, and rates*, Industrial & Engineering Chemistry Research 33 (4) (1994) 790-799

62. C. Chevalier; J. Warnatz; H. Melenk, *Automatic generation of reaction mechanisms for the description of the oxidation of higher hydrocarbons*, Berichte der Bunsengesellschaft für physikalische Chemie 94 (11) (1990) 1362-1367

63. E. Ranzi; T. Faravelli; P. Gaffuri; E. Garavaglia; A. Goldaniga, *Primary pyrolysis and oxidation reactions of linear and branched alkanes*, Industrial & engineering chemistry research 36 (8) (1997) 3336-3344

64. E. Ranzi; A. Frassoldati; S. Granata; T. Faravelli, *Wide-range kinetic modeling study of the pyrolysis, partial oxidation, and combustion of heavy n-alkanes*, Industrial & engineering chemistry research 44 (14) (2005) 5170-5183

65. *Chemkin-Pro 15101*, Reaction Design, San Diego, CA (2010)

66. A. Cuoci; A. Frassoldati; T. Faravelli; E. Ranzi, *OpenSMOKE++: An object-oriented framework for the numerical modeling of reactive systems with detailed kinetic mechanisms*, Computer Physics Communications 192 (2015) 237-264

67. H. Wang; D. A. Sheen, *Combustion kinetic model uncertainty quantification, propagation and minimization*, Progress in Energy and Combustion Science 47 (2015) 1-31

68.   A. S. Tomlin, *The role of sensitivity and uncertainty analysis in combustion modelling*, Proceedings of the Combustion Institute 34 (1) (2013) 159-176

69.   W. H. Green, *Predictive kinetics: a new approach for the 21st century*, Advances in Chemical Engineering 32 (2007) 1-313

70.   C. Olm; I. G. Zsély; R. Pálvölgyi; T. Varga; T. Nagy; H. J. Curran; T. Turányi, *Comparison of the performance of several recent hydrogen combustion mechanisms*, Combustion and Flame 161 (9) (2014) 2219-2234

71.   M. Frenklach, *Transforming data into knowledge—process informatics for combustion chemistry*, Proceedings of the combustion Institute 31 (1) (2007) 125-140

72.   E. Ranzi; C. Cavallotti; A. Cuoci; A. Frassoldati; M. Pelucchi; T. Faravelli, *New reaction classes in the kinetic modeling of low temperature oxidation of n-alkanes*, Combustion and flame 162 (5) (2015) 1679-1691

73.   M. Pelucchi; M. Bissoli; C. Cavallotti; A. Cuoci; T. Faravelli; A. Frassoldati; E. Ranzi; A. Stagni, *Improved kinetic model of the low-temperature oxidation of n-heptane*, Energy & Fuels 28 (11) (2014) 7178-7193

74.   M. Bernardi; M. Pelucchi; A. Stagni; L. Sangalli; A. Cuoci; A. Frassoldati; P. Secchi; T. Faravelli, *Curve matching, a generalized framework for models/experiments comparison: An application to n-heptane combustion kinetic mechanisms*, Combustion and Flame 168 (2016) 186-203

75.   D. Nativel; M. Pelucchi; A. Frassoldati; A. Comandini; A. Cuoci; E. Ranzi; N. Chaumeix; T. Faravelli, *Laminar flame speeds of pentanol isomers: An experimental and modeling study*, Combustion and Flame 166 (2016) 1-18

76.   M. Pelucchi; C. Cavallotti; E. Ranzi; A. Frassoldati; T. Faravelli, *Relative Reactivity of Oxygenated Fuels: Alcohols, Aldehydes, Ketones, and Methyl Esters*, Energy & Fuels 30 (10) (2016) 8665-8679

77.   M. Pelucchi; E. Ranzi; A. Frassoldati; T. Faravelli, *Alkyl radicals rule the low temperature oxidation of long chain aldehydes*, Proceedings of the Combustion Institute (2016)

78.   M. Pelucchi; K. P. Somers; K. Yasunaga; U. Burke; A. Frassoldati; E. Ranzi; H. J. Curran; T. Faravelli, *An experimental and kinetic modeling study of the pyrolysis and oxidation of n-C 3 C 5 aldehydes in shock tubes*, Combustion and Flame 162 (2) (2015) 265-286

79.   C. K. Westbrook; F. L. Dryer, *Simplified reaction mechanisms for the oxidation of hydrocarbon fuels in flames*, Combustion science and technology 27 (1-2) (1981) 31-43

80.   M. J. Pilling; P. W. Seakins, Reaction kinetics, Oxford University Press, 1996, p.^pp.

81.   P. W. Atkins; R. S. Friedman, Molecular quantum mechanics, Oxford university press, 2011, p.^pp.

82.   R. G. Gilbert; S. C. Smith, Theory of unimolecular and recombination reactions, Blackwell Scientific Publications; Publishers' Business Services [distributor], 1990, p.^pp.

83.   J. Warnatz; U. Maas; R. W. Dibble; J. Warnatz, Combustion, Springer, 2001, p.^pp.

84.   G. Dixon-Lewis; P. Marshall; B. Ruscic; A. Burcat; E. Goos; A. Cuoci; A. Frassoldati; T. Faravelli; P. Glarborg, *Inhibition of hydrogen oxidation by HBr and Br 2*, Combustion and Flame 159 (2) (2012) 528-540

85.   J. H. Van't Hoff, Etudes de dynamique chimique, Muller, 1884, p.^pp.

86.   S. Arrhenius, *On the reaction rate of the inversion of non-refined sugar upon souring*, Z. Phys. Chem 4 (1889) 226-248

87.   F. Lindemann; S. Arrhenius; I. Langmuir; N. Dhar; J. Perrin; W. M. Lewis, *Discussion on "the radiation theory of chemical action"*, Trans. Faraday Soc. 17 (1922) 598-606

88.   M. Evans; M. Polanyi, *Further considerations on the thermodynamics of chemical equilibria and reaction rates*, Transactions of the Faraday Society 32 (1936) 1333-1360

89.   H.-H. Carstensen; A. M. Dean, *Development of detailed kinetic models for the thermal conversion of biomass via first principle methods and rate estimation rules*, Computational Modeling in Lignocellulosic Biofuel Production, Oxford University Press, Oxford, UK 201 (2010)

90.   H. Curran, *Rate constant estimation for C1 to C4 alkyl and alkoxyl radical decomposition*, International journal of chemical kinetics 38 (4) (2006) 250-275

91.   E. R. Ritter; J. W. Bozzelli, *THERM: Thermodynamic property estimation for gas phase radicals and molecules*, International Journal of Chemical Kinetics 23 (9) (1991) 767-778

92.   C. Muller; V. Michel; G. Scacchi; G.-M. Côme, *THERGAS: a computer program for the evaluation of thermochemical data of molecules and free radicals in the gas phase*, Journal de chimie physique 92 (5) (1995) 1154-1178

93.   J. M. Simmie; K. P. Somers, *Benchmarking Compound Methods (CBS-QB3, CBS-APNO, G3, G4, W1BD) against the Active Thermochemical Tables: A Litmus Test for Cost-Effective Molecular Formation Enthalpies*, The Journal of Physical Chemistry A 119 (28) (2015) 7235-7246

94.   K. P. Somers; J. M. Simmie, *Benchmarking Compound Methods (CBS-QB3, CBS-APNO, G3, G4, W1BD) against the Active Thermochemical Tables: Formation Enthalpies of Radicals*, The Journal of Physical Chemistry A 119 (33) (2015) 8922-8933

95.   M. E. Harding; J. Vázquez; B. Ruscic; A. K. Wilson; J. Gauss; J. F. Stanton, *High-accuracy extrapolated ab initio thermochemistry. III. Additional improvements and overview*, The Journal of chemical physics 128 (11) (2008) 114111

96.   B. Ruscic; R. E. Pinzon; M. L. Morton; G. von Laszevski; S. J. Bittner; S. G. Nijsure; K. A. Amin; M. Minkoff; A. F. Wagner, *Introduction to active thermochemical tables: Several "key" enthalpies of formation revisited*, The Journal of Physical Chemistry A 108 (45) (2004) 9979-9997

97.   B. Ruscic; R. E. Pinzon; G. Von Laszewski; D. Kodeboyina; A. Burcat; D. Leahy; D. Montoy; A. F. Wagner in: *Active Thermochemical Tables: thermochemistry for the 21st century*, Journal of Physics: Conference Series, 2005; IOP Publishing: 2005; p 561.

98.   A. Burcat; B. Ruscic, Third millenium ideal gas and condensed phase thermochemical database for combustion with updates from active thermochemical tables, Argonne National Laboratory Argonne, IL, 2005, p.^pp.

99.   B. Ruscic, *Uncertainty quantification in thermochemistry, benchmarking electronic structure computations, and Active Thermochemical Tables*, International Journal of Quantum Chemistry 114 (17) (2014) 1097-1101

100.   S. Burke; J. Simmie; H. Curran, *Critical Evaluation of Thermochemical Properties of C1–C4 Species: Updated Group-Contributions to Estimate Thermochemical Properties*, Journal of Physical and Chemical Reference Data 44 (1) (2015) 013101

101.   E. Ranzi; A. Frassoldati; R. Grana; A. Cuoci; T. Faravelli; A. Kelley; C. Law, *Hierarchical and comparative kinetic modeling of laminar flame speeds of hydrocarbon and oxygenated fuels*, Progress in Energy and Combustion Science 38 (4) (2012) 468-501

102.   J. O. Hirschfelder; C. F. Curtiss; R. B. Bird; M. G. Mayer, Molecular theory of gases and liquids, Wiley New York, 1954, p.^pp.

103.   R. B. Bird, *Transport phenomena*, Applied Mechanics Reviews 55 (1) (2002) R1-R4

104.   J. E. Lennard-Jones, *Cohesion*, Proceedings of the Physical Society 43 (5) (1931) 461

105.   W. H. Stockmayer, *Second virial coefficients of polar gases*, The Journal of Chemical Physics 9 (5) (1941) 398-402

106.   N. J. Brown; L. A. Bastien; P. N. Price, *Transport properties for combustion modeling*, Progress in Energy and Combustion Science 37 (5) (2011) 565-582

107.   C. Ji; E. Dames; Y. L. Wang; H. Wang; F. N. Egolfopoulos, *Propagation and extinction of premixed C 5–C 12 n-alkane flames*, Combustion and Flame 157 (2) (2010) 277-287

108.   S. Gordon; B. McBride, *Computer program for calculation of complex equilibrium composition, rocket performance, incident and reflected shocks and Chapman-Jouguet detonations*, NASA SP-273 168 (1971)

109.   P. Sabia; M. L. Lavadera; P. Giudicianni; G. Sorrentino; R. Ragucci; M. de Joannon, *CO 2 and H 2 O effect on propane auto-ignition delay times under mild combustion operative conditions*, Combustion and Flame 162 (3) (2015) 533-543

110.   M. P. Burke; R. Song, *Evaluating Mixture Rules for Multi-Component Pressure Dependence: H+ O 2 (+ M)= HO 2 (+ M)*, Proceedings of the Combustion Institute   (2016)

111.   E. Ranzi; A. Sogaro; P. Gaffuri; G. Pennati; C. Westbrook; W. Pitz, *A new comprehensive reaction mechanism for combustion of hydrocarbon fuels*, Combustion and Flame 99 (2) (1994) 201-211

112.   M. Bissoli; A. Cuoci; A. Frassoldati; T. Faravelli; E. Ranzi; T. Lucchini; G. D'Errico; F. Contino, *Detailed kinetic analysis of HCCI combustion using a new multi-zone model and CFD simulations*, SAE International Journal of Engines 6 (2013-24-0021) (2013) 1594-1609

113.   M. Bissoli; A. Frassoldati; A. Cuoci; E. Ranzi; M. Mehl; T. Faravelli, *A new predictive multi-zone model for HCCI engine combustion*, Applied Energy 178 (2016) 826-843

114.   A. Frassoldati; A. Cuoci; T. Faravelli; E. Ranzi; S. Colantuoni; P. D. Martino; G. Cinque, *Experimental and modeling study of a low NOx combustor for aero-engine turbofan*, Combustion Science and Technology 181 (3) (2009) 483-495

115.   A. Cuoci; A. Frassoldati; T. Faravelli; E. Ranzi, *Numerical modeling of auto-ignition of isolated fuel droplets in microgravity*, Proceedings of the Combustion Institute 35 (2) (2015) 1621-1627

116.   A. Cuoci; M. Mehl; G. Buzzi-Ferraris; T. Faravelli; D. Manca; E. Ranzi, *Autoignition and burning rates of fuel droplets under microgravity*, Combustion and Flame 143 (3) (2005) 211-226

117.   A. Goossens; M. Dente; E. Ranzi, *Improve steam cracker operation*, Hydrocarbon processing 57 (9) (1978) 227-236

118.   L. Cai; H. Pitsch, *Optimized chemical mechanism for combustion of gasoline surrogate fuels*, Combustion and Flame 162 (5) (2015) 1623-1637

119.   H. Hakka; R. Cracknell; A. Pekalski; P.-A. Glaude; F. Battin-Leclerc, *Experimental and modeling study of ultra-rich oxidation of n-heptane*, Fuel 144 (2015) 358-368

120.   L. Seidel; K. Moshammer; X. Wang; T. Zeuch; K. Kohse-Höinghaus; F. Mauss, *Comprehensive kinetic modeling and experimental study of a fuel-rich, premixed n-heptane flame*, Combustion and Flame 162 (5) (2015) 2045-2058

121.   R. Sivaramakrishnan; M.-C. Su; J. Michael; S. Klippenstein; L. Harding; B. Ruscic, *Rate constants for the thermal decomposition of ethanol and its bimolecular reactions with OH and D: Reflected shock tube and theoretical studies*, The Journal of Physical Chemistry A 114 (35) (2010) 9425-9439

122.   J. Badra; A. Elwardany; A. Farooq, *Shock tube measurements of the rate constants for seven large alkanes+ OH*, Proceedings of the Combustion Institute 35 (1) (2015) 189-196

123.   D. M. Matheu; W. H. Green; J. M. Grenda, *Capturing pressure-dependence in automated mechanism generation: Reactions through cycloalkyl intermediates*, International journal of chemical kinetics 35 (3) (2003) 95-119

124.   J. A. Miller; S. J. Klippenstein; S. H. Robertson, *A theoretical analysis of the reaction between ethyl and molecular oxygen*, Proceedings of the Combustion Institute 28 (2) (2000) 1479-1486

125.   J. D. DeSain; S. J. Klippenstein; J. A. Miller; C. A. Taatjes, *Measurements, theory, and modeling of OH formation in ethyl+ O2 and propyl+ O2 reactions*, The Journal of Physical Chemistry A 107 (22) (2003) 4415-4427

126.   C. F. Goldsmith; W. H. Green; S. J. Klippenstein, *Role of O2+ QOOH in low-temperature ignition of propane. 1. Temperature and pressure dependent rate coefficients*, The Journal of Physical Chemistry A 116 (13) (2012) 3325-3346

127.   J. Bugler; B. Marks; O. Mathieu; R. Archuleta; A. Camou; C. Grégoire; K. A. Heufer; E. L. Petersen; H. J. Curran, *An ignition delay time and chemical kinetic modeling study of the pentane isomers*, Combustion and Flame 163 (2016) 138-156

128.   J. Bugler; A. Rodriguez; O. Herbinet; F. Battin-Leclerc; C. Togbé; G. Dayma; P. Dagaut; H. J. Curran, *An experimental and modelling study of n-pentane oxidation in two jet-stirred reactors: The importance of pressure-dependent kinetics and new reaction pathways*, Proceedings of the Combustion Institute (2016)

129.   S. M. Villano; L. K. Huynh; H.-H. Carstensen; A. M. Dean, *High-pressure rate rules for alkyl+ O2 reactions. 1. The dissociation, concerted elimination, and isomerization channels of the alkyl peroxy radical*, The Journal of Physical Chemistry A 115 (46) (2011) 13425-13442

130.   A. Miyoshi, *Molecular size dependent falloff rate constants for the recombination reactions of alkyl radicals with O2 and implications for simplified kinetics of alkylperoxy radicals*, International Journal of Chemical Kinetics 44 (1) (2012) 59-74

131.   L. K. Huynh; H.-H. Carstensen; A. M. Dean, *Detailed modeling of low-temperature propane oxidation: 1. The role of the propyl+ O2 reaction*, The Journal of Physical Chemistry A 114 (24) (2010) 6594-6607

132.   C. Y. Sheng; J. W. Bozzelli; A. M. Dean; A. Y. Chang, *Detailed kinetics and thermochemistry of C2H5+ O2: reaction kinetics of the chemically-activated and stabilized CH3CH2OO adduct*, The Journal of Physical Chemistry A 106 (32) (2002) 7276-7293

133.   H. Sun; J. W. Bozzelli, *Thermochemical and kinetic analysis on the reactions of neopentyl and hydroperoxy-neopentyl radicals with oxygen: Part I. OH and initial stable HC product formation*, The Journal of Physical Chemistry A 108 (10) (2004) 1694-1711

134.   J. A. Miller; S. J. Klippenstein, *The reaction between ethyl and molecular oxygen II: Further analysis*, International Journal of Chemical Kinetics 33 (11) (2001) 654-668

135.   J. D. DeSain; C. A. Taatjes; J. A. Miller; S. J. Klippenstein; D. K. Hahn, *Infrared frequency-modulation probing of product formation in alkyl+ O 2 reactions. Part IV. Reactions of propyl and butyl radicals with O 2*, Faraday discussions 119 (2002) 101-120

136.   J. Griffiths; S. Scott, *Thermokinetic interactions: Fundamentals of spontaneous ignition and cool flames*, Progress in energy and combustion science 13 (3) (1987) 161-197

137.   P. Lignola; E. Reverchon, *Cool flames*, Progress in energy and combustion science 13 (1) (1987) 75-96

138.   K. Zhang; C. Banyon; J. Bugler; H. J. Curran; A. Rodriguez; O. Herbinet; F. Battin-Leclerc; C. B'Chir; K. A. Heufer, *An updated experimental and kinetic modeling study of n-heptane oxidation*, Combustion and Flame 172 (2016) 116-135

139.   I. O. Antonov; J. Zádor; B. Rotavera; E. Papajak; D. L. Osborn; C. A. Taatjes; L. Sheps, *Pressure-dependent competition among reaction pathways from first-and second-O2 additions in the low-temperature oxidation of tetrahydrofuran*, The Journal of Physical Chemistry A 120 (33) (2016) 6582-6595

140.   Z. Wang; S. M. Sarathy, *Third O 2 addition reactions promote the low-temperature auto-ignition of n-alkanes*, Combustion and Flame 165 (2016) 364-372

141.   Z. Wang; L. Zhang; K. Moshammer; D. M. Popolan-Vaida; V. S. B. Shankar; A. Lucassen; C. Hemken; C. A. Taatjes; S. R. Leone; K. Kohse-Höinghaus, *Additional chain-branching pathways in the low-temperature oxidation of branched alkanes*, Combustion and Flame 164 (2016) 386-396

142.   C. F. Goldsmith; M. P. Burke; Y. Georgievskii; S. J. Klippenstein, *Effect of non-thermal product energy distributions on ketohydroperoxide decomposition kinetics*, Proceedings of the Combustion Institute 35 (1) (2015) 283-290

143.   S. Sharma; S. Raman; W. H. Green, *Intramolecular hydrogen migration in alkylperoxy and hydroperoxyalkylperoxy radicals: accurate treatment of hindered rotors*, The Journal of Physical Chemistry A 114 (18) (2010) 5689-5701

144.   A. Miyoshi, *Systematic computational study on the unimolecular reactions of alkylperoxy (RO2), hydroperoxyalkyl (QOOH), and hydroperoxyalkylperoxy (O2QOOH) radicals*, The Journal of Physical Chemistry A 115 (15) (2011) 3301-3325

145.   R. Minetti; M. Carlier; M. Ribaucour; E. Therssen; L. Sochet in: *Comparison of oxidation and autoignition of the two primary reference fuels by rapid compression*, Symposium (International) on Combustion, 1996; Elsevier: 1996; pp 747-753.

146.   H. Ciezki; G. Adomeit, *Shock-tube investigation of self-ignition of n-heptane-air mixtures under engine relevant conditions*, Combustion and flame 93 (4) (1993) 421-433

147.   S. M. Villano; L. K. Huynh; H.-H. Carstensen; A. M. Dean, *High-pressure rate rules for alkyl+ O2 reactions. 2. The isomerization, cyclic ether formation, and β-scission reactions of hydroperoxy alkyl radicals*, The Journal of Physical Chemistry A 116 (21) (2012) 5068-5089

148.   J. Bugler; J. Power; H. J. Curran, *A theoretical study of cyclic ether formation reactions*, Proceedings of the Combustion Institute   (2016)

149.   O. Herbinet; B. Husson; Z. Serinyel; M. Cord; V. Warth; R. Fournet; P.-A. Glaude; B. Sirjean; F. Battin-Leclerc; Z. Wang, *Experimental and modeling investigation of the low-temperature oxidation of n-heptane*, Combustion and flame 159 (12) (2012) 3455-3471

150.   E. Silke. Influence of Fuel Structure on Combustion as Demonstrated by the Isomers of Heptane: a Rapid Compression Machine Study & Detailed Kinetic Modelling of n-Heptane. National University of Ireland, Galway, Galway, 2005.

151.   H. Huang; M. Fairweather; J. Griffiths; A. Tomlin; R. Brad, *A systematic lumping approach for the reduction of comprehensive kinetic models*, Proceedings of the Combustion Institute 30 (1) (2005) 1309-1316

152.   M. Dente; G. Bozzano; T. Faravelli; A. Marongiu; S. Pierucci; E. Ranzi, *Kinetic modelling of pyrolysis processes in gas and condensed phase*, Advances in chemical engineering 32 (2007) 51-166

153.   K. Zhang; C. Banyon; C. Togbé; P. Dagaut; J. Bugler; H. J. Curran, *An experimental and kinetic modeling study of n-hexane oxidation*, Combustion and Flame 162 (11) (2015) 4194-4207

154.   F. Jensen, Introduction to computational chemistry, John Wiley & Sons, 2013, p.^pp.

155.   E. Schrödinger, *An undulatory theory of the mechanics of atoms and molecules*, Physical Review 28 (6) (1926) 1049

156.   D. Hartree; W. Hartree, *Self-consistent field, with exchange, for beryllium*, Proceedings of the Royal Society of London. Series A, Mathematical and Physical Sciences 150 (869) (1935) 9-33

157.   J. C. Slater, *Note on Hartree's method*, Physical Review 35 (2) (1930) 210

158.   V. Fock, *Näherungsmethode zur Lösung des quantenmechanischen Mehrkörperproblems*, Zeitschrift für Physik 61 (1-2) (1930) 126-148

159.   M. Urban; J. Noga; S. J. Cole; R. J. Bartlett, *Towards a full CCSDT model for electron correlation*, The Journal of chemical physics 83 (8) (1985) 4041-4046

160.   K. Raghavachari; G. W. Trucks; J. A. Pople; M. Head-Gordon, *A fifth-order perturbation comparison of electron correlation theories*, Chemical Physics Letters 157 (6) (1989) 479-483

161.   P. J. Knowles; H.-J. Werner, *An efficient second-order MC SCF method for long configuration expansions*, Chemical physics letters 115 (3) (1985) 259-267

162.   H. J. Werner; P. J. Knowles, *A second order multiconfiguration SCF procedure with optimum convergence*, The Journal of chemical physics 82 (11) (1985) 5053-5063

163.   H.-J. Werner, *Third-order multireference perturbation theory The CASPT3 method*, Molecular Physics 89 (2) (1996) 645-661

164.   P. Celani; H.-J. Werner, *Multireference perturbation theory for large restricted and selected active space reference wave functions*, The Journal of Chemical Physics 112 (13) (2000) 5546-5557

165.   P. Hohenberg; W. Kohn, *Inhomogeneous electron gas*, Physical review 136 (3B) (1964) B864

166.   C. Lee; W. Yang; R. G. Parr, *Development of the Colle-Salvetti correlation-energy formula into a functional of the electron density*, Physical review B 37 (2) (1988) 785

167.   A. D. Becke, *Density-functional thermochemistry. III. The role of exact exchange*, The Journal of chemical physics 98 (7) (1993) 5648-5652

168.   Y. Zhao; D. G. Truhlar, *The M06 suite of density functionals for main group thermochemistry, thermochemical kinetics, noncovalent interactions, excited states, and transition elements: two new functionals and systematic testing of four M06-class functionals and 12 other functionals*, Theoretical Chemistry Accounts 120 (1-3) (2008) 215-241

169.   S. Grimme, *Semiempirical hybrid density functional with perturbative second-order correlation*, The Journal of chemical physics 124 (3) (2006) 034108

170.   S. Grimme; J. Antony; S. Ehrlich; H. Krieg, *A consistent and accurate ab initio parametrization of density functional dispersion correction (DFT-D) for the 94 elements H-Pu*, The Journal of chemical physics 132 (15) (2010) 154104

171.   J. A. Montgomery Jr; M. J. Frisch; J. W. Ochterski; G. A. Petersson, *A complete basis set model chemistry. VI. Use of density functional geometries and frequencies*, The Journal of chemical physics 110 (6) (1999) 2822-2827

172.   L. A. Curtiss; P. C. Redfern; K. Raghavachari, *Gaussian-4 theory*, The Journal of chemical physics 126 (8) (2007) 084108

173.   A. D. Boese; M. Oren; O. Atasoylu; J. M. Martin; M. Kállay; J. Gauss, *W3 theory: robust computational thermochemistry in the kJ/mol accuracy range*, The Journal of chemical physics 120 (9) (2004) 4129-4141

174.   J. M. Martin; G. de Oliveira, *Towards standard methods for benchmark quality ab initio thermochemistry—W1 and W2 theory*, The Journal of chemical physics 111 (5) (1999) 1843-1856

175.   Y. J. Bomble; J. Vázquez; M. Kállay; C. Michauk; P. G. Szalay; A. G. Császár; J. Gauss; J. F. Stanton, *High-accuracy extrapolated ab initio thermochemistry. II. Minor improvements to the protocol and a vital simplification*, The Journal of chemical physics 125 (6) (2006) 064108

176.   A. Tajti; P. G. Szalay; A. G. Császár; M. Kállay; J. Gauss; E. F. Valeev; B. A. Flowers; J. Vázquez; J. F. Stanton, *HEAT: High accuracy extrapolated ab initio thermochemistry*, The Journal of chemical physics 121 (23) (2004) 11599-11613

177.   S. J. Klippenstein Ab Initio theoretical chemical kinetics. https://www.princeton.edu/cefrc/combustion-summer-school/archived-programs/2010-summer-school/lecture-notes/

178.   J. R. Barker, *Multiple-Well, multiple-path unimolecular reaction systems. I. MultiWell computer program suite*, International Journal of Chemical Kinetics 33 (4) (2001) 232-245

179.   D. G. Truhlar, *A simple approximation for the vibrational partition function of a hindered internal rotation*, Journal of computational chemistry 12 (2) (1991) 266-270

180.   P. Y. Ayala; H. B. Schlegel, *Identification and treatment of internal rotation in normal mode vibrational analysis*, The Journal of chemical physics 108 (6) (1998) 2314-2325

181.   Y.-Y. Chuang; D. G. Truhlar, *Statistical thermodynamics of bond torsional modes*, The Journal of Chemical Physics 112 (3) (2000) 1221-1228

182.   S. J. Klippenstein; V. S. Pande; D. G. Truhlar, *Chemical kinetics and mechanisms of complex systems: A perspective on recent theoretical advances*, Journal of the American Chemical Society 136 (2) (2014) 528-546

183.   H. Eyring, *The activated complex in chemical reactions*, The Journal of Chemical Physics 3 (2) (1935) 107-115

184.   M. G. Evans; M. Polanyi, *Some applications of the transition state method to the calculation of reaction velocities, especially in solution*, Transactions of the Faraday Society 31 (1935) 875-894

185.   J. Zheng; P. Seal; D. G. Truhlar, *Role of conformational structures and torsional anharmonicity in controlling chemical reaction rates and relative yields: butanal+ HO 2 reactions*, Chemical Science 4 (1) (2013) 200-212

186.   C. Eckart, *The penetration of a potential barrier by electrons*, Physical Review 35 (11) (1930) 1303

187.   R. Marcus; M. E. Coltrin, *A new tunneling path for reactions such as H+ H2→ H2+ H*, The Journal of Chemical Physics 67 (6) (1977) 2609-2613

188.   W. H. Miller; N. C. Handy; J. E. Adams, *Reaction path Hamiltonian for polyatomic molecules*, The Journal of chemical physics 72 (1) (1980) 99-112

189.   R. T. Skodje; D. G. Truhlar; B. C. Garrett, *A general small-curvature approximation for transition-state-theory transmission coefficients*, The Journal of Physical Chemistry 85 (21) (1981) 3019-3023

190.   F. Leonori; N. Balucani; V. Nevrly; A. Bergeat; S. Falcinelli; G. Vanuzzo; P. Casavecchia; C. Cavallotti, *Experimental and Theoretical Studies on the Dynamics of the O (3P)+ Propene Reaction: Primary Products, Branching Ratios, and Role of Intersystem Crossing*, The Journal of Physical Chemistry C 119 (26) (2015) 14632-14652

191.   X. Li; A. W. Jasper; J. Zádor; J. A. Miller; S. J. Klippenstein, *Theoretical kinetics of O+ C 2 H 4*, Proceedings of the Combustion Institute (2016)

192.   M. Pelucchi; C. Cavallotti; E. Ranzi; A. Frassoldati; T. Faravelli, *Theoretical calculation of the rate coefficient for CH3Cl+M=CH3+Cl+M and kinetic modeling study of chloromethane pyrolysis and oxidation*, Proceedings of the Combustion Institute, not accepted, in preparation for re-submission (2016)

193.   O. K. Rice; H. C. Ramsperger, *Theories of unimolecular gas reactions at low pressures*, Journal of the American Chemical Society 49 (7) (1927) 1617-1629

194.   O. K. Rice; H. C. Ramsperger, *Theories of unimolecular gas reactions at low pressures. II*, Journal of the American Chemical Society 50 (3) (1928) 617-620

195.   L. Kassel, *Studies in homogeneous gas reactions. II. Introduction of quantum theory*, The Journal of Physical Chemistry 32 (7) (1928) 1065-1079

196.   R. Marcus, *Unimolecular dissociations and free radical recombination reactions*, The Journal of Chemical Physics 20 (3) (1952) 359-364

197.   R. Marcus; O. Rice, *The Kinetics of the Recombination of Methyl Radicals and Iodine Atoms*, The Journal of Physical Chemistry 55 (6) (1951) 894-908

198.   G. Whitten; B. Rabinovitch, *Accurate and Facile Approximation for Vibrational Energy-Level Sums*, The Journal of Chemical Physics 38 (10) (1963) 2466-2473

199.   S. E. Stein; B. Rabinovitch, *Accurate evaluation of internal energy level sums and densities including anharmonic oscillators and hindered rotors*, The Journal of Chemical Physics 58 (6) (1973) 2438-2445

200.   G. Whitten; B. Rabinovitch, *Approximation for Rotation—Vibration Energy Level Sums*, The Journal of Chemical Physics 41 (6) (1964) 1883-1883

201.   T. Beyer; D. Swinehart, *Algorithm 448: number of multiply-restricted partitions*, Communications of the ACM 16 (6) (1973) 379

202.   A. P. Penner; W. Forst, *Analytic solution of relaxation in a system with exponential transition probabilities*, The Journal of Chemical Physics 67 (11) (1977) 5296-5307

203.   Y. Georgievskii; J. A. Miller; M. P. Burke; S. J. Klippenstein, *Reformulation and solution of the master equation for multiple-well chemical reactions*, The Journal of Physical Chemistry A 117 (46) (2013) 12146-12154

204.   Y. Georgievskii; S. J. Klippenstein, *Transition state theory for multichannel addition reactions: Multifaceted dividing surfaces*, The Journal of Physical Chemistry A 107 (46) (2003) 9776-9781

205.   Y. Georgievskii; S. J. Klippenstein, *Variable reaction coordinate transition state theory: Analytic results and application to the C2H3+ H$\rightarrow$ C2H4 reaction*, The Journal of chemical physics 118 (12) (2003) 5442-5455

206.   S. J. Klippenstein, *A bond length reaction coordinate for unimolecular reactions. II. Microcanonical and canonical implementations with application to the dissociation of NCNO*, The Journal of chemical physics 94 (10) (1991) 6469-6482

207.   S. J. Klippenstein, *Variational optimizations in the Rice–Ramsperger–Kassel–Marcus theory calculations for unimolecular dissociations with no reverse barrier*, The Journal of chemical physics 96 (1) (1992) 367-371

208.   R. J. Kee; M. E. Coltrin; P. Glarborg, Chemically reacting flow: theory and practice, John Wiley & Sons, 2005, p.^pp.

209.   A. W. Jasper; J. A. Miller, *Collisional Energy Transfer in Unimolecular Reactions: Direct Classical Trajectories for CH4$\rightleftarrows$ CH3+ H in Helium*, The Journal of Physical Chemistry A 113 (19) (2009) 5612-5619

210.   A. W. Jasper; C. M. Oana; J. A. Miller, *"Third-body" collision efficiencies for combustion modeling: Hydrocarbons in atomic and diatomic baths*, Proceedings of the Combustion Institute 35 (1) (2015) 197-204

211.   D. R. Glowacki; C.-H. Liang; C. Morley; M. J. Pilling; S. H. Robertson, *MESMER: an open-source master equation solver for multi-energy well reactions*, The Journal of Physical Chemistry A 116 (38) (2012) 9545-9560

212.   A. Barbato; C. Seghi; C. Cavallotti, *An ab initio Rice-Ramsperger-Kassel-Marcus/master equation investigation of SiH4 decomposition kinetics using a kinetic Monte Carlo approach*, The Journal of chemical physics 130 (7) (2009) 074108

213.   S. Klippenstein; A. Wagner; R. Dunbar; D. Wardlaw; S. Robertson, *VARIFLEX, version 1.00*, Argonne National Laboratory, Argonne, IL   (1999)

214.   A. Chang; J. Bozzelli; A. Dean, *Kinetic analysis of complex chemical activation and unimolecular dissociation reactions using QRRK theory and the modified strong collision approximation*, Zeitschrift für Physikalische Chemie International journal of research in physical chemistry and chemical physics 214 (11/2000) (2000) 1533

215.   A. Dean, *Predictions of pressure and temperature effects upon radical addition and recombination reactions*, The Journal of Physical Chemistry 89 (21) (1985) 4600-4608

216.   K. A. Holbrook; M. J. Pilling; S. H. Robertson, Unimolecular reactions, Wiley, 1996, p.^pp.

217.   K. P. Somers. On the Pyrolysis and Combustion of Furans: Quantum Chemical, Statistical Rate Theory and Chemical Kinetic Modelling Studies. Ph. D, National University of Ireland Galway, 2014.

218.   Y. Zhang; K. P. Somers; M. Mehl; W. J. Pitz; R. F. Cracknell; H. J. Curran, *Probing the antagonistic effect of toluene as a component in surrogate fuel models at low temperatures and high pressures. A case study of toluene/dimethyl ether mixtures*, Proceedings of the Combustion Institute   (2016)

219.   K. P. Somers; R. F. Cracknell; H. J. Curran, *Simulating the Octane Appetite of SI Engines: The Influence of Chemical Mechanisms*)

220.   J. Zádor; C. A. Taatjes; R. X. Fernandes, *Kinetics of elementary reactions in low-temperature autoignition chemistry*, Progress in Energy and Combustion Science 37 (4) (2011) 371-421

221.   J. M. Simmie, *Detailed chemical kinetic models for the combustion of hydrocarbon fuels*, Progress in Energy and Combustion Science 29 (6) (2003) 599-634

222.   R. Pollard, *Comprehensive chemical kinetics*, by CH Bamford and CFH Tipper, Elsevier, New York 17 (1977) 249-367

223.   M. J. Pilling, Low-temperature combustion and autoignition, Elsevier, 1997, p.^pp.

224.   F. Battin-Leclerc; O. Herbinet; P.-A. Glaude; R. Fournet; Z. Zhou; L. Deng; H. Guo; M. Xie; F. Qi, *New experimental evidences about the formation and consumption of ketohydroperoxides*, Proceedings of the Combustion Institute 33 (1) (2011) 325-331

225.   O. Herbinet; F. Battin-Leclerc; S. Bax; H. Le Gall; P.-A. Glaude; R. Fournet; Z. Zhou; L. Deng; H. Guo; M. Xie, *Detailed product analysis during the low temperature oxidation of n-butane*, Physical Chemistry Chemical Physics 13 (1) (2011) 296-308

226.   O. Herbinet; B. Husson; Z. Serinyel; M. Cord; V. Warth; R. Fournet; P.-A. Glaude; B. Sirjean; F. Battin-Leclerc; Z. Wang, *Experimental and modeling investigation of the low-temperature oxidation of< i> n</i>-heptane*, Combustion and flame 159 (12) (2012) 3455-3471

227.   M. Cord; B. Husson; J. C. Lizardo Huerta; O. Herbinet; P.-A. Glaude; R. Fournet; B. Sirjean; F. Battin-Leclerc; M. Ruiz-Lopez; Z. Wang, *Study of the low temperature oxidation of propane*, The Journal of Physical Chemistry A 116 (50) (2012) 12214-12228

228.   M. Cord; B. Sirjean; R. Fournet; A. Tomlin; M. Ruiz-Lopez; F. d. r. Battin-Leclerc, *Improvement of the modeling of the low-temperature oxidation of n-butane: study of the primary reactions*, The Journal of Physical Chemistry A 116 (24) (2012) 6142-6158

229.   C. Bahrini; O. Herbinet; P.-A. Glaude; C. Schoemaecker; C. Fittschen; F. Battin-Leclerc, *Quantification of hydrogen peroxide during the low-temperature oxidation of alkanes*, Journal of the American Chemical Society 134 (29) (2012) 11944-11947

230.   C. Bahrini; P. Morajkar; C. Schoemaecker; O. Frottier; O. Herbinet; P.-A. Glaude; F. Battin-Leclerc; C. Fittschen, *Experimental and modeling study of the oxidation of n-butane in a jet stirred reactor using cw-CRDS measurements*, Physical Chemistry Chemical Physics 15 (45) (2013) 19686-19698

231.   P. Dagaut; M. Reuillon; M. Cathonnet, *Experimental study of the oxidation of< i> n</i>-heptane in a jet stirred reactor from low to high temperature and pressures up to 40 atm*, Combustion and flame 101 (1) (1995) 132-140

232.   R. Minetti; M. Carlier; M. Ribaucour; E. Therssen; L. Sochet, *A rapid compression machine investigation of oxidation and auto-ignition of< i> n</i>-Heptane: Measurements and modeling*, Combustion and flame 102 (3) (1995) 298-309

233.   H. Curran; P. Gaffuri; W. J. Pitz; C. K. Westbrook, *A comprehensive modeling study of n-heptane oxidation*, Combustion and flame 114 (1-2) (1998) 149-177

234.   J. Biet; M. H. Hakka; V. Warth; P.-A. Glaude; F. Battin-Leclerc, *Experimental and modeling study of the low-temperature oxidation of large alkanes*, Energy & Fuels 22 (4) (2008) 2258-2269

235.   C. Westbrook; W. Pitz; M. Mehl; H. Curran, *Detailed chemical kinetic reaction mechanisms for primary reference fuels for diesel cetane number and spark-ignition octane number*, Proceedings of the Combustion Institute 33 (1) (2011) 185-192

236.   S. Sarathy; C. Westbrook; M. Mehl; W. Pitz; C. Togbe; P. Dagaut; H. Wang; M. Oehlschlaeger; U. Niemann; K. Seshadri, *Comprehensive chemical kinetic modeling of the oxidation of 2-methylalkanes from C< sub> 7</sub> to C< sub> 20</sub>*, Combustion and flame 158 (12) (2011) 2338-2357

237.   C. K. Westbrook; J. Warnatz; W. J. Pitz in: *A detailed chemical kinetic reaction mechanism for the oxidation of iso-octane and< i> n</i>-heptane over an extended temperature range and its application to analysis of engine knock*, Symposium (international) on combustion, 1989; Elsevier: 1989; pp 893-901.

238.   F. Buda; R. Bounaceur; V. Warth; P.-A. Glaude; R. Fournet; F. Battin-Leclerc, *Progress toward a unified detailed kinetic model for the autoignition of alkanes from C< sub> 4</sub> to C< sub> 10</sub> between 600 and 1200 K*, Combustion and flame 142 (1) (2005) 170-186

239.   E. Ranzi; T. Faravelli; P. Gaffuri; G. Pennatti; A. Sogaro, *A wide range modeling study of propane and n-butane oxidation*, Combustion science and technology 100 (1-6) (1994) 299-330

240.   H. J. Curran; P. Gaffuri; W. Pitz; C. Westbrook, *A comprehensive modeling study of iso-octane oxidation*, Combustion and flame 129 (3) (2002) 253-280

241.   R. Fournet; F. Battin-Leclerc; P. Glaude; B. Judenherc; V. Warth; G. Come; G. Scacchi; A. Ristori; G. Pengloan; P. Dagaut, *The gas-phase oxidation of n-hexadecane*, International Journal of Chemical Kinetics 33 (10) (2001) 574-586

242.   C. K. Westbrook; W. J. Pitz; O. Herbinet; H. J. Curran; E. J. Silke, *A comprehensive detailed chemical kinetic reaction mechanism for combustion of< i> n</i>-alkane hydrocarbons from< i> n</i>-octane to< i> n</i>-hexadecane*, Combustion and flame 156 (1) (2009) 181-199

243.   E. Ranzi; A. Frassoldati; T. Faravelli; A. Cuoci, *Lumped kinetic modeling of the oxidation of isocetane (2, 2, 4, 4, 6, 8, 8-Heptamethylnonane) in a jet-stirred reactor (JSR)*, Energy & Fuels 23 (10) (2009) 5287-5289

244.   F. Battin-Leclerc; A. Konnov; J.-L. Jaffrezo; M. Legrand, *To better understand the formation of short-chain acids in combustion systems*, Combustion science and technology 180 (2) (2007) 343-370

245.   O. Herbinet; F. Battin-Leclerc, *Progress in Understanding Low-Temperature Organic Compound Oxidation Using a Jet-Stirred Reactor*, International Journal of Chemical Kinetics 46 (10) (2014) 619-639

246.   R. Atkinson; D. Baulch; R. Cox; J. Crowley; R. Hampson; R. Hynes; M. Jenkin; M. Rossi; J. Troe; I. Subcommittee, *Evaluated kinetic and photochemical data for atmospheric chemistry: Volume II–gas phase reactions of organic species*, Atmospheric Chemistry and Physics 6 (11) (2006) 3625-4055

247.   A. S. Hasson; G. S. Tyndall; J. J. Orlando, *A product yield study of the reaction of HO2 radicals with ethyl peroxy (C2H5O2), acetyl peroxy (CH3C (O) O2), and acetonyl peroxy (CH3C (O) CH2O2) radicals*, The Journal of Physical Chemistry A 108 (28) (2004) 5979-5989

248.   J. J. Orlando; G. S. Tyndall; T. J. Wallington, *The atmospheric chemistry of alkoxy radicals*, Chemical reviews 103 (12) (2003) 4657-4690

249.   A. Jalan; I. M. Alecu; R. n. Meana-Pañeda; J. Aguilera-Iparraguirre; K. R. Yang; S. S. Merchant; D. G. Truhlar; W. H. Green, *New pathways for formation of acids and carbonyl products in low-temperature oxidation: the korcek decomposition of γ-ketohydroperoxides*, Journal of the American Chemical Society 135 (30) (2013) 11100-11114

250.   E. Ranzi; A. Sogaro; P. Gaffuri; G. Pennati; T. Faravelli, *A wide range modeling study of methane oxidation*, Combustion Science and Technology 96 (4-6) (1994) 279-325

251.   J. M. Martin, *Ab initio total atomization energies of small molecules—towards the basis set limit*, Chemical physics letters 259 (5) (1996) 669-678

252.   D. E. Woon; T. H. Dunning Jr, *Gaussian basis sets for use in correlated molecular calculations. V. Core-valence basis sets for boron through neon*, The Journal of chemical physics 103 (11) (1995) 4572-4585

253.   M. Frisch; G. Trucks; H. Schlegel; G. Scuseria; M. Robb; J. Cheeseman; G. Scalmani; V. Barone; B. Mennucci; G. Petersson, in: Inc: 2009.

254.   H. Werner; P. Knowles; R. Lindh; F. Manby; M. Schütz, in: MOLPRO, version: 2008.

255.   C. Cavallotti; D. Polino; A. Frassoldati; E. Ranzi, *Analysis of Some Reaction Pathways Active during Cyclopentadiene Pyrolysis*, The Journal of Physical Chemistry A 116 (13) (2012) 3313-3324

256.   F. Battin-Leclerc; O. Herbinet, in: Personal Communication, 2014.

257.   P. Dagaut; M. Reuillon; M. Cathonnet, *Experimental study of the oxidation of n-heptane in a jet stirred reactor from low to high temperature and pressures up to 40 atm*, Combustion and Flame 101 (1) (1995) 132-140 http://dx.doi.org/10.1016/0010-2180(94)00184-T.

258.   E. Ranzi; P. Gaffuri; T. Faravelli; P. Dagaut, *A Wide-Range Modeling Study of N-Heptane Oxidation*, Combustion and Flame 103 (1-2) (1995) 91-106 Doi 10.1016/0010-2180(95)00091-J.

259.   H. Ciezki; G. Adomeit, *Shock-tube investigation of self-ignition of< i> n</i>-heptane-air mixtures under engine relevant conditions*, Combustion and flame 93 (4) (1993) 421-433

260.   H.-P. S. Shen; J. Steinberg; J. Vanderover; M. A. Oehlschlaeger, *A shock tube study of the ignition of n-heptane, n-decane, n-dodecane, and n-tetradecane at elevated pressures*, Energy & Fuels 23 (5) (2009) 2482-2489

261.   J. Herzler; L. Jerig; P. Roth, *Shock tube study of the ignition of lean< i> n</i>-heptane/air mixtures at intermediate temperatures and high pressures*, Proceedings of the Combustion Institute 30 (1) (2005) 1147-1153

262.   J. M. Smith; J. M. Simmie; H. J. Curran, *Autoignition of heptanes; experiments and modeling*, International journal of chemical kinetics 37 (12) (2005) 728-736

263.   D. Davidson; M. Oehlschlaeger; R. Hanson, *Methyl concentration time-histories during< i> iso</i>-octane and< i> n</i>-heptane oxidation and pyrolysis*, Proceedings of the Combustion Institute 31 (1) (2007) 321-328

264.   D. Davidson; Z. Hong; G. Pilla; A. Farooq; R. Cook; R. Hanson, *Multi-species time-history measurements during< i> n</i>-heptane oxidation behind reflected shock waves*, Combustion and flame 157 (10) (2010) 1899-1905

265.   B. Akih-Kumgeh; J. M. Bergthorson, *Comparative study of methyl butanoate and n-heptane high temperature autoignition*, Energy & Fuels 24 (4) (2010) 2439-2448

266.   E. J. Silke; H. J. Curran; J. M. Simmie, *The influence of fuel structure on combustion as demonstrated by the isomers of heptane: a rapid compression machine study*, Proceedings of the Combustion Institute 30 (2) (2005) 2639-2647

267.   S. Tanaka; F. Ayala; J. C. Keck, *A reduced chemical kinetic model for HCCI combustion of primary reference fuels in a rapid compression machine*, Combustion and flame 133 (4) (2003) 467-481

268.   J. Griffiths; P. Halford-Maw; C. Mohamed, *Spontaneous ignition delays as a diagnostic of the propensity of alkanes to cause engine knock*, Combustion and flame 111 (4) (1997) 327-337

269.   A. Cox; J. Griffiths; C. Mohamed; H. Curran; W. Pit; C. Westbrook in: *Extents of alkane combustion during rapid compression leading to single-and two-stage ignition*, Symposium (International) on Combustion, 1996; Elsevier: 1996; pp 2685-2692.

270.   D. Karwat; S. W. Wagnon; M. S. Wooldridge; C. K. Westbrook, *Low-temperature speciation and chemical kinetic studies of< i> n</i>-heptane*, Combustion and flame 160 (12) (2013) 2693-2706

271.   T. Held; A. Marchese; F. Dryer, *A semi-empirical reaction mechanism for n-heptane oxidation and pyrolysis*, Combustion Science and Technology 123 (1-6) (1997) 107-146

272.   P. Veloo; S. Jahangirian; F. Dryer in: *An experimental and kinetic modeling study of the two stage autoignition kinetic behavior of C 7, C 10, C 12, and C 14 n-alkanes*, Spring Technical Meeting, Central States Section of the Combustion Institute, 2012; 2012.

273.   S. Davis; C. Law, *Determination of and fuel structure effects on laminar flame speeds of C1 to C8 hydrocarbons*, Combustion Science and Technology 140 (1-6) (1998) 427-449

274.   K. Kumar; J. Freeh; C. Sung; Y. Huang, *Laminar flame speeds of preheated iso-octane/O2/N2 and n-heptane/O2/N2 mixtures*, Journal of propulsion and power 23 (2) (2007) 428-436

275.   Y. Huang; C. Sung; J. Eng, *Laminar flame speeds of primary reference fuels and reformer gas mixtures*, Combustion and flame 139 (3) (2004) 239-251

276.   A. Smallbone; W. Liu; C. Law; X. You; H. Wang, *Experimental and modeling study of laminar flame speed and non-premixed counterflow ignition of< i> n</i>-heptane*, Proceedings of the Combustion Institute 32 (1) (2009) 1245-1252

277.   P. Dirrenberger; P.-A. Glaude; R. Bounaceur; H. Le Gall; A. P. da Cruz; A. Konnov; F. Battin-Leclerc, *Laminar burning velocity of gasolines with addition of ethanol*, Fuel 115 (2014) 162-169

278.   J. P. Szybist; A. L. Boehman; D. C. Haworth; H. Koga, *Premixed ignition behavior of alternative diesel fuel-relevant compounds in a motored engine experiment*, Combustion and flame 149 (1) (2007) 112-128

279.   M. Tanabe; T. Bolik; C. Eigenbrod; H. Rath; J. Sato; M. Kono in: *Spontaneous ignition of liquid droplets from a view of non-homogeneous mixture formation and transient chemical reactions*, Symposium (International) on Combustion, 1996; Elsevier: 1996; pp 1637-1643.

280. S. Schnaubelt; O. Moriue; T. Coordes; C. Eigenbrod; H. Rath Zarm, *Detailed numerical simulations of the multistage self-ignition process of< i> n</i>-heptane, isolated droplets and their verification by comparison with microgravity experiments*, Proceedings of the Combustion Institute 28 (1) (2000) 953-960

281. E. Ranzi; C. Cavallotti; A. Cuoci; A. Frassoldati; M. Pelucchi; T. Faravelli, *New Reaction Classes in the Kinetic Modeling of Low Temperature Oxidation of n-alkanes.*, Combustion and flame (submitted) (2014)

282. M. S. Kurman; R. H. Natelson; N. P. Cernansky; D. L. Miller, *Speciation of the reaction intermediates from< i> n</i>-dodecane oxidation in the low temperature regime*, Proceedings of the Combustion Institute 33 (1) (2011) 159-166

283. P. Dagaut; M. Reuillon; M. Cathonnet, *High pressure oxidation of liquid fuels from low to high temperature. 1. n-Heptane and iso-Octane*, Combustion Science and Technology 95 (1-6) (1993) 233-260

284. A. Cuoci; A. Frassoldati; T. Faravelli; E. Ranzi in: *Low-temperature chemistry in auto-ignition of isolated droplets in microgravity conditions*, Proceedings of the Combustion Institute, 2014; 2014.

285. A. Kazakov; J. Conley; F. L. Dryer, *Detailed modeling of an isolated, ethanol droplet combustion under microgravity conditions*, Combustion and Flame 134 (4) (2003) 301-314

286. R. J. Hall, *The radiative source term for plane-parallel layers of reacting combustion gases*, Journal of Quantitative Spectroscopy and Radiative Transfer 49 (1993) 517-523

287. G. Buzzi-Ferraris; F. Manenti, *BzzMath: Library overview and recent advances in numerical methods*, Computer Aided Chemical Engineering 30 (2) (2012) 1312-1316

288. M. Yao; Z. Zheng; H. Liu, *Progress and recent trends in homogeneous charge compression ignition (HCCI) engines*, Progress in Energy and Combustion Science 35 (5) (2009) 398-437

289. C. K. Westbrook; Y. Mizobuchi; T. J. Poinsot; P. J. Smith; J. Warnatz, *Computational combustion*, Proceedings of the Combustion Institute 30 (1) (2005) 125-157

290. N. Komninos; C. Rakopoulos, *Modeling HCCI combustion of biofuels: A review*, Renewable and Sustainable Energy Reviews 16 (3) (2012) 1588-1610

291. M. Bissoli; A. Cuoci; A. Frassoldati; T. Faravelli; E. Ranzi; T. Lucchini; G. D'Errico; F. Contino, *Detailed Kinetic Analysis of HCCI Combustion Using a New Multi-Zone Model and CFD Simulations*, SAE International Journal of Engines 6 (3) (2013) 1594-1609

292. J. Andrae, *Comprehensive chemical kinetic modeling of toluene reference fuels oxidation*, Fuel 107 (2013) 740-748

293. J. C. Andrae; P. Björnbom; R. Cracknell; G. Kalghatgi, *Autoignition of toluene reference fuels at high pressures modeled with detailed chemical kinetics*, Combustion and Flame 149 (1) (2007) 2-24

294. W. Yuan; Y. Li; P. Dagaut; J. Yang; F. Qi, *Investigation on the pyrolysis and oxidation of toluene over a wide range conditions. I. Flow reactor pyrolysis and jet stirred reactor oxidation*, Combustion and Flame 162 (1) (2015) 3-21

295. W. Yuan; Y. Li; P. Dagaut; J. Yang; F. Qi, *Investigation on the pyrolysis and oxidation of toluene over a wide range conditions. II. A comprehensive kinetic modeling study*, Combustion and Flame 162 (1) (2015) 22-40

296. G. da Silva; J. W. Bozzelli, *Kinetic modeling of the benzyl+ HO 2 reaction*, Proceedings of the Combustion Institute 32 (1) (2009) 287-294

297. G. da Silva; J. W. Bozzelli, *Benzoxyl radical decomposition kinetics: Formation of benzaldehyde+ H, phenyl+ CH2O, and benzene+ HCO*, The Journal of Physical Chemistry A 113 (25) (2009) 6979-6986

298. G. da Silva; M. R. Hamdan; J. W. Bozzelli, *Oxidation of the benzyl radical: mechanism, thermochemistry, and kinetics for the reactions of benzyl hydroperoxide*, Journal of chemical theory and computation 5 (12) (2009) 3185-3194

299. R. Perry; R. Atkinson; J. N. Pitts Jr, *Kinetics and mechanism of the gas phase reaction of hydroxyl radicals with aromatic hydrocarbons over the temperature range 296-473 K*, The Journal of Physical Chemistry 81 (4) (1977) 296-304

300. F. Markert; P. Pagsberg, *UV spectra and kinetics of radicals produced in the gas phase reactions of Cl, F and OH with toluene*, Chemical physics letters 209 (5) (1993) 445-454

301. V. Vasudevan; D. F. Davidson; R. K. Hanson, *High-temperature measurements of the reactions of OH with toluene and acetone*, The Journal of Physical Chemistry A 109 (15) (2005) 3352-3359

302. F. Tully; A. Ravishankara; R. Thompson; J. Nicovich; R. Shah; N. Kreutter; P. Wine, *Kinetics of the reactions of hydroxyl radical with benzene and toluene*, The Journal of Physical Chemistry 85 (15) (1981) 2262-2269

303. R. Knispel; R. Koch; M. Siese; C. Zetzsch, *Adduct formation of OH radicals with benzene, toluene, and phenol and consecutive reactions of the adducts with NOx and O2*, Berichte der Bunsengesellschaft für physikalische Chemie 94 (11) (1990) 1375-1379

304. T. Seta; M. Nakajima; A. Miyoshi, *High-temperature reactions of OH radicals with benzene and toluene*, The Journal of Physical Chemistry A 110 (15) (2006) 5081-5090

305. A. G. Baboul; L. A. Curtiss; P. C. Redfern; K. Raghavachari, *Gaussian-3 theory using density functional geometries and zero-point energies*, The Journal of chemical physics 110 (16) (1999) 7650

306. A. Hoffmann; M. Klatt; H. G. Wagner, *An Investigation of the Reaction between O (3P) and Toluene at High Temperatures*, Zeitschrift für Physikalische Chemie 168 (Part_1) (1990) 1-12

307. R. Eng; C. Fittschen; A. Gebert; P. Hibomvschi; H. Hippler; A.-N. Unterreiner in: *Kinetic investigations of the reactions of toluene and of p-xylene with molecular oxygen between 1050 and 1400 K*, Symposium (International) on Combustion, 1998; Elsevier: 1998; pp 211-218.

308. M. A. Oehlschlaeger; D. F. Davidson; R. K. Hanson, *Investigation of the reaction of toluene with molecular oxygen in shock-heated gases*, Combustion and flame 147 (3) (2006) 195-208

309. S.-H. Li; J. Guo; R. Li; F. Wang; X.-Y. Li, *Theoretical Prediction of Rate Constants for Hydrogen Abstraction by OH, H, O, CH3 and HO2 Radicals from Toluene*, The Journal of Physical Chemistry A (2016)

310. H.-J. Werner; F. R. Manby; P. J. Knowles, *Fast linear scaling second-order Møller-Plesset perturbation theory (MP2) using local and density fitting approximations*, The Journal of chemical physics 118 (18) (2003) 8149-8160

311. H.-P. S. Shen; J. Vanderover; M. A. Oehlschlaeger, *A shock tube study of the auto-ignition of toluene/air mixtures at high pressures*, Proceedings of the Combustion Institute 32 (1) (2009) 165-172

312. D. Baulch; C. Cobos; R. Cox; P. Frank; G. Hayman; T. Just; J. Kerr; T. Murrells; M. Pilling; J. Troe, *Evaluated kinetic data for combustion modeling. Supplement I*, Journal of Physical and Chemical Reference Data 23 (6) (1994) 847-848

313. M. Altarawneh; A. A. H. Al-Muhtaseb; B. Z. Dlugogorski; E. M. Kennedy; J. C. Mackie, *Rate constants for hydrogen abstraction reactions by the hydroperoxyl radical from methanol, ethenol, acetaldehyde, toluene, and phenol*, Journal of computational chemistry 32 (8) (2011) 1725-1733

314. Y. Zhao; B. J. Lynch; D. G. Truhlar, *Development and assessment of a new hybrid density functional model for thermochemical kinetics*, The Journal of Physical Chemistry A 108 (14) (2004) 2715-2719

315. J. Zádor; S. J. Klippenstein; J. A. Miller, *Pressure-Dependent OH Yields in Alkene+ HO2 Reactions: A Theoretical Study*, The Journal of Physical Chemistry A 115 (36) (2011) 10218-10225

316. S. J. Klippenstein; J. A. Miller, *From the time-dependent, multiple-well master equation to phenomenological rate coefficients*, The Journal of Physical Chemistry A 106 (40) (2002) 9267-9277

317. J. A. Miller; S. J. Klippenstein, *Master equation methods in gas phase chemical kinetics*, The Journal of Physical Chemistry A 110 (36) (2006) 10528-10544

318. K. Narayanaswamy; G. Blanquart; H. Pitsch, *A consistent chemical mechanism for oxidation of substituted aromatic species*, Combustion and Flame 157 (10) (2010) 1879-1898

319. Y. Li; C.-W. Zhou; K. P. Somers; K. Zhang; H. J. Curran, *The oxidation of 2-butene: a high pressure ignition delay, kinetic modeling study and reactivity comparison with isobutene and 1-butene*, Proceedings of the Combustion Institute (2016)

320. C.-W. Zhou; Y. Li; E. O'Connor; K. P. Somers; S. Thion; C. Keesee; O. Mathieu; E. L. Petersen; T. A. DeVerter; M. A. Oehlschlaeger, *A comprehensive experimental and modeling study of isobutene oxidation*, Combustion and Flame 167 (2016) 353-379

321. C. K. Westbrook; W. J. Pitz; M. Mehl; P.-A. Glaude; O. Herbinet; S. Bax; F. Battin-Leclerc; O. Mathieu; E. L. Petersen; J. Bugler, *Experimental and kinetic modeling study of 2-methyl-2-butene: allylic hydrocarbon kinetics*, The Journal of Physical Chemistry A 119 (28) (2015) 7462-7480

322. X. Fan; G. Wang; Y. Li; Z. Wang; W. Yuan; L. Zhao, *Experimental and kinetic modeling study of 1-hexene combustion at various pressures*, Combustion and Flame 173 (2016) 151-160

323. M. K. Altarawneh; B. Z. Dlugogorski; E. M. Kennedy; J. C. Mackie, *Rate constants for reactions of ethylbenzene with hydroperoxyl radical*, Combustion and Flame 160 (1) (2013) 9-16

324. T. Ingham; R. Walker; R. Woolford in: *Kinetic parameters for the initiation reaction RH+ O 2→ R+ HO 2*, Symposium (International) on Combustion, 1994; Elsevier: 1994; pp 767-774.

325. C.-J. Chen; J. W. Bozzelli, *Thermochemical property, pathway and kinetic analysis on the reactions of allylic isobutenyl radical with O2: an elementary reaction mechanism for isobutene oxidation*, The Journal of Physical Chemistry A 104 (43) (2000) 9715-9732

326. Y. Murakami; T. Oguchi; K. Hashimoto; Y. Nosaka, *Theoretical study of the benzyl+ O2 reaction: kinetics, mechanism, and product branching ratios*, The Journal of Physical Chemistry A 111 (50) (2007) 13200-13208

327. P. Clothier; D. Shen; H. Pritchard, *Stimulation of diesel-fuel ignition by benzyl radicals*, Combustion and flame 101 (3) (1995) 383-386

328. S. Canneaux; F. Louis; M. Ribaucour; R. Minetti; A. El Bakali; J.-F. Pauwels, *A theoretical study of the kinetics of the benzylperoxy radical isomerization*, The Journal of Physical Chemistry A 112 (26) (2008) 6045-6052

329. C. Ellis; M. S. Scott; R. W. Walker, *Addition of toluene and ethylbenzene to mixtures of H 2 and O 2 at 772 K: Part 2: formation of products and determination of kinetic data for H+ additive and for other elementary reactions involved*, Combustion and flame 132 (3) (2003) 291-304

330. G. Knizia; T. B. Adler; H.-J. Werner, *Simplified CCSD (T)-F12 methods: Theory and benchmarks*, The Journal of Chemical Physics 130 (5) (2009) 054104

331. T. B. Adler; G. Knizia; H.-J. Werner, *A simple and efficient CCSD (T)-F12 approximation*, Journal of Chemical Physics 127 (22) (2007) 221106-224100

332. F. R. Manby; H.-J. Werner; T. B. Adler; A. J. May, *Explicitly correlated local second-order perturbation theory with a frozen geminal correlation factor*, The Journal of chemical physics 124 (9) (2006) 094103

333. F. Zhang; A. Nicolle; L. Xing; S. J. Klippenstein, *Recombination of aromatic radicals with molecular oxygen*, Proceedings of the Combustion Institute (2016)

334. L. Elmaimouni; R. Minetti; J. Sawerysyn; P. Devolder, *Kinetics and thermochemistry of the reaction of benzyl radical with O2: Investigations by discharge flow/laser induced fluorescence between 393 and 433 K*, International journal of chemical kinetics 25 (5) (1993) 399-413

335. F. F. Fenter; B. Nozière; F. Caralp; R. Lesclaux, *Study of the kinetics and equilibrium of the benzyl-radical association reaction with molecular oxygen*, International journal of chemical kinetics 26 (1) (1994) 171-189

336. J. Finley; P.-Å. Malmqvist; B. O. Roos; L. Serrano-Andrés, *The multi-state CASPT2 method*, Chemical physics letters 288 (2) (1998) 299-306

337. K. Hoyermann; J. Seeba in: *A direct study of the reaction of benzyl radicals with molecular oxygen: Kinetics and thermochemistry*, Symposium (International) on Combustion, 1994; Elsevier: 1994; pp 851-858.

338. H. Nelson; J. McDonald, *Reaction of the benzyl radical with oxygen and chlorine*, The Journal of Physical Chemistry 86 (8) (1982) 1242-1244

339. K. Pamidimukkala; R. Kern; M. Patel; H. Wei; J. Kiefer, *High-temperature pyrolysis of toluene*, Journal of Physical Chemistry 91 (8) (1987) 2148-2154

340. M. Braun-Unkhoff; P. Frank; T. Just in: *A shock tube study on the thermal decomposition of toluene and of the phenyl radical at high temperatures*, Symposium (International) on Combustion, 1989; Elsevier: 1989; pp 1053-1061.

341. R. A. Eng; A. Gebert; E. Goos; H. Hippler; C. Kachiani, *Incubation times, fall-off and branching ratios in the thermal decomposition of toluene: Experiments and theory*, Physical Chemistry Chemical Physics 4 (16) (2002) 3989-3996

342. M. Colket; D. Seery in: *Reaction mechanisms for toluene pyrolysis*, Symposium (International) on Combustion, 1994; Elsevier: 1994; pp 883-891.

343. R. Sivaramakrishnan; R. S. Tranter; K. Brezinsky, *High pressure pyrolysis of toluene. 2. Modeling benzyl decomposition and formation of soot precursors*, The Journal of Physical Chemistry A 110 (30) (2006) 9400-9404

344.   S. D. Klotz; K. Brezinsky; I. Glassman in: *Modeling the combustion of toluene-butane blends*, Symposium (International) on Combustion, 1998; Elsevier: 1998; pp 337-344.

345.   R. Bounaceur; I. Da Costa; R. Fournet; F. Billaud; F. Battin-Leclerc, *Experimental and modeling study of the oxidation of toluene*, International journal of chemical kinetics 37 (1) (2005) 25-49

346.   P. Dagaut; G. Pengloan; A. Ristori, *Oxidation, ignition and combustion of toluene: Experimental and detailed chemical kinetic modeling*, Physical Chemistry Chemical Physics 4 (10) (2002) 1846-1854

347.   C. Ji; E. Dames; H. Wang; F. N. Egolfopoulos, *Propagation and extinction of benzene and alkylated benzene flames*, Combustion and Flame 159 (3) (2012) 1070-1081

348.   T. Hirasawa; C. Sung; A. Joshi; Z. Yang; H. Wang; C. Law, *Determination of laminar flame speeds using digital particle image velocimetry: binary fuel blends of ethylene, n-butane, and toluene*, Proceedings of the Combustion Institute 29 (2) (2002) 1427-1434

349.   X. Hui; A. K. Das; K. Kumar; C.-J. Sung; S. Dooley; F. L. Dryer, *Laminar flame speeds and extinction stretch rates of selected aromatic hydrocarbons*, Fuel 97 (2012) 695-702

350.   L. Sileghem; V. Alekseev; J. Vancoillie; K. Van Geem; E. Nilsson; S. Verhelst; A. Konnov, *Laminar burning velocity of gasoline and the gasoline surrogate components iso-octane, n-heptane and toluene*, Fuel 112 (2013) 355-365

351.   R. Johnston; J. Farrell, *Laminar burning velocities and Markstein lengths of aromatics at elevated temperature and pressure*, Proceedings of the combustion institute 30 (1) (2005) 217-224

352.   A. Burcat; C. Snyder; T. Brabbs, *Ignition delay times of benzene and toluene with oxygen in argon mixtures*,   (1985)

353.   V. Vasudevan; D. Davidson; R. Hanson, *Shock tube measurements of toluene ignition times and OH concentration time histories*, Proceedings of the Combustion Institute 30 (1) (2005) 1155-1163

354.   D. Davidson; B. Gauthier; R. Hanson, *Shock tube ignition measurements of iso-octane/air and toluene/air at high pressures*, Proceedings of the Combustion Institute 30 (1) (2005) 1175-1182

355.   R. Sivaramakrishnan; R. Tranter; K. Brezinsky, *High-pressure, high-temperature oxidation of toluene*, Combustion and flame 139 (4) (2004) 340-350

356.   G. Mittal; C.-J. Sung, *Autoignition of toluene and benzene at elevated pressures in a rapid compression machine*, Combustion and Flame 150 (4) (2007) 355-368

357.   C. Cavallotti; M. Derudi; R. Rota, *On the mechanism of decomposition of the benzyl radical*, Proceedings of the Combustion Institute 32 (1) (2009) 115-121

358.   D. Polino; C. Cavallotti, *Fulvenallene decomposition kinetics*, The Journal of Physical Chemistry A 115 (37) (2011) 10281-10289

359.   M. Derudi; D. Polino; C. Cavallotti, *Toluene and benzyl decomposition mechanisms: elementary reactions and kinetic simulations*, Physical Chemistry Chemical Physics 13 (48) (2011) 21308-21318

360.   S. J. Klippenstein; L. B. Harding; Y. Georgievskii, *On the formation and decomposition of C 7 H 8*, Proceedings of the Combustion Institute 31 (1) (2007) 221-229

361.   F. Battin-Leclerc, in: 2016.

362.   A. Rodriguez; O. Herbinet; F. Battin-Leclerc, *A study of the low-temperature oxidation of a long chain aldehyde: n-hexanal*, Proceedings of the Combustion Institute   (2016)

363.   Q. Li; E. Hu; X. Zhang; Y. Cheng; Z. Huang, *Laminar flame speeds and flame instabilities of pentanol isomer–air mixtures at elevated temperatures and pressures*, Energy & Fuels 27 (2) (2013) 1141-1150

364.   C. Togbé; F. Halter; F. Foucher; C. Mounaim-Rousselle; P. Dagaut, *Experimental and detailed kinetic modeling study of 1-pentanol oxidation in a JSR and combustion in a bomb*, Proceedings of the Combustion Institute 33 (1) (2011) 367-374

365.   K. A. Heufer; S. M. Sarathy; H. J. Curran; A. C. Davis; C. K. Westbrook; W. J. Pitz, *Detailed kinetic modeling study of n-pentanol oxidation*, Energy & Fuels 26 (11) (2012) 6678-6685

366.   G. Dayma; C. Togbé; P. Dagaut, *Experimental and detailed kinetic modeling study of isoamyl alcohol (isopentanol) oxidation in a jet-stirred reactor at elevated pressure*, Energy Fuels 25 (11) (2011) 4986-4998

367.   S. M. Sarathy; S. Park; B. W. Weber; W. Wang; P. S. Veloo; A. C. Davis; C. Togbe; C. K. Westbrook; O. Park; G. Dayma, *A comprehensive experimental and modeling study of iso-pentanol combustion*, Combustion and flame 160 (12) (2013) 2712-2728

368.   A. Frassoldati; A. Cuoci; T. Faravelli; E. Ranzi, *Kinetic modeling of the oxidation of ethanol and gasoline surrogate mixtures*, Combustion Science and Technology 182 (4-6) (2010) 653-667

369.   R. Grana; A. Frassoldati; T. Faravelli; U. Niemann; E. Ranzi; R. Seiser; R. Cattolica; K. Seshadri, *An experimental and kinetic modeling study of combustion of isomers of butanol*, Combustion and Flame 157 (11) (2010) 2137-2154

370.   A. Frassoldati; R. Grana; T. Faravelli; E. Ranzi; P. Oßwald; K. Kohse-Höinghaus, *Detailed kinetic modeling of the combustion of the four butanol isomers in premixed low-pressure flames*, Combustion and Flame 159 (7) (2012) 2295-2311

371.   L. Zhao; L. Ye; F. Zhang; L. Zhang, *Thermal decomposition of 1-pentanol and its isomers: A theoretical study*, The Journal of Physical Chemistry A 116 (37) (2012) 9238-9244

372.   L. B. Harding; Y. Georgievskii; S. J. Klippenstein, *Predictive theory for hydrogen atom-hydrocarbon radical association kinetics*, The Journal of Physical Chemistry A 109 (21) (2005) 4646-4656

373.   J. Moc; J. M. Simmie; H. J. Curran, *The elimination of water from a conformationally complex alcohol: A computational study of the gas phase dehydration of n-butanol*, Journal of Molecular Structure 928 (1) (2009) 149-157

374.   S. Mani Sarathy; S. Park; B. W. Weber; W. Wang; P. S. Veloo; A. C. Davis; C. Togbe; C. K. Westbrook; O. Park; G. Dayma; Z. Luo; M. A. Oehlschlaeger; F. N. Egolfopoulos; T. Lu; W. J. Pitz; C.-J. Sung; P. Dagaut, *A comprehensive experimental and modeling study of iso-pentanol combustion*, Combustion and Flame 160 (12) (2013) 2712-2728 http://dx.doi.org/10.1016/j.combustflame.2013.06.022.

375.   C. Tang; L. Wei; X. Man; J. Zhang; Z. Huang; C. K. Law, *High temperature ignition delay times of C5 primary alcohols*, Combustion and Flame 160 (3) (2013) 520-529

376.   J. Zádor; R. X. Fernandes; Y. Georgievskii; G. Meloni; C. A. Taatjes; J. A. Miller, *The reaction of hydroxyethyl radicals with O 2: A theoretical analysis and experimental product study*, Proceedings of the Combustion Institute 32 (1) (2009) 271-277

377.   G. da Silva; J. W. Bozzelli; L. Liang; J. T. Farrell, *Ethanol oxidation: Kinetics of the α-hydroxyethyl radical+ O2 reaction*, The Journal of Physical Chemistry A 113 (31) (2009) 8923-8933

378.   B. W. Weber; K. Kumar; Y. Zhang; C.-J. Sung, *Autoignition of n-butanol at elevated pressure and low-to-intermediate temperature*, Combustion and Flame 158 (5) (2011) 809-819

379.   P. Dagaut; S. Sarathy; M. Thomson, *A chemical kinetic study of n-butanol oxidation at elevated pressure in a jet stirred reactor*, Proceedings of the combustion Institute 32 (1) (2009) 229-237

380.   K. Heufer; R. Fernandes; H. Olivier; J. Beeckmann; O. Röhl; N. Peters, *Shock tube investigations of ignition delays of n-butanol at elevated pressures between 770 and 1250K*, Proceedings of the Combustion Institute 33 (1) (2011) 359-366

381.   S. Vranckx; K. Heufer; C. Lee; H. Olivier; L. Schill; W. Kopp; K. Leonhard; C. Taatjes; R. Fernandes, *Role of peroxy chemistry in the high-pressure ignition of n-butanol–Experiments and detailed kinetic modelling*, combustion and flame 158 (8) (2011) 1444-1455

382.   K. Heufer; J. Bugler; H. Curran, *A comparison of longer alkane and alcohol ignition including new experimental results for n-pentanol and n-hexanol*, Proceedings of the Combustion Institute 34 (1) (2013) 511-518

383.   C. Togbé; A. Mzé-Ahmed; P. Dagaut, *Kinetics of oxidation of 2-butanol and isobutanol in a jet-stirred reactor: experimental study and modeling investigation*, Energy & Fuels 24 (9) (2010) 5244-5256

384.   C. Togbe; P. Dagaut; A. Mzé-Ahmed; P. Diévart; F. Halter; F. Foucher, *Experimental and detailed kinetic modeling study of 1-hexanol oxidation in a pressurized jet-stirred reactor and a combustion bomb*, Energy & Fuels 24 (11) (2010) 5859-5875

385.   L. Cai; Y. Uygun; C. Togbé; H. Pitsch; H. Olivier; P. Dagaut; S. M. Sarathy, *An experimental and modeling study of n-octanol combustion*, Proceedings of the Combustion Institute 35 (1) (2015) 419-427

386.   D. Grosjean, *Formaldehyde and other carbonyls in Los Angeles ambient air*, Environmental Science & Technology 16 (5) (1982) 254-262

387.   C. Togbé; P. Dagaut; F. Halter; F. Foucher, *2-Propanol Oxidation in a Pressurized Jet-Stirred Reactor (JSR) and Combustion Bomb: Experimental and Detailed Kinetic Modeling Study*, Energy & Fuels 25 (2) (2011) 676-683 10.1021/ef101485q.

388. B. Galmiche; C. Togbé; P. Dagaut; F. Halter; F. Foucher, *Experimental and Detailed Kinetic Modeling Study of the Oxidation of 1-Propanol in a Pressurized Jet-Stirred Reactor (JSR) and a Combustion Bomb*, Energy & Fuels 25 (5) (2011) 2013-2021 10.1021/ef2003552.

389. K. Yasunaga; T. Mikajiri; S. M. Sarathy; T. Koike; F. Gillespie; T. Nagy; J. M. Simmie; H. J. Curran, *A shock tube and chemical kinetic modeling study of the pyrolysis and oxidation of butanols*, Combustion and Flame 159 (6) (2012) 2009-2027 http://dx.doi.org/10.1016/j.combustflame.2012.02.008.

390. G. Black; H. J. Curran; S. Pichon; J. M. Simmie; V. Zhukov, *Bio-butanol: Combustion properties and detailed chemical kinetic model*, Combustion and Flame 157 (2) (2010) 363-373 http://dx.doi.org/10.1016/j.combustflame.2009.07.007.

391. S. M. Sarathy; M. J. Thomson; C. Togbé; P. Dagaut; F. Halter; C. Mounaim-Rousselle, *An experimental and kinetic modeling study of n-butanol combustion*, Combustion and Flame 156 (4) (2009) 852-864 http://dx.doi.org/10.1016/j.combustflame.2008.11.019.

392. S. M. Sarathy; S. Vranckx; K. Yasunaga; M. Mehl; P. Oßwald; W. K. Metcalfe; C. K. Westbrook; W. J. Pitz; K. Kohse-Höinghaus; R. X. Fernandes; H. J. Curran, *A comprehensive chemical kinetic combustion model for the four butanol isomers*, Combustion and Flame 159 (6) (2012) 2028-2055 http://dx.doi.org/10.1016/j.combustflame.2011.12.017.

393. S. S. Vasu; S. M. Sarathy, *On the High-Temperature Combustion of n-Butanol: Shock Tube Data and an Improved Kinetic Model*, Energy & Fuels 27 (11) (2013) 7072-7080 10.1021/ef401406z.

394. P.-J. He; J.-F. Tang; N. Yang; J.-J. Fang; X. He; L.-M. Shao, *The emission patterns of volatile organic compounds during aerobic biotreatment of municipal solid waste using continuous and intermittent aeration*, Journal of the Air & Waste Management Association 62 (4) (2012) 461-470 10.1080/10962247.2012.658954.

395. D. Grosjean; E. Grosjean; A. W. Gertler, *On-Road Emissions of Carbonyls from Light-Duty and Heavy-Duty Vehicles*, Environmental Science & Technology 35 (1) (2000) 45-53 10.1021/es001326a.

396. E. Zervas, *Regulated and non-regulated pollutants emitted from two aliphatic and a commercial diesel fuel*, Fuel 87 (7) (2008) 1141-1147 http://dx.doi.org/10.1016/j.fuel.2007.06.010.

397. G. Karavalakis; S. Poulopoulos; E. Zervas, *Impact of diesel fuels on the emissions of non-regulated pollutants*, Fuel 102 (0) (2012) 85-91 http://dx.doi.org/10.1016/j.fuel.2012.05.030.

398. R. d. Abrantes; J. V. d. Assunção; E. Y. Hirai, *Caracterização das emissões de aldeídos de veículos do ciclo diesel*, Revista de Saúde Pública 39 (2005) 479-485

399. M. M. Roy, *HPLC analysis of aldehydes in automobile exhaust gas: Comparison of exhaust odor and irritation in different types of gasoline and diesel engines*, Energy Conversion and Management 49 (5) (2008) 1111-1118 http://dx.doi.org/10.1016/j.enconman.2007.09.014.

400. J. J. Schauer; M. J. Kleeman; G. R. Cass; B. R. T. Simoneit, *Measurement of Emissions from Air Pollution Sources. 5. C1−C32 Organic Compounds from Gasoline-Powered Motor Vehicles*, Environmental Science & Technology 36 (6) (2002) 1169-1180 10.1021/es0108077.

401. S. G. Poulopoulos; D. P. Samaras; C. J. Philippopoulos, *Regulated and unregulated emissions from an internal combustion engine operating on ethanol-containing fuels*, Atmospheric Environment 35 (26) (2001) 4399-4406 http://dx.doi.org/10.1016/S1352-2310(01)00248-5.

402. B.-Q. He; S.-J. Shuai; J.-X. Wang; H. He, *The effect of ethanol blended diesel fuels on emissions from a diesel engine*, Atmospheric Environment 37 (35) (2003) 4965-4971 http://dx.doi.org/10.1016/j.atmosenv.2003.08.029.

403. S. Machado Corrêa; G. Arbilla, *Carbonyl emissions in diesel and biodiesel exhaust*, Atmospheric Environment 42 (4) (2008) 769-775 http://dx.doi.org/10.1016/j.atmosenv.2007.09.073.

404. T. M. Cahill; R. A. Okamoto, *Emissions of Acrolein and Other Aldehydes from Biodiesel-Fueled Heavy-Duty Vehicles*, Environmental Science & Technology 46 (15) (2012) 8382-8388 10.1021/es301659u.

405. R. Ballesteros; J. J. Hernández; J. Guillén-Flores, *Carbonyls speciation in a typical European automotive diesel engine using bioethanol/butanol–diesel blends*, Fuel 95 (0) (2012) 136-145 http://dx.doi.org/10.1016/j.fuel.2011.09.012.

406. E. Ranzi; M. Corbetta; F. Manenti; S. Pierucci, *Kinetic modeling of the thermal degradation and combustion of biomass*, Chemical Engineering Science (0)) http://dx.doi.org/10.1016/j.ces.2013.08.014.

407.   A. M. Dean; R. L. Johnson; D. C. Steiner, *Shock-tube studies of formaldehyde oxidation*, Combustion and Flame 37 (0) (1980) 41-62 http://dx.doi.org/10.1016/0010-2180(80)90070-X.

408.   S. Hochgreb; F. L. Dryer, *A comprehensive study on CH2O oxidation kinetics*, Combustion and Flame 91 (3–4) (1992) 257-284 http://dx.doi.org/10.1016/0010-2180(92)90058-W.

409.   Y. Román-Leshkov; C. J. Barrett; Z. Y. Liu; J. A. Dumesic, *Production of dimethylfuran for liquid fuels from biomass-derived carbohydrates*, Nature 447 (7147) (2007) 982-985

410.   G. Friedrichs; D. F. Davidson; R. K. Hanson, *Direct measurements of the reaction H + CH2O → H2 + HCO behind shock waves by means of Vis–UV detection of formaldehyde*, International Journal of Chemical Kinetics 34 (6) (2002) 374-386 10.1002/kin.10059.

411.   B. Eiteneer; C. L. Yu; M. Goldenberg; M. Frenklach, *Determination of Rate Coefficients for Reactions of Formaldehyde Pyrolysis and Oxidation in the Gas Phase*, The Journal of Physical Chemistry A 102 (27) (1998) 5196-5205 10.1021/jp981184v.

412.   Y. Hidaka; T. Taniguchi; H. Tanaka; T. Kamesawa; K. Inami; H. Kawano, *Shock-tube study of CH2O pyrolysis and oxidation*, Combustion and Flame 92 (4) (1993) 365-376 http://dx.doi.org/10.1016/0010-2180(93)90149-W.

413.   P. Glarborg; M. U. Alzueta; K. Kjærgaard; K. Dam-Johansen, *Oxidation of formaldehyde and its interaction with nitric oxide in a flow reactor*, Combustion and Flame 132 (4) (2003) 629-638 http://dx.doi.org/10.1016/S0010-2180(02)00535-7.

414.   Y. Hidaka; T. Taniguchi; T. Kamesawa; H. Masaoka; K. Inami; H. Kawano, *High temperature pyrolysis of formaldehyde in shock waves*, International Journal of Chemical Kinetics 25 (4) (1993) 305-322

415.   A. M. Dean; R. L. Johnson; D. C. Steiner, *Shock-tube studies of formaldehyde oxidation*, Combustion and Flame 37 (1980) 41-62

416.   J. Li; Z. Zhao; A. Kazakov; M. Chaos; F. L. Dryer; J. J. Scire, *A comprehensive kinetic mechanism for CO, CH2O, and CH3OH combustion*, International Journal of Chemical Kinetics 39 (3) (2007) 109-136 10.1002/kin.20218.

417.   M. P. Halstead; A. Prothero; C. P. Quinn, *A Mathematical Model of the Cool-Flame Oxidation of Acetaldehyde*, Proceedings of the Royal Society of London. A. Mathematical and Physical Sciences 322 (1550) (1971) 377-403 10.1098/rspa.1971.0074.

418.   P. Gray; J. F. Griffiths; S. M. Hasko; P.-G. Lignola, *Oscillatory Ignitions and Cool Flames Accompanying the Non-Isothermal Oxidation of Acetaldehyde in a Well Stirred, Flow Reactor*, Proceedings of the Royal Society of London. A. Mathematical and Physical Sciences 374 (1758) (1981) 313-339 10.1098/rspa.1981.0025.

419.   J. Cavanagh; R. A. Cox; G. Olson, *Computer modeling of cool flames and ignition of acetaldehyde*, Combustion and Flame 82 (1) (1990) 15-39 http://dx.doi.org/10.1016/0010-2180(90)90075-3.

420.   F. P. Di Maio; P. G. Lignola; P. Talarico, *Thermokinetic Oscillations in Acetaldehyde CSTR Combustion*, Combustion Science and Technology 91 (1-3) (1993) 119-142 10.1080/00102209308907636.

421.   E. W. Kaiser; C. K. Westbrook; W. J. Pitz, *Acetaldehyde oxidation in the negative temperature coefficient regime: Experimental and modeling results*, International Journal of Chemical Kinetics 18 (6) (1986) 655-688 10.1002/kin.550180606.

422.   P. Dagaut; M. Reuillon; D. Voisin; M. Cathonnet; M. McGuinness; J. M. Simmie, *Acetaldehyde Oxidation in a JSR and Ignition in Shock Waves: Experimental and Comprehensive Kinetic Modeling*, Combustion Science and Technology 107 (4-6) (1995) 301-316 10.1080/00102209508907809.

423.   Y. Hidaka; S. Kubo; T. Hoshikawa; H. Wakamatsu, in: Shock Waves, Z. Jiang, (Ed.) Springer Berlin Heidelberg: 2005; pp 603-608.

424.   K. Yasunaga; S. Kubo; H. Hoshikawa; T. Kamesawa; Y. Hidaka, *Shock-tube and modeling study of acetaldehyde pyrolysis and oxidation*, International Journal of Chemical Kinetics 40 (2) (2008) 73-102 10.1002/kin.20294.

425.   G. da Silva; J. W. Bozzelli, *Enthalpies of Formation, Bond Dissociation Energies, and Molecular Structures of the n-Aldehydes (Acetaldehyde, Propanal, Butanal, Pentanal, Hexanal, and Heptanal) and Their Radicals*, The Journal of Physical Chemistry A 110 (48) (2006) 13058-13067 10.1021/jp063772b.

426.   E. W. Kaiser, *A modeling study of the oxidation of propionaldehyde in the negative temperature coefficient regime*, International Journal of Chemical Kinetics 19 (5) (1987) 457-486 10.1002/kin.550190506.

427.   A. Lifshitz; C. Tamburu; A. Suslensky, *Decomposition of propanal at elevated temperatures: experimental and modeling study*, The Journal of Physical Chemistry 94 (7) (1990) 2966-2972 10.1021/j100370a043.

428.   T. Kasper; U. Struckmeier; P. Oßwald; K. Kohse-Höinghaus, *Structure of a stoichiometric propanal flame at low pressure*, Proceedings of the Combustion Institute 32 (1) (2009) 1285-1292 http://dx.doi.org/10.1016/j.proci.2008.06.040.

429.   B. Akih-Kumgeh; J. M. Bergthorson, *Ignition of C3 oxygenated hydrocarbons and chemical kinetic modeling of propanal oxidation*, Combustion and Flame 158 (10) (2011) 1877-1889 http://dx.doi.org/10.1016/j.combustflame.2011.02.015.

430.   P. S. Veloo; P. Dagaut; C. Togbe; G. Dayma; S. M. Sarathy; C. K. Westbrook; F. N. Egolfopoulos, *Jet-stirred reactor and flame studies of propanal oxidation*, Proceedings of the Combustion Institute 34 (1) (2013) 599-606 http://dx.doi.org/10.1016/j.proci.2012.06.138.

431.   P. S. Veloo; P. Dagaut; C. Togbé; G. Dayma; S. M. Sarathy; C. K. Westbrook; F. N. Egolfopoulos, *Experimental and modeling study of the oxidation of n- and iso-butanal*, Combustion and Flame 160 (9) (2013) 1609-1626 http://dx.doi.org/10.1016/j.combustflame.2013.03.018.

432.   D. Davidson; S. Ranganath; K.-Y. Lam; M. Liaw; Z. Hong, *Ignition delay time measurements of normal alkanes and simple oxygenates*, Journal of Propulsion and Power 26 (2) (2010) 280-287

433.   S. Dooley; H. J. Curran; J. M. Simmie, *Autoignition measurements and a validated kinetic model for the biodiesel surrogate, methyl butanoate*, Combustion and Flame 153 (1–2) (2008) 2-32 http://dx.doi.org/10.1016/j.combustflame.2008.01.005.

434.   J. Zhang; L. Pan; J. Mo; J. Gong; Z. Huang; C. K. Law, *A shock tube and kinetic modeling study of n-butanal oxidation*, Combustion and Flame 160 (9) (2013) 1541-1549 http://dx.doi.org/10.1016/j.combustflame.2013.04.002.

435.   J. Zhang; L. Pan; Z. Zhang; J. Mo; Z. Huang, *Shock Tube and Kinetic Modeling Study of Isobutanal Oxidation*, Energy & Fuels 27 (5) (2013) 2804-2810 10.1021/ef302164n.

436.   D. Healy; N. Donato; C. Aul; E. Petersen; C. Zinner; G. Bourque; H. Curran, *< i> n</i>-Butane: Ignition delay measurements at high pressure and detailed chemical kinetic simulations*, Combustion and Flame 157 (8) (2010) 1526-1539

437.   D. Healy; D. M. Kalitan; C. J. Aul; E. L. Petersen; G. Bourque; H. J. Curran, *Oxidation of C1–C5 Alkane Quinternary Natural Gas Mixtures at High Pressures*, Energy & Fuels 24 (3) (2010) 1521-1528 10.1021/ef9011005.

438.   D. Healy; M. M. Kopp; N. L. Polley; E. L. Petersen; G. Bourque; H. J. Curran, *Methane/n-Butane Ignition Delay Measurements at High Pressure and Detailed Chemical Kinetic Simulations*, Energy & Fuels 24 (3) (2010) 1617-1627 10.1021/ef901292j.

439.   S. Burke. Development of a Chemical Kinetic Mechanism for Small Hydrocarbons. Ph.D. Thesis, National University of Ireland Galway, 2013.

440.   W. K. Metcalfe; S. M. Burke; S. S. Ahmed; H. J. Curran, *A Hierarchical and Comparative Kinetic Modeling Study of C1 – C2 Hydrocarbon and Oxygenated Fuels*, International Journal of Chemical Kinetics 45 (10) (2013) 638-675 10.1002/kin.20802.

441.   A. Kéromnès; W. K. Metcalfe; K. A. Heufer; N. Donohoe; A. K. Das; C.-J. Sung; J. Herzler; C. Naumann; P. Griebel; O. Mathieu; M. C. Krejci; E. L. Petersen; W. J. Pitz; H. J. Curran, *An experimental and detailed chemical kinetic modeling study of hydrogen and syngas mixture oxidation at elevated pressures*, Combustion and Flame 160 (6) (2013) 995-1011 http://dx.doi.org/10.1016/j.combustflame.2013.01.001.

442.   E. Ranzi; A. Frassoldati; R. Grana; A. Cuoci; T. Faravelli; A. P. Kelley; C. K. Law, *Hierarchical and comparative kinetic modeling of laminar flame speeds of hydrocarbon and oxygenated fuels*, Progress in Energy and Combustion Science 38 (4) (2012) 468-501 DOI 10.1016/j.pecs.2012.03.004.

443.   A. M. Dean, *Predictions of pressure and temperature effects upon radical addition and recombination reactions*, The Journal of Physical Chemistry 89 (21) (1985) 4600-4608 10.1021/j100267a038.

444.   A. Chang; J. Bozzelli; A. Dean, *Kinetic analysis of complex chemical activation and unimolecular dissociation reactions using QRRK theory and the modified strong collision approximation*, Zeitschrift für Physikalische Chemie 214 (11/2000) (2000) 1533

445.   L. S. Kassel, *Studies in Homogeneous Gas Reactions. I*, The Journal of Physical Chemistry 32 (2) (1928) 225-242

446.   C. Lee; W. Yang; R. Parr, *Phys. Re V. 1988*, B37 785 (1988) 789

447.   J. Zádor; A. W. Jasper; J. A. Miller, *The reaction between propene and hydroxyl*, Physical Chemistry Chemical Physics 11 (46) (2009) 11040-11053

448.   P. Zhang; S. J. Klippenstein; C. K. Law, *Ab Initio Kinetics for the Decomposition of Hydroxybutyl and Butoxy Radicals of n-Butanol*, The Journal of Physical Chemistry A 117 (9) (2013) 1890-1906

449.   D. R. Lide, CRC handbook of chemistry and physics, CRC press, 2004, p.^pp.

450.   J. R. Barker, *Energy transfer in master equation simulations: A new approach*, International Journal of Chemical Kinetics 41 (12) (2009) 748-763

451.   M. A. Oehlschlaeger; D. F. Davidson; R. K. Hanson, *High-temperature ethane and propane decomposition*, Proceedings of the Combustion Institute 30 (1) (2005) 1119-1127

452.   M. A. Oehlschlaeger; D. F. Davidson; R. K. Hanson, *High-temperature thermal decomposition of isobutane and n-butane behind shock waves*, The Journal of Physical Chemistry A 108 (19) (2004) 4247-4253

453.   Z. Serinyel; N. Chaumeix; G. Black; J. Simmie; H. Curran, *Experimental and Chemical Kinetic Modeling Study of 3-Pentanone Oxidation*, The Journal of Physical Chemistry A 114 (46) (2010) 12176-12186

454.   J. P. Orme; H. J. Curran; J. M. Simmie, *Experimental and Modeling Study of Methyl Cyclohexane Pyrolysis and Oxidation*, The Journal of Physical Chemistry A 110 (1) (2005) 114-131 10.1021/jp0543678.

455.   E. Ranzi; A. Sogaro; P. Gaffuri; G. Pennati; C. K. Westbrook; W. J. Pitz, *A new comprehensive reaction mechanism for combustion of hydrocarbon fuels*, Combustion and Flame 99 (2) (1994) 201-211

456.   J. M. Simmie, *Kinetics and Thermochemistry of 2,5-Dimethyltetrahydrofuran and Related Oxolanes: Next Next-Generation Biofuels*, The Journal of Physical Chemistry A 116 (18) (2012) 4528-4538 10.1021/jp301870w.

457.   H. J. Curran, *Rate constant estimation for C1 to C4 alkyl and alkoxyl radical decomposition*, International Journal of Chemical Kinetics 38 (4) (2006) 250-275 10.1002/kin.20153.

458.   L. K. Huynh; A. Violi in: *Ab Initio Study on the Methyl Butanoate Decomposition*, The 2007 Annual Meeting, 2007; 2007.

459.   D. M. Matheu; W. H. Green; J. M. Grenda, *Capturing pressure-dependence in automated mechanism generation: Reactions through cycloalkyl intermediates*, International Journal of Chemical Kinetics 35 (3) (2003) 95-119 10.1002/kin.10106.

460.   M. Dente; G. Bozzano; T. Faravelli; A. Marongiu; S. Pierucci; E. Ranzi, in: Advances in Chemical Engineering, B. M. Guy, (Ed.) Academic Press: 2007; Vol. Volume 32, pp 51-166.

461.   H. J. Curran; P. Gaffuri; W. J. Pitz; C. K. Westbrook, *A Comprehensive Modeling Study of n-Heptane Oxidation*, Combustion and Flame 114 (1,Äì2) (1998) 149-177 http://dx.doi.org/10.1016/S0010-2180(97)00282-4.

462.   K. P. Somers; J. M. Simmie; F. Gillespie; C. Conroy; G. Black; W. K. Metcalfe; F. Battin-Leclerc; P. Dirrenberger; O. Herbinet; P.-A. Glaude, *A comprehensive experimental and detailed chemical kinetic modelling study of 2, 5-dimethylfuran pyrolysis and oxidation*, Combustion and Flame 160 (11) (2013) 2291-2318

463.   C.-W. Zhou; J. M. Simmie; H. J. Curran, *Ab initio and kinetic study of the reaction of ketones with ȮH for T= 500–2000 K. Part I: hydrogen-abstraction from H3CC (O) CH3–x (CH3) x, x= 0↦ 2*, Physical Chemistry Chemical Physics 13 (23) (2011) 11175-11192

464.   J. Mendes; C.-W. Zhou; H. J. Curran, *Theoretical and Kinetic Study of the Reactions of Ketones with HȮ2 Radicals. Part I: Abstraction Reaction Channels*, The Journal of Physical Chemistry A 117 (22) (2013) 4515-4525 10.1021/jp4000413.

465.   S. Wang; D. F. Davidson; R. K. Hanson, *High temperature measurements for the rate constants of C1–C4 aldehydes with OH in a shock tube*, Proceedings of the Combustion Institute (in press) (2014) http://dx.doi.org/10.1016/j.proci.2014.06.112.

466.   R. J. Kee; F. M. Rupley; J. A. Miller, in: Sandia National Labs., Livermore, CA (USA): 1989.

467.   A. Burcat; B. Ruscic; Chemistry; T.-I. I. o. Tech., in: 2005; p Medium: ED.

468.   S. W. Benson, Thermochemical kinetics: methods for the estimation of thermochemical data and rate parameters, Wiley New York, 1976, p.^pp.

469.   C. V. Naik; K. V. Puduppakkam; E. Meeks, *An Improved Core Reaction Mechanism for Saturated C0-C4 Fuels*, Journal of engineering for gas turbines and power 134 (2) (2012)

470.   J. Mendes; C.-W. Zhou; H. J. Curran, *Theoretical Chemical Kinetic Study of the H-Atom Abstraction Reactions from Aldehydes and Acids by Ḣ Atoms and ȮH, HȮ2, and ĊH3 Radicals*, The Journal of Physical Chemistry A 118 (51) (2014) 12089-12104

471.   S. Wang; D. F. Davidson; R. K. Hanson, *High temperature measurements for the rate constants of C 1–C 4 aldehydes with OH in a shock tube*, Proceedings of the Combustion Institute 35 (1) (2015) 473-480

472.   S. Jagiella; H. Libuda; F. Zabel, *Thermal stability of carbonyl radicals Part I. Straight-chain and branched C 4 and C 5 acyl radicals*, Physical Chemistry Chemical Physics 2 (6) (2000) 1175-1181

473.   R. Méreau; M.-T. Rayez; J.-C. Rayez; F. Caralp; R. Lesclaux, *Theoretical study on the atmospheric fate of carbonyl radicals: kinetics of decomposition reactions*, Physical Chemistry Chemical Physics 3 (21) (2001) 4712-4717

474.   A. Tomas; E. Villenave; R. Lesclaux, *Kinetics of the (CH 3) 2 CHCO and (CH 3) 3 CCO radical decomposition: temperature and pressure dependences*, Physical Chemistry Chemical Physics 2 (6) (2000) 1165-1174

475.   E. Kaiser; C. Westbrook; W. Pitz, *Acetaldehyde oxidation in the negative temperature coefficient regime: Experimental and modeling results*, International journal of chemical kinetics 18 (6) (1986) 655-688

476.   J. P. Senosiain; S. J. Klippenstein; J. A. Miller, *Pathways and rate coefficients for the decomposition of vinoxy and acetyl radicals*, The Journal of Physical Chemistry A 110 (17) (2006) 5772-5781

477.   J. Lee; C.-J. Chen; J. W. Bozzelli, *Thermochemical and kinetic analysis of the acetyl radical (CH3CO)+ O2 Reaction System*, The Journal of Physical Chemistry A 106 (31) (2002) 7155-7170

478.   H. Hou; A. Li; H. Hu; Y. Li; H. Li; B. Wang, *Mechanistic and kinetic study of the CH3CO+ O2 reaction*, The Journal of chemical physics 122 (22) (2005) 224304-224304

479.   T. Pokidova; E. Denisov; A. Shestakov, *Kinetic parameters and geometry of the transition state of acyl radical decarbonylation*, Kinetics and Catalysis 50 (5) (2009) 647-655

480.   A. Ajanovic; R. Haas, *Economic challenges for the future relevance of biofuels in transport in EU countries*, Energy 35 (8) (2010) 3340-3348

481.   F. Hoppe; U. Burke; M. Thewes; A. Heufer; F. Kremer; S. Pischinger, *Tailor-Made Fuels from Biomass: Potentials of 2-butanone and 2-methylfuran in direct injection spark ignition engines*, Fuel 167 (2016) 106-117

482.   U. Burke; J. Beeckmann; W. A. Kopp; Y. Uygun; H. Olivier; K. Leonhard; H. Pitsch; K. A. Heufer, *A comprehensive experimental and kinetic modeling study of butanone*, Combustion and Flame 168 (2016) 296-309

483.   A. Demirbas, *Progress and recent trends in biofuels*, Progress in energy and combustion science 33 (1) (2007) 1-18

484.   J. Y. Lai; K. C. Lin; A. Violi, *Biodiesel combustion: advances in chemical kinetic modeling*, Progress in Energy and Combustion Science 37 (1) (2011) 1-14

485.   L. Coniglio; H. Bennadji; P. A. Glaude; O. Herbinet; F. Billaud, *Combustion chemical kinetics of biodiesel and related compounds (methyl and ethyl esters): experiments and modeling–advances and future refinements*, Progress in Energy and Combustion Science 39 (4) (2013) 340-382

486.   H.-H. Carstensen; A. M. Dean, *Rate Constant Rules for the Automated Generation of Gas-Phase Reaction Mechanisms†*, The Journal of Physical Chemistry A 113 (2) (2008) 367-380

487.   A. Sudholt; L. Cai; J. Heyne; F. M. Haas; H. Pitsch; F. L. Dryer, *Ignition characteristics of a bio-derived class of saturated and unsaturated furans for engine applications*, Proceedings of the Combustion Institute 35 (3) (2015) 2957-2965

488.   K. P. Somers; J. M. Simmie; F. Gillespie; U. Burke; J. Connolly; W. K. Metcalfe; F. Battin-Leclerc; P. Dirrenberger; O. Herbinet; P.-A. Glaude, *A high temperature and atmospheric pressure experimental and*

detailed chemical kinetic modelling study of 2-methyl furan oxidation, Proceedings of the Combustion Institute 34 (1) (2013) 225-232

489.   V. B. Oyeyemi; J. A. Keith; E. A. Carter, *Trends in Bond Dissociation Energies of Alcohols and Aldehydes Computed with Multireference Averaged Coupled-Pair Functional Theory*, The Journal of Physical Chemistry A 118 (17) (2014) 3039-3050

490.   V. B. Oyeyemi; J. A. Keith; E. A. Carter, *Accurate bond energies of biodiesel methyl esters from multireference averaged coupled-pair functional calculations*, The Journal of Physical Chemistry A 118 (35) (2014) 7392-7403

491.   V. B. Oyeyemi; D. B. Krisiloff; J. A. Keith; F. Libisch; M. Pavone; E. A. Carter, *Size-extensivity-corrected multireference configuration interaction schemes to accurately predict bond dissociation energies of oxygenated hydrocarbons*, The Journal of chemical physics 140 (4) (2014) 044317

492.   P. J. Linstrom; W. Mallard, *NIST Chemistry webbook; NIST standard reference database No. 69*, (2001)

493.   R. Grana; A. Frassoldati; A. Cuoci; T. Faravelli; E. Ranzi, *A wide range kinetic modeling study of pyrolysis and oxidation of methyl butanoate and methyl decanoate. Note I: Lumped kinetic model of methyl butanoate and small methyl esters*, Energy 43 (1) (2012) 124-139

494.   M. H. Hakka; H. Bennadji; J. Biet; M. Yahyaoui; B. Sirjean; V. Warth; L. Coniglio; O. Herbinet; P.-A. Glaude; F. Billaud, *Oxidation of methyl and ethyl butanoates*, International Journal of Chemical Kinetics 42 (4) (2010) 226-252

495.   J. Mendes; C.-W. Zhou; H. J. Curran, *Theoretical Study of the Rate Constants for the Hydrogen Atom Abstraction Reactions of Esters with• OH Radicals*, The Journal of Physical Chemistry A 118 (27) (2014) 4889-4899

496.   T. Tan; X. Yang; Y. Ju; E. A. Carter, *Ab initio kinetics studies of hydrogen atom abstraction from methyl propanoate*, Physical Chemistry Chemical Physics 18 (6) (2016) 4594-4607

497.   K.-Y. Lam; D. F. Davidson; R. K. Hanson, *High-temperature measurements of the reactions of OH with small methyl esters: methyl formate, methyl acetate, methyl propanoate, and methyl butanoate*, The Journal of Physical Chemistry A 116 (50) (2012) 12229-12241

498.   D. Felsmann; H. Zhao; Q. Wang; I. Graf; T. Tan; X. Yang; E. A. Carter; Y. Ju; K. Kohse-Höinghaus, *Contributions to improving small ester combustion chemistry: Theory, model and experiments*, Proceedings of the Combustion Institute   (2016)

499.   S. Gaïl; M. J. Thomson; S. M. Sarathy; S. A. Syed; P. Dagaut; P. Diévart; A. J. Marchese; F. L. Dryer, *A wide-ranging kinetic modeling study of methyl butanoate combustion*, Proceedings of the Combustion Institute 31 (1) (2007) 305-311

500.   S. Walton; M. Wooldridge; C. Westbrook, *An experimental investigation of structural effects on the auto-ignition properties of two C 5 esters*, Proceedings of the Combustion Institute 32 (1) (2009) 255-262

501.   R. Grana; A. Frassoldati; C. Saggese; T. Faravelli; E. Ranzi, *A wide range kinetic modeling study of pyrolysis and oxidation of methyl butanoate and methyl decanoate–Note II: Lumped kinetic model of decomposition and combustion of methyl esters up to methyl decanoate*, Combustion and Flame 159 (7) (2012) 2280-2294

502.   A. Rodriguez; O. Herbinet; F. Battin-Leclerc; A. Frassoldati; T. Faravelli; E. Ranzi, *Experimental and modeling investigation of the effect of the unsaturation degree on the gas-phase oxidation of fatty acid methyl esters found in biodiesel fuels*, Combustion and Flame 164 (2016) 346-362

503.   H. Minwegen; U. Burke; K. A. Heufer, *An experimental and theoretical comparison of C 3–C 5 linear ketones*, Proceedings of the Combustion Institute   (2016)

504.   K.-Y. Lam; D. F. Davidson; R. K. Hanson, *High-Temperature Measurements of the Reactions of OH with a Series of Ketones: Acetone, 2-Butanone, 3-Pentanone, and 2-Pentanone*, The Journal of Physical Chemistry A 116 (23) (2012) 5549-5559

505.   K.-Y. Lam; W. Ren; S. H. Pyun; A. Farooq; D. F. Davidson; R. K. Hanson, *Multi-species time-history measurements during high-temperature acetone and 2-butanone pyrolysis*, Proceedings of the Combustion Institute 34 (1) (2013) 607-615

506.   J. Badra; A. E. Elwardany; F. Khaled; S. S. Vasu; A. Farooq, *A shock tube and laser absorption study of ignition delay times and OH reaction rates of ketones: 2-Butanone and 3-buten-2-one*, Combustion and Flame 161 (3) (2014) 725-734

507.   Z. Serinyel; G. Black; H. Curran; J. Simmie, *A shock tube and chemical kinetic modeling study of methy ethyl ketone oxidation*, Combustion Science and Technology 182 (4-6) (2010) 574-587

508.   N. Sebbar; J. Bozzelli; H. Bockhorn, *Thermochemistry and Kinetics for 2-Butanone-1-yl Radical (CH2· C (▯ O) CH2CH3) Reactions with O2*, The Journal of Physical Chemistry A 118 (1) (2013) 21-37

509.   J. W. Allen; A. M. Scheer; C. W. Gao; S. S. Merchant; S. S. Vasu; O. Welz; J. D. Savee; D. L. Osborn; C. Lee; S. Vranckx, *A coordinated investigation of the combustion chemistry of diisopropyl ketone, a prototype for biofuels produced by endophytic fungi*, Combustion and Flame 161 (3) (2014) 711-724

510.   K. HadjAli; M. Crochet; G. Vanhove; M. Ribaucour; R. Minetti, *A study of the low temperature autoignition of methyl esters*, Proceedings of the Combustion Institute 32 (1) (2009) 239-246

511.   S. Gaïl; S. Sarathy; M. Thomson; P. Diévart; P. Dagaut, *Experimental and chemical kinetic modeling study of small methyl esters oxidation: Methyl (E)-2-butenoate and methyl butanoate*, Combustion and Flame 155 (4) (2008) 635-650

512.   P. Dagaut; C. Togbé, *Experimental and modeling study of the kinetics of oxidation of butanol– n-heptane mixtures in a jet-stirred reactor*, Energy & Fuels 23 (7) (2009) 3527-3535

513.   K. Moshammer; A. W. Jasper; D. M. Popolan-Vaida; A. Lucassen; P. Diévart; H. Selim; A. J. Eskola; C. A. Taatjes; S. R. Leone; S. M. Sarathy; Y. Ju; P. Dagaut; K. Kohse-Höinghaus; N. Hansen, *Detection and Identification of the Keto-Hydroperoxide (HOOCH2OCHO) and Other Intermediates during Low-Temperature Oxidation of Dimethyl Ether*, The Journal of Physical Chemistry A   (2015)

514.   A. Frassoldati; G. D'Errico; T. Lucchini; A. Stagni; A. Cuoci; T. Faravelli; A. Onorati; E. Ranzi, *Reduced kinetic mechanisms of diesel fuel surrogate for engine CFD simulations*, Combustion and Flame   (2015)

515.   R. Sargent, Chapter IX in Progress in Modelling and Simulation: Verification and validation of simulation Models, London: Academic Press, 1982, p.^pp. 159-169.

516.   A. S. Tomlin, *The use of global uncertainty methods for the evaluation of combustion mechanisms*, Reliability Engineering & System Safety 91 (10) (2006) 1219-1231

517.   J. Zádor; I. G. Zsely; T. Turányi, *Local and global uncertainty analysis of complex chemical kinetic systems*, Reliability Engineering & System Safety 91 (10) (2006) 1232-1240

518.   C. Olm; I. G. Zsély; T. Varga; H. J. Curran; T. Turányi, *Comparison of the performance of several recent syngas combustion mechanisms*, Combustion and Flame 162 (5) (2015) 1793-1812

519.   G. Mittal; C. J. Sung; R. A. Yetter, *Autoignition of H2/CO at elevated pressures in a rapid compression machine*, International Journal of Chemical Kinetics 38 (8) (2006) 516-529

520.   J. O. Ramsay; B. W. Silverman, Functional data analysis, Springer New York, 2005, p.^pp. 81-110.

521.   L. M. Sangalli; P. Secchi; S. Vantini, *Analysis of AneuRisk65 data: $ k $-mean alignment*, Electronic Journal of Statistics 8 (2) (2014) 1891-1904

522.   L. M. Sangalli; P. Secchi; S. Vantini; V. Vitelli, *K-mean alignment for curve clustering*, Computational Statistics & Data Analysis 54 (5) (2010) 1219-1233

523.   T. Varga; T. Nagy; C. Olm; I. G. Zsély; R. Pálvölgyi; É. Valkó; G. Vincze; M. Cserháti; H. Curran; T. Turányi, *Optimization of a hydrogen combustion mechanism using both direct and indirect measurements*, Proceedings of the Combustion Institute 35 (1) (2015) 589-596

524.   F. L. Dryer; F. M. Haas; J. Santner; T. I. Farouk; M. Chaos, *Interpreting chemical kinetics from complex reaction–advection–diffusion systems: Modeling of flow reactors and related experiments*, Progress in Energy and Combustion Science 44 (2014) 19-39

525.   D. G. Goodwin; H. K. Moffat; R. L. Speth, in: *Cantera an object-oriented software toolkit for chemical kinetics, thermodynamics, and transport processes, version 2.1. 1*, Caltech, Pasadena, CA, 2014.

526.   D. Mishra, Experimental Combustion: An Introduction, CRC Press, 2014, p.^pp.

527.   A. Cuoci; A. Frassoldati; T. Faravelli; E. Ranzi, *Formation of soot and nitrogen oxides in unsteady counterflow diffusion flames*, Combustion and Flame 156 (10) (2009) 2010-2022

528.   S. Jerzembeck; N. Peters; P. Pepiot-Desjardins; H. Pitsch, *Laminar burning velocities at high pressure for primary reference fuels and gasoline: Experimental and numerical investigation*, Combustion and Flame 156 (2) (2009) 292-301

529.   A. Kelley; A. Smallbone; D. Zhu; C. Law, *Laminar flame speeds of C 5 to C 8 n-alkanes at elevated pressures: Experimental determination, fuel similarity, and stretch sensitivity*, Proceedings of the Combustion Institute 33 (1) (2011) 963-970

530.   R. Minetti; M. Carlier; M. Ribaucour; E. Therssen; L. Sochet, *A rapid compression machine investigation of oxidation and auto-ignition of n-heptane: measurements and modeling*, Combustion and Flame 102 (3) (1995) 298-309

531.   D. Horning; D. Davidson; R. Hanson, *Study of the high-temperature autoignition of n-alkane/O/Ar mixtures*, Journal of Propulsion and Power 18 (2) (2002) 363-371

532.   J. Herzler; L. Jerig; P. Roth, *Shock tube study of the ignition of lean n-heptane/air mixtures at intermediate temperatures and high pressures*, Proceedings of the Combustion Institute 30 (1) (2005) 1147-1153

533.   P. Veloo; S. Jahangirian; F. Dryer in: *An experimental and kinetic modeling study of the two stage autoignition kinetic behavior of C7, C10, C12, and C14 n-alkanes*, Spring Technical Meeting, Central States Section of the Combustion Institute, 2012; 2012.

534.   S. Davis; C. Law in: *Laminar flame speeds and oxidation kinetics of iso-octane-air and n-heptane-air flames*, Symposium (international) on combustion, 1998; Elsevier: 1998; pp 521-527.

535.   A. El Bakali; J.-L. Delfau; C. Vovelle, *Kinetic modeling of a rich, atmospheric pressure, premixed n-heptane/O 2/N 2 flame*, Combustion and Flame 118 (3) (1999) 381-398

536.   CRECK Modeling Group. http://creckmodeling.chem.polimi.it

537.   A. Stagni; A. Frassoldati; A. Cuoci; T. Faravelli; E. Ranzi, *Skeletal mechanism reduction through species-targeted sensitivity analysis*, Combustion and Flame Submitted (2015)

538.   M. Mehl; W. Pitz; M. Sjöberg; J. E. Dec, in: SAE Technical Paper: 2009.

539.   R. Seiser; H. Pitsch; K. Seshadri; W. Pitz; H. Curran, *Extinction and autoignition of n-heptane in counterflow configuration*, Proceedings of the Combustion Institute 28 (2) (2000) 2029-2037

540.   J. C. Prince; F. A. Williams; G. E. Ovando, *A short mechanism for the low-temperature ignition of n-heptane at high pressures*, Fuel 149 (2015) 138-142

541.   D. Davidson; R. Hanson, *Interpreting shock tube ignition data*, International Journal of Chemical Kinetics 36 (9) (2004) 510-523

542.   M. Chaos; F. L. Dryer, *Chemical-kinetic modeling of ignition delay: Considerations in interpreting shock tube data*, International Journal of Chemical Kinetics 42 (3) (2010) 143-150

543.   G. Mittal; C.-J. Sung, *A rapid compression machine for chemical kinetics studies at elevated pressures and temperatures*, Combustion Science and Technology 179 (3) (2007) 497-530

544.   C. Cavallotti; S. J. Klippenstein; M. Pelucchi; Y. Georgievskii, *From electronic structure to k(T,p): EStoKTP an automatic tool for theoretical rate constant calculation.*, in progress   (2017)

545.   C. Cavallotti, *A systematic approach to investigate potential energy surfaces of reacting systems*, (2016)

546.   P. E. A. Debiagi; G. Gentile; M. Pelucchi; A. Frassoldati; A. Cuoci; T. Faravelli; E. Ranzi, *Detailed kinetic mechanism of gas-phase reactions of volatiles released from biomass pyrolysis*, Biomass and Bioenergy 93 (2016) 60-71

547.   M. Pelucchi; A. Frassoldati; T. Faravelli; B. Ruscic; P. Glarborg, *High-temperature chemistry of HCl and Cl 2*, Combustion and Flame 162 (6) (2015) 2693-2704